ASTROPARTICLE PHYSICS WITH PARTICLE DARK MATTER MODELS, NEUTRINOS AND GRAVITATIONAL WAVES FROM FIRST ORDER ELECTROWEAK PHASE TRANSITION

By

MADHURIMA PANDEY

PHYS05201504019

Saha Institute of Nuclear Physics, Kolkata

A thesis submitted to the

Board of Studies in Physical Sciences

In partial fulfillment of requirements

For the Degree of

DOCTOR OF PHILOSOPHY

of

HOMI BHABHA NATIONAL INSTITUTE

June, 2021

Homi Bhabha National Institute

Recommendations of the Viva Voce Committee

As members of the Viva Voce Committee, we certify that we have read the dissertation prepared by **Madhurima Pandey** entitled **"Astroparticle Physics with Particle Dark Matter Models, Neutrinos and Gravitational Waves from First Order Electroweak Phase Transition"** and recommend that it may be accepted as fulfilling the thesis requirement for the award of Degree of Doctor of Philosophy.

Debades Bandyopadhyay Date: 26.06.2021

Chairman - Professor Debades Bandyopadhyay

Debasish Majumdar Date: 26/06/2021

Guide / Convener - Professor Debasish Majumdar

Narendra Sahu Date: 26/06/2021

Examiner - Dr. Narendra Sahu

Date: 26/06/2021

Member 1 - Professor Satyajit Saha

Ambar Ghosal Date: 26/06/2021

Member 2 - Professor Ambar Ghosal

Final approval and acceptance of this thesis is contingent upon the candidate's submission of the final copies of the thesis to HBNI.

I/We hereby certify that I/we have read this thesis prepared under my/our direction and recommend that it may be accepted as fulfilling the thesis requirement.

Date: 26/06/2021

Place: Kolkata

Guide: Debasish Majumdar

तस्मादसक्तः सततं कार्यं कर्म समाचर ।
असक्तो ह्याचरन्कर्म परमाप्नोति पूरुषः ।।

-**Karmayoga,** Shrimad Bhagavad Gita

"Therefore, without attachment, perform always the work that has to be done, for man attains to the highest by doing work without attachment."

Translated by
-Prof. Sarvepalli RadhaKrishnan

STATEMENT BY AUTHOR

This dissertation has been submitted in partial fulfillment of requirements for an advanced degree at Homi Bhabha National Institute (HBNI) and is deposited in the Library to be made available to borrowers under rules of the HBNI.

Brief quotations from this dissertation are allowable without special permission, provided that accurate acknowledgement of source is made. Requests for permission for extended quotation from or reproduction of this manuscript in whole or in part may be granted by the Competent Authority of HBNI when in his or her judgment the proposed use of the material is in the interests of scholarship. In all other instances, however, permission must be obtained from the author.

Madhurima Pandey

Madhurima Pandey

DECLARATION

I, hereby declare that the investigation presented in the thesis has been carried out by me. The work is original and has not been submitted earlier as a whole or in part for a degree / diploma at this or any other Institution / University.

Madhurima Pandey

Madhurima Pandey

Certified By –

Debasish Majumdar

Prof. Debasish Majumdar

(Guide)

Senior Professor H

Astroparticle Physics and Cosmology Division

Saha Institute of Nuclear Physics

1/AF, Bidhannagar, Kolkata – 700064

INDIA

LIST OF PUBLICATIONS ARISING FROM THE THESIS

Publications included in the thesis

Journal:

1. "Two component WIMP - FImP dark matter model with singlet fermion, scalar and pseudo scalar", Amit Dutta Banik, **Madhurima Pandey**, Debasish Majumdar and Anirban Biswas, *Eur. Phys. J. C*, **2017**, *77*, 657, [1612.08621].

2. "Two Component Feebly Interacting Massive Particle (FIMP) Dark Matter", **Madhurima Pandey**, Debasish Majumdar and Kamakshya Prasad Modak, *JCAP*, **2018**, *1806*, 023, [1709.05955].

3. "Probing a four flavor vis-a-vis three flavor neutrino mixing for ultrahigh energy neutrino signals at a 1 Km^2 detector", **Madhurima Pandey**, Debasish Majumdar and Amit Dutta Banik, *Phys. Rev. D*, **2018**, *97*, 103015, [1711.05018].

4. "Unparticle decay of neutrinos and its possible signatures at Km^2 detector for (3+1) flavour framework", **Madhurima Pandey**, *JHEP*, **2019**, *1901*, 066, [1804.07241].

5. "Mass and Life Time of Heavy Dark Matter Decaying into IceCube PeV Neutrinos", **Madhurima Pandey**, Debasish Majumdar, Ashadul Halder and Shibaji Banerjee, *Phys. Lett. B*, **2019**, *797*, 134910, [1905.08662].

6. "Implications of a proton blazar inspired model on correlated observations of neutrinos with gamma-ray flaring blazars", Prabir Banik, Arunava Bhadra, **Madhurima Pandey** and Debasish Majumdar, *Phys. Rev. D*, **2020**, *101*, 063024, [1909.01993].

7. "Addressing γ-ray emissions from dark matter annihilations in 45 milky way satellite galaxies and in extragalactic sources with particle dark matter models", Ashadul Halder, Shibaji Banerjee, **Madhurima Pandey** and Debasish Majumdar, *MNRAS*, **2020**, *500*, 5589, [1910.02322].

Conference:

1. "Mass and Life Time of Heavy Dark Matter Decaying into IceCube PeV Neutrinos", **Madhurima Pandey**, Debasish Majumdar, Ashadul Halder and Shibaji Banerjee, *Springer Proc. Phys.*, **2020**, *248*, 311-316, [1735865].

2. "Probing the Effects of Unparticle Decay of Neutrinos on the Possible Ultrahigh Energy Neutrino Signals at a Km^2 Detector for 4-Flavour Scenario", **Madhurima Pandey**, *Springer Proc. Phys.*, **2021**, *261*, 497-503, [1865702].

Preprint:

1. "IceCube PeV Neutrino Events from the Decay of Superheavy Dark Matter; an Analysis", **Madhurima Pandey**, Debasish Majumdar and Ashadul Halder, [1909.06839v1].

2. "The Violation of Equivalence Principle and Four Neutrino Oscillations for Long Baseline Neutrinos", **Madhurima Pandey**, Debasish Majumdar, Amit Dutta Banik and Ashadul Halder, [2003.02102v1].

3. "Gravitational Wave Emissions from First Order Phase Transitions with Two Component FIMP Dark Matter", **Madhurima Pandey** and Avik Paul, [2003.08828v2].

Other publications/Communicated (not included in the thesis)

1. "Effects of Violation of Equivalence Principle on UHE Neutrinos at IceCube in 4 Flavour Scenario", **Madhurima Pandey**, [1812.11570v2].

2. "Estimation of Baryon Asymmetry from Dark Matter Decaying into IceCube Neutrinos", Tista Mukherjee, **Madhurima Pandey**, Debasish Majumdar and Ashadul Halder, *Int. J. Mod. Phys. A*, **2021**, *36*, 2150078, [1911.10148v3].

3. "Bounds on Dark Matter Annihilation Cross-sections from Inert Doublet Model in the context of 21 cm Cosmology of Dark Ages", Rupa Basu, Shibaji Banerjee, **Madhurima Pandey** and Debasish Majumdar, [2010.11007v2], accepted for the publication in the International Journal of Modern Physics A (*Int. J. Mod. Phys. A*).

4. "Investigating the Effect of PBH, Dark Matter – Baryon and Dark Matter – Dark Energy Interaction on EDGES in 21cm Signal", Ashadul Halder and **Madhurima Pandey**, [2101.05228v2].

5. "Exploring multimessenger signals from heavy dark matter decay with EDGES 21-cm result and IceCube", Ashadul Halder, **Madhurima Pandey**, Debasish Majumdar and Rupa Basu, [2105.14356v2].

Madhurima Pandey

Madhurima Pandey

Dedicated to my parents and brother

ACKNOWLEDGEMENTS

"When we express our gratitute, it grows" - Richie Norton

At the outset, I would like to convey my profound indebtedness towards my supervisor Prof. Debasish Majumdar for his effortless and continuous support during my Ph.D. research. He truely has the substance of a genious and his stupendous knowledge base transcends across both academic and non-academic sphere alike. He sowed the seed of scientific approach in me and relentlessly nurtured it so that I get a comprehensive understanding for several areas of Astroparticle Physics. I can not envisage having a better supervisor for my Ph.D. research. He is the epitome of a friend, philisopher and guide who has persistently steered me towards the right direction. The innumerable discussions with Prof. Majumdar on a wide spectrum of topics expanding across academia, literature and music will be etched in golden letters in my memory for the rest of my life.

I wish to acknowledge the Department of Science and Technology, Govt. of India for their financial support under the INSPIRE Fellowship scheme which assisted me in following my research interest and completing my Ph.D. research. I owe my gratitude to all the conference organizers from various institutes over the world who have given me with the opportunity to showcase my work in their forum. Special mention to Japan Society for the Promotion of Science (JSPS) for providing logistics support during the 11th Hope Meeting with Noble Laureates in Okinawa, Japan and "The Paris-Saclay AstroParticle Symposium 2019" for fully funding my academic trip to Orsay, France.

I sincerely express my deepest gratitude to all the members of my doctoral committee Prof. Debades Bandyopadhyay, Prof. Satyajit Saha and Prof. Ambar Ghosal for painstakingly assessing my progress reports and providing their valuable suggestions throughout

my Ph.D. research. Taking this opportunity to pay my special regards to Prof. Asit Kumar De, Prof. Palash Baran Pal, Prof. Amit Ghosh, Prof. Pradip Kumar Mahanty, Prof. Munshi Golam Mustafa, Prof. Prakash Mathews and Prof. Pratik Majumdar who were always available for solving any research related doubts as well as explaining in details about various aspects of scientific research. During my Ph.D. tenure, I got the privilege of collaborating with Dr. Anriban Biswas, Dr. Amit Dutta Banik, Dr. Kamakshya Prasad Modak, Dr. Prabir Banik, Prof. Arunava Bhadra, Prof. Shibaji Banerjee, Avik Paul, Ashadul Halder, Rupa Basu and Tista Mukherjee. It was an absolutely enriching experience and I will definitely look forward to collaborate more with them in the coming days.

Let me take this time to recognize the invaluable assistance of all the members of Saha Institute of Nuclear Physiscs, especially faculty, students, post-doctoral fellows and non-academic stuffs of Astroparticle Physics and Cosmology (APC) Division. I am grateful to my institute for providing me with the best working environment and appropriate infrastructure support during my Ph.D. tenure. I would like to thank Pradyut Da, Pradip Da and Dipak Da from the core of my heart for helping me in all official matters. I will cherish and remember the great moments that I have shared with Dola Di and Sangeeta di in the last few years. It is my pleasure to have Anirban da, Amit da, Kamakshya da, Rome da, Anshu da, Biswajit da, Rupam da, Mugdha da, Sukannya di, Mairayee di, Mainak da, Prasanta da and Susnata di as my seniors who guided and extended help as when required. Avik Paul, Satyabrata, Suraj, Aman, Habib, Sunita, Vimal, Upala, Sayan, Bithika and Aranya are among the most dynamic juniors that I have interacted with and wish them very best for their future endeavours. I will dearly miss the vibrant atmosphere of APC scholar room and all the cultural events with which I had been associated during my Ph.D. tenure. Conveying my thanks to Avik Banerjee, Augniva, Sajad, Samanwaya and Aritra for being the best batchmates I could have ever wished for. Big shout out to my MSA II hostel mates

Rajkamal, Pallavi and Biswajit Da for breathing fresh life into my otherwise mundane hostel stay. I am thankful to the hostel security, bus services for ensuring safe and secure stay and canteen services for providing delicious foods.

"A good friend is like a four-leaf clover; hard to find and lucky to have". I consider myself really lucky to have found my set of four-leaf clovers in Debalina, Payel, Ritwik and Songshaptak with whom I have shared all my happiness and sadness alike. Samadrita, Sanchari, Sumit, Supriya, Chayan, Suchira, Suparna, Atanu, Rounak, Dibyashree, and Amit are some of the wonderful souls with whom I cherished all the mesmerizing moments of life. I am really fortunate enough to have Sampad, my forever best friend, by my side through thick and thin. I am extremely thankful to him for understanding me and for giving me immense emotional support.

Sampa Kundu Vaskar, one of the kindest person I have met in life, has always been there for me to shower her blessings and unconditional love. I am grateful to Juna aunty and Atreyi for their loving and caring gestures towards me.

This acknowledgement will not be complete without paying tribute to my family, my mother Sudipta Pandey, my father Tapas Kumar Pandey and my little brother Alekhya Pandey. They have been my perpetual source of motivation and pillar of moral support that have helped me to overcome all professional and personal impediments throughout my academic career. I am obligated to my parents for supporting me in pursuing my dreams by defending me from the benighted perspective of the stereotypical mentality.

Lastly I thank all the tax payers of my country for their indirect support.

Madhurima Pandey

Madhurima Pandey

CONTENTS

LIST OF FIGURES

LIST OF TABLES

CHAPTER 14

CONCLUSIONS AND FUTURE OUTLOOK

In the thesis, three important aspects of Astroparticle Physics have been addressed, namely, particle dark matter (DM) phenomenology, neutrino oscillation and primordial Gravitational Waves (GWs) from first order electroweak phase transition.

The known luminous object in the Universe accounts for only about 4.9 $\%$ of the total mass-energy budget of the Universe. The analysis of satellite borne PLANCK experiment on the anisotropy of Cosmic Microwave Background Raditaion or CMBR suggests that the Universe ovewhelmingly contains unknown DM and dark energy. The former one is an unseen unknown matter, whose only definite evidence so far is due to their gravitational effects, makes up for around 26.8 $\%$ of the Universe's contents. The rest around 68.3 $\%$ is yet another unknown energy known as dark energy thought to invoke a negative pressure opposite to gravity and cause the recent accelerated expansion of the Universe. Although Standard Model (SM) of particle physics very satisfactorily explains the known fundamental particles in nature with which the luminous matter of the Universe is made up of, it cannot explain the particle nature of DM. SM cannot also explain the neutrino mass and hence mass induced oscillation. Theories are proposed in the thesis for particle DM by simple extension of SM, by a scalar, a pseudo scalar or a fermion or combinations of all. It is then shown in the

thesis that such models can well explain some of the possible indirect DM signatures from different astrophysical bodies such as Galactic Centre (GC), dwarf galaxies etc.

A two component DM model is proposed in the thesis where the SM is extended by a scalar, a fermion and a pseudo scalar. The scalar and the fermion constitute each of the components of this two component DM while the fermion component is of Weakly Interacting Massive Particle or WIMP in nature, the other scalar component is the Feebly Interacting Massive Particle or FIMP. The stability of the fermionic component is assured by imposing a global $\mathrm{U}(1)_{\mathrm{DM}}$ symmetry on this fermion such that this Dirac fermion is a singlet under SM gauge group and it has a global $\mathrm{U}(1)_{\mathrm{DM}}$ charge. On the other hand, a Z_2 symmetry is imposed on the scalar component to ensure its stability. It is shown in the thesis that, while the annihilation end product of the fermionic component can explain the observed gamma-ray (γ-ray) excess from GC in the 1-3 GeV energy range, the other scalar component accounts for the emission of 3.55 keV X-ray lines reported to have observed from Persues and Andromeda galaxies. The FIMP component is also found to be useful in explaining the self interaction of DM. The experimental bound for the cross-section of this self interaction is $\sigma_{\mathrm{DM}}/m < 0.47\,\mathrm{cm}^2/\mathrm{gm}$ [217].

A two component DM model where both the components are scalars and FIMPs are also proposed and explored in the thesis in order to explain the DM self interaction.

Dwarf satellite galaxies of Milky Way can be rich in DM. The Fermi-LAT satellite borne experiment provided upper bounds of the γ-ray flux observed from dwarf satellite galaxies. Proposing that the γ-rays from the dwarf galaxies are produced by the annihilations of DM present in the dwarf galaxies, γ-rays from 45 dwarf galaxies are analysed in the thesis with two different particle DM models. One is the WIMP-FImP model proposed in the thesis by simple extension of SM while the other is Kaluza-Klein or KK DM in theories of extra dimension - a beyond SM theory. These two DM candidates are also explored to explain the extragalactic γ-ray flux observed by Fermi-LAT. It is seen that the γ-rays from annihilation of KK DM when added to other possible background sources for γ-rays such as BL LAC objects, Gamma Ray Bursts (GRBs) etc. very well satisfy the

Fermi-LAT data for extragalactic γ-rays.

It is also explored in the thesis, whether the decay of primordial superheavy dark matter (SHDM) may produce the ultrahigh energy (UHE) neutrinos as a secondary product. Southpole based IceCube observatory reported UHE neutrinos in the energy range $\sim$ 120 TeV to $\sim$ 50 PeV from their 6 year data analysis known as HESE (High Energy Starting Event) data. From a through χ^2 analysis of HESE energy region of IceCube ($\sim 10^5$ GeV - $\sim 5 \times 10^6$ GeV), in the thesis a prediction is made for the mass and lifetime of a primordial SHDM that can explain the HESE results of UHE neutrino. It is found that the decay of a primordial SHDM mass $\sim 10^8$ GeV with a lifetime $\sim 10^{28}$ sec, can explain the HESE results of UHE neutrinos. The SHDM undergoes cascading decay and such decay process can proceed through two decay channels namely hadronic and leptonic. While the former study was only assuming the hadronic decay cascade, the scope of the analysis has latter been broadened by including the leptonic channel as well. In addition, the energy range of the analysis has been extended further in the lower energy regime to include the two IceCube data of astrophysical origin. A combined analysis is then performed in the thesis including the astrophysical flux and the hadronic and leptonic decay channels of the SHDM of the 7.5 year IceCube HESE data and the two astrophysical neutrino data. From this analysis, again the SHDM mass and decay lifetime are obtained.

The possible existence of a sterile fourth neutrino in addition to the usual 3 active neutrino flavours is a long standing issue. Although it is not conclusively confirmed but several terrestrial neutrino detectors analyse their experimental data for neutrino ocillations assuming 4 neutrino (3 active + 1 sterile) oscillations and determined bounds on various 4 neutrino oscillation parameters. In the thesis, this issue of sterile neutrino has been explored. Considering the UHE neutrinos from distant GRB sources, the possible detection yields of the observed UHE signal at a km^2 detector such as IceCube have been computed in the thesis for both 3-flavour and 4-flavour scenarios. For this case, a detailed formalism for 4-flavour mixing matrix and 4-flavour neutrino oscillations have been worked out in the thesis. It is to be noted that due to astronomical distances between the Earth

and the UHE neutrino sources, the oscillatory part of a neutrino oscillation probability equation is averaged to $\frac{1}{2}$ and a neutrino flavour would suffer flavour suppression instead of flavour oscillation while traversing such astronomical baselines. To this end, a ratio of muon yields to shower yields at the detector induced by such UHE neutrinos is defined for the purpose. It is seen that this ratio grossly differs for the two cases of 3-flavour and 4-flavour oscillation formalisms. Thus, this ratio for UHE neutrino events in a km^2 detector could be a viable probe for the existence of sterile neutrinos.

On September 22, 2017 the IceCube collaboration detected a cosmic neutrino event IceCube-170922A of energy $\sim$ 290 TeV from the direction of the Blazar TXS 0506+056. The Fermi-LAT collaboration also reported a state of enhanced γ-ray emission of the same Blazar around that time. This revealations of multimessenger astronomy suggest a common high energy cosmic source of neutrinos and γ-rays. In addition 13 neutrino events IceCube-141209A are also observed by IceCube during 2014-2015 from the direction of the Blazars PKS 0502+049/TXS 0506+056 and GB6 J1040+0617. All of them were found to be in the state of enhanced γ-ray emission during these detections suggesting blazars to be a source of cosmic rays and their acceleration in blazar jets. The UHE γ-rays and neutrinos can be produced either by the interaction of cosmic rays accelerated by blazar jets with the surrounding photons or electromagnetic radiations ($p\gamma$ interaction) or by the interaction of blazar-accelerated cosmic rays with ambient matter (pure hadronic (pp) interactions). In the thesis, a proton blazar model for the blazars has been explored to show that it not only can explain consistently the spectral behaviour of the high energy bump of electromagnetic spectral energy distribution (SED) but also the observed neutrinos from the three blazars mentioned above. This model is more realistic than cloud-in-jet model.

The Standard Model (SM) of particle physics does not have scale invariance since most of the SM particles are massive and scale invariance is manifestly broken by the masses of SM particles. But the scale invariance may be restored at a much higher scale. But it had been observed by Georgi that if an unseen scale invariant sector exists at low energy and interacts very weakly with

SM particles then this non trivial scale invariant sector is characterised by “Unparticles". In this theoretical set up, scale invariance sector sets in at an energy scale $\Lambda_{\mathcal{U}}$ and the renormalizable couplings of the fields of the scale invariant sector induce dimensional transmutation at $\Lambda_{\mathcal{U}}$ and the particles are described by massless unparticles. Below $\Lambda_{\mathcal{U}}$ the scale invariant fields match onto unparticle operators. The scale dimension $d_{\mathcal{U}}$ of unparticles is a non-integral number. The unparticle physics may lead to very unexpected phenomenologies. In the thesis, the consequences of neutrino decay to unparticles has been explored in a 4 neutrino framework with UHE neutrinos from distant GRB by explicitly writing the analytical expressions for the neutrino flux undergoing such unparticle decay and then computing their possible signatures at a km^2 detector. The effect of unparticle coupling strength and the scaling dimension $d_{\mathcal{U}}$ on the detector yield are also addressed.

A consequence of the principle of equivalence is that all the three types of neutrinos couple with same strength G with gravity. Although the equivalence principle is not reported to be violated in nature but even a very weak violation of equivalence principle or VEP would result in different coupling strengths with which different types of neutrinos interact with gravity. This in turn would induce a phase difference between two types of neutrinos in a coherent neutrino beam while traversing a distance in a gravitation field. In the event therefore, if the neutrinos in gravitational basis are not identical to that in gravity basis, this results in flavour-gravity mixing of neutrinos in addition to the mass-flavour mixing and would lead to gravity induced oscillations along with the usual mass-flavour oscillations. In the thesis, a possibility is explored to probe a very tiny violation of equivalence principle in case of a long baseline (LBL) neutrino experiment by considering a 4 neutrino framework. Since for an LBL neutrino experiment, the accelerator neutrinos (in a neutrino factory) would travel through different layers of Earth matter before reaching a distant detector, in the thesis, a rigorous analytical expressions for neutrino oscillation probabilities in matter are derived where matter induced mass-flavour oscillations along with gravity induced oscillations are considered in the same framework for 4-flavour neutrino scenario. This is accomplished in the thesis by explicitly diagonalising the relevant 4×4 matrices and elaborate computation of the same

as the neutrinos propagate through different density layers within the Earth matter to reach the far detector. Finally in the thesis, wrong sign (in appearence channel, where a ν_e oscillates to ν_μ) and right sign (in disappearence channel, where the ν_μ flux is suppressed due to oscillation of ν_μ) muon yields are computed at the far detector assumed to be at a baseline length of $\sim$ 7000 km from the neutrino source. The detector is taken to be a 50 kTon iron calorimeter (ICAL) with magnetic field applied across it so that the neutrino induced μ^+ and μ^- could be identified at the detector (and hence the incident neutrino or an antineutrino could be differentiated). From this study, two important observations have been made in the thesis. One is that the VEP effect on neutrino oscillations is very prominent if violation is as small as $\sim 10^{-23}$ in comparison to no VEP case for both the 3-flavour and 4-flavour scenarios. The other is that the computed wrong sign muon yields for the 3-flavour case are found to be remarkably suppressed than the same when computed for the 4-flavour scenario for both VEP and no VEP considerations. These studies indicate that the LBL neutrinos could not only offer viable mechanisms to probe very small VEP, if exists, but is suitable as well to investigate the possible existence of sterile neutrinos.

The emissions of the Gravitational Waves (GWs) from a strong first-order electroweak phase transition have been explored in the thesis. To this end, a dark matter model has been investigated in Feebly Interacting Massive Particle (FIMP) scenario, where the dark matter particles are produced through "freeze-in" mechanism in the early Universe. The first-order phase transition has been studied within the framework of this present model. Both analytical and numerical computations have been done to calculate the consequent production of GWs and then the detectabilities of such GWs have been investigated at the future space-based detectors such as LISA, BBO, ALIA, DECIGO, aLIGO and aLIGO+, etc. It is also observed that the smaller Higgs portal couplings plays a signifant role in the relic density calculations for the considered two component FIMP dark matter model whereas the dark matter self-couplings has a considerable influence on GW production in the present scenario.

Future Outlook

The topics of Astroparticle Physics that has been addressed in the thesis have very wide scope for future expansion and studies. In the following, some of the future research topics are mentioned.

- An interesting FIMP scenario is the Clockwork FIMP scenario involving a number of Beyond Standard Model Fields and their interactions through which FIMPs are produced. In one such approach discussed in A. Goudelis *et al.*, [600], the scalar FIMP DM has been considered to have originated from the consideration of the spontaneous breakdown of a global symmetry $\Pi_{i=0}^{N} \otimes \mathrm{U}(1)_{\mathrm{i}}$ at scales f_is (for each $\mathrm{U}(1)_{\mathrm{i}}$) where $f = f_i$ is assumed to be leading to the gereration of $N+1$ massless Goldstone bosons and this $\mathrm{U}(1)^{N+1}$ is further softly broken giving rise to mass parameters. The resulting mass matrix, on diagonalisation produces a tower of discrete levels of masses much like the Kaluza-Klein tower in extra-dimensional theories, the lowest one of which is attributed to a FIMP candidate. The self interaction of such a Clockwork FIMP candidate will also be addressed where in addition to $2 \to 2$ processes, $4 \to 2$ and $3 \to 2$ processes can also be investigated.

- It is also interesting to investigate the possibility of one of the three right handed (RH) neutrinos (singlets) introduced in see-saw mechanism to be a DM candidate. This RH neutrino is almost decoupled from the Yukawa interaction term of the Lagrangian and is produced by the freeze-in mechanism assisted by a thermalized scalar singlet having odd Z_2 parity. The Yukawa couplings of other two heavy neutrinos which are related to the light neutrino masses and mixing also play a crucial role in the DM production. A successful hierarchical leptogenesis will also be addressed while the Yukawa couplings are expressed in terms of the low energy parameters via Casas-Ibarra parametrization.

- Primordial Black Holes (PBH) are believed to be formed during the radiation dominated era due to the collapse of the overdensity region characterized by the size of the region which should be greater than the Jeans length. The PBHs may account for DM or it may evaporate DM along with other SM particles. The evaporation of Primordial Black Holes can inject

more energy to the system. This may affect the 21 cm signal of hydrogen from the dark ages of the Universe as well as the 21 cm signal from the epoch of reionisation (EoR). It will be an important topic for further investigation.

- Fuzzy dark matter or FDM is considered to be composed of scalar particles with mass as low as 10^{-22} eV. Therefore the de Broglie wavelength is of the order of astrophysical scales ($\sim$ kpc) and is hypothesised to address the cusp-core problem of DM density profile. The FDM is well motivated by the ubiquitous presence of ultra-light scalars (such as axion like particles) in beyond Standard Model theories. The implications of FDM as against the ususal cold dark matter (CDM) can be investigated via the fluctuations in 21 cm signal of hydrogen during the EoR along with the Lyman-α background as also from the dark ages. The future data from upcoming radio telescope, the square kilometer array or SKA would help obtain tighter bounds on FDM. These also is a topic for future exploration.

- The long baseline (LBL) accelerator neutrinos will be probed mainly with respect to DUNE, NOνA and other LBL neutrino experiments and the questions such as CP violations in neutrino sector, the possibility of a fourth sterile neutrino, neutrino mixing angle and neutrino mass hierarchy will be a study worth pursued in future. The origin of neutrino mass and its possible DM origin is also be probed.

- When a discrete symmetry is spontaneously broken it leads to the formation of domain walls. These are in fact topological defects. In general, the average number of domain walls per Hubble horizon remains constant, which may lead to overclosure of the Universe due to the slower decrease of their energy densities with respect to radiation or matter. Thus the domain wall has to be unstable and should eventually break down. The domain wall could be unstable if the discrete symmetry is approximate. The domain walls are annihilated when the pressure on the walls induced by the energy bias between the true and false vacua superceeds the tensions of the domain walls. The process of annihilations of such domain walls triggers

Gravitational Wave emissions and these GWs retain in them the information of the physics following which these were created. Thus, study of such domain wall induced relic GWs may enable us to probe events in the early Universe and the ultraviolet physics as well. The study of such GWs for several possible discrete symmetries in the early Universe era is worth pursuing. Possible generations of baryon asymmetry from domain wall annihilations may also be looked into.

SUMMARY

The thesis explores three very important aspects of Astroparticle Physics namely particle dark matter (DM) phenomenology, neutrinos and primordial Gravitational Waves (GWs) from first order electroweak phase transition (FOEWPT). The known luminous matter in the Universe accounts for only about a meagre 4.9 $\%$ of the total mass and energy content of the Universe. The presence of enormous unknown mass, known as DM, constitutes about 26.8 $\%$ of the Universe's content and its evidence is overwhelmingly gravitational (it has perhaps very feeble interaction, if at all, with other known SM particles). The Standard Model (SM) of particle physics cannot explain the particle nature of DM. In this thesis, the particle nature of DM and its phenomenology are explored by proposing some particle physics models of DM by extending the SM with scalars, fermions or both and also adopting the beyond Standard Model (BSM) theory of extra dimension. In the framework where DM consists of two particle components instead of just one component, the thesis addresses and explains various possible indirect signatures of DM from astrophysical sources such as Galactic Centre (GC), dwarf galaxies etc. Simultaneously such models also explain the self interaction of DM considering Feebly Interacting Massive Particles or FIMPs created in the Universe by "freeze-in" mechanism in contrast to Weakly Interacting Massive Particles or

WIMPs produced by "freeze-out" mechanism. In addition, gamma-ray (γ-ray) fluxes from 45 dwarf spheroidal galaxies (dSphs) of Milky Way are analysed by considering that these γ-rays are produced by possible DM annihilation of dwarf galaxies. The DM can also induce the electroweak phase transition (EWPT) to be of first order such that primordial GWs can be emitted by bubble nucleation and tunneling during this phase transition. With a two component particle DM model, in the thesis it is shown that the EWPT is of first order and the frequency of such GW is estimated. Their detection possibilities are also addressed. The thesis then probes the possible sterile neutrino signatures in case of ultrahigh energy (UHE) neutrinos at a large Km^2 detector such as IceCube. A blazar model is proposed in the thesis which can beautifully explain the multimessenger signals of γ-ray (by Fermi-LAT telescope) and high energy neutrinos from blazar TXS 0506+056 (at IceCube). Other signals from PKS 0502+049 and GB6 J1040+0617 are computed and compared with experimental results. In addition, assuming the UHE neutrinos are produced from the cascade decay of very heavy DM that could have been produced gravitationally by other quantum effects during or just after (reheating) inflation, a detailed analysis of IceCube High Energy Starting Event (HESE) data are performed to estimate mass and lifetime of such DM. The neutrino oscillation physics is also an useful mechanism to address other exotic phenomena such as possible violation of equivalence principle (VEP) that can induce neutrino flavour oscillation. In nature, there are no such signatures that the equivalence principle in Einstein's theory of relativity is violated. It is demonstrated in the thesis that, even a very tiny amount of VEP can be probed by gravity induced neutrino oscillations in long baseline (LBL) experiments on Earth. In addition to this, the thesis also addresses the decay of neutrinos to unparticles proposed by Georgi. Unparticles can be produced from the theory of scale invariance and dimensional transmutation at lower energy.

CHAPTER 1

INTRODUCTION

"The Universe is full of magical things

patiently waiting for our wits to grow sharper"

- EDEN PHILLPOTTS

The unfathomable mysteries that the Universe offers have always enchanted the human race. The movements of heavenly bodies across the vault of the sky, the innumerable twinkling stars and distant placid planets that adorn the night sky cast a spell of incantation on human mind and human intellect from time immemorial. Human wondered at the layout of groups of stars in imaginative formation that appears to represent the impressions of several earthlings. The visible cosmic events such as eclipses, the appearences of comets or Supernovae events invoked within them a sense of awe and inspire their inquisitive faculties. The invention of the telescope by Galileo Galilei was a giant leap in this direction and took the study of the heavenly bodies to a whole new level. The theoretical development of Tycho Brahe and later Kepler's law of planetary motion provided a fresh perspective in understanding the dynamics of heavenly bodies. With the groundbreaking

discovery of gravitation by Newton, the inverse square law of the force of gravity and more importantly the introduction of the brilliant idea of "free fall" not only consolidated the mathematical foundation but pave the way to more comprehensive understanding of the observed behaviour of celestial objects. The deviation of known celestial body's observed motion from what was expected from such theories would then serve as an indicator of the presence of the objects which are unknown to us and it calls for the modifications of the formulated theories. Later with the advent of Einstein's theory of relativity both "speical" and "general", along with Hubble's astounding discovery that the Universe is in fact expanding, had ushered in a new perspective in the study of cosmos in general and the evolution of the Universe in particular. Simultaneous advances in the physics of microscopic world with the development in quantum mechanics, atomic and nuclear physics, particle physics and gauge theory, GUT, electroweak and quantum chromodynamics (QCD) phase transitions add much deeper insight to the evolution and symmetries of the Universe. This lead to the advent of fundamental particles and fields as consequences of those symmetries and the breaking of those symmetries. For example, an electroweak phase transition (EWPT) occured at the temperature $\sim$ 200 GeV of the Universe when $\mathrm{SU}(2)_L \times \mathrm{U}(1)_Y$ electroweak gauge symmetry is broken resulting in the separation of electromagnetic (EM) and weak forces and the presently known fundamental particles being massive is another consequence. The $\mathrm{SU}(2)_L \times \mathrm{U}(1)_Y$ electroweak theory is a gauge theory of Standard Model (SM) of particle physics, the most successful theory in explaining the behaviour of fundamental particles (or bulding blocks) of nature and their interactions. If this EWPT is of first order then Gravitational Waves (GWs) can be emitted during this phase transition. Also electroweak baryogenesis could be a possibility. A first order phase transition (FOPT) is a violent phenomenon and is initiated by the bubble nucleation of a true vacuum state whereby the bubbles undergo tension, collisions and eventual collapse producing GW.

The GW from a FOPT at the electroweak scale can be detectable by future space-based detector such as the Laser Interferometer Space Antenna (LISA) GW detector and other detectors. But within the framework of SM, EWPT is a smooth cross-over from one phase to another. However, the electroweak theory, successfully represented by SM of particle physics if minimally extended by, say a spinless scalar field then EWPT of the Universe can be shown to be of first order. Also it renders a viable candidate of particle dark matter (DM), an unknown particle that does not belong to the family of known fundamental particles described by the electroweak theory of SM of particle physics but is found by other indirect evidences (mostly gravitational), to have constitute more than 80% of the matter content of the Universe (whereas the known Universe with the known SM fundamental particles account for a paltry $\sim 4.9\%$ of the total Universe).

The known fundamental particles which are the basic building blocks of nature are very well described by SM of particle physics. The theory of SM in fact is a theory that unifies two different fundamental forces of nature namely weak interaction and EM interaction. It is based on the group symmetry of some groups with which different interactions can be represented. Thus the weak interaction is described in terms of $\mathrm{SU}(2)_L$ group while the EM interaction, by $\mathrm{U}(1)_{\mathrm{EM}}$ group. But the unified group structure of electroweak group is $\mathrm{SU}(2)_L \times \mathrm{U}(1)_Y$ where L represents the left chirality and Y is called the hypercharge. These group symmetries are also called gauge symmetries and SM of electroweak interaction is a gauge theory of local invariance of $\mathrm{SU}(2)_L \times \mathrm{U}(1)_Y$ group. It encompasses the fundamental particles which are fermions, the interacting bosons that mediated the weak ($W^{\pm}$ and Z bosons) and EM interaction (γ). The fundamental particles also include a scalar (spin 0) called Higgs boson. So long as electroweak symmetry ($\mathrm{SU}(2)_L \times \mathrm{U}(1)_Y$) is in place, all the force carrier bosons namely $W^{\pm}$, Z and γ as also the fermions are massless. But this symmetry is broken by the process called Higgs mechanism leading to unbroken

$\mathrm{U}(1)_{\mathrm{EM}}$ group. This separates weak and EM interactions and the weak interaction carrier bosons become massive. The EM force carrier γ (photon) does not acquire any mass as $\mathrm{U}(1)_{\mathrm{EM}}$ group remains unbroken. As a result of this spontaneous symmetry breaking (SSB), the massless fundamental fermions also acquire masses by interactions with Higgs. The fermion sector of SM contains three generations of quarks and leptons and their antiparticles. Each generation consists of one up type and one down type quark. There are thus three up type quarks and three down type quarks (three generations). The leptonic part also contains three generations of particles. Each generation of flavour consists of charged lepton and a neutral one. Thus electron and electron neutrino (e^- and ν_e) constitute first generation of flavour while muon, muon neutrino (μ, ν_ν) and tau, tau neutrino (τ, ν_τ) are respectively the second and third generation of flavour. It is not clear why there are only three generations of leptons or quarks in nature. It is also an enigma why a mass hierarchy exists from one generation of flavour to the other although they follow the same symmetry group ($\mathrm{SU}(2)$). The weak interaction changes parity (where parity is an operator that inverts a 3-D space through the origin) and weak interaction current contains only left handed particles. The handedness is a property principally attributed to a particle depending on its momentum and spin direction. For massive particles, the concept of chirality is used. Thus the left handed components of each lepton generation form a doublet under weak interaction while the right handed parts of the same leptons are singlets under weak interaction. The form of the weak interaction is $(V-A)$ type (Vector - Axial vector) and is parity violating. This interaction when mediated by charged bosons $W^{\pm}$, is called charged current (CC) interaction whereas for the weak interaction with neutral boson Z mediator is called neutral current (NC) interaction. It is also an enigma that for neutrinos, only left handed neutrinos and right handed antineutrinos are observed. The fermions are described by Dirac equation. The Dirac equation has a kinetic term and a mass term for fermions. The Dirac mass term

involves both left and right handed particle fields. The absence of right handed neutrino therefore does not allow any neutrino mass term in the SM. But one adopts the presence of a right handed neutrino to generate neutrino mass in theories such as See-Saw model (heavy right handed neutrino) as also as a fourth generation sterile neutrino. But their existence has so far not been established. Neutrinos (and antneutrinos) of different energy ranges can originate from various sources, both natural and man made. The natural sources include Sun (eV to MeV range), Supernovae (upto hundreds of MeV), atmosphere (hundreds of MeV to few GeV), Ultrahigh energy (UHE) cosmic sources such as Active Galactic Nuclei (AGN), Blazars, Gamma Ray Bursts (GRBs) or possibly decay of superheavy dark matter (SHDM) (hundreds of GeV to EeV range). The man made neutrino sources are reactor neutrinos (eV to MeV energy range), accelerator neutrinos (upto tens of GeV energy) etc. Neutrino being a neutral particle could serve as a very useful signal for locating and analyzing the properties of the cosmic sources of their origins as they propagate through cosmos or other medium almost unperturbed by the influence of any possible magnetic or electric field along their path of travel. Thus neutrinos are useful probe in studying astrophysical objects. Neutrinos exhibit an important property called "neutrino oscillation". A coherent neutrino beam of one flavour can change into a different flavour (for example $\nu_e \rightarrow \nu_\mu$) after traversing a certain distance. The flavour oscillations exhibited by neutrinos are caused by the mixing of neutrino flavour and mass eigenstates, which arises since the weak interaction eigenstates or flavour eigenstates of neutrinos ($|\nu_e\rangle, |\nu_\mu\rangle, |\nu_\tau\rangle$) and their mass eigenstates ($|\nu_1\rangle, |\nu_2\rangle, |\nu_3\rangle$) are not same. As a result of this, a flavour eigenstate can be written in terms of the superposition of their mass eigenstates ($|\nu_1\rangle, |\nu_2\rangle, |\nu_3\rangle$ etc.) and vice versa. Thus different flavour eigenstates are expressed as different mixtures of mass eigenstates. As superposed mass eigenstates (constituting a flavour eigenstate) propagate in vacuum or through a medium, different mass eigenstates in a flavour eigenstate evolve

with different phases giving rise to a phase difference betwen any two mass eigenstates. As a result, the propagating flavour eigenstate develops different mixtures of mass eigenstates and thus the initial flavour eigenstate of the neutrino also suffers a change of flavour. This phenomena will therefore cause depletion or increase of neutrinos of a particular flavour if the neutrinos are allowed to traverse from the source to a distant detector. There are ample evidences of neutrino oscillations for scalar, atmospheric and man made neutrinos from the data of several neutrino oscillation experiments. The oscillation of neutrino is therefore a consolidated evidence that neutrinos are massive, no matter how negligible the masses are and therefore can be an useful window for physics beyond Standard Model (BSM). The neutrino oscillation can also however be realised in principle by mixing of neutrino flavour eigenstates with exotic neutrino eigenstates other than the mass eigenstates. The possibility of such situations arises, if for example, equivalence principle is weakly violated. In such a scenario three types of neutrinos would not couple to gravity with the same strength and the gravity eigenstates will not be the same as flavour eigenstates. This gravity induced oscillation, if exists could also be possibly probed by oscillation experiments. Also if a fourth generation sterile neutrino is envisaged which does not have any interaction except gravity, then utilising the properties of neutrino oscillations, existence of such sterile neutrino can also be addressed.

After years of observations and mathematical calculations, the scientists are of the opinion that the beginning of the Universe is from an undefined point called a "singularity" following a huge explosion termed as "Big Bang" around 13.8 billion years ago [1] and immediately after, the Universe was being inflated at a super rapid pace. The expansion of the Universe eventually slowed down heralding the end of this inflationary phase but the

[1] Although recent researches using loop quantum gravity replace the idea of Big Bang singularity by the one in which the Universe emerged from a super compressed mass arising out of the contraction of the Universe in its preceeding phase.

Universe however, continues to expand. The very primordial Universe was filled with radiation having temperature and energy of immensely high magnitude. In this respect this can be mentioned that PLANCK set up "units for length, mass, time and temperature ... which retain their meanings for all ..." and these are constructed by taking suitable ratios of scientifically measurable fundamental constants of nature such as velocity of light c, gravitational constant G, PLANCK constant h (or $\hbar = \frac{h}{2\pi}$), Boltzmann constant $k_{\rm B}$ etc. The time, length and energy obtained from such ratios (of suitable combinations of those constants) are respectively $\sim 10^{-44}$ sec, $\sim 10^{-35}$ cm and $\sim 10^{19}$ GeV. These are called PLANCK time, PLANCK length and PLANCK energy scales respectively. But these are not smallest time scales or shortest length scales or highest energy scale. Only these are the scales beyond which the known physics breaks down. With the eventual cooling down of the Universe as its expansion progresses, different types of fundamental particles start appearing as particle-antiparticle pair from the radiation and the four fundamental forces of nature namely the gravitational force, the strong nuclear force, the weak force (that causes the beta decay to happen) and the EM force as we know them at present, are manifested as separate entities and not as a part of one unified force. It is not fully understood yet how in the early Universe, a very tiny excess is generated in favour of the particles over their antiparticles which transcends into the domination of particles over antiparticles; otherwise both would have been perpetually created and annihilated in pairs and the creation would not have been possible. In the early Universe, a certain type of particles may interact with other type of particles, may coexist with radiation, undergo annihilations by colliding with a particle of same kind or species and produce other particle species or these particles may be recreated by the process of annihilation of particles of other species. A state of equilibrium is maintained between the particles and the hot early Universe through these processes. This equilibrium is known as "thermal equilibrium". Since the Universe contin-

ually expands and gains in size, the number densities of these particles also endure gradual decline. But if the particles of a particular species are drifted away from each other, due to the expansion of the Universe, at a rate faster than the rate at which they interact with each other then they can never come together and interact. In such an event, these particles float in the Universe as non-interacting relics being out of the thermal equilibrium of the Universe's plasma with its numbers "frozen". Particles in the Universe can also be created by the decay of heavier particle as also through the process of interaction with other particles and their nature of interaction could be so feeble that they couldn't attain thermal equilibrium. The radiation photons and the particles coexist till the formation of neutral atoms after a series of processes that include the binding of the quarks to form a proton or neutron (hadronization), the process of nucleosynthesis whereby nuclei are formed by the bindings of protons and neutrons etc. and finally the formation of neutral atoms, where electrons are captured by the positively charged nucleus into their orbits. The era of formation of the neutral atom is called the era or epoch of recombination. Before recombination, the electron density was so dense that photons suffer multiple scattering off the electrons via Thomson scattering and photons were in thermal equilibrium with the contents of the Universe. In this era therefore, the Universe was opaque. Thus photon spectrum is the one of smooth black body spectrum. After recombination, as electrons are not available for the photons to scatter with, the free photons stream out and propagate with the expansion of the Universe retaining their expected black body spectrum. The wavelengths of these photons are also stretched with the expansion of the Universe and at the present epoch, the wavelengths of those primordial gamma photons are of microwave order as they form a microwave background in the cosmos known as Cosmic Microwave Background Radiation or CMBR. Although the ionization energy of the hydrogen atom is 13.6 eV, the decoupling of photon at the recombination epoch occurs at around a temperature ($T_{\rm dec}$) of 0.3 eV or ~ 300

K. This delay is due to the fact that the photons emitted following the capture of electrons at the ground state of hydrogen further ionize newly recombined atoms. At a temperature around 0.3 eV when almost all the electrons are captured by the positive nuclei, the thermal photons decouple from the matter of the Universe and they free stream. Therefore, this is the epoch when matter and radiation decouple. Before the photons decouple from the matter, the Universe was an almost smooth primordial soup. This was not perfectly smooth though and at certain regions it is slightly (may be a thousand of a percent) denser than the rest. While gravity tends to push the matter together, the scattering of photons tends to push them apart. In the process, the less dense region becomes denser while the denser region gets thinner. This push and pull between the high and low density regions exhibit a sound wave like oscillations in the medium and the signatures of this acquastic oscillations at the time of decoupling remains frozen in CMBR. The photon that is emitted from such denser region at the time of decoupling will have a slightly higher temperature than the photon that is emitted from the less denser region. This induces tiny anisotropies over the average smooth CMBR spectrum and on analysing these anisotropies in the CMBR background the matter content of the Universe is estimated. Although the spectrum of the CMBR is expected to be smooth and uniform (black body) irrespective of any directions in the sky, any fluctuations in the spectrum would indicate the existence of overdense regions back in time that could be the seed for the formation of different structures in the Universe like the galaxy, galaxy clusters as we see today. These fluctuations would appear as different peaks of different heights in the CMBR spectrum, indicating the magnitude of overdense regions. A small fraction of CMB is polarized, meaning that it vibrates in a preferred direction. The polarization is due to the last scattering of photon by an electron and this polarization is in the direction of the motion of that electron. But substantial polarization of CMBR photons demands an anisotropic distribution of photons that scatter off electrons on the last scat-

tering surface. Since the couplings between the electrons and photons are strong before the last scattering, these lead to an approximately isotropic distribution of photons before the recombination. Therefore, the CMBR photons are only weakly polarized. This is due to small but finite photon diffusion caused by small quadrupole moment. The so called E mode polarization in CMBR is due to scalar perturbations (inhomogeneities) at linear order. In this kind of polarization the inhomogeneities that give rise to such anisotropies produce the polarization in the same direction as the wave propagates. Several satellite borne observations of these fluctuations or anisotropies in CMBR (namely Wilkinson Microwave Anisotropy Probe (WMAP) and PLANCK) and rigorous analyses of data have now established the presence of unknown matter or DM which are not made up of known particles or matters in the Universe. Estimates of the energy-mass content of the Universe from these observations also reveal that the matter content of the Universe is about 31.7% out of which only about a paltry amount of 4.9% accounts for all the known particles and matters with which this trillions of stars, galaxies and all other known entities are made up of and these known matters are generally referred as "baryonic matter". The rest about 26.8% of matter is completely of unknown nature with no interaction with photons (and hence are not visible) and perhaps having no or very weak interactions with other particles and this unknown matter is termed as DM. The remaining 68.3% is filled up with unknown energy entitled as dark energy and is attributed to the recent speeding up of the expansion rate of the Universe.

The existence of this unknown matter in galaxies, clusters of galaxies and beyond are known even earlier. The fact that the estimation of mass based on the gravitational effect always far supersedes the estimation of mass from the measurements based on the light or EM radiation from the luminous objects indicates the presence of unseen matter. The gravitational mass can be estimated by the motion or velocity of stars in a galaxy or in a

galaxy cluster as they move in the gravitational potential of these objects. They are also estimated by gravitational lensing effects whereby light from a background object bends due to the gravity of a foreground object much the same way as an optical lens works and this phenomenon produces distorted or multiple images of the background object. From these measurements it is also established now that a galaxy or a galaxy cluster is embedded in a huge halo of DM.

The particle constituents of DM cannot overwhelmingly be the known fundamental particles since in that case they would have "seen" or detected by now. Since they are not visible and hence has no EM interaction, they must be neutral particles and they should be stable enough for not being decayed into known particles in which event too they would have been detected by now. This is evident that the DM particles are not SM particles. Neutrinos however could be a DM candidate among SM particles but their relic densities are far low to account for the 26.8% of DM in the Universe. There could be other astrophysical objects such as black holes, MACHOS (Massive Astrophysical Halo Objects) or other baryonic DM but they are way off the total amount of DM present in the Universe. Therefore for a viable DM particle theory one needs a BSM theory. A particle DM candidate can be theoretically proposed the framework of the established BSM theories such as supersymmetry (SUSY), theory of extra dimension or little Higgs but the signatures of none of these BSM theories have so far been established by Large Hadron Collider (LHC) or other accelerator experiments. Viable particle DM candidates can also be proposed by simple extension of the SM such as by extending the SM by a singlet or doublet or some other particle. Then applying suitable symmetries, discrete or other, the stability of DM candidate can be ensured by the Higgs portal models for particle DM.

Any attempt to detect the DM through their direct impact with a detection material did not yield any positive results although there are continuing rigorous experimental endeav-

ours such as LUX, XENON100, CDMS, CoGeNT, DAMA etc. But there are cosmological observational results of γ-ray excess around an energy region of 1-3 GeV from Galactic Centre (GC), an X-ray line of energy 3.55 keV from several galaxies including Andromeda and other such excesses which cannot be explained by known astrophysical phenomena and could well be indirect signatures for DM. As such DM being relic particles decoupled from the soup of the Universe will not undergo pair annihilation but if they are trapped in considerable numbers over a long period, inside a massive gravitating body such as GC then they can again undergo pair annihilation process and produce the known particles like γ-rays, fermion-antifermion pairs such as $e^+e^-, p\bar{p}, \nu\bar{\nu}$ etc. The γ-ray excess from GC has been reported by Fermi-LAT, which is a ground based experiment and also by several earthbound experiments namely HESS, MAGIC etc. could have DM origin. A substantial searches are being taken into account for the detection of antiparticles in the Universe at some satellite borne experiments like PAMELA, AMS etc. and these experiments detect an excess of positrons at positron energy beyond 10 GeV and the ratio $\left(\frac{e^+}{e^+ + e^-}\right)$ of positrons to positrons + electrons appears at positron energy of around 350 GeV. Neutrino detectors auch as IceCube (a 1 Km^2 detector within the South Pole ice in Antarctica designed to detect neutrinos from very high energetic astrophysical sources like exploding stars, GRBs, AGN etc.) and ANTARES (located under the Mediterranean sea) are meant to observe the neutrino fluxes from the cosmic origin. Also recent observations on collisions of several galaxy clusters where the luminous matter in those clusters suffers distortion and offset while the surrounding halos of DM pass through almost unscathed, surprisingly reveal that the DM have "self interactions" which means they can scatter among themselves and these observations produce an upper bound to these too. It appears that in order to explain all these results, a single type of DM particle may not be suffice and one needs perhaps a multicomponent DM. Therefore new theories are to be formulated to predict

new particles which are not the known basic fundamental particles governed by the SM of particle physics such as the charged particles like electrons, muons, tauons, the six types of quarks etc.

CHAPTER 2

STANDARD MODEL BASICS

The fundamental building blocks of nature known so far that constitute only about 4.9% of the content of the Universe (also referred to as visible matter) consist of fermionic fundamental particles that include six types of quarks and six types of leptons, twelve vector bosons (also known as gauge bosons) responsible for mediating the three fundamental interactions of nature namely strong, weak and electromagnetic (EM) and a neutral scalar boson with spin 0 namely Higgs boson. Out of the twelve gauge bosons, the gluons which are eight of them and the photon, responsible for mediating strong and EM interactions respectively are massless gauge bosons and do not carry any electric charge while the remaining three gauge bosons namely $W^{\pm}$ and Z are massive. While W is charged gauge boson carrying both positive and negative electric charges, Z is neutral. These three bosons get their masses by spontaneous breaking of electroweak symmetry (that unifies weak and EM forces) via Higgs mechanism whereby weak and EM forces are separated in nature.

The Higgs boson however is responsible for the fermionic fundamental particles to acquire their bare masses through the latter's interaction with Higgs boson. The theory of

Standard Model (SM) which is basically a perturbative field theory can well explain the behaviour of the known fundamental particles although how one type of leptons namely neutrinos get their masses, cannot be explained within the framework of SM of particle physics. There are other drawbacks of SM though, such as it has no explanation regarding the dark matter (DM) phenomena or the particle nature of DM, the problem of hierarchy of mass in lepton and quark family, the naturalness problem etc. However, the theory of SM has remained enormously successful in explaining most of the experimental results related to particle physics to the level of high precision.

Any theory of elementary particles should be consistent with the principles of special relativity. The combinations of special relativity, quantum mechanics and electromagnetism lead to the Dirac equations that describe the motion of the charged fermions. Dirac equation correctly predicts the existence of antiparticle of same mass and spin but of opposite charge for each massive charged fermion. One obtains quantum electrodynamics (QED) that basically describes the interactions of electrons with EM field, by quantizing the Dirac field. The SM is a theory of interacting fields and is developed by the principles of mathematical symmetries provided by the group theories. The connection between the symmetries and particle physics can be envisaged by Noether's theorem which states that for every continuous symmetry there is a corresponding conservation law. Such symmetries and breaking of symmetries are at the root of the theory of SM.

The SM is a theory of fields. This field theory is 'local', which means that there is no action at a distance. This is very crucial for the theory of SM. Other than the scalar and the vector fields there is a new kind of field called the spinor field which follows the solution of the Dirac equation. The scalar field can be represented by the Klein-Gordan Lagrangian

density

$$\mathcal{L} = \frac{1}{2}[g^{\mu\nu}\partial_\mu\phi\partial_\nu\phi - m^2\phi^2] = \frac{1}{2}[\partial_\mu\phi\partial^\mu\phi - m^2\phi^2] \ . \tag{2.1}$$

The field equation is obtained from Euler-Lagrange equation

$$\frac{\partial\mathcal{L}}{\partial\phi} - \partial_\mu\left(\frac{\partial\mathcal{L}}{\partial(\partial_\mu\phi)}\right) \ = \ 0 \tag{2.2}$$

as

$$(\partial_\mu\partial^\mu + m^2)\phi \ = \ 0 \ . \tag{2.3}$$

The general solution of the above equation is given as

$$\phi(\vec{r},t) \ = \ \frac{1}{\sqrt{V}}\sum_K\left(\frac{a_K}{\sqrt{2w_K}}e^{i(\vec{K}\cdot\vec{r}-wt)} + \frac{a_K^*}{\sqrt{2w_K}}e^{-i(\vec{K}\cdot\vec{r}-wt)}\right) \ , \tag{2.4}$$

where V represents the volume and a_K is the complex wave amplitude. The Lagrangian density of the massive vector field can be written as

$$\mathcal{L} \ = \ -\frac{1}{4}F_{\mu\nu}F^{\mu\nu} + \frac{1}{2}m^2A_\mu A^\mu - j^\mu A_\mu \ , \tag{2.5}$$

where $F_{\mu\nu}$ is the field tensor, A_μ represents the vector field and j_μ is the current. The field equation follows as

$$\partial_\mu F^{\mu\nu} + m^2A^\nu \ = \ j^\nu \ . \tag{2.6}$$

But since $\partial_\nu \partial_\mu F^{\mu\nu} = 0$, one obtains

$$m^2 \partial_\nu A^\nu \;\; = \;\; \partial_\nu j^\nu \; . \tag{2.7}$$

The above equation (Eq. 2.7) is a consequence of the field equation [1]. On solving the field equation

$$\frac{\partial^2 A^\nu}{\partial t^2} - \nabla^2 A^\nu + m^2 A^\nu \;\; = \;\; 0 \; , \tag{2.8}$$

a particle of mass m with a four component field is obtained out of which three components are independent.

The spinors on the other hand follow from the solution of the Dirac equation as four component Dirac field. They come as a pair of two component fields. In other words, two component complex quantities, that transform under Lorentz transformation as

$$\psi'_L(x') = \mathcal{M}\psi_L(x) \; , \;\; \psi'_R(x') = \mathcal{N}\psi_R(x) \; , \tag{2.9}$$

are called the left handed and right handed spinors repectively. In the above $\mathcal{M}$ and $\mathcal{N}$ are two 2×2 matrices with determinant 1, which follows the property

$$\mathcal{M}^\dagger \tilde{\sigma}^\nu \mathcal{M} \;\; = \;\; L^\nu_\mu \tilde{\sigma}^\mu \; , \tag{2.10}$$

$$\mathcal{N}^\dagger \sigma^\nu \mathcal{N} \;\; = \;\; L^\nu_\mu \sigma^\mu \; , \tag{2.11}$$

where σ^0 is a 2×2 unit matrix, $\sigma^i (i = 1, 2, 3)$ are three Pauli matrices and $\sigma^\nu = (\sigma^0, \sigma^1, \sigma^2, \sigma^3)$, $\tilde{\sigma}^\nu = (\sigma^0, -\sigma^1, -\sigma^2, -\sigma^3)$. The matrices $\mathcal{M}$ and $\mathcal{N}$ are related by $\mathcal{M}^\dagger \mathcal{N} = \mathcal{N}^\dagger \mathcal{M} = 1$.

[1] This implies that the field A_ν is not independent in contrast to the Lorentz gauge condition $\partial_\mu A_\mu = 0$ (gauge fixing condition).

In the above L^{ν}_{μ} is a proper Lorentz transformation. The transformations in Eq. 2.9 ensure that the spinor field equations take the same form in every inertial frame. This four component Dirac fields or Dirac spinors can also be combined in pairs. Such combinations can give rise to scalars ($(\psi_L^\dagger \psi_R + \psi_R^\dagger \psi_L)$, a Lorentz invariant quantity), pseudo scalar ($(\psi_L^\dagger \psi_R - \psi_R^\dagger \psi_L)$, Lorentz invariant but changes sign under space inversion), four vector ($(\psi_L^\dagger \sigma^\mu \psi_L + \psi_R^\dagger \sigma^\mu \psi_R)$, changes sign under space inversion) and axial four vector ($(\psi_L^\dagger \sigma^\mu \psi_L - \psi_R^\dagger \sigma^\mu \psi_R)$, does not change sign under space inversion). In fact using Dirac γ matrices one can construct sixteen set of linearly independent combinations for Dirac spinors, which are $\bar{\psi}\psi$ (components-1, scalar), $\bar{\psi}\gamma^\mu\psi$ (components-4, vector), $\bar{\psi}\sigma^{\mu\nu}\psi$ (components-6, tensor), $\bar{\psi}\gamma^5\psi$ (components-1, pseudo scalar), $\bar{\psi}\gamma^5\gamma^\mu\psi$ (components-4, axial vector), where $\sigma^{\mu\nu} = \dfrac{i}{2}(\gamma^\mu\gamma^\nu - \gamma^\nu\gamma^\mu)$. Here $\bar{\psi} = \psi^\dagger\gamma^0$ and γ^μ are the Dirac γ matrices. The matrix γ^5 is associated with the projection operators $P_L = \dfrac{1-\gamma^5}{2}$ and $P_R = \dfrac{1+\gamma^5}{2}$ such that $P_L\psi = \psi_L$ and $P_R\psi = \psi_R$ (projects out left or right handed components of the spinor ψ).

The SM can be attributed to a theory that provides a unified framework to describe three of the fundamental forces of nature namely, EM, weak and strong forces. However, here we will mainly restrict to the electroweak sector (unified EM and weak forces or interactions (electroweak interaction)) of the SM and the separation of EM and weak forces following the spontaneous breaking of electroweak symmetry by the process of Higgs mechanism.

The theory of unification of EM and weak forces are proposed by Sheldon Glashow [1], Abdus Salam [2] and Steven Weinberg [3]. The Glashow-Weinberg-Salam (GWS) theory of electroweak interaction of the SM is based on the local invariance of gauge symmetry inspired by the symmetry of the group $\mathrm{SU}(2)_L \times \mathrm{U}(1)_Y$. Here '$L$' represents the left chirality while 'Y' denotes weak hypercharge. One recognises that the theory of QED is a gauge theory based on U(1) group.

Here we consider a manifestly covariant formulation of QED in Lagrangian density approach. In electrodynamics the potential is given as $A^\mu = (\phi, \vec{A})$. A Lorentz covariant term with the covariant derivative operator ∂_μ and A^μ can be obtained as $F_{\mu\nu} = \partial_\mu A_\nu - \partial_\nu A_\mu$. The quantity $F_{\mu\nu}$ is antisymmetric, i.e. $F_{\mu\nu} = -F_{\nu\mu}$, which implies that $F_{00} = -F_{00}$. This means all the diagonal elements of $F_{\mu\nu}$ tensor are zero. It can be easily checked that $F_{01} = E_x, F_{12} = -B_z$ etc. ($F_{\mu\nu}$ contains only $\vec{E}$ and $\vec{B}$). Therefore the EM interaction Lagrangian is constructed by contracting $F^{\mu\nu}$ and $F_{\mu\nu}$ as

$$\mathcal{L}_{\rm EM} \;=\; -\frac{1}{4} F_{\mu\nu} F^{\mu\nu} \;, \tag{2.12}$$

where $-\frac{1}{4}$ is an appropriate constant related to the units ($\mathcal{L}$ is scalar). Now the Dirac Lagrangian ($\mathcal{L}_{\rm Dirac}$) is given by

$$\mathcal{L}_{\rm Dirac} \;=\; \bar{\psi}(i\gamma^\mu \partial_\mu - m)\psi \;. \tag{2.13}$$

One can easily identify that it has a global U(1) symmetry in the sense that under the transformation $\psi(x) \rightarrow e^{i\alpha}\psi(x)$ (α is independent of space time; global U(1) transformation) the Dirac Lagrangian remains invariant. Hence there exists a conserved current given by

$$j^\mu \;=\; -e\bar{\psi}\gamma^\mu\psi \;, \tag{2.14}$$

where e is the electronic charge. The interaction Lagrangian for the EM field is therefore

$$\mathcal{L}_{\rm int} \;=\; -j^\mu A_\mu \;. \tag{2.15}$$

Thus the QED Lagrangian takes the form

$$\begin{aligned}\mathcal{L}(\psi, A) &= \mathcal{L}_{\rm EM} + \mathcal{L}_{\rm Dirac} + \mathcal{L}_{\rm int} \ , &(2.16)\\ &= -\frac{1}{4}F_{\mu\nu}F^{\mu\nu} + \bar{\psi}(i\gamma^{\mu}\partial_{\mu} - m)\psi - j^{\mu}A_{\mu} \ . &(2.17)\end{aligned}$$

Substituting Eq. 2.14, Eq. 2.17 becomes

$$\mathcal{L}(\psi, A) = -\frac{1}{4}F_{\mu\nu}F^{\mu\nu} + \bar{\psi}(i\gamma^{\mu}\partial_{\mu} - m)\psi + e\bar{\psi}\gamma^{\mu}\psi A_{\mu} \ . \quad (2.18)$$

Now instead of global U(1) transformation it will be worthwhile to see how the Dirac Lagrangian and the EM Lagrangian behave under a local transformation given by $\psi'(x) \rightarrow e^{-i\alpha(x)}\psi(x)$, where $\alpha(x)$ is now dependent on the space time coordinate x. It is evident that the Dirac Lagrangian is not invariant under this U(1) phase transformation.

$$\begin{aligned}\mathcal{L}_{\rm Dirac}(\psi') &= \bar{\psi}'(i\gamma^{\mu}\partial_{\mu} - m)\psi' \ , \\ &= \bar{\psi}e^{i\alpha(x)}(i\gamma^{\mu}\partial_{\mu} - m)e^{-i\alpha(x)}\psi \ , \\ &= \bar{\psi}(i\gamma^{\mu}\partial_{\mu} - m)\psi + \bar{\psi}\gamma^{\mu}(\partial_{\mu}\alpha(x))\psi \ . &(2.19)\end{aligned}$$

Therefore the QED Lagrangian becomes

$$\mathcal{L}(\psi', A) = \mathcal{L}_{\rm Dirac}(\psi) + \mathcal{L}_{\rm EM}(A) + e\bar{\psi}\gamma^{\mu}\psi\left(A_{\mu} + \frac{1}{e}\partial_{\mu}\alpha(x)\right) \ . \quad (2.20)$$

The transformation $\psi' \rightarrow e^{-i\alpha(x)}\psi$ is not infact a gauge transformation, it is a U(1) phase transformation. A gauge transformation is to be incorporated when we replace A_{μ} by $A_{\mu} - \frac{1}{e}\partial_{\mu}\alpha(x)$, to keep the local QED Lagrangian invariant under local U(1) phase and

gauge transformation. After this gauge transformation,

$$\mathcal{L}(\psi', A') \;\; = \;\; \mathcal{L}(\psi, A) \; . \tag{2.21}$$

Now the Dirac Lagrangian and the interaction Lagrangian are written in terms of covariant derivative D_μ as

$$\mathcal{L}(\psi, A) = \bar{\psi} i\gamma^\mu \partial_\mu \psi + \bar{\psi} e \gamma^\mu A_\mu \psi = \bar{\psi} i \gamma^\mu D_\mu \psi \; . \tag{2.22}$$

In the above, the structure of D_μ will be

$$D_\mu \;\; = \;\; \partial_\mu - ieA_\mu \tag{2.23}$$

for the electrons and correspondingly

$$D_\mu \;\; = \;\; \partial_\mu + iQeA_\mu \; , \tag{2.24}$$

where a field of charge Qe is considered. The purpose is to write the Dirac Lagrangian with the EM interaction in manifestly covariant form. Therefore, under the local gauge transformation $\psi' \rightarrow e^{-i\alpha(x)}\psi$,

$$D_\mu \psi \rightarrow D'_\mu \psi' = e^{-i\alpha(x)} D_\mu \psi \tag{2.25}$$

provided we have a gauge transformation of A_μ as

$$A_\mu \longrightarrow A'_\mu = A_\mu - \left(\frac{1}{e}\right) \partial_\mu \alpha(x) \; . \tag{2.26}$$

By this construction, $\partial_\mu \alpha(x)$ term cancels and under the local phase transformation $D_\mu \psi$ does not generate any terms involving any derivatives. From Eq. 2.23, one easily sees that such a construction with gauge and phase invariance immediately gives rise to the interaction term $j^\mu A_\mu$. It can be easily noted that a Lie group transformation is given by $\psi \rightarrow e^{i\vec{G}\cdot\vec{\alpha}}\psi$, where $\vec{G}$ are the generator of the group while $\vec{\alpha}$ are the parameter of the group transformation. In this case of U(1) group, $e^{i\alpha}$ is a number, which may be associated with 1×1 unitary matrix. Considering the transformation for the field of charge Qe, i.e. $\psi' = e^{iQe\alpha(x)}\psi$, one identifies that in this case the charge is the generator of U(1) group in QED.

Now under the local gauge symmetry, A_μ is to be replaced by $A_\mu - \frac{1}{e}\partial_\mu \alpha(x)$. Therefore, under the gauge transformation, the mass terms of the Lagrangian in Eq. 2.5 is reduced to

$$m^2 A^\mu A_\mu \rightarrow m^2 \left(A^\mu - \frac{1}{e}\partial^\mu \alpha\right)\left(A_\mu - \frac{1}{e}\partial_\mu \alpha\right) \ , \tag{2.27}$$

which is not invariant as the extra terms related to $\partial^\mu \alpha(x)$ do not cancel. Thus the gauge particles are massless.

2.1 SU(2) Gauge Theory

The group SU(2) consists of a set of 2×2 unitary matrices, whose determinant is 1. Now U(2) symmetry can be written as

$$\mathrm{U}(2) \ = \ \mathrm{U}(1) \otimes \mathrm{SU}(2) \ . \tag{2.28}$$

This can be seen in the following way. A unitary matrix U can be expressed as

$$U = \exp(iH) \ , \tag{2.29}$$

where H is a Hermitian matrix, $H = H^\dagger$ and H has the same order as U. Now a 2×2 Hermitian matrix can be expressed as

$$H = \theta \mathbf{1} + \tau_a \alpha_a \ , \tag{2.30}$$

where $\mathbf{1}$ is the 2×2 unit matrix and $\tau_a (a = 1, 2, 3)$ are the three Pauli spin matrices. Thus

$$\begin{aligned} U &= \exp[i(\theta \mathbf{1} + \tau_a \alpha_a)] \ , \\ &= \exp(i\theta) \exp(i\tau_a \alpha_a) \ , \end{aligned} \tag{2.31}$$

where $\exp(i\theta)$ corresponds to the global U(1) transformation of Dirac Lagrangian and has been already explored. The matrix $\exp(i\tau_a \alpha_a)$ has a determinant 1 and it belongs to the group SU(2). The free Lagrangian $\mathcal{L}$ has a SU(2) global symmetry along with the U(1) global symmetry.

Symmetry of 2 Dirac particles of same mass: Yang-Mills Theory

The Lagrangian of two Dirac particles of masses m_1 and m_2 respectively, is given by

$$\begin{aligned} \mathcal{L} &= \bar{\psi}_1 (i\gamma^\mu \partial_\mu - m_1)\psi_1 + \bar{\psi}_2 (i\gamma^\mu \partial_\mu - m_2)\psi_2 \ , \\ &= \begin{pmatrix} \bar{\psi}_1 & \bar{\psi}_2 \end{pmatrix} \left[(i\gamma^\mu \partial_\mu) \begin{pmatrix} 1 & 0 \\ 0 & 1 \end{pmatrix} - \begin{pmatrix} m_1 & 0 \\ 0 & m_2 \end{pmatrix} \right] \begin{pmatrix} \psi_1 \\ \psi_2 \end{pmatrix} \ . \end{aligned} \tag{2.32}$$

This Lagrangian has a global U(2) symmetry only when $m_1 = m_2 = m$ and we write the Lagrangian in that case as

$$\begin{aligned} \mathcal{L} &= \begin{pmatrix} \bar{\psi}_1 & \bar{\psi}_2 \end{pmatrix} (i\gamma^\mu \partial_\mu - m) \begin{pmatrix} \psi_1 \\ \psi_2 \end{pmatrix} , \\ &= \bar{\Psi}(i\gamma^\mu \partial_\mu - m)\Psi , \end{aligned} \tag{2.33}$$

where $\Psi \equiv \begin{pmatrix} \psi_1 \\ \psi_2 \end{pmatrix}, \bar{\Psi} \equiv \begin{pmatrix} \bar{\psi}_1 & \bar{\psi}_2 \end{pmatrix}$. As stated above this Lagrangian is symmetric under the global U(2) transformation

$$\Psi \rightarrow \Psi' = U\Psi , \tag{2.34}$$

where U is a 2×2 unitary matrix ($UU^\dagger = U^\dagger U = 1$). As U(2) = U(1) $\otimes$ SU(2), the U(2) symmetry of the Lagrangian in Eq. 2.33 represents two fundamental symmetries of the Lagrangian - one is the U(1) symmetry originating because of particular form of Dirac Lagrangian of a single field and the other is the SU(2) symmetry owing to the fact that the field content in the Lagrangian is of two Dirac fields of equal masses. The U(1) symmetry has already been studied. Let us explore the physics arising out of the SU(2) symmetry of the Lagrangian. For this we take the field transformation which keeps the Lagrangian invariant as the following global SU(2) transformation

$$\Psi \rightarrow \Psi' = S\Psi , \tag{2.35}$$

where S is an element of the group of SU(2) matrices and therefore we can parameterize it by

$$S = \exp\left(i\sum_{a=1}^{3}\alpha_a\frac{\tau_a}{2}\right) , \tag{2.36}$$

where $\alpha_1, \alpha_2, \alpha_3$ are independent parameters which are space-time independent as long as the transformation considered is global and as we mentioned earlier τ_1, τ_2, τ_3 are Pauli matrices.

It is to be noted that the Lagrangian in Eq. 2.33 is not symmetric under the local SU(2) gauge transformation i.e. when α's and hence S becomes a function of space-time. For this we check how the Lagrangian in Eq. 2.33 transforms under the following local SU(2) transformation

$$\Psi \to \Psi' = S\Psi \quad \text{where} \quad S = \exp\left(i\sum_{a=1}^{3}\alpha_a(x)\frac{\tau_a}{2}\right) . \tag{2.37}$$

Transformation of $\bar{\Psi}(i\gamma^\mu\partial_\mu)\Psi$ and $m\bar{\Psi}\Psi$ under the transformation Eq. 2.37

$$\begin{aligned}
\bar{\Psi}(i\gamma^\mu\partial_\mu)\Psi \longrightarrow \bar{\Psi}'(i\gamma^\mu\partial_\mu)\Psi' &= \bar{\Psi}S^{-1}(i\gamma^\mu\partial_\mu)(S\Psi) , \\
&= \bar{\Psi}S^{-1}i\gamma^\mu(S(\partial_\mu\Psi) + (\partial_\mu S)\Psi) , \\
&= \bar{\Psi}S^{-1}Si\gamma^\mu\partial_\mu\Psi + i\bar{\Psi}\gamma^\mu S^{-1}(\partial_\mu S)\Psi , \\
&= \bar{\Psi}(i\gamma^\mu\partial_\mu)\Psi + i\bar{\Psi}\gamma^\mu S^{-1}(\partial_\mu S)\Psi .
\end{aligned} \tag{2.38}$$

$$
\begin{aligned}
m\bar{\Psi}\Psi \longrightarrow m\bar{\Psi}'\Psi' &= m\bar{\Psi}S^{-1}S\Psi \ , \\
&= m\bar{\Psi}\Psi \ . \qquad (2.39)
\end{aligned}
$$

Therefore under local SU(2) transformation, the Lagrangian transforms as

$$
\mathcal{L} \longrightarrow \mathcal{L} + i\bar{\Psi}\gamma^{\mu}S^{-1}(\partial_{\mu}S)\Psi = \mathcal{L} + i\bar{\Psi}\gamma^{\mu}\exp\left(\sum_{a=1}^{3} -i\alpha_a\frac{\tau_a}{2}\right)\left[\partial_{\mu}\exp\left(\sum_{b=1}^{3} i\alpha_b\frac{\tau_b}{2}\right)\right]\Psi \ . \qquad (2.40)
$$

We see that due to local SU(2) transformation of the fields, the original Lagrangian changes by an amount which is a function of three mutually independent functions $\alpha_1(x), \alpha_2(x), \alpha_3(x)$. So in order to construct the local symmetric Lagrangian out of the original one, we have to incorporate at least three independent fields with proper transformations such that the symmetry breaking term in Eq. 2.40 is absorbed by the transformation of the newly added term in the Lagrangian. The local gauge invariant Lagrangian is formulated in the following way. A covariant derivative D_{μ} is to be obtained such that the Lagrangian $\mathcal{L}_{\mathbf{loc}} = \bar{\Psi}(i\gamma^{\mu}D_{\mu} - m)\Psi$ is invariant under local transformation $\Psi \longrightarrow S\Psi$. For this it requires that $D_{\mu}\Psi$ should transform the same way as Ψ transforms under $\Psi \longrightarrow \Psi' = S\Psi$,

$$
(D_{\mu}\Psi) \longrightarrow (D'_{\mu}\Psi') = S(D_{\mu}\Psi) \ . \qquad (2.41)
$$

Now D_{μ} is to be written in the form $D_{\mu} = \partial_{\mu} + ()_{\mu}$ so that the quantity $()_{\mu}$ with a Lorentz index μ should transform in a way so as to cancel the term $i\bar{\Psi}\gamma^{\mu}S^{-1}(\partial_{\mu}S)\Psi$ arising from local phase transformation of the term $\bar{\Psi}i\gamma^{\mu}\partial_{\mu}\Psi$. Therefore it should contain at least 3

vector fields, say, $W^1_\mu, W^2_\mu, W^3_\mu$. We then choose to write $()_\mu = ig\frac{\tau_a}{2}W^a_\mu$ so that

$$D_\mu \equiv \partial_\mu + ig\frac{\tau_a}{2}W^a_\mu \ . \tag{2.42}$$

Therefore $(D'_\mu\Psi') \longrightarrow S(D_\mu\Psi)$ requires

$$\begin{aligned}
\partial_\mu(S\Psi) + ig\frac{\tau_a}{2}(W^a_\mu)'(S\Psi) &= S(\partial_\mu\Psi) + igS(\frac{\tau_a}{2}W^a_\mu\Psi) \ , \\
ig\frac{\tau_a}{2}(W^a_\mu)'(S\Psi) &= igS\frac{\tau_a}{2}W^a_\mu\Psi - (\partial_\mu S)\Psi \ , \\
ig\frac{\tau_a}{2}(W^a_\mu)'(S\Psi) &= igS\frac{\tau_a}{2}W^a_\mu S^{-1}(S\Psi) - (\partial_\mu S)S^{-1}(S\Psi) \ , \\
\frac{\tau_a}{2}(W^a_\mu)' &= S\left(\frac{\tau_a}{2}W^a_\mu\right)S^{-1} + \frac{i}{g}(\partial_\mu S)S^{-1} \ , \\
\left(\frac{\vec{\tau}}{2}\cdot\overrightarrow{W'_\mu}\right) &= S\left(\frac{\vec{\tau}}{2}\cdot\overrightarrow{W_\mu}\right)S^{-1} + \frac{i}{g}(\partial_\mu S)S^{-1} \ ,
\end{aligned} \tag{2.43}$$

where $\vec{\tau} = (\tau_1, \tau_2, \tau_3); \overrightarrow{W_\mu} = (W^1_\mu, W^2_\mu, W^3_\mu)$. Let us choose all of them to be infinitesimal. Therefore

$$S = \exp\left(i\frac{\vec{\tau}}{2}\cdot\vec{\alpha}\right) \approx 1 + i\frac{\vec{\tau}}{2}\cdot\vec{\alpha} \ , \tag{2.44}$$

$$S^{-1} = \exp\left(-i\frac{\vec{\tau}}{2}\cdot\vec{\alpha}\right) \approx 1 - i\frac{\vec{\tau}}{2}\cdot\vec{\alpha} \ , \tag{2.45}$$

$$(\partial_\mu S) \approx i\frac{\vec{\tau}}{2}\cdot(\partial_\mu\vec{\alpha}) \ , \tag{2.46}$$

where $\vec{\alpha} = (\alpha_1, \alpha_2, \alpha_3)$. Then using Eqs. 2.44 - 2.46 in Eq. 2.43 gives

$$\begin{aligned}
\left(\frac{\tau}{2}\cdot\overrightarrow{W'_\mu}\right) &\approx \left(1+i\frac{\vec{\tau}}{2}\cdot\vec{\alpha}\right)\left(\frac{\vec{\tau}}{2}\cdot\overrightarrow{W_\mu}\right)\left(1-i\frac{\vec{\tau}}{2}\cdot\vec{\alpha}\right)+\frac{i}{g}\cdot i\left[\frac{\vec{\tau}}{2}\cdot(\partial_\mu\vec{\alpha})\right]\left(1-i\frac{\vec{\tau}}{2}\cdot\vec{\alpha}\right) \ , \\
&\approx \left(\frac{\vec{\tau}}{2}\cdot\overrightarrow{W_\mu}\right)+i\left[\left(\frac{\vec{\tau}}{2}\cdot\vec{\alpha}\right),\left(\frac{\vec{\tau}}{2}\cdot\overrightarrow{W_\mu}\right)\right]_- -\frac{1}{g}\frac{\vec{\tau}}{2}\cdot(\partial_\mu\vec{\alpha})+O(\alpha^2) \ , \\
&\approx \left(\frac{\vec{\tau}}{2}\cdot\overrightarrow{W_\mu}\right)+i\left[\left(\frac{\vec{\tau}}{2}\cdot\vec{\alpha}\right),\left(\frac{\vec{\tau}}{2}\cdot\overrightarrow{W_\mu}\right)\right]_- -\frac{1}{g}\frac{\vec{\tau}}{2}\cdot(\partial_\mu\vec{\alpha}) \ . \qquad (2.47)
\end{aligned}$$

The above commutation form can be achieved in the following way. We know for non-Abelian Lie group, the generators follow the commutation relations

$$\left[\frac{\vec{\tau_a}}{2},\frac{\vec{\tau_b}}{2}\right] = if_{abc}\frac{\vec{\tau_c}}{2};\ (f_{abc} = \text{structure constants}) \ . \qquad (2.48)$$

Now,

$$\begin{aligned}
\left[\left(\frac{\vec{\tau}}{2}\cdot\vec{\alpha}\right),\left(\frac{\vec{\tau}}{2}\cdot\overrightarrow{W_\mu}\right)\right]_- &= \left[\frac{\vec{\tau_b}}{2}\alpha^b,\frac{\vec{\tau_c}}{2}W_\mu^c\right]_- \ (\text{Einstein's summation convension implied}) \\
&= \alpha^b W_\mu^c\left[\frac{\vec{\tau_b}}{2},\frac{\vec{\tau_c}}{2}\right]_- \ (\text{commutator is distributive}) \\
&= if_{abc}\alpha^b W_\mu^c\frac{\vec{\tau_a}}{2} \ , \qquad (2.49)
\end{aligned}$$

where f_{abc} is antisymmetric under interchange of any pair of indices. Therefore, using Eq. 2.49 in Eq. 2.47 gives

$$\begin{aligned}
\left(\frac{\vec{\tau}}{2}\cdot\overrightarrow{W'_\mu}\right) &\approx \left(\frac{\vec{\tau}}{2}\cdot\overrightarrow{W_\mu}\right) + i\cdot i f_{abc}\alpha^b W_\mu^c\frac{\tau_a}{2} - \frac{1}{g}\frac{\vec{\tau}}{2}\cdot(\partial_\mu\vec{\alpha}) \ , \\
\frac{\tau_a}{2}W'^a_\mu &\approx \frac{\tau_a}{2}W^a_\mu - f_{bca}\alpha^b W_\mu^c\frac{\tau_a}{2} - \frac{1}{g}\frac{\tau_a}{2}(\partial_\mu\alpha^a) \ , \\
W'^a_\mu &\approx W^a_\mu - \frac{1}{g}(\partial_\mu\alpha^a) - f_{bca}\alpha^b W^c_\mu \ , \\
W'^a_\mu &\approx W^a_\mu - \frac{1}{g}(\partial_\mu\alpha^a) - \epsilon_{abc}\alpha^b W^c_\mu \ . \qquad (2.50)
\end{aligned}$$

Since $f_{abc} = f_{bca}$ and we replace f_{abc} by the Levicivita symbol ϵ_{abc} in the last step of Eq. 2.50. Therefore, the Lagrangian

$$\begin{aligned}
\mathcal{L}_{\rm loc} = \bar{\Psi}(i\gamma^\mu D_\mu - m)\Psi &= \bar{\Psi}\left[i\gamma^\mu(\partial_\mu + ig\frac{\tau_a}{2}W^a_\mu) - m\right]\Psi \\
&= \bar{\Psi}(i\gamma^\mu\partial_\mu - m)\Psi - g(\bar{\Psi}\gamma^\mu\frac{\tau_a}{2}\Psi)W^a_\mu \qquad (2.51)
\end{aligned}$$

is invariant under the local SU(2) gauge transformation

$$\begin{aligned}
\Psi(x) &\longrightarrow \exp(i\frac{\tau_a}{2}\alpha^a(x))\Psi(x) \approx (1 + i\frac{\tau_a}{2}\alpha^a(x))\Psi(x) \ , \qquad (2.52) \\
W'^a_\mu &\longrightarrow W^a_\mu - \frac{1}{g}(\partial_\mu\alpha^a) - \epsilon_{abc}\alpha^b W^c_\mu \ . \qquad (2.53)
\end{aligned}$$

Similar to the discussions for QED one may also add a term of the type $W^{\mu\nu}W_{\mu\nu}$ but in this case $W^{\mu\nu}$ is to be so constructed in terms of W^μ such that the term $W^{\mu\nu}W_{\mu\nu}$ remains invariant under this (SU(2) gauge) transformation. In order to obtain an expression for $W^{\mu\nu}$ that satisfies these criteria, the following procedure is adopted. Using the relation

$$(\vec{A}\times\vec{B})^a = \epsilon_{abc}A^b B^c \ , \qquad (2.54)$$

the expression for W'^{a}_{μ} in Eq. 2.53 is written as

$$\begin{aligned}
\overrightarrow{W'_\mu} &= \overrightarrow{W_\mu} - \frac{1}{g}(\partial_\mu \vec{\alpha}) - (\vec{\alpha} \times \overrightarrow{W_\mu}) && (2.55)\\
(\partial_\mu \overrightarrow{W'_\nu} - \partial_\nu \overrightarrow{W'_\mu}) &= \partial_\mu \left(\overrightarrow{W_\nu} - \frac{1}{g}(\partial_\nu \vec{\alpha}) - (\vec{\alpha} \times \overrightarrow{W_\nu}) \right) \\
&\quad -\partial_\nu \left(\overrightarrow{W_\mu} - \frac{1}{g}(\partial_\mu \vec{\alpha}) - (\vec{\alpha} \times \overrightarrow{W_\mu}) \right) \\
&= (\partial_\mu \overrightarrow{W_\nu} - \partial_\nu \overrightarrow{W_\mu}) - \left[\partial_\mu (\vec{\alpha} \times \overrightarrow{W_\nu}) - \partial_\nu (\vec{\alpha} \times \overrightarrow{W_\mu}) \right] && (2.56)\\
\overrightarrow{W'_\mu} \times \overrightarrow{W'_\nu} &= \left(\overrightarrow{W_\mu} - \frac{1}{g}(\partial_\nu \vec{\alpha}) - (\vec{\alpha} \times \overrightarrow{W_\mu}) \right) \times \left(\overrightarrow{W_\nu} - \frac{1}{g}(\partial_\nu \vec{\alpha}) - (\vec{\alpha} \times \overrightarrow{W_\nu}) \right) \\
&= (\overrightarrow{W_\mu} \times \overrightarrow{W_\nu}) - \frac{1}{g} \left[(\partial_\mu \vec{\alpha}) \times \overrightarrow{W_\nu} + \overrightarrow{W_\mu} \times (\partial_\nu \vec{\alpha}) \right] \\
&\quad - \left[\overrightarrow{W_\mu} \times (\vec{\alpha} \times \overrightarrow{W_\nu}) + (\vec{\alpha} \times \overrightarrow{W_\mu}) \times \overrightarrow{W_\nu} \right] && (2.57)
\end{aligned}$$

$$\begin{aligned}
\left[(\partial_\mu \overrightarrow{W'_\nu} - \partial_\nu \overrightarrow{W'_\mu}) \right] - g(\overrightarrow{W'_\mu} \times \overrightarrow{W'_\nu}) &= \left[(\partial_\mu \overrightarrow{W_\nu} - \partial_\nu \overrightarrow{W_\mu}) - g(\overrightarrow{W_\mu} \times \overrightarrow{W_\nu}) \right] \\
&\quad - \left[\partial_\mu (\vec{\alpha} \times \overrightarrow{W_\nu}) - \partial_\nu (\vec{\alpha} \times \overrightarrow{W_\mu}) \right. \\
&\quad \left. -(\partial_\mu \vec{\alpha}) \times \overrightarrow{W_\nu} - \overrightarrow{W_\mu} \times (\partial_\nu \vec{\alpha}) \right] \\
&\quad + g \left[\overrightarrow{W_\mu} \times (\vec{\alpha} \times \overrightarrow{W_\nu}) + (\vec{\alpha} \times \overrightarrow{W_\mu}) \times \overrightarrow{W_\nu} \right] \\
&= \left[(\partial_\mu \overrightarrow{W_\nu} - \partial_\nu \overrightarrow{W_\mu}) - g(\overrightarrow{W_\mu} \times \overrightarrow{W_\nu}) \right] \\
&\quad - \vec{\alpha} \times (\partial_\mu \overrightarrow{W_\nu} - \partial_\nu \overrightarrow{W_\mu}) \\
&\quad + g \left[\overrightarrow{W_\mu} \times (\vec{\alpha} \times \overrightarrow{W_\nu}) + (\vec{\alpha} \times \overrightarrow{W_\mu}) \times \overrightarrow{W_\nu} \right] . \qquad (2.58)
\end{aligned}$$

In evaluating the RHS of the above expression (Eq. 2.58), we need to use the Jacobi identity which is derived as follow and the relation $(\vec{A} \times \vec{B})^a = \epsilon_{abc} A^b B^c$ (Eq. 2.54)

$$\begin{aligned}
\left[\frac{\tau_a}{2}, \left[\frac{\tau_b}{2}, \frac{\tau_c}{2}\right]_-\right]_- + \left[\frac{\tau_b}{2}, \left[\frac{\tau_c}{2}, \frac{\tau_a}{2}\right]_-\right]_- + \left[\frac{\tau_c}{2}, \left[\frac{\tau_a}{2}, \frac{\tau_b}{2}\right]_-\right]_- &= 0 \ , \qquad (2.59) \\
\left[\frac{\tau_a}{2}, i\epsilon_{bcp}\frac{\tau_p}{2}\right]_- + \left[\frac{\tau_b}{2}, i\epsilon_{cap}\frac{\tau_p}{2}\right]_- + \left[\frac{\tau_c}{2}, i\epsilon_{abp}\frac{\tau_p}{2}\right]_- &= 0 \ , \\
\epsilon_{bcp}\left[\frac{\tau_a}{2}, \frac{\tau_p}{2}\right]_- + \epsilon_{cap}\left[\frac{\tau_b}{2}, \frac{\tau_p}{2}\right]_- + \epsilon_{abp}\left[\frac{\tau_c}{2}, \frac{\tau_p}{2}\right]_- &= 0 \ , \\
\epsilon_{bcp} i\epsilon_{apq}\frac{\tau_q}{2} + \epsilon_{cap} i\epsilon_{bpq}\frac{\tau_q}{2} + \epsilon_{abp} i\epsilon_{cpq}\frac{\tau_q}{2} &= 0 \ , \\
\epsilon_{bcp}\epsilon_{apq} + \epsilon_{cap}\epsilon_{bpq} + \epsilon_{abp}\epsilon_{cpq} &= 0 \ , \qquad (2.60) \\
\epsilon_{bcp}\epsilon_{pqa} + \epsilon_{cap}\epsilon_{pqb} + \epsilon_{abp}\epsilon_{pqc} &= 0 \ . \qquad (2.61)
\end{aligned}$$

Now

$$\begin{aligned}
(\overrightarrow{W_\mu} \times (\vec{\alpha} \times \overrightarrow{W_\nu}))_a = \epsilon_{aqp} W_\mu^q (\vec{\alpha} \times \overrightarrow{W_\nu})^p = \epsilon_{aqp} W_\nu^q \epsilon_{pbc} \alpha^b W_\mu^c = \\
\epsilon_{aqp}\epsilon_{pbc}\alpha^b W_\mu^q W_\nu^c = -\epsilon_{bcp}\epsilon_{pqa}\alpha^b W_\mu^q W_\mu^c \qquad (2.62)
\end{aligned}$$

and

$$\begin{aligned}
((\vec{\alpha} \times \overrightarrow{W_\mu}) \times \overrightarrow{W_\nu})_a = -(\overrightarrow{W_\nu} \times (\vec{\alpha} \times \overrightarrow{W_\mu}))_a = -\epsilon_{acp} W_\nu^c (\vec{\alpha} \times \overrightarrow{W_\mu})^p = \\
-\epsilon_{acp} W_\nu^c \epsilon_{pbq} \alpha^b W_\mu^q = -\epsilon_{acp}\epsilon_{pbq}\alpha^b W_\mu^q W_\nu^c = -\epsilon_{cap}\epsilon_{pqb}\alpha^b W_\mu^q W_\nu^c \ . \qquad (2.63)
\end{aligned}$$

Therefore,

$$
\begin{aligned}
g\left[\overrightarrow{W_\mu}\times(\vec{\alpha}\times\overrightarrow{W_\nu})+(\vec{\alpha}\times\overrightarrow{W_\mu})\times\overrightarrow{W_\nu}\right]_a &= -g(\epsilon_{bcp}\epsilon_{pqa}+\epsilon_{cap}\epsilon_{pqb})\alpha^b W_\mu^q W_\nu^c \ , \\
&= g\epsilon_{abp}\epsilon_{pqc}\alpha^b W_\mu^q W_\nu^c \ , \text{ using Eq. 2.61} \\
&= g\epsilon_{abp}\alpha^b(\epsilon_{pqc}W_\mu^q W_\mu^c) \ , \\
&= g\epsilon_{abp}\alpha^b(\overrightarrow{W_\mu}\times\overrightarrow{W_\nu})^p \ , \\
&= g(\vec{\alpha}\times(\overrightarrow{W_\mu}\times\overrightarrow{W_\nu}))_a \ . \qquad (2.64)
\end{aligned}
$$

In all the above equations, use has been made of the relation given in Eq. 2.54. So from Eq. 2.58 we have

$$
\begin{aligned}
\left[(\partial_\mu\overrightarrow{W_\nu'}-\partial_\nu\overrightarrow{W_\mu'}\right]-g(\overrightarrow{W_\mu'}\times\overrightarrow{W_\nu'}) &= \left[(\partial_\mu\overrightarrow{W_\nu}-\partial_\nu\overrightarrow{W_\mu})-g(\overrightarrow{W_\mu}\times\overrightarrow{W_\nu})\right] \\
&\quad -\vec{\alpha}\times(\partial_\mu\overrightarrow{W_\nu}-\partial_\nu\overrightarrow{W_\mu})+g(\vec{\alpha}\times(\overrightarrow{W_\mu}\times\overrightarrow{W_\nu})) \ , \\
&= \left[(\partial_\mu\overrightarrow{W_\nu}-\partial_\nu\overrightarrow{W_\mu})-g(\overrightarrow{W_\mu}\times\overrightarrow{W_\nu})\right] \\
&\quad -\vec{\alpha}\times\left[(\partial_\mu\overrightarrow{W_\nu}-\partial_\nu\overrightarrow{W_\mu})-g(\overrightarrow{W_\mu}\times\overrightarrow{W_\nu})\right] \ . \qquad (2.65)
\end{aligned}
$$

Identifying

$$
\overrightarrow{W_{\mu\nu}} = \left[(\partial_\mu\overrightarrow{W_\nu}-\partial_\nu\overrightarrow{W_\mu})-g(\overrightarrow{W_\mu}\times\overrightarrow{W_\nu})\right] \ , \qquad (2.66)
$$

i.e.

$$
W_{\mu\nu}^a = \left[(\partial_\mu\overrightarrow{W_\nu}-\partial_\nu\overrightarrow{W_\mu})-g\epsilon_{abc}W_\mu^b W_\nu^c\right] \ . \qquad (2.67)
$$

We see from Eq. 2.65 that

$$\overrightarrow{W'_{\mu\nu}} = \overrightarrow{W_{\mu\nu}} - \vec{\alpha} \times \overrightarrow{W_{\mu\nu}} \ . \tag{2.68}$$

Now

$$\begin{aligned} \overrightarrow{W'^{\mu\nu}} \cdot \overrightarrow{W'_{\mu\nu}} &= (\overrightarrow{W^{\mu\nu}} - \vec{\alpha} \times \overrightarrow{W^{\mu\nu}}) \cdot (\overrightarrow{W_{\mu\nu}} - \vec{\alpha} \times \overrightarrow{W_{\mu\nu}}) \ , \\ &= \overrightarrow{W^{\mu\nu}} \cdot \overrightarrow{W_{\mu\nu}} - \overrightarrow{W^{\mu\nu}} \cdot (\vec{\alpha} \times \overrightarrow{W_{\mu\nu}}) - (\vec{\alpha} \times \overrightarrow{W^{\mu\nu}}) \cdot \overrightarrow{W_{\mu\nu}} \ , \\ &= \overrightarrow{W^{\mu\nu}} \cdot \overrightarrow{W_{\mu\nu}} \ . \end{aligned} \tag{2.69}$$

Eq. 2.69 is achieved by identifying $\overrightarrow{W^{\mu\nu}} \cdot (\vec{\alpha} \times \overrightarrow{W_{\mu\nu}}) = -(\vec{\alpha} \times \overrightarrow{W^{\mu\nu}}) \cdot \overrightarrow{W_{\mu\nu}}$. This can be shown in the following way

$$\begin{aligned} \overrightarrow{W^{\mu\nu}} \cdot (\vec{\alpha} \times \overrightarrow{W_{\mu\nu}}) = W_a^{\mu\nu} (\vec{\alpha} \times \overrightarrow{W_{\mu\nu}})^a = W_a^{\mu\nu} \epsilon_{abc} \alpha^b W_{\mu\nu}^c = \epsilon_{abc} \alpha^b W_a^{\mu\nu} W_{\mu\nu}^c = \\ -\epsilon_{cba} \alpha^b W_a^{\mu\nu} W_{\mu\nu}^c = (-\epsilon_{abc} \alpha^b W_c^{\mu\nu}) W_{\mu\nu}^a = -(\vec{\alpha} \times \overrightarrow{W^{\mu\nu}}) \cdot \overrightarrow{W_{\mu\nu}} \ . \end{aligned} \tag{2.70}$$

Therefore $\overrightarrow{W^{\mu\nu}} \cdot \overrightarrow{W_{\mu\nu}}$ remains invariant under the transformation (Eq. 2.53) and in Eqs. 2.66, 2.67, one expresses $W_{\mu\nu}$ in terms of W_μ. Therefore we can now construct the locally invariant Lagrangian as

$$\begin{aligned} \mathcal{L}_{\text{loc}} &= \bar{\Psi}(i\gamma^\mu \partial_\mu - m)\Psi - g\left(\bar{\psi}\gamma^\mu \frac{\tau_a}{2} \Psi\right) W_\mu^a - \frac{1}{4} W_{\mu\nu}^a W_a^{\mu\nu} \ , \\ &= \bar{\Psi}(i\gamma^\mu \partial_\mu - m)\Psi - g\left(\bar{\psi}\gamma^\mu \frac{\tau_a}{2} \Psi\right) W_\mu^a - \frac{1}{4} \left[(\partial_\mu W_\nu^a - \partial_\nu W_\mu^a) - g\epsilon_{abc} W_\mu^b W_\nu^c\right] \\ &\quad \left[(\partial^\mu W_a^\nu - \partial^\nu W_a^\mu) - g\epsilon_{abc} W_b^\mu W_c^\nu\right] \ . \end{aligned} \tag{2.71}$$

This Lagrangian is symmetric under the folowing local transformations

$$\bar{\Psi}(x) \longrightarrow \exp\left(i\frac{\tau_a}{2}\alpha_a(x)\right)\Psi(x) \approx \left(1+i\frac{\tau_a}{2}\alpha_a(x)\right)\Psi(x)\ , \tag{2.72}$$

$$W_\mu^a \longrightarrow W_\mu^a - \frac{1}{g}(\partial_\mu\alpha^a) - \epsilon_{abc}\alpha^b W_\mu^c\ . \tag{2.73}$$

This Lagrangian describes two equal mass Dirac fields in interaction with three massless vector gauge fields which have self interaction between themselves. The origin of this self interaction lies in the non-Abelian nature of the symmetry group (SU(2)). Note that the gauge fields are massless because of non-occurrence of terms quadratic in the gauge field. This is a consequence of local SU(2) invariance of the original Dirac Lagrangian of two massless fields. The Dirac fields in this case generate three currents

$$j_a^\mu = g\bar{\Psi}\gamma^\mu\frac{\tau_a}{2}\Psi\ , \tag{2.74}$$

which act as sources of gauge fields. The gauge Lagrangian is given by

$$\begin{aligned}\mathcal{L}_{\text{gauge}} &= -g\left(\bar{\Psi}\gamma^\mu\frac{\tau_a}{2}\Psi\right)W_\mu^a - \frac{1}{4}W_{\mu\nu}^a W_a^{\mu\nu}\ , \\ &= -j_a^\mu W_\mu^a - \frac{1}{4}W_{\mu\nu}^a W_a^{\mu\nu}\ .\end{aligned} \tag{2.75}$$

The implementations of the principle of local gauge invariance may be complicated at two points

1. the local transformation rule for gauge fields,

2. the expression for $W_a^{\mu\nu}$ in terms of W_a^μ.

Both complications originate from the fact that the symmetry group SU(2) is non-Abelian in nature (U(1) is Abelian) so that

$$W_{\mu\nu}W^{\mu\nu} = \left[(\partial_\mu W_\nu - \partial_\nu W_\mu) - g\epsilon_{abc}W_\mu W_\nu)\right]\left[(\partial^\mu W^\nu - \partial^\nu W^\mu) - g\epsilon_{abc}W^\mu W^\nu\right].$$

One can readily see that three and four gauge boson vertices appear for SU(2) gauge theories. In fact this is a feature in all non-Abelian gauge theories. This may be considered as a consequence of the fact that an invariant has to be obtained when the gauge fields are contracted with generators in the covariant derivatives. This means that the field must absorbs the term $\partial_\mu\alpha$. This process forms a non-trivial adjoint representation of the group with α playing the key role. If an invariant is to be produced from such a contraction, the gauge fields must form an adjoint representation of the group. Also since the group is non-Abelian, the generators form a non-trivial representation of the group and the generators do not commute. Therefore for non-Abelian gauge groups, (a) both the gauge fields and the generators must form adjoint representations of the gauge group and this means the gauge fields must possess group "charge", (b) the gauge fields can have three gauge particle interaction vertices as well as four gauge particle interaction vertices. This may also be seen that introduction of a mass term ($m^2\overrightarrow{W_\mu}\cdot\overrightarrow{W^\mu}$) destroys the local gauge symmetry. Therefore, as for the Abelian U(1) case (photon), SU(2) gauge fields are also massless.

Yang-Mills theory in its original form turned out to be of little use. After all, it starts from the premise that there exists two elementary spin $\frac{1}{2}$ particles of equal masses, and as far as we know there are no such pairs exist in nature. When non-Abelian gauge theory finally came into its own, it was in the context of colour (SU(3)) symmetry in strong interactions and weak isospin-hypercharge (SU(2) $\times$ U(1)) in the weak interactions.

2.2 $\mathrm{SU}(2)_L \times \mathrm{U}(1)_Y$ Electroweak Gauge Theory

The electroweak theory of Glashow-Weinberg-Salam, as stated earlier is based on the symmetry of the group $\mathrm{SU}(2)_L \times \mathrm{U}(1)_Y$, where L represents the left handedness and Y represents the hypercharge which will be illustrated shortly.

Indications may be obtained from the earlier discussion that QED is intimately related with the weak interaction. Similar to the QED interaction term which is $j^\mu A_\mu$, the weak interaction also can be described by $j^\mu_{\rm weak} W_\mu$. The structure of the weak current arises from the famous $(V-A)$ coupling, which is a parity violating interaction since the relative signs between V and A change under parity inversion. Here V and A represents vector $(\bar{\Psi}\gamma^\mu\Psi)$ and axial vector $(\bar{\Psi}\gamma^\mu\gamma_5\Psi)$ respectively. Thus the structure $j^\mu_{\rm weak}$ can be written in the form

$$\begin{aligned} j^\mu_{\rm weak} &= \frac{1}{2}\bar{\Psi}_A(\gamma^\mu - \gamma^\mu\gamma_5)\Psi_B \ , \\ &= \Psi^\dagger_A P_L \gamma^0\gamma^\mu P_L \Psi_B \ , \\ &= \bar{\Psi}_{AL}\gamma^\mu\Psi_{BL} \ . \end{aligned} \tag{2.76}$$

Therefore SU(2) weak interaction is operating on left handed particles. The theory must be explicitly mirror asymmetry. This asymmetry is realised by the fact that the left handed components of the fermion i.e. $\Psi_L = \frac{1}{2}(1-\gamma_5)\Psi$ form the weak isospin doublet of the $\mathrm{SU}(2)_L$ group. Thus the lepton sector are the three doublet families namely,

$$\begin{pmatrix} \nu_e \\ e^- \end{pmatrix}_L , \begin{pmatrix} \nu_\mu \\ \mu^- \end{pmatrix}_L , \begin{pmatrix} \nu_\tau \\ \tau^- \end{pmatrix}_L$$

and for the quarks

$$\begin{pmatrix} u \\ d \end{pmatrix}_L, \begin{pmatrix} c \\ s \end{pmatrix}_L, \begin{pmatrix} t \\ b \end{pmatrix}_L,$$

while the right handed components are SU(2)$_L$ singlets (weak isospin singlets) given by $\Psi_R = \frac{1}{2}(1+\gamma_5)\Psi$. These are

$$e_R^-, \mu_R^-, \tau_R^-, u_R, c_R, t_R, d_R, s_R, b_R.$$

Note that the neutrino singlets are absent. No right handed neutrinos are found in nature [2].

Since j^μ_{weak} is of the form $\bar{\Psi}_A \gamma^\mu \Psi_B$, which is similar to the form of EM current, the state A and state B with different values of electric charge can also interact mediated by the SU(2) gauge field W_μ. Since charge has to be conserved, therefore W_μ should also carry electric charge. The current j^μ_{weak} can be operative between leptons as also in quarks.

In SU(2) gauge theory, there is one neutral gauge boson W_3 appears in the covariant derivative term as $ig\frac{\tau_3}{2}W_3$ (=igI_3W_3, where I_3 is the isospin component). Since the isospin of a neutrino, $I_3 = \pm 1/2$, W_3 couples to neutrinos. But W_3 cannot be photon since neutrinos are neutral particles. In this context, it may be mentioned that, the weak interaction are of two types namely charged current (CC) and neutral current (NC) interactions. In the CC interaction, which is mediated by the charged gauge bosons $W^\pm$, fermion charge is changed. The NC interaction is mediated by the neutral component of the gauge boson where no charge exchanges take place. Therefore, a larger group is required to accommodate both weak and EM interactions in a single framework and this larger group is given by SU(2)$_L\times$ U(1). This group has two independent transformations namely the isorotation and independent U(1) rotation. It is already mentioned that the $(V-A)$ coupling is acting

[2]Therefore in GWS theory the neutrinos are massless.

Particle	Handedness	I_3	Y	Q
ν_L	Left	$\frac{1}{2}$	$-\frac{1}{2}$	0
ν_R	Right	0	0	0
e_L	Left	$-\frac{1}{2}$	$-\frac{1}{2}$	-1
e_R	Right	0	-1	-1
u_L	Left	$\frac{1}{2}$	$\frac{1}{6}$	$\frac{2}{3}$
u_R	Right	0	$\frac{2}{3}$	$\frac{2}{3}$
d_L	Left	$-\frac{1}{2}$	$\frac{1}{6}$	$-\frac{1}{3}$
d_R	Right	0	$-\frac{1}{3}$	$-\frac{1}{3}$

Table 2.1: The first generation of the lepton sector in SM.

only for the left handed particle operator, hence the subscript L is introduced for SU(2). Needless to mention that the EM interaction has no handedness. In this context, the electric charge is redefined as

$$Q \;=\; I_3 + \frac{Y}{2}\,, \tag{2.77}$$

where I_3 is the third component of the weak isospin and $\dfrac{Y}{2}$ is the generator of U(1), where Y is known as the weak hypercharge. Thus the resulting group should be given by $\mathrm{SU}(2)_L \times \mathrm{U}(1)_Y$, which is in fact the basis of electroweak theory where $\mathrm{SU}(2)_L$ represents a group of weak isospin and $\mathrm{U}(1)_Y$ represents a group of weak hypercharge. In Table 2.1 we furnish the values of the weak isospin (I_3), weak hypercharge (Y), electric charge (Q) as well as the handedness of the first generation of the lepton sector in the SM.

Following our previous discussions, the covariant derivative of this gauge group is writ-

ten as

$$D_\mu \;=\; \partial_\mu - ig_1\frac{Y}{2}B_\mu - ig_2\frac{\tau_a}{2}W_\mu^a \;, \tag{2.78}$$

where g_1 and g_2 are the respective couplings of U(1)$_Y$ and SU(2)$_L$. The gauge field B_μ is corresponding to the U(1)$_Y$ gauge group, while W_μ^a is the gauge field as in the Yang-Mills theory. The Lagrangian in the leptonic sector can be written as

$$\mathcal{L}_{\text{lepton}} \;=\; \sum_{\alpha=1}^{3}\left[\bar{\Psi}_L^\alpha i\gamma^\mu D_\mu^L\Psi_L^\alpha + \bar{\Psi}_R^\alpha i\gamma^\mu D_\mu^R\Psi_R^\alpha\right] \;, \tag{2.79}$$

where

$$\begin{aligned} D_\mu^L\Psi_L^\alpha &= \left(\partial_\mu - ig_1\frac{Y_L}{2}B_\mu - i\frac{g_2}{2}\sum_{a=1}^{3}\tau_a W_\mu^a\right)\Psi_L^\alpha \;, \\ D_\mu^R\Psi_R^\alpha &= \left(\partial_\mu - ig_1\frac{Y_R}{2}B_\mu\right)\Psi_R^\alpha \;. \end{aligned} \tag{2.80}$$

D_μ^L and D_μ^R are the covariant derivatives for the left and right chiral leptons, while α denotes the generation index. Now considering the first generation of leptons

$$\left(\Psi_L^1 = \begin{pmatrix}\nu_e\\ e^-\end{pmatrix}_L, \Psi_R^1 = e_R\right)$$

we have

$$\begin{aligned}
\mathcal{L}_{\text{lepton}} \supset & \begin{pmatrix} \bar{\nu}_L & \bar{e}_L^- \end{pmatrix} \gamma^\mu i \left(\partial_\mu - i g_1 \frac{Y_L}{2} B_\mu - i g_2 \frac{\tau_a}{2} W_\mu^a \right) \begin{pmatrix} \nu_L \\ e_L^- \end{pmatrix} \\
& + (e_R^-) \gamma^\mu i \left(\partial_\mu - i g_1 \frac{Y_R}{2} B_\mu \right) (e_R^-) \ , \qquad (2.81) \\
= & \ i \bar{\nu}_L \gamma^\mu \partial_\mu \nu_L + i \bar{e}_L^- \gamma^\mu \partial_\mu e_L^- + g_1 \frac{Y_L}{2} \left[\begin{pmatrix} \bar{\nu}_L & \bar{e}_L^- \end{pmatrix} \gamma^\mu \begin{pmatrix} \nu_L \\ e_L^- \end{pmatrix} \right] B_\mu \\
& + \frac{g_2}{2} \left[\begin{pmatrix} \bar{\nu}_L & \bar{e}_L^- \end{pmatrix} \gamma^\mu \begin{pmatrix} W_\mu^3 & W_\mu^1 - i W_\mu^2 \\ W_\mu^1 + i W_\mu^2 & -W_\mu^3 \end{pmatrix} \begin{pmatrix} \nu_L \\ e_L^- \end{pmatrix} \right] \\
& + i \bar{e}_R^- \gamma^\mu \partial_\mu e_R^- + g_1 \frac{Y_R}{2} \bar{e}_R^- \gamma^\mu e_R^- B_\mu \ . \qquad (2.82)
\end{aligned}$$

Here we made use of the relation

$$\begin{aligned}
\vec{\tau} \cdot \overrightarrow{W_\mu} &= \tau_1 W_\mu^1 + \tau_2 W_\mu^2 + \tau_3 W_\mu^3 \ , \\
&= \begin{pmatrix} 0 & 1 \\ 1 & 0 \end{pmatrix} W_\mu^1 + \begin{pmatrix} 0 & -i \\ i & 0 \end{pmatrix} W_\mu^2 + \begin{pmatrix} 1 & 0 \\ 0 & -1 \end{pmatrix} W_\mu^3 \ , \\
&= \begin{pmatrix} W_\mu^3 & W_\mu^1 - i W_\mu^2 \\ W_\mu^1 + i W_\mu^2 & -W_\mu^3 \end{pmatrix} \ . \qquad (2.83)
\end{aligned}$$

Now with $W_\mu^\pm = \frac{1}{\sqrt{2}}(W_\mu^1 \pm i W_\mu^2)$, fourth term of Eq. 2.82 takes the form

$$\frac{g_2}{2} \left[\bar{\nu}_L \gamma^\mu \nu_L W_\mu^3 + \sqrt{2} \bar{\nu}_L \gamma^\mu e_L W_\mu^- + \sqrt{2} \bar{e}_L^- \gamma^\mu \nu_L W_\mu^+ - \bar{e}_L^- \gamma^\mu e_L^- W_\mu^3 \right] \ .$$

In the Lagrangian $\mathcal{L}_{\text{lepton}}$, we have a neutrino current $\bar{\nu}_L \gamma^\mu \nu_L$ associated with the neutral

gauge fields given by

$$\bar{\nu}_L \gamma^\mu \nu_L \left(\frac{g_1}{2} Y_L B_\mu + \frac{g_2}{2} W_\mu^3 \right) \ .$$

Since neutrino has no electric charge, the above interaction is not an EM interaction, but it is a part of weak interaction. In fact it is a NC interaction, where the neutral gauge fields (or a linear combination of them) couple to neutral neutrino current. This linear combination of neutral gauge fields can be expressed as the gauge field Z_μ as

$$Z_\mu \ \propto \ (g_1 Y_L B_\mu + g_2 W_\mu^3) \ , \tag{2.84}$$

which under proper normalization takes the form

$$Z_\mu \ = \ \frac{(-g_1 B_\mu + g_2 W_\mu^3)}{\sqrt{g_1^2 + g_2^2}} \ , (\text{using } Y_L = -1) \ . \tag{2.85}$$

As the sum of the squares of the coefficients is 1, Z_μ can also be written as

$$Z_\mu \ = \ \cos\theta_{\rm W} W_\mu^3 - \sin\theta_{\rm W} B_\mu \ , \tag{2.86}$$

where $\cos\theta_{\rm W} = \dfrac{g_2}{\sqrt{g_1^2 + g_2^2}}$ and $\sin\theta_{\rm W} = \dfrac{g_1}{\sqrt{g_1^2 + g_2^2}}$. We also have another current namely $\bar{e_L^-} \gamma^\mu e_L^-$ associated with B_μ and W_μ^3 given as

$$\bar{e_L^-} \gamma^\mu e_L^- \left[\frac{g_1}{2} Y_L B_\mu - \frac{g_2}{2} W_\mu^3 \right] \ .$$

This combination of the neutral gauge fields should correspond to the EM photon field operator A_μ. Since A_μ cannot couple to neutrino current, it should be orthogonal to Z_μ and

A_μ is expressed as

$$\begin{aligned} A_\mu &= \sin\theta_{\rm W} W^3_\mu + \cos\theta_{\rm W} B_\mu \ , \\ &= \left(\frac{g_2 B_\mu + g_1 W^3_\mu}{\sqrt{g_1^2 + g_2^2}} \right) \ , \end{aligned} \tag{2.87}$$

where $\theta_{\rm W}$ is the Weinberg angle. Now exploring the coupling of the electron currents to the gauge fields, we get

$$\begin{aligned} \bar{e_L^-}\gamma^\mu e_L^- \left(-\frac{g_1}{2} B_\mu - \frac{g_2}{2} W^3_\mu \right) + (e_R^-)^\dagger \gamma^\mu e_R (-g_1 B_\mu) = \bar{e}_L^- \gamma^\mu e_L^- \left(A_\mu \frac{-g_1 g_2}{\sqrt{g_1^2+g_2^2}} + Z_\mu \frac{g_1^2 - g_2^2}{\sqrt{g_1^2+g_2^2}} \right) \\ + (e_R^-)^\dagger \gamma^\mu e_R \left(A_\mu \frac{-g_1 g_2}{\sqrt{g_1^2+g_2^2}} + Z_\mu \frac{g_1^2}{\sqrt{g_1^2+g_2^2}} \right) \ . \end{aligned} \tag{2.88}$$

In the above equation, it is clear that both right handed and left handed electrons couple to the EM field A_μ with equal strengths. Therefore, this effective EM coupling should be equal to electronic charge e for the agreement with the experiments. Thus $e = \dfrac{g_1 g_2}{\sqrt{g_1^2+g_2^2}}$, with the Weinberg angle θ_W given as (from the measurements) $\sin^2\theta_W \equiv 0.2325, \theta_W \equiv 28^\circ$. One readily sees that $g_1 \approx 1.14e$ and $g_2 \approx 2.07e$. This seems to indicate that the weak interaction is stronger than the EM interaction, which is not the case in reality [3]. Also the gauge theories with symmetries do not generate any masses for the gauge fields. But as the interaction strength goes inversely as the mass of the gauge mediator of that interaction, we certainly have the range of EM interaction is infinite since photons are massless. Therefore the range of weak interaction will also be infinite, which is not at all the case in reality. In

[3] In the units of Heavyside-Lorentz, the electronic charge is defined as the fine structure constant α, where $\alpha = \dfrac{e^2}{4\pi\hbar c}$. In natural units $\alpha = \dfrac{e^2}{4\pi} = \dfrac{1}{137}$. In terms of these units, g_1 and g_2 are expressed as $\alpha_1 \equiv \dfrac{g_1^2}{4\pi} \approx \dfrac{1}{100}$ and $\alpha_2 \equiv \dfrac{g_2^2}{4\pi} \approx \dfrac{1}{30}$.

fact the weak interaction is a very short range interaction indicating that the gauge particles are massive. Thus $\mathrm{SU}(2)_L \times \mathrm{U}(1)_Y$ symmetry must be a broken symmetry.

The masses of the gauge bosons may be invoked by just adding a mass term in a Lagrangian. But that can upset the renormalizability of the theory. A non-renormalizable theory makes no sense because this gives rise to infinities. The mechanism which can make the $\mathrm{SU}(2)_L \times \mathrm{U}(1)_Y$ theory viable is known as spontaneous symmetry breaking (SSB). The SSB is described as a mechanism when the ground state does not respect the original symmetry. This phenomenon is used to give a mass to the gauge boson and this mechanism is known as Higgs mechanism. Therefore, for a symmetry transformation of the type $\exp(i\alpha_a \frac{\tau_a}{2})$, the ground state $|0\rangle$ will not remain invariant which implies

$$\exp(i\alpha_a \frac{\tau_a}{2})|0\rangle \neq |0\rangle \ ,$$

meaning that $\tau_a|0\rangle \neq 0$. Thus for a SSB in case of this type of gauge transformation, there has to be at least one generator τ_a, which does not annihilate the vaccum state of the system.

Let us consider a complex scalar field ϕ. The Lagrangian for such a field can be written as

$$\mathcal{L} = (\partial^\mu \phi)^* (\partial_\mu \phi) - \mu^2 \phi^* \phi - \lambda^2 (\phi^* \phi)^2 \ , \tag{2.89}$$

with $\lambda >> 0$, such that

$$V \ = \ \mu^2 \phi^* \phi + \lambda^2 (\phi^* \phi)^2 \ , \tag{2.90}$$

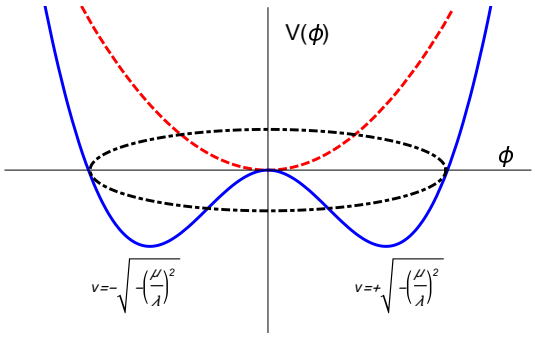

Figure 2.1: Variation of the potential $V(\phi)$ with the scalar field ϕ for $\mu^2 > 0$ (red dotted line) and $\mu^2 < 0$ (blue solid line).

considering $\phi = \dfrac{\phi_1 + i\phi_2}{\sqrt{2}}$, where ϕ_1 and ϕ_2 are real scalar fields, the potential V takes the form

$$\begin{aligned} V &= \frac{1}{2}\mu^2(\phi_1^2 + \phi_2^2) + \frac{\lambda^2}{4}(\phi_1^2 + \phi_2^2)^2 \ , \\ &= \frac{1}{2}\mu^2\zeta^2 + \frac{\lambda^2}{4}\zeta^4 \ , \end{aligned} \tag{2.91}$$

where $\zeta^2 = (\phi_1^2 + \phi_2^2)$. For the minima of the potential, we should have $\dfrac{\partial V}{\partial \phi_1} = 0, \dfrac{\partial V}{\partial \phi_2} = 0$, i.e. $(\mu^2 + \lambda^2\zeta^2)\phi_1 = 0, (\mu^2 + \lambda^2\zeta^2)\phi_2 = 0$. Now one sees that for $\mu^2 > 0$, the minimum lies at $\phi_1 = \phi_2 = 0$, but for $\mu^2 < 0$, the minimum occurs when $\zeta^2 = -\left(\dfrac{\mu}{\lambda}\right)^2$. This means that the set of potential satisfies $\phi_{1\text{min}}^2 + \phi_{2\text{min}}^2 = -\left(\dfrac{\mu}{\lambda}\right)^2$ for the potential to be realised. That is to say the minima of the potential lies on a circle in the $\phi_1 - \phi_2$ plane. Obviously there are infinite number of degenerate ground states forming the continuous circle in $\phi_1 - \phi_2$ plane. Now $\phi_1 = \phi_2 = 0$ does not correspond to the ground state or true minima. But this does not break the symmetry of the Lagrangian. This can be seen in Fig. 2.1. With $v = \pm\sqrt{-\left(\dfrac{\mu}{\lambda}\right)^2}$, where v is the expectation value of the field ϕ, the two minima of $V(\phi)$ are at $\langle\phi\rangle = \pm v/\sqrt{2}$. Fig. 2.1 shows the two cases $\mu^2 > 0$ and $\mu^2 < 0$. It has seen that for $\mu^2 < 0$, one has more than one minima.

Let us consider a simple Abelian U(1) complex scalar field (ϕ) satisfying the local symmetry condition. The Lagrangian for such a complex scalar field, which is coupled to itself and the EM field (A_μ) can be written as

$$\mathcal{L} \;=\; -\frac{1}{4}F_{\mu\nu}F^{\nu\nu} + D_\mu\phi^* D^\mu\phi - V(\phi)\ , \tag{2.92}$$

where D_μ is the covariant derivative and $V(\phi)$ is the scalar potential

$$V(\phi) \;=\; \mu^2\phi^*\phi + \lambda(\phi^*\phi)^2\ . \tag{2.93}$$

Under the local U(1) transformation, $\phi(x) \longrightarrow e^{-i\alpha(x)}\phi(x), A_\mu(x) \longrightarrow A_\mu(x) - \frac{1}{e}\partial_\mu\alpha(x)$, the Lagrangian is invariant.

For $\mu^2 > 0$, the Lagrangian (Eq. 2.92) behaves as the QED Lagrangian for a charged scalar particle having mass μ and ϕ^4 self-interactions. On the other hand, the field $\phi(x)$ will acquire a vacuum expectation value (VEV) for $\mu^2 < 0$ and the minimum of $V(\phi)$ will be obtained at

$$\langle\phi\rangle_0 \equiv \langle 0|\phi|0\rangle = \left(-\frac{\mu^2}{2\lambda}\right)^{1/2} \equiv \frac{v}{\sqrt{2}}\ . \tag{2.94}$$

The complex scalar field (ϕ) around the vacuum state ($\langle\phi\rangle$) can be expanded as

$$\phi(x) = \frac{1}{\sqrt{2}}[v + \phi_1(x) + i\phi_2(x)]\ . \tag{2.95}$$

Therefore, using Eq. 2.95 and $D_\mu = \partial_\mu - ieA_\mu$, the Lagrangian in Eq. 2.92 can be written

as

$$\begin{aligned}\mathcal{L} &= -\frac{1}{4}F_{\mu\nu}F^{\nu\nu} + (\partial^{\mu} + ieA^{\mu})\phi^{*}(\partial_{\mu} - ieA_{\mu})\phi - \mu^{2}\phi^{*}\phi + \lambda(\phi^{*}\phi)^{2} \ , \\ &= -\frac{1}{4}F_{\mu\nu}F^{\nu\nu} + \frac{1}{2}(\partial_{\mu}\phi_{1})^{2} + \frac{1}{2}(\partial_{\mu}\phi_{2})^{2} - v^{2}\lambda\phi_{1}^{2} + \frac{1}{2}e^{2}v^{2}A_{\mu}A^{\mu} - evA_{\mu}\partial^{\mu}\phi_{2} \ .\end{aligned} \tag{2.96}$$

We can make three remarks in this present scenario:

1. The Lagrangian (Eq. 2.96) contains a photon mass term: $\frac{1}{2}M_{A}^{2}A_{\mu}A^{\mu}$ where $M_{A} = ev = -e\mu^{2}/\lambda$.

2. A sclar particle ϕ_1 having mass $M_{\phi_1}^{2} = -2\mu^{2}$ still appears.

3. Apparently, there is a massless particle ϕ_2 and that is a would-be Nambu-Goldstone boson.

We still have a problem which is needed to be addressed. Initially there are four degrees of freedom in the theory - two for ϕ (the complex scalar field) and two for A_{μ} (the massless EM field). But now we are seemingly dealing with five degrees of freedom including one for ϕ_1, one for ϕ_2 and three for the massive photon A_{μ}. Therefore at the end a non physical field appears and indeed a bilinear term is there in the Lagrangian (Eq. 2.96), which is required to be eliminated. For this purpose, we have noticed that at first order the complex field ϕ can be written as

$$\phi(x) = \frac{1}{\sqrt{2}}[v + \phi_{1}(x) + i\phi_{2}(x)] \equiv \frac{1}{\sqrt{2}}[v + \eta(x)]e^{i\zeta(x)/v} \ . \tag{2.97}$$

By considering the freedom of gauge transformations as well as by performing the substi-

tution

$$A_\mu \longrightarrow A_\mu - \frac{1}{ev}\partial_\mu \zeta(x) \tag{2.98}$$

we can neglect all ζ terms such as $A_\mu \partial^\mu \zeta$ term from the above Lagrangian (Eq. 2.96). Therefore, this choice of gauge for which the non physical particles are disappeared from the Lagrangian i.e. the Lagrangian contains only the physical particles, is named as the unitary gauge. Thus, the would-be Nambu-Goldstone boson (having one degree of freedom) has been absorbed by the photon (having two degrees of freedom) and it turns to be massive with three degrees of freedom. The U(1) gauge symmetry is no longer valid and we can phrase it as the U(1) gauge symmetry is spontaneously broken. This is called the Higgs mechanism [4] and depending on this mechanism the masses for the gauge bosons can be generated.

In the non-Abelian case of the SM, the masses of the three gauge bosons ($W^\pm$ and Z) are needed to be generated but the same for photon should remain zero and QED must satisfy an exact symmetry. Therefore, a least three degrees of freedom are required for the scalar fields. For a SU(2) complex scalar doublet H, the Lagrangian is written as

$$\mathcal{L}_{\text{Higgs}} = (D_\mu H)^\dagger (D^\mu H) - V(H) \ , \tag{2.99}$$

where $V(H)$ is the potential term [4]

$$V(H) = \mu^2 (H^\dagger H) + \lambda^2 (H^\dagger H)^2 \ . \tag{2.100}$$

[4]Note that higher order terms in $H^\dagger H$ cannot be present because that will break the renormalizability of the theory.

The doublet Higgs is represented as

$$H = \begin{pmatrix} H^+ \\ H^0 \end{pmatrix} , \; Y_H = +1 \; . \tag{2.101}$$

where H^+ and H^0 are two complex scalar fields having electric charges 1 and 0 respectively. [5] For $\mu^2 < 0, H^0$ (the neutral component of H) will acquire a vacuum expectation value [the charged components of H (H^+) will not develop any VEV and as a result

[5] Writing $H^0 = \frac{h' + iG}{\sqrt{2}}$, the doublet H takes the form

$$H = \begin{pmatrix} H^+ \\ \frac{h' + iG}{\sqrt{2}} \end{pmatrix} ,$$

where h' and G are two real scalars. The covariant derivative D_μ in the Lagrangian $\mathcal{L}_{\text{Higgs}}$ (Eq. 2.99) is given as

$$D_\mu H = \left(\partial_\mu - i g_1 \frac{Y}{2} B_\mu - i \frac{g_2}{2} \sum_{a=1}^{3} \tau_a W_\mu^a \right) H \; . \tag{2.102}$$

The above equation can also be written with $H = \begin{pmatrix} H^+ \\ H^0 \end{pmatrix}$ as

$$D_\mu H = \left[\partial_\mu - \frac{i}{2} \begin{pmatrix} g_2 W_\mu^3 + g_1 B\mu & \sqrt{2} g_2 W_\mu^+ \\ \sqrt{2} g_2 W_\mu^- & -g_2 W_\mu^3 + g_1 B\mu \end{pmatrix} \right] \begin{pmatrix} H^+ \\ H^0 \end{pmatrix} \; . \tag{2.103}$$

As discussed earlier, one can show that for $\mu^2 < 0$, $\langle H \rangle = 0$, does not represent a true minima of $V(H)$. But instead we have two minima $\langle H \rangle = \pm v/\sqrt{2}$. Since both the minima are equally probable, the system can choose any of them. But once it is chosen, the symmetry is broken. Note that this choice does not affect the original gauge symmetry of the Lagrangian since both the ground states do not possess gauge symmetry.

Now let us consider the preferred ground state to be $\langle H \rangle = v/\sqrt{2}$. Redefining h' as $h' = h + v$, we get

$$H = \begin{pmatrix} H^+ \\ \frac{h + v + iG}{\sqrt{2}} \end{pmatrix} \; . \tag{2.104}$$

Here v is the VEV of the field h' and h, G are the two real scalar fields.

$\mathrm{U(1)_{QED}}$ is preserved].

$$\langle H\rangle_0 \equiv \langle 0|H|0\rangle = \begin{pmatrix} 0 \\ \frac{v}{\sqrt{2}} \end{pmatrix} \text{ with } v = \left(-\frac{\mu^2}{\lambda}\right)^{1/2} . \tag{2.105}$$

The doublet Higgs field H can be expressed in terms of four fields $\theta_{1,2,3}(x)$ and $h(x)$ at first order as

$$H(x) = \begin{pmatrix} \theta_2 + i\theta_1 \\ \frac{v+h}{\sqrt{2}} - i\theta_3 \end{pmatrix} = e^{i\theta_a(x)\tau^a(x)/v} \begin{pmatrix} 0 \\ \frac{v+h(x)}{\sqrt{2}} \end{pmatrix} . \tag{2.106}$$

We can move this field $H(x)$ to the unitary gauge by making a gauge transformation as

$$H(x) \longrightarrow e^{-i\theta_a(x)\tau^a(x)} H(x) = \frac{1}{\sqrt{2}} \begin{pmatrix} 0 \\ v+h(x) \end{pmatrix} . \tag{2.107}$$

Now the mass term of the physical Higgs field is obtained as

$$m_h^2 \;=\; \mu^2 + 3\lambda v^2 . \tag{2.108}$$

Using $v = \sqrt{-\left(\frac{\mu}{\lambda}\right)^2}$, we get $m_h^2 = 2\lambda v^2$. [6]

Since the gauge bosons also have to be massive through some gauge invariant way, this should be realised by the spontaneous breaking of $\mathrm{SU(2)}_L \times \mathrm{U(1)}_Y$ symmetry through Higgs mechanism, whereby a non zero VEV is developed for the Higgs doublet H. Here it is to be mentioned that the Higgs doublet H after SSB $\left[H = \begin{pmatrix} H^+ \\ \frac{h+v+iG}{\sqrt{2}} \end{pmatrix}\right]$ reduces

[6] Therefore after SSB, one obtains two massless Nambu-Goldstone bosons (H^+ and G) and one massive physical Higgs boson (h).

to $H = \begin{pmatrix} 0 \\ \frac{h+v}{\sqrt{2}} \end{pmatrix}$ since the massless Goldstone bosons H^+ and G disappear (see later).

Now replacing $H = \begin{pmatrix} 0 \\ \frac{h+v}{\sqrt{2}} \end{pmatrix}$ in Eq. 2.99 and after a simple algebra, one obtains

$$\mathcal{L}_{\text{Higgs}} \supset \frac{1}{4}g_2^2 v^2 W_\mu^+ W_\mu^- + \frac{1}{8}v^2(-g_2 W_\mu^3 + g_1 B_\mu)(-g_2 W^{3\mu} + g_1 B_\mu) \ . \tag{2.109}$$

It can be readily seen that the first term is the mass term of the charged gauge bosons $W^\pm$. Therefore the mass of $W^\pm$ is

$$M_W \ = \ \frac{1}{2}g_2 v \ . \tag{2.110}$$

The remaining part can be written in terms of a mass matrix W_μ^3 and B_μ as

$$\frac{1}{8}v^2(-g_2 W_\mu^3 + g_1 B_\mu)(-g_2 W^{3\mu} + g_1 B_\mu) \ = \ \frac{1}{2}A^T \mathcal{M}^2_{W^3 B} A \ , \tag{2.111}$$

where the mass squared mixing matrix $\mathcal{M}^2_{W^3 B}$ is given by

$$\mathcal{M}^2_{W^3 B} = \frac{1}{4}v^2 \begin{pmatrix} g_2^2 & -g_1 g_2 \\ -g_1 g_2 & g_1^2 \end{pmatrix} \text{ and } A = \begin{pmatrix} W_\mu^3 \\ B_\mu \end{pmatrix} \ . \tag{2.112}$$

The eigenstates of $\mathcal{M}^2_{W^3 B}$ (symmetric matrix) can be obtained by diagonalizing this matrix using an orthogonal transformation

$$\begin{pmatrix} Z_\mu \\ A_\mu \end{pmatrix} \ = \ \begin{pmatrix} \cos\theta_{\text{W}} & -\sin\theta_{\text{W}} \\ \sin\theta_{\text{W}} & \cos\theta_{\text{W}} \end{pmatrix} \begin{pmatrix} W_\mu^3 \\ B_\mu \end{pmatrix} \ . \tag{2.113}$$

The masses of Z_μ is obtained as

$$M_z = \frac{1}{2}\left(\sqrt{g_1^2 + g_2^2}\right) v = \frac{M_W}{\cos\theta_{\rm W}} \tag{2.114}$$

and for A_μ the mass is zero. So A_μ remains massless after the SSB. This has to be the case because the determinant of the mass squared mixing matrix is zero and one of the eigenvalues must vanish. As A_μ remains massless, the symmetry corresponds to this, i.e. U(1) should remain unbroken after the SSB. Note that A_μ arises out of the mixture of W_μ^3 and B_μ associated with $\mathrm{SU}(2)_L$ and $\mathrm{U}(1)_Y$ respectively, but the U(1) group corresponding to A_μ which remains unbroken is not $\mathrm{U}(1)_Y$. Now it is demonstrated that this A_μ is indeed a photon and therefore this U(1) (associated with A_μ) corresponds to the U(1) group of electromagnetism and therefore $\mathrm{U}(1) \equiv \mathrm{U}(1)_{\rm EM}$.
The ratio of masses of charged gauge bosons ($W^\pm$) and neutral gauge boson (Z) of $\mathrm{SU}(2)_L \times \mathrm{U}(1)_Y$ interaction is known as the ρ-parameter, which is defined as

$$\rho \;=\; \frac{M_W}{M_Z \cos\theta_{\rm W}} \;. \tag{2.115}$$

In the case of electroweak interaction with $M_Z = \dfrac{M_W}{\cos\theta_{\rm W}}$ (using Eq. 2.114), one can find that $\rho = 1$.

The disappearence of the Goldstone bosons namely H^+, G (see footnote earlier) from the electroweak theory is closely connected to the appearence of mass terms for the gauge fields. Massless vector boson (photon of the electroweak interaction) has solely two transverse modes of polarization (i.e. transverse to the direction of its three momentum). The longitudinal mode of the polarization vector is forbidden by the unbroken gauge symmetry as it is related to the massless gauge field. If the gauge symmetry associated with the gauge

boson breaks spontaneously, then that boson becomes massive. Therefore for a spin-1 massive particles we have longitudinal mode of polarization in addition to the two transverse states of polarization. Before symmetry breaking there are four massless gauge fields and two complex scalar fields. Therefore, in the unbroken Lagrangian the total number of independent degrees of freedom is twelve. Three out of four gauge fields acquire masses after symmetry breaking while the rest remains massless. Similarly, the scalar sector contains one massive real scalar field as well as two massless Goldstone bosons (one charged scalar H^+ and one neutral scalar G). Therefore, after symmetry breaking there are total 15 independent degrees of freedom. But this can be unfeasible since the total number of degrees of freedom in a system cannot be changed by the phenomena of symmetry breaking. Therefore the Goldstone bosons [7] should disappear from the system to obtain a physically viable situation. Metaphorically, one can say that the three gauge bosons ($W^{\pm}, Z$) have "eaten up" the Goldstone bosons (H^+, G) to get their masses.

The Higgs couplings to fermions, gauge bosons (massive) and the Higgs self-couplings in the SM are given in Fig. 2.2, where the couplings are expressed in terms of both v (VEV) and G_μ (Fermi constant).

2.2.1 Gauge Fixing

It has been seen in the discussions for Abelian gauge theory that a new massless field A_μ identified as photon field has to be introduced to maintain the U(1) symmetry. This field A_μ which maintains the gauge invariance has four real components. But a physical photon has two polarisation states. In order to take into account this property of the observable

[7] The contribution of the Goldstone bosons (H^+, G) to the total number independent degrees of freedom is three.

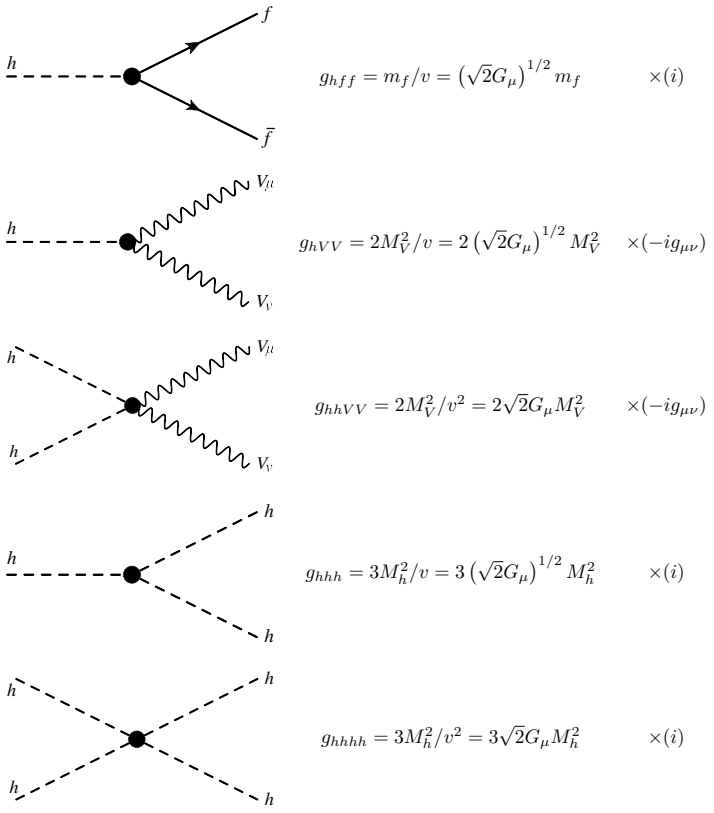

Figure 2.2: The Higgs couplings to fermions, gauge bosons and the Higgs self-couplings.

different from what has been considered for the gauge symmetry, it appears to break this symmetry. In fact the problem arises when attempts are made to quantise this photon field or photon propagator calculations. This problem is circumvented by introducing a gauge fixing term in the Lagrangian so that the gauge symmetry is maintained in the observable. In fact, the fixing of gauge is performed to make a calculation.

Let us now consider the QED Lagrangian. The part, quadratic in photon field is $-14F^{\mu\nu} = -12A^\mu(-g_{\mu\nu}\partial^\sigma\partial_\sigma + \partial_\mu\partial_\nu)A^\nu$. In momentum space this part of the action is written as

$$S = \int d^4p \frac{1}{2} A^\mu(-p)(-g_\mu\nu p^2 + p_\mu p_\nu)A^\nu(p) \ . \tag{2.116}$$

Now inverse does not exist for the operator $-g_\mu\nu p^2 + p_\mu p_\nu$[8]. Therefore the photon propagator cannot be written. In order to circumvent this problem such that a photon propagator can be obtained for computation of physical quantities, a *gauge fixing* term of the form $-\frac{1}{2(1-\xi)}(\partial_\mu A^\mu)(\partial_\nu A^\nu)$ is added to the Lagrangian density where ξ can have arbitrary values. This added term however is not arbitrary since we have the condition $\partial_\mu A^\mu = 0$. From the classical consideration, although this gauge fixing term is zero but quantum mechanically it helps in physical calculations. But the physical amplitude of any process is independent of ξ.

The action mentioned above can now be written as $S = \int d^4p \frac{1}{2}\tilde{A}^\mu(-p)(-g_{\mu\nu}p^2 - \frac{\xi}{1-\xi}p_\mu p_\nu)\tilde{A}^\nu(p)$. It can be seen that the photon propagator takes the form

$$-i\left(g_{\mu\nu} - \xi\frac{p_\mu p_\nu}{p^2}\right)\frac{1}{p^2}\,. \tag{2.117}$$

The choice of ξ is completely arbitrary. Since the final result does not depend on the value of the parameter ξ, let us choose $\xi = 0$. In that case the proton prapagator takes the form $\frac{-ig_{\mu\nu}}{p^2}$. This choice of parameter ξ is known as 't Hooft-Feynman gauge.

For the case of symmetry broken Lagrangian (Higgs mechanism), considering the term of the form [5]

$$\frac{1}{2}\left(D_\mu v\right)^\dagger\left(\partial^\mu(H+i\zeta)\right) + \frac{1}{2}\left(\partial_\mu(H+i\zeta)\right)^\dagger + \left(D_\mu v\right)\ ,$$

where $D_\mu v = ieA_\mu v$ and then the above term is

$$-\frac{1}{2}ievA_\mu\left(\partial^\mu(H+i\zeta)\right) + \text{h.c.} = M_A A_\mu \partial^\mu\zeta\ ,$$

[8] $(-g_\mu\nu p^2 + p_\mu p_\nu)p^\nu = 0$. Therefore, the eigenvector of this operator is p^ν with zero eigenvalue.

with $M_A = ev$, the mass of the vector field (Lagrangian density $\mathcal{L} = (D_\mu\phi)^\dagger(D^\mu\phi) - V(\phi) - \frac{1}{4}F_{\mu\nu}F^{\mu\nu}$, $F_{\mu\nu}$ is the field-strength tensor for gauge field A_μ). Now, this poses a problem since being a quadratic term this can be a part of free Lagrangian but then it is not clear whose free Lagrangian, A_μ or ζ, this term is relevant for. Adding a gauge fixing term of the form $\mathcal{L}_{GF} = -\frac{1}{2\zeta}(\partial_\mu A_\mu - \xi M_A\zeta)^2$, where ξ is a parameter (gauge parameter) similar what to discussed above (physical amplitude does not depend on ξ and this parameter can take any arbitrary value ('t Hooft-Fynman gauge)) to the Lagrangian density (mentioned above), the quadratic term in question takes the form $M_A\partial^\mu(A_\mu\xi)$. This being a total derivative is inconsequential and thus using the gauge fixing term, the problem of the quadratic term of different fields as mentioned above is addressed effectively.

The Lagrangian for the scalar field ζ can be written as

$$\mathcal{L}^\zeta = \frac{1}{2}(\partial_\mu\zeta)(\partial^\mu\zeta) - \frac{1}{2}\xi M_A^2\xi^2$$

and the propagator for the scalar field as

$$\frac{i}{p^2 - \xi M_A^2} \ .$$

Unitary Gauge

The parameter ξ is now chosen in the limit $\xi \to \infty$. In this limit, the propagator for ξ is zero which signifies that for a process or a Feynman diagram with propagatar ξ, the amplitude is zero. This is unitary gauge. The implication of this can be understood if a scalar field written in the form $\phi(x) = \frac{1}{2}(v + H(x) + i\xi(x))$, after spontaneous symmetry

breaking (H(x) and $\xi(x)$ have zero VEV), is represented as

$$\phi(x) = \frac{1}{\sqrt{2}}(v + H(x)) \exp(\frac{i\xi(x)}{v}) \, .$$

Now changing the phase of $\phi(x)$ by $\exp(-i\xi(x)/v)$ (local symmetry transformation), the physics of the theory will not change but $\phi(x)$ can be written as

$$\phi(x) = \frac{1}{\sqrt{2}}(v + H(x)) \ .$$

With this $\phi(x)$, the Lagrangian will not involve any term with ξ. For global symmetry however, this ξ field would be a Goldstone boson.

Therefore, the gauge fixing term is essential to derive the propagator of the gauge boson and thereby to perform calculations for physical processes. For this purpose, we have to add the term $-\frac{1}{2}(\partial^\mu A^a_\mu)^2$ to the Lagrangian density in the case of Feynman gauge and the propagator in momentum space takes a form $-i\frac{g_{\mu\nu}}{p^2}$. This gauge fixing term is also needed to perform higher order loop calculations in the case of non-Abelian gauge theories, although one unfortunate complication arises here.

It is seen that the extra loop diagrams at higher orders emerge when we go through the formalism of gauge fixing in details. Some additional particles are involved in these diagrams, which are equivalent to interacting scalar particles and these are referred as "Faddeev-Popov ghosts". Such a ghost field appears for each gauge field. We cannot interpret this particles as physical scalar particles, but these particles can be observed experimentally as a part of the gauge-fixing programme. This is the reason for which these particles are named as "ghosts". They have two anomalies, which are following:

1. These ghost particles only appear inside loops instead of occuring in intial or final

states as they are not really physical particles. The sole purpose of introducing these particles to wash out a difficulty, which is arised through the gauge-fixing mechanism.

2. They behave similarly to fermions although their spins are zero (scalars). This indicates that in any Feynman diagram we have to consider a minus sign for each loop of Faddeev-Popov ghosts.

2.2.2 Fermion masses

From Dirac Lagrangian $\mathcal{L}_{\rm Dirac} = \bar{\Psi}(i\gamma^\mu\partial_\mu - m)\Psi$, the mass term can be obtained as

$$\begin{aligned} \mathcal{L}_{\rm mass} &= -m\bar{\Psi}\Psi \ , \\ &= -m(\bar{\Psi}_L\Psi_R + \bar{\Psi}_R\Psi_L) \ . \end{aligned} \tag{2.118}$$

One notices that, the transformation properties of left chiral and right chiral projections of leptons are different. Also within the gauge group of SM, the left chiral fermions are doublets and the right chiral ones are singlets. Therefore, the $\bar{\Psi}_L\Psi_R$ and its Hermitian conjugate $\bar{\Psi}_R\Psi_L$ are not invariant under $\mathrm{SU}(2)_L \times \mathrm{U}(1)_Y$. In order to generate fermionic mass within the framework of the invariance of SM gauge group, the Yukawa type interaction is invoked to connect the left chiral and right chiral projections and the Higgs. The interaction Lagrangian for the first generation of leptons is given by

$$\mathcal{L}_{\rm Yukawa} = g_\Psi \left[\bar{\Psi}^1_L H \Psi^1_R + \bar{\Psi}^1_R H^\dagger \Psi^1_L\right] \ , \tag{2.119}$$

where g_Ψ is the Yukawa coupling. After SSB of $\mathrm{SU}(2)_L \times \mathrm{U}(1)_Y$ symmetry, one obtains

$$H = \begin{pmatrix} 0 \\ \dfrac{h+v}{\sqrt{2}} \end{pmatrix} .$$

Now since $\bar{e}_L$ is a doublet $\begin{pmatrix} \nu_e \\ e \end{pmatrix}_L$ therefore we get

$$\begin{pmatrix} \bar{\nu}_L & \bar{e}_L \end{pmatrix} \frac{1}{\sqrt{2}} \begin{pmatrix} 0 \\ v + h(x) \end{pmatrix} e_R = \frac{1}{\sqrt{2}} \bar{e}_L (v+h) e_R \, . \tag{2.120}$$

Similarly doing the same thing for the second term of Eq. 2.119, one obtains

$$\mathcal{L}_{\text{Yukawa}} = g_e \left[\frac{v}{\sqrt{2}} [\bar{e}_L e_R + \bar{e}_R e_L] + \frac{h}{\sqrt{2}} [\bar{e}_L e_R + \bar{e}_R e_L] \right] , \tag{2.121}$$

where we consider $g_\Psi \equiv g_e$ for the first generation of leptons. Now comparing with the Dirac mass term $m(\bar{\Psi}_L \Psi_R + \bar{\Psi}_R \Psi_L)$, one sees that mass of the electron is

$$m_e = \frac{g_e v}{\sqrt{2}} \, . \tag{2.122}$$

Therefore, the Higgs electron coupling strength g_e is given by

$$\frac{g_e}{\sqrt{2}} = \frac{m_e}{v} \, . \tag{2.123}$$

Thus $\mathcal{L}_{\text{Yukawa}}$ now can be written as

$$\mathcal{L}_{\text{Yukawa}} \;=\; m_e \bar{e}e + \frac{m_e}{v}\bar{e}eh \;. \tag{2.124}$$

Quark masses

Similar to the lepton masses the quark masses also can be generated using the same scalar field H. The $\mathrm{SU}(2)_L \times \mathrm{U}(1)_Y$ Lagrangian for any fermion generation is given by

$$\mathcal{L}_F \;=\; -\lambda_e \bar{e}_L H e_R - \lambda_d \bar{Q}_L H d_R - \lambda_u \bar{Q}_L \tilde{H} u_R + \text{h.c.} \;, \tag{2.125}$$

where Q represents quark doublet of first generation $\left[\begin{pmatrix} u \\ d \end{pmatrix}_L\right]$. Note that the isodublet $\tilde{H} = i\tau_2 H^*$, which has hypercharge $Y = -1$ [9]. This has to be introduced to make the above Yukawa Lagrangian, $\mathrm{SU}(2)_L \times \mathrm{U}(1)_Y$ invariant. With this now we obtain

$$m_u = \frac{\lambda_u v}{\sqrt{2}}, \;\; m_d = \frac{\lambda_d v}{\sqrt{2}} \;.$$

Notice that the quark doublets taking part in the weak interaction (weak current operator) are not the same as those appear in a definite generation having a definite mass. This problem has been addressed by the generation mixing in the quark sector and this is the mixed generation that appears in the weak current operator for the quarks. For example, the strangeness-changing decays could be understood if the doublet partners of u, i.e. down quark d is in fact the mixture of strange quark (s) and the down quark member of the definite generation $\begin{pmatrix} u \\ d \end{pmatrix}$. Thus the down quark d_c is expressed as the mixed state of the

[9] In order to generate the up quark mass, one has to invoke that $\tilde{H} = i\tau_2 H^*$, which is an SU(2) invariant. Therefore, the Yukawa Lagrangian for up quark is $\mathcal{L}_u = -\lambda_u \bar{Q}_L \tilde{H} u_R + \text{h.c.}$.

d quark and strange quark s

$$d_c \;=\; d\cos\theta_c + s\sin\theta_c \;, \tag{2.126}$$

where s is the strange quark, θ_c is the Cabibbo angle. The doublet corresponding to the weak current is

$$\begin{pmatrix} u \\ d_c \end{pmatrix} \;=\; \begin{pmatrix} u \\ d\cos\theta_c + s\sin\theta_c \end{pmatrix} \;. \tag{2.127}$$

This indeed changes the coupling strength of the $u - d - W$ vertex, where $d \equiv d\cos\theta_c$. This is known as flavour mixing. For the above example of d and s quark, this mixing is given by

$$\begin{pmatrix} d_c \\ s_c \end{pmatrix} \;=\; \begin{pmatrix} \cos\theta_c & \sin\theta_c \\ -\sin\theta_c & \cos\theta_c \end{pmatrix} \begin{pmatrix} d \\ s \end{pmatrix} \;. \tag{2.128}$$

In case of three generation, the mixing matrix will be a (3×3) matrix known as Cabibbo-Kobayashi-Maskawa (CKM) mixing matrix [6–8] [10].

2.3 Drawbacks of Standard Model

Inspite of the phenomenal success of SM, it suffers from some serious drawbacks. First of all, SM has nineteen unknown parameters. The values of the masses of the fermions cannot be obtained from the SM. In the following, we briefly discuss the drawbacks of SM.

[10] It is to be noted that in all experiments the individual lepton numbers are found to be conserved. The conservation of lepton numbers are not related to any gauge theory, but because of this conservation, there can be no generation mixing in the weak leptonic current.

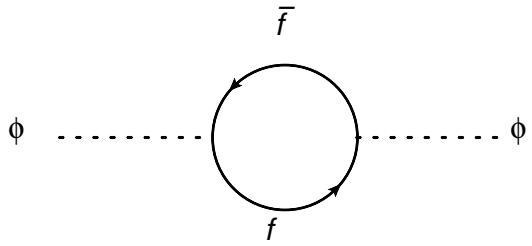

Figure 2.3: The contribution of fermion antifermion to the self energy of the Higgs Boson in SM.

Naturalness

One glaring drawback of SM manifests itself as the problem of naturalness. This arises when the quantum corrections of Higgs boson mass is calculated. This can be obtained by the fermion loop shown in Fig. 2.3. The correction from this loop is given by

$$\begin{aligned} \pi^f_{\phi\phi}(0) &= -N(f)\int \frac{d^4k}{(2\pi)^4}\mathrm{Tr}\left[\left(i\frac{\lambda_f}{\sqrt{2}}\right)\frac{i}{\not{k}-m_f}\left(i\frac{\lambda_f}{\sqrt{2}}\right)\frac{i}{\not{k}-m_f}\right] , \\ &= -2N(f)\lambda_f^2\int \frac{d^4k}{(2\pi)^4}\frac{k^2+m_f^2}{(k^2-m_f^2)^2} , \end{aligned} \tag{2.129}$$

where $\phi \sim \dfrac{(h-v)}{\sqrt{2}}$ and λ_f is the $hf\bar{f}$ coupling. Integrating in the momentum space upto a cut off scale Λ, the correction term is obtained as

$$\delta M_h^2 = -\frac{\lambda_f^2}{8\pi^2}\Lambda^2 + ... , \tag{2.130}$$

i.e. the Higgs boson mass is quadratically divergent on the high scale cut off Λ. In contrast, the fermionic mass correction is logarithmically divergent and the correction is proportional to fermionic mass m_f. This can be seen by calculating fermion self energy in one loop as shown in Fig. 2.4. In this case, the correction is obtained by calculating this loop as

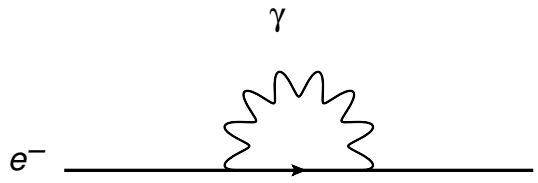

Figure 2.4: The electron self energy in QED.

$$\begin{aligned}\pi_{ee}(0) &= \int \frac{d^4k}{(2\pi)^4}(-ie\gamma_\mu)\frac{i}{\not{k} - m_e}(-ie\gamma_\nu)\frac{-ig^{\mu\nu}}{k^2} \ , \\ &= -4e^2 m_e \int \frac{d^4k}{(2\pi)^4}\frac{1}{k^2(k^2 - m_e^2)} \ . \end{aligned} \tag{2.131}$$

The above integral has a logarithmic divergence in the Ultraviolet (UV) limit and the correction in mass term can be written as

$$\delta m_e \simeq 2\frac{\alpha_{\rm EM}}{\pi} m_e \log\frac{m_{\rm PL}}{m_e} \simeq 0.24 m_e \ . \tag{2.132}$$

Even if we consider the cutoff scale Λ is the largest scale in particle physics, i.e. the PLANCK scale, one sees that the correction is proportional to m_e. But if $m_e \to 0$, the correction vanishes. This has implications with the chiral symmetry rotation $\Psi_e \to \exp(i\gamma_5\theta)\Psi_e$, which is an exact symmetry if $m_e = 0$. But the Yukawa coupling slightly breaks the chiral symmetry and we obtain $\delta m_e \neq 0$. One can say that the fermion mass is chirally protected. But we have seen it is not the case for Higgs which suffers a quadratic divergence in higher order corrections and SM has no remedy for this. This problem is known as the problem of naturalness.

Triviality

The necessity of "triviality bound" for any particular model can be ensured by one of the conditions that the quartic coupling constant of such model should not be pushed to an infinite value up to the ultraviolet cut-off scale (Λ) of the model by the evolution of the

renormalization group. For this purpose, there is a requirement that the Landau pole of the Higgs boson should be larger than the energy scale Λ.

The triviality bounds (theoretical bounds) on the Higgs boson mass can be obtained by taking into account the variation of the Higgs boson quartic coupling with the energy scale. Let us have a look into the scalar sector of the SM.

$$V(\phi) \quad = \quad \mu^2|\phi^\dagger\phi| + \lambda^2(\phi^\dagger\phi)^2 \ . \tag{2.133}$$

In the above equation, λ is the quartic coupling, which can be expressed in terms of the Higgs mass (m_h) and VEV (v) as

$$\lambda \quad = \quad \frac{m_h^2}{2v^2} \ . \tag{2.134}$$

The quartic Higgs coupling λ varies with the effective energy scale Q due to the self-interactions of the scalar field ϕ.

$$\frac{d\lambda(Q^2)}{dt} \quad = \quad \frac{3}{4\pi^2}\lambda^2(Q^2) + \text{higher orders ... ,} \tag{2.135}$$

where $t = \log(Q^2/Q_0^2)$ and Q_0 indicates some referenece energy scale, which is chosen in such a way that it is similar to the electroweak symmetry breaking, $Q_0 = v$. The solution of Eq. 2.135 at one-loop can be written as

$$\lambda(Q^2) \quad = \quad \lambda(v^2)\left[1 - \frac{3}{4\pi^2}\lambda(v^2)\log\frac{Q^2}{v^2}\right]^{-1} \ . \tag{2.136}$$

It is reflected from Eq. 2.136 that, the quartic coupling changes logarithmically with Q^2.

If $Q^2 << v^2$, then $\lambda(Q^2)$ tends to zero ($\lambda(Q^2) \longrightarrow \lambda(v^2)/\log(\alpha) \longrightarrow 0_+$). It depicts

that the theory is trivial since λ is zero.

Alternatively, when $Q^2 >> v^2$ the quartic coupling grows and it eventually becomes infinite, $\lambda(Q^2) \sim \lambda(v^2)/(1-1) >> 1$. The point or the energy scale at which the quartic coupling becomes infinite, is called the Landau pole.

At a high scale $\Lambda(Q = \Lambda)$, the quartic coupling can be finite, if it satisfies

$$\frac{1}{\lambda(\Lambda)} > 0 \ . \tag{2.137}$$

Following this condition (Eq. 2.137) we can give a bound on Higgs mass

$$m_h^2 < \frac{8\pi v^2}{3\log(\Lambda^2/v^2)} \ . \tag{2.138}$$

According to the general triviality argument [9, 10], we can state that the scalar sector of the SM is ϕ^4 theory and this theory can maintain its perturbativity at all energy scales if the value of the quartic coupling is zero ($\lambda = 0$), which indicates that the theory is non interacting (Higgs boson is massless). However, one can understand this argument in a different manner. If the energy scale Λ is associated with the grand unified scales (Λ is large, $\Lambda \sim 10^{16}$ GeV), then from Eq. 2.138 we can obtain $m_h < 160$ GeV. Eq. 2.138 implies that if the SM is valid upto 10^{16} GeV, then the Higgs mass should be less than 160 GeV. On the other hand, if Λ becomes small, then the Higgs boson mass can be rather enlarged. For instance if $\Lambda \sim 10^3$ GeV, then $m_h \sim 1$ TeV.

Dark Matter (DM)

In the framework of SM, there are no particles that can account for the total content of the DM in the Universe. The particle nature of DM is still unknown. The only SM particle that could qualify to be a DM candidate, may be neutrinos. But their relic densities contribute

negligibly to the observed relic density of DM (PLANCK measurements).

Neutrino mass

Since, no right handed neutrinos are observed, the neutrinos are massless in the SM of electroweak interaction. But the undisputed evidence of neutrino oscillations indicates that the neutrinos are massive and no procedure is available within the SM framework for the gerneration of neutrino mass.

Charge quantization

In SM, the $\mathrm{SU}(2)_L \times \mathrm{U}(1)_Y$ electroweak theory is spontaneously broken to an unbroken residual $\mathrm{U}(1)_{\mathrm{EM}}$ symmetry. Therefore the electric charge remains conserved and it is given by $Q = I_3 + \dfrac{Y}{2}$, where Y is the hypercharge and I_3 is the isospin projection, which can take values $\pm 1/2$. Now Y being the weak hypercharge of a U(1) group, its value can be any number. But the charge of a particle cannot take just any value. In reality, the charge of a particle is expressed in terms of the integral multiple of a chosen unit charge. This is known as quantization of electric charge in which SM has no explanation.

Mass hierarchy problem in the fermionic sector

The fermions in SM which are quarks and leptons have three families. The left handed fermions form a doublet pair for each family, which is $\mathrm{SU}(2)_L$ invariant. But even though all the three families (left handed) respect the same symmetry, which is SU(2), the masses of the fermions vary from one family to the other. There exists a hierarchy in the fermionic masses where the third family is more massive than the second and the first family is the lightest. This is true for both quark and lepton families or generations. SM cannot explain the reason of this mass hierarchy between the fermionic families although they respect the same symmetry (SU(2)).

It may also be mentioned that an anomalous term appears during renormalization for each fermion in the quantum field theory (QFT) and can destroy the renormalizability of the

theory. Although this is not the case for the Abelian gauge theory, but it appears for the non-Abelian gauge theory. This is an anomaly and this anomaly $\propto$ [(sum of the charges of the left handed fundamental fermions) - (sum of the charges of the right handed fundamental fermions)] (their antiparticles are not counted). Since the fundamental fermions are all left handed, the renormalizability requires that $\sum_f Q_f = 0$, where Q_f is the charge of fermion f. This implies that the number of quark generations must be the same as the number of lepton generations.

CHAPTER 3

DARK MATTER BASICS

The presence of an unknown, non-luminous form of matter, called as the dark matter (DM), has now been firmly established by the observational results from the satellite borne experiment like Wilkinson Microwave Anisotropy Probe (WMAP) [11] and more recently PLANCK [12]. Their results reveal that more than 80 $\%$ matter content of the Universe is in the form of DM. The rest about $\sim$ 20 $\%$ matter content of the Universe is the "visible" part of the Universe, which is luminous and baryonic in nature. Though this "visible" matter can be successfully explained by the Standard Model (SM) of particle physics, but the particle nature of DM still remains unknown to us. Until now, only the gravitational interactions of DM have been manifested by most of its indirect evidences namely the gravitational lensing [13], the flatness of rotation curves of spiral galaxies [14], the Bullet cluster phenomena [15] and other various colliding galaxy clusters etc. Some basic concepts in DM physics (including observational evidences, classifications, detections of DM etc.) have been discussed in this Chapter.

3.1 Observational Evidences for Dark Matter

In this Section, we discuss a brief outline of various astrophysical evidences for DM observed in the range extending from galactic scale to cosmological scale. All of these enthralling evidences for DM are gravitational in nature.

1. **Gravitational Lensing**

   Einstein's general theory of relativity states how the presence of any mass concentration causes a distortion of the surrounding space-time geometry by curving it. The path of the light ray in the vicinity of any massive object will be deflected and bent as a result of such curved space-time. Therefore, the gravity due to an enormous amount of matter, like a cluster of galaxies, distorts the space in its vicinity such that the light rays from a background object suffer bending and convergence just as they behave in case of optical lens and magnifies the light. This phenomenon is named as gravitational lensing which has a direct connection with the theory of general relativity. The existence of invisible DM with enormous mass in the massive astrophysical objects such as galaxies, galaxy clusters and likes that may surpasses their visible masses, are known by the process of gravitational lensing of these objects.

   Due to the effect of gravitational lensing, the multiple, magnified or distorted images of the background luminous objects situated in the background of the gravitating object at a proper distance may be appeared to the forground observer. Thus the strong gravitational field of these gigantic masses present in between the background sources and the forground observers can behave as gravitational lens if the light rays coming from the distant background luminous object are deflected around the gravitating mass. The deflection of light was first observed by Arthur Eddington and the

collaborators [16] during the total solar eclipse of May 29, 1919. Their observations were performed by noting how the stars change their positions as they are passing near the sun or the celestial spehere. In 1979 D. Walsh, B. Carsweel and R. Weynman discovered the first gravitational lens, which is known as “Twin QSQ" (looked like two quasistellar objects) SBS 0957+561, using the Kitt Peak National Observatory 2.1 meter telescope [17]. Therefore, the observations of such gravitational lensing of the gravitating objects like galaxy cluster provide a powerful indication that the masses of the observed visible matters are way more smaller in comparison to the total mass of the cluster. This phenomenon confirms the presence of huge amount of unseen DM in the gravitating object.

The concept of gravitational lensing theory can be understood by writing a Minkowski space-time metric, which is locally perturbed, as

$$ds^2 = \left(1+2\frac{\phi}{c^2}\right)c^2dt^2 - \left(1-2\frac{\phi}{c^2}\right)dl^2 \ , \tag{3.1}$$

where the deflecting Newtonian gravitational potential ϕ have a very small amplitude (weak field limit is applicable in case $\phi \propto \sigma_v^2 \ll c^2$, where σ_v indicates the velocity dispersion of the lensing mass) and hence it causes a small lensing effect. The time taken by the light photons during their travel from the source (from where they emit) to the observer can be computed by using Fermat principle and this computation provides the relation for the angle of deflection at a position $\vec{\xi}$ in this weak field approximation.

$$\vec{\hat{\alpha}}(\vec{\xi}) = -\frac{2}{c^2}\int_{\text{source}}^{\text{observer}} \nabla_{\perp}\phi dl \ , \tag{3.2}$$

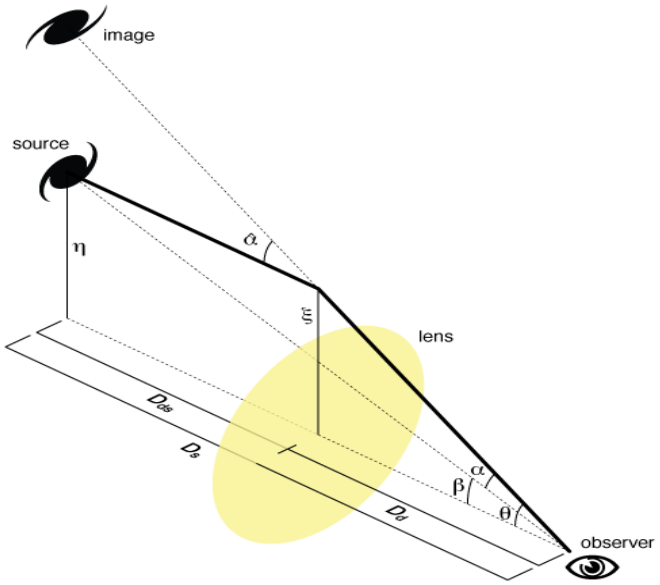

Figure 3.1: The geometry of lensing configuration. *Credit: the author Michael Sachs.*

where $\nabla_\perp$ defines the gradient perpendicular to the line of sight (l.o.s). The distribution of masses in the gravitating objects can be probed by observing the deflection angle of the light rays influenced by the immense gravitational potential of this massive astrophysical objects. In this case, the deflection can be written as a vector sum over point masses. In the continuum limit, this turns out to be an integral over the mass density (ρ) of the lens. It is also pointed out that, if the deflection is small then the gravitational potential along the direction of the deflected trajectory can be approximated by the potential along the trajectory, which is not deflected, similar to what adopted in the context of Born approximation in quantum mechanics. With this, the angle of deflection is given by

$$\vec{\hat{\alpha}}(\vec{\xi}) \;=\; \frac{4G}{c^2}\int d^2\xi' \int \rho(\vec{\xi}', z)\frac{\vec{\xi}-\vec{\xi}'}{|\vec{\xi}-\vec{\xi}'|^2}dz \;\;, \tag{3.3}$$

where z is the l.o.s coordinate. A schematic representation of gravitational lensing is

shown in Fig. 3.1. Shown in Fig. 3.1 are an observer, the lensing mass (in yellow) and a background object on the l.o.s of the observer situated at a distance behind the gravitational lens with respect to the observer. The distance from the source to lens and the distance from the observer to the source are indicated by D_{ds} and D_s respectively, whereas D_d is the distance between the observer and the lens. The deflection angle with the thin lens approximation can be written as [1]

$$\vec{\hat{\alpha}}(\vec{\xi}) \;=\; \frac{4G}{c^2}\int \Sigma(\vec{\xi'})\frac{\vec{\xi}-\vec{\xi'}}{|\vec{\xi}-\vec{\xi'}|^2}dz \;\;, \tag{3.4}$$

where $\Sigma(\vec{\xi'})(=\int \rho(\vec{\xi'},z)dz)$ is the projected mass density along the l.o.s. In the limit of this thin lens approximation, for a lens of point mass M, the mass density is reduced to Dirac distribution and the deflection angle is then given by

$$\vec{\hat{\alpha}} \;=\; \frac{4GM}{c^2\xi} \;\;, \tag{3.5}$$

where ξ is the impact parameter presenting the closest approach distance between the light ray and the point mass (M), G is the Newton's Universal constant of gravitation and c denotes the velocity of light in vacuum. The relation between the true position of the source in the source plane, the deflection angle and the apparent position of images in the lens plane is known as the lens equation, which is given by

$$\vec{\eta} \;=\; \frac{D_s}{D_d}\vec{\xi} - D_{ds}\vec{\hat{\alpha}}(\vec{\xi}) \;\;. \tag{3.6}$$

If some of the parameters like the deflection angle, the redshifts of the source and

[1] In the thin lens approximation, D_d and D_{ds} are way more larger than the size of the lens and this approximation is almost applicable for all astronomical objects.

the lens as well as the cosmological model are known, then the lensing configuration and the process through which the deflecting Newtonian potential recovers can be completely described by the lens equation (Eq. 3.6). We can also express the lens equation in terms of angles instead of using physical distances as

$$\vec{\beta} \;=\; \vec{\theta} - \vec{\alpha}(\vec{\theta}) \;, \tag{3.7}$$

where $\vec{\beta} = \frac{\vec{\eta}}{D_s}$, $\vec{\theta} = \frac{\vec{\xi}}{D_d}$ and $\vec{\alpha} = \frac{D_{ds}}{D_s}\vec{\hat{\alpha}}(\vec{\eta})$. If we replace the point mass by a circular mass distribution then the equation Eq. 3.7 will produce multiple solutions. Therefore, from Eq. 3.7 we can infer that the images of a lensed source are multiplied, magnified and distorted in addition to being deflected.

Depending on the types of images at the point of observation or how the light rays from the source are focused, the gravitational lensing can be categorized into three classes, namely, strong lensing, weak lensing and microlensing. In the case of strong lensing, there is extreme deflections of the light rays due to the presence of very massive gravitational lens aligned closely with the source and the observer. The effect of the strong lensing is so powerful that it may cause observable distortions of the images to adopt the form of a ring called as the Einstein ring [18] (also known as Einstein-Chwolson ring), arcs and multiple images. When the observer, the lensing massive object and the source are aligned along the same l.o.s, the light ray coming from the distant background source suffers a uniform distortion around the lens causing the appearence of a ring of images of the background object, which is called Einstein ring. The first partial Einstein ring was discovered by Hewitt *et al.* in 1988, where he made an observation of the radio source MG1131+0456 using the very large array and ten years later King *et al.* discovered the first complete Einstein ring

B1938+666 with the Hubble Space Telescope of a gravitational lens imaged with the Multi-Element Radio Linked Interferometer Network (MERLIN). Some examples of such strong lensing are given in Fig. 3.2.

If the alignment symmetry among the positions of the source, lens and the observer is partially broken, i.e., if they all do not lie along the same line, then we can observe the arcs or the multiple images of the distant object.

The observations of such Einstein ring or the giant arcs can lead to the estimation of the total mass of the gravitating lens assuming the projected mass density within a circle drawn by the ring or the arc ($\theta_{\rm Ring}$) is equivalent to the critical mass density as

$$M(\theta < \theta_{\rm Ring}) \quad = \quad \pi\theta^2_{\rm Ring} D_d^2 \Sigma_{\rm critical} \ . \tag{3.8}$$

After applying the above equation (Eq. 3.8) to the spectacular giant arc in Abell 370 considering the redshift of the source and the lens as $z_{\rm arc} = 0.724$ and $z_{\rm cluster} = 0.374$ respectively, it has been shown that the mass-to-luminosity ratio of the cluster is about 300, which is in good agreement with the values of the mass-to-luminosity ratio found later using more sophisticated lens model [20] Similar approach for the mass estimation has been applied to many other galaxy clusters and the mass-to-luminosity ratios obtained for these clusters are as similar as Abell 370 [21]. Though the accuracy of the mass estimation is penurious ($\sim \pm 20 - 40\%$), but such a large value of the mass-to-luminosity ratio makes a hint that the discovery of Einstein rings or the arcs produced under the influence of strong gravitational lensing provides a direct indication of the presence of huge unseen non-baryonic DM in the gravitating objects. On the other hand, there are a lensing phenomenon experienced by majority of the background sources that are far away from the caustic lines, where the grav-

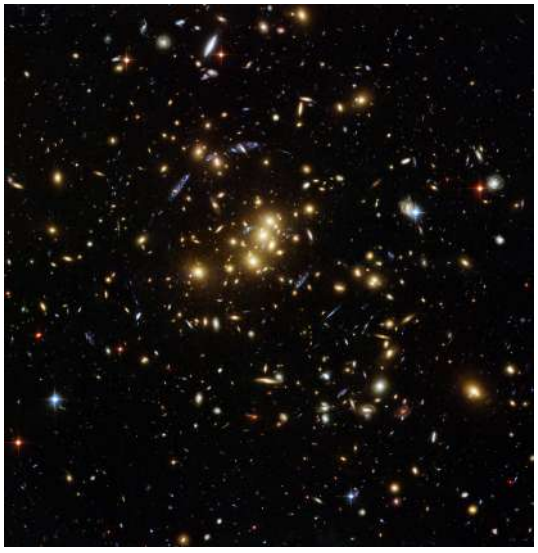

(a)

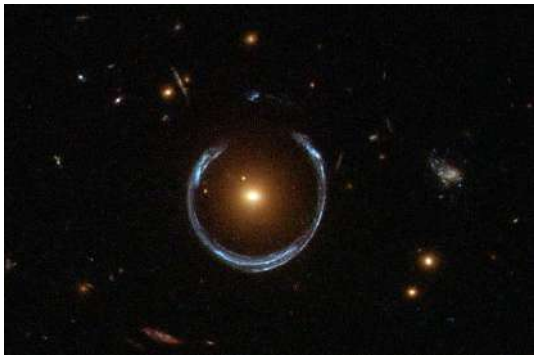

(b)

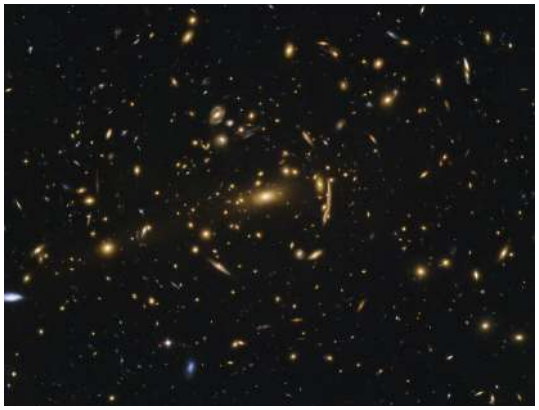

(c)

Figure 3.2: Some examples of strong gravitational lensing. (a) CL0024+1654 galaxy cluster; this cluster is enriched with DM. It behaves as a lens and innumerable blue images of a distant background galaxy appear as a result. *Credit: NASA, ESA, H. Lee & H. Ford (Johns Hopkins U.) [19].* (b) LRG 3-757; it belongs to the luminous red galaxies, which is a rare class of galaxies. It acts as a lens and due to its perfect alignment a ringlike image, named as 'the Cosmic Horseshoe', arises. *Credit: ESA/Hubble & NASA*. (c) MACS J1206.2-0847 cluster; due to its lensing phenomonon the image of a yellow-red distant galaxy is magnified and as a result it turns into a huge arc. *NASA, ESA, M. Postman (STScI) & the CLASH Team.*

itational shear causes a distortion of the images but their amplitude is not as strong as the same for the strong gravitational lensing. These lensing phenomena belong to

the category named as weak gravitational lensing. Since the distortion of the image for an individual background is very faint, a large number of background sources are used for probing the ensemble of the distorted images, which are coherent in nature. In general, for the purpose of analysis, the average properties of these sources are taken into account since their intrinsic properties are unknown to us. Therefore, the measurements of distortions as an effect of the weak lensing have been performed in a statistical manner. Observing and measuring the shapes and the orientations of such ensemble of distant objects (like galaxies), the gravitational shear of the lensing field can be estimated. This in turn can be used to reconstruct the background statistical distribution of DM in particular [13, 22]. For the case of microlensing, smaller objects (like individual stars) can act as gravitational lenses. The mass of this type of lens is too low compared to the cases of strong and weak lensing, where in general the large scale structure like galaxies and galaxy clusters caused the gravitational lensing. Hence with microlensing, it is very hard to observe the displacement of light. But when the forground lensing object aligns perfectly with the background object, then the light from the background source appears brighter as it is magnified by the gravitational lensing effect of the forground object. The alignment bewteen the lens and the background source may suffer a change as the lens passes by the background source in a resonable amount of time. Therefore, microlensing effect can be realized by monitoring the apparent brightness changes of the background source as it moves relative to the forground lens. Unlike the strong and weak lensing, microlensing event is a transient phenomena to the observer from the perspective of human time scale [23]. In the light curve, which represents the variation of brightness with time, a peak appears due to the effect of microlensing. As an example, the microlensing light curve of a star named OGLE-2005-BLG-006 is shown in Fig. 3.3. Thus the

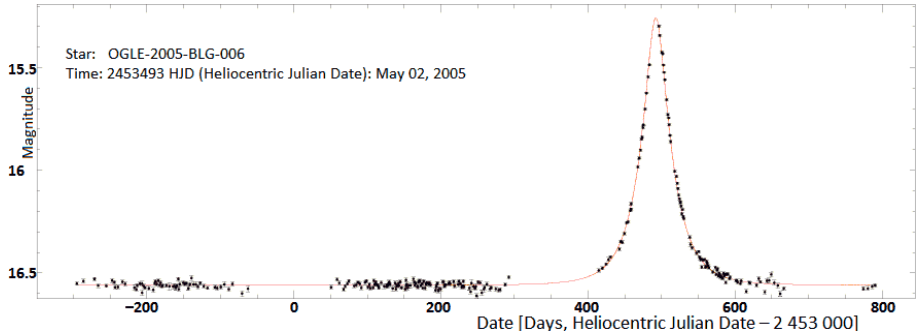

Figure 3.3: A microlensing light curve of the star OGLE-2005-BLG-006.

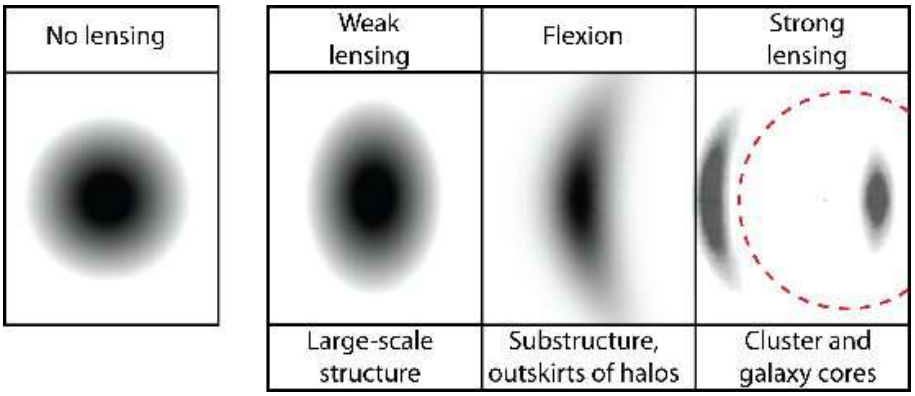

Figure 3.4: Distortions of the images due to different kinds of gravitational lensing (Ref. [24]).

lensing masses can be measured by studying such light curves. The different types of distortions created under the influences of various kinds of gravitational lensing effects are shown in Fig. 3.4.

2. **Flattening of Velocity Distribution Curves of Spiral Galaxy**

   The rotational curve (or velocity curve) shows how the orbital (or circular) velocities of stars vary with the radial distances of that stars from the galactic centre. The study of rotational curves of the spiral galaxies are one of the prominent indication for the existence of DM in the galaxy.

Spiral galaxies may be composed of several distinct components like a flat, rotating disk having interstellar matter and newly formed stars, a central stellar buldge where most of the masses of the visible matters namely old stars, supermassive black holes etc. are concentrated. Such galaxies also contain the spiral arms, which are patterns of gas, dust and younger stars shining brightly before their quick demise, that elongate over the disk. These spiral arms are formed by the density waves travelling through the outer disk which cause an accumulation of the gas and the stars at the galaxy.

Rotational curves of spiral galaxies are major tools for determining the circular (or rotational) velocity $v(r)$ of a star within the galaxy at a distance r from the Galactic Centre (GC). Let us assume that the DM halo has a spherical symmetry. Newtonian dynamics has been applied to a star moving in a circular orbit with a velocity $v(r)$ at a radial distance r from the centre of the galaxy. The equation which represents the balance between the gravitational force and the centrifugal force is given by

$$\frac{mv(r)^2}{r} = \frac{GM(r)m}{r^2} , \tag{3.9}$$

where m denotes the mass of the star and $M(r)$ is the mass enclosed within the radius r from the centre of the galaxy. If the star lies within the central buldge of the galaxy having very high average density of matter ρ, then we can estimate $M(r)$ as

$$M(r) = \frac{4}{3}\pi r^3 \rho . \tag{3.10}$$

The combined effect of the above two equations (Eqs. 3.9, 3.10) indicate that the rotational velocity of the star increases with the radial distance r in a proportional

manner,

$$v(r) \propto r \ . \tag{3.11}$$

When the star or gas is at a distance from the centre of the galaxy beyond the dense core (bulge) region of the galaxy, where the matter density is much less than that in the bulge, then the mass of the bulge can be taken to be a constant with respect to the motion of the star. Under this circumstance $M(r) = M$, where the galactic mass outside the central hub is neglected as it is much smaller than the mass contained within the central dense region of the galaxy. Hence in this case, the nature of the circular velocity of a star follows the radial distance as

$$v(r) \propto \frac{1}{\sqrt{r}} \ . \tag{3.12}$$

Therefore, it is inferred that when the radial distance r is smaller than the radius of the central buldge of the galaxy, then initially the rotational velocity should increase with r (Eq. 3.11) following a Keplerian decline (Eq. 3.12) in the region outside the central core of the galaxy. But a different behaviour of the velocity distribution curves for numerous spiral galaxies have been observed experimentally. These observations indicate that though initially $v(r)$ increases with r as expected but in the region away from the inner dense core of the galaxy (with large r), $v(r)$ becomes constant (instead of following the Keplerian decline nature ($r^{-1/2}$)). If we consider $v(r)$ as a constant in Eq. 3.9, then one gets

$$M(r) \propto r \ . \tag{3.13}$$

Thus the observed flatness of the rotational curves of several spiral galaxies imply the presence of immense matter, which is invisible in nature, in the galaxy much more than the visible mass present in the galaxy. In fact, this would lead us to believe that the huge amount of unseen matter would form a halo of DM. The reach of the dark halo, which embeds the visible galaxy, is way more robust than the visible reaches of the spiral galaxies.

In 1957, Henk van de Hulst and their collaboration made a detail study on the spiral galaxy M31 by using the Dwingeloo 25 meter telescope [25]. In the same year Maarte Schmidt showed that the rotational curve of M31 galaxy did not follow the Keplerian dynamics [26] at a very large radial distance. The same kind of behaviour of the rotational curve has been observed for the spiral galaxy M33 [27] in 1959. In the late 1960s and early 1970s, Vera Rubin and her collaborations [28] came up with their extensive studies on the measurement of the velocity of the rotational curve in and near the Andromeda nebula. They found a considerable amount of deviation of the velocity distribution curve from the predictions made by the virial theorem in the region which is far beyond the visible extremity of the galaxy. The idea regarding the existence of DM had been accepted widely after these observations. As an example, the velocity distribution curve (or rotational curve plotted against the radial distance r) for spiral galaxy NGC 6503 and M33 have been shown in Fig 3.5, which satisfies the characteristics mentioned above. In Fig. 3.5(a) the dash-dot curve denotes the velocity distribution curve for the dark halo while the contribution to the circular (rotational) velocity of the gas and the galactic disk residing inside the galaxy have been indicated by the dotted and the dashed curves repectively. The observational data points and the fitted curves passing through these points are also shown in both the Figures (Figs. 3.5(a), 3.5(b)).

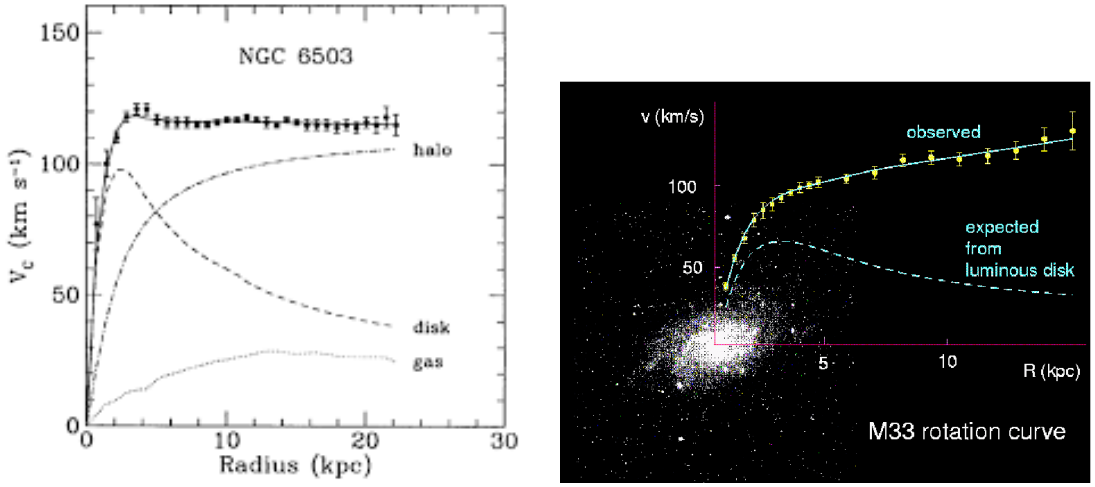

(a) (b)

Figure 3.5: The observed rotation curves for (a) NGC 6503 (sprial galaxy) [29, 30], (b) M33 (dwarf spiral galaxy) [31]. See text for details.

3. **Bullet Cluster**

The studies of the gravitational lensing phenomena of Bullet cluster or more explicitly the galaxy clusters 1E0657-56, 1E0657-558 etc. [15, 32] provide one of the most fruitful evidence for the existence of DM. The origin of Bullet cluster (for example 1E0657-56) phenomena follows from the collisions of two gigantic galaxy clusters at a comoving radial distance 1.141 Gpc (3.72 billion light-years) which has been known as one of the most energetic events happened in our Univese since the Big Bang. In the process of collision the smaller subcluster passes through the core of the larger one. Each of the colliding clusters mainly consists of the baryonic matters such as stars, gas etc. and the presumptive DM. Both these components behave in different ways during the collision. The galaxy clusters, besides having stars and galaxies are abundant in X-ray emitting hot gas. These remain unaffected by the

collisions and these stars can be slowed down other than unaltered by the gravitational effects. The hot gases of the two colliding clusters, detected by Chandra X-ray telescope, interact electromagnetically because of their baryonic nature. The X-ray analyses of the gases in two colliding clusters make it evident that due to the immensity of the collision, the mass distributions of the baryonic matters of the smaller cluster, at the time of passing through the core of the larger one, experience a distortion leading to a bullet-shaped formation and hence the name “Bullet" came into being. On the other hand, the studies of the weak and strong gravitational lensing on this cluster pair reveal that the putative DM halos of each of the colliding galaxy clusters remain unruffled and undistorted during the collision. In addition, as a result of this huge impact, the visible matters seen to have displaced from their central peak position within the respective DM halo of the colliding clusters. Thus the “Bullet cluster" phenomena not only provide a promising evidence of the presence of DM but also confirms the collisionless nature of the DM.

4. **Obeservations of X-ray**

   In addition to the galactic rotation curves, the observations of X-ray produced in the highly ionised hot gas bound by the gravitational potential of a galaxy also furnish an important evidence for the existence of DM in those particular sites and consequently such observations can also infer the density distribution of the galaxy. A theoretical estimation of such framework can be constructed by considering a thin shell of X-ray emitting hot gas situated on or near the exterior of the galaxy (may consist of stars, gas and DM). The mass of the galaxy (in particular the masses of its components like star, gas and DM) confined within the shell exerts the gravitational force which will pull the shell inward. On the other hand, the pressure gradient of the gas within the

shell will try to push the shell outward as the pressure decreases in outward direction. In hydrostatic equilibrium condition, these two forces balance with each other. We can deduce the gravitational mass of the galaxy via the evaluation of the pressure gradient from such obeservations of X-ray emitting gas outside the galaxy and hence the difference between the visible baryonic mass and the gravitational mass of the galaxy amounts to an indication of the DM's presence inside the galaxy [33].

For the sake of simplicity, let us consider that the elliptical galaxy is spherically symmetric. The gravitational force exerted on an annular shell of hot X-ray emitting gas at a particular radius r due to the mass enclosed by the shell is given as

$$F_{\rm grav} \;=\; \frac{GM_{<r}M_{\rm shell}}{r^2}\;, \tag{3.14}$$

where $M_{<r}$ is the total mass confined within the shell of radius r and $r+dr$ (thickness of the shell is dr). The total mass $M_{<r}$ entails the masses of the stars (M_*), gas ($M_{\rm gas}$) and DM ($M_{\rm DM}$) such that $M = M_* + M_{\rm gas} + M_{\rm DM}$. The mass of the shell is defined as

$$M_{\rm shell} \;=\; 4\pi r^2 \rho_{\rm gas}(r) dr\;. \tag{3.15}$$

The force exerted on a surface due to the pressure in the hot ionised gas can be expressed in terms of the pressure ($p(r)$) times the surface area ($4\pi r^2$) of the shell. The net outward force $F_p(r)$ (signifying the difference between the inward and outward forces) can be expressed as an Taylor series expansion of the pressure

$$F_p(r) \;=\; 4\pi r^2 (p(r) - p(r+dr)) = -4\pi r^2 \frac{dp}{dr} dr\;. \tag{3.16}$$

In this mechanism, the hydrostatic equilibrium sustains as the gravitational force and the pressure force balance. Therefore, the combination of the last three equations (Eqs. 3.14 - 3.16) implies

$$\frac{GM_{<r}}{r^2} 4\pi r^2 \rho_{\rm gas}(r) dr \;\; = \;\; -4\pi r^2 \frac{dp}{dr} dr \;\; , \tag{3.17}$$

and thus

$$\frac{GM_{<r}}{r^2} \;\; = \;\; -\frac{1}{\rho_{\rm gas}(r)} \frac{dp}{dr} \;\; . \tag{3.18}$$

Alternatively, the above equation (Eq. 3.18) can be written in terms of the gravitational potential (ϕ) as

$$\nabla \phi \;\; = \;\; -\nabla p / \rho_{\rm gas} \;\; . \tag{3.19}$$

Eq. 3.19 looks familiar to the hydrostatic equilibrium equation for the stars.

The determination of the hot gas temperature ($T_{\rm gas}(r)$) is pursued by modelling the spectrum of X-ray with respect to the position. We can also estimate the radial density of the X-ray emitting gas ($\rho_{\rm gas}(r)$) as the X-ray intensity, which is proportional to $\rho^2_{\rm gas} T^{1/2}_{\rm gas}$. The pressure ($p$) of the gas is $\propto \rho_{\rm gas} T_{\rm gas}$. Thus we can determine all the parameters in the right hand side (RHS) of Eq. 3.19. Using Eq. 3.19 one can reconstruct the gravitational potential and therefore the mass distribution can be inferred. A rough estimation of the density profile can be obtained by the observation that the temperature of the hot gas remains approximately constant. The pressure is given as

$$p \;\; = \;\; \frac{k_{\rm B} T_{\rm gas}}{\mu m_{\rm P}} \rho_{\rm gas} \;\; , \tag{3.20}$$

where $\mu, m_{\rm P}$ are the mean molecular weight (fixed to a chosen value 0.6) and the mass of hydrogen atom respectively. After substituting the expression for p (Eq. 3.20) in Eq. 3.18 and cosnidering the constant value of $T_{\rm gas}$, the Eq. 3.18 turns to be

$$GM_{<r} = -\frac{k_{\rm B}T_{\rm gas}}{\mu m_{\rm P}}\left(r^2\frac{d\ln\rho_{\rm gas}}{dr}\right) . \tag{3.21}$$

The derivative of both sides of the above equation (Eq. 3.21) with respect to r gives

$$G4\pi r^2\rho_{\rm Total} = -\frac{k_{\rm B}T_{\rm gas}}{\mu m_{\rm P}}\frac{d}{dr}\left(r^2\frac{d\ln\rho_{\rm gas}}{dr}\right) , \tag{3.22}$$

where the term $4\pi r^2\rho_{\rm Total}$ comes from the derivation of $M_{<r}$ with respect to r, i.e. $\frac{dM_{<r}}{dr} = \frac{d}{dr}\left(\frac{4}{3}\pi r^3\rho_{\rm Total}\right) = 4\pi r^2\rho_{\rm Total}$, $\rho_{\rm Total}$ being the total mass density (contributed by stars, gas and DM).

Now depending on the assumption that the gas density is proportional to the total mass density ($\rho_{\rm gas} \propto \rho_{\rm Total}$), if we substitute $\rho_{\rm Total}$ by the expression $\rho_0(r_0/r)^\beta$ then it shows that $\rho_{\rm Total} = \rho_0(r_0/r)^\beta$ will be a solution if $\beta = 2$, in which case

$$\rho_{\rm Total} = \frac{k_{\rm B}T_{\rm gas}}{2\pi G\mu m_{\rm P}}r^{-2} . \tag{3.23}$$

Therefore, the total mass density $\rho_{\rm Total}$ can be constrained by the measurement of $T_{\rm gas}$. The estimation of the stellar mass density from the luminosity and the gas density from the X-ray emissivity is useful to find the DM density as $\rho_{\rm DM} = \rho_{\rm Total} - \rho_* - \rho_{\rm gas}$. The more detailed analysis of this type of modelling confirms that also in the case of elliptical galaxies, most of their masses are in the form of DM.

The methods following the hydrostatic equilibrium condition, which is more advan-

tageous than the optical determination of mass, have been used to estimate the gravitational mass and the density distributions of the galaxy. Just like elliptical galaxies, clusters can also emit X-rays via the thermal bremsstrahlung process produced by the gravitationally bound highly ionised gas of the clusters. This method can be used to determine the mass required to bind the gas, as we have done in order to derive the equation Eq. 3.22 from making an assumption of the hydrostatic equilibrium condition in the hot ionised gas. Therefore, such analysis of the X-ray emitting gas in elliptical galaxies as well as the clusters strongly suggest the presence of DM in those sites. The most evident example is that of the M87 ellipitical galaxy in the Virgo cluster [34, 35], where the hydrostatic method has been applied for mapping the temperature and the density profiles of the hot gas emitting X-rays in detail. The obervations of X-rays at the site of M87 galaxy reveal that the total mass of the galaxy is consistent with the value of

$$M(r) = (3-6) \times 10^{13} M_{\odot} \frac{r}{300\text{kpc}} \ . \tag{3.24}$$

The total mass-to-luminosity ratio at a very large distance $r > 100$ kpc is $\left(\frac{M}{L_B}\right)_{\text{Total}} > 150\frac{M_{\odot}}{L_{\odot}}$ and a local value $\left(\frac{M}{L_B}\right)_{\text{local}} > 500\frac{M_{\odot}}{L_{\odot}}$ [35]. This provides an indication of the huge presence of unseen DM in M87 galaxy. Although the position of the DM halo in the region around M87 galaxy is yet unknown to us.

Besides M87 elliptical galaxay in the Virgo cluster, there are other clusters such as Coma and Persus in which the hydrostatic method has been widely implemented. In 1989 Hughes [36] made the derivation that the total mass of Coma cluster lies to be within the radial distance 5 Mpc as $2 \times 10^{15} M_{\odot}$ and the mass-to-luminosity ratio,

$\left(\frac{M}{L_B}\right)_{\text{Total}} \sim 165\frac{M_\odot}{L_\odot}$, whereas the estimated values show that the uncertainties are very high due to the lack of spatial and spectral resolutions. The studies by the several telescopes namely NASA's Chandra X-ray Observatory (of Persus cluster), a Japanese-led X-ray telescope known as Hitomi and the European Space Agency's (ESA) XMM-Newton [37], reveal an unusual spike of intensity in X-ray wavelengths and these waves are originating from the heated gas in the Persus galactic cluster. It is suggested that the presence of DM could be responsible for the phenomenon.

5. **Cosmic Microwave Background Radiation (CMBR)**

The observations of the Cosmic Microwave Background (CMB) are one of the most covincing evidences of DM and also the studies of CMB extract the information about the amount of the DM or more precisely the DM density present in the Universe. At a very early age, before the formation of any visible matters like stars, planets etc., the Universe was much hotter, denser and it was filled with uniform radiation from a white-hot fog of hydrogen plasma. As the Universe evolves, this hot plasma had cooled down and the protons and electrons started combining to form the atoms. At the recombination epoch during the formation of the baryonic matters, the free electrons became inaccessible to the protons to scatter with. The photons started to stream freely in the Universe rather than being scattered by the nuclei and electrons in plasma and this phenomena is referred to as photon decoupling. Heneceforth, these unscattered photons that existed during the time of photon decoupling have been disseminated and with the expansion of the Universe these photons are growing fainter and less energetic, which as a result form a background of the Universe. Since over the past few billion years, the evolution of the Universe causes an elongation of the background radiation towards longer wavelength, whereby at the present epoch

the wavelength of these photons appear in the microwave regime. This background is known as Cosmic Microwave Background Radiation or CMBR having a thermal blackbody spectrum at a temperature 2.73 K [38] where in the microwave range the CMB peaks at a wavelength of around 2 mm. PLANCK [12] and earlier WMAP [11] have observed the anisotropies in CMBR, which is basically the fluctuations in the temperature of the Universe. We can express these anisotropies in temperature in the form of spherical harmonics and thus we can obtain the CMB angular power spectrum. Now by comparing this angular spectrum data with various cosmological models, the best fit values of the parameters of different cosmological models such as $\Omega_b h^2$ (baryon density), $\Omega_m h^2$ (matter density), Λ (cosmological constant) etc. [2] are obtained. From the analysis of CMBR, PLANCK have made a prediction that $\Omega_b h^2$ = 0.022 and $\Omega_m h^2 = 0.1423 \pm 0.0029$ (with 68 $\%$ C.L.). Therefore, the observations of the anisotropies in CMBR ensure that most of the Universe's matter is composed of DM.

6. **Lyman Alpha Forest**

Lyman alpha (Lyα) system is serving an adjuvant source of information in physical cosmology. It is also an useful tool to decipher some of the DM properties. When an electron in the hydrogen atom undergoes a transition from the higher energy state to the ground state, the hydrogen atom emits some emission lines which are named as the Lyα lines. The reverse process can also occur, where an electromagnetic radiation with suitable energy, boost an electron from the ground state of the hydrogen atom to its higher orbit. Therefore, in this case, the hydrogen atom in the lower orbit (ground state) will absorb the energy of the electromagnetic wave. As a result,

[2] $\Omega = \frac{\rho}{\rho_c}$, where ρ and ρ_c are the density of a particular species and the critical density of the Universe respectively.

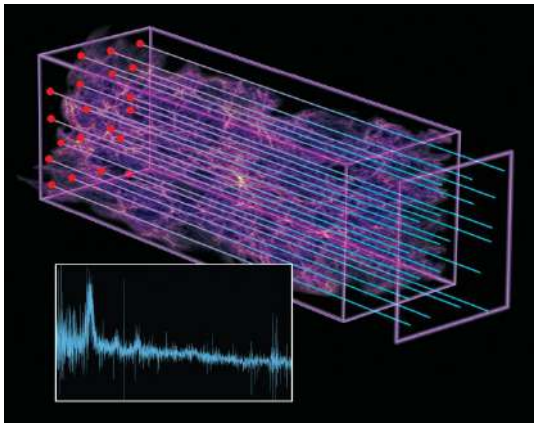

Figure 3.6: Lyα forest. The red dots in the figure indicate the distant quasars. When the light rays coming from these red dots pass through the intergalactic clouds, which is full of hydrogen gas, they are partially absorbed. As a result a forest of hydrogen absorption lines appear in the spectrum of each individual quasar (shown in the box figure). *Credit: Zosia Rostomian, Lawrence Berkeley National Laboratory; Nic Ross, BOSS Lyman-alpha team, Berkeley Lab; and Springel et al., Virgo Consortium and Max Planck Institute for Astrophysics.*

the wavelength corresponding to the absorbed energy will be absent from the energy spectra of hydrogen and this will appear as an absorption line to the observer. The intergalactic medium (IGM) accommodates a large number of neutral hydrogen atoms. Due to the excitation of these hydrogen atoms situated at its energy ground state, a series of absorption lines will appear which represent the series of energies required to excite these hydrogen atoms. This type of absorption phenomenon containing a series of absorption lines is named as the Lyα forest. As the Universe expands, each line of the Lyα forest is shifted towards longer wavelength (redshifted) by a different amount which varies proportionally with the distance between the distant absorbing gas cloud in the IGM and the observer. This is shown in Fig 3.6. Therefore, the Lyα forest is the only direct observational evidence we have by which we can investigate the existence and the properties of the IGM. In the year 1970, astronomer Rodger Lynds first discovered the Lyα forest in an observation of the quasar 4C 05.34 [39],

where surprisingly a large number of absorption lines have been observed in the spectrum of the quasar 4C 05.34. Initially there is an argument that the absorption lines in the Lyα forest are generated due to any physical interactions between the objects within the quasars. But later Jan Oort confirmed that these absorption features are due to the absorption undergoing inside the intergalactic gas clouds in superclusters [40].

We can make an estimation about the presence of hydrogen atoms and free electrons in space by studying the absorption or emission lines with proper wavelengths. If a large number of neutral hydrogen atoms exist in the ground state energy, then more radiation will be absorbed by them. Therefore, if a bunch of neutral hydrogen atoms in their ground state are exposed by a radiation having a certain wavelength $\sim$ 1215.67 Å in the Ultraviolet (UV) region, then the atoms will absorb the radiation and a dip will appear in the intensity curve at $\sim$ 1215.67 Å as the intensity is a function of the wavelength. Thus, the amount of light absorbed by the neutral hydrogen atom, which is known as optical depth, is proportional to the number of hydrogen atoms that exist along the path through which the photon propagates times the probability that the hydrogen atom will absorb the radiation (or cross-section).

The Lyα forest is the absorption phenomenon observed in the spectra of distant high redshift quasi stellar objects or QSOs (also referred to as quasars). Since QSOs are highly luminous and exceedingly energetic objects, they can emit radiations which include not only the visible band but also radio waves, UV, X-rays, optical and gamma-rays. On its way to the observer the electromagnetic radiation emitted from a bright QSO, a distant active galactic nuclei situated at the core of a massive galaxy, passes through the IGM including both the interceding intergalactic gas and the gas

clouds connected with forground objects like galaxies. The IGM is very rich in neutral hydrogen atoms, which can absorb the emitted light from QSOs. The absorption of radiation by the gas clouds of IGM modifies the spectra of the background object (QSO for example) and imprints the signatures of the physical and chemical state of the gas clouds on the observed background quasar and galaxy spectra. The whole arrangement is just like a reminiscent of a giant cosmic slide projector, where QSO is the light bulb that emits radiation and the intervening gas clouds play the role of slides which changes the wavelength or rather the colours of the light source by absorbing the part of the spectrum. The appearence of such optically absorbed quasar spectra is referred to as Lyα forest, which is basically the accumulation of series of sharp absorption lines, corresponding to the neutral hydrogen (HI) Lyα lines. The absorption lines in the Lyα forest are mostly associated with the atomic transition at ~ 1215.67 Å in UV region. The observation of this absorption spectra in the optical band having wavelength $\sim 4000-9000$ Å implies that the gas clouds causing the absorption are highly redshifted with the evolution of the Hubble parameter (expansion of the Universe). Hence such Lyα absorption spectra received at a distant observer is redshifted and the wavelength of this spectra corresponds to the wavelength of the radiation absorbed at the particular site of the IGM at an early state. Therefore, the Lyα forest is the only direct observational evidence by which we can investigate the existence of the IGM and its properties.

Before the advent of the DM concept, the general wisdom was that the absorption systems remained enclosed by the pressure of hotter and more fragile inter cloud medium and floating around the intergalactic region. But the model fails miserably to explain the evolution of the absorption phenomena with redshifts and to reproduce the clouds with higher column densities. Instead of a smooth IGM having

regions embedded on it, the evidences of lumpy regions have been reported by the observers. Therefore, the confrontation between the evidence of CMB observed by COBE (Cosmic Background Explorer) satellite and the idea of hot IGM discards the latter scenario. The Lyα forest along with the reliable computer simulations suggest that although the Lyα systems are not very massive in comparison to the objects like galaxies, certain structures arranged in filaments and sheets can be formed by the inetrstellar gas. Since the DM can interact gravitationally with the interstellar matter in cosmological scale, the structure formation in this scenario will be influenced by such DM distributions in large scale The luminous matters which are baryonic in nature can be trapped by the gravitational collapse of such putative DM. The generation of cold DM halos with the accretions of interstellar gas around them under the influence of gravity is based on the structure formation mechanism commenced by the cold DM. But the masses of such cold DM halos are much small to give birth to the massive bodies such as stars, galaxies etc. The collapse within the accreted intergalactic gas, which eventually forms a stable configuration, has been prevented by its thermal gas pressure. The only way to envisage such kind of structures is to study the absorption spectra of Lyα forest would provide an important probe of DM. On the other hand, it should be noticed that, the hot DM is inconsistent with the observational imprints of the Lyα forest.

7. **Dark Matter in Galaxy Clusters**

The virial theorem provides a conservation law for a system of interacting particles, which has attained dynamical equilibrium due to some kind of central force interactions. In 1870, Rudolf Clausis first gave the technical definition of the virial theorem [41], which states the relation between the time averaged total kinetic energy and the

time averaged total potential energy of a stable system containing discrete particles. Let n be the number of interacting non-relativistic particles of the system and the virial of such a system, W can be defined as

$$W = \sum_{k=1}^{n} \vec{F}_k \cdot \vec{r}_k \ , \tag{3.25}$$

where the net force acting on the kth particle, having a position vector $\vec{r}_k$ and mass m_k, is represented as $\vec{F}_k$, which is given as

$$\vec{F}_k = m_k \frac{d^2\vec{r}_k}{dt^2} \ . \tag{3.26}$$

After substituting the expression of the net force (Eq. 3.26) in Eq. 3.25, one obtains

$$\begin{aligned} W &= \sum_{k=1}^{n} m_k \frac{d^2\vec{r}_k}{dt^2} \cdot \vec{r}_k \ , \\ &= \sum_{k=1}^{n} m_k \frac{d}{dt}\left(\frac{d\vec{r}_k}{dt} \cdot \vec{r}_k\right) - \sum_{k=1}^{n} m_k \frac{d\vec{r}_k}{dt} \cdot \frac{d\vec{r}_k}{dt} \ , \\ &= \sum_{k=1}^{n} m_k \left[\frac{d^2\vec{r}_k}{dt^2} \cdot \vec{r}_k + \left(\frac{d\vec{r}_k}{dt}\right)^2\right] - \sum_{k=1}^{n} m_k \frac{d\vec{r}_k}{dt} \cdot \frac{d\vec{r}_k}{dt} \ , \\ &= \frac{1}{2}\sum_{k=1}^{n} \frac{d^2}{dt^2}\left(m_k\vec{r}_k \cdot \vec{r}_k\right) - \sum_{k=1}^{n} m_k \frac{d\vec{r}_k}{dt} \cdot \frac{d\vec{r}_k}{dt} \ . \end{aligned} \tag{3.27}$$

The first term in the above equation (Eq. 3.27) represents the moment of inertia, $I = m_k\vec{r}_k \cdot \vec{r}_k$ of the entire system about the origin and the second term indicates twice of the total translational kinetic energy (T). Therefore, Eq. 3.27 will take the form,

$$W = \frac{1}{2}\frac{d^2}{dt^2}I - 2T \ . \tag{3.28}$$

If the system attains dynamical equilibrium, then there will be no changes in moment of inertia I with time, which reflects the fact that $\frac{dI}{dt} = 0 = \frac{d^2I}{dt^2}$. From Eq. 3.28, one obtains

$$W + 2T = 0 \tag{3.29}$$

and thus the virial theorem in the case of dynamical equilibrium has been proved. The variations or changes of the moment of inertia (I) with time (the term $\frac{d^2I}{dt^2}$ in Eq. 3.28) exist till the virialisation process persists. The virial time scale of the system may refer to the time scale over which the virialisation process occurs. The total potential energy of the whole system is connected with the virial W. The central force between any two particles k and l of the system having position vector $\vec{r}_k$ and $\vec{r}_l$ respectively can be written as

$$\vec{F}_{kl} = f_{kl}(\vec{r}_k - \vec{r}_l) \ , \tag{3.30}$$

where $k \neq l$ and

$$f_{kl} = \frac{C_{kl}}{|\vec{r}_k - \vec{r}_l|^{n+1}} \ (k \neq l) \ , \tag{3.31}$$

where C_{kl} may have a dependence on the masses of the particles, m_k, m_l etc., but is independent on the mutual separation of the particles or on time. The virial W due to these central force can be written as

$$W = \sum_k \sum_{k \neq l} \vec{F}_{kl} \cdot \vec{r}_k \tag{3.32}$$

or

$$\begin{aligned} W &= \sum_k \sum_{k\neq l} f_{kl}(\vec{r}_k - \vec{r}_l) \cdot \left[\frac{1}{2}(\vec{r}_k - \vec{r}_l) + \frac{1}{2}(\vec{r}_k + \vec{r}_l)\right] \ , \\ &= \frac{1}{2}\sum_k \sum_{k\neq l} f_{kl}|\vec{r}_k - \vec{r}_l|^2 + \frac{1}{2}\sum_k \sum_{k\neq l} f_{kl}(\vec{r}_k - \vec{r}_l) \cdot (\vec{r}_k + \vec{r}_l) \ . \end{aligned} \tag{3.33}$$

The second term of the above equation (Eq. 3.33) is the summation of the product of the symmetric and the antisymmetric terms with respect to (k, l) and therefore, it vanishes. Thus Eq. 3.33 will take the form

$$\begin{aligned} W &= \frac{1}{2}\sum_k \sum_{k\neq l} f_{kl}|\vec{r}_k - \vec{r}_l|^2 \ , \\ &= \frac{1}{2}\sum_k \sum_{k\neq l} \frac{C_{kl}}{|\vec{r}_k - \vec{r}_l|^{n-1}} \ , \\ &= (n-1)V \ , \end{aligned} \tag{3.34}$$

where the total potential energy (V) of the system is given as

$$V = \frac{1}{2}\sum_k \sum_{k\neq l} \int_{\infty}^{(\vec{r}_k - \vec{r}_l)} \vec{F}_{kl} \cdot d(\vec{r}_k - \vec{r}_l) \ . \tag{3.35}$$

If there are no external forces acting on the system of mutually interacting particles, then the virial theorem of such a system under dynamical equilibrium is given as

$$2T = (1-n)V \ , \tag{3.36}$$

which yields that the force between any pair of particles obey an inverse law as

$$|\vec{F}_{kl}| \propto |\vec{r}_k - \vec{r}_l|^{-n} \ . \tag{3.37}$$

If the force of attraction between any two particles is gravitational in nature, then this force follows an inverse square law.

$$|\vec{F}_{kl}| = \sum_{k}\sum_{k\neq l} G m_k m_l \frac{(\vec{r}_k - \vec{r}_l)}{|\vec{r}_k - \vec{r}_l|^3} , \tag{3.38}$$

where m_k and m_l are the masses of the k and l particles among which the gravitational force interacts. In this particular case, we obtain $W = V$ from Eq. 3.36 (as $n = 2$) and hence

$$2T + V = 0 . \tag{3.39}$$

As an example, for a virialised homogeneous and self gravitating spherical galaxy cluster with radius R and mass M (density ρ), we can calculate the potential energy as

$$\begin{aligned} V &= -\int_0^R \frac{R\left(\frac{4}{3}\pi r^3\rho\right)(4\pi r^2\rho)}{r} dr , \\ &= -G\frac{R^5}{5}\left(\frac{4}{3}\pi r^3\rho\right)(4\pi r^2\rho) , \\ &= -\frac{3}{5}G\frac{\left(\frac{4}{3}\pi R^3\rho\right)\left(\frac{4}{3}\pi R^3\rho\right)}{R} , \\ &= -\frac{3}{5}\frac{GM^2}{R} . \end{aligned} \tag{3.40}$$

The total kinetic energy of such a spherical cluster of galaxies is given as $T = \frac{1}{2}M\bar{v}^2$, where $\bar{v}^2$ defines the root mean square (rms) velocity of the individual galaxy of the galaxy cluster. Thus, the mass of the galaxy cluster can be obtained by using the

virial theorem as

$$M = \frac{5}{3}\frac{R\bar{v}^2}{G} . \tag{3.41}$$

Therefore, from Eq. 3.41 we can estimate the gravitational mass of such a system (spherical galaxy cluster) if we can measure the radius R and the rms speed $\bar{v}^2$.

The measurement of the motion of such spherical galaxies embedded in the Coma cluster [3] as well as the estimation of the gravitational mass of the same cluster have been performed by Zwicky, the astounding physicist, in 1933 [42]. In order to calculate the rms velocity of the galaxy, Zwicky made use of the known radial velocities of seven galaxies in the Coma cluster. The Doppler shift measurements of the spectra of all the seven galaxies in the Coma cluster have been used to determine their radial velocities. Zwicky made an estimation of the gravitational mass of the Coma Cluster as $\sim 1.9 \times 10^{13} M_{\odot}$ (from Eq. 3.41) by using the concept of virial theorem mentioned in Eq. 3.39. Considering some rational assumptions on the distribution of star population in the galaxies [42, 43], the total mass of the visible matter can be estimated to be $\sim 8.0 \times 10^{11} M_{\odot}$. From the comparison between the dynamical (gravitational) mass and the total visible mass, it is observed that the former one is $\sim$ 400 times larger than the latter one. Later it was brought to light that the visible sector of the Coma cluster contains two parts. One of them is composed of the galaxies emitting the visible light and the other one consists an extensive amount of gas that emits X-rays which pervade through the galaxies (between and within the galaxies) of the cluster. In recent times, more masses in the Coma cluster have been discovered, which is found to be in the form of X-ray emitting gas and the estimated

[3] The galaxies in the Coma cluster are regular in shape of sphere and their masses immersed in the cluster are same.

(a) (b)

Figure 3.7: The inside of (a) Coma Cluster of galaxies [*Credit: NASA, ESA, Hubble Heritage (STScI/AURA); Acknowledgment: D. Carter (LJMU) et al. and the Coma HST ACS Treasury Team*], (b) Virgo Cluster of galaxies [*Credit and Copyright: Rogelio Bernal Andreo*]

.

mass in this case is $((1.0 \pm 0.2)h^{-1} + (5.48 + 0.98)h^{-5/2}) \times M_{\odot}$ [44]. After substituting the value of the Hubble parameter, $h = 0.673 \pm 0.012$ in terms of 100 km s^{-1} Mpc^{-1}, the above estimated mass appears to be $\sim 1.6 \times 10^{14} M_{\odot}$. Similar approach towards the measurement of the gravitational mass of the Virgo cluster has been taken into account by Sinclair Smith [45]. The Virgo cluster, which is irregular in shape, contains elliptical galaxies as well as flat spiral galaxies in a huge amount. The collective average motion of the Virgo cluster is affected by the irregular distribution as well as the random motion of the stars or gas inside the diffused elliptical galaxy. Smith also made a similar conclusions for Virgo cluster as given by Zwicky for Coma cluster. Therefore, the estimations of the dynamical masses of both the Coma and Virgo cluster demonstrate the existence of an enormous amount of unseen invisible DM in the galaxy cluster. In Fig 3.7 the interior of both the Coma and Virgo clusters are shown.

3.2 The Evolution of Thermally Generated Dark Matter and Relic Density

The Boltzmann equation governs the thermal evolution of the DM candidate generated at the early epoch of the Universe. We can calculate the relic abundances of the DM candidates by solving this Boltzmann equation numerically. The detailed formalism of the Boltzmann equation as well as the relic density calculation for the thermal DM candidate have been briefly discussed in this section.

The evolution of a single DM component having particle species ξ is governed by the Boltzmann equation, which is given by the Liouville equation

$$L[f_\xi(p_\xi^\mu, x^\mu)] \quad = \quad C[f_\xi(p_\xi^\mu, x^\mu)] \tag{3.42}$$

where $f_\xi(p_\xi^\mu, x^\mu)$ is the phase space distribution function of the particle species ξ and the four momentum of ξ at any point x^μ in space-time is denoted by p_ξ^μ. In Eq. 3.42 the Liouville operator $L[f_\xi(p_\xi^\mu, x^\mu)]$ represents the total rate of change of the phase space distribution function $f_\xi(p_\xi^\mu, x^\mu)$ with time while $C[f_\xi(p_\xi^\mu, x^\mu)]$ is the collision operator which represents the number of particles gained or lost during their collisions with other partices per unit time per volume of phase space. The hypothesis, on which the cosmological model [4] is based, is that the phase space density is isotropic and spatially homogeneous. The Liouville operator in the case of $f_\xi = f_\xi(E_\xi, t)$, where the phase space distribution function (f_ξ) of the particle species ξ is only the function of its time t and energy E_ξ, can be written

[4] This model is proposed by Friedmann-Robertson-Walker and this is generally named as FRW model of cosmology.

as

$$L[f_\xi(E_\xi,t)] \;=\; E_\xi\frac{\partial f_\xi}{\partial t} - \mathrm{H}|\vec{p}_\xi|^2\frac{\partial f_\xi}{\partial E_\xi}\;, \tag{3.43}$$

where the Hubble parameter is denoted by H (=$\frac{\dot{R}}{R}$, R indicates the scale factor of the Universe where $\dot{R}$ is the first order time derivative of R). We can define the number density of particle species ($n_\xi(t)$) at any moment of time t in terms of its internal degrees of freedom of ξ (g_ξ) and $f_\xi(E_\xi,t)$, the distribution function for ξ, as

$$n_\xi(t) \;=\; \frac{g_\xi}{(2\pi)^3}\int f_\xi(E_\xi,t)d^3p_\xi\;. \tag{3.44}$$

Now by integrating both sides of Eq. 3.43 along d^3p_ξ, one can obtain

$$\begin{aligned}\frac{g_\xi}{(2\pi)^3}\int\frac{L[f_\xi(E_\xi,t)]}{E_\xi}d^3p_\xi \;&=\; \frac{\partial}{\partial t}\left(\frac{g_\xi}{(2\pi)^3}\int f_\xi(E_\xi,t)d^3p_\xi\right)\\ &\quad -\frac{g_\xi}{(2\pi)^3}4\pi\mathrm{H}\int\frac{|p_\xi|^4}{E_\xi}\frac{\partial f_\xi}{\partial E_\xi}dp_\xi\;.\end{aligned} \tag{3.45}$$

We have changed the variable of the integration from p_ξ to E_ξ in the RHS of the above equation and used the definition of the particle number density $n_\xi(t)$ (Eq. 3.44) in Eq.

3.45. Therefore, one obtains

$$\begin{aligned}
\frac{g_\xi}{(2\pi)^3}\int \frac{L[f_\xi(E_\xi,t)]}{E_\xi}d^3p_\xi &= \frac{\partial n_\xi}{\partial t} - \frac{g_\xi}{(2\pi)^3}4\pi \mathrm{H}\int |\vec{p}_\xi|^3\frac{\partial f_\xi}{\partial E_\xi}dE_\xi \ , \\
&= \frac{\partial n_\xi}{\partial t} - \frac{g_\xi}{(2\pi)^3}4\pi \mathrm{H}\left[\left(|\vec{p}_\xi|^3 f\right) - 3\int |\vec{p}_\xi|^2\frac{\partial |p_\xi|}{\partial E_\xi}f_\xi dE_\xi\right] \ , \\
&= \frac{\partial n_\xi}{\partial t} + \frac{g_\xi}{(2\pi)^3}4\pi \mathrm{H}\int 3|\vec{p}_\xi|^2\frac{E_\xi}{|\vec{p}_\xi|}f_\xi dE_\xi \ , \\
&= \frac{\partial n_\xi}{\partial t} + 3\mathrm{H}\frac{g_\xi}{(2\pi)^3}\int f_\xi d^3p_\xi \ , \\
&= \frac{\partial n_\xi}{\partial t} + 3\mathrm{H}n_\xi \ . \qquad (3.46)
\end{aligned}$$

Using Eq. 3.46, the Boltzmann equation for $n_\xi(t)$ can now be written as (with Eq. 3.42)

$$\frac{\partial n_\xi}{\partial t} + 3\mathrm{H}n_\xi = \frac{g_\xi}{2\pi^3}\int \frac{C[f_\xi(E_\xi,t)]}{E_\xi}d^3p_\xi \ . \qquad (3.47)$$

The collision term of the Boltzmann equation, indicated by the RHS of Eq. 3.47, for a $2 \leftrightarrow 2$ type of interaction process (like $\xi + \psi \rightarrow a + b$) is given as

$$\begin{aligned}
\frac{g_\xi}{2\pi^3}\int \frac{C[f_\xi(E_\xi,t)]}{E_\xi}d^3p_\xi &= -\sum_{\text{spin}}\int d\Pi_\xi d\Pi_\psi d\Pi_a d\Pi_b (2\pi)^4\delta^4(p_\xi + p_\psi - p_a - p_b) \\
&\times \left[|M|^2_{\xi+\psi\rightarrow a+b}f_\xi f_\psi(1\pm f_a)(1\pm f_b)\right. \\
&\left. -|M|^2_{a+b\rightarrow \xi+\psi}f_a f_b(1\pm f_\xi)(1\pm f_\psi)\right] \ , \qquad (3.48)
\end{aligned}$$

where $f_i(= f_\xi, f_\psi, f_a, f_b)$ denote the phase space density function of the particle species $i(i = \xi, \psi, a, b$ respectively) and

$$d\Pi_{f_i} = \frac{d^3p_{f_i}}{2E_{f_i}(2\pi)^3} \ . \qquad (3.49)$$

In Eq. 3.48, $(1 \pm f_i)$ indicates the statistical mechanics factor where $+(-)$ is relevant for the bosonic (fermionic) particle species. The term $|M|^2_{\xi+\psi \,\to\, a+b}$ and $|M|^2_{a+b \,\to\, \xi+\psi}$, which are obtained by averaging over the spin states of the initial incoming particles and the final outgoing particles, represent the matrix square element for the forward and the backward process respectively. The momentum and energy conservation for the $2 \leftrightarrow 2$ interaction process is secured by the 4-dimensional delta function (δ^4). We can simplify the expression of the collision term (Eq. 3.48) by taking into account some well motivated assumptions, which are the followings.

1. The first assumption is that the final state particles (a, b) produced in the $2 \leftrightarrow 2$ ($\xi + \psi \to a + b$) process maintain thermal equilibrim with the thermal soup of the Universe. This assumption is truely applicable for the electrically charged particles interacting with the thermal photons as well as for the neutral final state outgoing particles. Therefore, the distribution functions f_a and f_b for the final state particles a and b can be replaced by their equilibrium density functions $f_a^{\rm eq}$ and $f_b^{\rm eq}$ respectively. From the application of the principle of detailed balance, we can obtain

$$f_a^{\rm eq} f_b^{\rm eq} \;\; = \;\; f_\xi^{\rm eq} f_\psi^{\rm eq} \; . \tag{3.50}$$

   Also in addition, the condition of the unitarity of S-matrix is given by

$$\begin{aligned} &\sum_{\rm spin} \int d\Pi_a d\Pi_b (2\pi)^4 \delta^4(p_\xi + p_\psi - p_a - p_b) |M|^2_{a+b \to \xi+\psi} \\ &= \sum_{\rm spin} \int d\Pi_a d\Pi_b (2\pi)^4 \delta^4(p_\xi + p_\psi - p_a - p_b) |M|^2_{\xi+\psi \to a+b} \; . \end{aligned} \tag{3.51}$$

2. Secondly, we assume the utilisation of the Maxwell-Botzmann (MB) statistics for all

particle species instead of using Fermi-Dirac (FD) and Bose-Einstein (BE) statistics for fermions and bosons respectively. The Fermi degeneracy and the Bose condensation do not exist anymore and therefore this reflects the fact that $1 \pm f_i \simeq 1$, where $f_i (= \exp[-(E_i - \mu_i)/k_{\rm B}T])$ is the phase space distribution function for all particles (initial and final particles of the $2 \leftrightarrow 2$ process) governed by the MB statistics.

We can define the cross-section ($\sigma_{\xi+\psi\rightarrow a+b}$) for the interaction process $\xi + \psi \rightarrow a + b$ as

$$\sigma_{\xi+\psi\rightarrow a+b} = \frac{1}{4E_\xi E_\psi g_\xi g_\psi v} \sum_{\rm spin} \int d\Pi_a d\Pi_b (2\pi)^4 \delta^4(p_\xi + p_\psi - p_a - p_b) |M|^2_{\sigma_{\xi+\psi\rightarrow a+b}} \ , \tag{3.52}$$

where g_ξ, g_ψ are the internal degrees of freedom of ξ, ψ (two intial state particles of the considered $2 \leftrightarrow 2$ process) respectively and v denotes the relative velocity between these two incoming intial particles, which is given by

$$v = \frac{\sqrt{(\vec{p}_\xi \vec{p}_\psi)^2 - m_\xi^2 m_\psi^2}}{E_\xi E_\psi} \ . \tag{3.53}$$

After applying the definition of the interaction cross-section (Eq. 3.52) as well as the two assumptions stated above, the collision term in Eq. 3.48 takes the following form [5]

$$\begin{aligned} \frac{g_\xi}{2\pi^3} \int \frac{C[f_\xi(E_\xi, t)]}{E_\xi} d^3 p_\xi &= -\int \sigma_{\xi+\psi\rightarrow a+b} v (dn_\xi dn_\psi - dn_\xi^{\rm eq} dn_\psi^{\rm eq}) \ , \\ &= -\langle \sigma_{\xi+\psi\rightarrow a+b} v \rangle (n_\xi n_\psi - n_\xi^{\rm eq} n_\psi^{\rm eq}) \ . \end{aligned} \tag{3.54}$$

[5] We make an assumption that the initial state annihilating particles for the $2 \leftrightarrow 2$ process ($\xi + \psi \rightarrow a + b$) maintain kinetic equilibrium throught their scattering process within the thermal soup of the Universe, in the course of their evolution, both before and after they decouple from the thermal bath. In addition to this, they are also remain in chemical equilibrium with other species before the decoupling temperature and after freeze-out the chemical equilibrium of the particles is not maintained.

In the above equation (Eq. 3.54), $\langle\sigma_{\xi+\psi\to a+b}v\rangle$ is the thermally averaged annihilation cross-section times relative velocity for the process $\xi+\psi\to a+b$, which can be written as

$$\langle\sigma_{\xi+\psi\to a+b}v\rangle \;=\; \frac{\int\sigma_{\xi+\psi\to a+b}v dn_{\xi}^{\rm eq}dn_{\psi}^{\rm eq}}{\int dn_{\xi}^{\rm eq}dn_{\psi}^{\rm eq}}\;. \tag{3.55}$$

If the two initial particles of the $\xi+\psi\to a+b$ interaction process (ξ,ψ) are identical or antiparticle to each other then $\langle\sigma_{\xi+\psi\to a+b}v\rangle$ is given by [46]

$$\langle\sigma_{\xi+\psi\to a+b}v\rangle \;=\; \frac{1}{8m^4TK_2^2(\frac{m}{T})}\int_{4m^2}^{\infty}\sigma_{\xi+\psi\to a+b}({\rm s}-4m^2)\sqrt{\rm s}K_1\left(\frac{\sqrt{\rm s}}{T}\right)d{\rm s}\;, \tag{3.56}$$

where T is the temperature of the thermal soup of the Universe, m denotes the mass of the particle species ξ and the centre of mass energy for the process $\xi+\psi\to a+b$ is represented by the Mandelstam variable 's'. The modified Bessel functions of order $i(=1,2)$ are defined by the factor $K_i(=K_1,K_2)$ in the above equation (Eq. 3.56). Finally, we substitute the RHS of Eq. 3.47 by the collision term derived in Eq. 3.54 and therefore the Boltzmann equation for ξ takes the following form

$$\frac{\partial n_{\xi}}{\partial t}+3{\rm H}n_{\xi} \;=\; -\langle\sigma_{\xi+\psi\to a+b}v\rangle(n_{\xi}n_{\psi}-n_{\xi}^{\rm eq}n_{\psi}^{\rm eq})\;. \tag{3.57}$$

It is to be noted that, the final state particles (a,b) of the process $\xi+\psi\to a+b$ can be produced from the initial state particles ξ and ψ through different interaction channels and these different channels may have an impact on the number densities of the DM particles. Therfore, after including all the different interaction channels the modified Boltzmann

equation can be written as

$$\frac{\partial n_\xi}{\partial t} + 3\mathrm{H}n_\xi \;=\; -\langle\sigma_{\rm total}v\rangle(n_\xi n_\psi - n_\xi^{\rm eq}n_\psi^{\rm eq}) \;, \tag{3.58}$$

where $\sigma_{\rm total}$ is the total cross-section obtained by considering the summation of the cross-section attributed to all possible channels, $\sigma_{\rm total} = \sum_{i,j}\sigma_{\xi+\psi\to a+b}$. Let us investigate the case where the initial particles of the $2 \leftrightarrow 2$ process (ξ and ψ) are identical with each other. Therefore, $n_\xi = n_\psi = n$ and $n_\xi^{\rm eq} = n_\psi^{\rm eq} = n_{\rm eq}$ (equilibrium values of the number densities of ξ and ψ are represented as $n_\xi^{\rm eq}$ and $n_\psi^{\rm eq}$ respectively). In this case, the Boltzmann equation will take the form

$$\frac{\partial n}{\partial t} + 3\mathrm{H}n \;=\; -\langle\sigma_{\rm total}v\rangle(n^2 - n_{\rm eq}^2) \;. \tag{3.59}$$

We consider another case when ψ is antiparticle of ξ and vice versa. In this situtaion, the number density $n = n_\xi + n_\psi$. As the chemical potential is negligible, i.e. $n_\xi = n_\psi$ and therefore, $n = 2n_\xi$. Thus the Boltzmann equations for both n_ξ and n_ψ are similar as given in Eq. 3.59. The double counting of the total number density of the species n can be avoided by multplying a factor of $\frac{1}{2}$ on the R.H.S. of Eq. 3.59. Therfore the evolution equation for the total number density n will be

$$\frac{\partial n}{\partial t} + 3\mathrm{H}n \;=\; -\frac{1}{2}\langle\sigma_{\rm total}v\rangle(n^2 - n_{\rm eq}^2) \;, \tag{3.60}$$

Throughout the remaining part of the Chapter, we will consider the case when the particle is its own antiparticle and $\sigma_{\rm total}$ will be replaced by σ. For further study, we define a useful dimensionless quantity, which is named as the comoving number density, $Y = n/S$, where S defines the entropy density of the Universe. After differentiating the comoving number

density (Y) with respect to time (t), one obtains

$$\dot{Y}S = \dot{n} + 3\mathrm{H}n \ . \tag{3.61}$$

In the above equation we use the relation $\dot{S}/S = -3\dot{R}/R$, which is obtained from the fact that the total entropy per comoving volume, $\mathcal{S} = SR^3$ remains constant in the absence of the entropy production. From Eq. 3.59 and Eq. 3.61, one can obtain

$$\dot{Y} = -S\langle\sigma v\rangle(Y^2 - Y_{\rm eq}^2) \ , \tag{3.62}$$

where $Y_{\rm eq}$ is the equilibrium counterpart of the comoving number density when $n = n_{\rm eq}$. Therefore, the evolution equation Eq. 3.62 will take the form

$$\frac{dY}{dR} = -\frac{1}{R\mathrm{H}}S\langle\sigma v\rangle(Y^2 - Y_{\rm eq}^2) \ . \tag{3.63}$$

In addition to the Y, one more dimensionless quantity (x) has been defined, where $x = m/T$, m and T are the mass of the particle and the photon temperature respectively. We can write Eq. 3.63 in terms of two dimensionless quantities Y and x as [47]

$$\frac{dY}{dx} = \frac{1}{3\mathrm{H}}\frac{dS}{dx}\langle\sigma v\rangle(Y^2 - Y_{\rm eq}^2) \ . \tag{3.64}$$

The Hubble parameter in the standard FRW cosmological model is given as

$$\mathrm{H} = \sqrt{8/3\pi G\rho} \ , \tag{3.65}$$

where G is the gravitational constant and the total energy density of the Universe is defined

by ρ. The total energy density (ρ) and the total entropy density (S) can be defined in terms of the effective degrees of freedom for energy ($g_{\rm eff}(T)$) and entropy ($h_{\rm eff}(T)$) respectively as

$$\rho = g_{\rm eff}(T)\frac{\pi^2}{30}T^4 \ , \tag{3.66}$$

$$S = h_{\rm eff}(T)\frac{2\pi^2}{45}T^3 \ . \tag{3.67}$$

Substituting Eqs. 3.64 - 3.67 into Eq. 3.63, the evolution equation for the comoving number density Y (Eq. 3.63) takes the following form [46]

$$\frac{dY}{dx} = -\left(\frac{45}{\pi}G\right)^{-1/2} \frac{g_*^{1/2}m}{x^2}\langle\sigma v\rangle(Y^2 - Y_{\rm eq}^2) \ , \tag{3.68}$$

where the quantity $g_*^{1/2}$ is defined as [46]

$$g_*^{1/2} = \frac{h_{\rm eff}(T)}{g_{\rm eff}(T)^{1/2}}\left(1 + \frac{1}{3}\frac{T}{h_{\rm eff}(T)}\frac{dh_{\rm eff}(T)}{dT}\right) \ . \tag{3.69}$$

The equilibrium value of the comoving number density ($Y_{\rm eq}$) can be expressed as

$$\begin{aligned} Y_{\rm eq} &= \frac{n_{\rm eq}}{s} \\ &= \frac{45g}{4\pi^5 h_{\rm eff}(T)T^3}\int \exp\left(-\frac{E}{k_{\rm B}T}\right)d^3p \ . \end{aligned} \tag{3.70}$$

For the cold relic species ($x = m/T >> 3$), $Y_{\rm eq}$ takes the following form

$$Y_{\rm eq} = \frac{45g}{4\pi^4}\frac{x^2K_2(x)}{h_{\rm eff}(m/x)} \ , \tag{3.71}$$

where g stands for the number of degrees of freedom of the species under consideration

and the modified Bessel function of order n is defined as $K_n(x)$. Let us define a quantity $\Delta(= Y - Y_{\rm eq})$ representing the deviation of Y from its equilibrium value, $Y_{\rm eq}$. Using $\Delta = Y - Y_{\rm eq}$, Eq. 3.68 becomes

$$\frac{d\Delta}{dx} = -\left(\frac{45}{\pi}G\right)^{-1/2}\frac{g_*^{1/2}m}{x^2}\langle\sigma v\rangle\Delta(\Delta+2Y_{\rm eq}) - \frac{dY_{\rm eq}}{dx} \ . \tag{3.72}$$

We can neglect the term $\frac{d\Delta}{dx}$ from Eq. 3.72 before decoupling because at $T > T_f$, where T and T_f are the temperature of the Universe and the freeze-out temperature [6], the deviation of Y from its equilibrium value ($Y_{\rm eq}$) is negligibly small ($\Delta = 0$ at $Y = Y_{\rm eq}$). At $T = T_f$, $\Delta = \delta Y_{\rm eq}$, where δ is a chosen number. Using Eq. 3.71, the codition for decouple or freeze-out of a cold relic can be written as

$$\left(\frac{45}{\pi}G\right)^{-1/2}\frac{45g}{4\pi^4}\frac{K_2(x)}{h_{\rm eff}(T)}g_*^{1/2}m\langle\sigma v\rangle\delta(\delta+2) = \frac{K_1(x)}{K_2(x)} - \frac{1}{x}\frac{d\ln h_c(T)}{d\ln T} \ . \tag{3.73}$$

One can write $g_*^{1/2}(T)$ in terms of $h_c(T)$ [7] as

$$g_*^{1/2}(T) = \frac{h_{\rm eff}(T)}{g_{\rm eff}(T)^{1/2}}\left(1+\frac{1}{3}\frac{d\ln h_c(T)}{d\ln T}\right) \ , \tag{3.74}$$

which implies $\frac{d\ln h_c(T)}{d\ln T} = 3\left(\frac{g_*^{1/2}(T)g_{\rm eff}^{1/2}(T)}{h_{\rm eff}(T)} - 1\right)$. After substituting the term $\frac{d\ln h_c(T)}{d\ln T}$ by its expression in Eq. 3.73 and inserting Eq. 3.71 into Eq. 3.73, we get

$$\left(\frac{45}{\pi}G\right)^{-1/2}\frac{45g}{4\pi^4}\frac{K_2(x)}{h_{\rm eff}(T)}g_*^{1/2}m\langle\sigma v\rangle\delta(\delta+2) = \frac{K_1(x)}{K_2(x)} - \frac{3}{x}\left(\frac{g_*^{1/2}(T)g_{\rm eff}^{1/2}(T)}{h_{\rm eff}(T)} - 1\right) \ . \tag{3.75}$$

[6] The temperature when the species decouple from the Universal plasma as the expansion rate of the Universe exceeds the interaction rate of species known as the freeze-out temperature.

[7] $h_c(T)$ is the contribution to $h_{\rm eff}(T)$ from all species which are coupled with the thermal plasma at temperature T ($T > T_f$).

In order to obtain the value of T_f or the value of $x_f(= \frac{m}{T_f})$, the above equation (Eq. 3.75) needs to be solved numerically and self consistently. The value of δ is taken to be 1.5 [46] while solving Eq. 3.75 for T_f (or x_f). Once we obtain T_f numerically, the comoving number density can be computed by using the Boltzmann equation (Eq. 3.68). After decoupling, the term $Y_{\rm eq}$ can be neglected in Eq. 3.68. Therefore, the comoving number density at the present epoch (Y_0) can be obtained by integrating Eq. 3.68 from T_f (freeze-out temperature) to T_0 (temperature at the present epoch), which is given by

$$\frac{1}{Y_0} = \left(\frac{45}{\pi}G\right)^{-1/2} \int_{T_0}^{T_f} g_*^{1/2} \langle\sigma v\rangle dT \ , \tag{3.76}$$

where the comoving number density at the freeze-out temperature (Y_f) has not been considered as its value is very small in comparison to the other terms present in Eq. 3.76. The expression for DM relic density is written as

$$\begin{aligned} \Omega_{\rm DM} &= \frac{\rho_{\rm DM}}{\rho_c} \ , \\ &= \frac{m_{\rm DM} s_0 Y_0}{\rho_c} \ . \end{aligned} \tag{3.77}$$

Substituting the numerical value of ρ_c (the critical density of the Universe) in Eq. 3.77, we get [46, 47]

$$\Omega_{\rm DM} h^2 = 2.755 \times 10^8 \ Y_0 \ \frac{m_{\rm DM}}{\rm GeV} \ , \tag{3.78}$$

where the Hubble parameter is redefined as $h = H/(100 \ {\rm Km \ s^{-1} \ Mpc^{-1}})$. Knowing the value of Y_0 from Eq. 3.76, the relic density for the cold relic particles can be computed by using the above equation (Eq. 3.78).

3.3 Classifications of Dark Matter

Although the exact particle nature of DM as well as their interaction with visible matter is still an enigma, the DM, whose existence is confirmed by different kinds of astrophysical observations principally through gravity effects, can be classified based on the following aspects,

- masses and the velocities (relativistic or non-relativistic) of the DM particle,
- the particle nature of the constituents of DM,
- possible production mechanism.

At the freeze-out temperature, the DM particles become relic with no interaction between them. The motion of the DM at the time of their decoupling can be either relativistic or non-relativistic, which can be determined by the DM mass (m) and the Universal temperature at the time of freeze-out (T_f). Depending on the velocities of DM particles, one can classify the DM candidates into three categories as [48]

Hot Dark Matter (HDM)

If the velocity of DM particle is relativistic in nature at the time of their decoupling (freeze-out), then this candidate of DM is termed as hot dark matter (HDM). For HDM, the factor $x_f(=\frac{m}{T_f}) \leq 3$ [47]. Since HDM candidates are in general of lighter masses (their masses are less than their kinetic energies), they are supposed to move with relativistic speeds during the galaxy formation era. After the formation of large scale structure (as the mean free path of HDM is long) such as a large sheet of many galaxies, they can be fragmented to form small scale structures such as dwarf galaxies, galaxy clusters etc. and this approach is referred as "top down" approach. In this case, HDM plays an effective role. The

small scale fluctuations of the matter density are smoothened by HDM due to its relativistic speed. Some of the popular HDM candidates are neutrinos (SM neutrinos having non zero masses), axions etc.

Cold Dark Matter (CDM)

On the other hand, the DM particle is referred to as cold dark matter (CDM), when they move with non-relativistic speeds at the time of freeze-out. In CDM scenario, m (the DM mass) is much greater than T_f and for CDM, the factor $x_f(=\frac{m}{T_f})$ is ≥ 3 [47]. The CDM particles have noteworthy success stories related to the large scale structure formation (N body simulations) irrespective of the fact that their free streaming has no cosmological importance because of their non-relativistic speeds. The CDM particles play an important role in the "bottom up" sequence of the structure formation. In this process initially the small clumps of CDM form in the presence of a tiny density fluctuation zones with a very high gravitational impact. The heavier mass and the non-relativistic speed of CDM are responsible for the formation of the seed for matter clumping in small scale. This small scale structure (small clumps of matter) grows into larger ones (small galaxies), eventually forming the large scale structures like the DM halos, galaxy clusters etc. One of the well known candidates for CDM is Weakly Interacting Massive Particles or WIMPs, which are used very frequently in several particle physics models for CDM and have a strong motivation in the cotext of extending the SM sector. Some of the most studied WIMPs in the existing literature are supersymmetric neutralino [49], scalar singlet DM [50–53], inert doublet DM [54–66], singlet fermionic DM [67–69], hidden sector vector DM [70–72] etc. In one of the Chapters in this thesis (Chapter 5), singlet fermionic WIMP DM have been discussed briefly. There are however discrepancies between CDM paradigm and the observational inferences which are known in the literature as 'cuspy halo' problem [73], 'missing satellite' problem [74], 'too-big-to-fail' problem [75] etc. Some alternatives to CDM paradigm

need to be considered to alleviate these discrepancies and there are propositions for warm DM, Fuzzy CDM [8] etc.

Warm Dark Matter (WDM)

The DM particles, which are neither cold nor hot in nature, are generally termed as warm dark matter (WDM). For the case of WDM the factor $x_f \sim 3$ [47]. The WDM partilces can also take part in structure formation, by both "bottom up" (above their free streaming scale) and "top down" (below their streaming scale) processes. Some examples of the WDM particles are sterile neutrinos, very light gravitions etc.

Based on the particle nature of the constituents of DM, they can also be distinguished into two sectors namely

Baryonic Dark Matter

Although the particle nature of DM is still a mystery to be resolved, the known fundamental particles following the SM theory cannot qualify for DM candidates or they cannot account on the DM content of the Universe. However only the visible matter of the Universe cannot satisfy the PLANCK results for baryon density. This indicates that some of the DM is composed of baryons and this is called baryonic DM.

The total contribution of baryonic DM towards the density (baryonic density) can be successfully inferred from the Big Bang Nucleosynthesis (BBN) models and the observation of CMBR. The bound on Ω_b given by the BBN, which explains the primordial nuclei (^{4}He, ^{1}D, ^{3}He and ^{7}Li) very well and the limit $\Omega_b h^2 = 0.02205 \pm 0.00028$ given by the PLANCK recent results [12] are roughly of the same order. Such baryonic dark matter may occur in the gas of IGM (Lyα), floating stars in galaxy clusters etc. It can also be present

[8] Fuzzy CDM is a hypothetical form of CDM. The main purpose of this kind of DM is to resolve the 'cuspy halo' problem. It would consist of scalar particles having extremely small masses ($\approx 10^{-22}$ eV).

in the so called Massive Astrophysical Compact Halo Objects (MACHOS), which are non luminous in nature and may include black holes or neutron stars as well as brown dwarfs [9], black dwarfs and unassociated planets. The particles like neutrinos, neutrons and the dense objects like jupiter [10], white dwarfs [11] [49, 76] can also be the possible candidates for baryonic DM.

Non-Baryonic Dark Matter

Non-baryonic DM interacts very weakly with the visible matter of the Universe and can account for more than 80% of the matter content of the Universe which is the amount of DM predicted by PLANCK results. The masses of non-baryonic dark matters (DMs) and their particle natures are yet to be ascertained. These non-baryonic DMs are supposed to be relic of the Big Bang and hence they should be massive enough to satisfy the observational result for the DM density of the Universe. Such non-baryonic DM candidates are exotic in nature. In most of the cases proposed particle physics models for these kind of DMs are attempted by simple extension of SM with scalar, fermion etc. One of the plausible candidates for non-baryonic DM in the literature are supersymmetry (SUSY) particles. Since most of the DMs are supposed to be non-baryonic in nature, the non-baryonic DM can be rephrased as DM. The lightest supersymmetric particle (LSP), which appears in SUSY models, is taken into account as a viable DM candidate, whose stability is ensured by R-parity conservation. Axinos, gravitinos, which are the superpartner of axions, gravitons respectively, can also be served as a well known DM candidates. There are also some non-SUSY DM models pursued in literature, for example sterile neutrino DM model, axion

[9] Brown dwarfs contain hydrogen and helium gas with masses $\sim 0.08 M_{\odot}$ or less. Due to their small masses, brown dwarfs cannot take part to form a dense cores required to commence hydrogen burning (failed star).

[10] Jupiter is a compact dense object having mass $\sim 0.001 M_{\odot}$.

[11] White dwarfs (also named as a degenerate dwarf) is a very dense object and its mass is compared to solar mass $M_{\odot}$. No fusion occurs inside white dwarfs as its luminosity faunts gradually and its volume is reduced to that of the Earth.

DM model etc. The lightest Kaluza-Klein particle (LKP) inspired by the theories of extra dimensions can also be a possible DM candidate [77] as well. We have considered only non-baryonic DM candidates in this thesis (see Chapter 5, 6 and 7 for more details).

On the basis of the production mechanism, the DM particles can be divided into two parts namely thermal DM and non-thermal DM.

Thermal Dark Matter

Thermal DM is attributed to the DM particles that maintain thermal and chemical equilibrium with the rest of the Universe's plasma before their decoupling. In the very early Universe, when the temperature T is much higher than the mass m_χ of the DM χ, then the number density n_χ of the DM follows a T^3 variation when in equilibrium [12]. The interaction rate $\chi\bar{\chi} \rightarrow f\bar{f}$ is the same as the rate of the process $f\bar{f} \rightarrow \chi\bar{\chi}$, such that the rates of annihilation and production of DM are same. Then the rate is given by

$$\Gamma_{\rm ann} \;=\; \langle \sigma_{\rm ann} v \rangle n_{\rm eq} \;, \tag{3.79}$$

where $\langle \sigma_{\rm ann} v \rangle$ is the annihilation cross-section and $n_{\rm eq}$ is the equilibrium number density of DM. As the temperature T decreases with the expansion of the Universe, the equilibrium number density is expressed by the Boltzmann distribution ($T << m_\chi$)

$$n_\chi^{\rm eq} \;=\; g \left(\frac{m_\chi T}{2\pi} \right)^{\frac{3}{2}} e^{-\frac{m_\chi}{T}} \;, \tag{3.80}$$

[12] At high temperature ($T >> m_\chi$), the number density n_χ is given as $\int \frac{8\pi}{(hc)^3} \frac{E^2 dE}{\exp\left(-\frac{E}{k_{\rm B}T}\right)}$, where h, c and $k_{\rm B}$ represent the PLANCK constant, the speed of light in vacuum and the Boltzmann constant respectively. Thus the integration is reduced to $n_\chi \sim T^3$.

where g is the effective number of degrees of freedom. Under this circumstance, the kinetic energy necessary for the particle - antiparticle collision to generate WIMP pairs can only be provided by the tail part of the Boltzmann distribution. With the progress of the expansion of the Universe, annihilation rate further depletes and when it lagss behind the expansion rate, the DM particles decouple from the rest of the plasma and become relics. Thus, this situation, is also known as the "freeze-out" of the DM species. The temperature at which this happens is known as the freeze-out temperature. It may be noted that relic density $\Omega_\chi \sim \frac{1}{\langle \sigma_{\rm ann} v \rangle}$. It may be noted that when the mean free path of collisions leading to the WIMP production becomes longer than the Hubble radius, the DM decouples and the number of DM in a comoving volume remains approximately constant. But the number density of the DM after decoupling decreases with the increase in volume of the Universe. WIMPs are a popular DM candidate which were in thermal equilibrium in the early Universe and decouple via freeze-out mechanism (i.e. when they decouple they move away from the thermal equilibrium).

Non-Thermal Dark Matter

Since in the cosmic history BBN is not known with certainty, it is possible that the DM particles never experienced chemical or thermal equilibrium in the early Universe. These species can be created in the early Universe but as the interaction of these particles with others are very feeble their numbers grow slowly but they never attain thermal equilibrium due to this very feeble coupling strength. This kind of DM particles, produced via non-thermal production mechanism, is named as non-thermal DM. The non-thermal production mechainsm may be realized as out of equilibrium decay of some heavy particles or scalar fields, gravitational effects etc. Some plausible candidates for non-thermal DMs are

1. *Feebly Interacting Massive Particles or FIMPS DM-*

Feebly Interacting Massive Particle (FIMP) is a well motivated mechanism alternative to the WIMP or thermal production mechanism. If the DM particles follow the FIMP mechanism, then they are termed as FIMP DM particles. In this mechanism, DM particles are slowly produced by decays or annihilations of SM particles in the thermal plasma. The interaction between the SM particles and FIMP DM particles are very feeble (coupling strength $\sim 10^{-11} - 10^{-12}$). Due to such small interaction these FIMP particles are unable to reach thermal equilibrium with the rest of Universe's plasma. In contrast to the thermal DM particles, their initial abundances are very negligible to undergo annihilation interaction among themselves. Therefore, they never attain thermal and chemical equilibrium with the Universe's plasma throughout their cosmological history. But their number densities grow gradually due to their very feeble couplings with the SM particles. While the thermal DM particles go away from the equilibrium, FIMP particles approach towards equilibrium.

2. *Superheavy dark matter (SHDM)* -

   The SHDM can be produced through the gravitational creation of matter in an expanding Universe. This production mechanism is similar to the Hawking radiation mechanism (radiation around black holes) and to the Unruh radiation mechanism that can occur in an accelerated frame of reference. The WIMPZILLAS, which are very massive relics from the Big Bang (mass $\sim 10^{13}$ GeV), can be taken as an example of SHDM. Such massive relics can also be produced at the end of the inflation era during the preheating or the reheating stage and in bubble collisions. The phase transition between the inflation and the radiation dominated Universe due to the non-adiabetic expansion of the Universe can be a possible production mechamism of the WIMZILLAS [78]. The relic abundances of such SHDM particles depend on their

masses rather than their interaction strength. This kind of very heavy DM particles are stable with lifetime $\sim$ the age of the Universe.

Another example of non-thermal DM produced from gravitational effect is Primordial Black Holes (PBH) [79]. PBH are believed to be formed during the radiation dominated era [13].

3. Axion -

Axions could also be another example of the non-thermal DM candidates. The existence of axion is envisaged by the Peccei-Quinn mechanism [80] related to the spontaneous breaking of an axial symmetry $\mathrm{U(1)_A}$. This mechanism is in fact required to counter an inevitable CP violating term arising in QCD Lagrangian. The QCD Lagrangian is written as

$$\mathcal{L}_{\mathrm{QCD}} = \bar{\psi}_i(i(\gamma^\mu D_\mu)_{ij} - m\delta_{ij})\psi_j - \frac{1}{4}G^a_{\mu\nu}G^{\mu\nu}_a - \frac{\alpha_s}{8\pi}\theta G^a_{\mu\nu}\tilde{G}^{\mu\nu}_a \ , \quad (3.81)$$

where D_μ is covariant derivative, $G^a_{\mu\nu}$ is the gluon field tensor, α_s is the strong interaction coupling and θ is a parameter. The $\tilde{G}^{\mu\nu}$ in the above expression (Eq. 3.81) is the dual of the tensor $G_{\mu\nu}$, which is given by

$$\tilde{G}^{\mu\nu} = \frac{1}{2}\epsilon^{\mu\nu ab}G_{ab} \ ,$$

This may be noted that, one cannot avoid the last term in the Lagrangian of a non-

[13] It forms due to the collapse of the overdense region characterized by the size of the region which should be greater than the Jeans length R_j, $R_j = \sqrt{\frac{1}{3G\rho}}$. Also the condition of the PBH formation is $\delta_{\mathrm{min}} \leq \delta \leq \delta_{\mathrm{max}}$, where δ is the density contrast. The maximum and mininum density contrast δ_{max} and δ_{min} respectively are governed by the value of $\delta\rho$, where the density $\rho = \rho_c + \delta\rho$, where ρ_c is the critical density for collapse. The δ_{min} is the threshold of PBH formation.

Abelian gauge theroy (Eq. 3.81).

$$G^a_{\mu\nu}\tilde{G}^{\mu\nu}_a = \frac{1}{2}\epsilon^{\mu\nu\lambda\rho}\left(2\partial_\mu G^a_\nu - g f_{bca} G^b_\mu G^c_\nu\right)\left(2\partial_\lambda G^a_\rho - g f_{dea} G^d_\lambda G^e_\rho\right) \ . \quad (3.82)$$

Applying the Jacobi identity, one can get

$$G^a_{\mu\nu}\tilde{G}^{\mu\nu}_a = 2\epsilon^{\mu\nu\lambda\rho}\left[(\partial_\mu G^a_\nu)(\partial_\lambda G^a_\rho) - g f_{bca}(\partial_\mu G^a_\nu) G^b_\lambda G^c_\rho\right] \ . \quad (3.83)$$

The RHS can be written in terms of total derivative K^μ, where K^μ is

$$K^\mu = 2\epsilon^{\mu\nu\lambda\rho}\left[G^a_\nu \partial_\lambda G^a_\rho - \frac{1}{3} g f_{bca} G^a_\nu G^b_\lambda G^c_\rho\right] \ . \quad (3.84)$$

Therefore, $G^a_{\mu\nu}\tilde{G}^{\mu\nu}_a = \partial_\mu K^\mu$, which is expressed as a total divergence. It appears that the action of this quantity, that leads to the volume integral on the RHS, is reduced to a surface integral. But in this case, for the energy to be conserved, although $G^a_{\mu\nu}$ vanishes at infinity, but not the fields. Therefore, $G\tilde{G}$ term will be there in the QCD non Abelian Lagrangian. One may also notice that the dual $\tilde{G}$ term contains the Levicivita symbol $\epsilon^{\mu\nu ab}$, such a term gives rise to the violation of parity and time reversal, hence this term is a CP violating term. The other possible source of CP violation is via the quark masses (the mass term is $m\bar{q}_L q_R$), but this apparently can be avoided by a chiral transformation $q_L \longrightarrow e^{i\theta_{1q}/2} q_L$ and $q_R \longrightarrow e^{-i\theta_{2q}/2} q_R$. One can write both the transformations in terms of single transformation such as $e^{i\theta_q} \simeq e^{i(\alpha+\beta\gamma_5)}$, where α, β are related to θ_{1q} and θ_{2q}. Here $e^{i\alpha}$ is a vector like symmetry which does not distinguish between left (L) and right (R) chiral fields and $e^{i\beta\gamma_5}$ is the chiral (left chiral and right chiral terms transform differently). But since the chiral transformation has a triangle anomaly, it is therefore not a real symmetry

in the theory. In fact due to this anomaly the axial current is not conserved and in QCD the divergence of this axial current is written as $\partial_\mu \tilde{J}_\mu = \frac{\alpha_s^2 N_F}{16\pi^2} G^a_{\mu\nu} \tilde{G}^{\mu\nu}_a$, where N_F is the number of flavours. Therefore, under the chiral rotation, the Lagrangian now transforms like (leaving aside the kinetic term)

$$\mathcal{L}_{\rm QCD} \rightarrow \mathcal{L}'_{\rm QCD} = \frac{1}{4} G^a_{\mu\nu} G^{\mu\nu}_a - |m_q|(\bar{q}_L q_R + \text{h.c.}) - \frac{\alpha_s}{8\pi}(\theta + N_F \theta_q) G^a_{\mu\nu} \tilde{G}^{\mu\nu}_a \ . \tag{3.85}$$

With $(\theta + N_F \theta_q) = \bar{\theta}$, the QCD CP violation term in the above Lagrangian (Eq. 3.85) can be written as

$$\frac{\alpha_s}{8\pi} \bar{\theta} G^a_{\mu\nu} \tilde{G}^{\mu\nu}_a \ ,$$

where $\bar{\theta}$ is a parameter and this parameter is a coefficient of an operator which violates parity (P) and time reversal (T) but not the charge (C). Therefore, the physical effects of $\bar{\theta}$ is to be looked in the context of electric dipole moments of strongly interacting particles. The electric dipole moment of a nucleon is written as

$$d_{(N)} \sim \frac{e \bar{\theta} m_\pi^2}{m_N^3} \ . \tag{3.86}$$

In the above expression of the dipole moment, electric charge (e) appears because of the QED coupling of photon and also recognising the fact that the pion mass, $m_\pi \neq 0$ and hence the chiral symmetry is explicitly broken (connected to m_π). Here the nucleon mass is represented as m_N. This electric dipole moment for the neutron from the expression Eq. 3.86 comes out to be

$$|d_{(N)}| \sim 5.2 \times 10^{-16} \ \bar{\theta} \ e \ \text{cm} \ . \tag{3.87}$$

But the experimental upper bound of $d_{(N)}$ is given by $|d_{(N)}| < 2.9 \times 10^{-26}\ e\ \mathrm{cm}$. Therefore, we must have $|\bar{\theta}| < 10^{-9}$, which is referred to as the strong CP problem. In order to address this problem, $\bar{\theta} \longrightarrow 0$ (in fact $\bar{\theta}$ should be exactly equal to zero). This can be realised by invoking a chiral symmetry in the Lagrangian. Since SM does not have the chiral symmetry (because of Yukawa couplings), one more scalar doublet field is to be introduced such that the two doublets namely ϕ_u and ϕ_d give the masses to the up quarks and down quarks respectively through the spontaneous symmetry breaking (SSB) and then generating two vacuum expectation values (VEVs) v_u and v_d. Now one can see that the Yukawa couplings are invariant under the chiral transformations

$$\phi_d \longrightarrow e^{-i\beta}\phi_d \ ; \ \phi_u \longrightarrow e^{i\beta}\phi_u \ .$$

This is clearly a chiral U(1) symmetry as left and right chiral fields transform separately. This formalism itself can make the strong CP violation disappear. This axial U(1) symmetry is called the Peccei-Quinn (PQ) symmetry. But because of the VEVs v_u and v_d, the PQ symmetry is broken spontaneously as well giving rise to a massless Goldstone boson. This boson is called axion (a). This is also to be noted that the two VEVs should be such that $v^2 = \sqrt{v_u^2 + v_d^2} \simeq 246$ GeV. So that the W boson mass is now given by

$$M_W^2 \ = \ \frac{1}{4}g^2(v_u^2 + v_d^2) \ . \tag{3.88}$$

The kinetic term for the axion can be written as

$$\mathcal{L}_a^{\mathrm{kin}} \ = \ \frac{1}{2}(\partial_\mu a)(\partial^\mu a) \ . \tag{3.89}$$

But in this approach the axion should have a remaining shift symmetry, $a \rightarrow a + 2\pi n f_a$, with $f_a = \dfrac{v_u v_d}{\sqrt{v_u^2 + v_d^2}}$ and $n \in \mathbf{N}$ [81]. Now the interaction term of the axions and gluons can be written as

$$\mathcal{L}_a^{\rm gl} \sim -\frac{\alpha_s}{8\pi}\frac{a}{f_a} G\tilde{G} \, . \tag{3.90}$$

Therefore, the total QCD Lagrangian with PQ symmetry and its breaking can be so written that $\bar{\theta} G\tilde{G}$ vacuum term can be absorbed by the axion-gluon interaction term. This can also be noticed that the static $\bar{\theta}$ parameter can now be compared with the dynamic axion field ($a(x)$) and $\bar{\theta} \longrightarrow \dfrac{a(x)}{f_a}$. Therefore, the QCD Lagrangian becomes free of the CP violating term. Though the axion is massless at high temperature, but at the QCD energy scale ($\sim$ a few hundred MeV) the axion potential "tilts" because of the QCD instanton [14] effects. Therefore, the axion oscillates around the minimum of the axion potential. Thus the minimum of the potential forces the $\bar{\theta}$ parameter to be zero and it can solve the strong CP problem. The mass of the axion can be around μeV scale; $m_a \simeq 5.7 \mu\text{eV} \left(\dfrac{10^{12}\ \text{GeV}}{f_a}\right)$.

3.4 Dark Matter Halo Density Profiles

The information about the variation of the DM density $\rho(r)$ with the radial distance r is provided by DM halo profile which is popularly based on spherically symmetric profile. No specific DM halo profile for Milky Way galaxy could be obtained as yet. This is because of the incomplete knowledge of the astrophysical behaviour of DM in the disk as well as in the

[14] When the winding number $(n) > 0$ in gauge field configuration then that gauge field configuration is called instanton and anti-instantons are those when $n < 0$. The winding number appears in relation to the surface integral of the nonvanishing derivative part of $G\tilde{G}$. The different values of n are related to the different topological sectors of the theory.

Halo Models	α	β	γ	κ	r_s (kpc)	ρ_s $(\mathrm{GeV/cm^3})$
Navarro, Frenk, White (NFW) [82, 83]	1	3	1	0	20	0.259
NFW with adiabetic compression [84]	0.8	2.7	1.45	0	20	0.257
Moore [85]	1.5	3.0	1.5	0	20	0.256
Moore II [86]	1.0	3.0	1.16	0	30.28	0.108
Isothermal [87]	2	2	0	0	3.5	2.069
Burkert [88]	2	3	1	1	12.67	0.729
Kravtsov [89]	2	3	0.2	0	10	0.361

Table 3.1: Values of parameters for DM halo density profiles.

halo of Milky Way. But astrophysicists arrive at certain halo profiles based on the observed astrophysical data and rigorous numerical simulations. These halo profiles describe the DM density at different radial distances from the centre of the galaxy. Empirically, this density profile is given by

$$\rho(r) = \frac{\rho_s}{\left(k+\left(\frac{r}{r_s}\right)^{\gamma}\right)\left(1+\left(\frac{r}{r_s}\right)^{\alpha}\right)^{\frac{\beta-\gamma}{\alpha}}}, \tag{3.91}$$

where α, β, γ and k are the parameters and their different sets of values represent different halo profiles tabulated in Table 3.1. The other parameters ρ_s and r_s represent the scale density and scale radius respectively which are also tabulated in Table 3.1.

Some of the halo density profiles that are generally used in the astrophysical calculations are furnished in the following equation.

$$
\begin{aligned}
\text{NFW} \qquad & \rho_{\rm NFW}(r) = \rho_s \frac{r_s}{r}\left(1+\frac{r}{r_s}\right)^{-2} , \\
\text{NFWII} \qquad & \rho_{\rm NFWII}(r) = \rho_s \left(\frac{r_s}{r}\right)^{1.45}\left(1+\left(\frac{r}{r_s}\right)^{0.8}\right)^{-1.5625} , \\
\text{Moore} \qquad & \rho_{\rm Moo}(r) = \rho_s \left(\frac{r_s}{r}\right)^{1.5}\left(1+\left(\frac{r}{r_s}\right)^{1.5}\right)^{-1} , \\
\text{MooreII} \qquad & \rho_{\rm MooII}(r) = \rho_s \left(\frac{r_s}{r}\right)^{1.16}\left(1+\frac{r}{r_s}\right)^{-1.84} , \\
\text{Isothermal} \qquad & \rho_{\rm Iso}(r) = \frac{\rho_s}{1+(r/r_s)^2} , \\
\text{Burkert} \qquad & \rho_{\rm Bur}(r) = \frac{\rho_s}{(1+r/r_s)\left(1+(r/r_s)^2\right)} , \\
\text{Kravtsov} \qquad & \rho_{\rm Krs}(r) = \rho_s \left(\frac{r_s}{r}\right)^{0.2}\left(1+\left(\frac{r}{r_s}\right)^{2}\right)^{-1.4} .
\end{aligned}
\tag{3.92}
$$

A different kind of halo profile namely Einasto halo [90, 91] profile is given as

$$
\text{Einasto}: \quad \rho_{\rm Ein}(r) = \rho_s \exp -\frac{2}{\tilde{\alpha}}\left[\left(\frac{r}{r_s}\right)^{\tilde{\alpha}} - 1\right] , \tag{3.93}
$$

where the value of the parameter $\tilde{\alpha}$ is chosen to be 0.17 and r_s is 20 kpc. The different DM halo density profiles are shown in Fig. 3.8.

3.5 Dark Matter Detection

Besides the evidence for DM, which is overwhelmingly gravitational in nature, the experimental searches for DM are being intensely pursued by several terrestrial as well as space-based experiments. These DM search experiments intend not only to confirm the

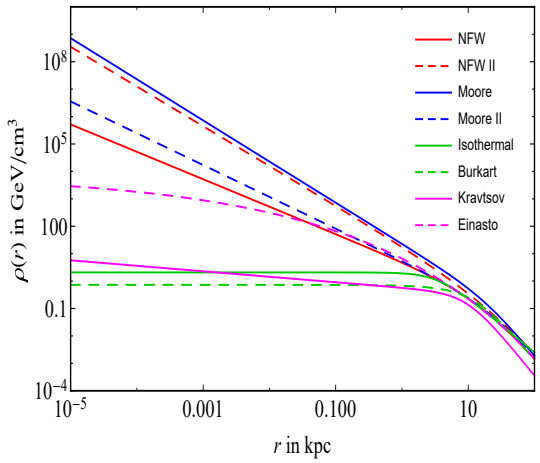

Figure 3.8: Variations of different DM halo density profiles with the radial distance r from the ceter of Milky Way galaxy.

presence of DM but also attempt to probe the particle nature and other properties. The experimental searches for DM broadly fall under three categories namely

1. Direct search experiments of DM,

2. Indirect detection of DM through the detection of products obtained from the decay or annihilation of DM,

3. Collider searches for the signature of DM.

The possible scattering of a DM particle off a detctor nuclei will lead to the direct detection of DM through its direct impact with the detector material. On the other hand, the searches for the indirect signature of DM rely on the detection of the end products obtained via the processes such as decay, annihilation etc. that the DM or the pair of DM may undergo. The colliders can also contribute to the search for particle DM in which case DM may be produced via the collisions of SM particles in the collider such as Large Hadron Collider (LHC). The schematic diagram of these three different DM detection methods has been shown in Fig. 3.9.

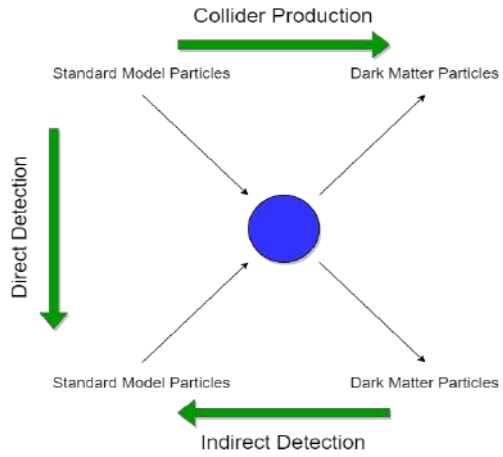

Figure 3.9: The schematic representation of possible DM detection channels. Different types of DM detection methods can be broadly envisaged depending on the direction of the time axis, which is indicated by green arrow.

1. **Direct Detection**

   One category of the well known experimental searches for DM is direct DM search experiment which relies on the possible scattering of the DM particle off the detector nucleus. In such eventual scattering of a DM particle off the detector nucleus, the nucleus suffers a recoil and the experiment attempts to measure the recoil energy by mechanisms of scintillation or ionisation or phonon excitations or several combinations of them. It may be mentioned here that these DM direct search experiments are aimed to detect WIMPs with mass few tens of GeV and beyond. Due to very weak interaction strength of DM, this recoil energy will be very low ($\sim$ keV). Therefore, in order to detect any signal from this low recoil energy of the scattered nuclei due to possible DM impact, detectors should be installed in a very low background environment shielded from cosmic rays, which is required for the precise measurement of such low recoil energy. The energy deposited by this recoiled nucleus is mainly detected by three different kinds of techniques, namely, (a) scintillation, used

by DAMA [92], ZEPLIN-I [93] experiments, (b) ionisation, used by CoGeNT [94], DRIFT [95] experiments and (c) phonon excitation, used by the experiment CRESST [96]. Multiple detection techniques have also been used in some of the ongoing experiments, for example, both ionization and phonon methods are used by CDMS-II [97], superCDMS [98], EDELWEISS-II [99] experiments, the combination of scintillation and ionisation methods are used by the experimets namely XENON 100 [100], LUX [101] and ZEPLIN-III [102], while the phonon and scintillation methods are used together by CRESST-II [103], EURECA [104] etc.

The scattering of a cold DM WIMP off a detector nucleus is elastic in nature. At the fundamental level, WIMP interacts with quarks (and gluons) inside the nucleon. Since the coupling of this type of interaction depends on the particle candidate of CDM for a chosen particle physics model, the coupling is a model dependent parameter. Also the scattering of WIMP off a target nucleus is of concern here. Therefore, the interactions at the fundamental level is to be translated to the nucleonic level using proper matrix elements of quarks and gluons (hadronic matrix elements) in nucleonic state. The distribution of hadrons (quarks and gluons) in nucleons is also important for theoretical estimation of WIMP-nucleon elastic scattering cross-section. Thus the proper nuclear matrix elements can be obtained by evaluating the hadronic matrix elements (matrix elements of nucleon operator) in the nucleon state.

The elastic scattering can be classified into two types depending on the spin state of the detector nucleus with which the WIMP DM is interacting. These are spin independent (SI) and spin dependent (SD) scattering. The SI scattering involves the scalar or vector type interactions, where the scalar part arises from the term [15] $\chi\bar{\chi}q\bar{q}$ in the Lagrangian while the term $\chi\gamma^{\mu}\bar{\chi}q\gamma_{\mu}\bar{q}$ in the Lagrangian accounts for the vector

[15]The mediator of the scalar type t-channel interaction can be Higgs boson or any Higgs like scalar.

type interaction (χ and q ($\equiv u, d, s, c, b, t$) represent the DM candidate and the SM quark respectively). The scalar part of the SI cross-section is given by [105]

$$\sigma_{\rm scalar} \;=\; \frac{4\mu^2}{\pi}[Zf_p + (A-Z)f_n]^2 \;, \tag{3.94}$$

where α_q is the coupling and $f_p = \sum_{\text{all } q} \frac{\alpha_q}{m_q} m_p f_q^p$; $f_n = \sum_{\text{all } q} \frac{\alpha_q}{m_q} m_n f_q^n$, f_p and f_n are factors that include the contribution of light quarks and the contribution of interaction with gluons in the nucleons. These factors are dependent on the scalar matrix elements. The factor $m_p f^p_{T_q} = \langle p|m_q\bar{q}q|p\rangle = m_q B_q$ where B_q is the scalar matrix element. The product $m_q B_q$ is invariant under renormalization and therefore is a physical quantity. For the lighter quarks, the values of $f^x_{T_q}$ ($x = p$ or n) are given as [105] $f^p_{T_u} = 0.020, f^p_{T_d} = 0.026, f^p_{T_s} = 0.118, f^n_{T_u} = 0.014, f^n_{T_d} = 0.036, f^n_{T_s} = 0.118$. For the heavier quarks, $f^x_{T_{c,b,t}} = \frac{2}{27}(1 - f^x_{T_u} - f^x_{T_d} - f^x_{T_s})$. The term μ in Eq. 3.94 is the reduced mass, $\mu = \frac{m_\chi m_{\rm nucleus}}{m_\chi + m_{\rm nucleus}}$, where m_χ and $m_{\rm nucleus}$ are the masses of DM (χ) and nucleus respectively. For the case of $f_p \simeq f_n$, Eq. 3.94 will take the form

$$\sigma_{\rm scalar} \;=\; \frac{4\mu^2 f_p^2 A^2}{\pi} \;. \tag{3.95}$$

Now for a single nucleon 'n', we can write the SI WIMP scalar scattering cross-section as (considering $f_p = f_n$) $\sigma^{\rm n}_{\rm scalar} = \frac{4\mu_{\rm n}^2 f_n^2}{\pi}$, where $\mu_{\rm n} = \frac{m_\chi m_{\rm n}}{m_\chi + m_{\rm n}}$, $m_{\rm n}$ defines the mass of 'n'. In terms of $\sigma^{\rm n}_{\rm scalar}$, Eq. 3.95 can be written as

$$\sigma_{\rm scalar} \;=\; \sigma^{\rm n}_{\rm scalar}\frac{\mu^2}{\mu_{\rm n}^2}A^2 \;. \tag{3.96}$$

The multiplicative factor $\frac{\mu^2}{\mu_{\rm n}^2}A^2$, which connects $\sigma_{\rm scalar}$ and $\sigma^{\rm n}_{\rm scalar}$, will be different

for different mass number A (i.e. different target nuclei).

The axial vector type interaction term in the Lagrangian ($\bar{\chi}\gamma^{\mu}\gamma_5\chi\bar{q}\gamma_{\mu}\gamma_5 q$) becomes relevant for SD interaction. The SD scattering cross-section is considered when the target nucleus has non zero ground state spin [16] [17]. The SD scattering cross section is directly proportional to the factor $j(j+1)$, j being the nuclear angular momentum of the detector nucleus at its ground state. The SI scattering is relevant for the direct DM search experiments like XENON100 [105], LUX [101], CDMS [97], SuperCDMS [98], CoGeNT [94], DAMA [92], EDELWEISS-II [99], CRESST [96] etc. while for PICASSO [106], PICO [107] etc. experiments it is the SD scattering of DM off detector nucleus, which is more important. However, in the absence of convincing results from these DM direct detection experiments, these experiments give upper bounds for DM-nucleon SI and SD interactions for different masses of WIMP DM. Most stringent among them is by LUX (liquid Xenon) detector. For example, for a 50 GeV DM, the upper bound, given by LUX experiment, for SI WIMP-nucleon elastic cross-section $\sigma_{\rm SI} > 2.2 \times 10^{-46}$ cm^2 at 40% C.L. [108]. On the other hand, the most stringent present upper bound on DM-proton SD scattering cross-section is $\sigma_{\rm SD} \sim 5 \times 10^{-40}$ cm^2 [109, 110]. This may be mentioned that with more and more data accumulated from these experiments, their analyses bring down these upper bounds further and approaches towards the regime of coherent neutrino-nucleon scattering cross-section (the "neutrino floor"). Going by this trend, the $\sigma_{\rm SI}$ upper bound may overlap with the "neutrino floor". In this scenario, it will be difficult to discriminate a DM signal from that of background neutrinos. However, if the DM

[16] The axial vector type interaction (SD interaction) may proceed through the t-channel exchange of neutral vector bosons.

[17] Apart from the above mentioned scalar and axial current interaction, there can also have the neutral current interaction between the WIMPs (χ) and quarks (q), where SM Z boson or Z' boson (extra neutral gauge boson) acts as a possible mediator. This is a vector type spin independent interaction.

is indeed detected in direct direction experiments then that will be a "smoking gun signature" of the existence of beyond Standard Model (BSM) scenario as the SM of particle physics does not have any viable CDM candidate.

2. **Indirect Detection of Dark Matter**

Besides the direct detection searches for DM, there are another promising detection method of DM through which we can detect the annihilation or decay products of DM trapped in the heavy dense region of celestial objects namely core of the Sun, GC (GC), dwarf galaxies etc. A primordial SHDM may undergo cascade decays to produce SM particles as the end products. The information about the particle nature of DM can be revealed by probing the secondary particles, which are obtained via the DM annihilation or decay mechanism, such as gamma ray, neutrinos, charged cosmic rays including electrons, protons and their antiparticles positrons, antiprotons respectively etc. This type of detection method is known as the indirect detection of DM. Detection of these highly energetic gamma rays (by satellite-borne telescope-like Fermi-LAT [111] as also several earthbound experiments like H.E.S.S [112], VARITUS [113] etc.) or neutrinos (by experiments like ICECUBE [114], ANTARES [115] etc.), positrons (by satellite-borne experiments like PAMELA [116], AMS [117]), provide insightful information about the particle nature of DM.

Formalism of Indirect Detection of DM

The annihilation rate of the DM particles can be derived by taking into account that the DM particles are either self conjugate or not. Let us consider, $m_\chi(m_{\bar{\chi}})$ is the mass of DM particle χ ($\bar{\chi}$, antiDM particle) and the density of DM (antiDM) is defined as

$\rho_\chi(\rho_{\bar{\chi}})$. The annihilation rate per DM or antiDM can be written as

$$\sum_i^{\text{channels}} \frac{\rho_\chi}{m_\chi}\langle\sigma_{\text{ann}}v\rangle_i \quad \text{or} \quad \sum_i^{\text{channels}} \frac{\rho_{\bar{\chi}}}{m_{\bar{\chi}}}\langle\sigma_{\text{ann}}v\rangle_i \ , \tag{3.97}$$

where $\langle\sigma_{\text{ann}}v\rangle_i$ is the thermally averaged annihilation cross-section and the subscript 'i' represents the DM annihilation channel. In Eq. 3.97 the summation over all possible annihilation channels has been considered. The number of DM (antiDM) particles exist in the interaction volume V is $\frac{\rho V}{m_\chi}\left(\frac{\rho V}{m_{\bar{\chi}}}\right)$. Therefore, the number of possible DM - antiDM pairs per unit volume is given as

$$\frac{\rho_\chi V}{m_\chi}\frac{\rho_{\bar{\chi}} V}{m_{\bar{\chi}}}\frac{1}{V} \ . \tag{3.98}$$

The total annihilation rate in V can be expressed as the product of the annihilation rate per DM (antiDM) particle and the number of possible pairs of DM-antiDM particles in V as

$$\left(\sum_i^{\text{channels}} \frac{\rho_\chi}{m_\chi}\langle\sigma_{\text{ann}}v\rangle_i\right)\cdot\left(\frac{\rho_{\bar{\chi}}V}{m_{\bar{\chi}}}\right) \ . \tag{3.99}$$

Assuming, $\rho_\chi = \rho_{\bar{\chi}} = \rho/2$ (say) and $m_\chi = m_{\bar{\chi}} = m$ (say), the annihilation rate in the infinitesimal interaction volume is given by

$$\Gamma_{\text{ann}} \ = \ \frac{\rho^2}{4m^2}dV \sum_i^{\text{channels}} \langle\sigma_{\text{ann}}v\rangle_i \ . \tag{3.100}$$

In case of self conjugate DM

$$\Gamma_{\text{ann}} \ = \ \frac{\rho^2}{2m^2}dV \sum_i^{\text{channels}} \langle\sigma_{\text{ann}}v\rangle_i \ , \tag{3.101}$$

as the number of particles is doubled. Thus in general the rate of annihilation can be written as

$$\Gamma_{\rm ann} \;=\; \frac{\rho^2}{2\alpha m^2} dV \sum_i^{\rm channels} \langle \sigma_{\rm ann} v \rangle_i \;, \tag{3.102}$$

where $\alpha = 1$ for self conjugate case and $\alpha = 2$ otherwise. Now, dV can be written as $dV = l^2 d\Omega dl$, l being the distance between the location of the volume element and the observer and $d\Omega$ is the infinitesimal solid angle subtended by the source (volume element) at the observer. The differential flux of the end products (photons (γ) or neurtinos (ν) say), which may be obtained from the DM self annihilation, at a distance l from the observer can be written as

$$\left(\frac{d\Phi}{dE}\right)_{\gamma,\nu} \;=\; \frac{1}{4\pi l^2} \frac{\rho^2 \langle \sigma_{\rm ann} v \rangle}{2\alpha m^2} \sum_i^{\rm channels} \mathcal{B}_i \frac{dN^i}{dE} l^2 dl d\Omega \;. \tag{3.103}$$

where $\dfrac{dN^i}{dE}$ is the differential energy spectrum of the end products 'i', that gives the spectral shape of the signal. The branching fraction to different annihilation channels (i) is denoted by $\mathcal{B}_i$. One can readily see that the DM annihilation rate ($\Gamma_{\rm ann}$) is proportional to the square of DM density (ρ). The differential flux of ν or γ in the galactic halo produced by the DM annihilation in an angular direction that subtends a solid angle $d\Omega$ is given by [12]

$$\left(\frac{d\Phi}{d\Omega dE}\right)_{\gamma,\nu} \;=\; \frac{1}{8\pi\alpha m^2} \langle \sigma_{\rm ann} v \rangle \sum_i^{\rm channels} \mathcal{B}_i \frac{dN^i}{dE} \int_{\rm l.o.s} dl \rho[r(l,\theta)]^2 \;. \tag{3.104}$$

In the DM decay case, the decay rate can be written as

$$\mathcal{D}_{\rm decay} \;=\; \frac{\rho}{\alpha m} dV \sum_{i}^{\rm channels} \Gamma_i \;, \tag{3.105}$$

where the DM decay width for decay channel i is denoted as Γ_i. Therefore, for the case of decaying DM, the differential flux of the decay products (ν or γ) in the galactic halo can be written as, i.e.

$$\left(\frac{d\Phi}{d\Omega dE}\right)_{\gamma,\nu} \;=\; \frac{1}{4\pi\alpha m}\Gamma_{\rm decay} \sum_{i}^{\rm channels} \mathcal{B}_i \frac{dN^i}{dE} \int_{\rm l.o.s} dl \rho[r(l,\theta)] \;. \tag{3.106}$$

where $\Gamma_{\rm decay}$ represents total decay width, which is obtained by considering the summation over all possible DM decay channels. In contrast to the DM annihilation scenario, the differential flux of the decay products for the case of decaying DM is proportional to the single power of $\rho(r)$.

In both Eqs. 3.104, 3.106, r represents the distance at which the target is located from the centre of the DM halo and it is given by

$$r \;=\; \sqrt{r_\odot^2 + l^2 - 2 r_\odot l \cos\theta} \;, \tag{3.107}$$

where l denotes the l.o.s distance and θ is the aperture angle i.e. the angle between the direction of the l.o.s and the line connecting the observer and the GC. The distance between the observer (located at the solar system) and the GC is denoted as $r_\odot$ (~ 8.5 kpc). Different DM halo density profiles are used in the astrophysical calculation of the DM density ($\rho(r)$), which is discussed elaborately in Section 3.4.

Now we introduce a term named as the astrophysical J-factor, which indicates the

total DM contained within the solid angle $d\Omega$. In case of both annihilating DM and decaying DM, this J-factor can be written as

$$J_{\rm ann} = \int_{\rm l.o.s} dl(\rho[r(l,\theta])^2 \quad \text{(annihilation)} \ , \tag{3.108}$$

$$J_{\rm dec} = \int_{\rm l.o.s} dl\rho[r(l,\theta)] \quad \text{(decay)} \ . \tag{3.109}$$

Therefore, in terms of the astrophysical J-factor Eq. 3.104 and Eq. 3.106 can be expressed as

$$\left(\frac{d\Phi}{d\Omega dE}\right)_{\gamma,\nu} = \frac{1}{8\pi\alpha m^2}\langle\sigma_{\rm ann}v\rangle \sum_i^{\rm channels} \mathcal{B}_i \frac{dN^i}{dE} J_{\rm ann} \ \text{(annihilation)} \tag{3.110}$$

$$\left(\frac{d\Phi}{d\Omega dE}\right)_{\gamma,\nu} = \frac{1}{4\pi\alpha m}\Gamma_{\rm dec} \sum_i^{\rm channels} \mathcal{B}_i \frac{dN^i}{dE} J_{\rm dec} \quad \text{(decay)} \ . \tag{3.111}$$

3. Collider Searches

Although collider is the most successful tool to probe much about the properties of ordinary matter, the collider experiment is also utilised for probing the DM and more importantly its particle nature [118–120]. The DM production at collider relies on the interactions between the DM particles and the colliding SM particles. DM, if produced at the particle accelerators like LHC, may escape the collider remaining undetected since the DM is stable and if at all it interacts, it does so very weakly with the SM particles. But its signature may be traced in the form of missing energy, which would be acquired during the reconstruction of momentum for the event. Observation of such missing energy may lead to ascertain the signature of DM. Moreover, there are some alternative proposals of collider searches of DM, such as production of DM at collider from invisible decay of Higgs boson or Z boson, where the in-

visible decay branchings of these bosons are constrained by LHC, LEP experiments, which is used to put further bounds on the couplings of such invisible decay of these Higgs or Z bosons into DM. There are both advantages and disadvantages of the collider searches for DM. For the lighter DM search at the collider, the seacrh becomes more sensitive as they do not suffer from threshold effect, compared to both direct and indirect searches, which are less sensitive because of the smallness of the interaction energy of this lighter DM particles. On the other hand, direct and indirect detection of DM are more appropriate for the case of heavy DM particles in comparison to their collider searches as sufficiently high amount of energy is required to generate such heavy DM. The collider searches for DM also suffer from certain uncertainties such as the basic understandings of the signatures that might have been caused by "true" DM or some other unstable particles.

CHAPTER 4

INTRODUCTION TO NEUTRINOS AND NEUTRINO OSCILLATIONS

It was James Chadwick in the early 20th century who noticed that the electrons in β decay have a continuous spectrum rather than being a line spectrum. But this observation appears to violate the law of conservation. Wolfgang Pauli in 1930 proposed the existence of a low mass neutral particle, emitting along with the β decay and thereby sharing energy with β decay electrons. This however could explain the continuous nature of the β decay spectrum. As a result the existence of a new particle namely neutrino (ν) came to be known.

As discussed in the previous chapter, in the framework of the Standard Model (SM) of particle physics, neutrinos are known to be of three flavours namely electron neutrino (ν_e), muon neutrino (ν_μ) and tau neutrino (ν_τ) and are the partners of e, μ and τ in their respective $\mathrm{SU}(2)$ doublets. Within SM, neutrinos cannot have mass because of the absence of right handed neutrinos but various neutrino oscillation experiments conclusively prove that neutrinos are massive. Therefore, neutrinos could serve as a window to explore the

physics beyond SM. As various experiments suggest that even though neutrinos are massive their masses are extremely small, the neutrinos are therefore related to very low mass scale physics and the behaviour of new physics in such low mass scale neutrinos can also play an important role in understanding fermion mass generation.

Similar to the mixing in quark sector, in the leptonic sector also the mixing matrix arises through the charged current (CC) term. This mixing matrix is called Pontecorvo-Maki-Nakagawa-Sakata (PMNS) matrix [121]. The CC interaction for the lepton is given as

$$\begin{aligned} \mathcal{L} &= -\frac{g}{2\sqrt{2}}[\bar{\nu}_\alpha \gamma^\mu (1-\gamma^5) l_\beta W_\mu^+ + h.c.] \ , \\ &= -\frac{g}{2\sqrt{2}}[\bar{\nu}_\alpha U_\nu^\dagger U_l \gamma^\mu (1-\gamma^5) l_\beta W_\mu^+ + h.c.] \ , \end{aligned} \tag{4.1}$$

where

$$U_{\rm PMNS} = U_\nu^\dagger U_l = \begin{pmatrix} c_{12}c_{13} & s_{12}s_{13} & s_{13}e^{-i\delta} \\ -s_{12}c_{23} - c_{12}s_{23}s_{13}e^{i\delta} & c_{12}c_{23} - s_{12}s_{23}s_{13}e^{i\delta} & s_{23}c_{13} \\ s_{12}s_{23} - c_{12}c_{23}s_{13}e^{i\delta} & -c_{12}s_{23} - s_{12}c_{23}s_{13}e^{i\delta} & c_{23}c_{13} \end{pmatrix} . \tag{4.2}$$

In the above $c_{ij} = \cos\theta_{ij}, s_{ij} = \sin\theta_{ij}$ and δ is CP phase, $\theta_{ij}(i,j = 1,2,3)$ are the neutrino mixing angles. The problem of CP violation in the leptonic sector can be addressed by studying the neutrino oscillation in general and baseline neutrino experiments in particular. The experimental discovery of neutrino oscillations had been initiated by solar and atmospheric neutrino experiments for example by Chlorine (Homestake) experiment [122], SNO experiments (Sudbury Neutrino Observatory) [123] for solar neutrinos and mainly Kamiokande and Super-Kamiokande (SK) experiments [124] for atmospheric neutrinos. Neutrino oscillations had been further studied by reactor neutrino experiments like

KamLAND [125, 126], Daya Bay [127–133], Reactor Experiment for Neutrino Oscillation (RENO) [134], Double Chooz [135] experiments and long baseline (LBL) accelerator neutrino experiments such as K2K [136], MINOS [137–148], T2K [149] etc. Recently more such experiments namely Deep Underground Neutrino Experiment (DUNE) [150–153] and Noνa long baseline experiments [154–159] are coming up. The neutrino oscillations for coherent neutrinos on their propagation, take place by the presence of neutrino mixing (of neutrino mass eigenstates ($|\nu_i\rangle$) and flavour eigenstate $|\nu_\alpha\rangle$) and the phase difference that the neutrino mass eigenstates acquire during their propagation. The phase differences can be expressed in terms of the mass square difference between two neutrinos (Δm^2_{ij}) and the distance traversed by them. The probabilities of the neutrino oscillations also depend on the mixing angles (θ_{ij}) appearing in PMNS matrix (Eq. 4.2) and the CP phase δ. Several neutrino oscillation experiments therefore measure the values of Δm^2_{ij} and θ_{ij} but could not determine the absolute masses of the neutrinos. But yet there are issues that can still be probed by neutrino oscillation experiments such as the order of mass hierarchy of the neutrinos, the CP phase and whether neutrino oscillations can be affected by other exotic mechanisms e.g., the possible weak violation of equivalence principle (VEP), Lorentz violation, possible differences in velocities of different types of neutrinos etc. If there exists a fourth sterile neutrino in addition to three active neutrinos (ν_e, ν_μ and ν_τ), then the existence of such a sterile neutrino is also investigated through neutrino oscillations where a four flavour oscillation formalism is to be invoked.

Neutrinos are also important in astrophysics and cosmology. Neutrinos carry away about 99% of the energy released during Supernova explosions. This is suggested that interactions of the neutrinos in the Supernova core greatly influence the Supernova explosion mechanism. Also since these neutrinos are emitted from Supernova or solar cores (for the case of solar neutrinos) they carry information of the Supernova or solar cores which are

not accessible by other optical observations. The very and ultrahigh energy (UHE) neutrinos (of energy range from TeV upto EeV) could be possibly produced in high energy phenomena at cosmological UHE sources such as Gamma Ray Bursts (GRBs), Blazars, Active Galactic Nuclei (AGN) etc. through the likely process of energetic $p\gamma$ interactions (through the production of Δ which decays to pions (π) and the pions eventually produce ν_μ and ν_e). Study of these UHE neutrinos by Cherenkov detectors, e.g. IceCube [160], PINGU [161], Deepcore [162] at South Pole, Astronomy with a Neutrino Telescope and Abyss Environment Research (ANTARES) [163] at Mediterranean Sea can reveal the natures and mechanisms of the cosmic UHE sources. The simultaneous detections of both neutrino signals and the high energy γ-ray signals (and possibly Gravitational Wave signals) from such high energy sources constitute the multimessenger study of these sources and could provide better understandings of the UHE processes in them. Therefore with these UHE neutrinos, it is possible to probe the energy scale as high as PeV (or EeV) which is otherwise inaccessible in collider experiments.

The big bang nucleosynthesis (BBN) is influenced by neutrino interactions, number of neutrino species as also the neutrino oscillations. The number of relativistic neutrino species influences the mass fraction of $^2\mathrm{He}$ and the relative number density of Deuterium. But again this limit depends on baryon density ($\Omega_b h^2$) which in turn is given by the Cosmic Microwave Background Radiation (CMBR) measurements.

Active-sterile neutrino oscillations, in case a fourth neutrino or sterile neutrino ν_s exists may influence the primordial abundances of the light elements. If active neutrinos oscillate to sterile neutrinos before the decoupling of active neutrinos, then an increase of mass fraction of $^2\mathrm{He}$ and Deuterium results. Alternatively if ν_e to ν_s oscillation happens after ν_e decoupling then it leads to larger $^2\mathrm{He}$ fraction although the total energy density of all neutrinos would remain same. A deficit of ν_e due to oscillations at high energies results

in smaller $^2\mathrm{He}$ fraction while the deficit of ν_e at low energy increases the mass fraction of $^2\mathrm{He}$. If neutrino oscillation creates an asymmetry between ν_e and $\bar{\nu}_e$ then the behaviour of n/p ratio may not remain as $n/p \sim \exp(-\mu_\nu/T)$, where n and p define neutron and proton respectively. Present data can permit an asymmetry between ν_e and $\bar{\nu}_e$ much higher than the standard asymmetry of 10^{-10}.

The active neutrinos can contribute to hot dark matter (HDM) while if a sterile neutrino is in the mass range of keV then they could form cosmologically interesting warm dark matter (WDM). A massive neutrino can decay to lighter neutrinos or other particles such as photons, light scalar bosons or a pair of light fermions. But if neutrino decays into photons then these photons could be directly observable in such a way that they would not contradict other astronomical data on cosmic photons. If neutrino decays before hydrogen recombination then the decay products may distort the CMBR spectrum. On the other hand, if the neutrino decays after the hydrogen recombination or still later then it will produce electromagnetic (EM) radiation all across its spectrum. The neutrino mass in eV range and decays of neutrinos with lifetime $\sim 10^{13}$ sec influence the spectrum of CMBR angular fluctuations. If neutrinos decay to photon and e^+e^- pairs then the perfect Planckian spectrum of CMBR could be distorted. This will also happen if neutrinos decay into invisible modes such as $\nu_h \to \nu_l + \phi$ where ϕ is a light and massless scalar, ν_h and ν_l are heavy and light neutrinos respectively.

The large scale structure strongly depends upon the primordial spectrum of densiy fluctuations. Although this spectrum is assumed to be flat (predicted by the simplest inflationary models), the spectrum depends upon the relative mass fraction of cold dark matter (CDM) and HDM. If neutrinos are HDM candidates then their number denisties are fixed (112 cm^{-3}) and the relic density (Ω_{HDM}) is determined by the masses of the neutrinos. The density fluctuation at small scale is more suppressed for higher mass and hence for higher

$\Omega_{\rm HDM}$. But at the large scale the growth rate for density fluctuations for the case of HDM coincides with that for CDM. Therefore, at large scale the structure formation processes with neutrinos coincide with that for CDM (neutrino velocity reduces at large scale).

The fundamental charged fermions in SM are generally differentiated from their antiparticles by their charges. An antiparticle has an opposite charge to that of a particle. But neutrinos being neutral particles, the particle-antiparticle discrimination on the basis of their charges are not possible for neutrinos. In nature, the neutrinos appear with left handed chirality while the antineutrinos appear with right handed chirality. This may be mentioned here that for massless particles the chirality $(1\pm\gamma_5)$ is a good quantum number but for massive particles chirality is not a good quantum number. This means, in principle there could be a mixture of the "wrong" chirality with the "right" chirality but this admixture is $\sim m_\nu/e$, where m_ν is the mass of the particle, in this case neutrino and E is its energy. Since m_ν is very small, this admixture is also negligibly small. Thus for a relativistic particle like neutrino, the chirality is nearly conserved and descriptions of neutrinos in terms of their chiral states are useful.

If a particle is not identical with its antiparticle then it is a Dirac particle while in case they are identical, the particles are called Majorana particles. Therefore, if neutrinos are Majorana particles then the lepton number is violated by 2 units. The operator that connects the particle and the antiparticle is called the charge conjugation operator C. Operating C on a fermion field ψ one obtains,

$$\psi \xrightarrow{C} \psi^c \equiv C\psi C^{-1} = \eta_c C\bar{\psi}^{\intercal} \ , \tag{4.3}$$

where η_c is a phase factor with $|\eta_c| = 1$ and particle-antiparticle conjugation operator C has the form of a 4×4 matrix given by $C = i\gamma_2\gamma_0$ which follows the properties $C^\dagger =$

$C^{\intercal} = C^{-1} = -C,\ C\gamma_\mu C^{-1} = -\gamma_\mu^{\intercal}$ (using the properties of Dirac γ matrices). Also,

$$(\psi^c)^c = \psi,\ \overline{\psi^c} = \psi^{\intercal} C,\ \overline{\psi_1}\psi_2^c = \overline{\psi_2^c}\psi_1,\ \overline{\psi_1} A \psi_2 = \overline{\psi_2^c}(CA^{\intercal}C^{-1})\psi_1^c\ , \tag{4.4}$$

where ψ, ψ_1, ψ_2 etc. are the four component Dirac spinors and A has the form of an arbitrary 4×4 matrix. Again operating the projection operators

$$P_L\psi = \psi_L;\ C:\ \psi_L \to P_L\psi^c = (\psi_L)^c = (\psi^c)_R\ . \tag{4.5}$$

Similarly,

$$P_R\psi = \psi_R;\ C:\ \psi_R \to P_R\psi^c = (\psi_R)^c = (\psi^c)_L\ . \tag{4.6}$$

Eqs. 4.5, 4.6 can be achieved by using the properties of Dirac γ matrices. It is therefore clear from the above equations that the antiparticle of the left handed fermion is right handed and vice versa. The mass term of a massive fermion is written as

$$\mathcal{L}_{\text{mass}} = m\bar{\psi}\psi = \overline{(\psi_L + \psi_R)}(\psi_L + \psi_R) = \overline{\psi_L}\psi_R + \overline{\psi_R}\psi_L\ . \tag{4.7}$$

Therefore, a massive fermion field has both L and R components. If the right handed component is completely independent of the left handed component of a fermion field then that fermion is called a Dirac fermion. On the other hand, if the right handed field is a charge conjugate field of the left handed component such that $\psi_R = (\psi_L)^c = (\psi^c)_R$ then it is called a Majorana fermion. Therefore the Majorana field is expressed as $\psi = \psi_L + \psi_R = \psi_L + \eta(\psi_L)^c$. In order to construct a massive Dirac field one should include the fields $\psi_L, \psi_R, \psi_L^c, \psi_R^c$ and thus it has four degrees of freedom. For Majorana field however we

have only two degrees of freedom namely ψ_L and $(\psi_L)^c = \psi_R^c$. It can also be observed that $\bar{\psi}\psi$ is invariant under U(1) transformation of type $\psi \rightarrow e^{i\alpha}\psi$. This means the Dirac mass term conserves the charges (electric charge, lepton and baryon number etc.). But since the Majorana mass term has only two components, it breaks all charges by 2 units. Therefore, no charge particle can have Majorana mass since electric charge is conserved exactly. Thus among the known fermions it is only the neutrinos that can be a Majorana particle.
The parity transformation of a field $\psi(\vec{x}, t)$ by operating the parity operator P is defined as

$$\psi(\vec{x}, t) \xrightarrow{P} P\psi(\vec{x}, t)P^{-1} = \eta_P \gamma_0 \psi(-\vec{x}, t) \ , \tag{4.8}$$

where η_P is the phase and $\eta_P = \pm 1$. Therefore for the charge conjugated field ψ,

$$\psi^c = \eta_C C \bar{\psi}^\intercal \xrightarrow{P} \eta_C \eta_P^* C \gamma_0^\intercal \bar{\psi}^\intercal = -\eta_P^* \gamma_0 \psi^c \ . \tag{4.9}$$

This equation signifies that a fermion and an antifermion have opposite parity. For a Majorana particle however $\psi^c = \pm\psi$. This implies $\eta_P = -\eta_P^*$. Therefore a Majorana field now can be written as

$$\psi_M \ = \ \frac{1}{\sqrt{2}}(\psi + \eta_C \psi^c) \ , \tag{4.10}$$

where $\eta_C = \lambda_C e^{2i\phi}, \lambda_C = \pm 1$. On applying a phase transition on ψ_M, one obtains

$$\psi_M \rightarrow \psi_M e^{-i\phi} = \frac{1}{\sqrt{2}}(\psi e^{-i\phi} + \lambda_C \psi^c e^{i\phi}) = \frac{1}{\sqrt{2}}(\psi + \lambda_C \psi^c) \equiv \psi_M \ . \tag{4.11}$$

Also

$$\psi_M^c = \frac{1}{\sqrt{2}}(\psi^c + \lambda_C \psi) = \lambda_C \psi_M \ . \tag{4.12}$$

Therefore, ψ_M is an eigenstate with respect to charge conjugation operator (C) and the eigen values are $\lambda_C = \pm 1$. This demonstrates again that ψ_M and ψ_M^c are indistinguisable and Majorana particle is its own antiparticle. With respect to the operation of both C and P on ψ_M, one gets

$$\begin{aligned} \psi_M(\vec{x}, t) \xrightarrow{C} \psi_M^c = \lambda_C \psi_M \xrightarrow{P} \frac{\lambda_C}{\sqrt{2}}(\eta_P \gamma_0 \psi - \lambda_C \eta_P^* \gamma_0 \psi^c) \\ = \lambda_C \eta_P \gamma_0 \psi_M = \pm i \gamma_0 \psi_M(-\bar{x}, t) \ . \end{aligned} \tag{4.13}$$

In the above, the use has been made of the relations $\eta_P^* = -\eta_P$. This implies that $\eta_P = \pm i$ for $\lambda_C = \pm 1$. Therefore, the parity of a Majorana particle is imaginary. Again from the above discussions, one also has

$$(\gamma_5 \psi_M)^c = \eta_C C \gamma_5 \overline{\psi_M}^{\mathsf{T}} = -\eta_C C \gamma_5^{\mathsf{T}} \overline{\psi_M}^{\mathsf{T}} = -\gamma_5 \psi_M^c = -\lambda_C \gamma_5 \psi_M \ . \tag{4.14}$$

Now

$$\gamma_5 \overline{\psi_M} = (\gamma_5 \psi_M)^\dagger \gamma_0 = \psi_M^\dagger \gamma_5 \gamma_0 = -\overline{\psi_M} \gamma_5 \ . \tag{4.15}$$

Applying the projection operator ($P_{L,R}\psi = \psi_{L,R}$), one can obtain

$$\psi_{L,R} \xrightarrow{C} P_{L,R} \psi^c = (\psi^c)_{L,R} = (\psi_{L,R})^c \ . \tag{4.16}$$

Therefore, an eigenstate of charge conjugation operator (C) can not simultaneously be an eigenstate of chirality operator. Thus Majorana neutrino has no fixed chirality. But ψ_M obeys Dirac equation since both ψ and ψ^c obey Dirac equation. Dirac mass term has been discussed earlier. A more general treatment for the mass term involving ψ^c requires to identify the combination of the spinors ψ and ψ^c which behaves like Lorentz scalars. These combinations could be $\bar{\psi^c}\psi^c, \bar{\psi}\psi^c$ and $\bar{\psi^c}\psi$. But $\bar{\psi^c}\psi^c$ is equivalent to $\bar{\psi}\psi$. Thus we have additional mass terms which are hermitian conjugate (h.c.) to each other (since $\bar{\psi}\psi^c$ is hermitian conjugate to $\bar{\psi^c}\psi$). This additional mass term is called Majorana mass term and is given by

$$\begin{aligned} \mathcal{L} &= \frac{1}{2}(m_M \bar{\psi}\psi^c + m_M^* \bar{\psi^c}\psi) \ , \\ &= \frac{1}{2} m_M \bar{\psi}\psi^c + h.c. \ . \end{aligned} \tag{4.17}$$

4.1 Sources of Neutrinos

Broadly, there can be two types of sources namely the natural sources and man made sources from which neutrinos can be obtained. In the former case, neutrinos are produced due to various reaction and interaction processes within several astrophysical objects such as solar and Supernova core, in AGN, GRB as also in Earth's atmosphere and within the Earth (through radioactive decay). They can also be artificially produced in man made nuclear reactors or other accelerator based experiments.

Solar Neutrinos

Solar neutrinos are produced in solar core following the thermonuclear reactions such as $\mathrm{p} + \mathrm{p} \rightarrow {}^2\mathrm{H} + e^+ + \nu_e, {}^7\mathrm{Be} + e^- \rightarrow {}^7\mathrm{Li} + \nu_e, {}^8\mathrm{B} \rightarrow {}^8\mathrm{Be}^* + e^+ + \nu_e$. The reaction such as ${}^7\mathrm{Be} + e^- \rightarrow {}^7\mathrm{Li} + \nu_e$ emits monoenergetic neutrinos whereas other continuous neutrino

spectrum is obtained from the other two interactions mentioned above. The solar neutrino energy range can be upto $\sim$ 19 MeV. Solar neutrino suffers matter induced oscillations within the solar matter, while traversing from the core to the surface of the sun.

Supernova Neutrinos

Towards the end of the life cycle of massive stars (> 10 $M_{\odot}$), the final stage is achieved by an explosion. This happens when the spontaneous nucleosynthesis is stopped in an around $^{56}\mathrm{Fe}$ nucleus and other fp shell nuclei around the mass number of 56, a core mostly made up of $^{56}\mathrm{Fe}$ nuclei is formed. The materials from the outer shell of this Supernova core make infall on the core due to gravity, while a shock wave is generated which moves outward in enormous energy rapturing all the outer shells. The dying star then glows with enormous brightness for sometime before being extinguished. The neutrinos from Supernova generally emit in two stages, one is during the pre-Supernova stage just before the infall of the outer layers and the consequent shock wave productions and the other is during the actual Supernova explosions. At the pre-Supernova stage, the neutrinos are produced by β decay or neutron capture interaction and its energy remains within tens of MeV, while during the later stage of the Supernova process neutrinos are produced following pair annihilation in the Supernova plasma, whose energy ranges between few 100 MeV. Most of the Supernova energy is carried away by neutrinos during the Supernova explosion. Supernova can be of two types, namely Type I and Type II. While Type I Supernova does not have any hydrogen line, the Type II Supernova can be recognised by their hydrogen lines. So far, the only neutrino from a Supernova explosions detected by a terrestrial detector (Kamiokande experiment) is from the SN 1987A Supernova event.

Atmospheric Neutrinos

Atmospheric neutrinos are generated mainly due to the decay products of the particles collected by the cosmic ray bombardment on the Earth's atmosphere. These secondary

particles created by cosmic rays in the atmosphere are pions (π), kaons (K) and muons (μ). The production of neutrinos from the π decay will be mainly in the ratio 2:1 for ν_μ and ν_e. The atmospheric neutrino spectrum peaks at around 1-2 GeV but its tail can go upto 10 keV or far beyond. The Earth's atmosphere extends around 12 Km above the surface of the Earth. Atmospheric neutrinos suffer oscillations while traversing within the Earth and being detected at the opposite hemisphere of the Earth.

Geoneutrinos

Geoneutrinos are produced in the interior of the Earth due to the radioactive decays of the radioactive nuclei present inside the Earth. Most of the geoneutrinos are $\bar{\nu_e}$ and produced via β^- decay. The process also includes heating effects of Earth's interior. Other than KamLAND [125, 126] and Borexino [164] experiments, the SNO+ experiment [165] and JUNO experiment [166] also look for geoneutrinos. The energy of such neutrinos vary from a few MeV to tens of MeV.

Ultrahigh Energy (UHE) Neutrinos

Ultrahigh energy (UHE) neutrinos are astrophysical neutrinos produced with higher energy. The UHE neutrinos play an important role such as cosmic messengers via which we can understand the extreme astrophysical objects and environments as well as these neutrinos can also be useful for probing new physics. These may include the existence of sterile neutrinos etc. The cosmic rays having energy beyond 10^{20} eV, observed by the Fly's Eye and AGASA air shower arrays [167], support the obeservations of neutrinos upto this energy range. Such high energetic neutrinos can be produced through particle acceleration mechanism. The accelerated protons produced in an astrophysical accelerator with high energy interact with γ's via a cosmic beam dump. This interaction produces secondary mesons like pions ($\pi^\pm, \pi^0$). The neutral pion (π^0) further decays to photons as $\pi^0 \rightarrow \gamma + \gamma$ and these photons creating a high energy γ-ray flux while the charged pions ($\pi^\pm$) decay to UHE neu-

trinos via $\pi^+(\pi^-) \rightarrow \mu^+(\mu^-) + \nu_\mu(\bar{\nu}_\mu)$ followed by $\mu^+(\mu^-) \rightarrow e^+(e^-) + \bar{\nu}_\mu(\nu_\mu) + \nu_e(\bar{\nu}_e)$. This acceleration production mechanism for UHE neutrinos can be splitted into those of galactic and extragalactic origin. The possible galactic point sources of UHE neutrinos are young Supernova remnants [168], binary systems, protons interacting with the interstellar medium like molecular clouds, whereas the possible extragalactic sources are AGN [169], GRBs [170] etc. Other than acceleration processes there are also proposals that UHE neutrinos can be produced from the decay or annihilation of heavy particles, for example evaporating black holes, topological defects and annihilation or decay of superheavy dark matter (SHDM). The detectors, which are suited for detecting the UHE neutrinos, are ANTARES telescope under the Mediterranean Sea off the coast of Toulon, France (detects neutrinos in the range 10 GeV to 100 TeV) [163], IceCube Neutrino Observatory at the Amundsen-Scott South Pole Station in Antarctica [160] (it is designed to look for point sources in the energy range 10^{11} to 10^{21} eV), the Cubic Kilometre Neutrino Telescope or KM3NeT [171] located at the bottom of the Mediterranean Sea detecting high energetic cosmic neutrinos vary from TeV to PeV etc.

Accelerator Neutrinos

In the case of accelerator neutrinos, high energy neutrino beams are produced by the decay of pions in a long decay channel. In the actual production, a proton beam is accelerated and is made to collide with a suitable target, whereby pions and also kaons are produced as secondary mesons. These hadrons are then focused in a forward direction when these hadrons decay into muons and muon neutrinos through the processes $\pi^\pm \rightarrow \mu^\pm + \nu_\mu(\bar{\nu_\mu})$ (branching ratio 99.98 %) and through the process of Kaon decay $K^\pm \rightarrow \mu^\pm + \nu_\mu(\bar{\nu_\mu})$. The produced muons are stored and allowed to decay in a ring and the neutrinos produced via the process $\mu^\pm \rightarrow e^\pm + \nu_e(\bar{\nu_e}) + \bar{\nu_\mu}(\nu_\mu)$. The decay ring contains a long straight section which points in a suitable direction through which the produced neutrinos are sent towards

a detector at some distance (baseline length) from the neutrino factory. It can be noted that the muon lifetime is about 100 times more than the pion lifetime. Accordingly the decay length of the muons are also longer. For example, a 20 MeV muon have a decay length $\gamma c\tau = 126$ Km. This long decay length of muon is accommodated by allowing the muon to decay in the muon storage ring. Also one observes that decay of muon produces both $\nu_\mu(\bar{\nu_\mu})$ and $\nu_e(\bar{\nu_e})$ beams. Typically the energy of the accelerator neutrinos are $\sim$ tens of GeV. The neutrinos, after being directed by the long straight section of the muon stroage ring towards a desire detector, traverse a baseline length of the distance between the neutrino factory and the detector. In the process neutrinos travel to the Earth matter and show oscillation signatures at the far detector. The long baseline neutrino experiments with such accelertor neutrinos have enormous physics potentials in terms of probing the CP violation in the neutrino sector, any possible nonstandard neutrino interactions, neutrino mass hierarchy, the neutrio mixing angles as also any possible other sources of neutrino oscillations such as oscillations induced by VEP, Lorentz violation etc.

Reactor Neutrinos

Nuclear reactors are also intense sources of neutrinos (mainly electrons and antineutrinos). In a nuclear reactor, energy is produced by the fission process of nucleus and the fission products when undergoes β decay, produce flux of pure $\overline{\nu_e}$. For average fission energy of 250 MeV, six neutrinos can be produced per fission through the process of β decay. This process can emit $\sim 2 \times 10^{20}$ neutrinos per second in a 4π solid angle in case of a 1 GW reactor. These neutrinos are useful in probing, among other things, the θ_{13} mixing angle, the existence of a fourth sterile neutrino etc.

4.2 Neutrino Oscillations

This has been discussed earlier that the neutrinos are obtained in three types of flavours ν_e, ν_μ and ν_τ and their antineutrinos. If neutrinos are massive, then the mass eigenstates and the flavour or weak eigenstates are not identical. This includes mixing between two types of neutrinos and consequently oscillations of neutrinos from one flavour to another after traversing a distance. This means that the flavour eigenstates $|\nu_\alpha\rangle$ contains several mass eigenstates $|\nu_i\rangle$ components. If the mass differences $m_i - m_j$ of the two types of neutrinos are small enough (here small refers to the amount smaller than the resolution of an experiment) then the flavour eigenstates $|\nu_\alpha\rangle$ can be described by the coherent and quantum mechanical superposition of the mass eigenstates $|\nu_i\rangle$ as

$$|\nu_\alpha\rangle \;=\; \sum_i U_{\alpha i}|\nu_i\rangle \;, \tag{4.18}$$

where $U_{\alpha i}$ are the elements of a unitary mixing matrix U. This matrix should be a unitary matrix because it relates two orthonormal bases with one another. Therefore the mixing matrix U should have the following properties $U^\dagger = U^{-1}$, $\sum_\alpha U_{i\alpha}U^\dagger_{\alpha j} = \delta_{ij}$. If CP conservation is assumed then all the elements of U are real.

Neutrinos are always produced with a definite flavour. Let us consider, a neutrino is produced at a time $t = 0$ with flavour α and with fixed energy and momentum, E and p respectively. This neutrino state can then be expressed as the superposition of different

mass eigenkets, which is given as

$$\begin{aligned} |\nu(\vec{x},0)\rangle = |\nu_\alpha\rangle &= \sum_\alpha U_{\alpha i}|\nu_i(\vec{x},0)\rangle \ , \\ &= \sum_i U_{\alpha i}\text{exp}(-i\vec{p_i}\vec{x})|\nu_i\rangle \ . \end{aligned} \tag{4.19}$$

After traversing for a time t the eigenket of the neutrino is represented as $|\nu(\vec{x},t)\rangle$, which will be the time evolution of the mass eigenket

$$\begin{aligned} |\nu(\vec{x},t)\rangle &= \sum_i U_{\alpha i}\text{exp}\left(i(\vec{p_i}\vec{x}-E_i t)\right)|\nu_i\rangle \ , \\ &= \sum_i U_{\alpha i}\text{exp}(i\vec{p_i}\vec{x})\text{exp}(-iE_i t)|\nu_i\rangle \ . \end{aligned} \tag{4.20}$$

For ultrarelativistic neutrinos, the neutrino energy

$$E_i = \sqrt{m_i^2+p_i^2} \simeq p_i\left(1+\frac{m_i^2}{2p_i^2}\right) = p_i + \frac{m_i^2}{2p_i} \ . \tag{4.21}$$

If the neutrino masses are very small, i.e. $m_i << p_i$, then the mass eigenstates move with the speed of light c, so that the distance traversed (x) by the neutrino is given by $x = ct$ or $x = t$ (in natural units, $\hbar = c = 1$). With this,

$$\begin{aligned} |\nu(\vec{x},t)\rangle &= \sum_i U_{\alpha i}\text{exp}(ip_i x)\text{exp}\left[-i\left(p_i+\frac{m_i^2}{2p_i}\right)t\right]|\nu_i\rangle \ , \\ &= \sum_i U_{\alpha i}\text{exp}\left(-i\frac{m_i^2}{2p_i}t\right)|\nu_i\rangle \ . \end{aligned} \tag{4.22}$$

The mass eigenstates $|\nu_i\rangle$ relate to the weak interaction eigenstates $|\nu_\beta\rangle$ as

$$|\nu_i\rangle = \sum_\beta U^*_{\beta i}|\nu_\beta\rangle \ . \tag{4.23}$$

After substituting Eq. 4.23 into Eq. 4.22, we have

$$|\nu(\vec{x},t)\rangle \;=\; \sum_{\beta}\left[\sum_{i} U^{*}_{\beta i}U_{\alpha i}\exp(-i\frac{m_i^2}{2p_i}t)\right]|\nu_\beta\rangle \ . \tag{4.24}$$

Although the wavefunction $\nu(\vec{x},t)$ describes a neutrino of flavour α at time $t=0$, but from Eq. 4.24 it is clear that the wavefunction $\nu(\vec{x},t)$ at time t is represented as a superposition of all neutrino mass eigenstates.

Let us consider, a neutrino having flavour α ($|\nu_\alpha\rangle$) oscillates to a neutrino of flavour β ($|\nu_\beta\rangle$). The probability amplitude for this neutrino oscillation can be written as

$$\begin{aligned} A_{\nu_\alpha\to\nu_\beta}(t) &= \langle\nu_\beta|\nu(\vec{x},t)\rangle \ , \\ &= \sum_{\beta'}\sum_{i} U^{*}_{\beta' i}U_{\alpha i}\exp(-i\frac{m_i^2}{2p_i}t)\langle\nu_\beta|\nu'_\beta\rangle \ , \\ &= \sum_{i} U^{*}_{\beta i}U_{\alpha i}\exp(-i\frac{m_i^2}{2p_i}t) \end{aligned} \tag{4.25}$$

and for antineutrinos, the probability amplitude can be expressed as

$$A_{\bar{\nu}_\alpha\to\bar{\nu}_\beta}(t) \;=\; \sum_{i} U_{\beta i}U^{*}_{\alpha i}\exp(-i\frac{m_i^2}{2p_i}t) \ . \tag{4.26}$$

Assuming there is no CP violation in the neutrino sector, which indicates that the probability amplitude is same for both neutrinos and antineutrinos

$$A_{\nu_\alpha\to\nu_\beta}(t) \;=\; A_{\bar{\nu}_\alpha\to\bar{\nu}_\beta}(t) \tag{4.27}$$

since the unitary mixing matrices U are real. The probability of the neutrino oscillation from flavour α to flavour β ($P_{\nu_\alpha\to\nu_\beta}$) can be obtained by considering the square of the

absolute value of the probability amplitude (Eq. 4.25) as

$$\begin{aligned} P_{\nu_\alpha \to \nu_\beta}(t) &= |A_{\nu_\alpha \to \nu_\beta}(t)|^2 \ , \\ &= \sum_i \sum_j U^*_{\beta i} U_{\alpha i} U_{\beta j} U^*_{\alpha j} \exp\left[-i\left(\frac{m_i^2}{2p_i} - \frac{m_j^2}{2p_j}\right) t\right] \ . \end{aligned} \tag{4.28}$$

From the assumption $m_i << p_i$, we can write $p_i = p_j = p$. Therefore Eq. 4.28 turns out to be

$$P_{\nu_\alpha \to \nu_\beta}(t) = \sum_i \sum_j U_{\alpha i} U^*_{\alpha j} U^*_{\beta i} U_{\beta j} \exp(-i \frac{\Delta m^2_{ij}}{2p} t) \ . \tag{4.29}$$

In the above, $\Delta m^2_{ij} = m_i^2 - m_j^2$. Moreover, the neutrino oscillation probability can also be expressed in terms of its diagonal and non-diagonal terms as

$$P_{\nu_\alpha \to \nu_\beta}(t) = \sum_i |U_{\alpha i}|^2 |U_{\beta i}|^2 + \sum_{i \neq j} U_{\alpha i} U^*_{\alpha j} U^*_{\beta i} U_{\beta j} \exp(-i \frac{\Delta m^2_{ij}}{2p} t) \ , \tag{4.30}$$

where the diagonal term (first term on R.H.S of Eq. 4.30) is the time independent term and it represents an average transition probability which can be modulated by the second term of Eq. 4.30, which is dependent on time. The survival probability, defining the transition between two neutrinos having same flavours, is given by

$$P_{\nu_\alpha \to \nu_\alpha}(t) = 1 - \sum_{\alpha \neq \beta} P_{\nu_\alpha \to \nu_\beta}(t) \ . \tag{4.31}$$

The oscillatory behaviour of neutrino as a function of time and position (since $\hbar = c = 1$, we have $x = t$) can be nicely exhibited by Eq. 4.30. The time dependent term of the neutrino oscillation probability (Eq. 4.30) may be decomposed into real and imaginary

parts as

$$P_{\nu_\alpha \to \nu_\beta}(t) = \sum_i |U_{\alpha i}|^2 |U_{\beta i}|^2 + \sum_{i \neq j} \mathrm{Re}(U_{\alpha i} U^*_{\alpha j} U^*_{\beta i} U_{\beta j}) \cos(\frac{\Delta m^2_{ij}}{2p} t) + \sum_{i \neq j} \mathrm{Im}(U_{\alpha i} U^*_{\alpha j} U^*_{\beta i} U_{\beta j}) \sin(\frac{\Delta m^2_{ij}}{2p} t) \ . \quad (4.32)$$

The imaginary term (the last term in Eq. 4.32) will be vanished in the case of CP conservation. Therefore,

$$P_{\nu_\alpha \to \nu_\beta}(t) = \sum_i |U_{\alpha i}|^2 |U_{\beta i}|^2 + \sum_{i \neq j} \mathrm{Re}(U_{\alpha i} U^*_{\alpha j} U^*_{\beta i} U_{\beta j}) \cos(\frac{\Delta m^2_{ij}}{2p} t) \ . \quad (4.33)$$

The variation of the transition probability with time (t) and the distance (x) traversed by neutrinos from the source is periodic in nature. Therefore, the oscillation length (L_{osc}), which characterises the periodicity, is given as

$$L_{\mathrm{osc}} = \frac{4\pi p}{\Delta m^2_{ij}} = \frac{4\pi E}{\Delta m^2_{ij}} \ , \quad (4.34)$$

where for relativistic neutrinos $p = E$. The oscillation length $L_{\mathrm{osc}} \to \infty$ if all the masses of neutrinos are identical, which in particular indicates that if all neutrino masses vanish. Also there will be no oscillations into a flavour different from α in case $|\nu_\alpha\rangle = |\nu_i\rangle$, i.e. the neutrino is already in a mass eigenstate. Therefore, the phenomena of neutrino mass-flavour oscillations indicate that neutrinos should be massive and there will be a mixing between the mass and the flavour eigenstates.

4.3 Neutrino Oscillations in Two Neutrino Flavour case

The features of neutrino oscillations can be described by considering a simple model with two neutrino flavours, ν_e and ν_μ for example. The lepton mixing matrix, in the case of two state neutrino mixing, is a 2×2 unitary matrix having the form

$$U_{(2\times2)} = \begin{pmatrix} \cos\theta & e^{i\phi}\sin\theta \\ -e^{-i\phi}\sin\theta & \cos\theta \end{pmatrix} , \tag{4.35}$$

where θ defines the mixing angle between ν_e and ν_μ and $e^{\pm i\phi}$ indicate the CP phases. This phase factor is irrelevant as far as the neutrino oscillation phenomenon is concerned, but it plays an important role for the case of double beta decay. Therefore, we assume that there is no CP violation in the neutrino sector and with this assumption Eq. 4.35 will take the form

$$U_{(2\times2)} = \begin{pmatrix} \cos\theta & \sin\theta \\ -\sin\theta & \cos\theta \end{pmatrix} . \tag{4.36}$$

The neutrino flavour eigenstates $|\nu_e\rangle$ and $|\nu_\mu\rangle$ can be written in terms of the mass eigenstates $|\nu_1\rangle$ and $|\nu_2\rangle$ as

$$|\nu_e\rangle = \cos\theta|\nu_1\rangle + \sin\theta|\nu_2\rangle , \tag{4.37}$$

$$|\nu_\mu\rangle = -\sin\theta|\nu_1\rangle + \cos\theta|\nu_2\rangle . \tag{4.38}$$

The mixing angle is limited within the range $0 \leq \theta \leq \pi/4$. As the neutrinos are relativistic in nature (i.e. if the neutrinos are moving at the speed of light, $v = c = 1$), we can replace

the time 't' by distance 'x' and vice versa. From Eq. 4.33 it follows that, in 2-flavour case the transition probability of finding a ν_e, which is emitted at $x = 0$ having energy E_ν, as ν_μ at a distance x is given by

$$\begin{aligned} P_{\nu_e \to \nu_\mu}(x) &= 2\cos^2\theta \sin^2\theta - 2\sin^2\theta\cos^2\theta \cos\left(\frac{\Delta m^2}{2p_\nu}x\right) , \\ &= \frac{1}{2}\sin^2(2\theta)\left[1 - \cos\left(\frac{\Delta m^2}{2p_\nu}x\right)\right] , \\ &= \frac{1}{2}\sin^2(2\theta)\left[1 - \cos\left(\frac{2\pi x}{L_{\rm osc}}\right)\right] , \\ &= \sin^2(2\theta)\sin^2\left(\frac{\pi x}{L_{\rm osc}}\right) . \end{aligned} \tag{4.39}$$

where, $\Delta m^2 = |m_1^2 - m_2^2|$ and the oscillation length $L_{\rm osc}$ is obtained by equating the phase to 2π (as $L_{\rm osc}$ signifies time or length for one complete oscillation). Thus

$$\frac{\Delta m^2}{2p_\nu}L_{\rm osc} = 2\pi \Longrightarrow L_{\rm osc} = \frac{4\pi p_\nu}{\Delta m^2} = \frac{4\pi E}{\Delta m^2} \simeq 2.48{\rm m}\frac{E({\rm MeV})}{\Delta m^2({\rm eV}^2)} = 2.48{\rm Km}\frac{E({\rm GeV})}{\Delta m^2({\rm eV}^2)} . \tag{4.40}$$

The distance between any two closest maxima and the minima of the transition probability is defined as the oscillation length (Fig. 4.1). It is to be noted that the oscillation length relates with the energy difference of the neutrino mass eigenstates in an inversely proportional manner, i.e. $L_{\rm osc} = \dfrac{2\pi}{(E_2 - E_1)}$. In addition to the transition probability, correspondingly we have the survival probability

$$\begin{aligned} P_{\nu_e \to \nu_e}(x) &= 1 - P_{\nu_e \to \nu_\mu}(x) , \\ &= 1 - \sin^2(2\theta)\sin^2\left(\frac{\pi x}{L_{\rm osc}}\right) . \end{aligned} \tag{4.41}$$

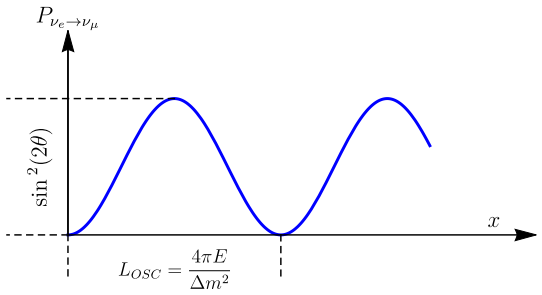

Figure 4.1: Two flavour neutrino oscillations. See text for details.

In Fig. 4.1, a schematic diagram for the neutrino oscillation probability for 2-flavour cases (Eq. 4.39) is shown. Here the oscillation probability contains two factors

1. The first one $\sin^2(2\theta)$ describes the amplitude (or the depth) of the neutrino oscillations and it is independent of the distance travelled by neutrinos. The oscillation amplitude is maximal ($\simeq 1$) when θ (mixing angle) $= 45°$, which corresponds to the maximal mixing between two neutrino species. On the other hand, when the alignment between the flavour and the mass eigenstates are nearly same, i.e. $\theta \simeq 0$ or $\theta \simeq 90°$, the oscillation amplitude turns out to be small and correspondingly the mixing between two neutrino species is very small.

2. The expression $\sin^2\left(\frac{\pi x}{L_{\rm osc}}\right)$ is the oscillatory factor and regulates the oscillations with the distance x traversed by neutrinos. The oscillation phase is proportional to $\frac{\Delta m^2}{2E}$, where $\Delta m^2 = |m_1^2 - m_2^2|$ and to the distance x. For the very large oscillation phase, the transition probability oscillates very fast. The transition probability in this case becomes

$$\overline{P_{\nu_e \to \nu_\mu}} = \overline{P_{\nu_\mu \to \nu_e}} = \frac{1}{2}\sin^2(2\theta) \ , \tag{4.42}$$

where the neutrino oscillations have been averaged out by considering an average over small intervals of energy (which corresponds to the finite amount of the energy resolution of the detector) or over small variations of the distance between the neutrino source and the detector (both are having finite sizes).

4.4 Neutrino Oscillations in Matter: Evolution Equation

When neutirno propagates through a dense matter, their properties are affected by the interactions between those neutrinos and the matter. The types of these effects can be either coherent or incoherent. The characteristic cross-section for an incoherent and inelastic neutrino-proton ($\nu - p$) scattering is very negligible

$$\sigma \sim \frac{G_F^2 s}{\pi} \sim 10^{-43}\mathrm{cm}^2 \left(\frac{E}{1\mathrm{MeV}}\right)^2 . \tag{4.43}$$

The irony of such a small cross-section is that if a beam of 10^{10} neutrinos having energy $E \sim 1$ MeV propagate through a matter (Earth matter, for example) then only one neutrino would be deflected by the medium of the Earth. It seems that the matter is irrelevant for neutrinos. However, there is no contribution of the coherent elastic scattering in Eq. 4.43. The medium remains unchanged in coherent interactions and there is a possibility of having interference between the scattered and unscattered neutrino waves, which enhances the effect. The evolution equations of the neutrinos can be decoupled from the equations of the medium due to coherence. In this approximation, the matter effect can be described by an effective potential depending on the matter density and the composition of the matter [172].

There is a very significant differnce between the neutrino oscillations in matter and in

vacuum. All the three kind of neutrino flavours, i.e. ν_e, ν_μ and ν_τ have neutral current (NC) interaction with the matter (to be specific, electrons, protons and neutrons of the matter) and this NC interaction is mediated by Z^0 bosons. In addition to this, ν_e can interact with the electrons of the medium through CC interaction mediated by $W^\pm$ boson. The effective potential, describing the evolution of ν_e in a dense medium with electrons due to CC interactions, can be derived. The effective Hamiltonian for the relevant neutrino interaction at low energies of neutrinos is given by

$$H_W = \frac{G_F}{\sqrt{2}}[\bar{\nu}_e(x)\gamma_\alpha(1-\gamma_5)e(x)] \times [\bar{e}(x)\gamma_\alpha(1-\gamma_5)\gamma_e(x)] \ . \tag{4.44}$$

Also the effective CC Hamiltonian for the electrons in the medium can be written as

$$\begin{aligned} H_{\rm CC}^{(e)} &= \frac{G_F}{\sqrt{2}} \int d^3p_e f(E_e,T) \langle\langle e(s,p_e)|\bar{e}(x)\gamma_\alpha(1-\gamma_5)\nu_e(x)\bar{\nu}_e(x)\gamma_\alpha(1-\gamma_5)e(x)|e(s,p_e)\rangle\rangle \ , \\ &= \frac{G_F}{\sqrt{2}}\bar{\nu}_e(x)\gamma_\alpha(1-\gamma_5)\nu_e(x) \int d^3p_e f(E_e,T) \langle\langle e(s,p_e)|\bar{e}(x)\gamma_\alpha(1-\gamma_5)e(x)|e(s,p_e)\rangle\rangle \ , \end{aligned} \tag{4.45}$$

where s and p_e are the spin and momentum of the electron respectively. The term $f(E_e,T)$ in the above equation (Eq. 4.45) is the energy distribution function of the electrons in matter. This energy distribution function $f(E_e,T)$ is assumed to be isotropic and homogeneous and it can be normalized as $\int d^3p_e f(E_e,T) = 1$. We consider an average over the electron spinors and take a summation over all the electrons in the medium and this whole phenomena are denoted by $\langle....\rangle$ in the above equation. In order to obtain forward coherent scattering, both s and p_e are same for initial and final electrons.

After considering the expansion of $e(x)$ (the electron field) in plane waves, we can find

$$\begin{aligned}\langle e(s,p_e)|\bar{e}(x)\gamma_\alpha(1-\gamma_5)e(x)|e(s,p_e)\rangle &= \frac{1}{V}\langle e(s,p_e)|\bar{U}_s(p_e)a_s^\dagger(p_e)\gamma_\alpha(1-\gamma_5) \\ & \quad a_s(p_e)u_s(p_e)|e(s,p_e)\rangle \ , \end{aligned} \tag{4.46}$$

where the factor V defines volume normalization. The averaging gives

$$\frac{1}{V}\langle\langle e(s,p_e)|a_s^\dagger(p_e)a_s(p_e)|e(s,p_e)\rangle\rangle = N_e(p_e)\frac{1}{2}\sum_s \ , \tag{4.47}$$

where the number densities of electrons having momentum p_e is denoted by $N_e(p_e)$. We make an assumption that the numbers of spin +1/2 and spin -1/2 electrons in the medium are equal and the number operator $\tilde{N}_e^{(s)}(p_e) = a_s^\dagger(p_e)a_s(p_e)$ has been used. Therefore, we obtain

$$\begin{aligned}\langle\langle e(s,p_e)|\bar{e}(x)\gamma_\alpha(1-\gamma_5)e(x)|e(s,p_e)\rangle\rangle &= N_e(p_e)\frac{1}{2}\sum_s \bar{u}_s(p_e)\gamma_\alpha(1-\gamma_5)u_s(p_e) \ , \\ &= \frac{N_e(p_e)}{2}\mathrm{Tr}\left[\frac{m_e+\not{p}}{2E_e}\gamma_\alpha(1-\gamma_5)\right] \ , \\ &= N_r(p_e)\frac{p_e^\alpha}{E_e} \ . \end{aligned} \tag{4.48}$$

From isotropy, we can write $\int d^3p_e\vec{p}_e f(E_e,T) = 0$. Therefore the term, which only contributes to integration, is p with $\int d^3p_e f(E_e,T)N_e(p_e) = N_e$. Substituting Eq. 4.48 in Eq. 4.45 one can obtain

$$H_{\mathrm{CC}}^{(e)} = \frac{G_F N_e}{\sqrt{2}}\bar{\nu}_e(x)\gamma_0(1-\gamma_5)\nu_e(x) \ . \tag{4.49}$$

The effective potential ($V_{\mathrm{CC}}^{(e)}$) for ν_e induced due to its CC interaction with electrons in

medium can be written as

$$V_{\rm CC}^{(e)} = \langle \nu_e | \int d^3x H_{\rm CC}^{(e)} | \nu_e \rangle = \frac{G_F N_e}{\sqrt{2}} \frac{2}{V} \int d^3x u_\nu^+ u_\nu = \sqrt{2} G_F N_e \ . \tag{4.50}$$

For $\bar{\nu}_e$, $V \to -V$. We can also express $V_{\rm CC}^{(e)}$ in terms of the matter density ρ as

$$V_{\rm CC}^{(e)} \equiv V_{\rm CC} = \sqrt{2} G_F N_e = 7.6 Y_e \frac{\rho}{10^{14} {\rm g/cm^3}} {\rm eV} \ . \tag{4.51}$$

In the above equation (Eq. 4.51), the relative number density of electrons is defined as $Y_e = \dfrac{N_e}{N_p + N_n}$, where N_e, N_p and N_n are the number densities of electron, proton and neutron respectively.

On the other hand, the contributions of the NC interactions towards the effective potential is needed to be considered. These contributions are same for all three flavours of neutrinos since the NC interactions do not depend on flavour. N_e and N_p coincide with each other in an electrically neutral medium and their corresponding contributions to $V_{\rm NC}$ is cancelled out. Therefore only the NC interactions of neutrinos with neutrons in matter have been taken into account and the effective neutral current potential in this case is given by

$$V_{\rm NC}^{\alpha} \ = \ -\frac{G_F N_n}{\sqrt{2}} \ . \tag{4.52}$$

From both the equations Eq. 4.52 and Eq. 4.51, we find

$$V_e = \sqrt{2} G_F (N_e - \frac{N_n}{2}) \ , \tag{4.53}$$

$$V_\mu = V_\tau = \sqrt{2} G_F (-\frac{N_n}{2}) \ . \tag{4.54}$$

Let us consider a system of oscillating neutrinos as well as how this system evolves in matter. Although the evolution of the neutrino oscillations in vacuum is more convenient in the mass basis, but in matter it is most easily followed in the flavour eigenstate basis as the effective potential of neutrinos are diagonal in this flavour basis. For the two flavour cases, the neutrino eigenstates in the flavour basis ($|\nu_{\rm fl}\rangle$) can relate to the neutrino fields in the mass eigenstate basis through the transformation

$$|\nu_{\rm fl}\rangle \ = \ U|\nu_{\rm m}\rangle \ , \tag{4.55}$$

where both the neutrino fields $\nu_{\rm fl}$ and $\nu_{\rm m}$ are two component vectors and the mixing matrix U is given in Eq. 4.2. In vacuum, the evolution equation in mass eigenstate basis $|\nu_{\rm m}\rangle$ can be written as

$$i\left(\frac{d}{dt}\right)|\nu_{\rm m}\rangle \ = \ H_{\rm m}|\nu_m\rangle \ , \tag{4.56}$$

where $H_{\rm m} = diag(E_1, E_2)$, E_1 and E_2 are the energy eigen values of neutrinos corresponding to the mass eigenstates $|\nu_1\rangle$ and $|\nu_2\rangle$ respectively. Now replacing $|\nu_{\rm m}\rangle = U^\dagger|\nu_{\rm fl}\rangle$ in Eq. 4.56, we have

$$i\left(\frac{d}{dt}\right)U^\dagger|\nu_{\rm fl}\rangle \ = \ H_{\rm m}U^\dagger|\nu_{\rm fl}\rangle \ , \tag{4.57}$$

$$i\left(\frac{d}{dt}\right)|\nu_{\rm fl}\rangle \ = \ UH_{\rm m}U^\dagger|\nu_{\rm fl}\rangle \ . \tag{4.58}$$

Therefore, the evolution equation in the flavour basis takes the form

$$i\left(\frac{d}{dt}\right)|\nu_{\rm fl}\rangle \;=\; H_{\rm fl}|\nu_{\rm fl}\rangle\;, \tag{4.59}$$

where $H_{\rm fl} = U H_{\rm m} U^{\dagger}$. For neutrinos moving with the speed of light (relativistic neutrinos), the energy eigen values in the mass basis can be written as $E_i (i = 1, 2) \simeq p + \dfrac{m_i^2}{2E}$ and therefore, the evolution equation in the flavour basis takes the form

$$i\frac{d}{dt}\begin{pmatrix} |\nu_e\rangle \\ |\nu_\mu\rangle \end{pmatrix} = \begin{pmatrix} \left(p + \dfrac{m_1^2+m_2^2}{4E}\right) - \dfrac{\Delta m^2}{4E}\cos 2\theta & \dfrac{\Delta m^2}{4E}\sin 2\theta \\ \dfrac{\Delta m^2}{4E}\sin 2\theta & \left(p + \dfrac{m_1^2+m_2^2}{4E}\right) + \dfrac{\Delta m^2}{4E}\cos 2\theta \end{pmatrix} \times \begin{pmatrix} |\nu_e\rangle \\ |\nu_\mu\rangle \end{pmatrix} . \tag{4.60}$$

The term $\left(p + \dfrac{m_1^2+m_2^2}{4E}\right)$ in the diagonal elements of the effective Hamiltonian in Eq. 4.60 can be omitted as this term has no contribution in the generation of the phase differences and hence for the neutrino oscillations. Thus one can rewrite the evolution equation in the flavour basis in vacuum as

$$i\frac{d}{dt}\begin{pmatrix} |\nu_e\rangle \\ |\nu_\mu\rangle \end{pmatrix} = \begin{pmatrix} -\dfrac{\Delta m^2}{4E}\cos 2\theta & \dfrac{\Delta m^2}{4E}\sin 2\theta \\ \dfrac{\Delta m^2}{4E}\sin 2\theta & \dfrac{\Delta m^2}{4E}\cos 2\theta \end{pmatrix} \begin{pmatrix} |\nu_e\rangle \\ |\nu_\mu\rangle \end{pmatrix} . \tag{4.61}$$

In the presence of matter, the matter induced potential V_e and V_μ (which are in the flavour basis) are now can be added to the diagonal elements of $H_{\rm fl}$ in Eq. 4.61. It is to be noted that both V_e and V_μ contain a similar term, which occurs due to NC interactions (see Eqs. 4.53, 4.54). As we have already mentioned, such common terms in the diagonal element have no effects on the neutrino

oscillations (no phase differences) and therefore we can neglect these terms. Thus one obtains

$$i\frac{d}{dt}\begin{pmatrix} |\nu_e\rangle \\ |\nu_\mu\rangle \end{pmatrix} = \begin{pmatrix} -\frac{\Delta m^2}{4E}\cos 2\theta + \sqrt{2}G_F N_e & \frac{\Delta m^2}{4E}\sin 2\theta \\ \frac{\Delta m^2}{4E}\sin 2\theta & \frac{\Delta m^2}{4E}\cos 2\theta \end{pmatrix}\begin{pmatrix} |\nu_e\rangle \\ |\nu_\mu\rangle \end{pmatrix} . \quad (4.62)$$

Eq. 4.62 describes $\nu_e \leftrightarrow \nu_\mu$ oscillations in matter for two flavour case. The evolution equation for $\nu_e \leftrightarrow \nu_\tau$ oscillation takes the same form as $\nu_e \leftrightarrow \nu_\mu$ oscillation. Since $V_\mu = V_\tau$, the oscillations between V_μ and V_τ in the 2-flavour approximation are not modified in matter, but in the 3-flavour framework the $\nu_\mu \leftrightarrow \nu_\tau$ oscillations will be significant because of the mixing with ν_e.

Constant matter density

If the matter has a constant electron number density, i.e. N_e = const, then after diagonalising the effective Hamiltonian in Eq. 4.62, one can obtain the neutrino mass eigenstates $|\nu_A\rangle$ and $|\nu_B\rangle$ in matter as

$$\begin{aligned} |\nu_A\rangle &= |\nu_e\rangle\cos\theta_{\rm m} + |\nu_\mu\rangle\sin\theta_{\rm m} , \\ |\nu_B\rangle &= -|\nu_e\rangle\sin\theta_{\rm m} + |\nu_\mu\rangle\cos\theta_{\rm m} , \end{aligned} \quad (4.63)$$

where the neutrino mixing angle in matter ($\theta_{\rm m}$) is given by

$$\tan 2\theta_{\rm m} = \frac{\frac{\Delta m^2}{2E}\sin 2\theta}{\frac{\Delta m^2}{2E}\cos 2\theta - \sqrt{2}G_F N_e} . \quad (4.64)$$

The mixing angle in matter ($\theta_{\rm m}$) is different from vacuum mixing angle (θ). The energy eigenvalues corresponding to mass eigenstates $|\nu_A\rangle$ and $|\nu_B\rangle$ in matter are E_A and E_B respectively. The differences $E_A - E_B$ is given as

$$E_A - E_B = \sqrt{\left(\frac{\Delta m^2}{2E}\cos 2\theta - \sqrt{2}G_F N_e\right)^2 + \left(\frac{\Delta m^2}{2E}\right)^2 \sin^2 2\theta} . \quad (4.65)$$

Similar to the vacuum oscillation case, The probability of $\nu_e \leftrightarrow \nu_\mu$ oscillations in matter with constant density can now be written as,

$$P'_{\nu_e \to \nu_\mu}(x) \quad = \quad \sin^2 2\theta_{\rm m} \sin^2 \left(\frac{\pi x}{L_m} \right) \ , \tag{4.66}$$

where

$$L_{\rm m} = \frac{2\pi}{E_A - E_B} = \frac{2\pi}{\sqrt{\left(\frac{\Delta m^2}{2E} \cos 2\theta - \sqrt{2} G_F N_e \right)^2 + \left(\frac{\Delta m^2}{2E} \right)^2 \sin^2 2\theta}} \tag{4.67}$$

is the oscillation length in matter. If we replace $\theta_{\rm m}$ by θ and $L_{\rm m}$ by $L_{\rm osc}$, i.e. considering no matter effect, then Eq. 4.66 assumes the vacuum oscillation probability equation (Eq. 4.39). The amplitude of the neutrino oscillations in matter is given by

$$\sin^2 2\theta_{\rm m} \quad = \quad \frac{\left(\frac{\Delta m^2}{2E} \right)^2 \sin^2 2\theta}{\left(\frac{\Delta m^2}{2E} \cos 2\theta - \sqrt{2} G_F N_e \right)^2 + \left(\frac{\Delta m^2}{2E} \right)^2 \sin^2 2\theta} \ . \tag{4.68}$$

It has a typical resonance form and the maximum value ($\sin^2 2\theta_{\rm m} = 1$) will be achieved when

$$\sqrt{2} G_F N_e \quad = \quad \frac{\Delta m^2}{2E} \cos 2\theta \ . \tag{4.69}$$

This condition is called the Mikheyev-Smirnov-Wolfenstein (MSW) [172, 173] resonance condition. From both Eqs. 4.64 and 4.68, it is clear that when the MSW resonance condition is fulfilled the neutrino mixing in matter is maximal ($\theta_{\rm m} = 45^\circ$), which has no dependency on θ (vacuum mixing angle). Therefore $P'_{\nu_e \to \nu_\mu}(x)$ can be large irrespective of the fact that θ is very small.

The above formalism can be extended to the case when the density of the medium varies with distance and also for the case of more than two flavours. For example, when neutrinos pass through the Earth matter it may be assumed that the neutrinos have to pass through different layers of fixed

densities and thicknesses. In such circumstances the propagations of neutrinos and their subsequent oscillations are to be numerically obtained as the neutrino eigenkets change while travelling from one such layer to another of different densities.

4.5 Neutrino Experiment

The neutrinos and their oscillations have been discovered by the serveral experiments over the year and their experimental discovery is still going on. In this section a brief account of neutrino experimental endeavour (both ongoing and near future experiments) have been furnished.

There are several experiments on neutrinos originating from nuclear reactions. In 1956, the neutrino discovery experiment situated at the Savannah River nuclearpower plant, had given the first evidence of neutrino interactions. In this experiment the detector was made of two compartments, which contains 200 liters of water with cadium chloride and organic liquid scintillators. The scintillator detector has also been used for the reactor neutrinos at Bugey (near Lyon, France) [174] where the detector was a pseudocumene based liquid scintillator with H/C ratio 1.4 and doped with ^{6}Li. This experiment provided the first constraints on the $\nu_e - \nu_\mu$ oscillation parameters. The Bugey-3 experiment [148] had obtained the last results in 1996. The underground detector known as Chooz detector (1995-1999) was situated in France, 1 km away from the Chooz nuclear plant. As a detector material 300 liters of liquid scintillator doped with gadolinium had been used in this experiment. This experiment had provided a limit on the neutrino mixing angles as well as the neutrino mass squared differences as $\sin^2(2\theta_{13}) < 0.17$ for large value of Δm^2 and $\Delta m^2 > 8 \times 10^{-4}$ eV^2 for maximal mixing and this is the last result obtained by this experiment in the year 1999. This experiment had later been upgraded to a new short baseline experiment (2003-2017), namely Double Chooz experiment [135] with neutrinos from Chooz nuclear reactor. The near detector was at 400 metre and the far detector was at 1050 metre away from the detector. The purpose of this was also to probe the oscillation of $\bar{n}u_e$ and measurement of 13 mixing angle θ_{13}. The first indication of

the nonzero value of θ_{13} mixing angle in reactor experiments had been observed by this experiment and this observation was published in 2011. The measurement of the mixing angle θ_{13} had been pursued by other reactor neutrino based short baseline experiments. The Daya Bay neutrino experiment (2011-2020) [127–133], located at Daya Bay (50 km north-east Hong Kong, China), used liquid scintillator as the detector material. The eight detectors of Daya Bay experiment are located within 1.9 km of six nuclear reactors. This experiment estimated the values of θ_{13} mixing angle. Another short baseline reactor neutrino experiment is RENO in South Korea [134], which is designed in the year 2011 to measure the mixing angle θ_{13}. This RENO experiment uses gadoliniumn doped liquid scintillator as the detector material. The RENO experiment confirmed the measurement of θ_{13}, which is published by the Daya Bay experiment in 2012. The RENO experiment is still collecting the data.

Based on the neutrinos produced in particle accelerators, a number of experiments have been proposed since 1962. The Liquid Scintillator Neutrino Detector (LSND) [175–177] is one of them in the year 1993, situated at Los Alamos National Laboratory. The LSND detector was made of 167 tons of mineral oil and 6.4 kg of organic scintillator, surrounded by 1220 photomultipliers. This neutrino oscillation experiment had first reported that the observed results cannot be explained by the usual three flavour neutrino oscillations and introduction of a fourth flavour "strile neutrino" (and four flavour neutrino oscillaions), appeared to be needed to explain this LSND anomaly. Unlike the neutrinos of three active flavours, this fourth sterile neutrino however would not have any interaction. Since the LSND anomaly, several experiments have been designed to probe this fourth sterile neutrino. In 2002, the MiniBooNE (Mini Booster Neutrino Experiment) experiment was proposed in Illinois, United States where mineral oil had been used as the detector material. The data from initial run suggested an excess in the results which is consistent with the LSND signal. Inspite of this observation, the existence of sterile neutrinos could not be established from the data analysis. But later in 2018, the MiniBooNE experiment and the data analysis [178] had produced modified results related to the sterile neutrino oscillation parameters. Beyond these accelerator-based

experiments, a number of radioactive source and reactor based experiments such as PROSPECT, STEREO, DANSS, CHANDLER and SOLID are expected to effectively probe, when operational, the issue of sterile neutrino through their possible oscillation effects. The electron antineutrino detector KamLAND (Kamioka Liquid Scintillator Antineutrino Detector) [125, 126] is an underground Cherenkov detector situated in the Kamioka mine, near Toyama, Japan where mineral oil and benzene are used for 1 kton of liquid scintillator detector material. The muon veto is provided by the 3.2 kton of water cherenkov detector surrounding the detector vessel. KamLAND detects the electron antineutrinos from 53 nuclear reactors that are situatated around KamLAND's location. In 2002, KamLAND started taking data and neutrino oscillation parameters namely Δ^2_{12} and θ_{12} are obtained from the analysis of their data. In 2008, the combined results of KamLAND and the solar neutrino disclosed the most precise determination of the oscillation parameters as $\Delta^2_{12} = (7.59 \pm 0.21) \times 10^{-5}$ eV^2 and $\tan^2\theta_{12} = 0.47 \pm 0.06$.

In 2005, a long baseline neutrino experiment known as MINOS (Main Injector Neutrino Oscillator Search) [137–148] is designed to observe neutrino oscillations. It consists of two detectors one is at Fermilab (near detector) and the other is in northern Minnesota (far detector). The oscillations of ν_μ beam generated at Fermilab are what they probed in both appearence and disappearence channels and it measures the neutrino mixing angle θ_{23}. An upgraded version of MINOS, MINOS+ experiment is operating since 2013. Another long baseline neutrino experiment OPERA (Oscillation Project with Emulsion tRacking Apparatus) [179] was installed at the Gran Sasso underground laboratory in 2008. The neutrino source for this experiment is the CNGS ν_μ beam from CERN. First observation of ν_τ had been made in May, 2010 by this OPFRA experiment. The NOνA (NuMI off - axis ν_e Appearence) experiment receives the muon neutrino beam genarated at Fermilab and here the baseline length is $\sim$ 735 km where the near detector is located at Fermilab.

A neutrino scattering experiment named as MINERVA, installed in 2010, which uses the ν_μ beam (produced at Fermilab) as a source. The main purpose of this experiment is to study the low energy neutrino interactions [180].

T2K (Tokai to Kamioka) experiment [149] is a very popular example of ongoing long baseline neutrino oscillation experiment, situated in Japan. In this case ν_μ beam produced by J-PARC is traverses a baseline length of 295 km to the Super-Kamiokande water-cherenkov detector. It is taking data since 2014. Prior to T2K experiment, an experiment of similar nature, namely K2K (KEK to Kamioka) [136] was operational (1999-2004). This experiment used the muon neutrino beam from particle accelerator of KEK which would be detected at Kamioka observatory. This K2K experiment studied the oscillation parameters and their results was in good agreement with those measured by Super-Kamiokande. The ν_μ disappearence was first observed by K2K.

Among the recent experiment, The Deep Underground Neutrino Experiment (DUNE) [150–153] is now in under construction. It will consist of two detectors, one is a detector near the source beam at Fermilab and the other is a far detector at the Sanford Underground Facility. The baseline length is $\sim$ 1300 km. The DUNE detector consists of 70kTon of liquid argon contained in cryogenic tank nearly a 1.5 km underground. However, the protoDUNE far detector at CERN has already started taking data. The scientific goals of DUNE are - investigation of neutrino oscillations to test CP violation in the leptonic sector, the neutrino mass ordering, searches for proton decay and neutrinos beyond the three active flavour.

The experimental discovery of solar neutrino oscillations had first been made by Homestake Chlorine experiment [122] proposed in 1968. This experiment was located in Homestake Gold Mine, South Dakota. A 380 m^3 tank of perchloroethylene had been used as the detector material. The threshold energy for this experiment had been chosen as $\sim$ 814 keV. There is an another solar neutrino detector in more recent times namely SNO (Sudbury Neutrino Observatory (1999-2006)) [123] situated 2100 m underground in the Creighton Mine in Sudbury, Ontario in Canada. The SNO detector consisted of a 12 m spherical vessel of 1000 m^3 of heavy water surroubded by 9600 photomultipliers. This detector was looking for the solar ν_eCC ininteraction as well as three neutrino types NC interactions. The upgraded version of SNO, known as SNO+ [165], where linear alkylbenzene has been used as detector material, is collecting data of solar neutrinos since 2014.

First observations of atmospheric neutrinos had been made in 1965 at Kolar Gold experiment in India while looking for proton decay. The Kamiokande experiment [124] was an underground detector in the Kamioka mine, in Japan. This water-cherenkov detector contained 3000 tons of pure water inside a tank and 1000 photomultiplier tubes installed throughout the inside wall of the tank. Some PMTs at the outer surface were used as vetos. It was collecting data till 1987 and it was one of the neutrino detector, which registered a few of neutrino events from supernova SN1987A. This cherenkov detector was also used for solar neutrino atmospheric neutrino oscillation studies. Its successor, Super-Kamiokande along with SNO results indicate the small mixing solution of the solar neutrino problem and extablished that $|\nu_2\rangle$ mass eigenstate is heavier than $|\nu_1\rangle$. SuperKamiokande experiment also measures the atmospheric neutrino oscillation and the values of the atmospheric neutrino oscillation parameters Δ^2_{23} and θ_{23}. A further upgraded experiment namely Hyper-Kamiokande is planned to have a fiducial volume 20 times that of Super-Kamiokande experiment and it is presently under construction. The proposed ICAL (Iron Calorimeter) detector, mainly designed to probe atmospheric neutrino oscillation as also for long baseline neutrino oscillations, at the proposed Indio-based Neutrino Observatory (INO) is proposed as a 50 kton magnetised iron calorimeter [181]. This muon neutrino detector, being magnetised, would be capable of identification of the charges of the secondary muons and hence identification of neutrinos or antineutrinos. This proposed detector is also expected to be capable of addressing the neutrino mass hierarchy as well.

Neutrinos are ideal messengers for astrophysics. There are several neutrino detectors, looking for UHE neutrinos like IceCube buried in the ice of the South Pole (ice-cherenkov detector) [160], GVD in Lake Baikal, ANTARES [163] and KM3NeT [171] in the Mediterranean sea. IceCube contains 5160 digital optical Modules (DOMs) within a volume of 1 km^3 ice. IceCube detects the cherenkov radiation, which is basically the consequence of neutrino interaction with the detector material i.e. ice. The number of color points and their size, which are observed by the IceCube detector, relate to the energy of the upcoming neutrino. From the colour code, we can get informa-

tion about the timimg and as a result we can reconstruct the direction of the produced muon. The spatial distribution of the hits or rather the topolgy of the event depicts the types of the neutrino flavours. The Icecube detector registers data having the energy range GeV - PeV. In 2013, IceCube announced first detection of high energy astrophysical neutrinos, which are referred as high energy starting event (HESE). Later in 2018, IceCube reported the first multi - messenger evidence of a flaring blazar in coincidence with the high energy neutrino event IC-170922A. A possible source candidate could be TXS 0506+056 and in this case 13 ± 5 events have been found in 2014-15 over 110 days in addition to the event detected in 2017. The low energy extension of the IceCube detectore, known as the PINGU (The Precision IceCube Next Generation Upgrade) detector [161] is proposed to observe the atmospheric meutrinos (sample of over 60,000 atmospheric neutrinos per year). This detector is embedded within the IceCube Deepcore and the effective mass of the detector material (ice) is $\sim$ 6 Mton. PINGU will make highly competitive measurements of neutrino oscillation parameters in an energy range over an order of magnitude higher than long baseline neutrino beam experiments. The scientific goals of the PINGU detector are to address $\sin^2\theta_{23}$ octant anomaly, ν_τ appearence, neurtino mass ordering. The ANTARES (Astronomy with a Neutrino Telescope and Abyss Environmental RESearch) telescope was proposed in 2006 at 2.5 km under the Mediterranean sea off coas of Toulon, France. This detector is monitoring one complete hemisphere of the sky (southern hemisphere) and it detects neutrinos emitted by transient astrophysical events. The three cases, which are performed with the ANTARES telescope, are (1) searches of neutrino candidates coincident with Swift and Fermi GRBs, (2) IceCube high energy neutrino events and (3) GW candidates observed by LIGO/VIRGO. The KM3NeT (The Cubic Kilometer Neutrino Telesecope) is undrt construction in the Mediterranean sea. This telescope has two different modes. One is ARCA (Astrophysical Research with Cosmic in the Abyss), searching for cosmic neutrino sources in TeV - PeV energy range and the other one is ORCA (Oscillation Research with Cosmic in the Abyss), which is optimized to detect GeV atmospheric neutrino. There is a balloon borne experiment named as ANITA (Antarctic Impulse Transient Antenna) [182] having altitude of 37

km and Horizon at 700 km at South Polw. The main purpose is to study UHE cosmic neutrinos by detecting the radio pulses emitted by their interactions with Antarctic ice sheet.

CHAPTER 5

TWO COMPONENT WIMP-FIMP DARK MATTER MODEL WITH SINGLET FERMION, SCALAR AND PSEUDO SCALAR

In this Chapter, we consider two component dark matter (DM) model, where one component is a Weakly Interacting Massive Particle (WIMP) and the other one is Feebly Interacting Massive Particle (FIMP). This has significance in exploring various possible DM indirect signatures that indicate the need of heavier DM (in the mass range $\sim$ 50 GeV) as also lighter DM (of mass $\sim$ 7.5 keV). In this Chapter, the DM in these two mass ranges are explored within a single theoretical framework by a two component WIMP-FIMP model and then it is shown that the observed gamma-ray (γ-ray) excess from the Galactic Centre (GC), self interaction of DM from colliding clusters as well as the 3.55 keV X-ray line from Perseus, Andromeda etc. can be simultaneously explained in the present two component DM model.

5.1 Introduction

The particle nature of DM still remains an enigma. Various direct DM search experiments such as LUX [108], XENON-1T [183], PandaX-II [184] etc. have been trying to investigate the particle nature of DM by measuring the recoil energy of the scattered detector nuclei. Moreover, these experiments are by and large intend to detect DM of mass range between few GeV to tens of GeV regime. However, these experiments give upper bounds on DM-nucleon scattering cross-sections for different DM masses and these are being modified as more and more data are being accumulated in these experiments. These experiments also probe the type of DM-nucleon interaction in the sense that they are spin independent (SI) or spin dependent (SD) types. However, the null results of these experiments have severely constrained the DM-nucleon spin independent scattering cross-section and thereby at present, $\sigma_{\rm SI} > 2.2 \times 10^{-46}$ cm^2 has been excluded by the LUX experiment [108] for the mass of a 50 GeV DM particle at 90% confidence limit (C.L.). Like the spin independent case, the present upper bound on DM-proton spin dependent scattering cross-section is $\sigma_{\rm SD} \sim 5 \times 10^{-40}$ cm^2 [109, 110] for a DM of mass $\sim$ 20 to 60 GeV. The DM-nucleon scattering cross-sections are approaching towards the regime of coherent neutrino-nucleon scattering cross-section and within next few years $\sigma_{\rm SI}$ may hit the "neutrino floor". Therefore, it will be difficult to discriminate the DM signal from that of background neutrinos. However, if the DM is detected in direct direction experiments then that will be a "smoking gun signature" of the existence of beyond Standard Model (BSM) scenario as the Standard Model (SM) of particle physics does not have any viable cold dark matter (CDM) candidate. In this respect indirect detection of DM plays a crucial role. In this Chapter, two possible indirect signatures of DM have been addressed, one is the 1-3 GeV γ-ray excess observed by Fermi-LAT from GC and the other is the 3.55 keV X-ray line observed by Chandra XMM Newton telescope from Andromeda galaxy and 73 other galaxy cluster.

In this Chapter, a two component DM model is proposed with one component to be a WIMP and the other component is a FIMP.

This has been mentioned in Chapter 3, that the WIMPs are a favourite class of thermal DM. The relevant properties of WIMPs such as their production mechanism, relic densities etc. are discussed in Chapter 3. In contrast the non-thermal production of FIMP which has never in thermal equilibrium and they are becoming relic via "freeze-in" mechanism are also discussed in Chapter 3 (Section 3.3). Detailed study of the γ-ray excess from GC by Calore *et al.* [185] also have reported that the γ-ray excess in 1-3 GeV energy range can be explained by DM annihilation into $b\bar{b}$ with annihilation cross-section $\langle\sigma v\rangle_{b\bar{b}} = 1.76^{+0.28}_{-0.27} \times 10^{-26}\ \mathrm{cm^3 s^{-1}}$ at GC having mass $49^{+6.4}_{-5.4}$ GeV. The analyses of γ-rays detected by 45 dwarf spheroidals (dSphs) or satellite galaxies of Milky Way by Fermi-LAT as also results of Dark Energy Survey (DES) indicate possible DM annihilations inside dwarf spheroidals (dSphs). A more detailed study for the observed γ-rays from dwarf galaxies is given in the latter Chapter (Chapter 7).

Apart from the GC γ-ray excess, unidentified 3.55 keV X-ray lines are also detected by XMM Chandra Newton telescope in Andromeda galaxy and 73 other galaxy cluster (Bulbul *et al.* [37] and Boyarsky *et al.* [186]).

This unknown X-ray line can be explained as a DM signal and several DM models are invoked to explain this phenomena [187–212]. However, there are attempts that argue this 3.55 keV X-ray line to be of astrophysical origin [213, 214]. Suggestions are that the molecular interactions in nebula may give rise to this 3.55 keV line (Hitomi collaboration [215]). But this needs further confirmation. In this Chapter, however DM origin for this 3.55 keV is considered and a two component particle DM model is proposed to this effect so as to explain both the phenomena namely the observed GC γ-ray excess and the 3.55 keV X-ray line. It may be noted that, while the GC γ-ray excess phenomenon requires annihilation of DM particles of mass $\sim$ 50 GeV, the 3.55 keV X-ray lines can be originated from the decay of a DM particle of mass as low as 7.5 keV. Therefore, in the proposed two component DM model in this Chapter, one is a heavier component (tens of GeV) while the other is a lighter component (a few keV).

Study of colliding galaxy clusters can also provide valuable information for DM self interac-

tion. An earlier attempt to calibrate the DM self interaction have been made by [216]. Recently an updated measurement for DM self interaction by Harvey *et al.* [217] have measured DM self interaction from the observations of the 72 colliding galaxy cluster. From their observation of spatial offset in collisions of galaxy cluster, DM self interaction is found to be $\sigma/m < 0.47$ cm^2/g with 95% C.L. DM self interaction observation from Abell 3827 cluster performed by [218] also suggests that $\sigma/m \sim 1.5$ cm^2/g. A study of DM self interaction by Campbell *et al.* [219] have reported that a light DM of mass lesser than 0.1 GeV, whose production is followed by freeze-in mechanism can explain the self interaction results from Abell 3827 by [218]. In the next Chapter (Chapter 6) it has been discussed that the FIMP DM is suitable for expalining the DM self interaction bounds.

Taking into considerations of these aspects, in the proposed two component particle DM model in this Chapter, one is a heavier WIMP component responsible for explaining the observed GC γ-ray excess from their annihilation principally to $b\bar{b}$ while the other is a lighter FIMP component, the decay of which would yield the observed 3.55 X-ray lines. In addition this is the FIMP component that also explains the DM self interaction (bounds).

The two component WIMP-FIMP DM model is proposed in this Chapter by first extending the SM with a singlet scalar S and a fermion χ. The added fermion χ and the singlet scalar S constitute the two components of the DM model. While the fermion is attributed to the heavier WIMP component, the lighter singlet scalar component is the FImP (denoted FImP instead of FIMP for being less massive) component of this WIMP-FImP two component DM model. In order to prevent the interactions between the fermion component and the SM fermions, a global $\mathrm{U}(1)_{\mathrm{DM}}$ symmetry is imposed on the added fermion. On the other hand, the lighter component – the singlet scalar – is subjected to a discrete Z_2 symmetry. This prevents the interaction between the singlet scalar and the SM particles. The singlet scalar S acquires a vacuum expectation value (VEV) on spontaneous breaking of Z_2 symmetry. This may give rise to domain walls, which has been discussed later. An additional pseudo scalar Φ is also introduced in the model. The fermion χ can interact with the pseudo scalar involving γ_5 operator. This is required for the following reason.

The self interaction (annihilation) of the fermionic component χ is a p-wave interaction and hence is velocity dependent. As the velocity of WIMP DM is much reduced at the present epoch, the annihilation cross-section will be much suppressed and cannot produce the γ-ray signal required to explain the GC γ-ray excess. However, interaction with the pseudo scalar increases this cross-section. Though the Lagrangian for Φ is CP invariant but CP symmetry is broken by the spontaneous breaking of CP symmetry and Φ acquires a VEV.

It may be mentioned that, in literature there are references of works with only WIMP DM for explaining the GC γ-ray excess or other DM candidates (also of FImP nature) for explaining only the 3.55 keV X-ray lines [220, 221]. There are even references for two component WIMP dark models but here in this Chapter we propose a two component DM model that encompasses both WIMP DM (from freeze-out mechanism) and FImP DM (from freeze-in mechanism) to explain both the GC γ-ray excess and the 3.55 keV X-ray line signature in the framework of a single model. The FImP component also satisfies the DM self interaction bounds.

5.2 Two Component Dark Matter Model

A renormalizable extension of SM is proposed where the SM is extended by a real singlet scalar field S, a singlet Dirac fermion χ and a pseudo scalar Φ. Therefore, in the present scenario the dark sector is composed of a Dira fermion χ and a real scalar S. As mentioned earlier, χ has a global $\mathrm{U(1)_{DM}}$ charge in order to prevent χ to couple with other SM fermions. This ensures its stability. A discrete Z_2 symmetry is imposed on the real scalar field S. This forbids any term with odd number of S field in the Lagrangian [1]. The discrete Z_2 symmetry breaks spontaneously with S acquiring a VEV. The Lagrangian is assumed to be CP invariant but on spontaneous breaking of CP symmetry the pseudo scalar acquires a VEV. Thus after spontaneous symmetry breaking (SSB)

[1] Instead of imposing a global U(1) on the singlet fermion and assuming a Z_2 on the scalar field, one can also assume two different discrete Z_2 symmetries on the scalar and the fermion. This would result in a framework with $Z_2^A \times Z_2^B$. However, we did not consider this framework in our model.

(of $\mathrm{SU}(2)_L \times \mathrm{U}(1)_Y$, Z_2 and CP) of the Lagrangian the scalar fields acquire VEVs and as a result the real components of H, Φ and S mix among each other. After diagonalisation of the 3×3 mass matrix, the lightest eigenstate is attributed to the FImP component of this two component WIMP-FImP model. The low mass eigenvalue corresponding to this eigenstate is achieved for sufficiently low values of relevant mixing angles.

The Lagrangian of the model thus can be written as

$$\mathcal{L} \;=\; \mathcal{L}_{\rm SM} + \mathcal{L}_{\rm DM} + \mathcal{L}_{\Phi} + \mathcal{L}_{\rm int}\ . \tag{5.1}$$

In the above, $\mathcal{L}_{\rm SM}$ represents the Lagrangian for the SM particles that includes the usual kinetic, quadratic and quartic terms for the Higgs doublet H. The dark sector Lagrangian $\mathcal{L}_{\rm DM}$ has two parts, the fermionic and the scalar,

$$\mathcal{L}_{\rm DM} \;=\; \bar{\chi}(i\gamma^{\mu}\partial_{\mu} - m)\chi + \mathcal{L}_S\ , \tag{5.2}$$

with

$$\mathcal{L}_S = \frac{1}{2}(\partial_{\mu}S)(\partial^{\mu}S) - \frac{\mu_S^2}{2}S^2 - \frac{\lambda_S}{4}S^4\,. \tag{5.3}$$

The Lagrangian $\mathcal{L}_{\Phi}$ for the pseudo scalar Φ is given by

$$\mathcal{L}_{\Phi} \;=\; \frac{1}{2}(\partial_{\mu}\Phi)^2 - \frac{\mu_{\Phi}^2}{2}\Phi^2 - \frac{\lambda_{\Phi}}{4}\Phi^4\ . \tag{5.4}$$

It is to be noted that the above Lagrangian does not have any odd term in Φ, which makes $\mathcal{L}_{\Phi}$ CP invariant. All the interaction terms are included in the Lagrangian $\mathcal{L}_{\rm int}$.

$$\mathcal{L}_{\rm int} \;=\; -\,i\,g\,\bar{\chi}\gamma_5\chi\,\Phi - V'(H,\Phi,S)\,. \tag{5.5}$$

The Lagrangian $\mathcal{L}_{\rm SM}$ encompasses the Yukawa type term between Φ (pseudo scalar) and the Dirac fermion χ ($ig\bar{\chi}\gamma^5\chi\Phi$) in addition to other possible mutual interaction terms among the scalars H, Φ and S ($V'(H,\, S,\, \Phi)$). The expression of V' is given as

$$V'(H,\, S,\, \Phi) = \lambda_{H\Phi} H^\dagger H\, \Phi^2 + \lambda_{HS} H^\dagger H\, S^2 + \lambda_{\Phi S} \Phi^2\, S^2\ . \tag{5.6}$$

A discussion is in order. Spontaneous breaking of Z_2 symmetry leads to the formation of domain walls in the Universe and the energy associated with the eventual breaking of such domain walls may overclose the Universe. One way to avoid such domain wall problem is to include an explicit Z_2 symmetry breaking term as given in Ref. [222] [2]. In this Chapter, this procedure has not been adopted. However, another way out to circumvent this problem requires the VEV v_3 to be small ([47] and the references therein). Such an approach to avoid the domain wall has been explored in the literature [199, 223]. In Ref. [199], it has been reported that the VEV of the scalar S considered should be $v_3 \leq 10.7$ MeV to be consistent with CMB (Cosmic Microwave Background) anisotropy measurements. Hence, we consider v_3 values within the above mentioned limit in this Chapter to avoid the domain wall problem.

After the SSB of SM gauge symmetry, Higgs acquires a VEV, v_1 ($\sim$ 246 GeV) and the fluctuating scalar field about this minima (v_1) is denoted as h. Denoting v_2 to be the VEV of the pseudo scalar Φ and v_3, the VEV that the singlet scalar S is assumed to acquire, we have

$$H = \frac{1}{\sqrt{2}} \begin{pmatrix} 0 \\ v_1 + h \end{pmatrix}\ ,\ \Phi = v_2 + \phi\ ,\ S = v_3 + s\,. \tag{5.7}$$

It is to be noted that the global $U(1)_{\rm DM}$ symmetry is conserved even after the SSB [3]. Let us consider

[2] In this Reference a term of the type $\sim |a| e^{i\Phi_a} S$ is introduced in the Lagrangian, a being a complex coefficient. The purpose was however to include a U(1) and Z_2 breaking linear term in this reference (Ref. [222].

[3] In fact global symmetry is also unbroken at the PLANCK scale to provide a stable DM canidate [224].

the scalar potential term V

$$\begin{aligned} V &= \mu_H^2\, H^\dagger H + \lambda_H\, (H^\dagger H)^2 + \frac{\mu_\Phi^2}{2}\Phi^2 + \frac{\lambda_\Phi}{4}\Phi^4 + \frac{\mu_S^2}{2}S^2 + \frac{\lambda_S}{4}S^4 \\ &\quad + \lambda_{H\Phi} H^\dagger H\, \Phi^2 + \lambda_{HS} H^\dagger H\, S^2 + \lambda_{\Phi S}\Phi^2\, S^2\,. \end{aligned} \tag{5.8}$$

After symmetry breaking, the scalar potential Eq. 5.8 takes the following form

$$\begin{aligned} V &= \frac{\mu_H^2}{2}(v_1+h)^2 + \frac{\lambda_H}{4}(v_1+h)^4 + \frac{\mu_\Phi^2}{2}(v_2+\phi)^2 + \frac{\lambda_\Phi}{4}(v_2+\phi)^4 \\ &\quad + \frac{\mu_S}{2}(v_3+s)^2 + \frac{\lambda_S}{4}(v_3+s)^4 + \frac{\lambda_{H\Phi}}{2}(v_1+h)^2(v_2+\phi)^2 \\ &\quad + \frac{\lambda_{HS}}{2}(v_1+h)^2(v_3+s)^2 + \lambda_{\Phi S}(v_2+\phi)^2(v_3+s)^2\,. \end{aligned} \tag{5.9}$$

Using the minimisation condition that

$$\left(\frac{\partial V}{\partial h}\right), \left(\frac{\partial V}{\partial \phi}\right), \left(\frac{\partial V}{\partial s}\right)\Bigg|_{h=0,\,\phi=0,\,s=0} = 0\,, \tag{5.10}$$

we obtain the three following conditions

$$\begin{aligned} \mu_H^2 + \lambda_H v_1^2 + \lambda_{H\Phi} v_2^2 + \lambda_{HS} v_3^2 &= 0\,, \\ \mu_\Phi^2 + \lambda_\Phi v_2^2 + \lambda_{H\Phi} v_1^2 + 2\lambda_{\Phi S} v_3^2 &= 0\,, \\ \mu_S^2 + \lambda_S v_3^2 + \lambda_{HS} v_1^2 + 2\lambda_{\Phi S} v_2^2 &= 0\,. \end{aligned} \tag{5.11}$$

The mass mixing matrix with respect to the basis h-ϕ-s can now be constructed by evaluating $\frac{\partial^2 V}{\partial h^2}$, $\frac{\partial^2 V}{\partial \phi^2}$, $\frac{\partial^2 V}{\partial s^2}$, $\frac{\partial^2 V}{\partial h \partial \phi}$, $\frac{\partial^2 V}{\partial h \partial s}$, $\frac{\partial^2 V}{\partial s \partial \phi}$ at $h = \phi = s = 0$ and is obtained as

$$\mathcal{M}^2_{\text{scalar}} = 2 \begin{pmatrix} \lambda_H\, v_1^2 & \lambda_{H\Phi}\, v_1\, v_2 & \lambda_{HS}\, v_1\, v_3 \\ \lambda_{H\Phi}\, v_1\, v_2 & \lambda_\Phi\, v_2^2 & 2\lambda_{\Phi S}\, v_2\, v_3 \\ \lambda_{HS}\, v_1\, v_3 & 2\lambda_{\Phi S}\, v_2\, v_3 & \lambda_S\, v_3^2 \end{pmatrix}. \tag{5.12}$$

Diagonalising the symmetric mass matrix (Eq. 5.12) by a unitary transformation we obtain three eigenvectors h_1, h_2 and h_3 which represent three physical scalars. Each of the new eigenstate is a mixture of old basis states h, ϕ and s depending on the mixing angles θ_{12}, θ_{23} and θ_{13} i.e.

$$\begin{pmatrix} h_1 \\ h_2 \\ h_3 \end{pmatrix} = U(\theta_{12}, \theta_{13}, \theta_{23}) \begin{pmatrix} h \\ \phi \\ s \end{pmatrix} , \tag{5.13}$$

where $U(\theta_{12}, \theta_{23}, \theta_{13})$ is the usual PMNS matrix with mixing angles are θ_{12}, θ_{23}, θ_{13} and complex phase $\delta = 0$. In this Chapter, we choose h_1 as the SM like Higgs boson which has been discovered few years ago by the LHC experiments [225, 226] at CERN. Therefore, throughout this Chapter we keep the mass (m_1) of $h_1 \sim 125.5$ GeV [4]. On the other hand as mentioned at the beginning of this Section, we consider h_2 is also heavy and the lightest scalar h_3 to be a component of DM (FImP candidate). For simplicity, Eq. 5.13 can be rewritten as

$$\begin{pmatrix} h_1 \\ h_2 \\ h_3 \end{pmatrix} = \begin{pmatrix} a_{11} & a_{12} & a_{13} \\ a_{21} & a_{22} & a_{23} \\ a_{31} & a_{32} & a_{33} \end{pmatrix} \begin{pmatrix} h \\ \phi \\ s \end{pmatrix} , \tag{5.14}$$

where a_{ij} are elements of PMNS matrix.

Further, in order to obtain a stable vacuum we have the following bounds on the quartic couplings derived following [227]

$$\begin{aligned} \lambda_H,\ \lambda_\Phi,\ \lambda_S &> 0 , \\ \lambda_{H\Phi} + \sqrt{\lambda_H \lambda_\Phi} &> 0 , \\ \lambda_{HS} + \sqrt{\lambda_H \lambda_S} &> 0 , \\ 2\lambda_{\Phi S} + \sqrt{\lambda_\Phi \lambda_S} &> 0 \end{aligned}$$

[4] We assume mass of physical scalars h_j to be m_j, $j = 1 - 3$.

and

$$\sqrt{2(\lambda_{H\Phi}+\sqrt{\lambda_H\lambda_\Phi})(\lambda_{HS}+\sqrt{\lambda_H\lambda_S})(2\lambda_{\Phi S}+\sqrt{\lambda_\Phi\lambda_S})}$$
$$+\sqrt{\lambda_H\lambda_\Phi\lambda_S}+\lambda_{H\Phi}\sqrt{\lambda_S}+\lambda_{HS}\sqrt{\lambda_\Phi}+2\lambda_{\Phi S}\sqrt{\lambda_H}>0\ . \tag{5.15}$$

In this model, the fermionic DM (WIMP DM candidate) has an interaction with the pseudo scalar Φ which should not be very large and be within the perturbative limit. For this purpose, we consider $g \leq 4\pi$ in this Chapter.

It is to be noted that, in general, spontaneous CP violation does not occur when singlet scalar acquires a VEV [228]. However, in this Chapter, we consider a pseudo scalar field Φ which acquires a VEV v_2. Consequently this would result in mixing between scalar and pseudo scalar fields and hence CP is violated [222]. Although the Lagrangian in Eq. 5.5 is CP conserving, any mixing between scalar and pseudo scalar (terms with $\lambda_{H\Phi}$ and $\lambda_{\Phi S}$) would break the CP symmetry of the Lagrangian. Hence Eq. 5.5 is the source of CP violation in the model.

5.3 Relic Density

The relic densities for the two component DM considered in the Chapter is obtained by solving the coupled Boltzmann equations for each of the DM components and total DM relic abundance is given by adding up the relic densities of each of the components.

The Boltzmann equation for the fermionic component χ in the present model is given by

$$\frac{dY_\chi}{dz} = -\sqrt{\frac{\pi g_\star(T)}{45G}}\frac{m_\chi}{z^2}\left[\langle\sigma v\rangle_{\bar{\chi}\chi\to x\bar{x}}\left(Y_\chi^2-(Y_\chi^{\rm eq})^2\right)+\langle\sigma v\rangle_{\bar{\chi}\chi\to h_3h_3}\left(Y_\chi^2-\frac{(Y_\chi^{\rm eq})^2}{(Y_{h_3}^{\rm eq})^2}Y_{h_3}^2\right)\right]\ , \tag{5.16}$$

where G is the gravitational constant. The fermionic DM in the present model follows usual freeze-out mechanism and becomes relic which behaves as a WIMP DM. However, evolution of

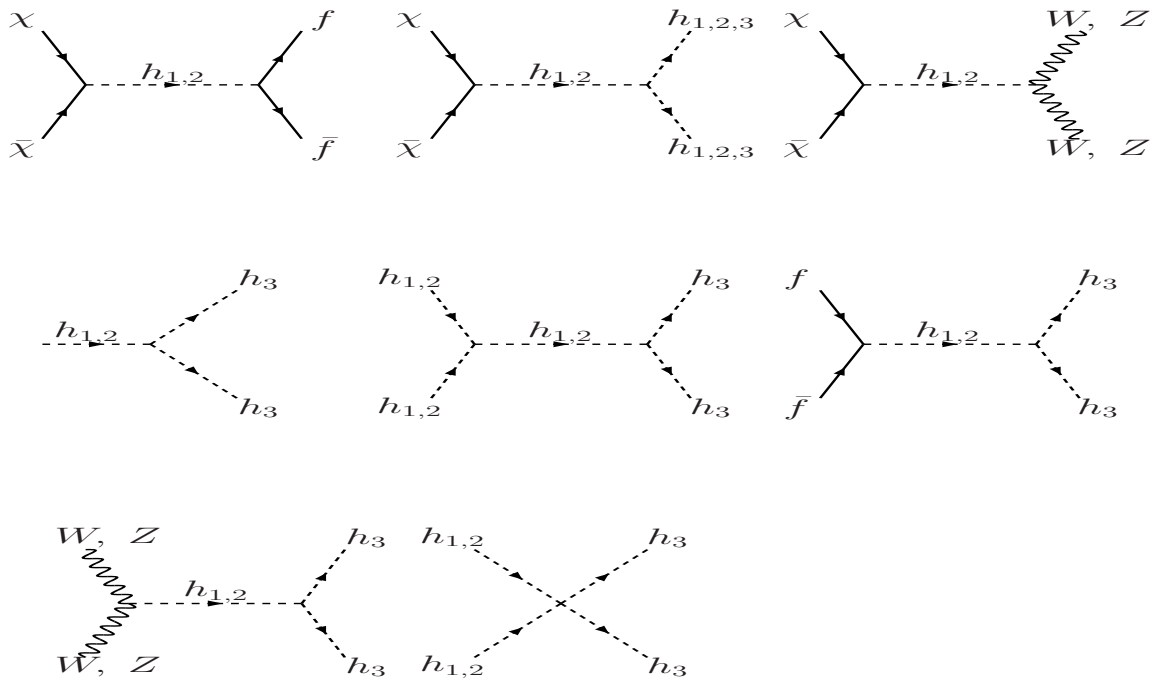

Figure 5.1: Feynman diagrams for the fermionic DM χ and scalar DM h_3.

light DM h_3 is different. We assume that the mixing between the scalar $h_j, j = 1-3$ are very small. Therefore, the scalar h_3 is produced from the decay or annihilation of heavier particles such as Higgs or gauge bosons which never reaches thermal equilibrium (therefore becomes non-thermal in nature) and its production saturates as the Universe expands and cools down. This is referred as freeze-in production of particle [229, 230] and the light DM resembles a FImP like DM. Hence, the initial abundance of h_3, $Y_{h_3} = 0$ in the present model. Thus Eq. 5.16 takes the form

$$\frac{dY_\chi}{dz} = -\sqrt{\frac{\pi g_\star(T)}{45G}}\frac{m_\chi}{z^2}\left[\langle\sigma v\rangle_{\bar{\chi}\chi\to x\bar{x}}(Y_\chi^2 - (Y_\chi^{\rm eq})^2) + \langle\sigma v\rangle_{\bar{\chi}\chi\to h_3h_3}Y_\chi^2\right] , \quad (5.17)$$

where $x(= f,\ W,\ Z,\ h_1,\ h_2)$ denotes the final state particles produced due to annihilation of DM

candidate χ. The Boltzmann equation for the scalar component h_3 in the present framework is given by

$$\begin{aligned}\frac{dY_{h_3}}{dz} &= -\frac{2m_{\rm PL}z}{1.66m^2}\frac{\sqrt{g_\star(T)}}{g_{\rm s}(T)}\left(\sum_i \langle\Gamma_{h_i\to h_3h_3}\rangle\left(Y_{h_3}-Y_{h_i}^{eq}\right)\right) - \\ &\quad \frac{4\pi^2}{45}\frac{m_{\rm PL}m}{1.66}\frac{\sqrt{g_\star(T)}}{z^2}\times \\ &\quad \left[\sum_{x=W,Z,f,h_1,h_2}\langle\sigma{\rm v}_{x\bar{x}\to h_3h_3}\rangle\,(Y_{h_3}^2-(Y_x^{\rm eq})^2) - \langle\sigma{\rm v}_{\bar{\chi}\chi\to h_3h_3}\rangle\left(Y_\chi^2-\frac{(Y_\chi^{\rm eq})^2}{(Y_{h_3}^{\rm eq})^2}Y_{h_3}^2\right)\right] .\end{aligned} \tag{5.18}$$

Since $Y_{h_3}=0$, Eq. 5.18 takes the form

$$\begin{aligned}\frac{dY_{h_3}}{dz} &= -\frac{2m_{\rm PL}z}{1.66m^2}\frac{\sqrt{g_\star(T)}}{g_{\rm s}(T)}\left(\sum_i \langle\Gamma_{h_i\to h_3h_3}\rangle\left(-Y_{h_i}^{eq}\right)\right) - \\ &\quad \frac{4\pi^2}{45}\frac{m_{\rm PL}m}{1.66}\frac{\sqrt{g_\star(T)}}{z^2}\times \\ &\quad \left[\sum_{x=W,Z,f,h_1,h_2}\langle\sigma{\rm v}_{x\bar{x}\to h_3h_3}\rangle\,(-(Y_x^{\rm eq})^2) - \langle\sigma{\rm v}_{\bar{\chi}\chi\to h_3h_3}\rangle Y_\chi^2\right] .\end{aligned} \tag{5.19}$$

In Eqs. 5.16 - 5.19, $Y_x=\frac{n_x}{S}$ is the comoving number density of DM candidate $x=\chi,\ h_3$ while the equilibrium number density is denoted by $Y_x^{\rm eq}$ and S is the entropy of the Universe. In the above $z=m/T$ where T is the photon temperature and m represents the mass. The PLANCK mass $m_{\rm PL}=1.22\times10^{22}$ GeV in Eqs. 5.18, 5.19 and the term $g_\star$ is expressed as [46]

$$\sqrt{g_\star(T)} = \frac{g_S(T)}{\sqrt{g_\rho(T)}}\left(1+\frac{1}{3}\frac{d\,\ln g_S(T)}{d\,\ln T}\right) . \tag{5.20}$$

Here g_S and g_ρ are the degrees of freedom corresponding to entropy and energy density of the

Universe and are expressed as [46]

$$S = g_S(T)\frac{2\pi^2}{45}T^3\,, \qquad \rho = g_\rho(T)\frac{\pi^2}{30}T^4\ . \tag{5.21}$$

The expressions for thermal average annihilation cross-sections ($\langle\sigma v\rangle$) and decay widths ($\langle\Gamma\rangle$) are given as

$$\begin{aligned}\langle\sigma \mathrm{v}\rangle_{aa\to bb} &= \frac{1}{8m_a^4\,T\,K_2^2(m_a/T)}\int_{4m_a^2}^{\infty} ds\;\sigma_{aa\to bb}\,(\mathrm{s}-4m_a^2)\,\sqrt{\mathrm{s}}\,K_1(\sqrt{\mathrm{s}}/T)\ ,\\ \langle\Gamma_{a\to bb}\rangle &= \Gamma_{a\to bb}\frac{K_1(z)}{K_2(z)}\ .\end{aligned} \tag{5.22}$$

The expressions of different annihilation cross-sections and decay processes along with the relevant couplings are given in Appendix A. Feynman diagrams that contribute to the annihilations of χ along with the production of scalar DM h_3 via decay and annihilation channels are shown in Fig. 5.1. It is to be noted that the diagram $\chi\chi \to h_3h_3$ will also contribute to the production of light scalar DM.

In Eq. 5.22, K_1 and K_2 are the modified Bessel functions and s represents the centre of momentum energy. The Boltzmann equations (Eqs. 5.17, 5.19) are solved using Eqs. 5.20 - 5.22 and the relic abundance for χ and h_3 are obtained as

$$\Omega_j h^2 = 2.755\times 10^8 Y_j(T_0)\left(\frac{m_j}{GeV}\right), \quad j=\chi, h_3 \tag{5.23}$$

where the present photon temperature is T_0 and h is Hubble parameter in the unit of 100 Km s^{-1} Mpc^{-1}. The total relic density of the two component WIMP-FImP DM is now obtained by adding up the individual relic densities of each component. The total relic density must satisfy the bound on DM relic density given by PLANCK observational results. Thus

$$\Omega_{\rm DM}h^2 = \Omega_\chi h^2 + \Omega_{h_3}h^2\ , \quad 0.1172 \le \Omega_{\rm DM}h^2 \le 0.1226\ . \tag{5.24}$$

5.4 Bounds from Collider Physics

In this Section, we briefly describe the collider physics bounds in the context of the present two component DM model. Note that three scalar particles are there in the present model namely the Higgs like scalar (h_1), the non SM scalar (h_2) (with mass 85 GeV $\leq m_2 \leq$ 110 GeV) and the light DM candidate (h_3). Therefore, the SM like scalar with mass $\sim$ 125.5 GeV should satisfy the bounds on SM scalar signal strength. The signal strength is defined as

$$R_1 = \frac{\sigma(pp \to h_1)}{\sigma^{\rm SM}(pp \to h)} \frac{{\rm Br}(h_1 \to xx)}{{\rm Br}^{\rm SM}(h \to xx)} \ . \tag{5.25}$$

In the above, $\sigma(pp \to h_1)$ defines the production cross-section of h_1 due to gluon fusion while $\sigma^{\rm SM}(pp \to h)$ is the same for SM Higgs. Similarly ${\rm Br}(h_1 \to xx)$ is defined as the decay branching ratio of h_1 into any final state particle whereas the same for SM Higgs is ${\rm Br}^{\rm SM}(h \to xx)$. The Higgs like scalar must satisfy the condition for SM Higgs signal strength $R_1 \geq 0.8$ [231]. Branching ratio to any final state particle for h_1 is given as ${\rm Br}(h_1 \to xx) = \frac{\Gamma(h_1 \to xx)}{\Gamma_1}$ (here $\Gamma(h_1 \to xx)$ is decay width of h_1 into final state particles and Γ_1 is the total decay width of h_1) and for SM Higgs with mass 125.5 GeV it can be expressed as ${\rm Br}^{\rm SM}(h \to xx) = \frac{\Gamma(h \to xx)}{\Gamma_{\rm SM}}$, where $\Gamma_{\rm SM}$ is total decay width of Higgs. Hence, Eq. 5.25 can be written as

$$R_1 = a_{11}^4 \frac{\Gamma_{\rm SM}}{\Gamma_1} \ , \tag{5.26}$$

where $\Gamma_1 = a_{11}^2 \Gamma_{\rm SM} + \Gamma_1^{\rm inv}$ is the total decay width and $\Gamma_1^{\rm inv}$ is the invisible decay width of h_1 into DM particles given as

$$\Gamma_1^{\rm inv} = \Gamma_{h_1 \to \chi\bar{\chi}} + \Gamma_{h_1 \to h_3 h_3} \ . \tag{5.27}$$

Similarly for h_2, the signal strength R_2 takes the form

$$R_2 = a_{21}^4 \frac{\Gamma'_{\rm SM}}{\Gamma_2} \tag{5.28}$$

with $\Gamma_2 = a_{21}^2 \Gamma'_{\rm SM} + \Gamma_2^{\rm inv}$ where $\Gamma'_{\rm SM}$ is the total decay width of non SM scalar of mass m_2 and $\Gamma_2^{\rm inv} = \Gamma_{h_2 \to \chi\bar{\chi}} + \Gamma_{h_2 \to h_3 h_3}$. The decay width $\Gamma(h_i \to \chi\bar{\chi}),\ i = 1, 2$ is expressed as

$$\begin{aligned} \Gamma_{h_1 \to \chi\bar{\chi}} &= \frac{m_1}{8\pi} g^2 a_{21}^2 \left(1 - \frac{4m_\chi^2}{m_1^2}\right)^{1/2}, \\ \Gamma_{h_2 \to \chi\bar{\chi}} &= \frac{m_2}{8\pi} g^2 a_{22}^2 \left(1 - \frac{4m_\chi^2}{m_2^2}\right)^{1/2}. \end{aligned} \tag{5.29}$$

The analytical forms for $\Gamma_{h_j \to h_3 h_3},\ j = 1, 2$ are given in Appendix A. The invisible decay branching ratio for the SM like Higgs is $\mathrm{Br}_{\rm inv}^1 = \frac{\Gamma_1^{\rm inv}}{\Gamma_1}$. The invisible decay branching ratio is assumed to be small and the condition $\mathrm{Br}_{\rm inv}^1 < 0.2$ [232] is adopted as the bound on the same in this Chapter.

5.5 Dark Matter Self Interaction

Study of DM self interaction have recently received attention and have been explored in literatures [216–218]. DM, though primarily assumed to be collisionless in nature, is found to have self interaction [217] with cross-section $\sigma_{DM}/m < 0.47$ cm^2/g at 95% C.L. In the present model we proposed two DM candidates χ (WIMP like fermion) and a light scalar DM h_3 (FImP). In this Chapter we will investigate whether any of these DM candidate can account for the observed DM self interaction cross-section. Study of DM self interaction by Campbell *et al.* [219] has reported that a light DM with mass below 0.1 GeV produced by freeze-in mechanism can provide the required amount of DM self interaction cross-section (contact interaction) in order to explain the observations of Abell 3827 [218] with $\sigma_{DM}/m \sim 1.5$ cm^2/g which is close to the bound obtained from [217]. Therefore, in this Chapter, we investigate whether the FImP DM h_3 can account for

the DM self interaction cross-section given by [217, 218]. The ratio to self interaction cross-section with mass m_3 for the scalar DM candidate in the present model is given as [199] [5]

$$\frac{\sigma_{h_3}}{m_3} \simeq \frac{9\lambda_S^2}{2\pi m_3^3} \ , \tag{5.30}$$

where the above expression of self interaction is obtained by replacing the quartic coupling λ_{3333} in terms of coupling λ_S for h_3 given in Appendix A. In the Eq. 5.30 we have considered contact interaction only and neglected the contributions from s-channel mediated diagrams since those are suppressed due to small coupling with scalars h_1 and h_2 and also due large mass terms in propagator. It is to be noted that since in the present model we have two DM components, the self interaction cross-section for a particular component should be modified in accordance with the fractional contribution of that component towards the DM relic density. For the light DM component h_3 in the present model, this factor is $f_{h_3} = \frac{\Omega_{h_3}}{\Omega_{\rm DM}}$. Again since the process of self interaction requires two DM particles to interact, the self interaction for the h_3 component should be modified by a factor $f_{h_3}^2$. We have shown later in Sect. 5.6 that although the lighter component of DM has smaller relic density, ($\Omega_{h_3}h^2 \sim 0.1\Omega_\chi h^2$), the number density of h_3 is very high compared to that of χ resulting in a smaller fractional density $r_\chi = \frac{n_\chi}{n_\chi + n_{h_3}} \sim 10^{-6}$ for the heavier DM candidate. As a result number of collisions will eventually be dominated by h_3 ($n_{h_3}^{\rm coll} >> n_\chi^{\rm coll}$). However, measurement of DM self interaction is difficult and depends on several other factors. Our calculation shows that the self interaction of the heavier component χ is very small in comparison to that of h_3. Therefore, the lighter component with large self interaction will suffer significant change in its spatial distribution while the same for χ will remain unaffected. However, in assessing the DM self interaction from the observational results (spatial offset as observed by [217]) of collisions of galaxy clusters, the mass distribution of DM (DM halo) in its totality has been considered (which in the present context signifies engaging both the DM components of the model). Moreover, if heavier component dominates the total contribution to relic density (as presented later in), will share large

[5] Using the condition $\mathrm{s} - 4m^2 << m^2$.

amount of mass of total DM halo. Then the gravitational effects between the DM components may affect the self interaction and the consequent observed spatial offset. Therefore, from the present study we may state that the effective self interaction ($\sim f_{h_3}^2 \frac{\sigma_{h_3}}{m_3}$) in our model is only an estimate and may be altered by these other factors. But this is for posterity.

5.5.1 3.55 keV X-ray Emission and Light DM Candidate

Independent study of XMM Newton observatory data by Bulbul *et al.* [37] and Boyarsky *et al.* [186] have reported a 3.55 keV X-ray emission line from extragalactic spectrum. Such an observation can not be explained by known astrophysical phenomena. Although the signal is not confirmed, if it remains to exist then such a signature can be explained by decay of heavy DM candidates [200] or annihilation of light DM directly into photon [199, 220]. The observations from Hitomi collaboration [215] also suggest that the 3.55 keV X-ray line can be caused by the charge exchange phenomena in molecular nebula which requires more sensitive observation to be confirmed. Since in the present framework, we propose a light DM candidate h_3 to circumvent the self interaction property of DM, we further investigate whether it can also explain the 3.55 keV X-ray signal. For this purpose, we assume that mass of the light FImP DM candidate h_3 is $m_3 \sim 7.1$ keV which decays into pair of photons. The expression for the decay of h_3 into 3.55 keV X-rays is given as

$$\Gamma_{h_3 \to \gamma\gamma} = \left(\frac{\alpha_{\rm em}}{4\pi}\right)^2 |F|^2 \; a_{31}^2 \; \frac{G_F m_3^3}{8\sqrt{2}\pi} \; , \tag{5.31}$$

where G_F is the Fermi constant and $\alpha_{\rm em} \sim \frac{1}{137}$ is the fine structure constant. The loop factor F in Eq. 5.31 is

$$F = F_W(\beta_W) + \sum_f N_c Q_f^2 F_f(\beta_f) \; , \tag{5.32}$$

m_1 GeV	m_2 GeV	m_3 GeV	λ_{12}	λ_{13}	λ_{23}	R_1	$\mathrm{Br}^1_{\mathrm{inv}}$	$f_{h_3}\Gamma_{h_3\to\gamma\gamma}$ 10^{-29} s^{-1}	g
∼125.5	85-110	∼7.1×10^{-6}	10^{-4}-0.1	10^{-10}-10^{-8}	10^{-11}-10^{-9}	0.8-1.0	0-0.2	2.5-25	0.01-5.0

Table 5.1: Constraints and chosen regions of model parameters for the two component DM model.

where

$$\begin{aligned} \beta_W &= \frac{4m_W^2}{m_3^2}, \;\; \beta_f = \frac{4m_f^2}{m_3^2}, \\ F_W(\beta) &= 2 + 3\beta + 3\beta(2-\beta)f(\beta), \\ F_f(\beta) &= -2\beta[1 + (1-\beta)f(\beta)], \\ f(\beta) &= \arcsin^2[\beta^{-1/2}] \, . \end{aligned}$$

N_c in the loop factor is the colour quantum number while Q_f denotes the charge of the fermion. It is to be noted that the decay width of h_3 must be in the range 2.5×10^{-29} s^{-1} $\leq f_{h_3}\Gamma_{h_3\to\gamma\gamma} \leq 2.5\times10^{-28}$ s^{-1} in order to produce the required extragalactic X-ray flux obtained from Andromeda, Perseus etc. Since in the present model we have two DM components, the decay width of h_3 must be multiplied by a factor $f_{h_3} = \frac{\Omega_{h_3}}{\Omega_{DM}}$, where f_{h_3} is the fractional contribution to DM relic density by h_3 component. Hence, in this work we will also test the viability of the light scalar DM candidate to explain the possible X-ray emission signal reported by [37, 186] along with DM self interaction results.

5.6 Calculations and Results

In this Section, we test the viability of the present two component DM model scanning over a range of model parameter space. In Table 5.1, we tabulate the range of model parameter space and relevant constraints used in this Chapter. Note that the coupling parameters $\lambda_{ij};\ i,j = 1-3,\ (i \neq j)$ are in agreement with the vacuum stability conditions mentioned earlier in Eqs. 5.15 and also satisfy

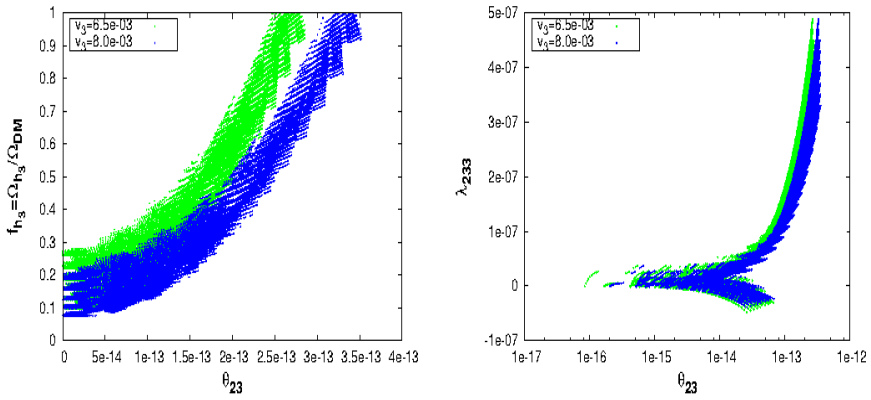

(a) (b)

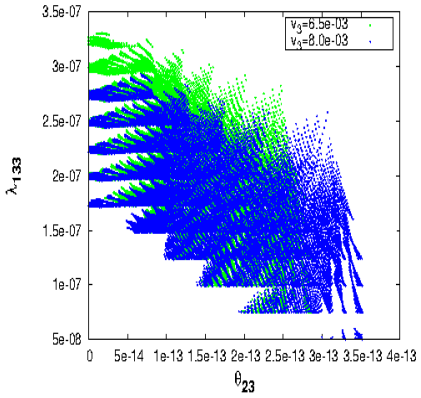

(c)

Figure 5.2: The upper left panel (a) shows the changes in f_{h_3} with mixing angle θ_{23}. Figs. (b-c) depict the allowed values of the couplings λ_{233} and λ_{133} plotted against θ_{23}.

perturbative unitarity condition. As we have mentioned earlier, h_1 is SM like scalar and h_2 is non SM scalar, we take $v_1 = 246$ GeV and $v_2 = 500$ GeV in the present framework. We further assume two choices of $v_3 = 6.5$ MeV and 8.0 MeV. These choices are consistent with the previous studies of light scalar DM of mass ~ 7.1 keV with bound 2.0 MeV $\leq v_3 \leq$ 10.0 MeV [199, 220]. We have also imposed the conditions on signal strength and invisible decay branching ratio of SM like scalar h_1 obtained from ATLAS and CMS at LHC ($R_1 \geq 0.8$ and $\text{Br}^1_{\text{inv}} \leq 0.2$). Using the range of model parameter space tabulated in Table 5.1 we solve the three scalar mass mixing matrix in order to find out the mixing angles of PMNS matrix and $a_{ij};\ i,j = 1-3$ elements. These

matrix elements are then used to calculate various couplings mentioned in Appendix A, which are necessary in order to calculate the decay widths and annihilation cross-sections of scalar DM candidate h_3. The coupling g ($\leq 4\pi$, bound from perturbative limit) between the pseudo scalar and the fermionic DM is also varied within the range mentioned in Table 5.1 to compute the annihilation cross-sections for fermionic DM. These decay widths and annihilation cross-sections of both DM candidates are then used to solve the coupled Boltzmann Eqs. 5.17, 5.19 and calculate the relic densities for each DM candidate satisfying the condition for total DM relic density Eq. 5.24. In Fig. 5.2 we show the valid range of model parameter space obtained using Table 5.1 and solving the coupled Boltzmann equations satisfying the condition $\Omega_\chi h^2 + \Omega_{h_3} h^2 = \Omega_{\rm DM} h^2$ as given by PLANCK satellite experiment. In Fig. 5.2(a) we plot the variation of allowed mixing angle θ_{23} with the fractional relic density f_{h_3} of the scalar DM in the present framework [6]. Plotted blue and green shaded regions depicted in all the three figures of Fig. 5.2 correspond to the choice of $v_3 = 6.5 \times 10^{-3}$ GeV and 8.0×10^{-3} GeV. The observation of Fig. 5.2(a) (in $\theta_{23} - f_{h_3}$ plane) shows that the relic density contribution of the scalar DM component increases with the increase in θ_{23}. It is to be noted that the maximum allowed range of θ_{23} depends on the choice of v_3 and we have found that for $v_3 = 6.5 \times 10^{-3}$ GeV, $\theta_{23}^{\rm max} \sim 2.8 \times 10^{-13}$ while the same obtained with $v_3 = 8.0 \times 10^{-3}$ GeV is $\theta_{23}^{\rm max} \sim 3.5 \times 10^{-13}$. This variation of θ_{23} with f_{h_3} shown in Fig. 5.2(a) is a direct consequence of the fact that increase in θ_{23} also increases the value of λ_{233} which is depicted in Fig. 5.2(b). In Fig. 5.2(b) the variation of θ_{23} is plotted against λ_{233}. It is easily seen from Fig. 5.2(b) that when θ_{23} is small $\sim 10^{-16} - 10^{-14}$, the value of λ_{233} is very small. However as θ_{23} increases further, there is a sharp increase in the value of $|\lambda_{233}|$. As a result the contribution from the decay channel $h_2 \to h_3 h_3$ enhances which then also raises the relic density contribution of scalar h_3. From Fig. 5.2(b) we notice that maximum allowed range of λ_{233} is $\sim 5 \times 10^{-7}$ for both the cases of v_3 considered in the Chapter. Finally in Fig. 5.2(c) θ_{23} is plotted against λ_{133} for the both the values of v_3 mentioned above. From Fig. 5.2(c) we notice that λ_{133} decreases steadily

[6] Mixing angles $\theta_{ij};\ i, j = 1 - 3, i \neq j$ are expressed in radian.

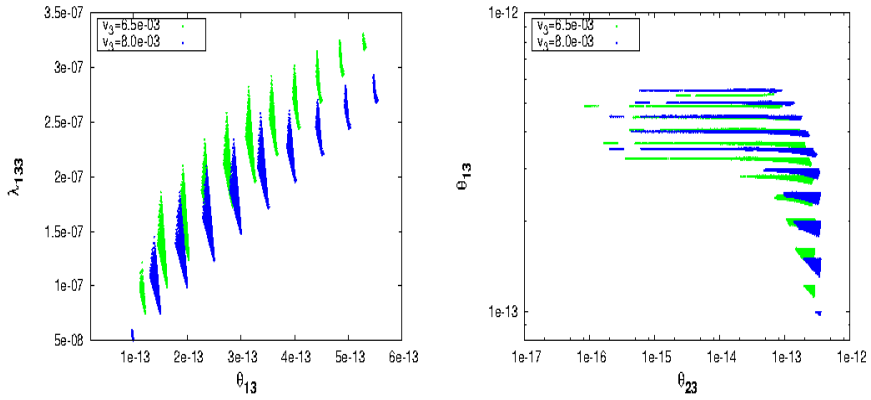

(a) (b)

Figure 5.3: The available model parameter space in $\theta_{13} - \lambda_{133}$ plane is shown in the left panel (a) while in the right panel (b) the same region is depicted when θ_{23} is varied against θ_{13}.

with enhancement in θ_{23} indicating an suppression in the contribution from h_1 (with $m_1 \sim 125.5$ GeV) decay into pair of h_3. The allowed range of λ_{133} for both the values of v_3 lie within the range $0.5 \times 10^{-8} - 3.5 \times 10^{-7}$. In this framework mass of h_2 is varied in the range $85 - 110$ GeV (i.e., $m_2 < m_1$) and decay width is inversely proportional to the mass of decaying particle (see Appendix A for expression). This indicates that the contribution of the non SM scalar to the freeze-in production of FImP DM h_3 is significant compared to the same obtained from SM like scalar when coupling λ_{233} is not small (i.e., $|\lambda_{233}| \sim \lambda_{133}$).

Fig. 5.3(a) depicts the allowed range of θ_{13} plotted against λ_{133} for both the values of v_3 considered in earlier plots of Fig. 5.2. We also use the similar colour scheme to indicate the values of v_3 satisfying the same conditions applied in order to plot Fig. 5.2. From Fig. 5.3(a) it can be easily observed that θ_{13} in the present model varies within the range $\sim 1.0 - 6.0 \times 10^{-13}$ for both the chosen values of $v_3 = 6.5 \times 10^{-3}$ GeV and $v_3 = 8.0 \times 10^{-3}$ GeV respectively. It can be also noticed from the plots in Fig. 5.3(a) that λ_{133} is proportional to the value of θ_{13}. This reveals that the decay width $h_1 \to h_3 h_3$ increases with increase in θ_{13} which can enhance the freeze-in pair production of h_3 via h_1. In Fig. 5.3(b) we show the allowed model parameter space in $\theta_{23} - \theta_{13}$ plane for the same set of

Set	m_1 GeV	m_2 GeV	m_3 GeV	v_3 GeV	θ_{12}	g
1	125.4	102.5	7.12×10^{-6}	6.5×10^{-3}	1.41×10^{-2}	0.01-5.0
2	125.5	107.2	7.15×10^{-6}	8.0×10^{-3}	5.78×10^{-2}	0.01-5.0

Table 5.2: Chosen parameter set for the plots in Fig. 5.4(a-c).

v_3 values and constraints used in earlier plots as well. Study of Fig. 5.3(b) reveals that for smaller values of $\theta_{23} \sim 10^{-16} - 10^{-14}$, θ_{13} maintains a value in range $\sim 3 \times 10^{-13} - 6 \times 10^{-13}$ indicating that contribution in the relic density is mostly from the decay of h_1 into two h_3 scalars. However, as θ_{23} increases the contribution of h_2 increases (due to increase in λ_{233}) which reduces the value of θ_{13} (as well as λ_{133}) in order to maintain the total DM relic density by h_3 and to avoid overabundance of DM (when we add up the contribution of DM relic density obtained from the fermionic DM component χ, i.e., $f_{h_3} + f_\chi = 1$). It is to be mentioned that the mixing angle θ_{12} varies within the range $0.003 \leq \theta_{12} \leq 0.183$ for the allowed model parameter space obtained using both sets of v_3 considered. Note that all the plots in Fig. 5.2 and Fig. 5.3 are in agreement with the constraints on decay width of 7.1 keV scalar h_3 into X-ray, $2.5 \times 10^{-29}\text{s}^{-1} \leq f_{h_3}\Gamma_{h_3\to\gamma\gamma} \leq 2.5 \times 10^{-28}\text{s}^{-1}$. We have also found that the signal strength of h_2, i.e., R_2 in the present formalism is very small to be observed at the LHC experiments due to smallness of mixing between SM like scalar h_1 with h_2.

So far, in this Chapter, we have only discussed about the available parameters for the two component DM model involving a fermion χ and a light scalar h_3 of mass ~ 7.1 keV in agreement with PLANCK DM relic density satisfying the condition $\Omega_\chi h^2 + \Omega_{h_3} h^2 = \Omega_{\rm DM} h^2$ (Fig. 5.2, 5.3). In Fig. 5.4(a-b) we show the $m_\chi - \Omega_\chi h^2$ plots while in Fig. 5.4(c) the variation of DM density $\Omega_{h_3} h^2$ for light DM candidate h_3 ($m_3 \sim 7.1$ keV) is plotted against the temperature T of Universe. Instead of scanning over the full range of parameter space obtained from Fig. 5.2 and Fig. 5.3 (for two values of v_3), we consider two valid set of parameters for the purpose of demonstration tabulated in Table 5.2. Therefore, the parameter sets in Table 5.2 are within the range of scan

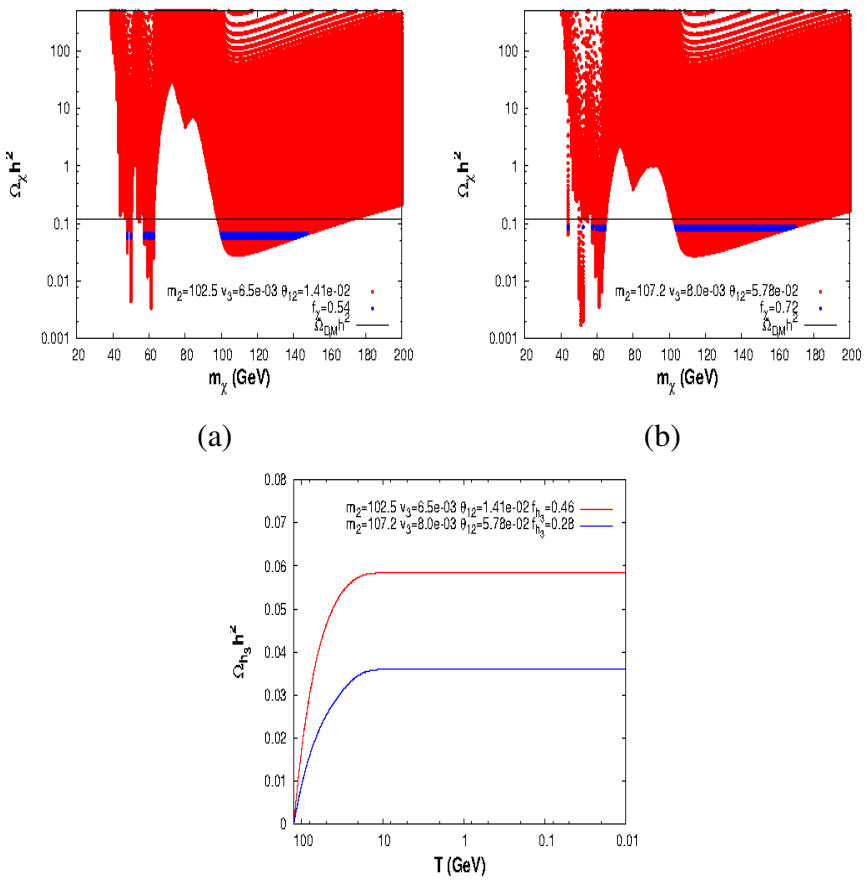

Figure 5.4: Plots in (a-b) show the $m_\chi - \Omega_\chi h^2$ parameter space for the set of parameters in table 5.2 for the fermionic DM. The variation of $\Omega_{h_3}h^2$ (for the scalar DM h_3) with temperature T for the same set of parameter is shown in (c).

performed using the Table 5.1 and also respect all other necessary conditions (such as vacuum stability, decay width of h_3, constrains from LHC etc.). Fermionic DM candidate can annihilate through s-channel annihilation mediated by scalars h_1 and h_2 (see Fig. 5.1). The mixing between the SM like scalar h_1 and non SM scalar h_2 given by θ_{12}, is necessary to calculate the parameters $a_{ij}(\ i,j\ =\ 1,2)$ and different annihilations of the fermionic DM. Since in this Chapter the range of coupling λ_{12} is larger compared to other couplings λ_{23} and λ_{13}, the parameters $a_{ij},\ i,j\ =\ 1,2$ will dominantly be determined by θ_{12}. This is also justified by the plots in Fig. 5.3(b) where θ_{23} is

varied with θ_{13} showing these mixing angles are very small. Therefore, we have chosen two values of θ_{12} for two set of v_3 values given in Table 5.2. Note that we have also considered the same set of v_3 values of light scalar S in our model along with $v_1 = 246$ GeV and $v_2 = 500$ GeV taken earlier in order to find out the valid range of parameter space obtained in Figs. 5.2, 5.3. Shown $m_\chi - \Omega_\chi h^2$ plot in Fig. 5.4(a) corresponds to the set of parameters with $v_3 = 6.5 \times 10^{-3}$ GeV and the same with other set of parameters (for $v_3 = 8.0 \times 10^{-3}$ GeV) is depicted in Fig. 5.4(b). The red regions in both the Figs. 5.4(a-b) are obtained by varying the coupling g within the range $0.01 \leq g \leq 5.0$ and also varying the fermionic DM mass m_χ from 20 GeV to 200 GeV. From both the Figs. 5.4(a-b) it can be observed that a very small region of parameter space (for these chosen sets in Table 5.2) lies below the total DM relic density bound given by PLANCK [12] (black horizontal line shown in both the plots Fig. 5.4(a-b)). We have found that relic density of fermionic DM becomes less abundant with respect to total DM relic density near the resonances of SM like Higgs (h_1) and non SM scalar h_2 when its mass $m_\chi \sim m_i/2,\ i = 1, 2$. Apart from that, there is also a region of parameter space with mass $\sim 100 - 180$ GeV (for $m_2 = 102.5$ GeV) and $\sim 100 - 190$ GeV (when $m_2 = 107.2$ GeV) where the condition $\Omega_\chi h^2 < \Omega_{\rm DM} h^2$ is satisfied. In this region the heavy fermionic DM annihilates into scalar h_1 and h_2. Thus the DM annihilation cross-section get enhanced which reduces the relic density $\Omega_\chi h^2$ of the fermionic DM candidate. The shaded blue horizontal regions shown in the plot Fig. 5.4(a) (Fig. 5.4(b)) are fractional contributions to the total DM relic density from the fermionic DM candidate χ with $f_\chi = 0.54$ ($f_\chi = 0.72$) where $f_\chi = \frac{\Omega_\chi}{\Omega_{DM}}$. In Fig. 5.4(c) we show the evolution of relic density $\Omega_{h_3} h^2$ of the light scalar DM h_3 as a function of temperature T of the Universe with the same set of parameters given in Table 5.2. The plot shown in red (blue) depicted in Fig. 5.4(a) (Fig. 5.4(b)) corresponds to the parameter set with $v_3 = 6.5 \times 10^{-3}$ GeV ($v_3 = 8.0 \times 10^{-3}$ GeV). Moreover, we have also satisfied the condition $f_\chi + f_{h_3} = 1$ in the plots of Fig. 5.4(c) (in order to produce the total DM relic abundance obtained from PLANCK results [12]) such that the fractional contribution of h_3 for each set of parameter in Table 5.2 is $f_{h_3} = 1 - f_\chi$, i.e., $f_{h_3} = 0.46\ (0.28)$ for the red (blue) plot depicted in Fig. 5.4(c).

It appears from the plots in Fig. 5.4(c) that the relic density of light scalar DM is very small (as initial abundance $Y_{h_3} = 0$), increases gradually with decreasing temperature and finally saturates near $T \sim 10$ GeV. The saturation of the relic density indicates that the production of h_3 ceases as the Universe expands and cools down due to rapid decrease in the number density of decaying or annihilating particles. Therefore, from Fig. 5.4(a-c) it can be concluded that the present model of two component DM with a WIMP (heavy fermion χ) and a FImP (light scalar h_3) can successfully provide the observed DM relic density predicted by PLANCK satellite data.

5.6.1 Direct Detection of DM

In this Section, we will investigate whether the allowed model parameter space is compatible with the results from direct detection of DM obtained from DM direct detection experiments. Direct detection experiments search for the evidences of DM-nucleon scattering and provide bounds on DM-nucleon scattering cross-section. DM candidates in the present model can undergo collision with detector nucleus and the recoil energy due to the scattering is calibrated. Since no such collision events have been observed yet by different DM direct detection experiments, these experiments provide an exclusion limit on DM-nucleon scattering cross-section. The most stringent bound on DM-nucleon spin independent (SI) cross-section is given by LUX [108], XENON-1T [183] and PandaX-II [184]. In the present model, both the DM components (WIMP and FImP) χ and h_3 can suffer SI elastic scattering with the detector nucleus. The fermionic DM χ in this Chapter can interact through pseudo scalar interaction via t-channel processes mediated by both h_1 and h_2. The expression of SI scattering cross-section for the fermionic DM χ is

$$\sigma_{SI}^{\chi} = \frac{g^2}{\pi} m_r^2 \left(\frac{a_{11} a_{12}}{m_1^2} + \frac{a_{22} a_{21}}{m_2^2} \right)^2 \lambda_p^2 \, v^2 \ , \tag{5.33}$$

where λ_p is given as [233]

$$\lambda_p = \frac{m_p}{v_1}\left[\sum_q f_q + \frac{2}{9}\left(1 - \sum_q f_q\right)\right] \simeq 1.3 \times 10^{-3} \tag{5.34}$$

and $m_r = \frac{m_\chi m_p}{m_\chi + m_p}$ denotes the reduced mass for the scattering. It is to be noted that due to the pseudo scalar interaction scattering cross-section on Eq. 5.33 is velocity suppressed and hence multiplied by a factor v^2 with $v \sim 10^{-3}$ being the velocity of DM particle. We have found that this velocity suppressed scattering cross-section is way below the latest limit on DM-nucleon scattering given by direct detection experiments [108, 183, 184]. This finding is also in agreement with the results obtained in a different work by Ghorbani [234]. Moreover, since we have two DM components in the model, the effective scattering cross-section for the fermionic DM (i.e., WIMP candidate) will be rescaled by a factor proportional to the fractional number density $r_\chi = \frac{n_\chi}{n_\chi + n_{h_3}}$ (n_x denotes the number density), i.e., $\sigma_{SI}^{'\chi} = r_\chi \sigma_{SI}^{\chi}$ (for further details see [220, 235]). The number density of both the DM components χ and h_3 can be obtained from the expression of individual relic density given in Eq. 5.23. In the present framework, the fermionic DM candidate χ is $\sim 10^6$ times heavier than the scalar h_3 DM. For example, if we consider that the contribution to the total relic density from h_3 is smaller with respect to that of fermion χ having value $\Omega_{h_3}h^2 \sim 0.1\Omega_\chi h^2$, the number density of h_3 is 10^6 times larger than that of n_χ. This indicates that the rescaling factor $r_\chi \sim 10^{-6}$ and $r_{h_3} \sim 1$. Therefore, the effective SI scattering cross-section $\sigma_{SI}^{'\chi}$ for fermionic DM candidate is further suppressed by the rescaling factor $r_\chi << 1$ making it much smaller than the most sensitive DM direct detection limits obtained from experiments like LUX, PandaX-II. Similarly, for the scalar FImP DM candidate the effective SI direct detection cross-section is given as $\sigma_{SI}^{'h_3} = r_{h_3}\sigma_{SI}^{h_3}$ where

$$\sigma_{SI}^{h_3} = \frac{m_r^{'2}}{4\pi}\frac{f^2}{v_1^2}\frac{m_p^2}{m_3^2}\left(\frac{\lambda_{133}a_{11}}{m_1^2} + \frac{\lambda_{233}a_{21}}{m_2^2}\right)^2 , \tag{5.35}$$

where $m'_r = \frac{m_3 m_p}{m_3+m_p}$ and $f \sim 0.3$ [236]. Since $m_3 << m_p$, $m'_r \sim m_3$ and Eq. 5.35 can be rewritten as

$$\sigma_{SI}^{h_3} = \frac{1}{4\pi}\frac{f^2}{v_1^2} m_p^2 \left(\frac{\lambda_{133} a_{11}}{m_1^2} + \frac{\lambda_{233} a_{21}}{m_2^2}\right)^2 . \tag{5.36}$$

Since h_3 in the present model has very small interaction with the SM bath particles and never reaches equilibrium after once produced, the couplings λ_{133} and λ_{233} are very small ($\sim 10^{-7}$, as seen from Fig. 5.2(b-c)). We have found that though the number density of h_3 is high $r_{h_3} \sim 1$ (as it is light), effective scattering cross-section $\sigma_{SI}^{'h_3} \sim \sigma_{SI}^{h_3}$ is also very small to be observed by any DM direct search experiments and remains far below the most stringent limit given by LUX [108], XENON-1T [183] and PandaX-II [184] due to smallness of couplings $\lambda_{j33},\ j = 1, 2$. Therefore, in the present scenario of two component DM model (with a WIMP and a FImP), we do not expect any bound on model parameter space from direct detection experimental constraints.

5.7 GC γ-ray Excess and DM Self Interaction

An excess of γ-ray in the energy range 1-3 GeV have been obtained from analysis of Fermi-LAT data [237] in the region of Galactic Centre. Such an excess can be interpreted as a result of DM annihilation in the GC region. DM particles can be trapped due to the immense gravitational pull of GC and also other astrophysical sites like dwarf galaxies, Sun etc. These sites are rich with particle DM which then undergo pair annihilation. Different particle physics models for DM are explored in order to provide a suitable explanation to this excess in γ-ray at GC as we have mentioned earlier in Sect. 5.1. An analysis of this 1-3 GeV GC excess of γ-ray by Calore, Cholis and Weniger (CCW) [185] using various galactic diffusion excess models suggests that Fermi-LAT data can be explained by DM annihilation at GC. Indeed, the γ-ray excess can be very well fitted with a DM of mass $49^{+6.4}_{-5.4}$ GeV which annihilates into pair of $b\bar{b}$ particles [7] with annihilation cross-section

[7] Produced pair of fermions undergo hadronization processes to finally annihilate into pair of photons via pion decay or bremsstrahlung.

BP1	m_1 GeV	m_2 GeV	m_χ GeV	v_3 10^{-3} GeV	g	R_1	$\mathrm{Br}^1_{\mathrm{inv}}$	f_χ	$f_\chi^2\langle\sigma v\rangle_{b\bar{b}}$ 10^{-26} $\mathrm{cm}^3\mathrm{s}^{-1}$	r_χ	$\sigma^{'\chi}_{SI}$ pb
1	125.5	102.4	47.5	3.5	0.22	0.92	0.082	0.88	1.68	1.04e-06	2.09e-26
2	125.4	104.9	50.0	4.5	0.11	0.99	0.021	0.89	1.62	1.14e-06	5.81e-28

Table 5.3: Benchmark points for calculation of GC γ-ray excess plotted in Fig. 5.5 with fermionic DM χ.

$\langle\sigma v\rangle_{b\bar{b}} = 1.76^{+0.28}_{-0.27} \times 10^{-26}\ \mathrm{cm}^3\mathrm{s}^{-1}$. In this section we will investigate whether the WIMP like fermionic DM candidate χ can account for the observed GC γ-ray excess results. In addition, self interaction study of the light scalar DM (FImP DM, mentioned earlier in Sect. 5.5) will also be addressed in this Section. Before we explore the DM interpretation of GC γ-ray excess, a discussion is in order. The study of γ-ray signatures from dwarf galaxies by Fermi-LAT and DES [238, 239] also provide limits on DM annihilation cross-section into various annihilation modes. The limits on DM annihilation cross-section into $b\bar{b}$ is consistent with the GC γ-ray excess analysis by CCW. However, apart from DM annihilation, the γ-ray excess at GC in the range 1-3 GeV can also be explained by various non DM phenomena such as contribution from point sources near GC [240] or millisecond pulsars [241]. Study by Clark *et al.* [242] also rule out the idea that the point like sources are DM substructures. However, in a recent work Fermi-LAT and DES collaboration have performed an analysis of γ-ray data with 45 confirmed dSphs [243]. The analysis of γ-ray emission data from these dSphs by Fermi-LAT and DES provides bound on DM annihilation cross-section into different final channel particles ($b\bar{b}$ and $\tau\bar{\tau}$). Although their analysis [243] of the data does not show any significant excess at these sites (dSphs), the limits obtained on DM annihilation cross-section in their analysis do not exclude the possibility of DM interpretation of GC γ-ray excess either. Therefore, in this Chapter, we will consider DM as the source to the γ-ray excess at GC observed by Fermi-LAT and test the viability of our model.

The expression for the differential γ-ray flux obtained in the region of the GC for the fermionic

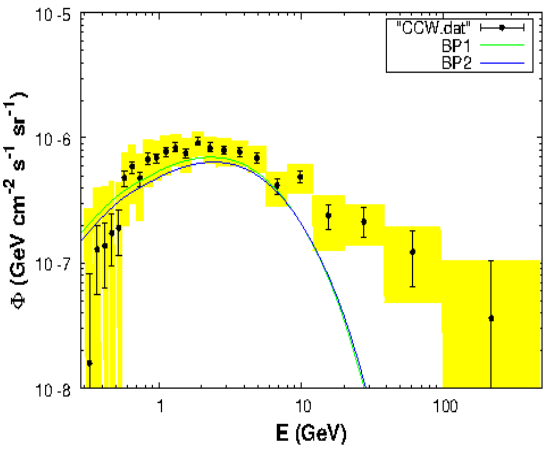

Figure 5.5: Comparison of the Fermi-LAT excess results from CCW [185] with the γ-ray flux obtained from benchmark points tabulated in Table 5.3.

BP1	m_1 GeV	m_2 GeV	m_3 keV	v_3 10^{-3} GeV	f_{h_3}	$f_{h_3}\Gamma_{h_3\to\gamma\gamma}$ 10^{-29} s^{-1}	r_{h_3}	λ_s	$f^2_{h_3}\frac{\sigma_{h_3}}{m_3}$ cm^2/g	$\sigma^{h_3}_{SI}$ pb
1	125.5	102.4	7.10	3.5	0.12	2.55	~ 1	2.06e-06	0.053	1.11e-23
2	125.4	104.9	7.11	4.5	0.11	2.63	~ 1	1.25e-06	0.017	9.10e-24

Table 5.4: Calculations of different observables for the scalar DM candidate for the same set of benchmark points given in Table 5.3.

DM candidate χ is

$$\frac{\mathrm{d}^2\Phi}{\mathrm{dEd}\Omega} = \frac{\langle\sigma\mathrm{v}\rangle_f}{8\pi m_\chi^2} J \frac{dN_\gamma^f}{dE_\gamma} \ , \tag{5.37}$$

performed over a solid angle $d\Omega$ for certain region of interest (ROI). From Eq. 5.37, it can be observed that the differential γ-ray flux depends on the thermal averaged annihilation cross-section $\langle\sigma v\rangle_f$ of DM into final state particles (fermions) and $\frac{dN_\gamma^f}{dE_\gamma}$, is the photon energy spectrum produced due to per annihilation into fermions. In the above Eq. 5.37, the factor J, the astrophysical factor

depending on the DM density ρ, is expressed as

$$J = \int_{\rm los} \rho^2(r(r', \theta))dr \ , \tag{5.38}$$

is the line of sight (l.o.s) integral where $r' = \sqrt{r_\odot^2 + r^2 - 2r_\odot r\cos\theta}$ with r being the distance from the region of annihilation (GC) to Earth and $r_\odot = 8.5$ kpc. The angle between l.o.s and line from GC is denoted by θ. In this Chapter, we assume the DM distribution is spherically symmetric which follows Navarro-Frenk-White (NFW) [83] profile given as

$$\rho(r) = \rho_s \frac{(r/r_s)^{-\gamma}}{(1 + r/r_s)^{3-\gamma}} \ . \tag{5.39}$$

In the expression of NFW halo profile $r_s = 20$ kpc and ρ_s is a typical scale density such that it produce the local DM density $\rho_\odot = 0.4$ GeV cm^{-3} at a distance $r_\odot$. The differential γ-ray flux is calculated using the ROI used in the work by CCW [185] ($|l| \leq 20^0$ and $2^0 \leq |b| \leq 20^0$) for $\gamma = 1.2$. The photon spectrum $\frac{dN_\gamma^f}{dE_\gamma}$ from the annihilation of DM is obtained from Cirelli [244]. In order to calculate the differential γ-ray flux obtained for the fermionic DM using Eqs. 5.37 - 5.39 and the specified ROI by CCW, we consider two benchmark points from the available model parameter space but with different values of v_3 (using the condition $v_3 \leq 10.7$ MeV to avoid domain wall problem as mentioned earlier in Sect. 5.2). We have used different values of v_3 for benchmark points keeping the range of parameter space (given in Table 5.1) unchanged. Imposing other relevant conditions (relic density, direct detection etc.) we have observed that the nature of plots and physics discussed earlier in Sect. 5.6 do not alter and conclusions remain same. Therefore, the new set of benchmark points are in agreement with all the limits and constraints such as vacuum stability, LHC bounds, limits on decay width of light scalar, DM relic density etc. The benchmark points are then used to calculate γ-ray flux in this Chapter is tabulated in Table 5.3. It is to be noted that since the DM candidate is fermion, one may think that the annihilation cross-section will be velocity suppressed. However, in the present model, the fermion DM has a pseudo scalar type interaction

which removes the velocity dependence of DM annihilation cross-section [234]. In Fig. 5.5, we compare the GC γ-ray flux produced using benchmark points BP1 and BP2 tabulated in Table 5.3 with the results from CCW [185] for GC γ-ray excess. It is to be noted that the annihilation cross-section for the fermionic DM χ into $b\bar{b}$, i.e., $\langle\sigma v\rangle_{b\bar{b}}$ will be multiplied by f_χ^2 (since annihilation requires two DM candidates)[8]. Hence in order to produce the required flux for excess GC γ-ray, the contribution to the relic density by the fermionic candidate f_χ should be large. In Fig. 5.5, the γ-ray flux obtained from BP1 (BP2) is plotted in green (blue) along with the data obtained from CCW [185]. From Fig. 5.5, it can be observed that the fermionic DM component χ (WIMP) in our model can account for the observed GC γ-ray excess results obtained by analysis of Fermi-LAT data. Moreover, from the benchmark points it can also be seen that the SI direct detection cross-section for the fermionic DM candidate calculated using Eqs. 5.33, 5.34 is very small and remains below the limits from most stringent constraints on DM-nucleon cross-section given by LUX [108], XENON-1T [183] etc.

As we have mentioned earlier, we now investigate whether the light scalar DM h_3 can satisfy the condition for DM self interaction with the same set of benchmark points. The relevant results for the scalar DM candidate h_3 for BP1 and BP2 are tabulated in Table. 5.4. From Table. 5.4, it can be easily seen that for both the benchmark points, the effective self interaction cross-section of light DM candidate h_3 remains below the observed limit $\sigma/m \leq 0.47\ \text{cm}^2/\text{g}$ ($\sim \frac{1}{10}$ of the observed upper limit) obtained from the study by Harvey *et al.* [217]. However, as we have discussed earlier in Sect. 5.5, it is to be noted that the result for effective self interaction in this model is only an estimate and the effective self interaction may change significantly by the influence of other effects such as gravitational interaction, mass distribution etc. of DM. The self interaction for the light scalar DM candidate is calculated using Eq. 5.30 and it is then scaled by a factor $f_{h_3}^2$ to find out the effective self interaction.

It can also be seen from Table 5.4 that the FImP like scalar DM can also explain the 3.55 keV

[8]This can be understood as the modified line of sight integral $J_{\text{eff}} = f_\chi^2 J$ as well depending on DM density.

X-ray emission as observed by XMM Newton observatory if confirmed later as well. Calculation of DM-nucleon scattering cross-section for the scalar DM (using Eq. 5.36) also indicates that direct detection of the candidate is not possible at present having a small $\sigma_{SI}^{\prime h_3}$ compared to the upper limit obtained LUX and other DM direct search experiments. Hence, at present, both the DM candidates (χ and h_3) are beyond the reach of ongoing direct DM search experiments with SI scattering cross-section lying far below the existing limits obtained from these experiments. This justifies our previous comments on the scattering cross-section for the DM particles with detector nucleon discussed in Sect. 5.6.1.

5.8 Summary

In this Chapter, we have explored the viability of a two component DM model with a fermionic DM that evolve thermally behaving like a WIMP and a non-thermal feebly interacting light singlet scalar DM which is produced via freeze-in mechanism (FImP). The fermionic DM candidate χ interacts with the SM sector through a pseudo scalar particle Φ as the pseudo scalar acquires a non zero VEV and thus CP symmetry of the Lagrangian is broken spontaneously. Similarly the Z_2 symmetry of the singlet scalar is also broken spontaneously when S is given a tiny non-zero VEV resulting three physical scalars. However, the global $\mathrm{U}(1)_{\mathrm{DM}}$ symmetry of the fermionic DM remains intact to provides us stable dark WIMP like DM candidate. On the other hand, the light scalar h_3 having a very small interaction with SM sector also serves as a FImP DM candidate produced via freeze-in mechanism. The $\mathrm{SU}(2)_L \times \mathrm{U}(1)_Y$ symmetry of SM Higgs field is also broken spontaneously which provide mass to the SM particles. Hence, in the present model we have three scalars which mix with each other. We identify one of the physical scalar h_1 to be SM like, h_2 as non SM Higgs and h_3 is the light scalar DM. We constrain the model parameter space by vacuum stability, unitarity, bounds from LHC results on SM scalar etc. to solve for the coupled Boltzmann equation in the present framework such that sum of relic densities of these DM candidates satisfies the ob-

served DM relic density by PLANCK. We test for the viability of the fermionic DM candidate in order to explain the GC γ-ray results obtained from the analysis of Fermi-LAT data [237] by CCW [185]. We show that excess of GC γ-ray in the energy range 1-3 GeV can be obtained from the annihilation of fermionic DM that produce the required amount of annihilation cross-section $\langle\sigma v\rangle_{b\bar{b}}$ having mass $\sim$ 50 GeV. There is also a valid region for the fermionic DM candidate χ with mass ranging from 100-190 GeV. In addition, we investigate whether the light scalar DM candidate can account for DM self interaction. We found that the DM self interaction cross-section for light scalar DM h_3 considered in the model is about ten times smaller than observed upper limit obtained from galaxy cluster collisions results. Moreover, we also test for viability of this light DM candidate to explain the possible 3.55 keV X-ray signal obtained from the study of extragalactic X-ray emission reported by Bulbul *et al.* [37]. Our study reveals that a light DM $m_3 \sim 7.1$ keV in the present model can serve as a viable candidate that produce the required flux (in agreement with the condition for decay width $h_3 \to \gamma\gamma$) if confirmed by the observations of extragalactic X-ray search experiments and also consistent with the DM self interaction results. Both the DM candidates in the present "WIMP-FImP" framework are insensitive to direct detection experimental bounds and SI direct detection cross-section is far below the upper limit given by LUX, PandaX-II DM direct search results.

CHAPTER 6

TWO COMPONENT FEEBLY INTERACTING MASSIVE PARTICLE (FIMP) DARK MATTER

In this Chapter, we consider a two component dark matter (DM) model where both the components are Feebly Interacting Massive Particles or FIMPs. FIMPs are produced via "freeze-in" mechanism in the very early Universe described in Chapter 3. After establishing the viability of this two component DM model, the viable mass ranges are explored for this FIMP scenario. From their self interaction limits FIMP masses in this two component scenario is also addressed.

6.1 Introduction

In this Chapter, a well motivated alternative to the WIMP mechanism, namely the FIMP (Feebly Interacting Massive Particle) [229, 230, 245, 246] mechanism is explored where the DM candidate that has two components and both of which are FIMPs, the production of which in the early Uni-

verse are assumed to be through the FIMP mechanism. In reality, it is not yet confirmed whether DM is of one or multi components. But indications from various direct and indirect searches tend to suggest that DM could be of multiple in nature. In fact in the literature there are several studies of DM with more than one component [247–276]. The FIMP mechanism is already described in Chapter 3. In this Chapter, a two component DM model is proposed in FIMP scenario. In this model, two distinct singlet scalars are proposed for the two components of the dark matter. The viablity of such two component singlet scalars in FIMP scenario to be DM candidates is demonstrated in this Chapter in the mass regimes spanning from GeV to keV. Three pairs of masses are considered for the DM components in the mass regimes GeV, MeV and keV. The model has been developed by extending the scalar sector of Standard Model (SM) by two real scalar fields S_2 and S_3, both of which are singlets under the SM gauge group $\mathrm{SU}(2)_L \times \mathrm{U}(1)_Y$. Both the scalars (in this two component model) could have been produced from the pair annihilation of SM particles such as fermions, gauge bosons and Higgs bosons. The scalars are chosen in such a way that they acquire no vacuum expectation values (VEV) at spontaneous symmetry breaking (SSB). Additionally, a $Z_2 \times Z_2'$ symmetry [277–279] is imposed on the model Lagrangian such that the dark sector is $Z_2 \times Z'_2$ odd while SM is even. This prevents the interactions of the two scalar components with the SM fermions or their decays. Here the discrete symmetries Z_2 and Z'_2 are imposed on the scalars S_2 and S_3 respectively. Also fermion masses are not affected as the VEV is zero for both the scalars after SSB. Such a scalar interacts with the SM sector only through a Higgs portal due to the interaction term (in inteaction Lagrangian) of the type $H^\dagger H S_i S_i$ (where $i = 2, 3$). The unknown couplings of these additional scalars are the parameters of the theory. These can be constrained by using the theoretical bounds on the Lagrangian as also by computing the relic densities and then comparing them with the same given by PLANCK experiment. Here a discussion on the relic density calculations for this two component FIMP DM is in order. The relic densities are in general written in terms of the ratios $Y_{s_2} = \frac{n_{s_2}}{S}$ and $Y_{s_3} = \frac{n_{s_3}}{S}$, n_{s_2}, n_{s_3} being the comoving number densities of scalar DM components s_2, s_3 and S is the entropy density of the Universe. At the present

epoch these are computed by solving self consistently the relevant coupled Boltzmann equations for the two components. In FIMP scenario the number density of a species evolves towards its equilibrium value from almost negligible initial abundance. This means initially $Y_{s_2} \approx 0 \approx Y_{s_3}$. Evolutions of these abundances require computations of the quantities such as the decay processes $h \to s_j s_j$ $(j = 2, 3)$, where h denotes the SM Higgs, the pair annihilation processes $x\bar{x} \to s_j s_j$, where x can be $W^{\pm}, Z, f(\bar{f}), h, s_2, s_3$ etc. The total DM relic density for the considered two component singlet scalar model in FIMP scenario is finally obtained by adding the computed individual abundances of each of the components as $\Omega_{\rm tot}\tilde{h}^2 = \Omega_{s_2}\tilde{h}^2 + \Omega_{s_3}\tilde{h}^2$, where the relic density Ω for a particular species is expressed in terms of $\Omega\tilde{h}^2$, $\tilde{h}$ being the Hubble parameter normalised to 100 Km s^{-1} Mpc^{-1}. The computed value of $\Omega_{\rm tot}\tilde{h}^2$ should be consistent with PLANCK [12] observational results, $0.1172 \leq \Omega_{\rm DM}\tilde{h}^2 \leq 0.1226$. The self interaction of DM is another important issue which is addressed in relation to this two component FIMP DM. From the observational results of the collisions of galaxy clusters (such as Bullet Cluster phenomenon and from more recent observations of 72 colliding galaxy clusters [217]), an upper bound for the DM self interaction per unit DM mass is given in the literature. This upper limit is used to obtain the upper bounds of masses for the present DM candidate.

6.2 Two Component DM Model

In the present two component FIMP DM, a renormalizable extension of the SM is considered by adding two real scalar fields S_2 and S_3 which do not acquire any VEVs after SSB. Thus the three scalars in the model (one is SM Higgs (physical scalar) and S_2, S_3) do not mix. These two real scalars are singlets under the SM gauge group and are stabilised by imposing a discrete $Z_2 \times Z_2'$ symmetry. The two scalars S_2 and S_3 represent the two components of the present DM model and they interact with other SM particles only through Higgs portal. The Lagrangian of the model can

be written as

$$\mathcal{L} = \mathcal{L}_{\rm SM} + \mathcal{L}_{\rm DM} + \mathcal{L}_{\rm int} \ , \tag{6.1}$$

where $\mathcal{L}_{\rm SM}$ is the SM Lagrangian that includes quadratic and quartic terms involving the Higgs doublet H as also the usual kinetic term for H. The dark sector Lagrangian is given as

$$\mathcal{L}_{\rm DM} = \mathcal{L}_{S_2} + \mathcal{L}_{S_3} \ , \tag{6.2}$$

with

$$\mathcal{L}_{S_2} = \frac{1}{2}(\partial_\mu S_2)(\partial^\mu S_2) - \frac{\mu_{S_2}^2}{2} S_2^2 - \frac{\lambda_{S_2}}{4} S_2^4 \ , \tag{6.3}$$

and

$$\mathcal{L}_{S_3} = \frac{1}{2}(\partial_\mu S_3)(\partial^\mu S_3) - \frac{\mu_{S_3}^2}{2} S_3^2 - \frac{\lambda_{S_3}}{4} S_3^4 \ . \tag{6.4}$$

The interaction Lagrangian $\mathcal{L}_{\rm int}$ encompasses all possible mutual interaction terms between the scalar fields H, S_2, S_3.

$$\mathcal{L}_{\rm int} = -V'(H, S_2, S_3) \ , \tag{6.5}$$

where $V'(H, S_2, S_3)$ can be written as

$$V'(H,\, S_2,\, S_3) = \lambda_{HS_2} H^\dagger H\, S_2^2 + \lambda_{HS_3} H^\dagger H\, S_3^2 + \lambda_{S_2S_3} S_2^2\, S_3^2 \ . \tag{6.6}$$

The renormalizable scalar potential V is follows as

$$\begin{aligned} V &= \mu_H^2\, H^\dagger H + \lambda_H\, (H^\dagger H)^2 + \frac{\mu_{S_2}^2}{2} S_2^2 + \frac{\lambda_{S_2}}{4} S_2^4 + \frac{\mu_{S_3}^2}{2} S_3^2 + \frac{\lambda_{S_3}}{4} S_3^4 \\ &\quad + \lambda_{HS_2} H^\dagger H\, S_2^2 + \lambda_{HS_3} H^\dagger H\, S_3^2 + \lambda_{S_2S_3} S_2^2\, S_3^2 \,. \end{aligned} \tag{6.7}$$

After the SSB

$$H = \frac{1}{\sqrt{2}} \begin{pmatrix} 0 \\ v + h \end{pmatrix} \;,\; \langle S_2 \rangle = 0 \;,\; \langle S_3 \rangle = 0 \;, \tag{6.8}$$

where v ($v \sim 246$ GeV) is the VEV acquired by SM Higgs. Therefore, after SSB we have $H \to h + v$, $S_2 = s_2 + 0$, $S_3 = s_3 + 0$ and the scalar potential V takes the form

$$\begin{aligned} V &= \frac{\mu_H^2}{2}(v+h)^2 + \frac{\lambda_H}{4}(v+h)^4 + \frac{\mu_{S_2}^2}{2} s_2^2 + \\ &\quad \frac{\lambda_{S_2}}{4} s_2^4 + \frac{\mu_{S_3}^2}{2} s_3^2 + \frac{\lambda_{S_3}}{4} s_3^4 + \\ &\quad \frac{\lambda_{HS_2}}{2}(v+h)^2 s_2^2 + \frac{\lambda_{HS_3}}{2}(v+h)^2 s_3^2 + \lambda_{S_2S_3} s_2^2 s_3^2 \;. \end{aligned} \tag{6.9}$$

Now from the minimisation condition

$$\left(\frac{\partial V}{\partial h}\right), \left(\frac{\partial V}{\partial s_2}\right), \left(\frac{\partial V}{\partial s_3}\right)\Bigg|_{h=0,\, s_2=0,\, s_3=0} = 0 \;, \tag{6.10}$$

we obtain

$$\mu_H^2 + \lambda_H v^2 = 0 \;. \tag{6.11}$$

The mass matrix in the basis $h - s_2 - s_3$ can now be constructed by evaluating $\frac{\partial^2 V}{\partial h^2}$, $\frac{\partial^2 V}{\partial s_2^2}$, $\frac{\partial^2 V}{\partial s_3^2}$, $\frac{\partial^2 V}{\partial h \partial s_2}$, $\frac{\partial^2 V}{\partial h \partial s_3}$, $\frac{\partial^2 V}{\partial s_3 \partial s_2}$ at $h = s_2 = s_3 = 0$,

$$\mathcal{M}^2_{\text{scalar}} = \begin{pmatrix} 2\lambda_H v^2 & 0 & 0 \\ 0 & \mu^2_{S_2} + \lambda_{HS_2} v^2 & 0 \\ 0 & 0 & \mu^2_{S_3} + \lambda_{HS_3} v^2 \end{pmatrix}. \tag{6.12}$$

Note that the mass matrix is diagonal as there is no mixing between h, s_2 and s_3.

6.3 Constraints on the Model

• **Vacuum Stability**: In the limit of large field values, the scalar potential has to be bounded from below along all possible directions of the field space. In this limit, the quartic terms in the scalar potential dominate over the mass and the cubic terms. The quartic part (V_4) of the scalar potential V (Eq. 6.7) is given as

$$\begin{aligned} V_4 &= \lambda_H \left(H^\dagger H\right)^2 + \frac{\lambda_{S_2}}{4} S_2^4 + \frac{\lambda_{S_3}}{4} S_3^4 + \lambda_{HS_2} H^\dagger H \, S_2^2 \\ &\quad + \lambda_{HS_3} H^\dagger H \, S_3^2 + \lambda_{S_2 S_3} S_2^2 \, S_3^2 \, . \end{aligned} \tag{6.13}$$

The vacuum stability condition imposes bounds on the above couplings as [227]

$$\begin{aligned} \lambda_H, \ \lambda_{S_2}, \ \lambda_{S_3} &> 0 \\ \lambda_{HS_2} + \sqrt{\lambda_H \lambda_{S_2}} &> 0 \\ \lambda_{HS_3} + \sqrt{\lambda_H \lambda_{S_3}} &> 0 \\ 2\lambda_{S_2 S_3} + \sqrt{\lambda_{S_2} \lambda_{S_3}} &> 0 \end{aligned} \tag{6.14}$$

and

$$\sqrt{2(\lambda_{HS_2}+\sqrt{\lambda_H\lambda_{S_2}})(\lambda_{HS_3}+\sqrt{\lambda_H\lambda_{S_3}})(2\lambda_{S_2S_3}+\sqrt{\lambda_{S_2}\lambda_{S_3}})}$$
$$+\sqrt{\lambda_H\lambda_{S_2}\lambda_{S_3}}+\lambda_{HS_2}\sqrt{\lambda_{S_3}}+\lambda_{HS_3}\sqrt{\lambda_{S_2}}+2\lambda_{S_2S_3}\sqrt{\lambda_H}>0\ . \tag{6.15}$$

• **Perturbativity**: The perturbative limit imposes bounds on the quartic couplings of the scalar potential in the present model which read as [11, 217, 227, 277–280]

$$\lambda_H,\ \lambda_{HS_2},\ \lambda_{HS_3}\leq 4\pi,$$
$$\lambda_{S_2},\ \lambda_{S_3},\ \lambda_{S_2S_3}\leq\frac{2\pi}{3}. \tag{6.16}$$

• **Relic Density**: The total relic density i.e. the sum of the relic densities of the DM components must satisfy PLANCK observational results for DM relic densities.

$$0.1172\leq\Omega_{\rm DM}\tilde{h}^2\leq 0.1226\ , \tag{6.17}$$

where $\Omega_{\rm DM}$ is the relic density of DM normalized to the critical density of the Universe and $\tilde{h}$ is the Hubble parameter in units of 100 Km s^{-1} Mpc^{-1}.

• **Collider Physics Bounds**: For a collider, the signal strength of Higgs like boson is defined as

$$R\ =\ \frac{\sigma(pp\to h)}{\sigma^{\rm SM}(pp\to h)}\frac{{\rm Br}(h\to xx)}{{\rm Br}^{\rm SM}(h\to xx)}\ , \tag{6.18}$$

where $\sigma(pp\to h)$ and ${\rm Br}(h\to xx)$ denote the production cross-section and the decay branching ratio of Higgs like particle decaying into SM particles (x) respectively. The $\sigma^{\rm SM}(pp\to h)$ and ${\rm Br}^{\rm SM}(h\to xx)$ respectively are those for SM Higgs. In the above ${\rm Br}(h\to xx)=\dfrac{\Gamma(h\to xx)}{\Gamma}$ and ${\rm Br}^{\rm SM}(h\to xx)=\dfrac{\Gamma^{\rm SM}(h\to xx)}{\Gamma^{\rm SM}}$, where $\Gamma(h\to xx)$ and $\Gamma^{\rm SM}(h\to xx)$ are the decay width of Higgs like boson and SM Higgs boson respectively and the quantities Γ and $\Gamma^{\rm SM}$ represent the

total decay width of Higgs like particle and SM Higgs boson respectively. Using these expressions for branching ratio in Eq. 6.18 one obtains

$$R = \frac{\sigma(pp \to h)}{\sigma^{\rm SM}(pp \to h)} \frac{\Gamma(h \to xx)}{\Gamma} \frac{\Gamma^{\rm SM}}{\Gamma^{\rm SM}(h \to xx)} \ . \tag{6.19}$$

Here, $\sigma(pp \to h) \equiv \sigma^{\rm SM}(pp \to h)$ and $\Gamma(h \to xx) \equiv \Gamma^{\rm SM}(h \to xx)$ since there is no mixing between the scalars (h, s_2 and s_3). Thus Eq. 6.19 takes the form

$$R = \frac{\Gamma^{\rm SM}}{\Gamma} \ . \tag{6.20}$$

The total decay width of Higgs like boson can be written as $\Gamma = \Gamma^{\rm SM} + \Gamma^{\rm inv}$. The invisible decay width $\Gamma^{\rm inv}$ of Higgs like boson decaying to DM particles is given as

$$\Gamma^{\rm inv} = \Gamma_{h \to s_2 s_2} + \Gamma_{h \to s_3 s_3} \ . \tag{6.21}$$

The decay width $\Gamma_{h \to s_i s_i}$ $(i = 2, 3)$ can be expressed as

$$\Gamma_{h \to s_i s_i} = \frac{g^2_{h s_i s_i}}{8\pi m_h} \sqrt{1 - \frac{4m^2_{s_i}}{m^2_h}} \ . \tag{6.22}$$

In Eq. 6.22, $g_{h s_i s_i}$ represents the coupling for the process $h \longrightarrow s_i s_i$. The invisible branching ratio for such invisible decay is then given as

$$\mathrm{Br}^{\rm inv} = \frac{\Gamma^{\rm inv}(h \to s_i s_i)}{\Gamma_h}, i = 2, 3 \ . \tag{6.23}$$

This has been computed within the framework of this model. Note that, $\mathrm{Br}^{\rm inv}$ has to be very small which is expected in this case as the couplings are small. However, the model parameters are constrained imposing the condition, $\mathrm{Br}^{\rm inv} < 0.2$ [232]. It is also adopted that that the Higgs like boson signal strength must satisfies the limit $R \geq 0.8$ [231].

6.4 Relic Density Calculations

The relic densities of this two component FIMP DM model are to be obtained by solving self consistently the two coupled Boltzmann equations at the present epoch (temperature $T_0 \sim 10^{-13}$ GeV) for the two DM candidate scalar candidates S_2 and S_3. These equations are

$$\begin{aligned}\frac{dn_{s_2}}{dt}+3\tilde{H}n_{s_2} &= -\langle\Gamma_{h\to s_2s_2}\rangle(n_{s_2}-n_{s_2}^{\rm eq})-\langle\sigma v\rangle_{s_2s_2\to x\bar{x}}(n_{s_2}^2-(n_{s_2}^{\rm eq})^2)\\ &\quad -\langle\sigma v\rangle_{s_2s_2\to s_3s_3}\left(n_{s_2}^2-\frac{(n_{s_2}^{\rm eq})^2}{(n_{s_3}^{\rm eq})^2}n_{s_3}^2\right)\\ &\quad +\langle\sigma v\rangle_{s_3s_3\to s_2s_2}\left(n_{s_3}^2-\frac{(n_{s_3}^{\rm eq})^2}{(n_{s_2}^{\rm eq})^2}n_{s_2}^2\right)\ , \end{aligned} \tag{6.24}$$

$$\begin{aligned}\frac{dn_{s_3}}{dt}+3\tilde{H}n_{s_3} &= -\langle\Gamma_{h\to s_3s_3}\rangle(n_{s_3}-n_{s_3}^{\rm eq})-\langle\sigma v\rangle_{s_3s_3\to x\bar{x}}(n_{s_3}^2-(n_{s_3}^{\rm eq})^2)\\ &\quad +\langle\sigma v\rangle_{s_2s_2\to s_3s_3}\left(n_{s_2}^2-\frac{(n_{s_2}^{\rm eq})^2}{(n_{s_3}^{\rm eq})^2}n_{s_3}^2\right)\\ &\quad -\langle\sigma v\rangle_{s_3s_3\to s_2s_2}\left(n_{s_3}^2-\frac{(n_{s_3}^{\rm eq})^2}{(n_{s_2}^{\rm eq})^2}n_{s_2}^2\right)\ . \end{aligned} \tag{6.25}$$

In the above, n_{s_i} and $n_{s_i}^{\rm eq}$ $(i=2,3)$ are the number densities (that evolve with time t) and equilibrium number densities respectively for the scalars s_2 and s_3, $\langle\sigma v\rangle_{s_is_i\to ab}$ represents the average annihilation cross-sections for the two scalars $s_i, i=2,3$ with a, b, the annihilation products and $\tilde{H}$ is the Hubble parameter. This may be mentioned here that the above two Boltzmann equations should also include the annihilation cross-sections of the processes such as $s_2s_2s_2s_2 \to s_2s_2, s_2s_2s_3s_3 \to s_2s_3, s_2s_2s_2 \to s_2s_2, s_2s_2s_3 \to s_2s_3$. These are the terms for $4 \to 2$ or $3 \to 2$ interaction processes. However, these terms are not found to be significant. For our cases we consider FIMP DM masses in three ranges namely keV, MeV and GeV. For FIMP in GeV mass range, such contributions are ruled out since for a significant contribution, the coupling is to be large enough which may violate perturbative limit [281]. In case of keV range FIMP, it has been checked in this Chapter

(also by Ref. [282]) that $4 \to 2$ interaction is insignificant due to smalleness of corresponding self couplings. It may be argued that for MeV range FIMP, these processes could be significant but it has been confined in this Chapter that for the chosen mass and the values of the couplings (obtained from theoretical constraints) the contribution is negligibly small even for MeV mass range FIMPs. From Fig. 3 of Ref. [283], one sees that for the present scenario the contribution for MeV mass range falls in the semi-relativistic region of the plot. Therefore these terms are not considered in the Boltzmann equations above.

In terms of $Y_{s_i}(= \frac{n_{S_i}}{S}, i = 2, 3$, defined earlier) and $Z = \frac{m_h}{T}$, T being the photon temperature, the Boltzmann equations in Eqs. 6.24, 6.25 take the form,

$$\begin{aligned}
\frac{dY_{s_2}}{dz} &= -\frac{2zm_{\rm Pl}}{1.66m_h^2}\frac{\sqrt{g_*(T)}}{\sqrt{g_S(T)}}\left(\langle\Gamma_{h\to s_2s_2}\rangle\left(Y_{s_2}-Y_h^{\rm eq}\right)\right) \\
&\quad -\frac{4\pi^2}{45}\frac{m_{\rm Pl}m_h}{1.66}\frac{\sqrt{g_*(T)}}{z^2}\times \\
&\quad \left[\sum_{x=W,Z,f,h}\langle\sigma v_{x\bar{x}\to s_2s_2}\rangle(Y_{s_2}^2-(Y_x^{\rm eq})^2)+\langle\sigma v_{s_2s_2\to s_3s_3}\rangle\left(Y_{s_2}^2-\frac{(Y_{s_2}^{\rm eq})^2}{(Y_{s_3}^{\rm eq})^2}Y_{s_3}^2\right)\right. \\
&\quad \left.-\langle\sigma v_{s_3s_3\to s_2s_2}\rangle\left(Y_{s_3}^2-\frac{(Y_{s_3}^{\rm eq})^2}{(Y_{s_2}^{\rm eq})^2}Y_{s_2}^2\right)\right] \qquad (6.26)
\end{aligned}$$

and

$$\begin{aligned}
\frac{dY_{s_3}}{dz} &= -\frac{2zm_{\rm Pl}}{1.66m_h^2}\frac{\sqrt{g_*(T)}}{\sqrt{g_S(T)}}\left(\langle\Gamma_{h\to s_3s_3}\rangle\left(Y_{s_3}-Y_h^{\rm eq}\right)\right) \\
&\quad -\frac{4\pi^2}{45}\frac{m_{\rm Pl}m_h}{1.66}\frac{\sqrt{g_*(T)}}{z^2}\times \\
&\quad \left[\sum_{x=W,Z,f,h}\langle\sigma v_{x\bar{x}\to s_3s_3}\rangle(Y_{s_3}^2-(Y_x^{\rm eq})^2)-\langle\sigma v_{s_2s_2\to s_3s_3}\rangle\left(Y_{s_2}^2-\frac{(Y_{s_2}^{\rm eq})^2}{(Y_{s_3}^{\rm eq})^2}Y_{s_3}^2\right)\right. \\
&\quad \left.+\langle\sigma v_{s_3s_3\to s_2s_2}\rangle\left(Y_{s_3}^2-\frac{(Y_{s_3}^{\rm eq})^2}{(Y_{s_2}^{\rm eq})^2}Y_{s_2}^2\right)\right] . \qquad (6.27)
\end{aligned}$$

It is mentioned that the initial abundance of FIMP [229, 230] DM candidate is negligible. Therefore assuming $Y_{s_2} = Y_{s_3} = 0$, Eqs. 6.26, 6.27 is written as

$$\begin{aligned}\frac{dY_{s_2}}{dz} &= -\frac{2zm_{\rm Pl}}{1.66m_h^2}\frac{\sqrt{g_*(T)}}{\sqrt{g_S(T)}}\left(\langle\Gamma_{h\to s_2s_2}\rangle\left(-Y_h^{\rm eq}\right)\right) \\ &\quad -\frac{4\pi^2}{45}\frac{m_{\rm Pl}m_h}{1.66}\frac{\sqrt{g_*(T)}}{z^2}\times \\ &\quad \left(\sum_{x=W,Z,f,h}\langle\sigma v_{x\bar{x}\to s_2s_2}\rangle(-Y_x^{\rm eq})^2\right) \end{aligned} \tag{6.28}$$

and

$$\begin{aligned}\frac{dY_{s_3}}{dz} &= -\frac{2zm_{\rm Pl}}{1.66m_h^2}\frac{\sqrt{g_*(T)}}{\sqrt{g_S(T)}}\left(\langle\Gamma_{h\to s_3s_3}\rangle\left(-Y_h^{\rm eq}\right)\right) \\ &\quad -\frac{4\pi^2}{45}\frac{m_{\rm Pl}m_h}{1.66}\frac{\sqrt{g_*(T)}}{z^2}\times \\ &\quad \left(\sum_{x=W,Z,f,h}\langle\sigma v_{x\bar{x}\to s_3s_3}\rangle(-Y_x^{\rm eq})^2\right) . \end{aligned} \tag{6.29}$$

In the above, $m_{\rm Pl}$ is the PLANCK mass, $m_{\rm Pl}$ = 1.22 $\times 10^{22}$ GeV and the term g_* is defined as [46]

$$\sqrt{g_*(T)} = \frac{g_S(T)}{\sqrt{g_\rho T}}\left(1+\frac{1}{3}\frac{{\rm d}\ {\rm ln}g_s(T)}{{\rm d}\ {\rm ln}T}\right) , \tag{6.30}$$

The two effective degrees of freedom $g_s(T)$ and $g_\rho(T)$ are expressed in relation to the energy and entropy densities of the Universe through the following relations,

$$S = g_S(T)\frac{2\pi^2}{45}T^3\ ,\ \rho = g_\rho(T)\frac{\pi^2}{30}T^4\ . \tag{6.31}$$

Also, the thermally averaged Higgs decay widths along with other annihilation cross-sections for various processes belong to the production of present DM candidates s_2, s_3 are given by,

$$\begin{aligned} \langle \Gamma_{h\to s_i s_i} \rangle &= \Gamma_{h\to s_i s_i} \frac{K_1(z)}{K_2(z)} \ , \\ \langle \sigma \mathrm{v} \rangle_{x\bar{x}\to s_i s_i} &= \frac{1}{8 m_x^4 \, T \, K_2^2(m_x/T)} \int_{4m_x^2}^{\infty} \sigma_{x\bar{x}\to s_i s_i}(\mathrm{s} - 4m_x^2)\sqrt{\mathrm{s}} K_1(\frac{\sqrt{\mathrm{s}}}{T}) ds \ . \end{aligned} \tag{6.32}$$

In Eq. 6.32, $i = 2, 3, x = W^{\pm}, Z, f, h, s_2, s_3$. K_1 and K_2 are the modified Bessel functions of order 1 and 2, s defines is the centre of mass energy. The decay widths $\Gamma_{h\to s_i s_i}$ and annihilation cross-sections $\sigma_{x\bar{x}\to s_i s_i}$ $(i = 2, 3)$ for different processes required to solve the Boltzmann equations

(Eqs. 6.26 - 6.29) are furnished below

$$
\begin{aligned}
\Gamma_{h\to s_i s_i} &= \frac{g^2_{hs_is_i}}{8\pi m_h}\sqrt{1-\frac{4m^2_{s_i}}{m^2_h}}\ , \\
\sigma_{hh\to s_i s_i} &= \frac{1}{2\pi s}\sqrt{\frac{s-4m^2_{s_i}}{s-4m^2_h}}\left\{g^2_{hhs_is_i}+\frac{9\ g^2_{hhh}g^2_{hs_is_i}}{[(s-m^2_h)^2+(\Gamma_h m_h)^2]}\right. \\
&\quad \left.-\frac{6\ g_{hhs_is_i}g_{hs_is_i}g_{hhh}(s-m^2_h)}{[(s-m^2_h)^2+(\Gamma_h m_h)^2]}\right\}\ , \\
\sigma_{s_2s_2\to s_3s_3} &= \frac{1}{2\pi s}\sqrt{\frac{s-4m^2_{s_3}}{s-4m^2_{s_2}}}\left\{g^2_{s_2s_2s_3s_3}+\frac{g^2_{s_2s_2h}g^2_{hs_3s_3}}{[(s-m^2_h)^2+(\Gamma_h m_h)^2]}\right. \\
&\quad \left.-\frac{2\ g_{s_2s_2s_3s_3}g_{s_2s_2h}g_{hs_3s_3}(s-m^2_h)}{[(s-m^2_h)^2+(\Gamma_h m_h)^2]}\right\}\ , \\
\sigma_{s_3s_3\to s_2s_2} &= \frac{1}{2\pi s}\sqrt{\frac{s-4m^2_{s_2}}{s-4m^2_{s_3}}}\left\{g^2_{s_2s_2s_3s_3}+\frac{g^2_{s_3s_3h}g^2_{hs_2s_2}}{[(s-m^2_h)^2+(\Gamma_h m_h)^2]}\right. \\
&\quad \left.-\frac{2g_{s_3s_3s_2s_2}g_{s_3s_3h}g_{hs_2s_2}(s-m^2_h)}{[(s-m^2_h)^2+(\Gamma_h m_h)^2]}\right\}\ , \\
\sigma_{WW\to s_i s_i} &= \frac{g^2_{WWh}g^2_{hs_is_i}}{72\pi s}\sqrt{\frac{s-4m^2_{s_i}}{s-4m^2_W}}\frac{\left(3-\frac{s}{m^2_W}+\frac{s^2}{4m^2_W}\right)}{(s-m^2_h)^2+(\Gamma_h m_h)^2}\ , \\
\sigma_{ZZ\to s_i s_i} &= \frac{g^2_{ZZh}g^2_{hs_is_i}}{18\pi s}\sqrt{\frac{s-4m^2_{s_i}}{s-4m^2_Z}}\frac{\left(3-\frac{s}{m^2_Z}+\frac{s^2}{4m^2_Z}\right)}{(s-m^2_h)^2+(\Gamma_h m_h)^2}\ , \\
\sigma_{f\bar{f}\to s_i s_i} &= \frac{N_c g^2_{ffh}g^2_{hs_is_i}}{16\pi s}\frac{\sqrt{(s-4m^2_{s_i})(s-4m^2_f)}}{(s-m^2_h)^2+(\Gamma_h m_h)^2}\ .
\end{aligned}
\tag{6.33}
$$

In the above equations, g_{abc} and g_{abcd} are the coupling of the vertices, where a, b, c, d denote various fields. The masses m_W, m_Z and m_f are the masses of the bosons W and Z and the fermions respectively. The quantity N_c in Eq. 6.33 denotes the colour quantum number. Detailed expressions for the couplings appearing in Eq. 6.33 are enlisted in the Appendix B. The relevant Feynman diagrams related to the above equations are also given in Fig. 6.1. The relic densities of each of the DM components s_2 and s_3 are finally obtained in terms of their respective masses and comoving

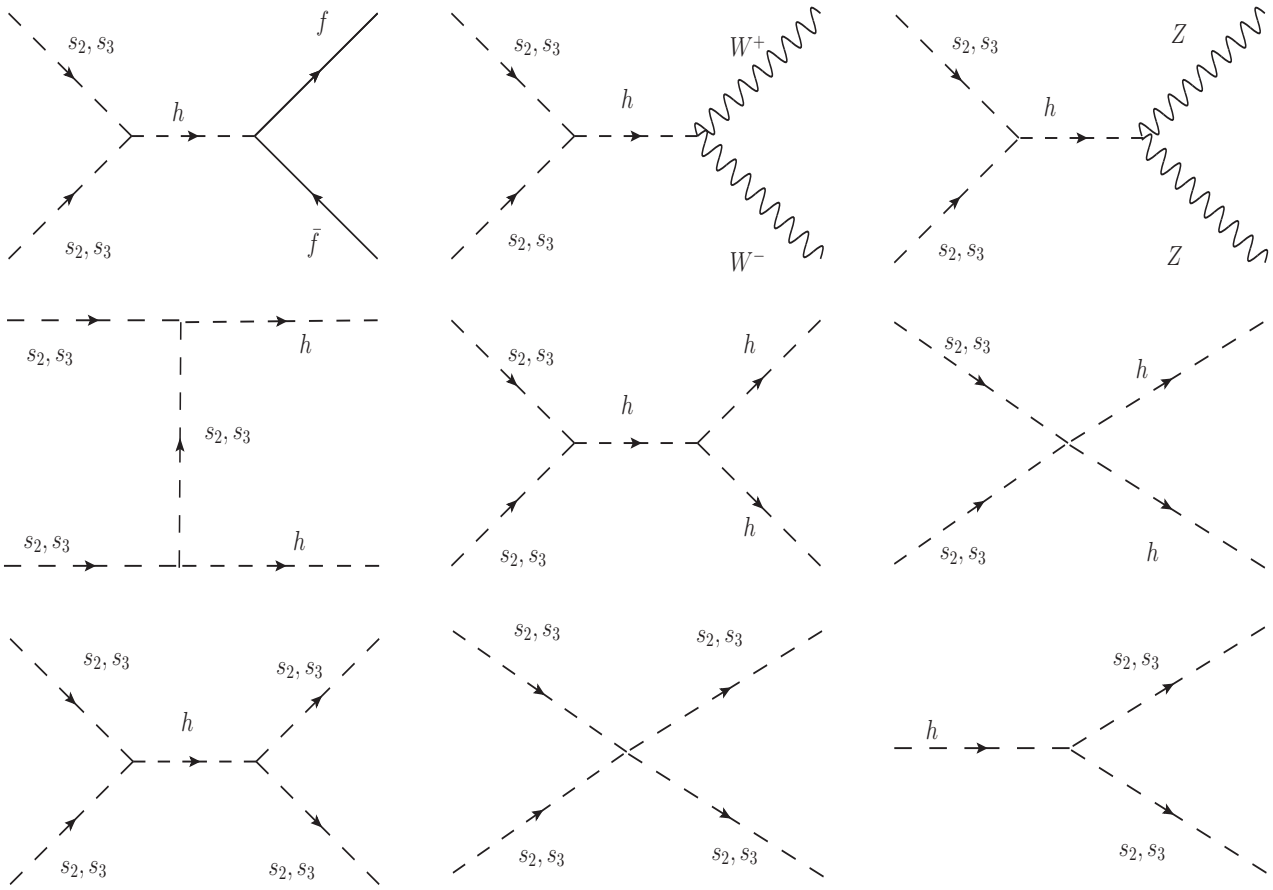

Figure 6.1: Feynman diagrams for both the scalar DM candidates s_2 and s_3.

number densities at the present epoch, as [284, 285]

$$\Omega_i \tilde{h}^2 = 2.755 \times 10^8 Y_i(T_0) \left(\frac{m_i}{\text{GeV}}\right) \ , \ i = s_2, s_3 \ . \tag{6.34}$$

Solving numerically the two coupled Boltzmann equations (Eqs. 6.26 - 6.29) alongwith Eq. 6.33 the comoving number densities $Y_i(T_0)$ are computed for both components of FIMP DM. The total relic density Ω_{tot} is then obtained by adding the relic densities of each of the components s_2 and s_3 as follows

$$\Omega_{\text{tot}} \tilde{h}^2 = \Omega_{s_2} \tilde{h}^2 + \Omega_{s_3} \tilde{h}^2 \ . \tag{6.35}$$

By computing the total relic density $\Omega_{\rm tot}\tilde{h}^2$ with the PLANCK measurement

$$0.1172 \leq \Omega_{\rm DM}\tilde{h}^2 \leq 0.1226 \ , \tag{6.36}$$

the unknown model parameters (unknown couplings etc.) are constrained. In Fig. 6.2 we furnish representative plots showing the evolutions of relic densities for each of the components of the present two component FIMP dark matter as well as the total relic densities for each of the chosen mass regimes namely GeV (Fig. 6.2(a)), MeV (Fig. 6.2(b)) and keV (Fig. 6.2(c)).

6.5 Calculations and Results

In order to demonstrate that over a wide range of masses (from GeV to keV) such a two component FIMP scalar DM is a viable DM candidate, in this analysis, the DM candidates in three mass regimes namely GeV, MeV and keV are chosen. The relic densities of the FIMP dark matter candidates in this proposed model. From our analysis it should be clear that the various unknown couplings ($\lambda_{HS_2}, \lambda_{HS_3}, \lambda_{S_2S_3}$ etc.) constitute the parameters of our model. We first constrain those parameters by using various theoretical bounds given in Eqs. 6.14 - 6.16 as also the collider bounds described in Eqs. 6.18 - 6.23. We have chosen a pair of values for two DM components in our two component scalar model in each of the three separate mass regimes GeV, MeV and keV. The relic densities of each components are first calculated using the Eqs. 6.24 - 6.34 by varying the parameter space within the constrained range. These are eventually added up (Eq. 6.35) to obtain the total relic density of the present two component DM model. The expressions for various couplings g_{x_1,x_2,x_3} and g_{x_1,x_2,x_3,x_4} (where x_i, $i = 1, 2, 3, 4$ represents different particles involving annihilation cross-sections or decay widths) required to compute the relic densities by solving the Boltzmann equations (Eqs. 6.26 - 6.29) in terms of the model parameters are given in the Appendix. The computed total relic density is then compared with the PLANCK observational measurements for the same (Eq. 6.36). Thus the model parameter space is further constrained by the observed

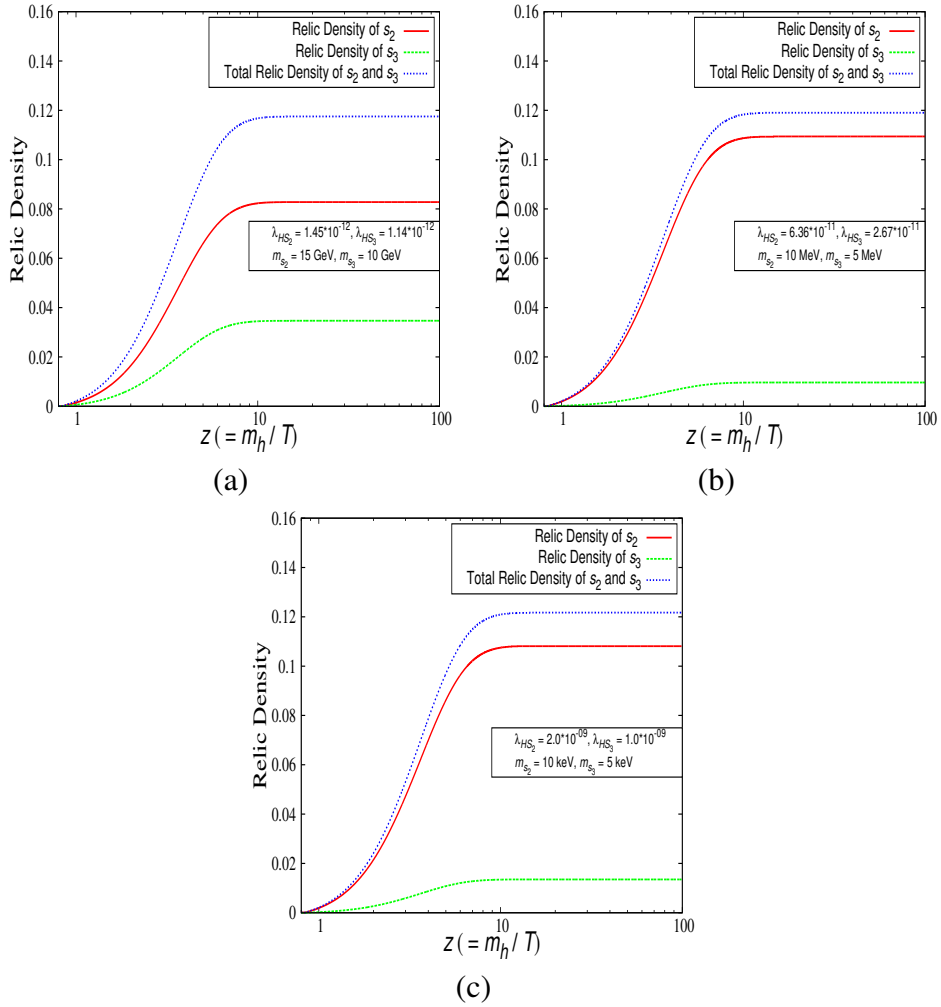

Figure 6.2: Variations of the relic densities of the two singlet scalar dark matter components s_2 and s_3 with z for different values of couplings $(\lambda_{HS_2}, \lambda_{HS_3})$ and masses (m_{s_2}, m_{s_3}) in the three mass regions (a) GeV, (b) MeV and (c) keV. In each of the three plots the red solid line and the green dashed line indicate the relic density of the components s_2 and s_3 respectively while the blue dotted line represents the total relic density. The PLANCK observational range for DM relic density is $0.1172 \leq \Omega_{\rm DM}\tilde{h}^2 \leq 0.1226$.

relic denisties for the DM. The elastic scatterings of DM (both the components) with nucleons are also computed using the constrained model parameters. It is observed that these elastic scattering cross-sections for the mass ranges considered here are well below the upper bounds given by recent direct DM search experiments such as LUX [108]. In the following we describe the analyses for the

two component FIMP DM in different mass regimes namely GeV, MeV and keV.

FIMP at GeV Mass Regime

In this regime, two scalar components with masses 15 GeV and 10 GeV are chosen for the two component FIMP DM model. The unknown model parameters are first constrained with the theoretical bounds and then further constrained using the collider bounds given in Section 6.3. These constrained parameter values (or the constrained range of parameter values) are then used to compute the relic densities of each of the components of the DM which are then added to obtain the total relic density. As mentioned earlier, the relic densities are obtained by numerically solving the coupled Boltzmann equations (Eqs. 6.28, 6.29) with Eqs. 6.33. The computed relic densities are then compared with the PLANCK relic density results and the range of allowed parameters are further constrained.

In Fig. 6.3 the variations of the total relic abundance $\Omega_{\rm tot}\tilde{h}^2$ (right panel) and the relic abundances $\Omega_{s_2,s_3}\tilde{h}^2$ for each of the components of the present DM model (left panel) with λ_{HS_3} are shown. Similar variations with coupling λ_{HS_2} are also shown in Fig. 6.4. The two parallel lines in both the figures indicate the PLANCK limit for $\Omega_{\rm DM}\tilde{h}^2$. It is observed from Figs. 6.3, 6.4 that with the increase of the parameters λ_{HS_3} and λ_{HS_2} the relic abundance increases. The parameters are then constrained by PLANCK results shown in Figs. 6.3, 6.4. In fact from Figs. 6.3, 6.4 one sees that for the chosen fixed FIMP component masses of 15 GeV and 10 GeV, the upper limits of the Higgs couplings with the scalar components λ_{HS_2} and λ_{HS_3} will be around 10^{-12}. For the WIMP DM, the relic density of DM would decrease with the increase of the Higgs couplings with the particle DM candidates. In contrast, for the case of FIMP DM the relic density increases with the Higgs couplings instead. This is one of the salient features of FIMP DM. This can also be seen from Figs. 6.3, 6.4 that the nature of variations of the relic abundances with $\lambda_{HS_i}(i = 2, 3)$ are parabolic which reflect the fact that $\Omega\tilde{h}^2 \sim \lambda^2_{HS_i}(i = 2, 3)$.

Further, in order to constrain the parameter space by the PLANCK observational results the two parameters λ_{HS_2} and λ_{HS_3} are simultaneously varied. The allowed region in the parameter space

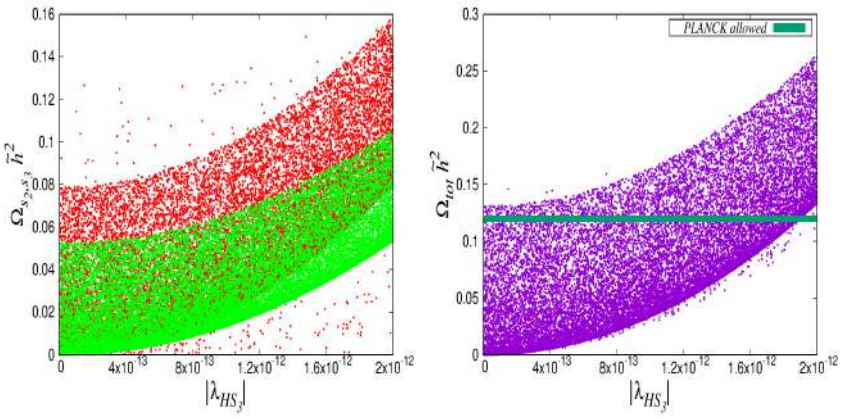

Figure 6.3: The variations of the relic abundances $\Omega_{s_2,s_3}\tilde{h}^2$ for each of the two DM components with the coupling λ_{HS_3}. The red and green regions represent the relic abundaces of s_2 and s_3 respectively. Right panel shows the variation of $\Omega_{\rm tot}\tilde{h}^2$ with λ_{HS_3}. The PLANCK limit is shown by the thick green line. See text for details.

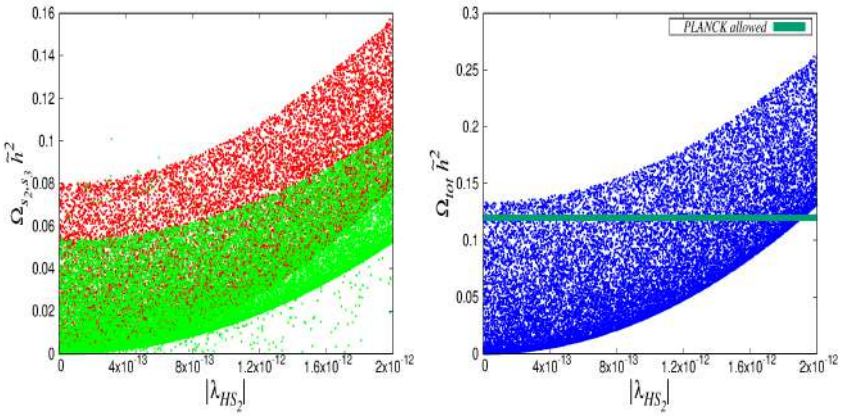

Figure 6.4: Same as Fig. 6.3 but for λ_{HS_2}. See text for details.

of $\lambda_{HS_2} - \lambda_{HS_3}$ that satisfy PLANCK relic density limits is shown in Fig. 6.5.

FIMP at MeV Mass Regime

In the MeV regime, the masses of the dark matter candidates are chosen to be 10 MeV and 5 MeV respectively. With these masses and using the formalism of two component FIMP DM model described in this Chapter the parameter space is constrained following the procedures similar to what is described in the case of GeV regime FIMP DM. In this mass regime too the parameter space is finally constrained by calculating the relic abundance and then comparing them with the

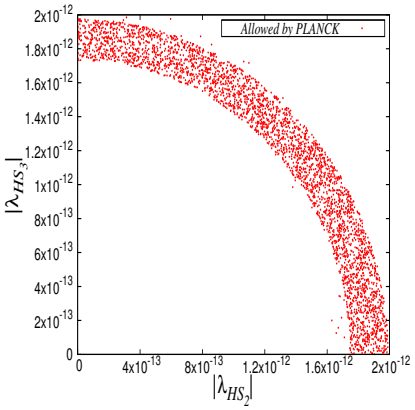

Figure 6.5: The region in $\lambda_{HS_2} - \lambda_{HS_3}$ parameter space constrained by the PLANCK results. See text for details.

PLANCK results. The results for the MeV mass regime are shown in Figs. 6.6, 6.7. Fig. 6.6 and Fig. 6.7 show the variations of relic abundances for each of the two components and the total abundance as well when the coupling parameters $\lambda_{HS_2}, \lambda_{HS_3}$ respectively are varied. Comparing the calculated relic abundances with the PLANCK results, upper limits for λ_{HS_3} and λ_{HS_2} are obtained. Both of them are found to be $\sim 8 \times 10^{-11}$. Fig. 6.8 shows the constrained region in $\lambda_{HS_2} - \lambda_{HS_3}$ parameter space for this case (MeV mass regime).

FIMP at keV Mass Regime

Tha analysis of the keV mass regime of the FIMP two component DM is performed with the masses of the two FIMP scalar components to be 10 keV and 5 keV and the analysis for restricting the parameter space, is also similar to what described for the cases of GeV and MeV regimes. The results are shown in Figs. 6.9, 6.10. Similar nature for variations of the relic abundances with the couplings (Figs. 6.9, 6.10) as also for the constrained parameter space (Fig. 6.11) are observed for keV case also. The upper limits for λ_{HS_3} and λ_{HS_2} are found to be around 2.2×10^{-9}.

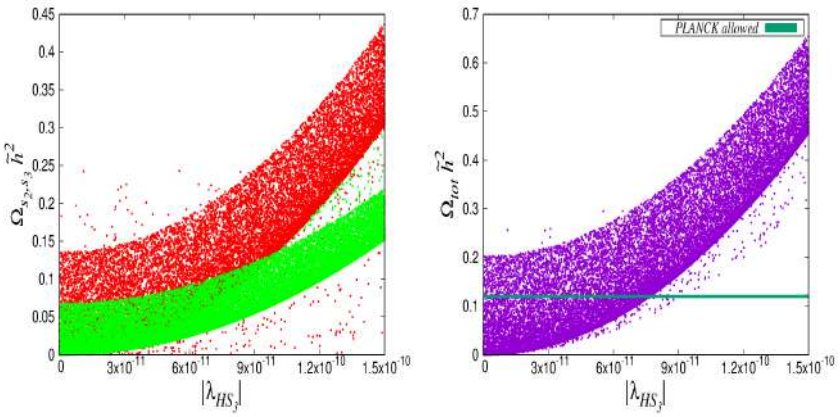

Figure 6.6: Same as Fig. 6.3 but for MeV mass regime. See text for details.

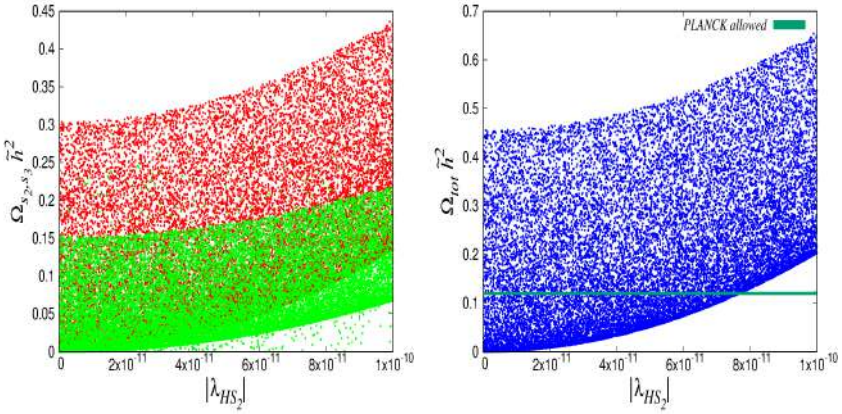

Figure 6.7: Same as Fig. 6.4 but for MeV mass regime. See text for details.

6.6 Self Interactions for Singlet Scalar Dark Matter

There are indications of DM self interactions [216–219, 286] from the observations of collisions of several galaxy clusters. The visible part of a galaxy is generally embedded inside a spherical halo of DM that extends far beyond the visible reaches of that galaxy. The DM halo makes up most of the galaxy masses. At the time of collisions between multiple galaxies, a larger galaxy among them pulls stars and other stellar material from a smaller galaxy and this process is called tidal stripping. Due to the presence of gravitational effect, one galaxy pulls in material from another and this can cause the DM to suffer a spatial offset from the stars in the galaxy. Recently the galaxy cluster

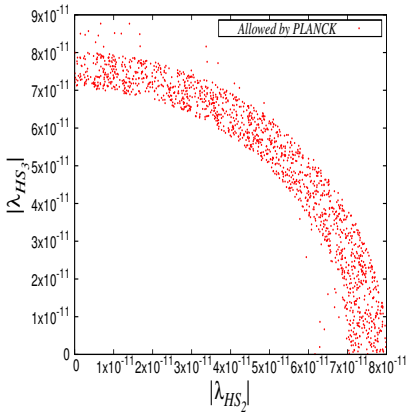

Figure 6.8: Same as Fig. 6.5 but for MeV mass regime. See text for details.

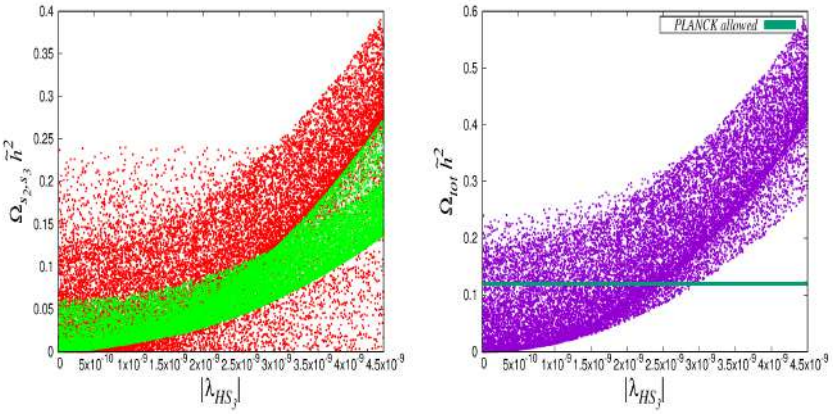

Figure 6.9: Same as Fig. 6.3 but for keV mass regime. See text for details.

Abell 3827 is observed by the Hubble Space Telescope [218]. The observations of the four elliptical galaxies falling into the inner 10 kpc core of galaxy cluster Abell 3827 indicate that the DM could be self interacting. The position of the DM halos of the four falling galaxies can be deciphered by using gravitational lensing and many other strongly lensed images of background objects. It is observed that one of the halos among these four galaxies is significantly separated from its stars by a distance of $\Delta = 1.62^{+0.47}_{-0.49}$ kpc. From the study of such spatial offsets observations in Abell 3827 cluster, an estimate of DM self interaction is deduced in terms of the ratio of DM self interaction cross-section $\sigma_{\rm DM}$ and DM mass m and this is given as $\sigma_{\rm DM}/m \sim 1.5\,{\rm cm}^2/{\rm gm}$. An involved observations on 72 colliding galaxy clusters [217] also set an upper limit on the DM self interaction cross-section to

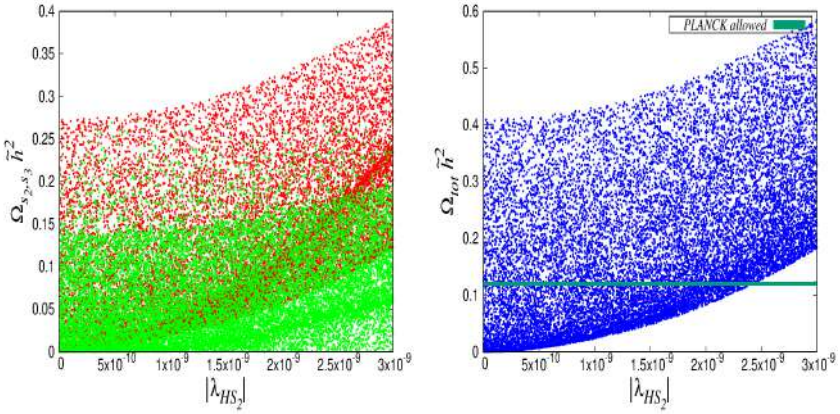

Figure 6.10: Same as Fig. 6.4 but for keV mass regime. See text for details.

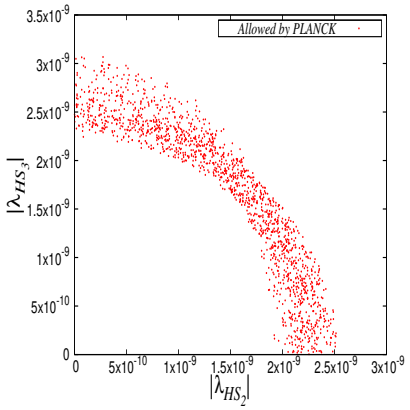

Figure 6.11: Same as Fig. 6.5 but for keV mass regime. See text for details.

DM mass ratio as $\sigma_{\rm DM}/m < 0.47\,{\rm cm}^2/{\rm gm}$ with 95% C.L. It appears from [219] that for the singlet scalar DM produced via thermal freeze-out mechanism cannot explain these deduced limits on DM self interaction cross-section. The DM candidates produced via freeze-in mechanism might explain these observed magnitude of DM self interactions. In the present model discussed in this Chapter, there are two scalar DM candidates (s_2 and s_3) constituting a two component scalar DM in FIMP scenario.

The self interaction scattering cross-section per unit DM mass (σ/m_s) for singlet scalar DM

scenario can be expressed as [219],

$$\frac{\sigma}{m_s} \simeq \frac{9\lambda^2}{2\pi m_s^3} \ , \tag{6.37}$$

where $\lambda = \lambda_S$ (λ_S being the 4-point DM self coupling), for mass of DM, m_s, to be much higher than mass of Higgs and $\lambda = \lambda_S - \frac{g^2}{8m_h^2}$ [219] when mass of DM is less than the mass of Higgs (m_h). Here, g denotes the Higgs-DM coupling. In this Chapter $g \leq 2\pi$ is adopted. In case of two scalar singlet model the above relation is modified and the effective scattering cross-section per unit effective DM mass can be expressed as,

$$\left.\frac{\sigma}{m}\right|_{\text{eff}} = f_{s_2}^2 \frac{9\lambda_{S_2}^2}{2\pi m_{s_2}^3} + f_{s_3}^2 \frac{9\lambda_{S_3}^2}{2\pi m_{s_3}^3} + f_{s_2} f_{s_3} \frac{9\lambda_{S_2S_3}^2}{2\pi \mu_s^3} \ , \tag{6.38}$$

where $\lambda_{S_2}, \lambda_{S_3}$ denote the 4-point self couplings among each of the scalars s_2, s_3 respectively while $\lambda_{S_2S_3}$ denotes the same between s_2 and s_3. In the above equation (Eq. 6.38), m_{s_2}, m_{s_3} and μ_S represent respectively the masses of s_2, s_3 and the reduced mass of s_2 and s_3. In Eq. 6.38, f_{s_2} and f_{s_3} are respectively the corresponding DM density fractions $f_i = \frac{\Omega_i}{\Omega_{\text{DM}}}$, $i = s_2, s_3$ [282, 287] for the components s_2 and s_3. Since $f_{s_2} + f_{s_3} = 1 (f_{s_2} = 1 - f_{s_3})$, Eq. 6.38 reduces to the form

$$\left.\frac{\sigma}{m}\right|_{\text{eff}} = f_{s_2}^2 \left(\frac{9\lambda_{S_2}^2}{2\pi m_{s_2}^3} + \frac{9\lambda_{S_3}^2}{2\pi m_{s_3}^3} - \frac{9\lambda_{S_2S_3}^2}{2\pi \mu_s^3} \right) + f_{s_2} \left(\frac{9\lambda_{S_2S_3}^2}{2\pi \mu_s^3} - 2\frac{9\lambda_{S_3}^2}{2\pi m_{s_3}^3} \right) + \frac{9\lambda_{S_3}^2}{2\pi m_{s_3}^3} \ . \tag{6.39}$$

Using the observational bounds on $\left.\frac{\sigma}{m}\right|_{\text{eff}}$, one may restrict the parameter space $f_{s_2} - m_{s_2} - m_{s_3}$ from Eq. 6.39. For this purpose, upper bounds $\left(\frac{2\pi}{3}\right)$ for the couplings $\lambda_{S_2}, \lambda_{S_3}$ and $\lambda_{S_2S_3}$ are adopted from perturbative unitarity conditions and vary the values of the couplings from 0 to $\frac{2\pi}{3}$. The masses m_{s_2} and m_{s_3} of the two scalars are also varied and $\frac{\sigma}{m}$ is computed using Eq. 6.39. Those values of m_{s_2} and m_{s_3} are so chosen that the upper limit of $\frac{\sigma}{m}$ is satisfied. Shown in Fig. 6.12 the limits of m_{s_2} and m_{s_3} for which the condition $\frac{\sigma}{m} = 0.47$ is satisfied for fixed different chosen values of f_{s_2} ($0 < f_{s_2} < 1$). Therefore, the region above each of the plots in $m_{s_2} - m_{s_3}$

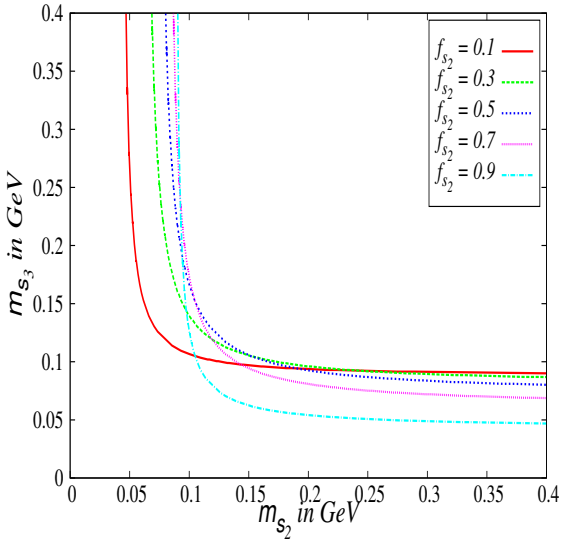

Figure 6.12: The limits for the masses of the scalar components m_{s_2} and m_{s_3} that satisfy the DM self interaction limit (from observations) for different chosen f_{s_2} component. See text for details.

plane (Fig. 6.12) satisfies the self interaction bound $\frac{\sigma}{m} < 0.47\ \mathrm{cm}^2/\mathrm{gm}$. From Eq. 6.38 it is evident that $\lambda_S^2 \sim m_s^3$ for a fixed value of $\frac{\sigma}{m}$. Therefore, the upper limit of λ_S should correspond to the upper limit of m_s (in this case m_{s_2} and m_{s_3}) for which a fixed considered value of $\frac{\sigma}{m}$ is satisfied. As an example, one can see from Fig. 6.12 that for the case of $f_{s_2} = 0.3$ when $m_{s_2} = 0.41$ the value of m_{s_3} cannot exceed a value of 0.18 in order to satisfy the upper limit of $\frac{\sigma}{m}$.

It should be worth mentioning here that such scalar DM can also be produced in the early Universe from the decay of the primordial scalar condensates. These condensates can be formed during the inflationary period and they may acquire nearly scale invariant fluctuations much the same way as a primordial Higgs condensates can be formed during the inflationary era [288–290]. These primordial scalar condensates can decay to produce non-thermal scalar DM [245]. Since these condensates were produced during the inflationary era, they contain the imprints of inflationary initial conditions. Thus the DM that is produced from the decay of primordial scalar condensates would be constrained by these initial conditions. For the case of Higgs portal models, where the SM is extended by scalar(s), such cosmological features can be addressed by the coupling of

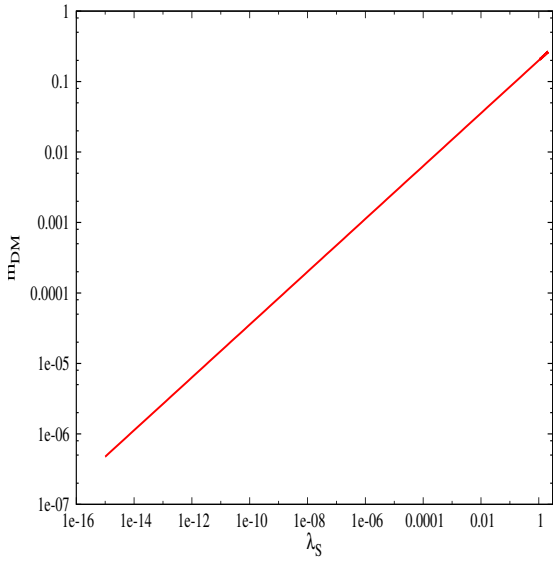

Figure 6.13: Variations of the DM self coupling (λ_S) with the scalar DM mass in the case when scalar DM is obtained from the decay of the primordial singlet condensate. See text for details.

these scalars with Higgs. In an elaborate work by K. Kainulainen *et al.* these issues are studied in detail [247]. They consider the primordial condensate to have originated from the inflationary fluctuations. These fluctuations therefore could transcend to the scalar DM from those condensates. Therefore, for any Higgs portal scalar DM from the primordial condensates is constrained by the isocurvature constraints as obtained from Cosmic Microwave Background Radiation (CMBR). Thus the treatment in the works of Ref. [247] explores the connection between freeze-in production of DM to the isocurvature constraints that leads to the very early era of the Universe. In this Ref. [247] the isocurvature constraints on the DM mass and singlet self coupling is expressed as $\left(\frac{m_{\rm DM}}{\rm GeV}\right) \leq 0.2\lambda_S^{3/8}\left(\frac{H_*}{10^{11}\rm GeV}\right)^{-3/2}$ for a small Higgs portal coupling λ_{HS} (λ_S being the scalar DM self coupling). Here H_* denotes the Hubble parameter value at the Horizon crossing. As mentioned earlier, in this Chapter the DM self coupling (λ_S) is so chosen that $\lambda_S \leq 2\pi/3$ [219]. Using $\lambda_S = 2\pi/3$ in the isocurvature constraint mentioned above, one obtains that the scalar DM mass should be ≤ 0.3 GeV in case these scalar DMs are produced from the decay of primordial scalar condensates. On that note, in Fig. 6.13 the variation of the DM self coupling (λ_S) with the

Table 6.1: Different ranges of the self ineteraction cross-section per unit mass (σ/m) of the scalar DM, produced from the decay of the primordial singlet condensate, for different values of f_{s_2} in both keV and MeV mass regime. See text for details.

$f_{s_2}\left(=\frac{\Omega_{s_2}}{\Omega_{\rm DM}}\right)$	σ/m for keV mass range in cm^2/gm	σ/m for MeV mass range in cm^2/gm
0.1	$1.06\times10^{-12}-1.40\times10^{-7}$	$1.89\times10^{-7}-0.06$
0.3	$7.89\times10^{-13}-1.04\times10^{-7}$	$1.41\times10^{-7}-0.05$
0.5	$6.99\times10^{-13}-9.19\times10^{-8}$	$1.24\times10^{-7}-0.04$
0.7	$7.89\times10^{-13}-1.04\times10^{-7}$	$1.41\times10^{-7}-0.05$
0.9	$1.06\times10^{-12}-1.40\times10^{-7}$	$1.89\times10^{-7}-0.06$

scalar DM mass ($m_{\rm DM}$) is shown while keeping in mind that both of the parameters satisfy the isocurvature constraint. The value of H_* is taken to be 10^{11} GeV in these calculations.

By using the isocurvature constraint connecting the DM mass and the self coupling of the scalar DM to the inflationary scale, the self interaction scattering cross-section per unit effective DM mass $\left(\frac{\sigma}{m}\Big|_{\rm eff}\right)$ for both keV and MeV mass range of the DM is now computed. Use has been made of Eq. 6.39 for this purpose where the values of m_{s_2}, m_{s_3} are chosen from Fig. 6.13 (and hence μ_s, the reduced mass). It is to be noted that $m_{\rm DM}\leq 0.3$ GeV in Fig. 6.13. The values of the couplings $\lambda_{S_2}, \lambda_{S_3}, \lambda_{S_2S_3}$ are then obtained using Fig. 6.13. Table 6.1 tabulates different ranges of the ratios of self interaction scattering cross-section and effective mass $\left(\frac{\sigma}{m}\Big|_{\rm eff}\right)$ corresponding to the different values of the DM density fractions (f_{s_2}) for both keV and MeV mass scales. Also from Table 6.1, it can be easily seen that for both the mass regimes, the scalar DM, produced from the decay of the primordial singlet condensate, can provide a self interaction cross-section, which satisfies the self interaction bound $\frac{\sigma}{m}<0.47$ cm^2/gm [217].

6.7 Summary

One important feature of FIMP DM is that they were never in thermal equilibrium because of their very feeble couplings with SM particles to the Universe's heat bath and they are produced

non-thermally and approach their "freeze-in" density. But they can assume significant role in cosmological or astrophysical contexts such as formation of small scale structures, signatures of the primordial initial conditions present in the Universe or even to address issues like “too-big-to-fail” problem etc. In this Chapter, the scalar sector of SM is extended by introducing two singlet scalars. These scalars are considered to have produced in the early Universe via “freeze-in” mechanism and constitute FIMP DM. Extensive phenomenology of such a model is performed to establish that the viabilities of this two component FIMP scalars for being possible DM candidates. Using the theoretical constraints on the interaction potential and the couplings and imposing the collider bounds as also by employing the PLANCK observed relic densities, this has been domonstrated that in the present FIMP scenario, the mass regime of such scalar FIMP DM candidates may have a range from GeV to keV. Also the self interaction for these DM candidates has also been addressed. The self interaction cross-section bound obtained from the results of 72 colliding galaxy clusters however restricts the viable mass range of this type of DM to upper limit values of around ~ 0.2 GeV. As the FIMP DM never attains thermal equilibrium due to their feeble couplings, the initial condition for such non-thermal production at early Universe is not washed away and can be probed via FIMP DM studies.

CHAPTER 7

ADDRESSING γ-EMISSIONS FROM DWARF GALAXIES AND EXTRAGALACTIC SOURCES WITH PARTICLE DARK MATTER THEORIES

In this Chapter, we consider 45 dwarf galaxies or the satellite galaxies of Milky Eay for which Fermi-LAT satellite borne telescope has made available the upper bound of γ-ray fluxes. Assuming these γ-rays of dwarf spheroidals (dSphs) are produced as an end product of dark matter (DM) annihilation inside the dwarf galaxies, this Chapter computes the γ-ray flux from each of the 45 dwarf galaxies for DM candidates in two types of particle DM models. It is then explored how well the γ-rays from DM annihilation for these two DM candidates agree when considered to interpret the Fermi-LAT data for extragalactic diffuse γ-ray flux.

7.1 Introduction

The indirect search for dark matter involves detection of the known Standard Model (SM) particles that can be produced by possible DM annihilation (or decay) in cosmos. It is mentioned in Chapter 3 that the DM can undergo self annihilation if it is accumulated in considerable magnitude by being captured, under the influence of gravity, inside massive astrophysical bodies. In Chapter 5, we have explored the possibility that DM annihilation in the Galactic Centre (GC) causes emissions of excess γ-rays from GC region (detected by Fermi-LAT satellite borne experiment). The dSphs are the satellite galaxies to the Milky Way and they fail to grow as matured galaxies. These dSphs are generally of low luminosities and contain population of older stars with little dust. The dwarf spheroidals could be very rich in DM. These galaxies would have been tidally disrupted but the presence of DM provides the necessary gravitational pull. The existence of DM in dSphs can also be realised by studying their mass-to-luminosity ratios. From several observations, the estimated mass-to-luminosity ratios (M/L) are found to be much more than the same for the sun $\left(\left|\frac{M}{L}\right|\right)$. The DM at dSphs can undergo self annihilation and produce γ-rays.

The Fermi-LAT satellite borne observations and Dark Energy Survey (DES) have reported the upper bounds of the γ-ray spectra for several dwarf galaxies [243, 291]. We consider two particle DM models (one is the simple extension of SM and the other is inspired by a beyond Standard Model (BSM) theory of particle physics) and for the DM candidates in each of these two models, we compute the expected γ-ray flux from all the 45 dSphs mentioned above by considering the DM annihilations at those dSphs. These computed results are then compared with the observational upper bounds for γ-ray flux for each of the 45 dSphs. The Fermi-LAT experiment also provides [292, 293] the observational results for extragalactic γ-ray flux. If the γ-rays (or a component of that) also originate from DM annihilation, then this too could be indirect signal of DM. The DM annihilation to γ-rays in extragalactic source is considered to add to the extragalactic γ-ray flux. To this end, we compute the extragalactic γ-ray flux from other possible sources such as Gamma Ray

Bursts (GRBs), BL Lac objects etc. and add to them the possible contribution to extragalactic γ-rays from DM annihilations (within the framework of the DM models considered in this Chapter). The sum total flux is then compared with Fermi-LAT results. This has also been shown in Chapter 5 that the WIMP component in the WIMP-FImP DM model (it is considered as Model I in this Chapter) would be a mass $\sim$ 50 GeV for this purpose. The DM candidate in the second model (Model II) adopted here is inspired by an established BSM theory namely theory of universal extra dimension [294]. This has been shown by [295, 296], that the DM mass in this model should be around 900 GeV in order that calculated relic density for such a DM in this model satisfies PLANCK relic density results. Being in a mass regime higher than that for the DM candidate in Model I, the γ-ray spectrum originated from this DM annihilation will have a wider energy range and thus raises the possibility of exploring the whole energy range given by the Fermi-LAT observed results for the upper bound of the γ-ray flux from all the 45 dwarf galaxies considered here. The same particle DM formalism is then adopted for the extragalactic γ-ray case.

As discussed in Chapter 5, the Model I is constructed by minimal extension of SM with a Dirac fermion χ, a real scalar S and a pseudo scalar Φ. While the fermion χ and the scalar S are singlets under SM gauge group, the fermion has an additional $\mathrm{U(1)_{DM}}$ charge. This prevents the fermion χ to interact with SM fermions ensuring its stability. A $\mathrm{Z_2}$ symmetry is imposed on the scalar S. The Lagrangian is CP invariant but the CP invariance is broken when the pseudo scalar Φ acquires a vacuum expectation value (VEV). On the other hand, the scalar develops a VEV when the $\mathrm{Z_2}$ symmetry is spontaneously broken. Thus after spontaneous breaking of the symmetries ($\mathrm{SU(2)}_L \times$ $\mathrm{U(1)}_Y$, $\mathrm{Z_2}$, CP), the scalars in the theory namely the Higgs H, S and Φ acquire VEV and their real components mix together. Three mass eigen states h_1, h_2 and h_3 are obtained (small mixing angles, $\theta_{12} \sim 10^{-2}$, $\theta_{13} \sim 10^{-13}$ and $\theta_{23} \sim 10^{-15}$) after diagonalisation of mass matrix while eigen state h_1 is identified with the physical Higgs with mass 125.5 GeV, h_2 is identified with the pseudo scalar considered in the model. In order to calculate the γ-rays from the annihilation of DM in each of the chosen 45 dwarf galaxies (as also the extragalactic γ-ray case), the WIMP component which is

the Dirac singlet fermion χ (in this WIMP-FImP [1] model) is useful. The WIMP candidate in this model interacts with SM sector through Higgs portal. The cross-section for the channel $\chi\chi \to b\bar{b}$ is calculated and computed in Chapter 5 for certain model benchmark points (BPs). The computations of annihilation cross-section of the process $\chi\chi \to b\bar{b}$ require the coupling and other factors (the expression for this cross-section is given in Appendix A). The process $\chi\chi \to b\bar{b}$ is mediated by the scalar h_1 and h_2 and one needs the coupling 'g' of the pseudo scalar (h_2) with the DM fermion χ as also the other couplings of χ with h_1. The fraction of WIMP component χ that contributes to generate required GC γ-ray excess in Chapter 5 is denoted by f_χ. The annihilation cross-section $\langle\sigma v\rangle_{\chi\chi\to b\bar{b}}$ will also be weighted by this fraction f_χ, the allowed ranges of which parameters are obtained by constraining the model interaction Lagrangian with theoretical (unitarity, perturbativity etc.) as well as experimental constraints (e.g. PLANCK relic density results) and collider constraints as given in Chapter 5. In this Chapter, we adopt one of the BPs considered in Chapter 5 and compute the γ-ray fluxes for all the 45 dSphs by similar consideration of annihilation of the WIMP component χ (of the two component model discussed above) to $b\bar{b}$ and compare them with the upper bounds of all those 45 dSphs given by Fermi-LAT experiment [243, 291]. This BP (set of values of the parameters) are shown in Table 7.1. The astrophysical J-factor values required to compute the fluxes are obtained from different observational groups for the dwarf galaxies.

The other particle DM candidate considered in this Chapter is from a BSM theory and this candidate is Kaluza-Klein (KK) DM (Model II) inspired by the theories of extra dimensions [294–297]. If only one spatial extra dimension is considered and this extra dimension is compactified over a circle of compactification radius R, say, then the effective four dimesional theory as obtained by integrating the extra spatial dimension over the periodic coordinate ($(y \to y + 2\pi R)$, compactification over a circle), gives rise to a tower of Kaluza-Klein modes with mass of each mode given by $m_{\rm k} = {\rm k}/R$, where k is called the Kaluza-Klein number or KK number. As KK number is associated with the quantized momentum in compactified dimension ($E^2 = \mathbf{p}^2 + m_{\rm k}^2$), the KK number is

[1] FIMP is denoted as FImP because of having very small mass

conserved and hence the Lightest Kaluza-Klein particle or LKP is stable and can be a candidate for DM.

In this Chapter, we consider a KK DM candidate in an extra dimensional model namely Universal Extra Dimensional model (UED) [294, 295, 298, 299]. In this model, each of the SM field can propagate in the extra dimension and every SM particle has a KK tower. But since the SM fermions are chiral, in order to obtain chiral KK counterpart of the SM fermions in UED model, the compactification of the extra dimension is to be made over a S^1/Z_2 orbifold (instead of compactifying just over a circle S^1 with compactification radius R), where a reflection symmetry Z_2 is imposed under which the extra coordinate $y \to -y$ and the fields are even or odd. Thus the chirality of a fermion can be identified in the extra dimension. The orbifold has now two boundary points at 0 and πR. But this breaks translational symmetry in the y direction and the KK momentum is no more conserved. Therefore the KK number (k) is also not conserved and the LKP is no more stable. But, for the transformation $y \to y + \pi R$, the KK modes remain invariant for even KK number but odd KK modes change sign. Thus we have a quantity called $(-1)^{\mathrm{KK}}$ - the KK parity - which is a good symmetry for this transformation and hence conserved. The conservation of KK parity ensures LKP in UED model is stable. In this Chapter, the LKP DM candidate in UED model is the first KK partner B^1 of the hypercharge gauge boson.

A range of masses for the chosen KK DM candidate B^1 are chosen and it is demonstrated how well the γ-rays produced from the annihilation of such a DM candidate agrees with the observational results for all the dwarf galaxies considered. The range of masses for these KK particles are so chosen that the PLANCK limits for the DM relic densities are satisfied. For continuum γ signal from B^1B^1 annihilation one needs to consider the channel $B^1B^1 \longrightarrow qq$ (q denotes the quarks). The annihilation cross-sections ($\langle\sigma_{qq}v\rangle$) for this channel are calculated following [294]. It is to be noted that the interaction coupling for the process $B^1B^1 \to qq$ is computable for a given mass of the DM candidate B^1 [294]. The only parameter here is the mass of q^1 which is the first KK partner of quark q in the UED model. The parameter is rewritten as $r = \dfrac{m_{q^1} - m_{B^1}}{m_{B^1}}$, where m_{q^1}, m_{B^1} are

Table 7.1: The model parameter considered for the calculation on γ-ray fluxes in Model I. v_1 is the vev of SM Higgs.

M_χ GeV	v_1 GeV	g	R_1	Br^1_{inv}	f_χ	$f_\chi^2\langle\sigma v\rangle_{b\bar{b}}$ $10^{-26}\mathrm{cm}^3\mathrm{s}^{-1}$
50	246	0.11	0.99	0.021	0.89	1.62

Table 7.2: The masses of the DM in both the models adopted in this Chapter.

Model	M_χ in GeV
Model I ([314])	50
Model II ([294, 295])	900

the masses of q^1 and B^1 respectively. In this Chapter, we have varied parameter r in such a way that m_{B^1} is in the allowed mass range (discussed earlier) and $m_{q^1} > m_{B^1}$ is maintained. We do not find any significant changes in the result.

We then extend our analyses for extragalactic γ-rays also. The observed extragalactic γ-ray signal may contain the component of γ-ray from DM annihilations at extragalactic sources [300–305]. The extragalactic γ-rays can have many components other than those possibly from DM annihilations. There are attempts to extract DM annihilation signals from the extragalactic γ-ray background or EGB [306–313]. The possible contribution to the EGB may come from BL Lac objects, millisecond pulsars, radio galaxies etc. More detailed knowledge and their possible contribution to the EGB not only helps to look for any such DM annihilation signals beyond the EGB but also is useful to put stringent bound on DM annihilation cross-sections. With both the particle DM models considered here, we have made an attempt to estimate whether any significant signal from the DM annihilation can be obtained from extragalactic sources. For the extragalactic also, the same BPs given in Table 7.1 and Table 7.2 are used.

7.2 Formalism for γ-ray Flux Calculations in Case of Dwarf Galaxies from DM Annihilation

The observed flux from cosmic DM source depends significantly on the DM annihilation cross-section $\langle\sigma v\rangle$ [291] as well as the total DM contained within the solid angle subtended by the source at the observer (the astrophysical $\mathcal{J}$-factor). The $\mathcal{J}$-factor can be calculated as

$$\mathcal{J} = \int_{l.o.s} \rho(r)^2 ds = r_\odot \rho_\odot^2 J. \tag{7.1}$$

In the above, $\rho_\odot$ ($0.3\ \mathrm{GeV/cm^3}$) is the DM density at the distance $r_\odot$ ($8.33\ \mathrm{kpc}$) from the GC (at the solar system). In the above equation, J represents the dimensionless form of $\mathcal{J}$-factor given by,

$$J = \int_{l.o.s} \frac{1}{r_\odot} \left(\frac{\rho(r)}{\rho_\odot}\right)^2 ds, \tag{7.2}$$

where $\rho(r)$ is the DM density at radial distance r from the GC and $\rho(r)$ is a DM halo can be parametrized as $\rho(r) = \rho_s g(r/r_s)$, where ρ_s is a scale density and $g(r/r_s)$ gives the nature of density function with r and r_s is a characteristic scale distance. In this case, $r_s = 20$ kpc for dwarf galaxy calculations. The radial distance r can be expressed in terms of the line of sight (l.o.s) s as,

$$r = \begin{array}{ll} \sqrt{s^2 + r_\odot^2 - 2sr_\odot \cos l \cos b} & l,\ b \text{ coordinate}, \\ \sqrt{s^2 + r_\odot^2 - 2sr_\odot \cos\theta} & r,\ \theta \text{ coordinate}. \end{array} \tag{7.3}$$

We adopt three density profiles namely NFW [82, 83], Einasto [90, 91] and Burkert [88] for computation of $\rho(r)$ and those three profiles are tabulated in the following table (this has also been discussed in details in Section 3.4 of Chapter 3).

Table 7.3: Dark matter halo profiles

NFW [82, 83]	$\rho_{\rm NFW}$	$=$	$\rho_s \frac{r_s}{r}\left(1+\frac{r}{r_s}\right)^{-2}$
Einasto [90, 91]	$\rho_{\rm Ein}$	$=$	$\rho_s \exp\left[-\frac{2}{\alpha}\left\{\left(\frac{r}{r_s}\right)^{\alpha}-1\right\}\right]$
Burkert [88]	$\rho_{\rm Bur}$	$=$	$\frac{\rho_s}{(1+r/r_s)\left(1+(r/r_s)^2\right)}$

The differential γ-ray flux due to DM annihilation of mass M_χ is given by

$$\frac{d\phi}{d\Omega dE_\gamma} = \frac{1}{8\pi\alpha}\sum_f \frac{\langle\sigma v\rangle_f}{M_\chi^2}\frac{dN_\gamma^f}{dE_\gamma}\mathcal{J}, \tag{7.4}$$

where $\alpha = 1$ and f indicates the final state particle.

For Model I (WIMP component of WIMP-FImP model) the expression of the cross-section for the process $\chi\chi \longrightarrow b\bar{b}$ is given in the Appendix A. The annihilation cross-section is computed to be $\langle\sigma v\rangle = 1.62\times10^{-26}\text{cm}^3\text{sec}^{-1}$. The couplings required to compute $\langle\sigma v\rangle$ are the particle DM model parameters and are discussed in Chapter 5. In Table 7.1 we furnish a set of benchmark values taken from the allowed region of these parameters discussed in Chapter 5. The set of values of the couplings is used in the present calculation. The parameters in Table 7.1 are within the allowed range of model parameter space and they also respect all the necessary constraints and bounds. Same set of coupling parameter value and the same formalism are adopted for extragalactic case also.

The other is a KK DM (B^1) in an extra dimensional model (Model II) having a mass of about 900 GeV (Table 7.2) which self annihilates to the primary product qq and yields γ-rays as the end product. For the case of B^1 DM, the annihilation cross-section $B^1B^1 \longrightarrow qq$ is computed from the expression [294]

$$\langle\sigma_{qq}v\rangle = \frac{q^4}{9\pi\cos^4\theta_W}\left[\frac{Y_{q_L^1}^4}{m_{B^1}^2+m_{q_L^1}^2}+L\rightarrow R\right], \tag{7.5}$$

where q_L^1 is the first KK partner of the quark q_L, $Y_{q_L^1}$ and $m_{q_L^1}$ are respectively the corresponding hypercharge and mass while θ_W is the Weinberg angle. The mass $m_{q_L^1}$ is fixed by defining a pa-

rameter $r = \frac{m_{q^1} - m_{B^1}}{m_{B^1}}$ ([294]) and then adopting a suitable value for r. It is also to be noted that the LKP DM candidate B^1 in this case is the first KK partner of the hypercharge gauge boson. It is seen that the mass of this DM candidate should be $\sim$ 900 GeV for its relic density to satisfy the PLANCK result [315]. In the limit in which electroweak symmetry breaking (EWSB) is neglected, there will be no channels with vector gauge bosons as primary products and only 2% of the annihilation goes into Higgs [295]. Moreover [294] shows that the channel $B^1B^1 \rightarrow e^+e^-$ yields narrow peaks for positrons and for the computation of continuum photon signal the relevant annihilation cross-section is $\langle\sigma_{qq}v\rangle$. The choice of DM masses in both the models are shown in Table 7.2. Same formalism of DM annihilation with same DM mass is adopted for the extragalactic γ-ray flux calculations.

The γ fluxes are calculated (for the chosen DM candidates) by computing the $\mathcal{J}$ factor with each of the three density profiles of Table 7.3. The fluxes are also computed with the $\mathcal{J}$ factors estimated and published by other groups [316, 317]. These density profile are plotted in Fig. 7.1.

7.3 The γ-ray Flux Calculations for the Dwarf Galaxies and their Comparison with the Observations

DM rich dSphs have turned out to be important cosmological sites to probe and understand the nature of DM and its astrophysical implications. The satellite observations by Fermi-LAT [318] as well as later DES and Fermi-LAT collaboration reveal a sum of 45 dSphs in the energy range $0.5 \sim 500$ GeV [291]. The details of these dSphs are furnished in Table 7.4. In Table 7.4 the $\mathcal{J}$ factors and their uncertainties are also given for those 45 dSphs. These Fermi-LAT observed upper bounds are obtained from [243, 291]. The upper bounds of γ-ray fluxes from those 45 dSphs are given in Figs. 7.2, 7.3.

In this Chapter, we have estimated γ-flux for all of those 45 dSphs tabulated in Table 7.4 assuming that the DM in those dSphs annihilate to produce γ. The computations for γ flux for each

of the two DM candidates have been performed following Eqs. 7.1 - 7.5. The DM candidates and models as also the chosen DM masses are already discussed and in Table 7.2 the benchmark mass points are given. Note that the cross-section given in Eq. 7.5 is for KK DM only (Model II).

Figs. 7.2 and 7.3 show upper bounds of γ-ray fluxes given by the Fermi-LAT observation as well as the computed γ-ray fluxes for the two particle DM candidates. In Figs. 7.2 and 7.3 the upper bounds of the γ-ray fluxes for all the 45 dSphs (as given by Fermi-LAT collaboration) are shown with green arrows pointing downwards. The numerical values of $\mathcal{J}$-factor for all dSphs (obtained from observational data) are tabulated in Table 7.4.

The computations of fluxes for the DM candidates in both the models are made as follows. Integrated $\mathcal{J}$-factor over a solid angle of $\Delta\Omega = 2.4 \times 10^{-4}$ sr (field of view of Fermi-LAT $\sim 0.5^o$) are measured from stellar kinematics data. The flux estimations for the case of both the Models I and II are first made using the $\mathcal{J}$-factors given in Table 7.4. The spread of each of these calculated fluxes due to the uncertainties of the $\mathcal{J}$-factors (given in Table 7.4) are also calculated in case of each of the two DM models considered. The fluxes and their spreads thus estimated with both the DM candidates for all the 45 dSphs are shown in Figs. 7.2 and 7.3. The γ-ray flux for DM in Model I (WIMP component χ with mass $\sim$50 GeV of two component WIMP-FImP model) are shown by a black line (for the central values of $\mathcal{J}$-factors in Table 7.4) and the estimated spread of these computed fluxes due to uncertainties in corresponding $\mathcal{J}$-factor values are shown by yellow bands in each of the 45 plots (for 45 dwarf galaxies) spreaded over Figs. 7.2 and 7.3. Similar estimations of the γ-ray flux and their uncertainties for the DM candidate B^1 (KK DM from extra dimensional model with mass $\sim$900 GeV; Model II) are shown with pink central lines with uncertainty spreads shown in pink in each of the 45 plots (of Figs. 7.2 and 7.3).

The fluxes are also estimated for both the DM candidates (Model I and Model II) following Eqs. 7.1-7.5 by explicitly computing the $\mathcal{J}$-factors with each of the three DM density profiles given in Table 7.3. These are NFW, Einasto and Burkert DM density profiles. They are shown in Figs. 7.2 and 7.3 in red, black and blue dashed lines respectively for the WIMP DM in Model I and in red,

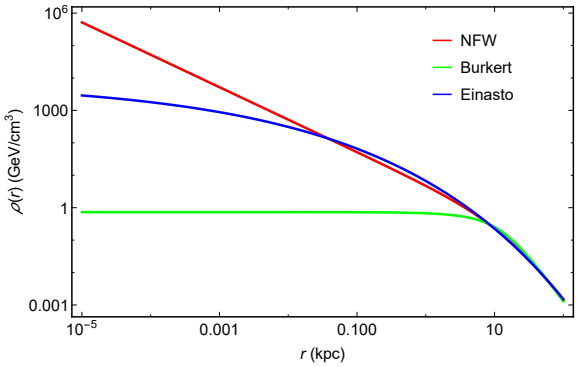

Figure 7.1: Galactic DM halo density profiles.

black and blue dotted lines for the KK DM of Model II. It can be seen that for most of the cases, the results using NFW profiles almost coincide with those using Einasto profile while distinction can be made for the flux results with Burkert profile. This may be understood from the natures of the profiles (Fig. 7.1). While both NFW and Einasto profiles are cuspy in nature, the Burkert profile is flat and isothermal in nature. Also Burkert profile has been used earlier to analyse the dwarf galaxy rotation curves ([88, 319]).

It appears from Figs. 7.2 and 7.3 that for Model I (the WIMP component of a WIMP-FImP model) with all the three density profiles, the fluxes are below the observational upper limits of all the 45 dSphs. Similar results for the KK DM in Model II (the Kaluza-Klein model) are shown in Figs. 7.2 and 7.3 with colour codes mentioned above. It can be seen that KK DM also respects the observational upper bounds of all the dSphs γ-ray fluxes considered here. Moreover, it can also be seen form Figs. 7.2 and 7.3 that wider range (in comparison to what obtained in case of Model I) of γ-ray flux can be achieved when KK DM (Model II) is considered.

Table 7.4: Latitude, longitude, distance and $\mathcal{J}$-factor for individual dSphs [316, 317].

dSphs name	Longitude l (deg)	Latitude b (deg)	Distance (kpc)	$\log_{10}\mathcal{J}$ ($\log_{10}\left[\mathrm{GeV}^2\mathrm{cm}^{-5}\mathrm{sr}\right]$)
Bootes I	358.1	69.6	66	18.17 ± 0.30
Bootes II	353.7	68.9	42	18.90 ± 0.60
Bootes III	35.4	75.4	47	18.80 ± 0.60
Canes Venatici I	74.3	79.8	218	17.42 ± 0.16
Canes Venatici II	113.6	82.7	160	17.82 ± 0.47
Carina	260.1	-22.2	105	17.83 ± 0.10
Cetus II	156.47	-78.53	30	19.10 ± 0.60
Columba I	231.62	-28.88	182	17.60 ± 0.60
Coma Berenices	241.9	83.6	44	19.00 ± 0.36
Draco	86.4	34.7	76	18.83 ± 0.12
Draco II	98.29	42.88	24	19.30 ± 0.60
Eridanus II	249.78	-51.65	330	17.28 ± 0.34
Eridanus III	274.95	-59.6	95	18.30 ± 0.40
Fornax	237.1	-65.7	147	18.09 ± 0.10
Grus I	338.68	-58.25	120	17.90 ± 0.60
Grus II	351.14	-51.94	53	18.70 ± 0.60
Hercules	28.7	36.9	132	17.37 ± 0.53
Horologium I	271.38	-54.74	87	18.40 ± 0.40
Horologium II	262.48	-54.14	78	18.30 ± 0.60
Hydra II	295.62	30.46	134	17.80 ± 0.60
Indus II	354	-37.4	214	17.40 ± 0.60
Kim 2	347.2	-42.1	69	18.60 ± 0.40
Leo I	226	49.1	254	17.64 ± 0.14
Leo II	220.2	67.2	233	17.76 ± 0.2
Leo IV	265.4	56.5	154	16.40 ± 1.15
Leo V	261.86	58.54	178	17.65 ± 0.97
Pegasus III	69.85	-41.81	205	18.30 ± 0.94
Phoenix II	323.69	-59.74	95	18.30 ± 0.40
Pictor I	257.29	-40.64	126	18.10 ± 0.40
Pisces II	79.21	-47.11	182	17.60 ± 0.40
Reticulum II	266.3	-49.74	32	18.68 ± 0.35
Reticulum III	273.88	-45.65	92	18.20 ± 0.60
Sagittarius II	18.94	-22.9	67	18.40 ± 0.60
Sculptor	287.5	-83.2	86	18.58 ± 0.05
Segue 1	220.5	50.4	23	19.12 ± 0.54
Sextans	243.5	42.3	86	17.73 ± 0.13
Triangulum II	140.9	-23.82	30	19.10 ± 0.60
Tucana II	328.04	-52.35	58	18.80 ± 0.40
Tucana III	315.38	-56.18	25	19.30 ± 0.60
Tucana IV	313.29	-55.29	48	18.70 ± 0.60
Tucana V	316.31	-51.89	55	18.60 ± 0.60
Ursa Major I	159.4	54.4	97	18.26 ± 0.28
Ursa Major II	152.5	37.4	32	19.44 ± 0.40
Ursa Minor	105	44.8	76	18.75 ± 0.12
Willman 1	158.6	56.8	38	18.90 ± 0.60

7.4 Extragalactic γ-ray Background and Extragalactic γ-rays from DM Annihilations

In this Section, the diffused extragalactic γ-ray flux from DM annihilation is computed and compared with different possible backgrounds. Here we like to mention that, the same models (Model I and Model II as described earlier) are adopted for particle DM candidates and the same set of model parameter values given in Table 7.1 and Table 7.2 are used for computing the DM annihilation cross-section in extragalactic case also. The γ-ray flux from DM annihilation could have extragalactic origins too and probing such γ-rays could be effective not only for indirect detection of extragalactic DM but also to understand their origins [300–305, 320–322]. But whether such γ-ray signals can be identified by terrestrial telescopes depend on the background γ-rays from different other types of extragalactic sources. Therefore, to study the γ-rays from extragalactic DM annihilation, one needs to estimate the flux from other possible sources that can contribute to the backgrounds for such observations.

In order to explore the possibilities that γ-ray signals from the extragalactic DM annihilations (indirect DM signals) could be detected with significance, we also compute the γ-ray signals from other possible non-DM origins of extragalactic γ-rays. Such non-DM origins include BL Lac objects, quasars, pulsars, GRBs etc. For many of these sources, the natures of spectra are found to follow roughly a power law. A list of such sources and the corresponding γ-ray flux (power law or other forms) from these sources are furnished later in Table 7.5.

The satellite borne experiment namely Fermi-LAT furnished their observed results for extragalactic γ-ray flux. In this Section, we compute the sum of the γ-rays from extragalactic DM annihilations (for each of the DM candidate in Model I and Model II) and from other possible non-DM sources. We then compare our results with those observed by Fermi-LAT [292, 293].

The rate of photons emitted from volume element dV from the sky depends on several factors mainly the halo mass function dn/dM as a function of mass M and redshift z, the differential

photon energy spectrum $\frac{d\mathcal{N}_\gamma}{dE}(E, M, z)$, the attenuation factor ($e^{-\tau}$) of the extragalactic γ-rays etc. The rate of photons emitted from volume element dV having energy ranges $E + dE$ and observed by detector having effective area dA (with time interval dt and redshifted energy interval dE such that $dtdE = \left[\frac{dt_0}{1+z}\right][(1+z)dE_0]$, where t_0 and E_0 are the time and energy respectively at $z = 0$) is given by,

$$dN_\gamma = e^{-\tau}\left[(1+z)^3 \int dM \frac{dn}{dM}(M, z) \times \frac{d\mathcal{N}_\gamma}{dE}(E, M, z)\right] \frac{dVdA}{4\pi(R_0 S_k(r))^2} dE_0 dt_0 \ . \tag{7.6}$$

In the above, the volume element dV is given by

$$dV = \frac{(R_0 S_k(r))^2 R_0}{(1+z)^3} dr d\Omega_{\text{detector}} \ . \tag{7.7}$$

where $S_k(r)$ is Universe's spatial curvature appearing in Robertson-Walker metric. In this case, we consider that the γ-rays are originated as the end product of the DM annihilation. Therefore, computation of DM cross-section is important for the calculation of $\frac{d\mathcal{N}_\gamma}{dE}$. The extragalactic γ-rays produced at a redshift z suffers attenuation during its passage through intergalactic medium (IGM). This attenuation of extragalactic γ-rays is due to the absorption of high energy γ-rays by extragalactic background light (EBL). Detailed studies for this attenuation are given in Cirelli *et al.* [323] and Fig. 7.4 is generated following Cirelli *et al.* [323]. This attenuation can be described by an exponential function in terms of the optical depth τ as $e^{-\tau(z, E_0)}$, E_0 being the energy at detection at $z = 0$. The optical depth is related to the pair production of baryonic matter, photon-photon scattering in ambient photon background radiation (PBR) and photon-photon pair production [323]. In Fig. 7.4 the dependence of the attenuation factor on redshift (z) and the energy E_0 at detection ($z = 0$) has been shown.

The PBR depends on the Cosmic Microwave Background (CMB), the intergalactic stellar light and the secondary Infrared (IR) radiation. Also the Ultraviolet (UV) background can be originated from

intergalactic stellar light that may come from the massive and hot stars that were ignited at very low redshift. The estimation of UV background are generally addressed by considering two UV models. One is the “no UV" case where the contribution of the UV is absent, while the other is “relativistic UV". The latter has been considered in blazar study and it has prescribed a certain value for the UV background proton density. But this value is lower than the values estimated in many of the other earlier analyses [324]. In the present analysis, a significant amount of contribution of the UV background has been taken into consideration as described in [324, 325]. The diffuse extragalactic γ-ray flux due to DM annihilation is written as,

$$\begin{aligned}\frac{d\phi_\gamma}{dE_0} =& \frac{dN_\gamma}{dAd\Omega dt_0 dE_0} \\ =& \frac{c}{4\pi}\int dz \frac{e^{-\tau(z,E_0)}}{H_0 h(z)} \int dM \frac{dn}{dM}(M,z) \\ & \frac{d\mathcal{N}_\gamma}{dE}\left(E_0(1+z), M, z\right), \end{aligned} \tag{7.8}$$

where c is the speed of light in vacuum, H_0 denotes the Hubble constant at the present epoch and M is the DM halo mass. For spatially flat Universe ($\Omega_k = 0$), $h(z) = \sqrt{\Omega_m(1+z)^3 + \Omega_\Lambda}$, where Ω_i $(i = m, \Lambda, k)$ represent the density parameters for matter (m) or dark energy (Λ) or curvature (k). The halo mass function $\frac{dn}{dM}$ is expressed in terms of the fluctuation, the overdensity in structure formation etc. Denoting $\sigma^2(M)$ to be the variance of the linear density field (rms density $= \sigma$) the mass function $f(\sigma)$ extrapolated to redshift z can be written following Press-Schechter model [326] as,

$$f(\sigma) = \sqrt{\frac{2}{\pi}}\frac{\delta_c}{\sigma}\exp\left(\frac{-\delta_c^2}{2\sigma^2}\right). \tag{7.9}$$

This expression arises out of the following assumption. After smoothening the linear density perturbations over a mass scale M, if in a fraction of space this smooth density field exceeds a threshold δ_c then this fraction of space collapses with mass greater than M. This δ_c is called critical overden-

sity for collapse [2]. In other word, this is the critical value of initial overdensity that is required for collapse at z. This mass function f is also written in terms of a quantity ν where ν $(= \delta_c/\sigma)$ is the overdensity in units of rms density σ. The ratio ν is related to mean square mass fluctuation $\sigma^2(M)$ that is also caused by the non-linear growth of fluctuation. The distribution $f(\nu)$ is the distribution of mass in isolated halos at a given epoch and is related to number densities of halos [3]. The mass density function $\frac{dn}{dM}(M, z)$ is written as [326]

$$\frac{dn}{dM} = \frac{\rho_{0,m}}{M^2}\nu f(\nu)\frac{d\log\nu}{d\log M} \ , \tag{7.10}$$

where $\rho_{0,m}$ is the matter density of the comoving background ($\rho_{0,m} = \rho_c\Omega_m(1+z)^3$, ρ_c is the critical density of the Universe), the ratio $\nu = \delta_c/\sigma(M)$ as discussed, where δ_c ($\simeq 1.686$, [327, 329]) is the critical overdensity for spherical collapse and $\sigma^2(M)$ is the variance of density fluctuations of a sphere containing mass M ($M \simeq (4/3)\pi R^3\rho_c(z_c)$ for collapse halos, R being the comoving length and z_c is the redshift at which the halo collapses). The term $\sigma^2(M)$ can be represented in terms of the power spectrum $P(k)$ of the initial density perturbation as [330]

$$\sigma^2(M) = \frac{1}{2\pi^2}\int_0^\infty d^3k\tilde{W}^2(kR)P(k) \ . \tag{7.11}$$

In the above, $\tilde{W}(kR)$ is the Fourier transform of the real space top hat window function of radius R [4]. The power spectrum is parameterized as $P(k) \propto k^n T^2(k)$ where n is the spectral index and T is a transfer function related to the DM and baryon density in the Universe. CMB data will be useful

[2] f is also defined as $f(\sigma, z) = \frac{M}{\rho_0}\frac{dn(M,z)}{d\ln\sigma^{-1}}$ where n signifies the halo abundance with mass $< M$ at redshift z and ρ_0 be the mean density of the Universe at that redshift [327].

[3] Press and Schechter proposed an ellipsoidal collapse model where the aspects of non spherical collapse are also addressed along with the spherical collapse. In this scenario, the critical overdensity ($\delta_{\rm sc}$) for spherical collapse is replaced by the same for ellipsoidal collapse ($\delta_{\rm ec}$). These are related as $\delta_{\rm ec}(\sigma, z) = \delta_{\rm sc}\left(z\left(1+\beta\left(\frac{\sigma^2}{\delta_{\rm sc}^2(z)}\right)^\gamma\right)\right)$ with $\beta = 0.47$ and $\gamma = 0.615$ [328]. For massive objects however $\sigma/\delta_{\rm sc} < 1$ and $\delta_{\rm ec}(\sigma, z) \simeq \delta_{\rm sc}(\sigma, z)$.

[4] $\tilde{W}(kR) = 3\frac{(\frac{\sin kR}{kR} - \cos kR)}{(kR)^2}$.

for its computation. In Fig. 7.5 the variation of $P(k)$ with wave number k for different z values is shown. The variation of variance σ with halo mass M has also been computed. These variations are plotted in Fig. 7.5(b) for the same set of z values as in Fig. 7.5(a). The multiplicity function $f(\nu)$ in Eq. 7.10 is computed using the relation [330]

$$\nu f(\nu) = 2A\left(1 + \frac{1}{\nu'^{2p}}\right)\left(\frac{\nu'^2}{2\pi}\right)^{1/2} \exp\left(-\frac{\nu'^2}{2}\right) , \tag{7.12}$$

where $\nu' = \sqrt{a}\nu$. Fitting the Eq. 7.10 with N-body simulation of Virgo consortium [331] the numerical values of a ($= 0.707$) and $p = 0.3$ can be obtained. The value of the parameter A in the above equation (Eq. 7.12) is adopted as $A = 0.322$ [330]. In terms of σ the mass function $f(\sigma)$ is written as (with $\nu = \delta_c/\sigma(M)$)

$$f(\sigma) = A\sqrt{\frac{2a}{\pi}}\left[1 + \left(\frac{\sigma^2}{a\delta_c^2}\right)^P\right]\frac{\delta_c}{a}\exp\left[-\frac{a\delta_c^2}{2\sigma^2}\right] . \tag{7.13}$$

The function $f(\nu)$ as well as the numerical values for ν can be computed by using Eq. 7.12. The variations of the mass collapse function $(f(\sigma))$ in the ellipsoidal models with the halo mass M for several values of redshift z (= 0 - 10) are demonstrated in Fig. 7.5(c). Fig. 7.5(d) describes the variations of the considered halo mass function $\frac{dn}{dM}$ of Sheth-Torman model [330] with redshift z and the halo mass M. Fig. 7.4 is just a demonstrative plot for the variation of optical depth with energy and redshift. In order to generate this demonstrative plot, all the necessary numerical calculations have been made by using HMFcalc [332] code.

According to the ΛCDM cosmological model, the DM halos are formed in the "bottom up" sequence. In this approach, initially small clumps of matter form in presence of a tiny density fluctuation zones having a very high gravitational impact. These small scale structures grow into larger ones, eventually forming the larger scale structures like the DM halos. From N-body simulation, the DM density profile is formulated as $\rho(r) = \rho(s)g(r/r_s)$, where r_s and ρ_s indicate the scale radius and the scale density for a particular halo model respectively. For the halo profile, NFW halo

profile [82, 83] is chosen and the nature of the function $g(r/r_s)$ is explained (mentioned in Table 7.3). The mass of any DM halo contained within the radius r_h is given as

$$M_h = 4\pi\rho_s r_h^3 f(r_s/r_h) \ , \tag{7.14}$$

where $f(x) = x^3[\ln(1+x)^{-1} - (1+x)^{-1}]$. The NFW profile has two parameters namely a characteristic inner radius r_s and a characteristic inner density ρ_s [333]. One of these characteristic parameter can be replaced by virial radius or virial mass where, virial mass $M_{\rm vir}$ is

$$M_h = M_{\rm vir} = \frac{4\pi}{3}\Delta_{\rm vir}\bar{\rho}(z)R_{\rm vir}^3 \ , \tag{7.15}$$

where $\Delta_{\rm vir}\bar{\rho}(z)$ is the mean density in the virial radius $R_{\rm vir}$ and $\Delta_{\rm vir}$ is the critical over density at virialisation. In the above, $\bar{\rho}(z)$ is the mean Universal density. For the flat Universe ($\Omega_k = 0$), the quantity $\Delta_{\rm vir}(z)$ takes the form [334]

$$\Delta_{\rm vir} \simeq (18\pi^2 + 82d - 39d^2) \ , \tag{7.16}$$

with $d \equiv d(z) = \frac{\Omega_m(1+z)^3}{(\Omega_m(1+z)^3+\Omega_\Lambda)} - 1$ $\left(d(z) \equiv \Omega(z) - 1 = \frac{\Omega_m(1+z)^3}{E(z)^2} - 1, \text{ where } E(z) = \frac{H(z)}{H_0}\right)$. The γ-ray energy spectrum $\frac{d\mathcal{N}}{dE}$ depends on the halo profile (here adopted to be NFW profile). The shape of the profile can be alternatively described in terms of a concentration parameter. As the name suggests this parameter is about the concentration of matter in the halo at different positions and hence is an effective alternative for the description of the shape of the halo density profile. In general, the concentration parameter is formally expressed in terms of the virial radius $R_{\rm vir}$ as $c_{\rm vir} = \frac{R_{\rm vir}}{r_s^{(-2)}}$ where $r_s^{(-2)}$ is the radius at which the logarithmic slope of the density profile is -2 $\left(\frac{d\log(\rho)}{dr} = -2\right)$ [335]. Considering the characteristic radius r_s of the halo to be the radius $r_s^{(-2)}$ and defining $x = \frac{r}{r_s^{(-2)}}$, the NFW density profile (Table 7.3) takes the form $\rho(r) = \rho_s g(r/r_s) = \frac{\rho_s}{x(1+x^2)}$. In the present computation, an r-dependent form is adopted as

$c_{\rm vir} r_{-2} = \frac{R_{\rm vir}}{r}$, where $r_{-2} = \frac{r_s^{(-2)}}{r_s}$. With this the γ-ray energy spectrum $\frac{d\mathcal{N}_\gamma}{dE}\left(E_0\,(1+z), M, z\right)$ for the γ-ray (Eq. 7.8) (induced by the DM annihilation with annhilation cross-section $\langle\sigma v\rangle$) emitted from a halo of mass M at redshift z can be written as,

$$\frac{d\mathcal{N}_\gamma}{dE}(E, M, z) = \frac{\langle\sigma v\rangle}{2}\frac{dN_\gamma(E)}{dE}\int dc'_{\rm vir}\mathcal{P}(c'_{\rm vir})\left(\frac{\rho'}{M_\chi}\right)^2 \int d^3 r g^2(r/a). \tag{7.17}$$

Here, the differential γ-ray spectrum is $\frac{dN_\gamma(E)}{dE}$ and $c_{\rm vir}$ is known as the concentration parameter whose lognormal distribution around a mean value (within 1σ [330]) for halos with mass M is denoted as $\mathcal{P}(c_{\rm vir})$. We finally have

$$\frac{d\mathcal{N}_\gamma}{dE}(E, M, z) = \frac{\sigma v}{2}\frac{dN_\gamma(E)}{dE}\frac{M}{M_\chi^2}\frac{\Delta_{\rm vir}\bar{\rho}(z)}{3} \int dc'_{\rm vir}\mathcal{P}(c'_{\rm vir})\frac{(c'_{\rm vir} r_{-2})^3}{\left[I_1(c'_{\rm vir}\, r_{-2})\right]^2} I_2(x_{min}, c'_{\rm vir} r_{-2})\ . \tag{7.18}$$

The integration $I_n(x_{min}, x_{max})$ is given by $I_n(x_{min}, x_{max}) = \int_{x_{min}}^{x_{max}} dx\, x^2 g^n(x)$. Finally the extragalactic γ-ray flux from DM annihilation takes the form [300]

$$\frac{d\phi_\gamma}{dE_0} = \frac{\sigma v}{8\pi}\frac{c}{H_0}\frac{\rho_0^2}{M_\chi^2}\int dz (1+z)^3 \frac{\Delta^2(z)}{h(z)}\frac{dN_\gamma(E_0(1+z))}{dE} e^{-\tau(z, E_0)}\ , \tag{7.19}$$

with

$$\Delta^2(z) \equiv \int dM \frac{\nu(z, M) f\left(\nu(z, M)\right)}{\sigma(M)}\left|\frac{d\sigma}{dM}\right| \Delta^2_M(z, M) \tag{7.20}$$

and $\left(c_{\rm vir} = \frac{R_{\rm vir}}{r_s^{(-2)}}\right)$,

$$\Delta^2_M(z, M) \equiv \frac{\Delta_{\rm vir}(z)}{3}\int dc'_{\rm vir}\ \mathcal{P}(c'_{\rm vir}) \frac{I_2(x_{min}, c'_{\rm vir}(z, M)\, r_{-2})}{\left[I_1(x_{min}, c'_{\rm vir}(z, M)\, r_{-2})\right]^2}(c'_{\rm vir}(z, M)\, r_{-2})^3. \tag{7.21}$$

Two forms for concentration parameter $c_{\rm vir}$ are adopted for the present computation of extragalactic γ-ray flux. The first form is $c_{\rm vir}(M,z) = k_{200}\,(\mathcal{H}(z_f(M))/\mathcal{H}(z))^{2/3}$ from Macciò *et al.* [336] with $k_{200} \simeq 3.9$, $\mathcal{H}(z) = H(z)/H_0$ and $z_c(M)$ is the effective redshift when a halo with mass M is formed. The second form for $c_{\rm vir}$ reads as $c_{\rm vir}(M,z) = 6.5\,\mathcal{H}(z)^{-2/3}\,(M/M_*)^{-0.1}$, $M_* = 3.37\times10^{12}h^{-1}M_\odot$. This follows from a power law model [336, 337]. In what follows this second form for $c_{\rm vir}$ is referred to as "Power law model for $c_{\rm vir}$" while the former form for $c_{\rm vir}$ is referred to as "Macciò *et al.* model for $c_{\rm vir}$". It is also to be noted that the DM substructure within a halo may form bound subhalos. The minimum mass for such subhalos are denoted by $M_{\rm min}$. These minimum masses $M_{\rm min}$ for such subhalos are determined from the decoupling temperature of DM. Two values for minimum subhalo mass namely $M_{\rm min} = 10^{-6}M_\odot$ and $10^{-9}\,M_\odot$ [338, 339] are chosen.

The extragalactic γ-ray flux (Eqs. 7.18, 7.19) induced by annihilation of DM is computed using Eqs. 7.6 - 7.17 alongwith Eqs. 7.20, 7.21. As mentioned, in order to explore the possibilities that the extragalactic γ-rays could be indirect DM signal, the calculations are performed for each of the two particle DM candidates mentioned in Section 7.3 as Model I and Model II. Exactly the same framework and the numerical values of the parameters (such as couplings) for the two DM candidates (WIMP DM and Kaluza-Klein DM (extra dimension model)) as used for dwarf galaxy calculations are also used for the extragalactic case. It may be noted that while one is a 50 GeV DM − the WIMP component of a two component WIMP-FImP DM model (Model I) the other (Model II) is a 900 GeV KK DM inspired by extra dimensional models (see Section 7.1).

We also estimate the background flux from different possible extragalactic astrophysical sources. The diffuse γ-ray background may include contributions from BL Lac objects, flat spectrum radio quasars (FSRQs), millisecond pulsars (MSPs), star forming galaxy (SFG), Fanarof-Riley (FR) radio galaxies of type I (FRI) and type II (FRII), ultrahigh energy cosmic rays (UHECRs), GRBs, star burst galaxy (SBG), ultrahigh energy protons interacting with the inter-cluster material (UHEp ICM) and gravitationally induced shock waves (IGS). These along with the nature of their empirical

power spectra [308] are tabulated in Table 7.5.

The sum total of computed γ-ray flux from the background (described above) and those involving from DM annihilation where the DM candidates are shown from Model I and Model II (50 GeV WIMP and 900 GeV KK DM from extra dimensional theory) are shown in Figs. 7.6 - 7.9. While the computed results with Model I are given in Figs. 7.6, 7.7, in Figs. 7.8, 7.9 the results for Model II are plotted. For each of the two cases, however the extragalactic backgrounds from each of the possible non-DM sources (Table 7.5) are also shown in Figs. 7.6 - 7.9. It is to be noted that for the computation of γ-rays from DM annihilation with each of the Model I and Model II DM candidates, two different forms for $c_{\rm vir}$ have been used, one follows from a power law consideration and the other as given by Maccio *et al.* [340]. Fig. 7.6 and Fig. 7.7 are for the two $c_{\rm vir}$ values respectively for Model I while Fig. 7.8 and Fig. 7.9 are for the same when Model II DM is considered. The results are computed with each of the two chosen values of minimun subhalo mass ($M_{\rm min} = 10^{-6} M_{\odot}$ and $M_{\rm min} = 10^{-9} M_{\odot}$) for each of the models Model I and Model II and are shown in Fig. 7.6 and Fig. 7.7 for the case of Model I and in Fig. 7.8 and Fig.7.9 when computations are made for the KK DM (Model II).

The observational results of Fermi-LAT for extragalactic are also plotted and compared with the computed sum total flux (γ-ray from DM annihilation considering both Model I and Model II for DM and the γ-rays estimation from the background). It is seen from Figs. 7.6 - 7.9 that for both Model I and Model II of DM, the sum total of calculated flux (both with $M_{\rm min} = 10^{-6} M_{\odot}$ and $M_{\rm min} = 10^{-9} M_{\odot}$) and background is always lower than the Fermi-LAT results for both the chosen values of M when the "Macciò *et al.* model for $c_{\rm vir}$" is used for the calculation of γ-ray flux from DM annihilation (Fig. 7.6 and Fig. 7.8) and hence no γ-ray signal from possible extragalactic DM annihilation can be detected above the background. The fluxes only due to the DM annihilation (no background) computed with each of the two chosen values of $M_{\rm min}$ are also shown in Figs. 7.6 - 7.9 by dashed plots. For all the cases considered in Figs. 7.6 - 7.9 for DM candidates in Model I and Model II, it is observed that the calculated flux with $M_{\rm min} = 10^{-9} M_{\odot}$ always lies above the flux

when computed with $M_{\rm min} = 10^{-6} M_{\odot}$. From Fig. 7.7 and Fig. 7.9, it is seen that the computed γ-ray flux (added with the background from non-DM sources) with "Power law model for $c_{\rm vir}$" and $M_{\rm min} = 10^{-9} M_{\odot}$ (solid black line) goes beyond the Fermi-LAT data upto around $E_{\gamma} = 10$ GeV for Model I (Fig. 7.7). Even only the computed flux for DM annihilation (without the background) with $M_{\rm min} = 10^{-9} M_{\odot}$ lies beyond the Fermi-LAT data within certain γ-energy range (Fig. 7.7).

Similar trends are also seen for the case of KK DM (Model II) also (Fig. 7.8 and Fig. 7.9). From Fig. 7.8, one sees that when "Macciò *et al.* model for $c_{\rm vir}$" is considered, the total computed flux (including non-DM background) always lies below the observed flux by Fermi-LAT in the considered range for E_{γ}. But here also the flux with $M_{\rm min} = 10^{-9} M_{\odot}$ are closer to the observed results than when computed with $M_{\rm min} = 10^{-6} M_{\odot}$. Interesting results are obtained for KK DM when "Power law model for $c_{\rm vir}$" is used in the calculations (Fig. 7.9). In Fig. 7.9 one observes that the total calculated flux (including the background) with $M_{\rm min} = 10^{-6} M_{\odot}$ agrees very well with the Fermi-LAT results for almost the whole considered range of E_{γ} upto the energy ~ 100 GeV. The total flux, when $M_{\rm min} = 10^{-9} M_{\odot}$, agrees with Fermi-LAT in lower energy region (upto ~ 1 GeV). Comparing with Fig. 7.7 (similar case for Model I) it appears that the extragalactic γ-rays from the annihilation of KK DM in extra dimensional model better agrees with experimental results than the WIMP DM of Model I with DM mass of 50 GeV. It can also be observed from Figs. 7.6 - 7.9 that "Power law model for $c_{\rm vir}$" (the concentration parameter), is more suited than the "Macciò *et al.* model for $c_{\rm vir}$" in the present calculations.

7.5 Summary

In this Chapter, we explore the observational upper limits of γ-ray fluxes from 45 dSphs and relate these to the γ-rays that could be produced from annihilation of DM in dSphs. For our analysis, we consider two DM candidates in two particle DM models. One is a two component WIMP-FImP model of which the WIMP component undergoes annihilation to produce the γ-ray flux. The WIMP

Table 7.5: The contributions of non-DM sources to the extragalactic γ-ray background.

Non-DM source	$\frac{dN}{dE}$ in $\mathrm{GeV^{-1}cm^{-2}s^{-1}sr^{-1}}$
BL Lacs	$3.9 \times 10^{-8} E_\gamma^{-2.23}$
FSRQ	$3.1 \times 10^{-8} E_\gamma^{-2.45}$
MSP	$1.8 \times 10^{-7} E_\gamma^{-1.5} \exp\left(-\frac{E_\gamma}{1.9}\right)$
SFG	$1.3 \times 10^{-7} E_\gamma^{-2.75}$
FR I and FR II	$5.7 \times 10^{-8} E_\gamma^{-2.39} \exp\left(-\frac{E_\gamma}{50.0}\right)$
UHECR	$4.8 \times 10^{-9} E_\gamma^{-1.8} \exp\left[-\left(\frac{E_\gamma}{100.0}\right)^{0.35}\right]$
GRB	$8.9 \times 10^{-9} E_\gamma^{-2.1}$
SBG	$0.3 \times 10^{-7} E_\gamma^{-2.4}$
UHEp ICM	$3.1 \times 10^{-9} E_\gamma^{-2.75}$
IGS	$0.87 \times 10^{-10} \times \begin{cases} \left(\frac{E_\gamma}{10.0}\right)^{-2.04} & \text{for } \mathrm{E_\gamma < 10GeV} \\ \left(\frac{E_\gamma}{10.0}\right)^{-2.13} & \text{for } \mathrm{E_\gamma > 10GeV} \end{cases}$

component is a Dirac singlet fermion and its additional $\mathrm{U(1)_{DM}}$ charge prevents its interaction with SM fermions. But the interaction between the WIMP fermion and the SM sector can be occurred via the Higgs portal. The benchmark mass for this DM is chosen to be 50 GeV for the present analysis. The other particle DM chosen for the analysis is KK DM inspired by models of extra dimensions. In Universal extra dimensional model B^1, the KK partner of hypercharge guage boson is chosen as the DM candidate. It appears from the analysis that for both the Higgs portal model and KK model, the DM annihilations to γ-rays for 45 dwarf galaxies are well within the observational upper bounds of the γ-ray fluxes for all the 45 dSphs considered. While the Higgs portal DM (Model I) covers a shorter range, the KK DM having higher mass range can probe the γ-ray flux at higher energy range.

We have also extended our analyses for the case of possible extragalactic signature of γ-rays from DM annihilations. If detected, such signals could be the indirect extragalactic DM signals. For this extragalactic case also, we adopt the same DM candidates and the model parameter values given in Tables 7.1 and 7.2 and discussed in Sections 7.1 and 7.2. But there can be many extragalactic

γ-ray sources other than possible DM annihilations. These non-DM sources for extragalactic γ-rays contribute to the background for the γ-rays produced via possible extragalactic DM annihilations. An estimation of the flux for such extragalactic sources has been made. The γ-ray flux from DM annihilations primarily depends on the annihilation cross-section of the particle DM candidate. In addition to this, the parameters which we need to taken into account for the γ-ray flux calculation are the DM halo mass function, the density fluctuation in the halo, the linear and non-linear growth of density perturbation and their collapse, the virial radius, the minimum mass $M_{\rm min}$ required for the formation of the subhalo within a DM halo, the γ-ray spectrum ($\frac{dN}{dE}$), the attenuation factor of these γ-rays during it's passage towards a terrestrial detector etc. It is also required to use a feasible model for DM halo density profile. In this calculations, NFW density profile has been considered and this NFW density profile is a function of concentration parameter ($c_{\rm vir}$), which plays a major role in computation of the extragalactic γ-ray flux originated from the DM annihilation. Two separate forms for $c_{\rm vir}$ has been adopted, where one is a power form and the other one is a form given by [336]. We have considered two distinct values for minimum mass $M_{\rm min}$, which are $M_{\rm min} = 10^{-6} M_{\odot}$ and $M_{\rm min} = 10^{-9} M_{\odot}$. The analyses in the thesis show that the power law choice for $c_{\rm vir}$ yields better results in comparison to the other choice. Better agreements are obtained for the KK DM candidate of UED model (Model II). The KK DM candidate is more massive ($\sim$ 900 GeV) than the WIMP DM candidate in Model I ($\sim$ 50 GeV). The computed flux for this KK DM candidate (for power law choice of $c_{\rm vir}$) agrees satisfactorily with the Fermi-LAT results for $M_{\rm min} = 10^{-6} M_{\odot}$ having a wider energy range than in case of the former DM candidate of Model I.

The present analyses therefore demonstrate the possibilities of detecting indirect signal of DM from extragalactic origins as well as from dSphs. The results also indicate that the particle nature of DM can be probed from the study of the γ-rays from both dwarf galaxies and extragalactic sources.

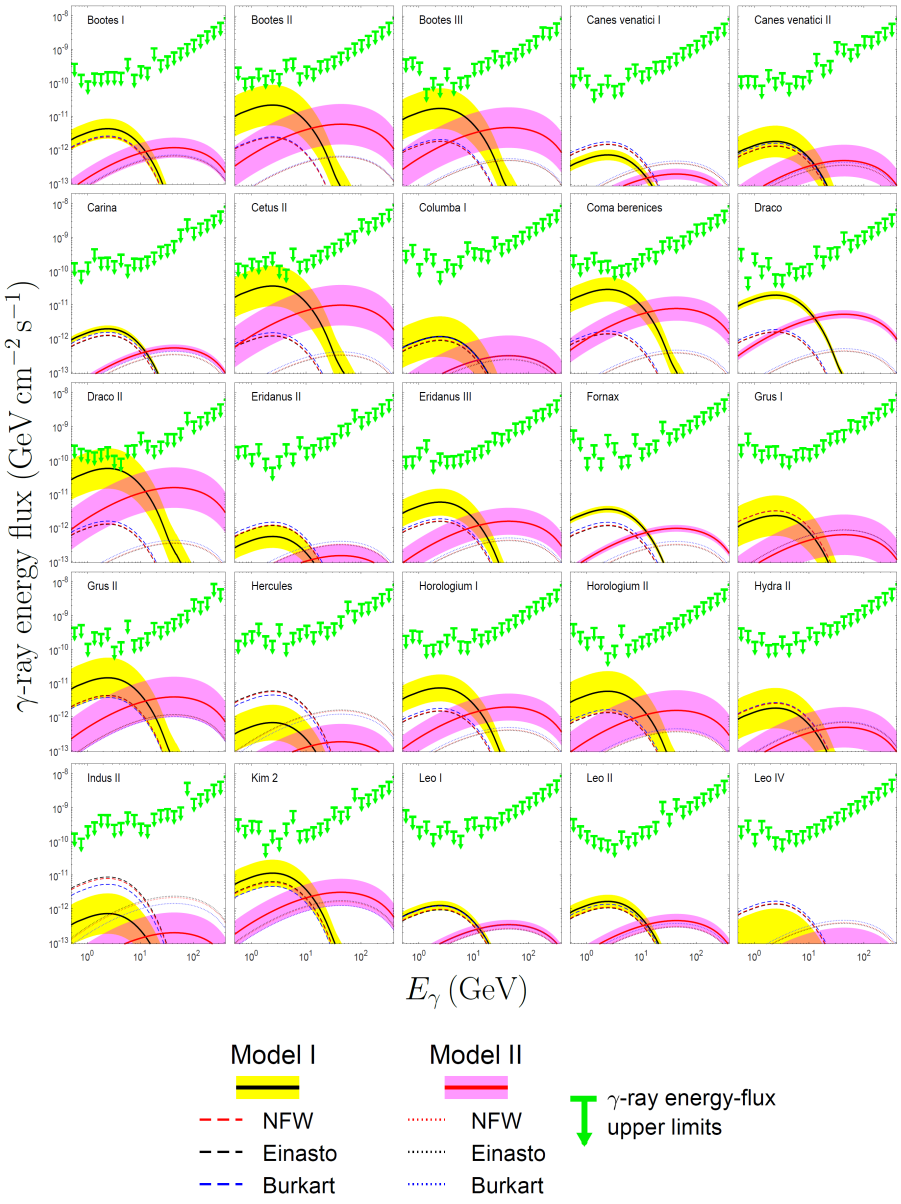

Figure 7.2: γ-ray fluxes from DM anihilations for each of the DM candidates in Model I (50 GeV fermionic WIMP) and Model II (900 GeV Kaluza-Klein DM) calculated for each of the 25 dwarf galaxies and their comparisons with experimental upper bounds of γ-ray flux (shown by green coloured downward arrows) for each of the dwarf spheroidals. The flux calculations with the $\mathcal{J}$-factors from Table 7.4 and its uncertainty spreads are shown by black solid line and yellow band respectively when Model I is considered and the same for the DM candidate of Model II are shown by pink solid line and pink band respectively. The estimated fluxes for both Model I and Model II using the $\mathcal{J}$-factors with each of the three DM density profiles are shown with dashed lines and dotted lines of different colours for comparisons. See text for details.

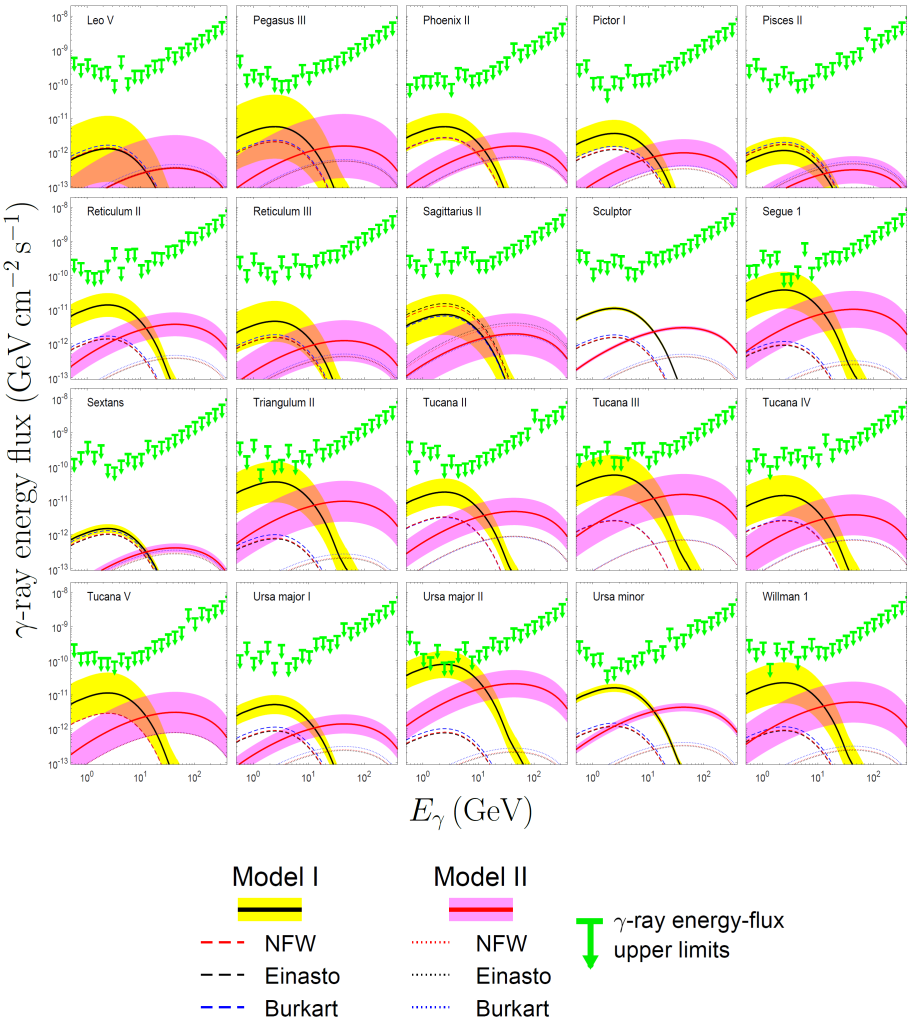

Figure 7.3: Same as Fig.7.2 but for the rest 20 dwarf galaxies. See text for details.

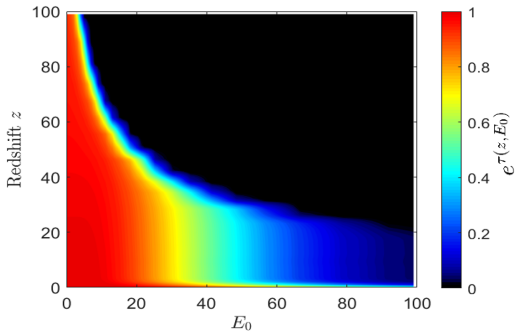

Figure 7.4: Variation of optical depth e^{τ} is described as function of energy E_0 and redshift z. The numerical values of the e^{τ} is described in the colourbar.

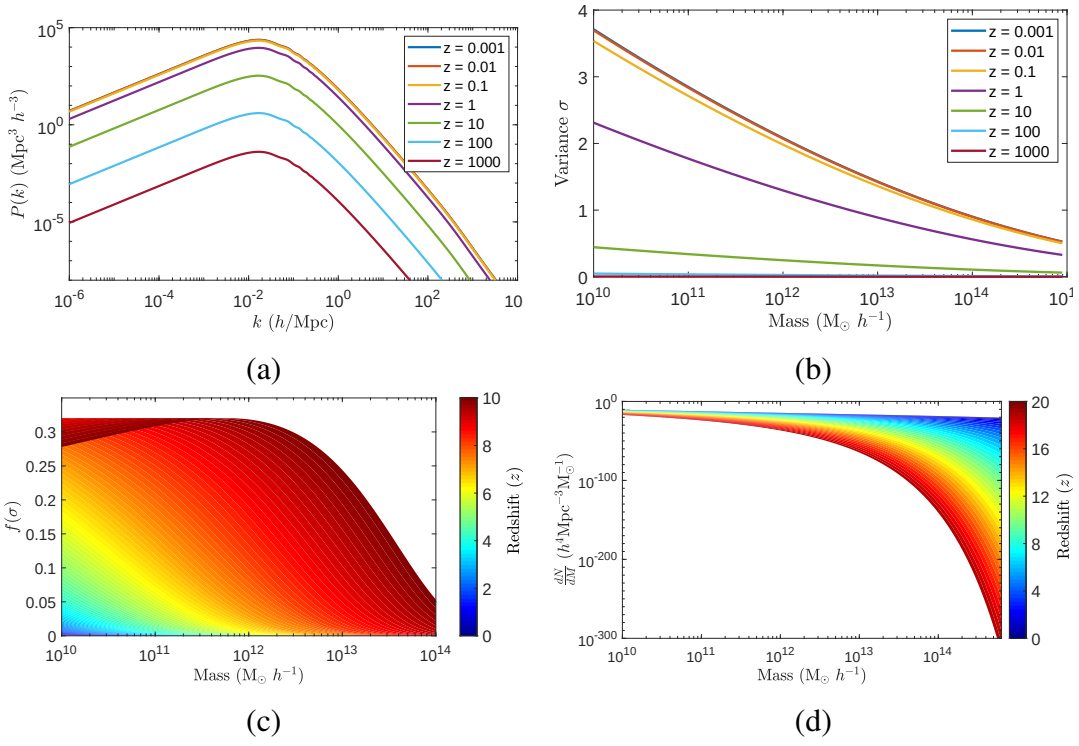

Figure 7.5: (a) Variation of the linear power spectrum $P(k)$ of matter density perturbations with the wave number k for different redshifts (z). (b) Variance σ of the density perturbations with halo mass for different redshifts (z). (c) Fraction of mass collapsed ($f(\sigma)$) for different redshifts z and halo masses M according to the Sheth-Torman model. (d) Variation of $\frac{dN}{dM}$ with halo mass M for different redshift z.

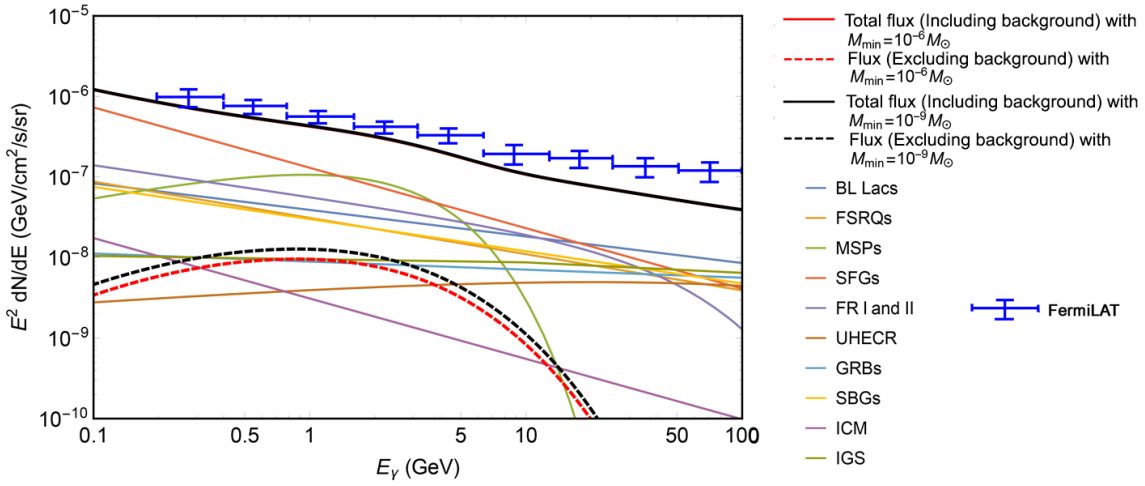

Figure 7.6: Observed extragalactic γ-ray fluxes by Fermi-LAT compared with the total γ-ray fluxes obtained from the DM annihilation for Model-I DM and other possible non-DM γ-rays extragalactic sources. For the flux calculation, we have taken into account concentration parameter ($c_{\rm vir}$), which is adopted from Macciò *et al.* See text for details.

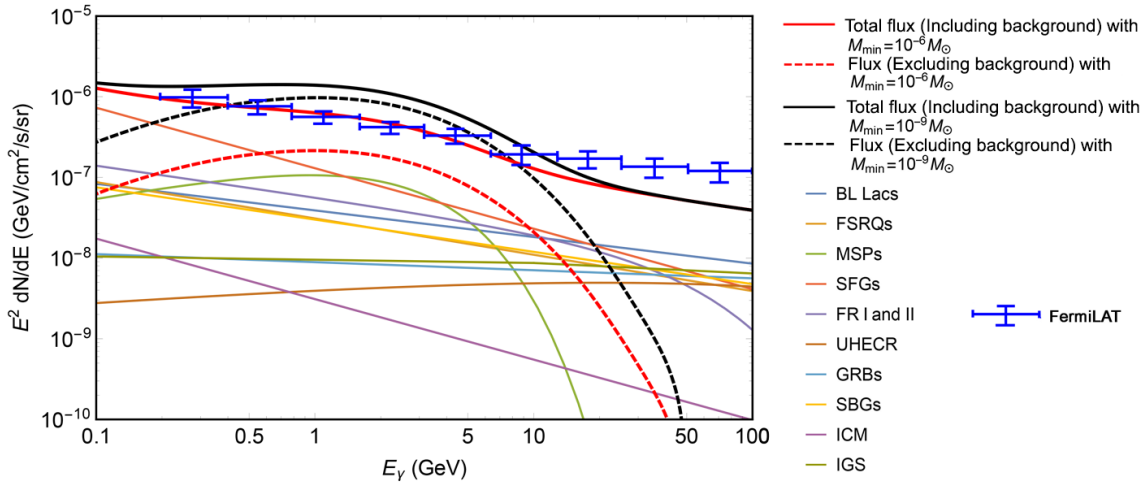

Figure 7.7: Observed extragalactic γ-ray fluxes by Fermi-LAT compared with the total γ-ray fluxes obtained from the DM annihilation for Model-I DM and other possible non-DM γ-rays extragalactic sources. In this case the power law for $c_{\rm vir}$ is used for the computation of flux. See text for details.

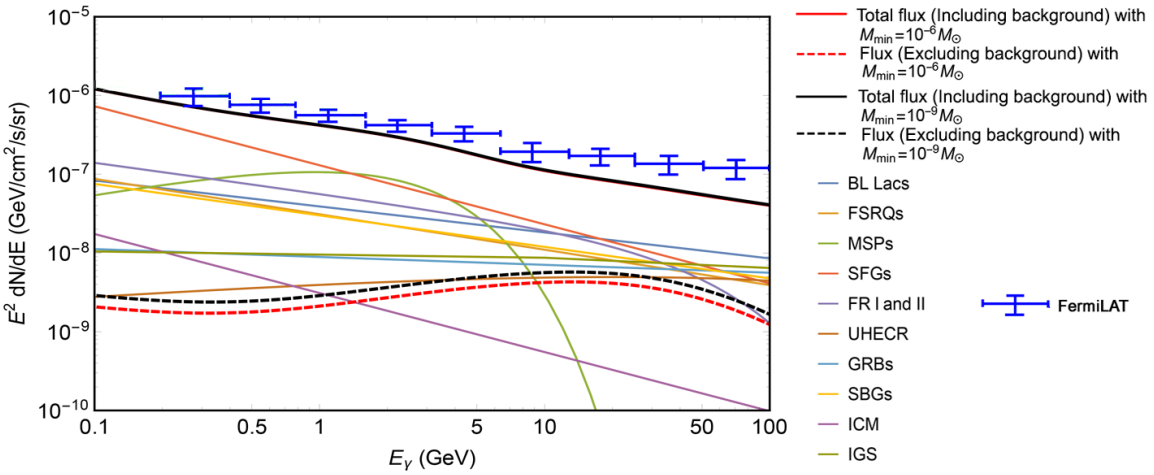

Figure 7.8: Same as Fig. 7.6 but for the DM candidate of Model II. See text for details.

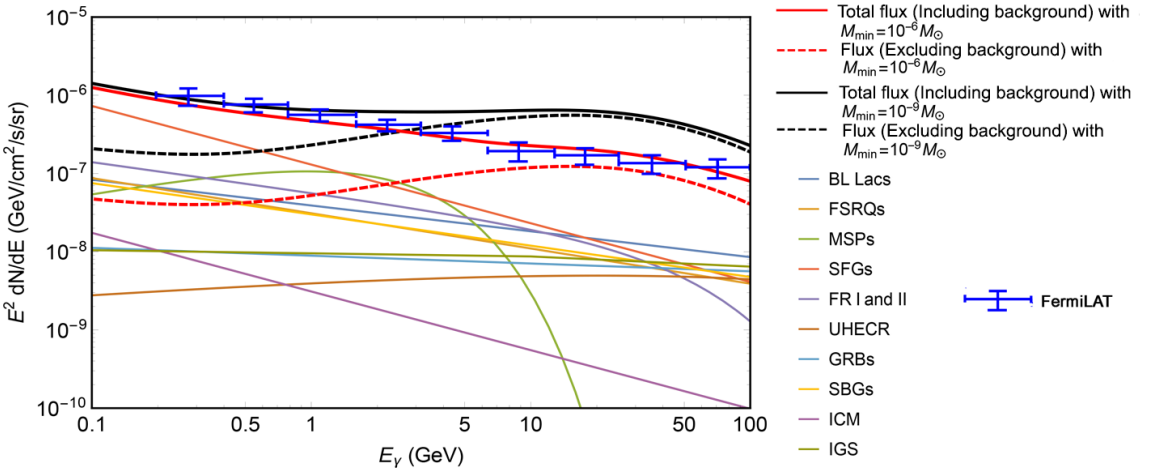

Figure 7.9: Same as Fig. 7.7 but for the DM candidate of Model II. See text for details.

CHAPTER 8

PROBING 4-FLAVOUR NEUTRINO MIXING WITH UHE NEUTRINO SIGNALS AT A 1 Km^2 DETECTOR

In this Chapter, a four neutrino (3 active + 1 sterile) framework is adopted to address the possible deviation of ultrahigh energy (UHE) neutrino signals at a Km^2 detector such as IceCube. To this end the possible UHE neutrino induced muon and shower yields are calculated for both 3-flavour and 4-flavour neutrino framework at a 1 Km^2 detector such as IceCube and the results are then compared. Such UHE neutrinos may originate from distant Gamma Ray Bursts (GRBs) and suffer flavour suppression while traversing astronomical baseline length before reaching the earthbound detector. This can be useful for probing the existence of a fourth sterile component using UHE neutrino flux.

8.1 Introduction

It has been discussed in Chapter 4 that neutrinos occur in three active flavours. But the existence of a fourth sterile neutrino has been proposed and pursued since long as also in recent times. The neutrino oscillation data from experiments like liquid scintillator neutrino detector or LSND [175–177] could not be satisfactorily explained by three neutrino oscillation framework. There are observed excess in LSND data that is consistent with $\bar{\nu}_\mu - \bar{\nu}_e$ oscillation with $0.2\ \mathrm{eV}^2 \leq \Delta m^2 \leq 10\ \mathrm{eV}^2$. But this mass squared difference is not consistent with Δm^2_{21} or Δm^2_{32} obtained from solar or atmospheric neutrino experiments. This is also substantiated from the analysis of excess observed by MiniBooNE experiment for both $\bar{\nu}_\mu - \bar{\nu}_e$ and $\nu_\mu - \nu_e$ oscillations [341, 342]. These results suggest the existence of an additional fourth neutrino with mass squared splitting $\Delta m^2_{41} >> \Delta m^2_{32}$. This fourth neutrino, if exists will not have other Standard Model (SM) couplings as indicated by the LEP experiment of Z boson decay width. Hence this additional neutrino if exists, is referred to as sterile neutrino. In addition, there are reactor neutrino anomalies reported by experiments where lower rates are found for $\bar{\nu_e}$ from nuclear reactors at a distance which is too short for any effective neutrino oscillation among standard neutrinos [343–345]. Lower rate has also been observed at 3σ for ν_e's from ^{51}Cr and ^{37}Ar sources in solar neutrino experiments with gallium [346–350].

Several current experiments are analyzing their data including a fourth sterile neutrino and give bounds on different oscillation parameters. The MINOS experiment [137] measures ν_μ oscillations using charged current (CC) and neutral current (NC) interactions in a long baseline (LBL) experiment with a far and near detector that has a LBL separation of 734 km. The MINOS and its upgraded MINOS+ experiment, from the analysis of their data have recently put constraints on sterile neutrino oscillation parameters (in $\sin^2\theta_{24} - \Delta m^2_{41}$ plane) [137, 138]. NOνA experiment on the other hand is another LBL neutrino experiment that look for $\nu_\mu - \nu_s$ oscillation (with ν_μ beam from NuMI at Fermilab) through NC interaction in a LBL experiment with a baseline distance from near and far detector of 810 km. NOνA experiment search for the oscillation in disappearance channel

of active neutrino flux in the near and far detector.

With new data from reactor and other short and LBL neutrino experiments such as MINOS [137–148], Daya Bay [127–133], Bugey [174] etc. and their analyses considering the active-sterile neutrino oscillation give new bounds on active-sterile mixing angles and Δm^2.

There are other future LBL experiments such as DUNE (Deep Underground neutrino experiment) [150–153], T2HK [351–353] etc. that may throw more light on neurtrino oscillation physics and the active-sterile neutrino oscillation search will be substantiated. For example, for DUNE which is a LBL experiment with the baseline length of about 1300 km between Fermilab, the neutrino source and the detector at Sanford Underground Research Facility or SURF at South Dakota, the NC data would be useful in case active neutrinos oscillate to sterile neutrinos [354].

A four (3+1) neutrino scheme is adopted in this Chapter where there are three active neutrinos and one sterile neutrino and a four flavour oscillation scenario. The usual three active neutrino scenario and the three flavour oscillations are also considered for comparison. The purpose is to explore an experimental signature that would or would not indicate the existence of a sterile neutrino. In doing this, the possible signature of UHE neutrinos from distant extragalactic sources at a large terrestrial neutrino telescope such as IceCube has been studied. High energy events such as GRBs can produce such neutrinos through their particle acceleration mechanism. GRBs are thought to occur when infalling accreted matter bounces off on a failed star that has possibly turned into a black hole. A powerful shock wave then progresses outwards with energies as high as $\sim 10^{53}$ ergs or more in the form of a “fireball". The protons inside such a fireball, being accelerated thus, interact with γ by the process of cosmic beam dump while the pions are produced which in turn decays to UHE neutrinos. This is commonly known as fireball (FB) model for GRBs. However there are also other type of mechanism such as cannonball (CB) model which can also explain GRB pulses and afterglow from core collapse Supernova [355–358]. In CB model, it is assumed that an accretion disk is formed around the exploding Supernova. When matters from the accretion disk fall into the compact object due to loss of rotational energy, a pair of cannonballs made up of matter

are ejected. Electrons in the cannonballs then undergo Compton scattering with photons to produce GRB energy. Every such CB generate a single GRB pulse. In contrast, in FB model of GRB, the synchrotron radiations of accreted matter are responsible for the pulses. In FB mechanism, the synchrotron radiations due to collision of conical outer shells with interstellar medium (ISM) also gives rise to GRB afterglows. On the other hand, in case of CB model, initially afterglow is due to thermal bremsstrahlung when the ejected CB expands rapidly and interacts with ISM and later it is governed by synchrotron [357]. For the present study, only fireball model is considered for neutrino production.

The UHE neutrinos therefore will ideally be produced from the decay of pions by GRB process in a ratio $\nu_e : \nu_\mu : \nu_\tau = 1 : 2 : 0$. These neutrinos will suffer flavour oscillations or suppressions while traversing to a terrestrial detector. Because of the astronomical baseline length of the GRBs from the Earth, the oscillation length $\frac{\Delta m^2}{4E}$ (Δm^2 is the mass squared difference between any two neutrinos and E is the neutrino energy) is much smaller than the baseline length and the neutrino suffer multiple oscillations in reaching the Earth from GRBs. Hence the oscillatory part $(\sin^2(\Delta m^2[L/4E]))$ in the oscillation probability equation averages out. Thus one is left with, in the oscillation probability equations, just three oscillation parameters namely the three mixing angles θ_{12}, θ_{23} and θ_{13} in case of three active neutrino scenario while for the four (3+1) neutrino scheme considered here, there are three additional mixing angles namely θ_{14}, θ_{24} and θ_{34} that account for the mixing of the three active neutrinos with the fourth sterile neutrino. In this Chapter, for the purpose of computation, the experimental best fit values for the three active neutrino mixing angles namely θ_{12}, θ_{23} and θ_{13} obtained from the analysis of data from solar neutrinos, atmospheric neutrinos, reactor and accelerator neutrinos etc. are adopted. But the active-sterile mixing angles are not known with certainty. However, as discussed earlier in this Section, bounds or limits on these unknown mixing angles are obtained from the data analyses of various other reactor or accelerator based neutrino experiments. With new LBL experiments coming up along with more and more data available from the existing experiments, these bounds are expected to be more stringent.

Two kinds of signals namely the muon track signal and the shower/cascade are computed for UHE neutrinos from GRBs in a Km^2 detector such as IceCube. The latter may be produced by the CC and NC interactions of GRB neutrinos during its passage through the Earth rock as also in a IceCube like detector. The muons are obtained when the UHE ν_μ from GRB reaches the Earth and interacts with the Earth's rock while moving through the Earth towards the detector. The CC interactions of ν_μ and ν_τ yield produce μ and τ respectively ($\nu_\alpha + N \longrightarrow \alpha + X$, where $\alpha \equiv \mu$ or τ). The muons are detected by the track events in an ice detector through its Cherenkov light. The τ can be detected by "double bang" events or "lollipop" events. The first bang of "double bang" events is produced at the site of first CC interaction $\nu_\tau + N \rightarrow \tau + X$ when a τ track followed by a cascade would be generated and the second bang of hadronic or electromagnetic (EM) shower occurs when ν_τ is regenerated from the decay of τ in the fiducial volume of the detector. A lollipop event is one when the first bang could not be detected but the τ track can be detected or reconstructed along with the second bang. In the case of an inverse lollipop event, the first bang and the neutrino track could be obtained while the second bang evades detection. In this Chapter, we do not consider these events related to ν_τ CC interaction as these detections are not very efficient and could be significant only in an energy window of $\sim 2\ \mathrm{PeV} - 10\ \mathrm{PeV}$. However, in this calculation, the muon track signals that can be obtained from ν_τ from the process $\nu_\tau \longrightarrow \tau \longrightarrow \bar{\nu}_\mu \mu \nu_\tau$ are also included. The CC interactions of ν_e produce EM showers. Shower events are also considered from the NC interactions of neutrinos of all active flavours. The computations for these events are performed for both (3+1) scheme and three active flavour scheme. The results are then compared for these two scenarios.

In addition, the effective Majorana mass m_{ee} for the present (3+1) neutrino (three active and one sterile) framework is also calculated and its variation with the mass of the lightest neutrino is studied. These results are then compared with the known bounds from the neutrino double beta decay experiments. It is found that for lower mass of the lightest neutrino, the inverted hierarchy of neutrino masses in (3+1) scenario may barely satisfy these limits.

8.2 Formalism

8.2.1 Four and Three Neutrino Oscillations for Distant UHE Neutrinos

In general as derived in Chapter 4, the probability for a neutrino $|\nu_\alpha\rangle$ of flavour α to oscillate to a neutrino $|\nu_\beta\rangle$ of flavour β is given by (considering no CP violation in neutrino sector)

$$P_{\nu_\alpha \to \nu_\beta} = \delta_{\alpha\beta} - 4 \sum_{j>i} U_{\alpha i} U_{\beta i} U_{\alpha j} U_{\beta j} \sin^2 \left(\frac{\pi L}{\lambda_{ij}} \right) . \tag{8.1}$$

In the above, i, j denote the mass indices, L is the baseline distance and $U_{\alpha i}$ etc. are the elements of the Pontecorvo-Maki-Nakagawa-Sakata (PMNS) mixing matrix [121] such that

$$|\nu_\alpha\rangle = \sum_i U_{\alpha i} |\nu_i\rangle , \tag{8.2}$$

$|\nu_i\rangle$ being the i^{th} mass eigenstate. The oscillation length λ_{ij} is given by

$$\lambda_{ij} = 2.47 \,\text{Km} \left(\frac{E}{\text{GeV}} \right) \left(\frac{\text{eV}^2}{\Delta m^2_{ij}} \right) , \tag{8.3}$$

with E being the neutrino energy and Δm^2_{ij} is the mass squared difference of i^{th} and j^{th} neutrino mass eigenstates. As discussed in Sect. 8.1, $\dfrac{\Delta m^2 L}{E} >> 1$ for UHE neutrinos from GRBs (very large L) and hence

$$\left\langle \sin^2 \left(\frac{\pi L}{\lambda_{ij}} \right) \right\rangle = \frac{1}{2} . \tag{8.4}$$

The probability equation (Eq. 8.1) is then reduced to

$$\begin{aligned} P_{\nu_\alpha \to \nu_\beta} &= \delta_{\alpha\beta} - 2\sum_{j>i} U_{\alpha i}U_{\beta i}U_{\alpha j}U_{\beta j} \ , \\ &= \delta_{\alpha\beta} - \sum_i U_{\alpha i}U_{\beta i}\left[\sum_{j\neq i} U_{\alpha j}U_{\beta j}\right] \ , \\ &= \sum_j |\ U_{\alpha j}\ |^2 |\ U_{\beta j}\ |^2 \ , \end{aligned} \tag{8.5}$$

where the use has been made of the unitarity condition

$$\sum_i U_{\alpha i}U_{\beta i} = \delta_{\alpha\beta} \ . \tag{8.6}$$

For four flavour scenario (with a fourth sterile neutrino ν_s) along with active flavours ν_e, ν_μ and ν_τ, the neutrino flavour eigenstates and mass eigenstates are related through

$$\begin{pmatrix} \nu_e \\ \nu_\mu \\ \nu_\tau \\ \nu_s \end{pmatrix} = \begin{pmatrix} \tilde{U}_{e1} & \tilde{U}_{e2} & \tilde{U}_{e3} & \tilde{U}_{e4} \\ \tilde{U}_{\mu 1} & \tilde{U}_{\mu 2} & \tilde{U}_{\mu 3} & \tilde{U}_{\mu 4} \\ \tilde{U}_{\tau 1} & \tilde{U}_{\tau 2} & \tilde{U}_{\tau 3} & \tilde{U}_{\tau 4} \\ \tilde{U}_{s1} & \tilde{U}_{s2} & \tilde{U}_{s3} & \tilde{U}_{s4} \end{pmatrix} \begin{pmatrix} \nu_1 \\ \nu_1 \\ \nu_3 \\ \nu_4 \end{pmatrix} , \tag{8.7}$$

where $\tilde{U}_{\alpha i}$ etc. (i being the mass index (i = 1,2,3,4) and α being the flavour index ($\alpha = e, \mu, \tau, s$)) are the elements of the PMNS mixing matrix for the 4-flavour case, which can be generated by the successive rotations (R) (in terms of six mixing angles θ_{14}, θ_{24}, θ_{34}, θ_{13}, θ_{12}, θ_{23}) [359] as

$$\tilde{U} = R_{34}(\theta_{34})R_{24}(\theta_{24})R_{14}(\theta_{14})R_{23}(\theta_{23})R_{13}(\theta_{13})R_{12}(\theta_{12}) \ . \tag{8.8}$$

No CP violation [1] in neutrino sector is assumed and hence the CP phases are absent. For the 4-flavour framework, the successive rotation terms (R) can be expressed as

$$
\begin{aligned}
R_{34}(\theta_{34}) &= \begin{pmatrix} 1 & 0 & 0 & 0 \\ 0 & 1 & 0 & 0 \\ 0 & 0 & c_{34} & s_{34} \\ 0 & 0 & -s_{34} & c_{34} \end{pmatrix}, R_{24}(\theta_{24}) = \begin{pmatrix} 1 & 0 & 0 & 0 \\ 0 & c_{24} & 0 & s_{24} \\ 0 & 0 & 1 & 0 \\ 0 & -s_{24} & 0 & c_{24} \end{pmatrix}, \\
R_{14}(\theta_{14}) &= \begin{pmatrix} c_{14} & 0 & 0 & s_{14} \\ 0 & 1 & 0 & 0 \\ 0 & 0 & 1 & 0 \\ -s_{14} & 0 & 0 & c_{14} \end{pmatrix}, R_{12}(\theta_{12}) = \begin{pmatrix} c_{12} & s_{12} & 0 & 0 \\ -s_{12} & c_{12} & 0 & 0 \\ 0 & 0 & 1 & 0 \\ 0 & 0 & 0 & 1 \end{pmatrix}, \\
R_{13}(\theta_{13}) &= \begin{pmatrix} c_{13} & 0 & s_{13} & 0 \\ 0 & 1 & 0 & 0 \\ -s_{13} & 0 & c_{13} & 0 \\ 0 & 0 & 0 & 1 \end{pmatrix}, R_{23}(\theta_{23}) = \begin{pmatrix} 1 & 0 & 0 & 0 \\ 0 & c_{23} & s_{23} & 0 \\ 0 & -s_{23} & c_{23} & 0 \\ 0 & 0 & 0 & 1 \end{pmatrix}. \qquad (8.9)
\end{aligned}
$$

Considering the present 4-flavour scenario to be the minimal extension of 3-flavour case by a sterile neutrino, the matrix $\tilde{U}$ can be written as

$$
\tilde{U}_{(4\times4)} = \begin{pmatrix} c_{14} & 0 & 0 & s_{14} \\ -s_{14}s_{24} & c_{24} & 0 & c_{14}s_{24} \\ -c_{24}s_{14}s_{34} & -s_{24}s_{34} & c_{34} & c_{14}c_{24}s_{34} \\ -c_{24}s_{14}c_{34} & -s_{24}c_{34} & -s_{34} & c_{14}c_{24}c_{34} \end{pmatrix} \times \begin{pmatrix} \mathcal{U}_{e1} & \mathcal{U}_{e2} & \mathcal{U}_{e3} & 0 \\ \mathcal{U}_{\mu1} & \mathcal{U}_{\mu2} & \mathcal{U}_{\mu3} & 0 \\ \mathcal{U}_{\tau1} & \mathcal{U}_{\tau2} & \mathcal{U}_{\tau3} & 0 \\ 0 & 0 & 0 & 1 \end{pmatrix}, \qquad (8.10)
$$

[1] Although the evidence of CP violation in lepton sector is yet to be established, an analysis of T2K data sets a best fit value of $\delta = -\pi/2$ but with only 2σ C.L. Hence we have neglected the CP violation in our present scenario.

$$= \begin{pmatrix} c_{14}\mathcal{U}_{e1} & c_{14}\mathcal{U}_{e2} & c_{14}\mathcal{U}_{e3} & s_{14} \\ -s_{14}s_{24}\mathcal{U}_{e1} + c_{24}\mathcal{U}_{\mu 1} & -s_{14}s_{24}\mathcal{U}_{e2} + c_{24}\mathcal{U}_{\mu 2} & -s_{14}s_{24}\mathcal{U}_{e3} + c_{24}\mathcal{U}_{\mu 3} & c_{14}s_{24} \\ \begin{matrix} -c_{24}s_{14}s_{34}\mathcal{U}_{e1} \\ -s24s34\mathcal{U}_{\mu 1} \\ +c_{34}\mathcal{U}_{\tau 1} \end{matrix} & \begin{matrix} -c_{24}s_{14}s_{34}\mathcal{U}_{e2} \\ -s24s34\mathcal{U}_{\mu 2} \\ +c_{34}\mathcal{U}_{\tau 2} \end{matrix} & \begin{matrix} -c_{24}s_{14}s_{34}\mathcal{U}_{e3} \\ -s24s34\mathcal{U}_{\mu 3} \\ +c_{34}\mathcal{U}_{\tau 3} \end{matrix} & c_{14}c_{24}s_{34} \\ \begin{matrix} -c_{24}c_{34}s_{14}\mathcal{U}_{e1} \\ -s_{24}c_{34}\mathcal{U}_{\mu 1} \\ -s_{34}\mathcal{U}_{\tau 1} \end{matrix} & \begin{matrix} -c_{24}c_{34}s_{14}\mathcal{U}_{e2} \\ -s_{24}c_{34}\mathcal{U}_{\mu 2} \\ -s_{34}\mathcal{U}_{\tau 2} \end{matrix} & \begin{matrix} -c_{24}c_{34}s_{14}\mathcal{U}_{e3} \\ -s_{24}c_{34}\mathcal{U}_{\mu 3} \\ -s_{34}\mathcal{U}_{\tau 3} \end{matrix} & c_{!4}c_{24}c_{34} \end{pmatrix} , \tag{8.11}$$

where $\mathcal{U}_{\alpha i}$ are the elements of 3-flavour neutrino mixing matrix

$$\mathcal{U}_{(3\times 3)} = \begin{pmatrix} \mathcal{U}_{e1} & \mathcal{U}_{e2} & \mathcal{U}_{e3} \\ \mathcal{U}_{\mu 1} & \mathcal{U}_{\mu 2} & \mathcal{U}_{\mu 3} \\ \mathcal{U}_{\tau 1} & \mathcal{U}_{\tau 2} & \mathcal{U}_{\tau 3} \end{pmatrix} . \tag{8.12}$$

The matrix $\mathcal{U}_{(3\times 3)}$ can be expressed as the successive rotations

$$\mathcal{U}_{(3\times 3)} = R_{23}R_{13}R_{12} , \tag{8.13}$$

where

$$R_{12} = \begin{pmatrix} c_{12} & s_{12} & 0 \\ -s_{12} & c_{12} & 0 \\ 0 & 0 & 1 \end{pmatrix}, R_{13} = \begin{pmatrix} c_{13} & 0 & s_{13} \\ 0 & 1 & 0 \\ -s_{13} & 0 & c_{13} \end{pmatrix}, R_{23} = \begin{pmatrix} 1 & 0 & 0 \\ 0 & c_{23} & s_{23} \\ 0 & -s_{23} & c_{23} \end{pmatrix} . \quad (8.14)$$

Therefore

$$\mathcal{U}_{(3\times3)} = \begin{pmatrix} c_{12}c_{13} & s_{12}c_{13} & s_{13} \\ -s_{12}c_{23} - c_{12}s_{23}s_{13} & c_{12}c_{23} - s_{12}s_{23}s_{13} & s_{23}c_{13} \\ s_{12}s_{23} - c_{12}c_{23}s_{13} & -c_{12}s_{23} - s_{12}c_{23}s_{13} & c_{23}c_{13} \end{pmatrix} . \quad (8.15)$$

Following Eq. 8.5 the oscillation probability $P^4_{\nu_\alpha \to \nu_\beta}$ (where α, β denote the flavour indices) for 4-flavour case can now be represented as [360]

$$P^4_{\nu_\alpha \to \nu_\beta} \equiv \begin{pmatrix} P_{ee} & P_{e\mu} & P_{e\tau} & P_{es} \\ P_{\mu e} & P_{\mu\mu} & P_{\mu\tau} & P_{\mu s} \\ P_{\tau e} & P_{\tau\mu} & P_{\tau\tau} & P_{\tau s} \\ P_{se} & P_{s\mu} & P_{s\tau} & P_{ss} \end{pmatrix} \equiv XX^T , \quad (8.16)$$

with

$$X = \begin{pmatrix} |\tilde{U}_{e1}|^2 & |\tilde{U}_{e2}|^2 & |\tilde{U}_{e3}|^2 & |\tilde{U}_{e4}|^2 \\ |\tilde{U}_{\mu1}|^2 & |\tilde{U}_{\mu2}|^2 & |\tilde{U}_{\mu3}|^2 & |\tilde{U}_{\mu4}|^2 \\ |\tilde{U}_{\tau1}|^2 & |\tilde{U}_{\tau2}|^2 & |\tilde{U}_{\tau3}|^2 & |\tilde{U}_{\tau4}|^2 \\ |\tilde{U}_{s1}|^2 & |\tilde{U}_{s2}|^2 & |\tilde{U}_{s3}|^2 & |\tilde{U}_{s4}|^2 \end{pmatrix} . \quad (8.17)$$

Similarly for 3-flavour scenario the probability $P^3_{\nu_\alpha \to \nu_\beta}$ takes the form

$$P^3_{\nu_\alpha \to \nu_\beta} = AA^T , \quad (8.18)$$

where

$$A = \begin{pmatrix} |\mathcal{U}_{e1}|^2 & |\mathcal{U}_{e2}|^2 & |\mathcal{U}_{e3}|^2 \\ |\mathcal{U}_{\mu 1}|^2 & |\mathcal{U}_{\mu 2}|^2 & |\mathcal{U}_{\mu 3}|^2 \\ |\mathcal{U}_{\tau 1}|^2 & |\mathcal{U}_{\tau 2}|^2 & |\mathcal{U}_{\tau 3}|^2 \end{pmatrix} . \tag{8.19}$$

8.2.2 UHE Neutrino Fluxes from GRBs

From the GRBs the neutrino (antineutrino) flavours are expected to produce in the ratio [2]

$$\nu_e : \nu_\mu : \nu_\tau = 1 : 2 : 0 .$$

The isotropic flux [170, 361] for ν_μ and $\bar{\nu}_\mu$ estimated by summing over all the sources is given as (Gandhi *et al.*) [362]

$$\mathcal{F}(E_\nu) = \frac{dN_{\nu_\mu + \bar{\nu}_\mu}}{dE_\nu} = \mathcal{N} \left(\frac{E_\nu}{1\text{GeV}} \right)^{-n} \text{cm}^{-2}\text{s}^{-1}\text{sr}^{-1}\text{GeV}^{-1} . \tag{8.20}$$

In the above,

$$\mathcal{N} = 4.0 \times 10^{-13} \qquad n = 1 \text{ for } E_\nu < 10^5 \text{ GeV} ,$$
$$\mathcal{N} = 4.0 \times 10^{-8} \qquad n = 2 \text{ for } E_\nu > 10^5 \text{ GeV} .$$

[2] In GRB (assuming fireball model) neutrinos are produced from the decay of pions. The pions are photoproduced by shocked protons in the photon field following $p\gamma \to \Delta \to \pi$.

Therefore, the fluxes of the corresponding flavours (same for both neutrinos and antineutrinos since no CP violation is considered in the neutrino sector) can be expressed as

$$\begin{aligned}
\frac{dN_{\nu_\mu}}{dE_\nu} &= \phi_{\nu_\mu} = \frac{dN_{\bar{\nu}_\mu}}{dE_\nu} = \phi_{\bar{\nu}_\mu} = 0.5\mathcal{F}(E_\nu)\,, \\
\frac{dN_{\nu_e}}{dE_\nu} &= \phi_{\nu_e} = \frac{dN_{\bar{\nu}_e}}{dE_\nu} = \phi_{\bar{\nu}_e} = 0.25\mathcal{F}(E_\nu)\ .
\end{aligned} \tag{8.21}$$

These neutrinos suffer flavour oscillations (suppressions) as they reach the terrestrial detector due to the astronomical baseline length. Thus in the process, the ν_μ can oscillate to ν_τ and/or to other flavours on reaching the Earth. The flux of neutrino flavours for four and three flavour cases, on reaching the Earth will respectively be

$$\begin{aligned}
F^4_{\nu_e} &= P^4_{\nu_e\to\nu_e}\phi_{\nu_e} + P^4_{\nu_\mu\to\nu_e}\phi_{\nu_\mu}\ , \\
F^4_{\nu_\mu} &= P^4_{\nu_\mu\to\nu_\mu}\phi_{\nu_\mu} + P^4_{\nu_e\to\nu_\mu}\phi_{\nu_e}\ , \\
F^4_{\nu_\tau} &= P^4_{\nu_e\to\nu_\tau}\phi_{\nu_e} + P^4_{\nu_\mu\to\nu_\tau}\phi_{\nu_\mu}\ , \\
F^4_{\nu_s} &= P^4_{\nu_e\to\nu_s}\phi_{\nu_e} + P^4_{\nu_\mu\to\nu_s}\phi_{\nu_\mu}
\end{aligned} \tag{8.22}$$

and

$$\begin{aligned}
F^3_{\nu_e} &= P^3_{\nu_e\to\nu_e}\phi_{\nu_e} + P^3_{\nu_\mu\to\nu_e}\phi_{\nu_\mu}\ , \\
F^3_{\nu_\mu} &= P^3_{\nu_\mu\to\nu_\mu}\phi_{\nu_\mu} + P^3_{\nu_e\to\nu_\mu}\phi_{\nu_e}\ , \\
F^3_{\nu_\tau} &= P^3_{\nu_e\to\nu_\tau}\phi_{\nu_e} + P^3_{\nu_\mu\to\nu_\tau}\phi_{\nu_\mu}\ .
\end{aligned} \tag{8.23}$$

In the above $F^4_{\nu_\alpha}(F^3_{\nu_\alpha})$ is the flux for the species ν_α, α being the flavour index and $P^4_{\nu_\alpha}(P^3_{\nu_\alpha})$ is the corresponding oscillation probability for 4(3) flavour scenario.

Cosmic neutrino flux (Eq. 8.22) in the far distance can be expressed as a product of $P_{(4\times4)}(=$

XX^T) and the intrinsic flux $\phi_{\nu_\alpha}(\alpha = e, \nu, \tau, s)$ in the matrix form

$$\begin{pmatrix} F^4_{\nu_e} \\ F^4_{\nu_\mu} \\ F^4_{\nu_\tau} \\ F^4_{\nu_s} \end{pmatrix} = XX^T \times \begin{pmatrix} \phi_{\nu_e} \\ \phi_{\nu_\mu} \\ \phi_{\nu_\tau} \\ \phi_{\nu_s} \end{pmatrix} . \tag{8.24}$$

Assuming the standard ratio of intrinsic neutrino flux i.e.

$$\phi_{\nu_e} : \phi_{\nu_\mu} : \phi_{\nu_\tau} : \phi_{\nu_s} = 1 : 2 : 0 : 0 \ .$$

Now by using the above assumption and Eq. 8.17, Eq. 8.24 can be rewritten as

$$\begin{pmatrix} F^4_{\nu_e} \\ F^4_{\nu_\mu} \\ F^4_{\nu_\tau} \\ F^4_{\nu_s} \end{pmatrix} = \begin{pmatrix} |\tilde{U}_{e1}|^2 & |\tilde{U}_{e2}|^2 & |\tilde{U}_{e3}|^2 & |\tilde{U}_{e4}|^2 \\ |\tilde{U}_{\mu1}|^2 & |\tilde{U}_{\mu2}|^2 & |\tilde{U}_{\mu3}|^2 & |\tilde{U}_{\mu4}|^2 \\ |\tilde{U}_{\tau1}|^2 & |\tilde{U}_{\tau2}|^2 & |\tilde{U}_{\tau3}|^2 & |\tilde{U}_{\tau4}|^2 \\ |\tilde{U}_{s1}|^2 & |\tilde{U}_{s2}|^2 & |\tilde{U}_{s3}|^2 & |\tilde{U}_{s4}|^2 \end{pmatrix} \begin{pmatrix} |\tilde{U}_{e1}|^2 & |\tilde{U}_{\mu1}|^2 & |\tilde{U}_{\tau1}|^2 & |\tilde{U}_{s1}|^2 \\ |\tilde{U}_{e2}|^2 & |\tilde{U}_{\mu2}|^2 & |\tilde{U}_{\tau2}|^2 & |\tilde{U}_{s2}|^2 \\ |\tilde{U}_{e3}|^2 & |\tilde{U}_{\mu3}|^2 & |\tilde{U}_{\tau3}|^2 & |\tilde{U}_{s3}|^2 \\ |\tilde{U}_{e4}|^2 & |\tilde{U}_{\mu4}|^2 & |\tilde{U}_{\tau4}|^2 & |\tilde{U}_{s4}|^2 \end{pmatrix} \times \begin{pmatrix} 1 \\ 2 \\ 0 \\ 0 \end{pmatrix} \phi_{\nu_e} \ . \tag{8.25}$$

Using the unitarity condition $\sum_{\alpha} |\tilde{U}|^2 = 1(\alpha \equiv e, \mu, \tau, s)$ the fluxes can be wriiten as

$$
\begin{aligned}
F^4_{\nu_e} &= [\mid \tilde{U}_{e1} \mid^2 (1 + \mid \tilde{U}_{\mu 1} \mid^2 - \mid \tilde{U}_{\tau 1} \mid^2 - \mid \tilde{U}_{s1} \mid^2) + \mid \tilde{U}_{e2} \mid^2 (1 + \mid \tilde{U}_{\mu 2} \mid^2 - \mid \tilde{U}_{\tau 2} \mid^2 - \mid \tilde{U}_{s2} \mid^2) \\
&\quad + \mid \tilde{U}_{e3} \mid^2 (1 + \mid \tilde{U}_{\mu 3} \mid^2 - \mid \tilde{U}_{\tau 3} \mid^2 - \mid \tilde{U}_{s3} \mid^2) + \mid \tilde{U}_{e4} \mid^2 (1 + \mid \tilde{U}_{\mu 4} \mid^2 - \mid \tilde{U}_{\tau 4} \mid^2 - \mid \tilde{U}_{s4} \mid^2)] \phi_{\nu_e} \ , \\
F^4_{\nu_\mu} &= [\mid \tilde{U}_{\mu 1} \mid^2 (1 + \mid \tilde{U}_{\mu 1} \mid^2 - \mid \tilde{U}_{\tau 1} \mid^2 - \mid \tilde{U}_{s1} \mid^2) + \mid \tilde{U}_{\mu 2} \mid^2 (1 + \mid \tilde{U}_{\mu 2} \mid^2 - \mid \tilde{U}_{\tau 2} \mid^2 - \mid \tilde{U}_{s2} \mid^2) \\
&\quad + \mid \tilde{U}_{\mu 3} \mid^2 (1 + \mid \tilde{U}_{\mu 3} \mid^2 - \mid \tilde{U}_{\tau 3} \mid^2 - \mid \tilde{U}_{s3} \mid^2) + \mid \tilde{U}_{\mu 4} \mid^2 (1 + \mid \tilde{U}_{\mu 4} \mid^2 - \mid \tilde{U}_{\tau 4} \mid^2 - \mid \tilde{U}_{s4} \mid^2)] \phi_{\nu_e} \ , \\
F^4_{\nu_\tau} &= [\mid \tilde{U}_{\tau 1} \mid^2 (1 + \mid \tilde{U}_{\mu 1} \mid^2 - \mid \tilde{U}_{\tau 1} \mid^2 - \mid \tilde{U}_{s1} \mid^2) + \mid \tilde{U}_{\tau 2} \mid^2 (1 + \mid \tilde{U}_{\mu 2} \mid^2 - \mid \tilde{U}_{\tau 2} \mid^2 - \mid \tilde{U}_{s2} \mid^2) \\
&\quad + \mid \tilde{U}_{\tau 3} \mid^2 (1 + \mid \tilde{U}_{\mu 3} \mid^2 - \mid \tilde{U}_{\tau 3} \mid^2 - \mid \tilde{U}_{s3} \mid^2) + \mid \tilde{U}_{\tau 4} \mid^2 (1 + \mid \tilde{U}_{\mu 4} \mid^2 - \mid \tilde{U}_{\tau 4} \mid^2 - \mid \tilde{U}_{s4} \mid^2)] \phi_{\nu_e} \ , \\
F^4_{\nu_s} &= [\mid \tilde{U}_{s1} \mid^2 (1 + \mid \tilde{U}_{\mu 1} \mid^2 - \mid \tilde{U}_{\tau 1} \mid^2 - \mid \tilde{U}_{s1} \mid^2) + \mid \tilde{U}_{s2} \mid^2 (1 + \mid \tilde{U}_{\mu 2} \mid^2 - \mid \tilde{U}_{\tau 2} \mid^2 - \mid \tilde{U}_{s2} \mid^2) \\
&\quad + \mid \tilde{U}_{s3} \mid^2 (1 + \mid \tilde{U}_{\mu 3} \mid^2 - \mid \tilde{U}_{\tau 3} \mid^2 - \mid \tilde{U}_{s3} \mid^2) \\
&\quad + \mid \tilde{U}_{s4} \mid^2 (1 + \mid \tilde{U}_{\mu 4} \mid^2 - \mid \tilde{U}_{\tau 4} \mid^2 - \mid \tilde{U}_{s4} \mid^2)] \phi_{\nu_e} \ . \qquad (8.26)
\end{aligned}
$$

Similarly for 3-flavour scenario we can write Eq. 8.23 by using Eqs. 8.18, 8.19 as

$$
\begin{pmatrix} F^3_{\nu_e} \\ F^3_{\nu_\mu} \\ F^3_{\nu_\tau} \end{pmatrix} = \begin{pmatrix} \mid \mathcal{U}_{e1} \mid^2 & \mid \mathcal{U}_{e2} \mid^2 & \mid \mathcal{U}_{e3} \mid^2 \\ \mid \mathcal{U}_{\mu 1} \mid^2 & \mid \mathcal{U}_{\mu 2} \mid^2 & \mid \mathcal{U}_{\mu 3} \mid^2 \\ \mid \mathcal{U}_{\tau 1} \mid^2 & \mid \mathcal{U}_{\tau 2} \mid^2 & \mid \mathcal{U}_{\tau 3} \mid^2 \end{pmatrix} \begin{pmatrix} \mid \mathcal{U}_{e1} \mid^2 & \mid \mathcal{U}_{\mu 1} \mid^2 & \mid \mathcal{U}_{\tau 1} \mid^2 \\ \mid \mathcal{U}_{e2} \mid^2 & \mid \mathcal{U}_{\mu 2} \mid^2 & \mid \mathcal{U}_{\tau 2} \mid^2 \\ \mid \mathcal{U}_{e3} \mid^2 & \mid \mathcal{U}_{\mu 3} \mid^2 & \mid \mathcal{U}_{\tau 3} \mid^2 \end{pmatrix} \times \begin{pmatrix} 1 \\ 2 \\ 0 \end{pmatrix} \phi_{\nu_e} \ . \qquad (8.27)
$$

Finally Eq. 8.27 can be written as

$$
\begin{aligned}
F^3_{\nu_e} &= [\mid \mathcal{U}_{e1} \mid^2 (1 + \mid \mathcal{U}_{\mu 1} \mid^2 - \mid \mathcal{U}_{\tau 1} \mid^2) + \mid \mathcal{U}_{e2} \mid^2 (1 + \mid \mathcal{U}_{\mu 2} \mid^2 - \mid \mathcal{U}_{\tau 2} \mid^2) \\
&\quad + \mid \mathcal{U}_{e3} \mid^2 (1 + \mid \mathcal{U}_{\mu 3} \mid^2 - \mid \mathcal{U}_{\tau 3} \mid^2)] \phi_{\nu_e} \ , \\
F^3_{\nu_\mu} &= [\mid \mathcal{U}_{\mu 1} \mid^2 (1 + \mid \mathcal{U}_{\mu 1} \mid^2 - \mid \mathcal{U}_{\tau 1} \mid^2) + \mid \mathcal{U}_{\mu 2} \mid^2 (1 + \mid \mathcal{U}_{\mu 2} \mid^2 - \mid \mathcal{U}_{\tau 2} \mid^2) \\
&\quad + \mid \mathcal{U}_{\mu 3} \mid^2 (1 + \mid \mathcal{U}_{\mu 3} \mid^2 - \mid \mathcal{U}_{\tau 3} \mid^2)] \phi_{\nu_e} \ , \\
F^3_{\nu_\tau} &= [\mid \mathcal{U}_{\tau 1} \mid^2 (1 + \mid \mathcal{U}_{\mu 1} \mid^2 - \mid \mathcal{U}_{\tau 1} \mid^2) + \mid \mathcal{U}_{\tau 2} \mid^2 (1 + \mid \mathcal{U}_{\mu 2} \mid^2 - \mid \mathcal{U}_{\tau 2} \mid^2) \\
&\quad + \mid \mathcal{U}_{\tau 3} \mid^2 (1 + \mid \mathcal{U}_{\mu 3} \mid^2 - \mid \mathcal{U}_{\tau 3} \mid^2)] \phi_{\nu_e} \ . \qquad (8.28)
\end{aligned}
$$

8.2.3 Detection of UHE Neutrinos from Diffused GRB Sources

Upward going muon signals at IceCube is induced by the CC interaction of upward going neutrinos. Such upward going muons can not be misidentified from muons produced in the atmosphere. The detection of ν_μ's from GRBs can be observed from the tracks of the secondary muons.

The total number of secondary muons that can be observed in a detector of unit area is estimated as (following [363–365])

$$
S = \int_{E_{\rm thr}}^{E_{\nu_{\rm max}}} dE_\nu \frac{dN_\nu}{dE_\nu} P_{\rm shadow}(E_\nu) P_\mu(E_\nu, E_{\rm thr}). \qquad (8.29)
$$

The phenomenon of Earth shielding is described by the shadow factor $P_{\rm shadow}(E_\nu)$, which is defined to be an effective solid angle divided by 2π for upward going muons. This is a function of the energy dependent neutrino-nucleon interaction length $L_{\rm int}(E_\nu)$ in the Earth and the column depth $z(\theta_z)$ for the incident neutrino zenith angle θ_z. For the case of isotropic fluxes, the attenuation can

be estimated by the shadow factor, $P_{\rm shadow}$ where,

$$P_{\rm shadow}(E_\nu) = \frac{1}{2\pi}\int_{-1}^{0} d\cos\theta_z \int d\phi \;\; \exp[-z(\theta_z)/L_{\rm int}(E_\nu)] \;, \tag{8.30}$$

with interaction length $L_{\rm int}(E_\nu)$ is given by

$$L_{\rm int} = \frac{1}{\sigma^{\rm tot}(E_\nu)N_A} \;. \tag{8.31}$$

In the above expression, N_A ($= 6.023\times10^{23}{\rm mol}^{-1} = 6.023\times10^{23}{\rm cm}^{-3}$) is the Avogadro number and $\sigma^{\rm tot}(=\sigma^{\rm NC}+\sigma^{\rm CC})$ is the total (CC plus NC) cross-section. The column depth $z(\theta_z)$ can be expressed as

$$z(\theta_z) = \int \rho(r(\theta_z, l))dl \;. \tag{8.32}$$

In Eq. 8.32, $\rho(r(\theta_z, l))$ represents the density of the Earth. A convenient representation of the matter density profile of the Earth, which is given by the Preliminary Earth Model [366] is adopted for the present analysis. The neutrino path length entering into the Earth is l.

The probability $P_\mu(E_\nu, E_{\rm thr})$ for a muon arriving in the detector with an energy threshold of $E_{\rm thr}$ is given by

$$P_\mu(E_\nu, E_{\rm thr}) = N_A\sigma^{\rm cc}(E_\nu)\langle R(E_\mu; E_{\rm thr})\rangle \;\; , \tag{8.33}$$

where $\langle R(E_\mu; E_{\rm thr})\rangle$ is the average range of a muon in rock, which can be expressed as

$$\langle R(E_\mu; E_{\rm thr})\rangle \;\; = \;\; \frac{1}{\sigma_{\rm CC}}\int_0^{(1-E_{\rm thr}/E_\nu)} dy R(E_\nu(1-y); E_{\rm thr}) \times \frac{d\sigma_{\rm CC}(E_\nu, y)}{dy} \;\; , \tag{8.34}$$

where $y = (E_\nu - E_\mu)/E_\nu$ is the energy loss fraction of a neutrino with energy E_ν that produced a secondary muon of energy E_μ via CC interaction. The range of detectable energy of such a muon

will then be from $E_{\rm thr}$ to E_μ. The range for a muon of energy E_μ is given by

$$R(E_\mu; E_{\rm thr}) = \int_{E_{\rm thr}}^{E_\mu} \frac{dE_\mu}{\langle dE_\mu/dX \rangle} \simeq \frac{1}{\xi} \ln\left(\frac{\alpha + \xi \mathrm{E}_\mu}{\alpha + \xi \mathrm{E}_{\rm thr}}\right) \ . \tag{8.35}$$

The energy loss rate of muons with energy E_μ due to ionization and catastrophic losses like bremsstrahlung, pair production and hadro production is expressed as [364]

$$\left\langle \frac{dE_\mu}{dX} \right\rangle = -\alpha - \xi E_\mu \ . \tag{8.36}$$

The constants α and ξ in Eq. 8.36 describe the energy losses and the catastrophic losses respectively in the rock. These two constants are computed as

$$\begin{aligned} \alpha &= 2.033 + 0.077 \ \ln[E_\mu(GeV)] \times 10^3 \ \text{GeV cm}^2 \ \text{gm}^{-1} \ , \\ \xi &= 2.033 + 0.077 \ \ln[E_\mu(GeV)] \times 10^{-6} \ \text{GeV cm}^2 \ \text{gm}^{-1} \ , \end{aligned} \tag{8.37}$$

for $E_\mu \ \leq \ 10^6$ GeV [367] and otherwise [368]

$$\begin{aligned} \alpha &= 2.033 \times 10^{-3} \ \text{GeV cm}^2 \ \text{gm}^{-1} \, , \\ \xi &= 3.9 \times 10^{-6} \ \text{GeV cm}^2 \ \text{gm}^{-1} \, . \end{aligned} \tag{8.38}$$

The muon events from CC interactions can be computed by replacing $\frac{dN_\nu}{dE_\nu}$ in Eq. 8.29 by $F^4_{\nu_\mu}$ from Eq. 8.26 and $F^3_{\nu_\mu}$ from Eq. 8.28 for the cases of 4-flavour and 3-flavour scenario respectively. As mentioned earlier, the muon events from the decay of τ are also included in the present calculation. These τs are produced via CC interaction of ν_τ at Earth through the process $\nu_\tau + N \to \tau + X$

This process of τ decay in this context is realised by the consideration that τ decays in a very short path length via $\tau \to \nu_\tau + \mu$ and the process occurs with the probability of 0.18 [369, 370]. Using Eqs. 8.29 - 8.38 the number of such muon events can be computed.

For the shower events, CC interaction of ν_e as also the NC interactions of all three active flavours

are taken into coniderations. For the shower case, the oscillation is made for the whole detector volume V and any specific track event is neglected. For the shower case the event rate is given by

$$S_{\rm sh} = V \int_{E_{\rm thr}}^{E_{\nu\rm max}} dE_\nu \frac{dN_\nu}{dE_\nu} P_{\rm shadow}(E_\nu) \int dy \frac{1}{\sigma^i} \frac{d\sigma^i}{dy} P_{\rm int}(E_\nu, y) \ . \tag{8.39}$$

In the above expression, $\sigma^i = \sigma^{\rm CC}$ for the EM shower and $\sigma^i = \sigma^{\rm NC}$ when ν_e, ν_μ NC interactions are considered. The probability that a shower produced by the neutrino interactions is given by

$$P_{\rm int} = \rho N_A \sigma^i L \ , \tag{8.40}$$

where ρ is the matter density and L is the length of the detector. For the case of shower events $\frac{dN_\nu}{dE_\nu}$ in Eq. 8.39 is replaced by $F^4_{\nu_e}$, $F^4_{\nu_\mu}$, $F^4_{\nu_\tau}$ from Eq. 8.26 and $F^3_{\nu_e}$, $F^3_{\nu_\mu}$, $F^3_{\nu_\tau}$ from Eq. 8.28 for the cases of 4-flavour and 3-flavour scenario respectively.

8.2.4 Detection of Neutrinos from a Single GRB

The estimation of muon events from the neutrinos for the case of a single GRB, similar approach (diffuse GRB case) is followed. But the expression for flux for a single GRB is different from that of the case for diffuse GRBs. For the single GRB case, the zenith angle θ_z (used in Eq. 8.30) for a particular GRB remains fixed. Thus the expression for $P_{\rm shadow}$ is now modified as

$$P_{\rm shadow} = \exp[-z(\theta_z)/L_{int}(E_\nu)] \ . \tag{8.41}$$

The Earth density should also be accordingly computed for a fixed θ_z.

For the case of isotropic emission from the source, the secondary neutrino flux $\frac{dN_{\nu 0}}{dE_{\nu\rm obs}}$ is given

by

$$\frac{dN_{\nu 0}}{dE_{\nu \rm obs}} = \frac{dN_\nu}{dE^s_\nu}\frac{1}{4\pi r^2(z')}(1+z') \ , \tag{8.42}$$

where the comoving radial coordinate distance ($r(z')$) of the source is expressed as

$$r(z') = \frac{c}{H_0}\int_0^{z'} \frac{dz''}{\sqrt{\Omega_\Lambda + \Omega_m(1+z'')^3}} \ . \tag{8.43}$$

In the above two equations, z' is the redshift of the GRB and $E_{\nu \rm obs}$ is the observed neutrino energy at the Earth. The secondary neutrino flux $\frac{dN_{\nu 0}}{dE_{\nu \rm obs}}$ (mentioned in Eq. 8.42) is the total number of secondary neutrinos emitted from a single GRB at redshift z' per unit observed neutrino energy $E_{\nu \rm obs}$ that are incident on the Earth. In a spatially flat Universe, $\Omega_\Lambda + \Omega_m = 1$, where Ω_Λ is the dark energy component normalized to the critical energy density of the Universe and Ω_m is the contribution of the matter density to the energy density of the Universe in units of the critical energy density. The speed of light is denoted as c and H_0 is the Hubble constant at the present epoch. The values of the constants adopted in our calculation are $\Omega_\Lambda = 0.684$, $\Omega_m = 0.316$ and $H_0 = 67.8$ Km sec^{-1} Mpc^{-1}.

The neutrino spectrum $\frac{dN_\nu}{dE^s_\nu}$ in Eq. 8.42 is expressed as

$$\frac{dN_\nu}{dE^s_\nu} = N \times \min\left(1, \frac{E_\nu}{E^{\rm brk}_\nu}\right)\frac{1}{E^2_\nu} \ . \tag{8.44}$$

In the above, N is the normalization constant and $E^{\rm brk}_\nu$ is the neutrino spectrum break energy. The latter ($E^{\rm brk}_\nu$) is a function of the Lorentz factor of the GRB (Γ), photon spectral break energy ($E^{\rm brk}_{\gamma,\rm MeV}$) and is given by the expression,

$$E^{\rm brk}_\nu \approx 10^6 \frac{\Gamma^2_{2.5}}{E^{\rm brk}_{\gamma,\rm MeV}} \rm GeV \ , \tag{8.45}$$

where, $\Gamma_{2.5} = \Gamma/10^{2.5}$. The normalization constant N can be written as

$$N = \frac{E_{\rm GRB}}{1 + \ln(\mathrm{E}^{\rm s}_{\nu \rm max}/\mathrm{E}^{\rm brk}_{\nu})} \ . \tag{8.46}$$

In the above $E^{s}_{\nu \rm max}, E^{s}_{\nu \rm min}$ respectively represent lower and upper cutoff energy of the neutrino spectrum. At the time of neutrino emission from a single GRB the total amount of energy released is $E_{\rm GRB}$, which is 10% of the total fireball proton energy.

With the neutrino flux from a single GRB computed using Eqs. 8.44 - 8.46, the same methodology as in the diffuse GRB case is now followed to obtain the muon and shower yield at a square kilometer detector such as IceCube.

8.3 Calculations and Results

In this Section, the calculations and results for the neutrino induced muons and the shower events as estimated for a $\rm Km^2$ detector are described. The UHE neutrinos considered here are a) from diffused neutrino flux and b) from a single GRB. As mentioned earlier, the computations for neutrino induced muons are done with both four and three flavour cases.

8.3.1 Diffused Neutrino Flux

The possible secondary muon and shower yields at a 1 $\rm Km^2$ detector such as IceCube for the cases of (3+1)-flavour as well as 3-flavour UHE neutrinos from distant GRB sources are calculated by using Eqs. 8.20 - 8.28 and Eqs. 8.29 - 8.40. The similar estimations are made for both 4-flavour and 3-flavour UHE neutrinos from single GRB sources by solving Eqs. 8.20 - 8.28 and Eqs. 8.41 - 8.46. The Preliminary Earth Reference Model from [366] is employed for Earth matter density profile. The νN interaction cross-sections including CC, NC and their sum are adopted from [362].

Waxman-Bahcall [170, 361] flux is used for diffuse GRB case and the detector threshold energy $E_{\rm thr}$ is taken to be $E_{\rm thr} = 1$ TeV. In the present calculations $E_{\nu \rm max}$ = 10^{11} GeV is assumed.

For the purpose of this analysis, a ratio R is defined as the ratio of the muon and the shower events, so that

$$R = \frac{T_\mu}{T_{\rm sh}} \ , \tag{8.47}$$

where

$$\begin{aligned} T_\mu &= S(\text{for } \nu_\mu) + S(\text{for } \nu_\tau) \\ T_{\rm sh} &= S_{\rm sh}(\text{for } \nu_e \text{ CC interaction}) \\ &\quad + S_{\rm sh}(\text{for } \nu_e \text{ NC interaction}) \\ &\quad + S_{\rm sh}(\text{for } \nu_\mu \text{ NC interaction}) \\ &\quad + S_{\rm sh}(\text{for } \nu_\tau \text{ NC interaction}) \end{aligned} \tag{8.48}$$

and the quantities S and $S_{\rm sh}$ are defined in Eq. 8.29 and Eq. 8.39 respectively. In 4-flavour and 3-flavour scenario the above mentioned ratio R is denoted as R_4 and R_3 respectively.

In order to address how the neutrino induced muon and the shower fluxes from distant UHE sources namely diffused GRB are affected in case a sterile neutrino exists in addition to the three active neutrinos, a comparison of the ratio R between the (3+1) scenario and 3 active neutrino scenario is made. The computations are done for two different sets of value of the sterile mixing angles namely θ_{14}, θ_{24} and θ_{34} while the mixing angles for 3 neutrino mixing are adopted as the current best fit values for them. As mentioned earlier, the oscillatory part in the oscillation probability expression that involves the parameter Δm^2 is averaged out due to astronomical baseline length. The limits on four flavour mixing angles ($\theta_{14},\ \theta_{24},\ \theta_{34}$) are chosen following the 4-flavour analyses of different experimental groups such as MINOS, Daya Bay, NOνA, Bugey [138, 148, 154–159, 174] The upper limits on θ_{24} and θ_{34} obtained from NOνA [155] are $\theta_{24} \leq 20.8^0$ and $\theta_{34} \leq 31.2^0$ assum-

Table 8.1: Comparison of the muon to shower ratio for a diffused GRB neutrino flux (Waxman-Bahcall flux) for the 4-flavour (3+1) case with the same for 3-flavour case for two sets of active-sterile neutrino mixing angle. See text for details.

θ_{14}	θ_{24}	θ_{34}	R_4 (in 4f)	R_3 (in 3f)
3°	5°	20°	9.48	1.80
4°	6°	15°	9.68	1.80

ing $\Delta m^2_{41} = 0.5$ eV^2. However according to MINOS analysis [138] $\theta_{24} \leq 7.3^0$ and $\theta_{34} \leq 26.6^0$ for the same value of Δm^2_{41}. IceCube-DeepCore [371] results considering $\Delta m^2_{41} = 1$ eV^2 suggest $\theta_{24} \leq 19.4^0$ and $\theta_{34} \leq 22.8^0$. Therefore, in this Chapter, we vary both θ_{24} and θ_{34} within the limit $2^0 \leq \theta_{24} \leq 20^0$ and $2^0 \leq \theta_{34} \leq 20^0$. The mixing angle θ_{14} is so chosen that $\theta_{14} \leq 4^0$. This is consistent with the results from the combined analysis by MINOS, Daya Bay and Bugey-3 [148] (in the range 0.2 eV^2 $\leq \Delta m^2_{41} \leq$ 2 eV^2). Using these limits on $\theta_{14}, \theta_{24}, \theta_{34}$ the ratio R_4 and R_3 for diffuse flux is computed. In Table 8.1, the computed values of R_4 are furnished for two representative sets of values for θ_{14}, θ_{24} and θ_{34}. The computed values for R_3, the muon to shower ratio for the three flavour case, are also given for comparison. From Table 8.1 it is obvious that the muon yield to shower ratio for four flavour scenario (R_4) increases considerably from the ratio for three flavour case (R_3). For the particular choices in Table 8.1, this increase is more than five times if a fourth sterile neutrino is assumed to be present in nature in addition to the three usual active neutrinos.

It is also explored how the ratio R_4 varies with different values of active-sterile mixing angles. In Fig. 8.1 we show the variations of R_4 with θ_{24} and θ_{34} for two fixed values of θ_{14} namely $\theta_{14} = 1^\circ$ (Fig. 8.1(a)) and $\theta_{14} = 4^\circ$ (Fig. 8.1(b)). From Fig. 8.1 it may be noted that the maximum value of the ratio R_4 is $\sim$ 6 times higher than R_3. So far, the calculations and comparisons of ratios R_4 and R_3 are made by adopting a diffuse GRB UHE neutrino flux given by Waxman-Bahcall [170, 361]. The calculations are repeated for another UHE neutrino flux obtained from the six year IceCube data. From the analysis of the high energy starting events (HESE) data, IceCube observation had furnished a best fit power law for neutrino flux as $E^2\phi(E) =$

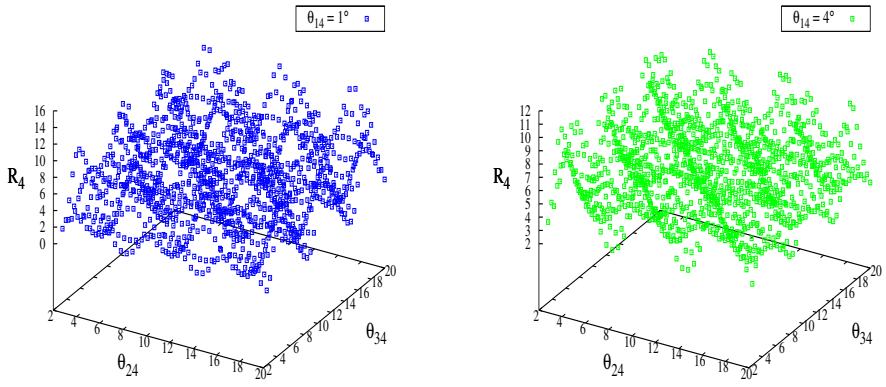

(a) (b)

Figure 8.1: Variation of R_4 with θ_{24} and θ_{34} for (a) $\theta_{14} = 1^\circ$ and (b) $\theta_{14} = 4^\circ$. See text for details.

Table 8.2: Same as Table 8.1, but here the diffused neutrino flux of UHE neutrinos is obtained from the recent analysis of the IceCube (HESE) data. See text for details.

θ_{14}	θ_{24}	θ_{34}	R_4 (in 4f)	R_3 (in 3f)
3°	5°	20°	2.01	0.55
4°	6°	15°	2.04	0.55

$2.46 \pm 0.8 \times 10^{-8} \left(\frac{E}{100\text{TeV}}\right)^{-0.92}$ GeV cm^{-2} s^{-1} sr^{-1}. Therefore, for one component fit (that is no broken power law) the neutrino flux $\phi(E) \sim E^{-\gamma}$, with the index $\gamma = 2.92$. In fact, their best fit spectral index is $\gamma = 2.92^{+0.33}_{-0.29}$. The ratios R_4, R_3 etc. are computed for this flux also. This is to be noted, following the astrophysical neutrino results from IceCube [372] that the neutrino above energy 60 TeV is to be considered for such calculations.

The results are furnished in Table 8.2. From the table it is seen that the ratio R_4 from the 4-flavour case ~ 2 for the chosen values of $\theta_{14}, \theta_{24}, \theta_{34}$. In contrast the track to shower ratio R_3 reduces to ~ 0.55 when 3-flavour case is employed. Although the ratios are different from what is given in Table 8.1 (with Waxman-Bahcall flux), yet the track to shower ratio R_4 is ~ 3.7 times than R_3. In Figs. 8.2(a), 8.2(b) the variations of R_4 with θ_{24} and θ_{34} are given for $\theta_{14} = 1^\circ$ and $\theta_{14} = 4^\circ$

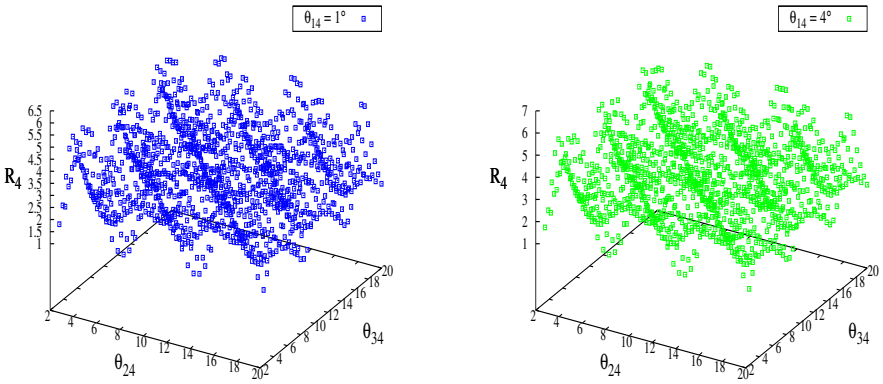

(a) (b)

Figure 8.2: Variation of R_4 with θ_{24} and θ_{34} for (a) $\theta_{14} = 1^\circ$ and (b) $\theta_{14} = 4^\circ$ (UHE neutrino diffused flux has been taken from the IceCube HESE six year data). See text for details.

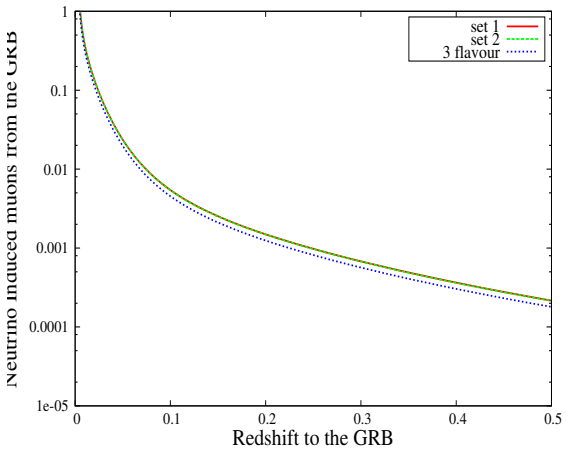

Figure 8.3: Variation of the neutrino induced muons from single GRBs with different redshifts at a fixed zenith angle $\theta_z = 10^\circ$. “set 1" and “set 2" correspond to the two sets of values for active-sterile mixing angles given in Table 8.1.

respectively.

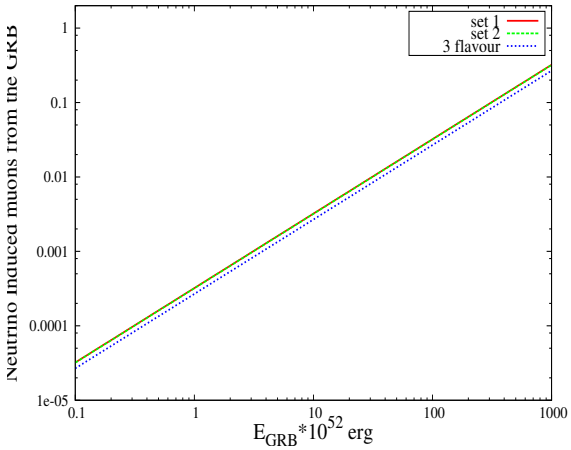

Figure 8.4: Variation of the neutrino induced muons from the GRB with different GRB energies at a fixed zenith angle ($\theta_z = 10^\circ$). “set 1" and “set 2" are as in Table 8.1.

8.3.2 Single GRB

A particular GRB occurs at a fixed zenith angle and at a definite redshift with respect to an observer at Earth [3] [4]. We have used two sets of active-sterile mixing angles for our calculations as given in Table 8.1 (and Table 8.2). The active neutrino mixing angles are fixed at their current experimental values. With these sets of parameters the neutrino induced muons are estimated in a Km^2 detector for the UHE neutrinos from a GRB at different redshifts. The results are obtained using Eqs. 8.41 - 8.46 and Eqs. 8.11 - 8.40. The values of the parameter such as the Lorentz factor Γ, photon spectral break energy $E^{\rm br}_{\gamma,\rm MeV}$ etc. required to calculate the neutrino flux from a single GRB are chosen as $\Gamma = 50.12$ and $E^{\rm br}_{\gamma,\rm MeV} = 0.794$. These values are adopted from Table 1 of ref [365]. The results are shown in Fig. 8.3. In Fig. 8.4 the variations of the neutrino induced muons with different GRB energies are shown. From both Fig. 8.3 and Fig. 8.4 it can be observed that the case of four flavour mixing cannot be distinguished from three flavour mixing as there is no significant deviation as observed in the case of diffused flux discussed earlier in Sect. 8.3.1.

[3] For the case of single GRB, although in principle one can make similar computation for R_4 and/or R_3 but being just a single burst event, simultanity of track and shower events may be difficult to determine.

[4] For the case of single GRBs, the neutrino induced muon events are estimated for both 4 and 3-flavour cases and the results are then compared.

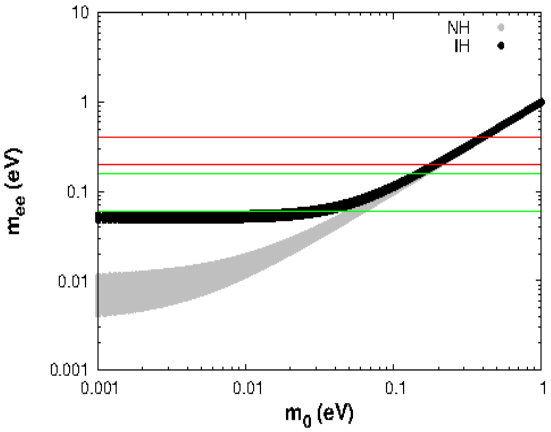

Figure 8.5: The variation of the effective Majorana neutrino mass with the lightest neutrino mass for normal hierarchy and inverted hierarchy in 4-flavour (3 active + 1 sterile) scenario. The pair of red lines and the pair of green lines indicate the limits obtained from different experiments (see text). For lower m_0 only inverted hierarchy satisfies experimental limits.

8.4 Neutrinoless Double Beta Decay in 3+1 Scenario

The studies made in the previous Section do not provide any information about the mass of the sterile neutrino or more precisely of Δm^2_{41} (Δm^2_{43}), for normal (inverted) hierarchy of neutrino mass. This is obvious as study of GRB fluxes involve large distance and mass squared oscillation is therefore averaged out. However, sterile neutrino in the present $3+1$ framework can affect the phenomenon of neutrinoless double beta decay. The effective Majorana mass for observable neutrinoless double beta decay in $3+1$ scenario is given as

$$m_{ee} = \sum_{i=1-4} |U_{ei}|^2 m_i \ , \tag{8.49}$$

where the Majorana phases have been neglected. The above Eq. 8.49 can be rewritten in terms of mixing angles

$$m_{ee} = |c_{14}c_{12}c_{13}|^2 m_1 + |c_{14}s_{12}c_{13}|^2 m_2 + |c_{14}s_{13}|^2 m_3 + |s_{14}|^2 m_4 \ . \tag{8.50}$$

The sterile neutrino with mass m_4 is assumed to be heavier than light active neutrinos. Therefore, the effective Majorana mass in case of normal ordering of active neutrinos is given as

$$\begin{aligned} m_{ee} &= |c_{14}c_{12}c_{13}|^2 m_1 + |c_{14}s_{12}c_{13}|^2\sqrt{m_1^2+\Delta m_{21}^2} + |c_{14}s_{13}|^2\sqrt{m_1^2+\Delta m_{31}^2} \\ &\quad + |s_{14}|^2\sqrt{m_1^2+\Delta m_{41}^2}\ . \end{aligned} \tag{8.51}$$

Similarly for the case of inverted hierarchy of active neutrinos, the expression in Eq. 8.50 can be rewritten as

$$\begin{aligned} m_{ee} &= |c_{14}c_{12}c_{13}|^2\sqrt{m_3^2+\Delta m_{23}^2-\Delta m_{21}^2} + |c_{14}s_{12}c_{13}|^2\sqrt{m_3^2+\Delta m_{23}^2} + |c_{14}s_{13}|^2 m_3 \\ &\quad + |s_{14}|^2\sqrt{m_3^2+\Delta m_{43}^2}\ . \end{aligned} \tag{8.52}$$

Hence, for normal (inverted) hierarchy, m_1 (m_3) is the lightest neutrino mass which will be denoted as m_0 for simplicity. From Eqs. 8.51-8.52, it can be easily observed that the effective Majorana mass m_{ee} depends on new physics involving sterile neutrino mixing angle θ_{14} and mass squared difference Δm_{41}^2 (or equivalently Δm_{43}^2). Here the effects of these parameters on effective Majorana mass for neutrinoless double beta decay are addressed. Since, m_3 is the lightest neutrino in case of inverted hierarchy, $\Delta m_{43}^2 = m_4^2 - m_0^2$ is equivalent to $\Delta m_{41}^2 = m_4^2 - m_0^2$ appearing in the expression of Eq. 8.51 for normal hierarchy. The variation of effective Majorana mass with lightest neutrino mass m_0 is computed and furnished in Fig. 8.5. The mass m_0 is varied within the range 10^{-3} eV $\leq m_0 \leq 1$ eV for both normal and inverted hierarchy of neutrino mass using best fit values of active neutrino mixing angles θ_{12} and θ_{13}. The shaded region shown in gray (black) in Fig. 8.5 corresponds to the normal (inverted) hierarchy of active neutrinos. A conservative limit on mixing angle θ_{14} is considered in the range $0^0 \leq \theta_{14} \leq 4^0$ and the range of Δm_{41}^2 is adopted to be from 0.2 eV^2 to 2 eV^2 consistent with the exclusion limits on θ_{14} obtained from combined results of MINOS, Daya Bay and Bugey-3 experiments ([148] and references therein) for normal hierarchy. Same range of θ_{14} and Δm_{43}^2 are also assumed for the case of inverted hierarchy of neutrino mixing.

From Fig. 8.5, it can be easily observed that for inverted hierarchy (IH), the specified range of m_0, θ_{14} and Δm^2_{43}, effective neutrino mass m_{ee} is almost constant for smaller values of m_0 (0.001 to 0.01 eV). For higher values of m_0, m_{ee} tends to increase proportionally with m_0. Similar trend is observed for normal hierarchy (NH) of neutrino mass when $m_0 \geq 0.1$ eV is considered. However, for smaller values of m_0 (≤ 0.1 eV), the effective neutrino mass m_{ee} in case of normal hierarchy tends to decrease. The observed upper limit on effective Majorana neutrino mass obtained from the combined analysis of KamLAND-Zen [125] and EXO-200 [373] is 0.2-0.4 eV corresponds to the region within the pair of red lines shown in Fig. 8.5. Therefore, in the above specified range NH and IH are indistinguishable. Stringent limit on m_{ee} is further obtained from KamLAND-Zen [126] (region within the horizontal green lines in Fig. 8.5) with $m_{ee} \sim 0.06 - 0.16$ eV probing the near inverted hierarchy regime. From Fig. 8.5 it can be easily observed that lightest neutrino mass m_0 must be larger than 0.1 eV for higher values of m_{ee}. However, for inverted hierarchy, lightest neutrino mass m_0 can be smaller ($\sim$ 0.02 eV) when the limits on m_{ee} from KamLAND [126] is taken into account. It is already mentioned that in the present discussion that the Majorana phases are neglected. However, in principle one should consider all the Majorana phases. Extensive study of effective neutrino mass including all the Majorana phases has been presented in [374] using $\sin^2\theta_{14} = 0.019$ for $\Delta m^2_{41} = 1.7$ eV^2. Vide Ref. [374] for further details and references therein.

8.5 Summary

The posible effects on UHE neutrino signatures obtained from GRB events in a Km^2 detector (such as IceCube) is addressed in case there exists a fourth sterile neutrino in nature in addition to three active neutrinos. The ratio of muon events to the shower events at the Km^2 detector are calculated for both the three flavour and four flavour cases which are denoted as R_3 and R_4 respectively. For this, two sets of UHE neutrino flux have been considered. The first one is the theoretical flux for diffused isotropic UHE neutrinos from GRBs given by Waxman-Bahcall, whereas the other such

flux is adopted from the analysis of the recent IceCube data. Using the present limits on active-sterile mixing obtained from different neutrino experiments along with the active neutrino mixing results, it is found that the maximum value of the ratio of muon events with respect to shower events R_4 can be six to eight times larger for 3+1 mechanism when compared with normal three active neutrino formalism R_3 if the Waxman-Bahcall flux is considered and R_4 can be three to four times of R_3 for the flux given by IceCube 6 year data (HESE data) analysis. Therefore, the present analysis shows that any excess of such events detected in a Km^2 detector over that predicted for three neutrino mixing case can clearly indicate the presence of active-sterile neutrino mixing. Thus UHE neutrinos from distant GRBs can be a probe to ascertain the existence of a sterile neutrino. In addition, neutrino induced muon events are computed from a single GRB in the present framework of 3+1 neutrino and the results are with the three flavour scenario. For a single GRB, with the observed bounds on active-sterile neutrino mixing, there is no significant deviation from three active neutrino results. Therefore, for a single GRB, it is difficult to discriminate between usual three neutrino and possible four flavour (3 active + 1 sterile) formalism. Further studies have been made on the bounds on light neutrino mass in the present four neutrino scheme obtained from neutrinoless double beta decay search results. For normal hierarchy, using the present bounds on active-sterile mixing and the bounds from neutrinoless double beta decay, the order of light neutrino mass has been estimated in this Chapter. It is found that for inverted hierarchy, lightest neutrino mass can be as small as ~ 0.02 eV when bounds from KamLAND is considered.

There are rooms for systematic and detector related uncertainties as also the uncertainty in estimating the GRB neutrino flux. Indeed the analysis of recent IceCube high energy starting event (HESE) data (6 year) estimated the diffused GRB neutrino flux as $E^2\phi(E) = 2.46 \pm 0.8 \times 10^{-8}\left(\frac{E}{100\mathrm{TeV}}\right)^{-0.92}$ $\mathrm{GeV\ cm^{-2}s^{-1}\ sr^{-1}}$. The uncertainty in the spectral index is also estimated to be $2.92^{+0.33}_{-0.29}$ in the same analysis. Uncertainties due to neutrino propagation and interactions inside the Earth, whereas detector and ice uncertainties also effect the observational data. Neutrino propagation inside the Earth is guided by the Earth density profile which in this case is pa-

rameterized by PREM model. In general the uncertainty in PREM model is considered by creating perturbations of the model. It is considered that the density gradient inside the Earth is negative in the core and mantle of the Earth. The local perturbation in the PREM model is not generally taken to be more than 10%. The shower and the track events are recorded by the Digital Optical Modules (DOMs). The uncertainty can arise from the DOMs as well as the ice immediately surrounding the DOMs. The cables attached to the DOMs and unknown local optical conditions can affect the optical efficiency, which in turn induces errors in the event distribution and in the detected energy. The systematic and the statistical error may also creep in for the absorptional coefficients as well as for the optical scattering in the ice. Even the glacial flows of the ice can contribute to the uncertainty due to the ice. These uncertainties affect the light deposited by the LED flashers in the DOMs. A Monte Carlo analysis of such ice uncertainties shows a $\sim 10\%$ variations [375]. The column of ice at the immediate vicinity of the DOMs may have different optical properties because of the possible trapping of gas during refreezing after their installation. This can induce an additional uncertainty in recording the actual events. The detailed analysis and comparisons with the Monte Carlo simulations is discussed in [375]. But when one evaluates a quantity from measurements which expressed in terms of the ratios of two observables, such as the one (track to shower ratio) considered in this Chapter, some of the errors are expected to be cancelled.

CHAPTER 9

IMPLICATIONS OF A PROTON BLAZAR INSPIRED MODEL ON CORRELATED OBSERVATIONS OF NEUTRINOS WITH GAMMA-RAY FLARING BLAZARS

The detection of the neutrino events IceCube-170922A, 13 muon neutrino events observed in 2014-2015 and IceCube-141209A by IceCube observatory from the Blazars, namely TXS 0506+056, PKS 0502+049/TXS 0506+056 and GB6 J1040+0617 respectively in the state of enhanced gamma-ray emission, indicates the acceleration of cosmic rays in the blazar jets. The photo-meson ($p\gamma$) interaction cannot explain the IceCube observations of 13 neutrino events. The non-detection of broadline emission in the optical spectra of the IceCube blazars, however, question the hadronuclear (pp) interaction interpretation through relativistic jet meets with a high density cloud. In this Chapter, a proton blazar model is investigated where non-relativistic protons under the charge neutrality condition of the blazar jet can be a viable target for pp interaction with shock-accelerated

protons, and describe the observed high energy gamma-rays (γ-rays) and neutrino signal from the said blazars. This is explored that the model is capable of explaining consistently, the observed electromagnetic (EM) spectrum in combination with the appropriate number of neutrino events from the corresponding blazars.

9.1 Introduction

The IceCube Neutrino Observatory reported the detection of a few reconstructed high energy (TeV energy and above) neutrino events in spatial coincidence with a couple of known γ-ray blazars which provide the first direct identification of sources of high energy cosmic rays. Gamma-ray blazars are a class of Active Galactic Nuclei (AGN) with powerful relativistic jets and are oriented close to the line of sight of the observer. These could very well contribute to the diffuse flux of high energy neutrinos detected by IceCube [376]. Blazars are usually sub-classified into BL Lac objects and flat spectrum radio quasars (FSRQs), depending on the emission line properties [377]. A common feature of the non-thermal EM spectral energy distribution (SED) of blazars is the double-hump structure $-$ one at the IR/optical/UV or X-ray regime and the other at high energy γ-ray bands. The lower energy bump is usually believed to produce from synchrotron radiation of primary electrons while most popular explanation of higher energy hump (the second hump) is inverse Compton (IC) scattering of synchrotron or external photons [378–380]. The leptonic scenarios, however, cannot explain some observed characteristics such as very fast variability almost in all observed bands [381, 382].

The first detection of cosmic ray sources happens on 22 September, 2017 when the IceCube collaboration observed a high energy muon neutrino event IceCube-170922A of energy ~ 290 TeV [383, 384] coming from the direction of the sky location of the known blazar TXS 0506+056, a BL Lac object [383, 385]. A follow-up observation by the Fermi Large Area Telescope (LAT) Collaboration [386] revealed that the γ-ray source TXS 0506+056 blazar was in a state of enhanced

emission in GeV energies with day-scale variability [387] on September 28, 2017. A significant very high energy γ-ray signal has been observed by the Major Atmospheric Gamma Imaging Cherenkov (MAGIC) Telescopes [388] with energies up to about 400 GeV on this day. As high energy neutrinos are believed to be produced only in hadronic processes, the observed association of the neutrino event with the γ-ray flaring blazar TXS 0506+056 has opened a new window to study the origin of cosmic rays in blazars using multimessenger astronomy.

After the discovery of TXS 0506+056 blazar flare, IceCube Collaboration, on reanalysis of archival 9.5 years of IceCube data at the position of TXS 0506+056 reported significant evidence for a flare of 13 muon neutrino events during September 2014 and March 2015 [383]. Assuming a power law distribution of the signal between 32 TeV and 3.6 PeV energy range, a statistical significance 3.5σ excess over the atmospheric neutrino background was found during a 158-day box-shaped time window from MJD 56937.81 to MJD 57096.21 [383]. It had also been noticed that time window of neutrino flare, the blazar TXS 0506+056 was in the quiescent state of both the radio and GeV emission [389]. A nearby FSRQ blazar, PKS 0502+049 which is only $\sim 1.2^0$ far from TXS 0506+056, was in a state of enhanced γ-ray emission state just before and after the period of the neutrino excess in 2014$-$2015 [389, 390]. Thus, the neutrinos produced in the jet of PKS 0502+049 blazar could have possible contribution to such neutrino flare in $2014 - 2015$ since PKS 0502+049 is spatially consistent with directional uncertainties of such observed muon neutrinos.

In addition, the IceCube Observatory reported the detection of a high energy neutrino event, designated as IceCube-141209A [391] which is in spatial coincidence with another known γ-ray blazar, GB6 J1040+0617 with the coincidence detection probability by chance is just 30%. The observed association of the neutrino suggests that the blazar GB6 J1040+0617 can be another plausible neutrino source candidate.

These observations suggest the blazars to be a common origin of both high energy γ-rays and neutrinos. Therefore, their production mechanisms in blazars are very relevant. The high energy neutrinos can be produced either in lepto-hadronic ($p\gamma$) or in pure hadronic (pp) interactions. The

high energy neutrinos and TeV γ-rays (totally or partially) are produced in the former scenario through the interaction of blazar accelerated cosmic rays with surrounding EM radiation whereas in the latter scenario they are produced in the interaction of the blazar accelerator cosmic rays with the ambient matter. Another issue is the maximum energy of the accelerated particles in the detected sources that led to the creation of such high energy neutrinos together with observed EM radiation from the sources. To this end, a proton blazar model in Ref. [392] is considered for this Chapetr. This proton Blazar model can describe consistently the observed high energy γ-rays and neutrino signal from the blazar TXS 0506+056 [392]. In this Chapter, we would like to demonstrate that this proton blazar model can consistently explain the spectral behavior of observed higher energy bump of the EM SED along with the observed association of neutrinos from all the three IceCube blazars at the flaring stage. Such a scenario appears to be more realistic than the scenario of the cloud-in-jet model as we discuss later.

9.2 The models of γ-rays and Neutrinos Production for the Blazars Probed by IceCube

There are efforts to interpret the production of the detected neutrino events together with the EM observations from TXS 0506+056. A common feature of all the proposed models is that protons are accelerated along with electrons to relativistic energies in the acceleration sites. The protons then interact with γ-rays or with ambient matter in blazar environment via $p\gamma$ interaction [385, 387, 393, 394] and/or pp interaction [395, 396] to produce high energy (HE) events. Ansoldi *et al.* (2018) [385] described the detected neutrino event along with the EM observations from the said blazar by assuming a dense field of external low energy photons originating in a possible structured-layer surrounding the jet as targets for photohadronic interactions. Keivani *et al.* (2018) [387] assumed a hybrid leptonic scenario of the blazar TXS 0506+056 where the production of high energy gamma-rays was described by external inverse Compton processes and high energy neutrinos are accounted

via a radiatively sub-dominant hadronic component. The said observation was interpreted recently in Gao *et al.* (2019) [393] by involving a compact radiation core for high photohadronic interaction rates.

In the hadronic (pp) interaction scenario, the high thermal plasma density is required for efficient high energy $\gamma-$ray production in AGN jet. Recently, Liu *et al.* [395] described the observed EM and neutrino fluxes from the blazar TXS 0506+056 by assuming the presence of clouds in the vicinity of the supermassive black hole (SMBH) that provides targets for inelastic pp collisions once they enter the jet. However, the non-detection of the broadline region (BLR) emission from TXS 0506+056 and other BL Lac objects [387] create doubt on the presence of BLR clouds in the vicinity of the SMBH of TXS 0506+056 [387]. The model by Murase *et al.* [397] can naively explain both of the 2017 and 2014-2015 neutrino flares of TXS 0506+056 when effective optical depth to the photodisintegration process is taken 0.1 and ≥ 1 respectively.

The composition of the bulk of the jet medium is not clearly known. For high luminous blazars, the proton component of plasma is necessary as suggested by some author e.g, Celotti & Fabian (1993) [398], Ghisellini *et al.* (2010) [399], in order to maintain the radiated power which would not exceed that carried by jet. In the proton blazar model in Ref. [392] by Banik *et al.*, the non-relativistic protons that come into existence under the charge neutrality condition of the blazar jet can offer sufficient target matter for pp interaction with shock-accelerated protons [392]. This model could explain simultaneously the EM observations and neutrino events from TXS 0506+056. This is to demonstrate that this model can well describe along with TXS 0506+056 results the 13 muon neutrino events at IceCube mentioned earlier.

9.3 The Flux Estimation in the Proton Blazar Model

The proton blazar model is described in Ref. [392]. In this proton blazar framework, a broken power law energy distribution is assumed for accelerated relativistic electrons in the blazar jet to

explain the low energy bump of the SED by synchrotron radiation and can be written as [392, 400]

$$\begin{aligned} N'_e(\gamma'_e) &= K_e \gamma'^{-\alpha_1}_e \qquad \text{if} \quad \gamma'_{e,min} \leq \gamma'_e \leq \gamma'_b \\ &= K_e \gamma'^{\alpha_2-\alpha_1}_b \gamma'^{-\alpha_2}_e \quad \text{if} \quad \gamma'_b < \gamma'_e \leq \gamma'_{e,max} \ , \end{aligned} \tag{9.1}$$

where α_1 and α_2 are the spectral indices before and after the spectral break at Lorentz factor γ'_b and $\gamma'_e = E'_e/m_e c^2$ is the Lorentz factor of electrons of energy E'_e. The normalization constant K_e can be found using the relation [392, 401]

$$L'_e = \pi R'^2_b \beta_j c \int_{\gamma'_{e,min}}^{\gamma'_{e,max}} m_e c^2 \gamma'_e N'_e(\gamma'_e) d\gamma'_e \ , \tag{9.2}$$

where L'_e represents the kinetic power of accelerated electrons in the comoving blazar jet frame. The energy density and number density of relativistic ('hot') electrons are $u'_e = \int m_e c^2 \gamma'_e N'_e(\gamma'_e) d\gamma'_e$ and $n'_{e,h} = \int N'_e(\gamma'_e) d\gamma'_e$ respectively.

It is often considered that all the electrons in such a scenario undergo Fermi acceleration. However, as pointed out by Eichler and Waxman [402] in the context of γ-ray bursts that the exact fraction of electrons (χ_e) participated in diffusive shock (Fermi) acceleration cannot be evaluated by current observations (the observationally admissible range is $m_e/m_p \leq \chi_e \leq 1$). When thermal ions/electrons encounter at any shock barrier, only about 25 $\%$ of them are reflected and when they encounter a shock barrier too weak to reflect them, they cross toward downstream and thus do not participate in the acceleration. A part of the impinged ions/electrons are reflected by shocks and energized up to a certain level via diffusive shock acceleration (DSA) also finally convected downstream. Only a small fraction of injected ions/electrons achieve sufficient energy via DSA and escape toward upstream [403]. Here $\chi_e \approx 10^{-3}$ is adopted, which is within the allowed range and consistent with the hybrid simulation results of DSA by parallel collisionless shock [404, 405]. Such a low value is also supported by the fact that electrons share nearly two order less total energy compare to total energy of protons [405, 406] and as mentioned already that only 0.04 fraction of

protons undergo Fermi acceleration. Note that it is not mandatory to strictly consider such low $\chi_e \sim 10^{-3}$. But, for instance $\chi_e \sim 10^{-2}$, the cosmic ray flux is to be increased appropriately i.e. signifying higher jet power. The total number of electrons including 'hot' and non-relativistic ('cold') electrons is $n'_e = n'_{e,h}/\chi_e$.

The detailed computation technique of EM and neutrino spectra at the Earth from a blazar in the framework of proton-blazar inspired model by Banik *et al.* is given in Ref. [392]. In order to compute the gamma spectrum in present proton blazar model one needs to attain the emissivity. The emissivity $Q_c(\epsilon'_c)$ of produced γ-ray photons of energy E'_c $(= m_e c^2 \epsilon'_c)$ due to IC scattering of primary accelerated electrons with the seed photons is given in [407, 408]. The seed photon density and spectra are estimated directly from the observed photon flux from the blazar [392, 409].

In the proton blazar framework, a power law behavior is assumed for the cosmic ray protons which are supposed to be accelerated to very high energies $E'_p = m_p c^2 \gamma'_p$ in the blob of a blazar jet [410, 411]

$$N'_p(\gamma'_p) = K_p {\gamma'_p}^{-\alpha_p}. \tag{9.3}$$

where γ'_p is the Lorentz factor of accelerated protons, α_p represents the spectral index, K_p indicates the proportionality constant which can be obtained from Eq. 9.2 (as the expression also holds for proton) using the corresponding jet power L'_p for relativistic protons. The energy density of relativistic protons is $u'_p = \int m_p c^2 \gamma'_p N'_p(\gamma'_p) d\gamma'_p$ and $n'_p = \int N'_p(\gamma'_p) d\gamma'_p$ represents the corresponding number density of relativistic protons.

Secondary particles (mainly pions) are produced when the shock accelerated cosmic rays interact with the cold matter (protons) of density $n_H = (n'_e - n'_p)$ in the blob of AGN jet. The emissivity of secondary particles has been calculated in this work following [395, 412–414].

The TeV-PeV γ-rays that may be produced from decay of π^0 is likely to be absorbed due to internal photon-photon ($\gamma\gamma$) interactions [415] while propagating through an isotropic source of low frequency radiation. This is generally assumed to be the observed synchrotron radiation photons produced by the relativistic electron population in the comoving jet. The γ-ray emissivity as a

function of γ-ray energy $E'_\gamma (= m_e c^2 \epsilon'_\gamma)$ has been computed following [413] and the emissivity of escaped γ-rays after internal $\gamma\gamma$-absorption within the source region is estimated following [401].

$$Q'_{\gamma,esc}(\epsilon'_\gamma) = Q'_\gamma(\epsilon'_\gamma).\left(\frac{1-e^{-\tau_{\gamma\gamma}}}{\tau_{\gamma\gamma}}\right). \tag{9.4}$$

where $\tau_{\gamma\gamma}(\epsilon'_\gamma)$ is the optical depth for the interaction and can be obtained as given by [392, 415].

The total number of high energy injected electrons/positrons (Q'_e) in the emission region of AGN jet are the sum of those created in $\gamma\gamma$ pair production and those produced directly due to the decay of $\pi^\pm$ mesons created in pp interaction. These injected electrons/positrons will initiate EM cascades in the AGN blob via the synchrotron radiation and the IC scattering. The secondary pair cascading processes were incorporated following the self consistent formalism of B*ö*ttcher *et al.* (2013) [401] after inclusion of IC mechanism.

The observable differential flux of γ-rays reaching the earth from a blazar can be written as

$$E_\gamma^2 \frac{d\Phi_\gamma}{dE_\gamma} = \frac{V'\delta^2\Gamma_j^2}{4\pi d_L^2}\frac{E'^2_\gamma}{m_e c^2} Q'_{\gamma,esc}(\epsilon'_\gamma).e^{-\tau_{\gamma\gamma}^{EBL}} \ , \tag{9.5}$$

where $Q'_{\gamma,esc}(\epsilon'_\gamma)$ is the total γ-ray emissivity from the blob of AGN jet with photon energies $E'_\gamma = m_e c^2 \epsilon'_\gamma$ in comoving jet frame including all processes stated above (the synchrotron and the IC radiation of accelerated electrons, the γ-rays produced in pp interaction and also the synchrotron photons of EM cascade electrons), $V' = \frac{4}{3}\pi R'^3_b$ is the volume of the emission region, $E_\gamma = \delta E'_\gamma/(1+z)$ [416] relates photon energies in the observer, d_L is the luminosity distance of the AGN from the Earth and comoving jet frame of red shift parameter z respectively. Here we introduce the effect of the absorption by the extragalactic background (EBL) light on γ-ray photons and $\tau_{\gamma\gamma}^{EBL}(\epsilon_\gamma, z)$ is the corresponding optical depth which can be obtained using the Franceschini-Rodighiero-Vaccari (FRV) model [324]. We have used the recent results on neutrino mixing angles to compute flavour ratio of various neutrino flavour after oscillations. As mentioned earlier, in this

Chapter the oscillation probability for a neutrino $|\nu_\alpha\rangle$ of flavour α to a neutrino $|\nu_\beta\rangle$ of flavour β after traversing a baseline distance d_L is given by

$$P_{\nu_\alpha \to \nu_\beta} = \delta_{\alpha\beta} - 4\sum_{j>i} U_{\alpha i}U_{\beta i}U_{\alpha j}U_{\beta j}\sin^2\left(\frac{\pi d_L}{\lambda_{ij}}\right) . \tag{9.6}$$

A neutrino $|\nu_\alpha\rangle$ of flavour α is related to its mass eigenstates $|\nu_i\rangle$ ($i = 1, 2, 3$, for three flavour case) by

$$|\nu_\alpha\rangle = \sum_i U_{\alpha i}|\nu_i\rangle . \tag{9.7}$$

If the neutrinos originate at distant blazar with the flavour ratio

$$\varphi_{\nu_e} : \varphi_{\nu_\mu} : \varphi_{\nu_\tau} = 1 : 2 : 0 ,$$

the flux $\Phi^3_{\nu_\alpha}$ on reaching the earth can be expressed as given in Eq. 8.28 ($\Phi^3_{\nu_\alpha}$ is equivalent to $F^3_{\nu_\alpha}$ of Eq. 8.28) earlier in the Chapter 8.

In this Chapter, the values of three mixing angles are adopted as $\theta_{12} = 32.96^o, \theta_{23} = 40.7^o$ and $\theta_{13} = 8.43^o$ [417] for the computation. Hence, the flavour ratio of neutrino flux reaching at Earth from the distant blazar after neutrino oscillation is evaluated to be $\Phi^3_{\nu_e} : \Phi^3_{\nu_\mu} : \Phi^3_{\nu_\tau} = 1.052 : 0.992 : 0.955$.

The corresponding muon neutrino flux reaching at the earth can be expressed as

$$E_\nu^2 \frac{d\Phi_{\nu_\mu}}{dE_\nu} = \xi . \frac{V'\delta^2\Gamma_j^2}{4\pi d_L^2}\frac{E_\nu'^2}{m_e c^2} Q'_{\nu,pp}(\epsilon'_\nu) , \tag{9.8}$$

where $\xi = 0.992/3$ is a fraction which is considered due to neutrino oscillation and $E_\nu = \delta E'_\nu/(1+z)$ [416] relates neutrino energies in the observer and comoving jet frame respectively. If the differential flux of muon neutrinos is known then the number of expected muon neutrino events at

IceCube detector in time τ can be obtained from the relation

$$N_{\nu_\mu} = \tau \int_{\epsilon_{\nu,min}}^{\epsilon_{\nu,max}} A_{eff}(\epsilon_\nu).\frac{d\Phi_{\nu_\mu}}{d\epsilon_\nu} d\epsilon_\nu \ , \tag{9.9}$$

where A_{eff} be the IceCube detector effective area at the declination of the blazars in the sky [163, 384, 389].

9.4 Gamma-rays and Neutrino Fluxes from the Icecube Detected Blazars

The γ-ray variability time scale of all three blazars can generally be assumed as $t_{ver} \leq 10^5$ s as found for TXS 0506+056 by analyzing the X-ray and γ-ray light curves [387]. The best fit spectral slope of the observed astrophysical neutrinos between 194 TeV and 7.8 PeV by IceCube observatory [418, 419] suggests that the spectral index of the energy spectrum of AGN accelerated cosmic rays can be taken as $\alpha_p \sim -2.1$ for all blazars. As the declination of the all blazars are nearly same, the same A_{eff} as provided by IceCube collaboration at the declination of the TXS 0506+056 in the sky has been usued for all three blazars [163, 384].

9.4.1 GB6 J1040+0617

An energy of 97.4 ± 9.6 TeV was deposited in the IceCube detector by the neutrino event, IceCube-141209A [391]. Although two neighbouring FSRQs 4C+06.41 and SDSS J104039.54+061521.5 of the object GB6 J1040+0617 were found to be positionally located within the 90% uncertainty of the well-reconstructed neutrino IceCube-141209A, they are less favoured as the likely neutrino counterpart [391] because no significant high energy gamma-ray emission was observed at the arrival of IceCube-141209A neutrino event. But being a BL Lac object, GB6 J1040+0617 displays a bright

optical flare detected by the All Sky Automated Survey for Supernovae observatory. This flare is associated with modest γ-ray activity at the neutrino arrival time. The blazar showed an increased γ-ray activity which started a few days before the neutrino event detection (IceCube-141209A) and lasted for 93 days. Moreover, the blazar is located near the equatorial plane at a similar declination as TXS 0506+056. This is the region in the sky for which IceCube is most sensitive to high energy neutrinos. If IceCube-141209A is astrophysical in origin, the low synchrotron peaked γ-ray blazar GB6 J1040+0617 appears to be a plausible neutrino source candidate based on its energetics and multiwavelength characteristics [391]. The redshift of the blazar has been estimated to be $z = 0.73$ [420, 421] and the luminosity distance of the blazar is evaluated to be $d_L \sim 4612.1$ Mpc with a consensus cosmology.

To explain the EM SED of GB6 J1040+0617 over the optical to γ-ray energy range, we have considered here the size of emission region is taken to be $R'_b = 5.2 \times 10^{16}$ cm with bulk Lorentz factor of AGN jet $\Gamma_j = 21$ and Doppler boosting factor $\delta = 30$. These are strongly consistent with the size suggested from the variability, namely $R'_b \lesssim \delta c t_{ver}/(1+z) \simeq 5.2 \times 10^{16}$ cm assuming $t_{ver} \simeq 10^5$ s (similar to that of the blazar TXS 0506+05). These are chosen to explain the SM SED of GB6 J1040+0617.

The lower energy bump of the experimental EM SED data can be explained well by the synchrotron emission of primary accelerated electron's distribution obeying a broken power law as given by Eq. 9.1 with spectral indices $\alpha_1 = 1.45$ and $\alpha_2 = 6.2$ respectively before and after the spectral break with the Lorentz factor $\gamma'_b = 1.35 \times 10^4$. The observed data are best explained when the magnetic field found to be $B' = 0.01$ G and $L'_e = 1.5 \times 10^{43}$ erg/s respectively. Also, IC scattering of primary relativistic electrons with this synchrotron photons comoving with the AGN jet is found to produce the lower part of the high energy bump of the EM spectrum.

Using the Eq. 9.5 the model can well explain the higher energy bump of observed EM SED. The required accelerated primary proton injection luminosity is estimated to be $L'_p = 2.7 \times 10^{45}$ erg/s and the best fitted spectral slope is $\alpha_p = -2.1$ under charge neutrality condition. The cold

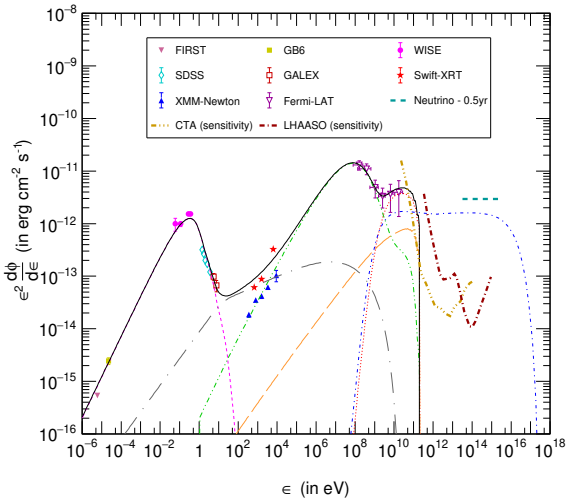

Figure 9.1: The estimated differential energy spectrum of γ-rays and neutrinos reaching the Earth from the blazar GB6 J1040+0617. The pink small-dashed line and green long-dash-double-dotted line indicate the EM spectrum due to the synchrotron emission and the IC emission of relativistic electrons respectively. The red dotted line shows the γ-ray flux produced from pp-interaction after $\gamma\gamma$-absorption. The gray big dash-dotted line and orange big dashed line denote the flux for synchrotron & IC emission by electrons/positrons in EM cascade after $\gamma\gamma$-absorption. The black continuous line represents the estimated overall differential EM SED. The blue small dash-single dotted line indicates the differential muon neutrino flux at the Earth. The yellow dash-triple-dotted line and brown long dash-single dotted line denote the detection sensitivity of the CTA detector for 1000 hours and the LHAASO detector for one year respectively. The expected level and energy range of the neutrino flux reaching the Earth, which are indicated by the cyan long dashed line, produce one muon neutrino in IceCube in 0.5 years, as observed.

proton number density in jet turns out to be 4.2×10^5 particles/cm^3 under charge neutrality condition which provides sufficient targets for hadronuclear interactions with accelerated protons under the assumption of a low acceleration efficiency of electrons in AGN jet of $\chi_e \approx 10^{-3}$. The contributions of the synchrotron and IC emission of the stationary electron/positron pairs produced in EM cascade induced by protons are estimated following [401]. The radiative cooling time due to IC losses inversely with the energy density of photons in comoving jet frame in equilibrium. The IC spectrum from cascade electrons is evaluated by considering seed photons from the observed EM energy

spectrum as a whole and not just using synchrotron seed photons. This leads to smaller IC cooling time and yields higher IC and lower synchrotron fluxes from cascade electrons. The IC process is incorporated with full Klein-Nishima formulation while implementing self consistent formalism of Bottcher *et al.* (2013) [401].

The total jet power is evaluated as $L^k_{jet} = \Gamma_j^2 \beta_j c\pi R_b'^2 \left[u'_e + u'_p + u'_B\right]$ [385] (in terms of relativistic electron, proton kinetic energy and magnetic field). This is computed to be 1.2×10^{48} erg/s and is consistent with the Eddington luminosity of the blazar if it is assumed that the system hosts a supermassive black hole of mass $M_{bh} \gtrsim 9.5 \times 10^9 M_\odot$, like AGN NGC 1281.

The estimated differential γ-ray and neutrino spectrum reaching at Earth from this blazar along with the different space and ground based observations is shown in Fig. 9.1. The XMM-Newton and the Swift-XRT data were collected in May, 2003 and during $2007-2011$ respectively [391]. Note that XMM-Newton and Swift-XRT data are not mutually consistent which may be due to dynamical behaviour of the source. Using Eq. 9.9 the expected muon neutrino event in IceCube detector from the blazar is evaluated to be about $N_{\nu_\mu} = 0.52$ events in 32 TeV and 7.5 PeV energy range in 0.5 years for the flaring very high energy (VHE) emission state with $E'_{p,max} = 20$ PeV.

9.4.2 TXS 0506+056

The high energy neutrino induced muon track detected by IceCube (IceCube-170922A) was found to coincide positionally with the known flaring $\gamma-$ray blazar, TXS 0506+056 with chance coincidence being rejected at a 3σ confidence level [383]. No additional excess of neutrinos was found from the direction of TXS 0506+056 near the time of the alert. Considering a spectral index of -2.13 (-2.0) for the spectrum of diffuse astrophysical muon neutrinos, the most probable energy of the neutrino event was estimated to be 290 TeV (311 TeV) with the 90% C.L. The lower and upper limits are 183 TeV (200 TeV) and 4.3 PeV (7.5 PeV), respectively [383, 385]. The Fermi-LAT observations suggest that the integrated γ-ray flux above 0.1 GeV from TXS 0506+056 elevates to the level $(5.3\pm0.6)\times10^{-7}$ cm$^{-2}s^{-1}$ in the week 4 to 11 July 2017 from its averaged integrated flux

of $(7.6 \pm 0.2) \times 10^{-8}$ cm$^{-2}s^{-1}$ above 0.1 GeV during 2008 to 2017. The Astro-Rivelatore Gamma a Immagini Leggero (AGILE) γ-ray telescope observed a flux of $(5.3 \pm 2.1) \times 10^{-7}$ cm$^{-2}s^{-1}$ during 10 to 23 September 2017. Thus all the extensive follow-up observations revealed TXS 0506+056 was active in all EM bands during the period July 2017 to September 2017 whereas the source was found to be in quiescent stage most of the time based on an archival study of the time dependent γ-ray data over about the last ten years. The redshift of the blazar has been recently estimated to be $z = 0.3365$ [422] and the luminosity distance of the blazar is evaluated to be $d_L \sim 1750$ Mpc [387] with a consensus cosmology. The size of emission region is chosen to be $R'_b = 5.5 \times 10^{16}$ cm with bulk Lorentz factor of AGN jet $\Gamma_j = 30$ and Doppler boosting factor $\delta = 30$. These are strongly consistent with the size inferred from the variability, namely $R'_b \lesssim \delta c t_{ver}/(1+z) \simeq 6.7 \times 10^{16}(\delta/30)(t_{ver}/10^5 s)$ cm [387] to describe the EM SED of TXS 0506+056 over the optical to γ-ray energy range.

This has been found in this Chapter, that the synchrotron emission by primary accelerated electrons, the distribution of which obeys a broken power law, can explain well the lower energy bump of the experimental EM SED data. The IC scattering of primary relativistic electrons with those synchrotron photons comoving with the AGN jet is found to produce lower part of the high energy bump of the EM spectrum. The adopted proton blazar model in which γ-rays are found to produce in interactions of relativistic protons with the ambient cold protons in the blob can explain consistently the observed higher energy bump of observed EM SED data as estimated following Eq. 9.5. The required accelerated primary proton injection luminosity is estimated to be $L'_p = 1.65 \times 10^{45}$ erg/s with the best fit spectral slope of $\alpha_p = -2.1$ and the total kinetic jet power turns out to be 1.5×10^{48} erg/s. The synchrotron & IC emissions of the stationary state electron/positron pairs produced in EM cascade induced by protons are evaluated and are found to explain well X-ray data as shown in Fig. 9.2. The estimated flux in the work from EM cascade for TXS 0506+056 is comparable with that of Liu *et al.* (2018) in which EM radiation absorption was also considered. The proton spectrum considered here is softer and this seems balance such effect of electromagnetic radiation

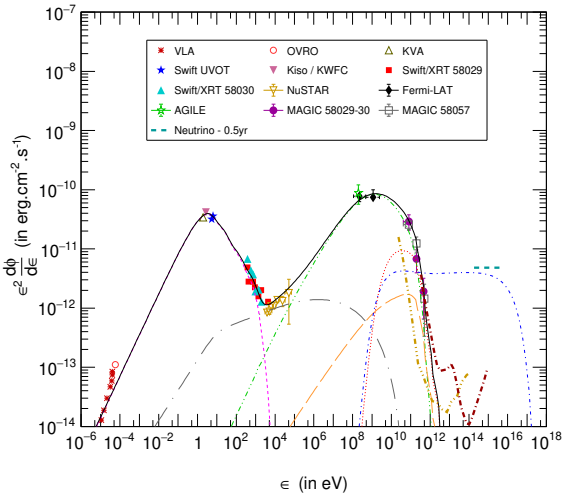

Figure 9.2: Same as Fig. 9.1, but for the blazar TXS 0506+056 during the active phase. The cyan long dashed line represents the expected level and energy range of the neutrino flux at the Earth to produce one muon neutrino event in IceCube in 0.5 years, as observed.

absorption considered by Liu *et al.* (2018). Our estimated cascade synchrotron emission is almost the same to that given by [396]. The effect of softer primary proton spectrum considered by [396] seems compensated by non-incorporation of IC process in his work. The model fitted parameters are shown in Table 9.1.

The calculated differential γ-ray and neutrino spectrum reaching at Earth from this blazar along with the different space- and ground-based observations are given in Fig. 9.2. Using Eq. 9.9 the expected muon neutrino event in IceCube detector from the blazar is found to be about $N_{\nu_\mu} = 0.74$ events in 200 TeV - 7.5 PeV energy range in 0.5 years for the flaring VHE emission state with $E'_{p,max} = 20$ PeV.

9.4.3 TXS 0506+056/PKS 0502+049

Reanalyzing the 9.5 years of data at the position of TXS 0506+056 Icecube collaboration reported significant evidence for a flare of 13 ± 5 muon neutrino events between September 2014 and March

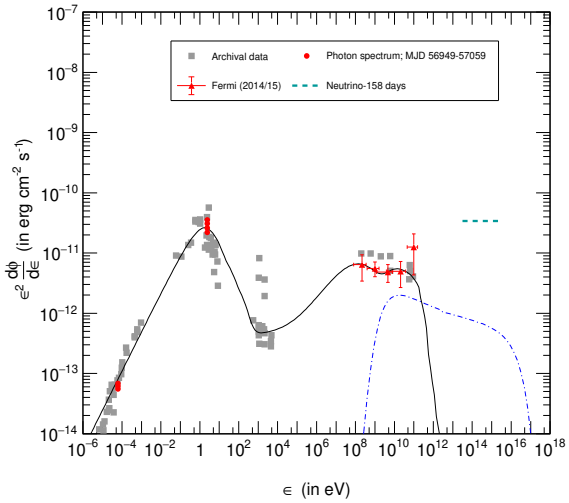

Figure 9.3: Evaluated differential energy spectrum of γ-rays and neutrinos reaching at the Earth from the blazar TXS 0506+056 in quiescent state (during MJD 56949$-$57059). The black continuous line and blue dash-dotted line indicate the estimated overall differential EM SED and neutrino spectrum respectively following our model. The cyan long dashed line represents the expected level and energy range of the neutrino flux reaching Earth to produce 13 muon neutrino events in IceCube in 158 days, as observed.

2015 [383]. Moreover, it is also reported that observed neutrino flare has 3.5σ excess over atmospheric neutrinos in an energy range (68 % C.L.) between 32 TeV and 3.6 PeV. But, the blazar TXS 0506+056 was appeared to be in the quiescent state in both the radio and GeV emission band at the arrival time window of such a neutrino flare [383]. The energy spectrum of detected neutrinos exhibits power law behavior with spectral slop around -2.1 to -2.2 depending on the choice of fitting window [384]. The spectral index of the accelerated proton spectrum has to be chosen accordingly.

The calculated differential γ-ray and neutrino spectrum reaching at the Earth from TXS 0506+056 during the window October 19, 2015 - February 06, 2015 (MJD 56949-57059) along with the different space- and ground-based observations are given in Fig. 9.3. It is found that overall differential multi wavelength EM SED of the blazar in quiescent state can be fitted using the present model with the parameters like Γ, δ, θ and R'_b are kept fixed to that of active state of the blazar. The mag-

netic field has to increase slightly to $B' = 0.068$ G and other parameters are adjusted as $\alpha_1 = 1.7$, $\alpha_2 = 4.5$, $\gamma'_b = 10^4$, $L'_e = 9.1 \times 10^{41}$ erg/s, $L'_p = 6.8 \times 10^{44}$ erg/s and $L^k_{jet} = 6.1 \times 10^{47}$ erg/s. The archival observed X-ray data restrict the spectral slope to $\alpha_p = -2.2$ and the expected muon neutrino event in IceCube detector from the blazar is found to be about $N_{\nu_\mu} = 0.19$ events in the energy range 32 TeV - 3.6 PeV energy range in 158 days.

Thus the blazar TXS 0506+056 which is in a quiescent state during MJD 56949-57059, is unlikely to contribute to the detected neutrino flare during the same period. It is found that a bright source PKS 0502+049 blazar which is located $\sim 1.2^0$ away from TXS 0506+056, had strong GeV flares around the neutrino flare phase in $2014-2015$. The light curve of the blazar displays two major active phases $-$ one in the periods of MJD 56860-56960 and another in the periods of MJD 57010-57120 which are partly overlapped with the 158-days box-shaped time window of IceCube neutrino flare from MJD 56937 to MJD 57096 [423]. The redshift of the blazar has been recently evaluated to be $z = 0.954$ and the luminosity distance of the blazar is estimated to be $d_L \sim 6.4$ Gpc with a consensus cosmology [424].

The EM SED of PKS 0502+049 over the optical to γ-ray energy range during MJD 56860-56960 has been described by considering the size of emission region of $R'_b = 6 \times 10^{16}$ cm with bulk Lorentz factor of AGN jet $\Gamma_j = 30$ and Doppler boosting factor $\delta = 40$. The value of R'_b is strongly consistent with the size inferred from the variability, namely $R'_b \lesssim \delta c t_{ver}/(1+z) \simeq 6.14 \times 10^{16}$ cm assuming $t_{ver} \simeq 10^5$ s (similar to the blazar TXS 0506+05).

During the first active phase, the synchrotron emission of primary accelerated electron's distribution is found to explain well the lower energy bump of the experimental EM SED data of the blazar PKS 0502+049. The required magnetic field and kinematic power of relativistic electrons in blazar jet as given by Eq. 9.2 are $B' = 0.023$ G and $L'_e = 1.7 \times 10^{43}$ erg/s respectively for reproduction of the EM spectrum. The IC scattering of primary relativistic electrons with this synchrotron photons comoving with the AGN jet are found to agree well with the lower part of the high energy bump of the EM spectrum.

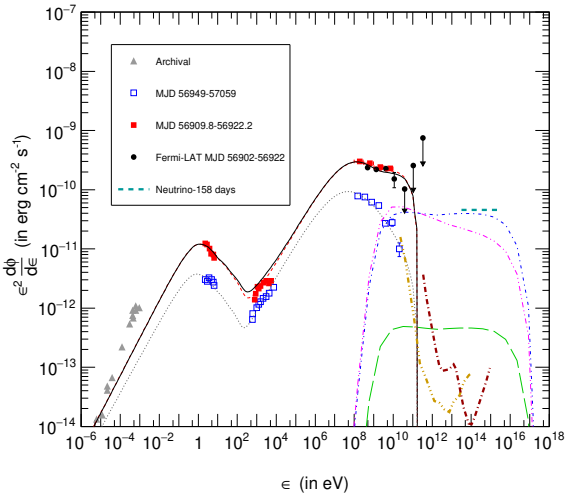

Figure 9.4: The estimated differential energy spectrum of γ-rays and neutrinos reaching the Earth from the blazar PKS 0502+049. The black continuous line (or, red small-dashed line) and blue small-dash-dotted line (or, pink small dash-double-dotted line) indicate the estimated overall differential EM SED and the differential muon neutrino flux at the Earth following our model using $\alpha_p = -2.1$ (or, -2.2) during first active phase in MJD 56909.8$-$56922.2. The gray dotted line and the green very-long dashed line represent the same with $\alpha_p = -2.1$ but for the quiescent state of the blazar during MJD 56949$-$57059. The yellow dash-triple-dotted line and brown long-dash-single-dotted line indicate the detection sensitivity of the CTA detector for 1000 hours and the LHAASO detector for one year, respectively. The cyan long dashed line represents the expected level and energy range of the neutrino flux reaching the Earth to produce 13 muon neutrino events in IceCube in 158 days, as observed.

Following the model as estimated using Eq. 9.5, the observed higher energy bump of observed EM SED data during first active phase can be explained well and the required accelerated primary proton injection luminosity is estimated to be $L'_p = 9.2 \times 10^{45}$ erg/s with the spectral slope of $\alpha_p = -2.1$ to -2.2. Here we have taken acceleration efficiency of the electrons in AGN jet as $\chi_e \approx 10^{-3}$ and the cold proton number density in jet turns out to be 1.4×10^6 particles/cm^3 under charge neutrality condition which provides sufficient targets for hadronuclear interactions with accelerated protons. The expected muon neutrino event in IceCube detector from the blazar is found to be about $N_{\nu_\mu} = 10.85$ and 5.2 events using $\alpha_p = -2.1$ and -2.2 respectively in 32 TeV

- 3.6 PeV energy range in 158 days for the flaring VHE emission state with $E'_{p,max} = 20$ PeV as estimated using Eq. 9.9.

The total jet power in the form of relativistic electron, proton kinetic energy and magnetic field is estimated to be $L^k_{jet} = 8.3 \times 10^{48}$ erg/s. The synchrotron and cascade emissions of the electrons/positrons pairs produced in EM cascade initiated by primary accelerated protons can explain the observed X-ray data.

On the other hand, the quiescent state of the blazar during MJD 56949-57059 found to be of leptonic origin where the observed low and high energy bump of observed EM SED data can be explained well by the synchrotron emission and IC scattering of primary accelerated electron's distribution of injection luminosity $L'_e = 1.3 \times 10^{43}$ erg/s with $B' = 0.017$ G. Because of harder spectral slope at GeV energies of observed EM SED, the second active phase during MJD 57010-57120 may also be originated in leptonic mechanism as suggested by Sahakyan (2019) [423]. The γ-ray and neutrino production via pp interaction may be sub-dominant and hence emission of neutrinos is not significant during this phase. The expected muon neutrino event in IceCube detector from the blazar is found to be about $N_{\nu_\mu} = 0.13$ with $L'_p = 8 \times 10^{43}$ erg/s and $\alpha_p = -2.1$ in 32 TeV - 3.6 PeV energy range in 158 days with $E'_{p,max} = 20$ PeV. The calculated differential γ-ray and neutrino spectrum reaching at Earth from this blazar along with the different space- and ground-based observations are shown in Fig. 9.4. The model fitting parameters to match the EM SED, as well as muon neutrino events from each of the blazars considered here, are shown in Table 9.1.

9.5 Summary

The coincident detection of the neutrino event, IceCube-170922A, 13 muon neutrino events observed in 2014-2015 and IceCube-141209A by IceCube observatory with the γ-ray flaring blazars, TXS 0506+056, PKS 0502+049 and GB6 J1040+0617 respectively provide support to the acceleration of cosmic rays in the blazar jet in diffusive shock acceleration process [383]. The $p\gamma$ reaction

Table 9.1: Model fitting parameters for TXS 0506+056, PKS 0502+049 and GB6 J1040+0617 according to proton blazar model.

Parameters	TXS 0506+056		PKS 0502+049	GB6 J1040+0617
	Active	Quiescent	Active	Active
1.5 δ	30	30	40	30
Γ_j	30	30	30	21
θ	1.9^0	1.9^0	1.35^0	1.7^0
z	0.3365	0.3365	0.954	0.73
R'_b (in cm)	5.5×10^{16}	5.5×10^{16}	6×10^{16}	5.2×10^{16}
B (in G)	0.034	0.068	0.023	0.01
α_1	-1.6	-1.7	-1.7	-1.45
α_2	-4.1	-4.5	-3.8	-6.2
γ'_b	1.8×10^4	10^4	1.3×10^4	1.35×10^4
$\gamma'_{e,min}$	1	1	1	1
$\gamma'_{e,max}$	3×10^5	10^5	1.4×10^5	10^5
L'_e (in erg/s)	2.3×10^{42}	9.1×10^{41}	1.7×10^{43}	1.5×10^{43}
n_H (in cm^{-3})	1.1×10^5	10^5	1.4×10^6	4.2×10^5
α_p	-2.1	-2.2	-2.1	-2.1
$E'_{p,max}$ (in eV)	2×10^{16}	2×10^{16}	2×10^{16}	2×10^{16}
L'_p (in erg/s)	1.65×10^{45}	6.8×10^{44}	9.2×10^{45}	2.7×10^{45}
L^k_{jet} (in erg/s)	1.5×10^{48}	6.1×10^{47}	8.3×10^{48}	1.2×10^{48}
N_{ν_μ}	0.74	0.19	10.85	0.52

is more widely used to explain the emission from blazars with major shortcomings of either low neutrino rates or complex geometry of the blazar jet required. More importantly, the lepto-hadronic model can not reproduce the neutrino flaring events from the direction of TXS 0506+056/PKS 0502+049 during the period 2014-15. On the other hand, the cloud-jet interaction scenario seems unlikely to be a common scenario for neutrino production in all IceCube blazars due to the absence of the broadline emission in the optical spectra of the sources.

In the framework of the proton blazar model, it is apparant that both the low and high energy bump of the multiwavelength EM SED as also the observed neutrino events from the corresponding blazars can be explained consistently with the relative contributions to the total jet power of cold protons, accelerated protons, accelerated electrons and magnetic field obtained based on charge neutrality. PKS 0502+049, the nearby flaring blazar of the TXS 0506+056, is found to contribute

mostly to the neutrino flare observed during 2014-2015 which can not be described by any model from TXS 0506+056 as origin [425].

The calculations in this Chapter suggest that the maximum energy of the cosmic ray particle achievable in the blazars is nearly one order less than the ankle energy of the cosmic ray energy spectrum in the observer frame and is required to explain consistently the observed γ-ray and neutrino signal from the IceCube sources. The upcoming γ-ray experiments like CTA [426] and LHAASO [427] (sensitive up to 100 TeV energies), may throw more light on the physical origin of γ-rays and maximum achievable energy of cosmic rays in AGN jets.

CHAPTER 10

UNPARTICLE DECAY OF NEUTRINOS AND ITS POSSIBLE SIGNATURES AT A Km^2 DETECTOR FOR (3+1) FLAVOUR FRAMEWORK

In this Chapter, we consider a scenario where ultrahigh energy (UHE) neutrinos undergo unparticle decay during its passage from its cosmological source to Earth. The idea of unparticle had been first proposed by Georgi by considering the possible existence of an unknown scale invariant sector at high energies and the unparticles in this sector manifest itself below a dimensional transmutation scale $\Lambda_{\mathcal{U}}$. The possible signatures of such decaying neutrinos to unparticles at a square kilometer detector such as IceCube are explored in this Chapter.

10.1 Introduction

Almost a decade back Georgi [428, 429] proposed the probable existence of a scale invariant sector. At a very high energy scale this scale invariance sector and the Standard Model (SM) sector may coexist and the fields of these two sectors can interact via a mediator messenger field of mass scale $M_{\mathcal{U}}$. This is the connector sector [430]. At low energies however, the scale invariance is manifestly broken since SM particles have masses. At a scale below $M_{\mathcal{U}}$ such interactions are suppressed by inverse powers of $M_{\mathcal{U}}$ and the effective theory at low energy can be expressed by a non-renormalizable operator. Note that in a scale invariant scenario the particle masses are zero and in the real world, the scale invariance is manifestly broken. It is observed by Georgi [428, 429] that at low energies such a scale invariance sector of scale dimension $d_{\mathcal{U}}$ manifests itself as non-integral number $d_{\mathcal{U}}$ of massless invisible particles called “unparticles". It is to be noted that in 4-D Quantum Field Theory (QFT), the conformal invariance is broken by renormalization group effects. But such a conformal invariance in 4-D can be described by a vector like non-Abelian gauge theory studied by Banks and Zaks (BZ) [431]. In this theory the scale invariant sector can flow to low energies with nontrivial infrared fixed points and the theory may be extended to low energy. Following Georgi's proposal, the interaction operator $\mathcal{O}_{\rm BZ}$ for the BZ fields with the operator $\mathcal{O}_{\rm SM}$ for SM fields can generically be represented by $\mathcal{O}_{\rm BZ}\mathcal{O}_{\rm SM}/(M_{\mathcal{U}}^k), k > 0$. In a massless non-Abelian gauge theory, the radiative corrections in the scale invariant sector induce dimensional transmutation [432] at another energy scale. As a result, another scale $\Lambda_{\mathcal{U}}$ appears and Georgi argued [428, 429] that below this scale the BZ field and field operator $\mathcal{O}_{\rm BZ}$ matches onto the unparticle operator $\mathcal{O}_{\mathcal{U}}$ with non-integral scaling dimension $d_{\mathcal{U}}$. Thus below $\Lambda_{\mathcal{U}}$, one has new low energy operator of the form $C_{\mathcal{O}_{\mathcal{U}}}\Lambda_{\mathcal{U}}^{d_{BZ}-d_{\mathcal{U}}}\mathcal{O}_{\rm SM}\mathcal{O}_{\mathcal{U}}/(M_{\mathcal{U}}^k)$, where $C_{\mathcal{O}_{\mathcal{U}}}$ is to be fixed from the matching conditions of BZ operator $\mathcal{O}_{\rm BZ}$ onto the unparticle operator $\mathcal{O}_{\mathcal{U}}$. In this operator, $d_{\rm BZ}$ denotes the scaling dimension of the operator $\mathcal{O}_{\rm BZ}$. Since at low energies BZ fields decouple from the SM fields, the infrared fixed points of the unparticles will remain unaffected by the couplings of the unparticle

and the SM particles. The unparticle physics gives rise to rich phenemenology of many unexpected processes. Several authors in the literatures used the concept of unparticles in a wide range of particle physics issues. For example, Kikuchi and Okada [433] addressed the unparticle couplings with Higgs and gauge bosons. The interactions of unpartilces with SM particles are addressed by various other authors [434–457]. The issues of dark matter and dark energy are discussed in the unparticle framework in the works of Refs. [458], [459]. We consider the unparticle decay of neutrinos and explore its consequences for UHE neutrinos from a distant Gamma Ray Bursts (GRBs). For this case, the decay length should be $\sim$ tens of Mpc for such decay is to be significant. Here we investigate the unparticle decay of neutrinos along with the mass-flavour suppression due to passage of such UHE neutrinos from a distant GRB to an Earth bound detector such as IceCube [372]. We also consider a four flavour scenario for the neutrino species where we assume a 4th sterile species (ν_s) along with the usual 3 active neutrinos (ν_e, ν_μ, ν_τ). The analyses of the data for reactor neutrinos, considering the existence of a fourth sterile neutrino along with three active neutrinos from the experiments (short and long baselines) such as MINOS [137–148], Daya Bay [127–133], Bugey [174] etc. have given bounds on the mixing parameters for active sterile mixing. We calculate the neutrino induced muon yield in such a scenario at a square kilometer detector such as IceCube.

10.2 UHE Neutrino Fluxes from a Single GRB with Neutrino Decay to Unparticles

GRBs [170] are some of the most energetic events in the Universe. We have considered the relativistically expanding fireball model, which is one of the few models that has been put forth to explain why GRBs tend to have such high energy levels. In this model, the Fermi mechanism in shocks developing in the GRB outflow can accelerate protons to energies as high as 10^{20} eV. These highly energetic accelerated protons interact with photons via a cosmic beam dump process

inside the fireball and the pions are produced through these interactions. In this Chapter, we consider the UHE neutrinos which are produced by the decay of these pions and the decay process is $\pi^+ \rightarrow \mu^+ + \nu_\mu$, which is followed by the muons decaying to $\mu^+ \rightarrow e^+ + \nu_e + \bar{\nu}_\mu$. There are some parameters, which are required to calculate the GRB neutrino spectrum, like Lorentz factor Γ (Γ plays an important role in the neutrino production mechanism of the GRB), neutrino break energy $E_\nu^{\rm brk}$, observed photon spectral break energy $E_{\gamma,{\rm MeV}}^{\rm brk}$, the total amount of energy released at the time of neutrino emission $E_{\rm GRB}$ ($E_{\rm GRB} = 10^{53}$ erg, which is 10% of the fireball photon energy), the wind variability time t_ν, redshift distance of GRB from the observer (z) and the wind luminosity L_w ($\simeq 10^{53}$ erg/sec) [365, 460]. The neutrino spectrum of the GRB [365, 460, 461] can be written as

$$\frac{dN_\nu}{dE_\nu^s} = N \times \min\left(1, \frac{E_\nu^s}{E_\nu^{\rm brk}}\right) \frac{1}{E_\nu^{s2}} \ . \tag{10.1}$$

In the above, N represents the normalization constant and E_ν^s is the neutrino energy. The neutrino spectrum break energy $E_\nu^{\rm brk}$ can be expressed in terms of Γ and $E_{\gamma,{\rm MeV}}^{\rm brk}$. The expressions for these quantities are given in Section 8.2.4 of the Chapter 8. At a particular distance of the GRB from the observer (z), the relation between the observed neutrino energy $E_\nu^{\rm obs}$ and the actual energy of neutrino at the source E_ν^s is given as $E_\nu^{\rm obs} = \dfrac{E_\nu^s}{(1+z)}$. Likewise for the upper cutoff energy of the source, the observed neutrino energy can be written as $E_{\nu{\rm max}}^{\rm obs} = \dfrac{E_{\nu{\rm max}}^s}{(1+z)}$. Thus in the absence of decay or oscillation the neutrino spectrum on reaching the Earth from a GRB at redshift z takes the form

$$\frac{dN_\nu}{dE_\nu^{\rm obs}} = \frac{dN_\nu}{dE_\nu^s} \frac{1}{4\pi L^2(z)} (1+z) \ . \tag{10.2}$$

In the absence of CP violation $\mathcal{F}(E_\nu^s) = \dfrac{dN_\nu}{dE_\nu^s} = \dfrac{dN_{\nu+\bar{\nu}}}{dE_\nu^s}$. The spectra for neutrinos will be $0.5\mathcal{F}(E_\nu^s)$. Now the neutrinos are produced in the GRB process in the proportion $\nu_e : \nu_\mu : \nu_\tau$:

$\nu_s = 1:2:0:0$. Therefore,

$$\phi^s_{\nu_e} = \frac{1}{6}\mathcal{F}(E^s_\nu)\ , \phi^s_{\nu_\mu} = \frac{2}{6}\mathcal{F}(E^s_\nu) = 2\phi^s_{\nu_e}\ , \phi^s_{\nu_\tau} = 0\ , \phi^s_{\nu_s} = 0\ , \tag{10.3}$$

where $\phi^s_{\nu_e}$, $\phi^s_{\nu_\mu}$, $\phi^s_{\nu_\tau}$ and $\phi^s_{\nu_s}$ are the fluxes of ν_e, ν_μ, ν_τ and ν_s at source repectively. In Eq. 10.2, $L(z)$ denotes the distance of the source (at a redshift z), which can be expressed as [462]

$$L(z) = \frac{c}{H_0}\int_0^z \frac{dz'}{\sqrt{\Omega_\Lambda + \Omega_m(1+z')^3}}\ , \tag{10.4}$$

where $\Omega_\Lambda + \Omega_m = 1$ for the spatially flat Universe (Ω_Λ and Ω_m have their usual meanings). In Eq. 10.4, c and H_0 denote respectively the speed of the light and the Hubble constant in the present epoch. The values of the constants which we have used in our calculations are $\Omega_\Lambda = 0.68$, $\Omega_m = 0.3$ and $H_0 = 67.8$ Km sec^{-1} Mpc^{-1}.

10.3 Unparticle Decay of GRB Neutrinos

After the Georgi's "Unparticle" proposal, extensive studies to investigate the unparticle phenomenology have been explored in the literature. Unparticle physics is a speculative theory that conjectures a form of matter that cannot be explained in terms of particles using the SM of particle physics, because its components are scale invariant. So the interaction between the unparticle and SM particles is speculative in nature. The presence of this unparticle operator can effect the processes, which are all measured in experiments. Some processes where the invisible unparticles ($\mathcal{U}$) have been considered as the final state are (1) the top quark decay $\tau \to u + \mathcal{U}$ [428], (2) the electron - positron annihilation $e^+ + e^- \to \gamma + \mathcal{U}$, (3) the hadronic processes such as $q + q \to g + \mathcal{U}$ [429, 430] etc. In this Chapter, we consider a decay phenomenon, where neutrino having mass eigenstate ν_j decays

to the invisible unparticle ($\mathcal{U}$) [463] and another light neutrino with mass eigenstate ν_i

$$\nu_j \to \mathcal{U} + \nu_i \ . \tag{10.5}$$

The effective Lagrangian for the above mentioned process takes the following form in the low energy regime as

$$\mathcal{L} = \frac{\lambda_\nu^{\alpha\beta}}{\Lambda_{\mathcal{U}}^{d_{\mathcal{U}}-1}} \bar{\nu}_\alpha \nu_\beta \mathcal{O}_{\mathcal{U}} \ , \tag{10.6}$$

where $\alpha, \beta = e, \mu, \tau, s$ are the flavour indices, $d_{\mathcal{U}}$ is the scaling dimension of the scalar unpartcile operator $\mathcal{O}_{\mathcal{U}}$. $\Lambda_{\mathcal{U}}$ and $\lambda_\nu^{\alpha\beta}$ indicate the dimension transmutation scale at which the scale invariance sets in and the relevant coupling constant respectively. From Eq. 10.5 note that a heavier neutrino decays into a lighter neutrino and an unparticle. The neutrino mass and flavour eigenstates are related through $|\nu_i\rangle = \sum_\alpha U_{\alpha i}^* |\nu_\alpha\rangle$, where $U_{\alpha i}$ are the elements of the Pontecorvo - Maki - Nakagawa - Sakata (PMNS) [121] mixing matrix. Working in the neutrino mass eigenstate basis is more convenient than the flavour eigenstate. So in this mass basis we can write the interaction term bettween neutrinos and the unparticles as $\lambda_\nu^{ij} \bar{\nu}_i \nu_j \mathcal{O}_{\mathcal{U}} / \Lambda_{\mathcal{U}}^{d_{\mathcal{U}}-1}$, where λ_ν^{ij} is the coupling constant in the mass eigenstate i, j. Now the above mentioned coupling constant can be expressed as

$$\lambda_\nu^{ij} \ = \ \sum_{\alpha,\beta} U_{\alpha i}^* \lambda_\nu^{\alpha\beta} U_{\beta j} \ . \tag{10.7}$$

The total decay rate Γ_j or equivalently the lifetime of neutrino $\tau_{\mathcal{U}} = 1/\Gamma_j$ is the most relevant quantity for the decay process $\nu_j \to \mathcal{U} + \nu_i$ [463]. The lifetime $\tau_{\mathcal{U}}$ can be written as

$$\frac{\tau_{\mathcal{U}}}{m_j} \ = \ \frac{16\pi^2 d_{\mathcal{U}} (d_{\mathcal{U}}^2 - 1)}{A_d |\lambda_\nu^{ij}|^2} \left(\frac{\Lambda_{\mathcal{U}}^2}{m_j^2} \right)^{d_{\mathcal{U}}-1} \frac{1}{m_j^2} \ , \tag{10.8}$$

where m_j is the mass of the decaying neutrino. The normalization constant [428] in the above equation (Eq. 10.8) is defined as

$$A_d = \frac{16\pi^{5/2}}{(2\pi)^{2d_{\mathcal{U}}}} \frac{\Gamma(d_{\mathcal{U}}+1/2)}{\Gamma(d_{\mathcal{U}}-1)\Gamma(2d_{\mathcal{U}})} . \tag{10.9}$$

In the decay process for the four flavour scenario the lightest mass state $|\nu_1\rangle$ is stable, because it does not decay and all other states $|\nu_2\rangle, |\nu_3\rangle$ and $|\nu_4\rangle$ are unstable. Also note that due to the astronomical baseline $L(z)$ for these neutrinos the oscillatory part ($\sin^2\left(\frac{\Delta m^2 L(z)}{4E_\nu}\right)$, Δm^2 being the mass squared difference of any two neutrinos) is averaged out to half and the flavour oscillation probability (from flavour α to a flavour β) is reduced to $P_{\nu_\alpha \to \nu_\beta} = \sum_j |U_{\alpha j}|^2 |U_{\beta j}|^2$, j being the mass index. In the absence of the decay therefore the neutrino flux at the detector for UHE neutrinos from distant GRB can be computed as $\phi_{\nu_\alpha}^{\rm detector}(E_\nu) = \sum_i \sum_\beta \left[\phi_{\nu_\beta}^s |U_{\beta i}|^2 |U_{\alpha i}|^2\right] a_1$, while in the presence of neutrino decay (we consider the unparticle decay of neutrinos in this Chapter) the expression for the neutrino flux at the detector is given as

$$\phi_{\nu_\alpha}^{\rm detector}(E_\nu) = \sum_i \sum_\beta \left[\phi_{\nu_\beta}^s |U_{\beta i}|^2 |U_{\alpha i}|^2 exp(-4\pi L(z)/(\lambda_d)_i)\right] a_1 , \tag{10.10}$$

where the baseline length, $L(z) = \frac{c}{H_0}\int_0^z \frac{dz'}{\sqrt{\Omega_\Lambda + \Omega_m(1+z')^3}}$, $a_1 = \frac{1}{4\pi L^2(z)}(1+z)$ and the decay length $(\lambda_d)_i = 4\pi\frac{E_\nu}{\alpha_i}$ with $\alpha_i = \frac{m_i}{\tau_{\mathcal{U}}}$. In Eq. 10.10 α, β indicate the flavour indices and i is defined as mass index. For the 4-flavour scenario, the elements of the PMNS mixing matrix can be generated by successive rotations (R) (in terms of six mixing angles $\theta_{14}, \theta_{24}, \theta_{34}, \theta_{13}, \theta_{12}, \theta_{23}$) as [359]

$$\tilde{U}_{4\times4} = R_{34}(\theta_{34})R_{24}(\theta_{24})R_{14}(\theta_{14})R_{23}(\theta_{23})R_{13}(\theta_{13})R_{12}(\theta_{12}) , \tag{10.11}$$

where we consider that there is no CP violation in the neutrino sector and hence the CP phases are omitted for simplicity. The expressions for the succesive rotation terms (R) in Eq. 10.11 are given

in the Chapter 8 (Eq. 8.14). For the 4-flavour scenario (the minimal extension of 3 flavour case by a sterile neutrino) the PMNS matrix can be written as

$$\tilde{U}_{(4\times4)} = \begin{pmatrix} c_{14}U_{e1} & c_{14}U_{e2} & c_{14}U_{e3} & s_{14} \\ -s_{14}s_{24}U_{e1} + c_{24}U_{\mu1} & -s_{14}s_{24}U_{e2} + c_{24}U_{\mu2} & -s_{14}s_{24}U_{e3} + c_{24}U_{\mu3} & c_{14}s_{24} \\ \begin{matrix} -c_{24}s_{14}s_{34}U_{e1} \\ -s24s34U_{\mu1} \\ +c_{34}U_{\tau1} \end{matrix} & \begin{matrix} -c_{24}s_{14}s_{34}U_{e2} \\ -s24s34U_{\mu2} \\ +c_{34}U_{\tau2} \end{matrix} & \begin{matrix} -c_{24}s_{14}s_{34}U_{e3} \\ -s24s34U_{\mu3} \\ +c_{34}U_{\tau3} \end{matrix} & c_{14}c_{24}s_{34} \\ \begin{matrix} -c_{24}c_{34}s_{14}U_{e1} \\ -s_{24}c_{34}U_{\mu1} \\ -s_{34}U_{\tau1} \end{matrix} & \begin{matrix} -c_{24}c_{34}s_{14}U_{e2} \\ -s_{24}c_{34}U_{\mu2} \\ -s_{34}U_{\tau2} \end{matrix} & \begin{matrix} -c_{24}c_{34}s_{14}U_{e3} \\ -s_{24}c_{34}U_{\mu3} \\ -s_{34}U_{\tau3} \end{matrix} & c_{!4}c_{24}c_{34} \end{pmatrix} , \tag{10.12}$$

where $U_{\alpha i}$ represents the matrix elements of 3-flavour neutrino mixing matrix U, which is given in Eq. 8.15 of Chapter 8

$$U = \begin{pmatrix} c_{12}c_{13} & s_{12}c_{13} & s_{13} \\ -s_{12}c_{23} - c_{12}s_{23}s_{13} & c_{12}c_{23} - s_{12}s_{23}s_{13} & s_{23}c_{13} \\ s_{12}s_{23} - c_{12}c_{23}s_{13} & -c_{12}s_{23} - s_{12}c_{23}s_{13} & c_{23}c_{13} \end{pmatrix} . \tag{10.13}$$

In Eq. 10.10, ϕ_{ν_α} represents the flux of ν_α and $\phi^s_{\nu_\beta}$ is the fluxe of neutrino having flavour β at the source. The decay length ($(\lambda_d)_i$) in the Eq. 10.10 can be expressed as

$$(\lambda_d)_i = 4\pi\frac{E_\nu}{\alpha_i} = 2.5 \text{ Km } \frac{E_\nu}{\text{GeV}}\frac{\text{eV}^2}{\alpha_i} , \tag{10.14}$$

where α_i is defined as $m_i/\tau_{\mathcal{U}}$, $\tau_{\mathcal{U}}$ being the neutrino decay lifetime [1]. Eq. 10.14 shows that the decay length ($(\lambda_d)_i$) is a function of neutrino energy (E).

Applying the equation Eq. 10.3 and by considering the condition that the lightest mass state $|\nu_1\rangle$ is stable we can write the fluxes of neutrino flavours for four flavour cases on reaching the Earth as [360, 464] (by assuming all the fluxes in terms of $\phi^s_{\nu_e}$ and using the unitarity condition $\sum_i U_{\alpha i}U^*_{\beta i} = \delta_{\alpha\beta}$).

$$\begin{aligned}\phi^{\text{detector}}_{\nu_e} \quad = \quad & \Big[\mid \tilde{U}_{e1} \mid^2 (1 + \mid \tilde{U}_{\mu 1} \mid^2 - \mid \tilde{U}_{\tau 1} \mid^2 - \mid \tilde{U}_{s1} \mid^2) \\ & + \mid \tilde{U}_{e2} \mid^2 (1 + \mid \tilde{U}_{\mu 2} \mid^2 - \mid \tilde{U}_{\tau 2} \mid^2 - \mid \tilde{U}_{s2} \mid^2) \exp(-4\pi L(z)/(\lambda_d)_2) \\ & + \mid \tilde{U}_{e3} \mid^2 (1 + \mid \tilde{U}_{\mu 3} \mid^2 - \mid \tilde{U}_{\tau 3} \mid^2 - \mid \tilde{U}_{s3} \mid^2) \exp(-4\pi L(z)/(\lambda_d)_3) \\ & + \mid \tilde{U}_{e4} \mid^2 (1 + \mid \tilde{U}_{\mu 4} \mid^2 - \mid \tilde{U}_{\tau 4} \mid^2 - \mid \tilde{U}_{s4} \mid^2) \exp(-4\pi L(z)/(\lambda_d)_4) \Big] \, \phi^s_{\nu_e} a_1 \ , \end{aligned} \tag{10.15}$$

$$\begin{aligned}\phi^{\text{detector}}_{\nu_\mu} \quad = \quad & \Big[\mid \tilde{U}_{\mu 1} \mid^2 (1 + \mid \tilde{U}_{\mu 1} \mid^2 - \mid \tilde{U}_{\tau 1} \mid^2 - \mid \tilde{U}_{s1} \mid^2) \\ & + \mid \tilde{U}_{\mu 2} \mid^2 (1 + \mid \tilde{U}_{\mu 2} \mid^2 - \mid \tilde{U}_{\tau 2} \mid^2 - \mid \tilde{U}_{s2} \mid^2) \exp(-4\pi L(z)/(\lambda_d)_2) \\ & + \mid \tilde{U}_{\mu 3} \mid^2 (1 + \mid \tilde{U}_{\mu 3} \mid^2 - \mid \tilde{U}_{\tau 3} \mid^2 - \mid \tilde{U}_{s3} \mid^2) \exp(-4\pi L(z)/(\lambda_d)_3) \\ & + \mid \tilde{U}_{\mu 4} \mid^2 (1 + \mid \tilde{U}_{\mu 4} \mid^2 - \mid \tilde{U}_{\tau 4} \mid^2 - \mid \tilde{U}_{s4} \mid^2) \exp(-4\pi L(z)/(\lambda_d)_4) \Big] \, \phi^s_{\nu_e} a_1 \ , \end{aligned} \tag{10.16}$$

[1] $\lambda_d = \frac{4\pi E_\nu}{\alpha_i}$, $\alpha_i = \frac{m_i}{\tau_{\mathcal{U}}}$; m in eV, E_ν in GeV, $\tau_{\mathcal{U}}$ is decay time. In natural units $\lambda_d \equiv 4\pi E_\nu[\text{GeV}] \times \frac{1}{\alpha_i} \times \frac{1}{[\text{GeV}]} \times \frac{1}{[\text{eV}]} = 4\pi \left(\frac{E_\nu}{\text{GeV}}\right)[\text{GeV}] \times \frac{1}{10^9} \times \frac{1}{[\text{eV}]^2} \times \left(\frac{\text{eV}^2}{\alpha_i}\right) = 4\pi \left(\frac{E_\nu}{\text{GeV}}\right) \left(\frac{\text{eV}^2}{\alpha_i}\right) \times \frac{[\text{GeV}][\text{GeV}]}{[\text{eV}]^2} \times 10^{-9} \times \frac{1}{[\text{GeV}]}$ $= 4\pi \left(\frac{E_\nu}{\text{GeV}}\right) \left(\frac{\text{eV}^2}{\alpha_i}\right) \times \frac{[\text{eV}]^2}{[\text{eV}]^2} \times \frac{10^9}{[\text{GeV}]} = \frac{4\pi}{5.6} \text{ Km } \left(\frac{E_\nu}{\text{GeV}}\right) \left(\frac{\text{eV}^2}{\alpha_i}\right) = 2.5 \text{ Km } \left(\frac{E_\nu}{\text{GeV}}\right) \left(\frac{\text{eV}^2}{\alpha_i}\right)$.

$$\begin{aligned}\phi^{\rm detector}_{\nu_\tau} &= \Big[|\,\tilde{U}_{\tau 1}\,|^2(1+|\,\tilde{U}_{\mu 1}\,|^2-|\,\tilde{U}_{\tau 1}\,|^2-|\,\tilde{U}_{s1}\,|^2)\\ &+|\,\tilde{U}_{\tau 2}\,|^2(1+|\,\tilde{U}_{\mu 2}\,|^2-|\,\tilde{U}_{\tau 2}\,|^2-|\,\tilde{U}_{s2}\,|^2)\exp(-4\pi L(z)/(\lambda_d)_2)\\ &+|\,\tilde{U}_{\tau 3}\,|^2(1+|\,\tilde{U}_{\mu 3}\,|^2-|\,\tilde{U}_{\tau 3}\,|^2-|\,\tilde{U}_{s3}\,|^2)\exp(-4\pi L(z)/(\lambda_d)_3)\\ &+|\,\tilde{U}_{\tau 4}\,|^2(1+|\,\tilde{U}_{\mu 4}\,|^2-|\,\tilde{U}_{\tau 4}\,|^2-|\,\tilde{U}_{s4}\,|^2)\exp(-4\pi L(z)/(\lambda_d)_4)\Big]\,\phi^s_{\nu_e}a_1\ ,\end{aligned} \tag{10.17}$$

$$\begin{aligned}\phi^{\rm detector}_{\nu_s} &= \Big[|\,\tilde{U}_{s1}\,|^2(1+|\,\tilde{U}_{\mu 1}\,|^2-|\,\tilde{U}_{\tau 1}\,|^2-|\,\tilde{U}_{s1}\,|^2)\\ &+|\,\tilde{U}_{s2}\,|^2(1+|\,\tilde{U}_{\mu 2}\,|^2-|\,\tilde{U}_{\tau 2}\,|^2-|\,\tilde{U}_{s2}\,|^2)\exp(-4\pi L(z)/(\lambda_d)_2)\\ &+|\,\tilde{U}_{s3}\,|^2(1+|\,\tilde{U}_{\mu 3}\,|^2-|\,\tilde{U}_{\tau 3}\,|^2-|\,\tilde{U}_{s3}\,|^2)\exp(-4\pi L(z)/(\lambda_d)_3)\\ &+|\,\tilde{U}_{s4}\,|^2(1+|\,\tilde{U}_{\mu 4}\,|^2-|\,\tilde{U}_{\tau 4}\,|^2-|\,\tilde{U}_{s4}\,|^2)\exp(-4\pi L(z)/(\lambda_d)_4)\Big]\,\phi^s_{\nu_e}a_1\ .\end{aligned} \tag{10.18}$$

In the above Eqs. 10.15 - 10.18, $\phi^{\rm detector}_{\nu_\alpha}$ represent the neutrino fluxes for four flavour cases on reaching the Earth. In case of $L(z) >> \lambda_d$, Eq. 10.10 is then reduced to

$$\phi^{\rm detector}_{\nu_\alpha}(E_\nu)(\text{no decay}) = \sum_{i(\text{stable}),\beta}(\phi^s_{\nu_\beta}|U_{\beta i}|^2|U_{\alpha i}|^2)a_1\ . \tag{10.19}$$

Eq. 10.19 indicates that with the condition $L(z) >> \lambda_d$, the decay term is removed because the neutrino decay is completed by the time it reaches the Earth. So only the stable state $|\nu_1\rangle$ exists. So the flavour ratio in 4-flavour scenario in this case is changed to $|U_{e1}|^2 : |U_{\mu 1}|^2 : |U_{\tau 1}|^2 : |U_{s1}|^2$ [465–467]. But when the decay length is close to the baseline length ($\lambda_d \sim L(z)$), then we cannot wash out the neutrino decay effect. Therefore, the exponential term survives in Eqs. 10.15 - 10.18 and $L(z)$ plays an important role. In such cases, considering GRB neutrino fluxes at a fixed redshift (z) is useful to explore the neutrino decay effects.

10.3.1 Detection of UHE Neutrinos from a Single GRB

Upward going muons [362] are produced by the interactions, which are weak in nature, of ν_μ or $\bar{\nu}_\mu$ with the rock surrounding the Super-Kamiokande detector. While muons from interactions above the detector cannot be sorted out from the continuous rain of muons created in cosmic ray showers in the atmosphere above the mountain, muons coming from below can only be due to neutrino (ν_μ) charged current (CC) interactions ($\nu_\mu + N \rightarrow \mu + X$), since cosmic ray muons cannot make it through from the other side of the Earth. Looking upward going muons is the most encouraging way to detect the UHE neutrinos. The secondary muon yields from the GRB neutrinos can be detected in a detector of unit area above a threshold energy $E_{\rm th}$ is given by [363–365]

$$S = \int_{E_{\rm th}}^{E_{\nu\rm max}} dE_\nu \phi_{\nu_\alpha}^{\rm detector} P_{\rm shadow}(E_\nu) P_\mu(E_\nu, E_{\rm th}) \ , \tag{10.20}$$

where $P_{\rm shadow}(E_\nu)$ represents the probability that a neutrino reaches the terrestrial detector such as IceCube being unabsorbed by the Earth. We can express this shadow factor in terms of the energy dependent neutrino-nucleon interaction length $L_{\rm int}(E_\nu)$ in the Earth and the effective path length $X(\theta_z)$ (θ_z is fixed for a particular single GRB). Thus $P_{\rm shadow}(E_\nu)$ takes the form.

$$P_{\rm shadow} = \exp[-X(\theta_z)/L_{int}(E_\nu)] \ , \tag{10.21}$$

where $L_{\rm int}(E_\nu)$, $X(\theta_z)$ are the interaction length, the effective path length respectively and these quantities are explained in details in Section 8.2.3 [Eqs. 8.31, 8.32 and the corresponding text] of the Chapter 8. In Eq. 10.20, $P_\mu(E_\nu, E_{\rm th})$ is the probability that a neutrino induced muon reaching the detector with an energy above $E_{\rm th}$. The expression for $P_\mu(E_\nu, E_{\rm th})$ and the quantities, which are required to calculate $P_\mu(E_\nu, E_{\rm th})$ have been briefly elaborated in Section 8.2.3 of the Chapter 8 (Eqs. 8.33 - 8.38 and the corresponding text)[2]. In the case of detecting muon events at a 1 Km^2

[2]In Chapter 8, threshold energy is represented as $E_{\rm thr}$ whereas in this Chapter we have addressed the threshold energy as $E_{\rm th}$ (both are same only the abbreviations are different).

detector such as IceCube the flux $\phi_{\nu_\alpha}^{\rm detector}$ in Eq. 10.20 is replaced by $\phi_{\nu_\mu}^{\rm detector}$ in Eqs. 10.15-10.18. Cosmic tau neutrinos undergo CC deep inelastic scattering with nuclei of the detector material and produces hadronic shower as well as tau lepton ($\nu_\tau + N \rightarrow \tau + X$). After traversing some distances, which is proportional to the energy of tau lepton, τ decays into ν_τ (having diminished energy) and in this process a second hadronic shower is induced. These whole double shower processes are introduced as a double bang event. The detection of these tau leptons, which are regenerated in the lollipop event, is very much complicated due to its non-interacting nature with the other particles as they lose energy very fast. The only possible way of the detection of tau leptons other than double bang event is the production of muons via the decay channel $\nu_\tau \rightarrow \tau \rightarrow \bar{\nu}_\mu \mu \nu_\tau$ with probability 0.18 [369, 370]. The number of such muon events can be computed by solving numerically Eqs 10.20, 10.21 and the corresponding equations mentioned in Section 8.2.3 of the Chapter 8 (Eqs. 8.31-8.38) and it is needless to say that $\phi_{\nu_\alpha}^{\rm detector}$ in Eq. 10.20 is equivalent to $\phi_{\nu_\tau}^{\rm detector}$ (Eq. 10.17).

10.4 Calculations and Results

In this Section, we explore the effect on a flux of neutrinos of different flavours on reaching the Earth from a distant astrophysical source, in case such neutrinos undergo unparticle decay along with the usual mass-flavour oscillations. For this purpose, we consider a specific example of UHE neutrinos from a single GRB and its detection at a Km^2 Cherenkov detector such as IceCube. We also assume the existence of a 4th sterile neutrino in addition to the usual three active flavour neutrinos (ν_e, ν_μ and ν_τ). The expression for the final flux for a neutrino flavour α on reaching the Earth is given in Eq. 10.10 along with Eqs. 10.12-10.18. It is to be noted that the decay part $(\exp(-4\pi L(z)/(\lambda_d)_i)$ for a neutrino mass eigenstate $|\nu_i\rangle$ will be meaningful and significant for $L(z) \sim (\lambda_d)_i$. This decay length depends on the neutrino-unparticle coupling $|\lambda_\nu^{ij}|$, the non-integral scaling dimension $d_{\mathcal{U}}$, the dimensional transmutation scale $\Lambda_{\mathcal{U}}$ etc. The neutrino flux from a single GRB is calculated using Eqs. 10.1 - 10.4. We have considered a GRB of energy $E_{\rm GRB} = 10^{53}$ GeV at a redshift $z = 0.1$ for

the present calculations. The measure of distance (Eq. 10.4) corresponding to the chosen redshift is computed as 10^{15} km from the Earth where the values of cosmological parameters ($\Omega_\Lambda = 0.68$ and $\Omega_m = 0.3$) are adopted from PLANCK 2015 data [468]. The value of photon spectrum break energy $E_\gamma^{\rm brk}$ is adopted from Table 1 of Ref. [365] for the Lorentz boost factor $\Gamma = 50.12$. We have considered the current best fit values for three neutrino mixing angles ($\theta_{12} = 33.48^\circ, \theta_{23} = 45^\circ$ and $\theta_{13} = 8.5^\circ$). The following four flavour analysis of different experimental group such as MINOS, Daya Bay, NOνA, Bugey [138, 148, 155–159, 174] suggest some limits on four flavour mixing angles ($\theta_{14}, \theta_{24}, \theta_{34}$) and these limits are briefly discussed in Section 8.3.1 of the Chapter 8. The limits on θ_{14} are chosen as $1^\circ \leq \theta_{14} \leq 4^\circ$ in the range $0.2\ {\rm eV}^2 < \Delta m^2_{41} < 2\ {\rm eV}^2$, which is consistent with the observational results from the combined experimental analysis by MINOS, Daya Bay and Bugey-3 [148]. By considering the above mentioned limits on four flavour mixing angles we have taken θ_{14}, θ_{24} and θ_{34} as $3^\circ, 5^\circ$ and 20° respectively for our calculations. It is to be noted that in the four flavour neutrino decay framework the normal hierarchy is evident and $|\nu_2\rangle, |\nu_3\rangle$ and $|\nu_4\rangle$, considering as unstable states, are subjected to undergo unparticle decay while only $|\nu_1\rangle$ is stable. In our calculations we consider m_2 and m_3 as $\sqrt{\Delta m^2_{32}}$ and $\sqrt{2.0 \times \Delta m^2_{32}}$, where $\Delta m^2_{32} = m_3^2 - m_2^2$ (normal hierarchy) [3] and $\Delta m^2_{32} = 2.4 \times 10^{-3}\ {\rm eV}^2$ (from atmospheric neutrino oscillation) respectively. The value of m_4 is estimated from $m_4 = \sqrt{\Delta m^2_{41}}$, where Δm^2_{41} lies within the range $0.2\ {\rm eV}^2 < \Delta m^2_{41} < 2\ {\rm eV}^2$. By using Eqs. 10.5 - 10.18 we now calculate the relevant neutrino flux from a single GRB reaching the detector with or without unparticle decay. The upgoing secondary muon yield from ν_μ in an earthbound detector can be computed by using Eqs. 10.20, 10.21 along with Eqs. 8.31 - 8.38 (Section 8.2.3 of Chapter 8). We have considered a Km^2 detector such as IceCube for our present calculations in case the neutrinos undergo unparticle decay. Note that we consider UHE neutrinos from a single GRB here. Therefore its directionality of the neutrino beam with respect to the detector is fixed. The effect of unparticle decay is characterised mainly by the three parameters namely, the neutrino-unparticle coupling $|\lambda_\nu^{ij}|$, the fractional dimension of

[3] $m_2 \simeq \sqrt{\Delta m^2_{32}},\ m_3 \simeq \sqrt{\Delta m^2_{32} + m_2^2} = \sqrt{\Delta m^2_{32} + \Delta m^2_{32}} = \sqrt{2\Delta m^2_{32}}$.

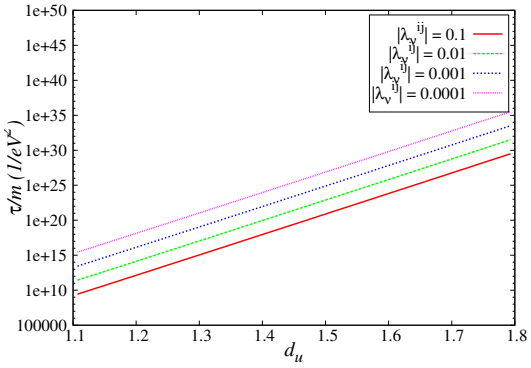

Figure 10.1: The Variations of the neutrino decay lifetime (τ/m) with the unparticle dimension ($d_{\mathcal{U}}$) are shown for four different values (0.1, 0.01, 0.001, 0.0001) of couplings $|\lambda_\nu^{ij}|$. See text for details.

unparticle ($d_{\mathcal{U}}$) and the transmutation scale $\Lambda_{\mathcal{U}}$. The scale $\Lambda_{\mathcal{U}}$ is fixed at 1 TeV for the present calculations. The effect of unparticle parameters $d_{\mathcal{U}}$ and $|\lambda_{\mathcal{U}}^{ij}|$ are varied to study how they affect the various quantities that can be measured at the detector.

We show the variations of decay life time of neutrino in terms of $\tau/m(=\tau_{\mathcal{U}}/m_j)$ for different fixed values of $|\lambda_\nu^{ij}|$ with the unparticle dimension $d_{\mathcal{U}}$ in Fig. 10.1. The plots clearly indicate the increasing nature of τ/m with the increase of $d_{\mathcal{U}}$, which is manifested in Eq. 10.8 along with Eq. 10.9. Fig. 10.1 also reflects the fact that τ/m increases with the reducing values of $|\lambda_\nu^{ij}|$ (Eq. 10.8).

Fig. 10.2 shows the variations of neutrino induced muons at IceCube considered here for neutrinos from different single GRBs at varied redshifts (z). We have shown the results for three fixed values of $|\lambda_\nu^{ij}|$ as well as for no decay case. All the plots in Fig. 10.2 exhibit decrease of neutrino induced muons with increasing z (the distance of the GRBs from the observer) as is evident from Eqs. 10.2, 10.4. It is to be noted that the decrease of the coupling $|\lambda_\nu^{ij}|$ causes λ_d to increase and therefore the depletion of the neutrino flux (and hence the induced muon yield) will be effective for neutrinos from GRBs at larger distances or redshifts. For example in Fig. 10.2, when $|\lambda_\nu^{ij}| = 0.0001$ the decay effect is significant for a GRB with $z \sim 0.1$ whereas for $|\lambda_\nu^{ij}| = 0.001$ the depletion due to decay is evident for neutrinos from a nearer GRB with $z \sim 0.001$. This is to be mentioned that the nature of the plots in Fig. 10.2 can be understood from the nature of the variation of the factor

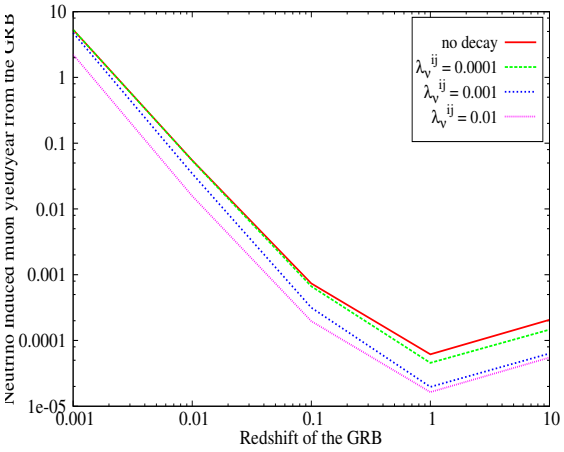

Figure 10.2: Variations of the neutrino induced muons per year from the GRB with different redshifts (z) for three different values of $|\lambda_\nu^{ij}|$ as well as for no decay case at a fixed zenith angle ($\theta_z = 160^\circ$). See text for details.

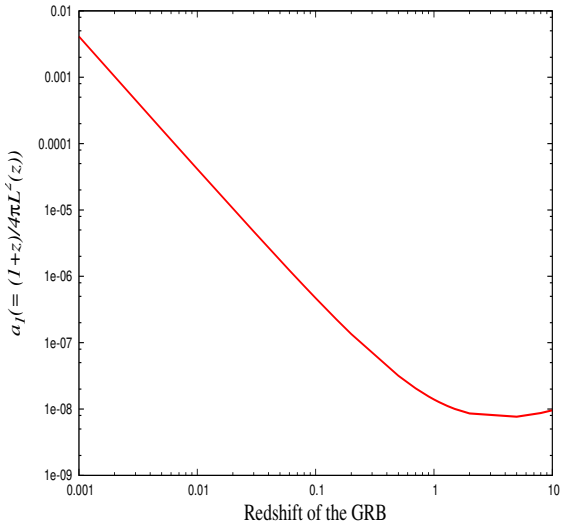

Figure 10.3: Variations of the factor $a_1(= \dfrac{1}{4\pi L^2(z)}(1+z))$ with different redshifts (z). See text for details.

$a_1(= \dfrac{1}{4\pi L^2(z)}(1+z))$ with z. This is demonstrated in Fig. 10.3. It is to be noted from Fig. 10.3 that around $z = 1$ there is a change in the nature of the plot which is reflected in the results shown in Fig. 10.2. In Figs. 10.4(a), 10.4(b) the effects of the unparticle parameters ($d_{\mathcal{U}}$ and $|\lambda_\nu^{ij}|$) on the unparticle decay of neutrinos are shown. Comparisons are also made with the cases when only

Table 10.1: The ratio of muon yields at IceCube for UHE neutrinos from a GRB with and without unparticle decay in a four neutrino framework. See text for details.

θ_{14}	θ_{24}	θ_{34}	$d_{\mathcal{U}}$	$\lvert\lambda_\nu^{ij}\rvert$	R
3°	5°	20°	1.2	10^{-4}	0.9
			1.3	10^{-2}	0.6

Table 10.2: Same as Table 10.1 but for the flux ratio for each flavour of active neutrinos in 4-flavour framework. See text for details.

θ_{14}	θ_{24}	θ_{34}	$d_{\mathcal{U}}$	$\lvert\lambda_\nu^{ij}\rvert$	$\phi_{\nu_e} : \phi_{\nu_\mu} : \phi_{\nu_\tau}$ (with decay and oscillation)	$\phi_{\nu_e} : \phi_{\nu_\mu} : \phi_{\nu_\tau}$ no decay (only oscillation)
3°	5°	20°	1.2	10^{-4}	0.349 : 0.621 : 0.489	0.449 : 0.979 : 0.834
			1.3	10^{-2}	0.344 : 0.265 : 9.5×10^{-2}	

mass-flavour oscillations are considered. Because of very long baseline the mass-flavour oscillations effect all the neutrino fluxes will be manifested only through an overall depletion of the flux depending on just the neutrino mixing angles. The variations of the neutrno induced muon yields at the detector considered with the unparticle dimension $d_{\mathcal{U}}$ for different fixed values of $|\lambda_\nu^{ij}|$ are shown in Fig. 10.4(a). The results with only mass-flavour oscillations (no unparticle decay) are also shown for comparison. All the calculations are made for UHE neutrinos from a GRB at $z = 0.1$ and at a zenith angle $\theta_z = 160°$. The decay effect is evident in Fig. 10.4(a) as the muon yield depletes by $\sim 70\%$ from what is expected for only the mass-flavour case. It can also be noted from Fig. 10.4(a) that higher the value of the coupling for unparticle decay of neutrinos, higher is the unparticle dimension at which the decay effect starts showing up. Since, here we consider a single GRB at a fixed redshift, the $L(z)$ is fixed. Therefore the exponential decay term $\exp(-L(z)/(\lambda_d)_i)$ depends only on $(\lambda_d)_i$. As the decay length depends on $\frac{\tau}{m}$ (Eq. 10.8) which in turn is a function of both $d_{\mathcal{U}}$ and $|\lambda_\nu^{ij}|$, the nature of the plots in Fig. 10.4(a) varies accordingly. Similar trends can also be seen when the neutrino induced muons are plotted with $|\lambda_\nu^{ij}|$ for different fixed values of $d_{\mathcal{U}}$ (Fig. 10.4(b)).

In order to quantify the possible effect on UHE neutrino signal at IceCube in case the UHE

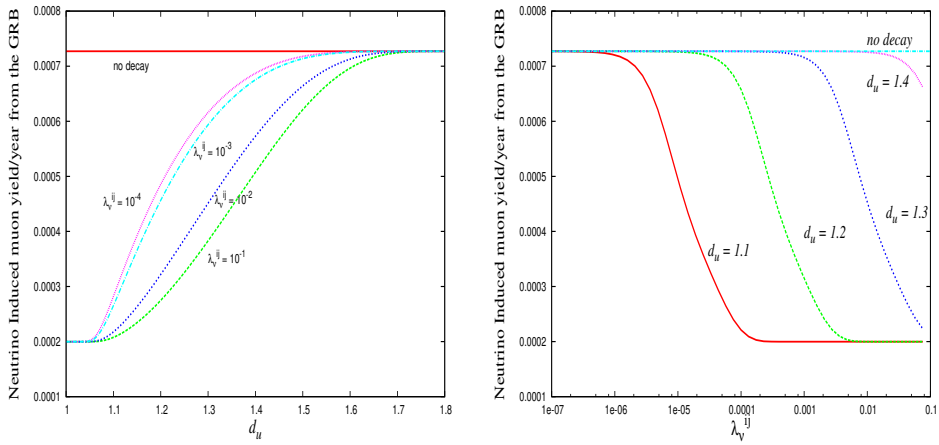

(a) (b)

Figure 10.4: The variations of the neutrino induced upward going muons per year from the GRB with (a) different values of $d_{\mathcal{U}}$ for four different fixed values of $|\lambda_\nu^{ij}|$ as well as for the mass-flavour case (no decay case), (b) different values of $|\lambda_\nu^{ij}|$ for four different fixed values of the unparticle dimension $d_{\mathcal{U}}$ (1.1, 1.2, 1.3, 1.4) and in addition for no decay case. See text for details.

neutrinos from a distant GRB undergo unparticle decay we define a ratio R of the expected muon yields per year with and without unparticle decay in addition to the 4-flavour oscillations as

$$R \;=\; \frac{\text{Rate}_{(\text{with decay})}}{\text{Rate}_{(\text{no decay})}} \;. \tag{10.22}$$

The results are given in Table 10.1 for a fixed set of values of the mixing angles θ_{14}, θ_{24}, θ_{34} and for two sets of values of decay parameters namely $d_{\mathcal{U}}$, $|\lambda_\nu^{ij}|$. It can be seen from Table 10.1 that for the decay parameter set $d_{\mathcal{U}} = 1.3$ and $|\lambda_\nu^{ij}| = 10^{-2}$ which may cause considerable decay (Fig. 10.4), this ratio R can be depleted to as low as a value of 0.6. We also estimate the flavour ratio for 3 active flavours in the present 4-flavour neutrino scenario for the case when these neutrinos undergo both oscillations and decay and when these neutrinos suffer only four flavour oscillations during its passage from the source GRB to the Earth. We have adopted same sets of values for the mixing angles and the decay parameters as chosen for Table 10.1. The results are shown in Table 10.2. It is seen from Table 10.2 that when $d_{\mathcal{U}} = 1.3$ and $|\lambda_\nu^{ij}| = 10^{-2}$ (decay is considerably strong (Fig.

10.4)) the flux for flavour ν_e suffers least depletion while the fluxes of ν_μ and ν_τ are considerably diminished. This is because of the fact that the $|\nu_1\rangle$ component in the flavour eigenstate $|\nu_e\rangle$ is dominant and $|\nu_2\rangle$ is the lightest component that undergoes no decay. The minimal change of ϕ_{ν_e} with decay in comparison to the case without decay (only 4-flavour oscillations) is due to the decay of small $|\nu_2\rangle$ and $|\nu_3\rangle$ components in $|\nu_e\rangle$. The depletion of ϕ_{ν_μ} and ϕ_{ν_τ} in comparison to the no decay case (only oscillation) can also be similarly understood (in $|\nu_\mu\rangle$, $|\nu_2\rangle$ component is dominant while in $|\nu_\tau\rangle$ the dominant component is $|\nu_3\rangle$).

10.5 Summary

In this Chapter, we have explored the possibility of unparticle decay of UHE neutrinos from a distant single GRB and its consequences on the neutrino induced muon yields at IceCube. The concept of unparticles first proposed by Georgi from the consideration of the presence of a yet unseen scale invariant sector which may be present in the four dimensions with non-renormalizable interactions with SM particles. The "particles" in this scale invariant sector are termed as "unparticles". The unparticle scenario and its interaction with SM particles such as neutrinos are expressed by an effective Lagrangian, which is expressed in terms of the effective couplings ($\lambda_\nu^{\alpha\beta}$, where α, β are the flavour indices) between neutrinos ($\nu_{\alpha,\beta}$) and the scalar unparticle operator ($\mathcal{O}_\mathcal{U}$), the scaling dimension ($d_\mathcal{U}$) and the dimension transmutaion scale ($\Lambda_\mathcal{U}$). In the case of the neutrino unparticle interaction, heavier neutrinos become unstable and can decay into the unparticles and lighter neutrinos. In order to explore the unparticle decay process, we have considered 3+1 neutrino framework. We estimate how the effect of an unparticle decay of neutrinos in addition to the mass-flavour oscillations can change the secondary muon yields from GRB neutrinos at a IceCube for a four flavour scenario. The advantage of choosing UHE neutrinos from GRB is that the oscillatory part is averaged out due to their astronomical baslines ($\Delta m^2 L/E >> 1$). In this Chapter, we consider the neutrino fluxes from a point like source such as a single GRB. We calculate the muon yield in this scenario. We also

investigate the effect of fractional unparticle dimension $d_{\mathcal{U}}$ as also the coupling $|\lambda_{\nu}^{ij}|$ on the muon yield and compare them with the case where only flavour suppression (without an unparticle decay) is considered. It is observed that the effect of unparticle decay considerably affects the muon yield. Also as is clear from Table 10.2, the tau neutrino flux would be affected substantially if the neutrinos undergo unparticle decay in comparison to the case when only oscillation is effective without any decay. This is a representative calculation to demonstrate the unparticle decay of neutrinos, which can indeed affect the neutrino flux from distant sources such as GRBs.

CHAPTER 11

MASS AND LIFE TIME OF HEAVY DARK MATTER DECAYING INTO ICECUBE PEV NEUTRINOS

In this Chapter, we consider that the ultrahigh energy (UHE) neutrino signals in the PeV range at IceCube to have originated from the decay of superheavy dark matter (SHDM). We analyse the IceCube 6 years and 7.5 years data of these UHE neutrinos with mass and decay lifetime of SHDM as parameters and thus estimate the values of these parameters. In our analysis the lower energy astrophysical neutrinos are also included.

11.1 Introduction

The ultrahigh energy (UHE) neutrino events at IceCube detector in the energy range TeV-PeV have immense implications as they enable to probe the UHE extra terrestrial sources. Analyses of such data coupled with other multimessenger signals generally lead to assess the nature of UHE neutrino

spectrum. They also help to understand the nature of the high energy sources from which these neutrinos (and other multimessenger signals) may originate. The IceCube data have by and large two components namely Medium Energy Starting Events (MESE) and High Energy Starting Events (HESE). The neutrinos with energies > 20 TeV are what consist of HESE data. In both the cases however the neutrino interaction vertex with the ice lie within the fiducial volume of detector ice of IceCube. There are several proposals in the literature for the possible sources of these IceCube high energy neutrino events. The possible sources may include the stellar remnants [469, 470], Gamma Ray Bursts (GRBS) [170], Supernovae and Hypernovae remnants [168], Active Galactic Nuclei (AGN) [169, 471] etc. Other than these astrophysical sources, the decay or annihilation of very heavy dark matter (DM) particles could well be a viable origin of UHE neutrino events [472–476]. The superheavy dark matters or SHDMs can produce neutrinos by rare long lived decay processes. After the discovery of PeV neutrinos at Icecube, the hypothesis of their DM origin gained a lot of interest [477–493]. The IceCube Collaboration had published 6 years data with 2078 data samples. Out of these 2078 samples that has been published by IceCube at ICRC 2017 conference [372], 82 track and shower events fall into HESE data category.

The IceCube Collaboration fitted their data of 82 events (HESE data [372]) (shower and track events) in the attempt to obtain a power law spectrum for the detected neutrino flux. The IceCube Collaboration has first fitted their 6 years data [372] and later with 7.5 years of data [494] to obtain unbroken single power law fit with the form of the spectral shape taken to be $\sim E^{-\gamma}$, γ being the spectral index. For an unbroken single power law fit they obtain a flux $\sim E^{-2.9}$ (index $\gamma \sim 2.9$, for $E^{-\gamma}$). This is what referred to as HESE data. But a fit of the data between the energy range ~ 120 TeV to ~ 5 PeV yielded a power law different from the HESE fit ($\gamma \sim 2.19$) indicating the possibility of a second component which is softer that the earlier one. This softer component around the PeV region had been represented as a pink band (specifying 1σ uncertainty) in Fig. 2 of Ref. [372]. Beyond the energy ~ 5 PeV the data points as shown in Fig. 2 of [372] are found to have no lower bound.

In this Chapter, considerations have been made that these neutrinos could have been created by the rare or long lived decay of SHDM in the Universe [495, 496]. The SHDM could be created during a spontaneous symmetry breaking (SSB) in Grand Unified scale and thus they were never in thermal equilibrium with the Universe. Thus their production is non-thermal in nature. Such particles can also be originated by the process of gravitational creation [495, 497] in the early Universe. This type of particle production is attributed to the fact that, in an expanding Universe with conformal time η and scale factor $a(\eta)$, an intial vacuum state does not remain a vacuum state at a later time. Here in this Chapter, we consider the decay of a SHDM to interpret the neutrinos in and around the PeV region (the pink region in Fig. 2 of Ref. [372]) reported by Icecube detector.

The decay of such massive particles much heavier than electroweak scale are discussed in the literature such as [496, 498–503]. The decays of superheavy particles are considered to proceed via the cascading of QCD partons. It is argued that although the QCD coupling is small the parton splitting is favoured by collinear parton emission [499]. Also these decay processes are enhanced by the electroweak radiative corrections at the TeV scale and above. In developing the computer codes for the QCD decay cascade process involving such decays, the Dokshitzer-Grivov-Lipatov-Altarelli-Parisi (DGLAP) equations [504, 505] are used. In order to treat the electroweak radiative corrections, evolution equations similar to DGLAP equations are developed valid for a spontaneously broken theory. The electroweak cascade experiences interactions of SU(3) $\times$ SU(2) $\times$ U(1) and the couplings are enhanced [499]. In this Chapter, a superheavy particle with mass $m_\chi \leq m_{\rm GUT}$ is considered that decays to produce $\nu\bar{\nu}$ ($\chi \rightarrow \nu\bar{\nu}$) as the final product. The electroweak cascade accompanies the usual QCD cascade when $m_\chi >> m_W$. The numerical evolution of the DGLAP equations that describe fragmentation function and Monte Carlo studies of such cascades yield the spectrum of the final product leptons. There can be two decay channels namely hadronic and leptonic decay channels through which the leptons and γ can be obtained as end products. In the hadronic decay channel, the decay proceeds through the QCD cascade whereby the decay of DM χ to $\bar{q}q$ ($\chi \rightarrow \bar{q}q$) is first produced which then hadronizes producing eventually the leptons as final

decay products. The numerical evolution of DGLAP equations can also be used for the case of electroweak radiative corrections. These are studied for a spontaneously broken theory [506]. Similar procedure for electroweak cascade attributes to the leptonic decay channel.

This Chapter describes several analyses of the IceCube neutrino signals of different energy ranges between 60 TeV to 5 PeV together or separately using either only the hadronic channel or extending to both hadronic and leptonic channels. It is to be noted that the two data points in the energy range 60 TeV to $\sim$ 120TeV are likely to be due to astrophysical neutrinos and the energy range between $\sim$ 120 TeV to 5 PeV are UHE neutrinos of possible different origin. In this Chapter, first hadronic channel is considered for the analysis of the neutrino energy range 120 TeV to 5 PeV and then both the hadronic and leptonic channels along with a power law spectrum of astrophysical flux have been used to analyse the IceCube data points for neutrinos in the total span of the considered energy range namely 60 TeV - 5 PeV. For each of the analyses however, χ^2 fits are performed to obtain best fit values for the mass of SHDM and its corresponding decay lifetime.

11.2 Formalism

11.2.1 Decay of SHDM through Hadronic and Leptonic Decay Channels

A. Hadronic decay channel

QCD cascade from the decay of superheavy particles plays a significant role to describe the production of hadrons. It is pointed out that even though the QCD coupling is small, the cascading in QCD parton appears due to the enhancement of the parton splitting in the presence of large logarithms for soft parton emission. The electroweak radiative corrections can also be dominated by similar logarithms. In the case of QCD cascade, we use the numerical code [496] for the evolution of the DGLAP equations. A similar kind of approach can be adopted by the electroweak radiative cor-

rections at the TeV energy scale or above [507–512] valid for spontaneously broken gauge group. In this Section, we discuss in particular the hadronic decay channel $\chi \to q\bar{q}$, where q indicates a quark with a flavour. In this decay channel, after the perturbative evolution of the QCD cascade, the partons are hadronized and finally, as the end product, the leptons are obtained by the subsequent decay of the unstable hadrons. In comparison to other theoretical uncertainties the effect of electroweak radiative corrections on the cascade development are insignificant. The neutrino spectrum can be written as [498]

$$\frac{dN_\nu}{dx} = 2R\int_{xR}^{1}\frac{dy}{y}D^{\pi^\pm}(y) + 2\int_{x}^{1}\frac{dz}{z}f_{\nu_i}\left(\frac{y}{z}\right)D_i^{\pi^\pm}(z)\ , \tag{11.1}$$

where $D_i^\pi(x,s)$ ($\equiv [D_q^\pi(x,s) + D_g^\pi(x,s)]$ is a fragmentation function of the pions from a parton $i(= q(= u,d,s,...),g)$. The total decay spectrum $F^h(x,s)$ can be obtained by the summation of the contributions of all possible parton (quarks, antiquarks and gluons) fragmentation functions ($D_i^\pi(x,s)$), where $x(\equiv 2E/m_\chi)$ - a dimensionless quantity - defines the fraction of energy transferred to the hadron and $\sqrt{s}$ is the centre of mass energy. In our calculation, we consider only the contribution of pion decays and the contribution ($\sim 10\%$) from other mesons are neglected following Ref. [496]. In Eq. 11.1, $R = \dfrac{1}{1-r}$, where $r = (m_\mu/m_\pi)^2 \simeq 0.573$ and the functions $f_{\nu_i}(x)$ are given as [414]

$$\begin{aligned}
f_{\nu_i}(x) &= g_{\nu_i}(x)\Theta(x-r) + (h_{\nu_i}^{(1)}(x) + h_{\nu_i}^{(2)}(x))\Theta(r-x)\ ,\\
g_{\nu_\mu}(x) &= \frac{3-2r}{9(1-r)^2}(9x^2 - 6\ln x - 4x^3 - 5)\ ,\\
h_{\nu_\mu}^{(1)}(x) &= \frac{3-2r}{9(1-r)^2}(9r^2 - 6\ln r - 4r^3 - 5)\ ,
\end{aligned}$$

$$
\begin{aligned}
h^{(2)}_{\nu_\mu}(x) &= \frac{(1+2r)(r-x)}{9r^2}[9(r+x)-4(r^2+rx+x^2)]\ , \\
g_{\nu_e}(x) &= \frac{2}{3(1-r)^2}[(1-x)(6(1-x)^2+r(5+5x-4x^2))+6r\ln x] \\
h^{(1)}_{\nu_e}(x) &= \frac{2}{3(1-r)^2}[(1-r)(6-7r+11r^2-4r^3)+6r\ln r]\ , \\
h^{(2)}_{\nu_e}(x) &= \frac{2(r-x)}{3r^2}(7r^2-4r^3+7xr-4xr^2-2x^2-4x^2r)\ . \qquad (11.2)
\end{aligned}
$$

B. Leptonic decay channel

The development of electroweak cascade can be illustrated by considering a tree level decay of superheavy particle χ with mass $m_\chi \leq m_{\rm GUT}$ to leptons. According to the Z-burst model, χ particles are decaying into $\bar{\ell}\ell$ pairs and $\chi \to \bar{\nu}\nu$ is the corresponding decay mode. For $m_\chi \gg m_Z$ (m_Z being the Z boson mass), considering the available momentum flow, ($Q^2 \leq \frac{m_\chi^2}{4}$) we can neglect the mass of the Z boson. The smallness of the QCD coupling can be compensated by very large logarithms $\ln(m_\chi^2/m_z^2)$, which is generated for soft or collinear singularities. Similarly for $m_\chi \gg m_W$ (m_W being the mass of W boson), due to large logarithms, the perturbation theory is no more valid and this initiates developing of the electroweak cascade, very similar to the known QCD cascade. There can be a mutual transmutation of electroweak and QCD cascades because the electroweak gauge bosons also split into quarks. This will modify the hadronic spectra to a limited extent while on the other hand the splitting like $W \to \bar{\nu}\nu$ contributes to the electroweak part of the cascade. In order to explain the effects of the SHDM particles decaying into the neutrinos as the final product via the leptonic decay channels, the MC simulations for both the QCD part [513] and the electroweak cascade [499] have been performed.

11.2.2 Components of Neutrino Fluxes

The neutrino flux from SHDM decay can have two origins namely galactic and extragalactic. The galactic neutrino flux from the decay of SHDM with mass m_χ and decay lifetime τ can be written

as

$$\frac{d\Phi_{\rm G}}{dE_\nu}(E_\nu) \;=\; \frac{1}{4\pi m_\chi \tau}\int_V \frac{\rho_\chi(R[r])}{4\pi r^2}\frac{dN}{dE}(E,l,b)dV \;, \tag{11.3}$$

where the neutrino spectrum from decaying SHDM particle is defined as $\frac{dN}{dE}(E,l,b)$, l and b are the galactic coordinates. In the above, $\rho_\chi(R[r])$ is the DM density, which is a function of the distance (R) from the Galactic Centre (GC) and r indicates the distance from the Earth. We adopt the Navarro-Frenk-White (NFW) profile for the DM density [82, 83] in this Chapter. The integration is made over the Milky Way halo for which the maximum value of R is chosen as $R_{\rm max} = 260$ kpc [244].

The isotropic extragalctic neutrino flux from similar decay is given as

$$\frac{d\Phi_{\rm EG}}{dE_\nu}(E_\nu) \;=\; \frac{1}{4\pi m_\chi \tau}\int_0^\infty \frac{\rho_0 c/H_0}{\sqrt{\Omega_m(1+z^3)+(1-\Omega_m)}}\frac{dN}{dE}[E(1+z)]dz \;. \tag{11.4}$$

In the above equation (Eq. 11.4), $c/H_0 = 1.37\times10^{28}$ cm signifies the Hubble radius and ρ_0 ($= 1.15\times10^{-6}$ GeV/cm^3) is the average cosmological DM density at the redshift $z = 0$ (present epoch). The contribution of the matter density to the energy density of the Universe in units of the critical energy density is defined as $\Omega_m = 0.316$. The injected neutrino energy spectrum obtained from the decay of superheavy particles is denoted as $\frac{dN}{dE_\nu}$, which is a function of the particle energy shift $E(z) = (1+z)E$. For both the galactic and extragalactic neutrino fluxes it is assumed that they reach Earth in the ratio 1:1:1 for three neutrino flavours (ν_e, ν_μ, ν_τ). Therefore, at source the ν_e flux can be taken to be Eq. 11.3 and Eq. 11.4 for galactic and extragalactic cases respectively. This is also to note that each of the fluxes $\frac{d\Phi_{\rm EG}}{dE}(E_\nu)$ and $\frac{d\Phi_{\rm G}}{dE}(E_\nu)$ in fact has two components namely the one that is of hadronic origin and the other which is obtained from leptonic decay channel. Therefore

$$\frac{d\Phi_{\rm EG}}{dE}(E_\nu) \;=\; \left(\frac{d\Phi_{\rm EG}}{dE}(E_\nu)\right)_{\rm had} + \left(\frac{d\Phi_{\rm EG}}{dE}(E_\nu)\right)_{\rm lep} \tag{11.5}$$

and

$$\frac{d\Phi_{\rm G}}{dE}(E_\nu) \;=\; \left(\frac{d\Phi_{\rm G}}{dE}(E_\nu)\right)_{\rm had} + \left(\frac{d\Phi_{\rm G}}{dE}(E_\nu)\right)_{\rm lep} \;. \tag{11.6}$$

Thus the total neutrino flux at the source due to the decay of SHDM can be written as

$$\phi^{\rm th}(E_\nu) \;=\; \left(\frac{d\Phi_{\rm EG}}{dE}(E_\nu)\right)_{\rm had} + \left(\frac{d\Phi_{\rm G}}{dE}(E_\nu)\right)_{\rm had} \;, \tag{11.7}$$

$$\phi^{\rm th}(E_\nu) \;=\; \left(\frac{d\Phi_{\rm EG}}{dE}(E_\nu)\right)_{\rm had} + \left(\frac{d\Phi_{\rm G}}{dE}(E_\nu)\right)_{\rm had} + \left(\frac{d\Phi_{\rm EG}}{dE}(E_\nu)\right)_{\rm lep} + \left(\frac{d\Phi_{\rm G}}{dE}(E_\nu)\right)_{\rm lep} \tag{11.8}$$

In Eq. 11.7 only hadronic channel is considered whereas in Eq. 11.8 both hadronic and leptonic channels are taken into account.

11.2.3 Astrophysical Neutrino Flux

Numerous astrophysical sources can produce high energy neutrinos through their highly energetic particle acceleration mechanism of protons, where the latter interact with themselves (pp interactions) or with photons ($p\gamma$ interactions) to finally produce neutrinos. Distant ultrahigh energy (UHE) sources like extragalctic SNR, AGN, GRBs etc. are proposed as the source of IceCube neutrino induced muon events in UHE regime. In this Chapter, we consider the source neutrino flux in the $\sim$ 60 TeV to $\sim$ 120 TeV energy range contributes to the astrophysical neutrino flux.

In order to consider the acceleration mechanism related to the astrophysical sources, the isotropic fluxes for the neutrinos are estimated by an unbroken power law (UPL) after summing over all the possible sources and is given as [514]

$$E_\nu^2 \frac{d\phi'_{\nu_{\rm Ast}}}{dE_\nu}(E_\nu) \;=\; N\left(\frac{E_\nu}{100{\rm TeV}}\right)^{-\gamma} \;{\rm GeV\ cm^{-2}\ s^{-1}\ sr^{-1}} \;, \tag{11.9}$$

where N represents the normalization factor of the flux and γ is the spectral index. We have chosen the values of N and γ for our analyses as 1×10^{-8} and 1.0 respectively for UPL [514]. Assuming the neutrinos are produced in the flavour ratio 1:2:0, the flux for ν_μ in this case at source will be $\frac{2}{3}\frac{d\phi'_{\nu_{\rm Ast}}}{dE_\nu} = \frac{d\phi_{\nu_{\rm Ast}}}{dE_\nu}$ and for ν_e, $\frac{1}{3}\frac{d\phi'_{\nu_{\rm Ast}}}{dE_\nu} = \frac{d\phi_{\nu_{\rm Ast}}}{dE_\nu}$.

Thus the total electron neutrino flux at the source, (diffuse astrophysical sources and the decay of SHDM (via both hadronic and leptonic channel), can be written as

$$\begin{aligned}\phi^{\rm th}(E_\nu) &= \frac{d\phi_{\nu_{\rm Ast}}}{dE_\nu}(E_\nu) + \left(\frac{d\Phi_{\rm EG}}{dE}(E_\nu)\right)_{\rm had} + \left(\frac{d\Phi_{\rm G}}{dE}(E_\nu)\right)_{\rm had} + \left(\frac{d\Phi_{\rm EG}}{dE}(E_\nu)\right)_{\rm lep} + \\ &\quad \left(\frac{d\Phi_{\rm G}}{dE}(E_\nu)\right)_{\rm lep}, \end{aligned} \tag{11.10}$$

11.3 Calculations and Results

The analyses are broadly classified into two parts. One is the analysis of the energy region between 10^5 GeV - 5×10^6 GeV with 6 years. This region is denoted by a pink band by IceCube Collaboration from the analysis of their 6 years of data. There are three actual data points in the pink band. For this analysis, the SHDM decay only through hadronic decay channel is considered and no astrophysical neutrino signal is taken into account (therefore, no astrophysical flux is added for this analysis). We refer this analysis as **Analysis A**. Thereafter, the whole range of energy from 60 TeV to 5 PeV probed by IceCube is taken into consideration. From the analysis of 7.5 years (instead of 6 years as in case of **Analysis A**) of IceCube data, the IceCube Collaboration has furnished two data points between the energy range 60 TeV to 120 TeV and a pink band has also been given for the energy range 120 TeV to 5 PeV with three actual data points within this range. For this analysis of 7.5 years of data the total theoretical flux is calculated by considering astrophysical flux as well as both hadronic and leptonic decay channles of SHDM that produce neutrinos as end products. As an **Analysis A**, here also a χ^2 fit is performed to obtain the mass and the decay lifetime of SHDM. We refer this latter analysis as **Analysis B**. In both the cases oscillations of neutrinos are taken into

Table 11.1: The data points (12 in all) used for the χ^2 fit. First three points (marked with "*") are the observed events by IceCube as shown in Fig. 11.1. See text for details.

Energy (in GeV)	Neutrino Flux ($E_\nu^2 \frac{d\Phi}{dE}$) (in GeV cm^{-2} s^{-1} sr^{-1})	Error
2.51189e+06*	4.16928e-09*	8.2726e-09*
1.19279e+06*	5.03649e-09*	7.5383e-09*
2.68960e+05*	7.50551e-09*	8.1583e-09*
3.54813e+06	5.25248e-09	4.1258e-09
2.30409e+06	5.71267e-09	4.1600e-09
1.52889e+06	6.21317e-09	3.9882e-09
1.05925e+06	6.61712e-09	3.7349e-09
7.18208e+05	7.04733e-09	3.9777e-09
4.46684e+05	7.66476e-09	3.6478e-09
2.86954e+05	8.16308e-09	4.1571e-09
1.90409e+05	8.87827e-09	6.2069e-09
1.43818e+05	9.65612e-09	6.8856e-09

consideration. The formalism of which is given in Chapter 8. Both **Analysis A** and **Analysis B** are performed for 3-flavour oscillations. For **Analysis B** 4 (3 active + 1 sterile)-flavour oscillations are also taken into account with no significant difference.

11.3.1 Analysis A

We have considered the energy region from $\sim 10^5$ GeV to $\sim 5\times10^6$ GeV for UHE neutrinos for our analysis. As mentioned earlier, this region is obtained by the analysis of the IceCube Collaboration for the UHE upgoing muon neutrino spectrum and shown as a pink band (for 1σ uncertainty) in Fig. 2 of Ref. [372]. For our analysis we have chosen all the three experimental points that are included in the pink band and have adopted several other points within the pink band along with their 1σ spread (the bandwidth of the pink band at the position of the chosen band). The chosen data sets for the fit are given in Table 11.1.

The pink band as given by the IceCube Collaboration in Ref. [372] along with the three observational points included in the band are reproduced in Fig. 11.1.

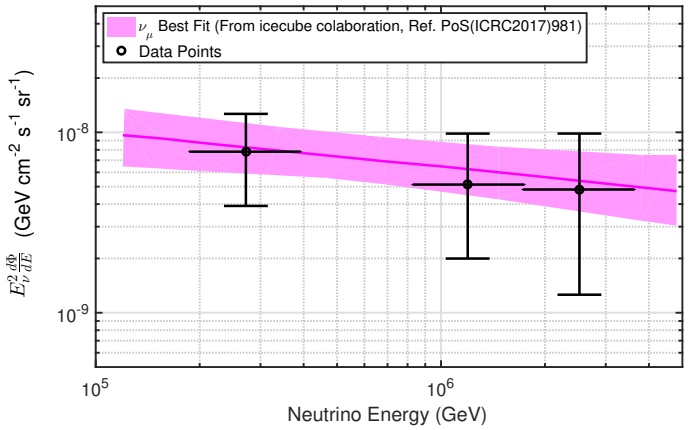

Figure 11.1: The region of IceCube observations adopted for the analysis **Analysis A** considering SHDM decay (reproduced from [372]).

The purpose is to find the best fit values of the mass of the SHDM (m_χ) and its decay lifetime (τ) that on its decay produce the UHE neutrinos in the region considered. The χ^2 for our fit is defined as

$$\chi^2 \;=\; \sum_{i=1}^{n} \left(\frac{E_i^2 \phi_i^{\rm th} - E_i^2 \phi_i^{\rm Ex}}{({\rm err})_{\rm i}} \right)^2 , \tag{11.11}$$

where $n(=12)$ is the number of chosen points (Table 11.1) and $E_i (i = 1, .., n)$ are the energies of the chosen points. In Eq. 11.11 $\phi_i^{\rm th}(E_\nu)$ (and hence $E_i^2 \phi_i^{\rm th}(E_\nu)$), the theoretical flux is obtained from Eq. 11.7 where $E_i^2 \phi_i^{\rm Ex}(E_\nu)$ (=$E_\nu^2 \frac{d\Phi}{dE}$) corresponding to experimental data are given in Table 1 and $({\rm err})_i$ is the $i^{\rm th}$ chosen experimental points (Table 11.1).

Chosing a range of m_χ and the decay lifetime τ we compute the χ^2 and one obtains the best fit values of m_χ and τ by minimizing the χ^2 and the minimum χ^2 denoted as $\chi^2_{\rm min}$. The 1σ, 2σ and 3σ ranges for m_χ and τ are also obtained. As the present χ^2 fit is a two parameter fit, the 1σ, 2σ and 3σ regions are obtained by adopting the range of χ^2 to be $\chi^2_{\rm min} + 2.30, \chi^2_{\rm min} + 4.61, \chi^2_{\rm min} + 9.21$

respectively. The results are shown in Fig. 11.2.

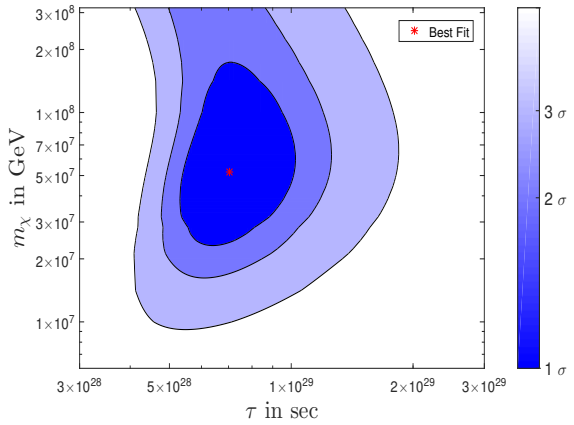

Figure 11.2: $m_\chi - \tau$ (two parameter) χ^2 fit corresponding to the $1\sigma, 2\sigma$, and 3σ level of confidence. See text for details.

The best fit values of m_χ and τ from our analysis are obtained as $m_\chi = 5.2 \times 10^7$ GeV, $\tau = 7.05 \times 10^{28}$ sec. This is denoted by a point in Fig. 11.2. The 1σ, 2σ and 3σ are also shown in Fig. 11.2 by different shades. From this analysis it can be said that in case the UHE neutrinos of the chosen energy range, adopted from IceCube experimental results, are generated from the decay of SHDM then the mass of such DM will be $\sim 5 \times 10^7$ GeV undergoing the rare decay with decay lifetime $\sim 7 \times 10^{28}$ sec. In Fig. 11.3 we show the neutrino flux in the PeV region calculated with these best fit values.

11.3.2 Analysis B

In this analysis, we have made a χ^2 analyses for the event data within a larger energy regime of ~ 60 TeV - ~ 5 PeV with 7.5 years of IceCube data and both the hadronic and leptonic decay channels of SHDM are considered. We also demonstrate that the two event data points in the energy range $\sim$ 60 TeV - $\sim$ 120 TeV [494], can be best explained if these two are considered to have astrophysical origin. Our analysis of the whole range of events (from $\sim$ 60 TeV to $\sim$ 5 PeV) suggests that this

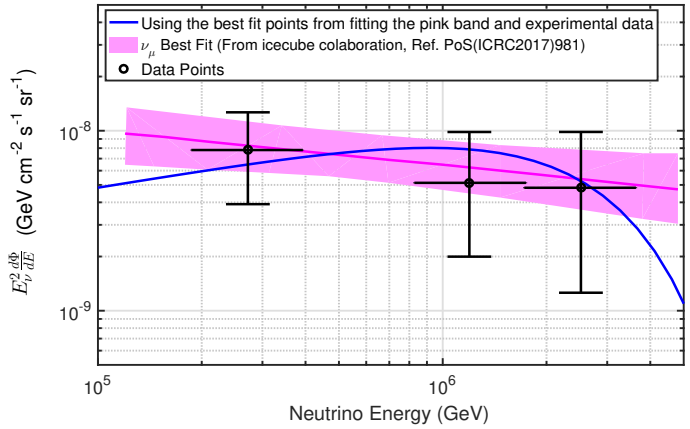

Figure 11.3: The neutrino flux with best fit values of m_χ and τ. Only hadronic channel is considered for SHDM decay.

range seems to have two parts in terms of the possible origins of neutrino events. The energy range spanning between $\sim$ 60 TeV - $\sim$ 120 TeV containing two event data points is the astrophysical component and the second component could have originated from the decay of SHDM.

In the present analysis, besides incorporating the possible astrophysical origin of neutrinos (diffuse flux), both the hadronic and leptonic channels of the decay cascade of these SHDMs that finally produce the UHE neutrinos are included along with the oscillations/suppressions that the neutrinos of a certain flavour would suffer while traversing the astronomical distance to reach the Earth. We consider three active neutrino flavours as also the four (3+1) neutrino scheme, where a sterile neutrino is added to the usual three flavour scenario and compare our results. But we find no significant change in results with those obtained for usual 3-flavour case.

The study of the IceCube data [494] in this regime shows that there are two data points in energy range $\sim$ 60 TeV - $\sim$ 120 TeV and three data points are in the energy regime greater than $\sim$ 120 TeV. As mentioned earlier, the first two data are supposed to be of astrophysical origin [514]. From the analysis, it appears that the SHDM decay considerations for UHE neutrino production is most relevant for the neutrinos with energies $>$ 120 TeV [494].

In this Chapter, we perform a χ^2 fit for the whole data-set. From the χ^2 analysis presented in

this Section (using 7.5 years of IceCube data [494]), the best fit values for the mass of the decaying SHDM and its decay lifetime are obtained.

The choice and data

In Fig. 11.4, we have reproduced the figure from Ref. [494], the energy range (and event data points) from which the data sets for the present analysis have been chosen.

1.Range $\sim$ 60 TeV to $\sim$ 120 TeV

There are two event points in the range $\sim$ 60 TeV-$\sim$ 120 TeV. These two points are adopted in our analysis.

2. Range $\sim 1.2 \times 10^5$ GeV - $\sim 5 \times 10^6$ GeV

There are four data points in the energy region $\sim 1.2 \times 10^5$ GeV to $\sim 5 \times 10^6$ GeV. For one of the four points, only upper limit is given. This region is designated by a pink band (Fig. 11.4).The width of the band indicates 1σ uncertainty. In our analysis we adopt three points in this region (given errors). In addition, we choose another 12 points from the pink band with the errors corresponding to a chosen point is adopted as the width of the band at that point. Thus, in this region we have a total of 15 points.

All the 17 event points (henceforth referred to as “data points") used in the present analyses are enlisted in Table 11.2.

Definition of χ^2

The χ^2 is already defined in Eq. 11.11. Note that $n = 17$ when the whole range of energy is considered. For the total energy range, therefore the total flux is as given in Eq. 11.10, while in case the analysis is performed with partial energy ranges, relevant fluxes or their sum will be considered. In Eq. 11.11, $\phi_i^{\rm Ex}$ denotes the experimental data point at energy E_i with error $(\text{err})_i$ (Table 11.2).

For the χ^2 fit, the theoretical fluxes for electron neutrinos are then computed using Eqs. 11.9, 11.10 alongwith Eqs. 11.3 - 11.6. After the neutrinos undergo oscillation on reaching the Earth, the muon neutrino flux on arrival is obtained from Eq. 8.28 (for 3-flavour case) or Eq. 8.26 (for 4-flavour case) in Chapter 8.

Energy (in GeV)	Neutrino Flux ($E_\nu^2 \frac{d\Phi}{dE}$) (in GeV cm^{-2} s^{-1} sr^{-1})	Error (in GeV cm^{-2} s^{-1} sr^{-1})
6.13446×10^{4} *	2.23637×10^{-8}	2.16107×10^{-8}
1.27832×10^{5} *	2.70154×10^{-8}	1.30356×10^{-8}
2.69271×10^{5} *	7.66476×10^{-9}	8.5082×10^{-9}
1.19479×10^{6} *	5.14335×10^{-9}	7.6982×10^{-9}
2.51676×10^{6} *	4.34808×10^{-9}	8.4481×10^{-9}
3.54813×10^{6}	5.25248×10^{-9}	4.1258×10^{-9}
2.30409×10^{6}	5.71267×10^{-9}	4.1600×10^{-9}
1.52889×10^{6}	6.21317×10^{-9}	3.9882×10^{-9}
1.05925×10^{6}	6.61712×10^{-9}	3.7349×10^{-9}
7.18208×10^{5}	7.04733×10^{-9}	3.9777×10^{-9}
4.46684×10^{5}	7.66476×10^{-9}	3.6478×10^{-9}
2.86954×10^{5}	8.16308×10^{-9}	4.1571×10^{-9}
1.90409×10^{5}	8.87827×10^{-9}	6.2069×10^{-9}
1.43818×10^{5}	9.65612×10^{-9}	6.8856×10^{-9}
2.51189×10^{6}	4.16928×10^{-9}	8.2726×10^{-9}
1.19279×10^{6}	5.03649×10^{-9}	7.5383×10^{-9}
2.68960×10^{5}	7.50551×10^{-9}	8.1583×10^{-9}

Table 11.2: The selected data points for the χ^2 fit. The points obeserved by the IceCube Collaboration (shown in Fig. 11.4) are marked with "*".

Following the formalism described above and Section 11.2.2, 11.2.3 we make the χ^2 fit by χ^2 minimisation with the data given in Table 11.2. The use has been made of Eqs. 11.9, 11.10 alongwith Eqs. 11.3 - 11.6 and Eqs. 8.28, 8.26 (Chapter 8) for computations of theoretical flux components namely astrophysical flux and those predicted from our proposition of the decay of a SHDM via the hadronic and leptonic channels. From the fit, the best fit values of the two unknown parameters of the formalism namely the mass m_χ and the lifetime τ of the decaying DM are obtained. The $1\sigma, 2\sigma$ and 3σ ranges for each of the χ^2 analysis are also computed and furnished along with the study of the quantity of fit for different chosen data sets from Table 11.2.

We furnish the analyses by considering four different cases. These are given below.

- Case I - All 17 points of the Table 11.2 is fitted with the theoretical flux at source as in Eq. 11.10 where astrophysical flux at source computed as in Eq. 11.9.

- Case II - All 17 points of Table 11.2. But the theoretical flux is computed without the astrophysical component (only the hadronic and leptonic channel of SHDM decay)

$$\phi^{\rm th}(E_\nu) = \left(\frac{d\Phi_{\rm EG}}{dE}(E_\nu)\right)_{\rm had} + \left(\frac{d\Phi_{\rm G}}{dE}(E_\nu)\right)_{\rm had} + \left(\frac{d\Phi_{\rm EG}}{dE}(E_\nu)\right)_{\rm lep} + \left(\frac{d\Phi_{\rm G}}{dE}(E_\nu)\right)_{\rm lep}.$$

- Case III- All 17 points of Table 11.2. Theoretical flux

$$\phi^{\rm th}(E_\nu) = \frac{d\phi_{\nu_{\rm Ast}}}{dE_\nu}(E_\nu) + \left(\frac{d\Phi_{\rm EG}}{dE}(E_\nu)\right)_{\rm had} + \left(\frac{d\Phi_{\rm G}}{dE}(E_\nu)\right)_{\rm had}$$

(no leptonic channel for SHDM decay, the astrophysical flux is from Eq. 11.9).

- Case IV- First 5 points of Table 11.2. Theoretical flux

$$\phi^{\rm th}(E_\nu) = \frac{d\phi_{\nu_{\rm Ast}}}{dE_\nu}(E_\nu) + \left(\frac{d\Phi_{\rm EG}}{dE}(E_\nu)\right)_{\rm had} + \left(\frac{d\Phi_{\rm G}}{dE}(E_\nu)\right)_{\rm had}$$

(the astrophysical flux is from Eq. 11.9).

In Figs. 11.5 - 11.8 we show (a) the fluxes calculated with the fitted values using corresponding theoretical flux formula and (b) the m_χ-τ contour plot with $1\sigma, 2\sigma$ and 3σ contours. The best fit values for m_χ and τ are also shown.

- It is shown from Figs. 11.5, 11.6 that the first two points of Table 11.2 (in the energy range $\sim$ 60 TeV - $\sim$ 120 TeV) cannot be fitted if astrophysical flux is not considered.

- The data points in the energy range ($\sim 1.2\times10^5$ GeV - $\sim 5\times10^6$ GeV) can be well explained from the consideration that these neutrinos originate from the decay of SHDM.

- The neutrino events within the energy range $\sim 1.2\times10^5$ GeV - $\sim 5\times10^6$ GeV (pink band) is very well represented by the neutrinos produced from the SHDM decay via hadronic channel.

Set	m_χ in GeV	τ in sec	Value of χ^2_{min}
All points, All channels (the astrophysical flux is taken from Eq. 11.9)	1.9724×10^8	6.3246×10^{28}	1.2115
All points, Leptonic channel, Hadronic channel	1.9055×10^7	3.3965×10^{28}	2.8674
All points, Hadronic channel Astrophysical flux (Eq. 11.9)	1.4962×10^8	5.2605×10^{28}	1.2126
First 5 points, Hadronic channel Astrophysical flux (Eq. 11.9)	4.5601×10^7	6.3405×10^{28}	0.9321

Table 11.3: Best fit values of m_χ and τ for different cases.

As mentioned, the best fit values of the parameters m_χ and τ (as well as $1\sigma, 2\sigma$ and 3σ contours) for each of the cases are shown in Fig. 11.5(b) - 11.8(b) respectively. These values along with the respective values for $\chi^2_{\rm min}$ are shown in Table 11.3.

From the above analyses therefore, it can be stated that the UHE neutrino events reported by IceCube in the energy range $\sim 1.2 \times 10^5$ GeV to $\sim 5 \times 10^6$ GeV can be well described to have originated from the decay of a SHDM of mass $\sim 10^7 - 10^8$ GeV and decay lifetime $\sim 10^{28}$ sec.

We also like to state that we repeat the entire analysis with 4-flavour oscillation scenario with no or any significant changes. For this purpose, the values of mixing angles are chosen as $\theta_{14} = 3.6^o, \theta_{24} = 4^o, \theta_{34} = 18.48^o$. These values are within the allowed limits of the analyses of NOνA [155], MINOS [137], Daya Bay [127] neutrino experiments.

In Fig. 11.9 we furnish a ternary plot showing the flavour ratios of the active neutrinos on reaching the Earth for both the 3-flavour and 4-flavour oscillation cases. The flavour $(\nu_e, \nu_\mu, \nu_\tau)$ ratio of 1:1:1 for active neutrinos are also shown for comparison. The assumed production ratio of 1:2:0 for the active neutrinos is also furnished. The flavour ratio barely changes when 4-flavour oscillation is considered.

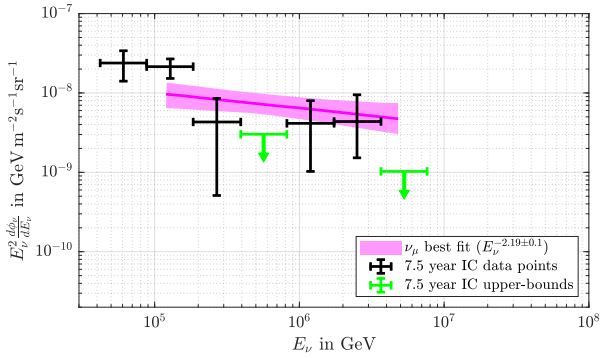

Figure 11.4: The data points and range of energy considered in the present analysis (**Analysis B**). The pink band is also shown. These are reproduced Ref. [494]

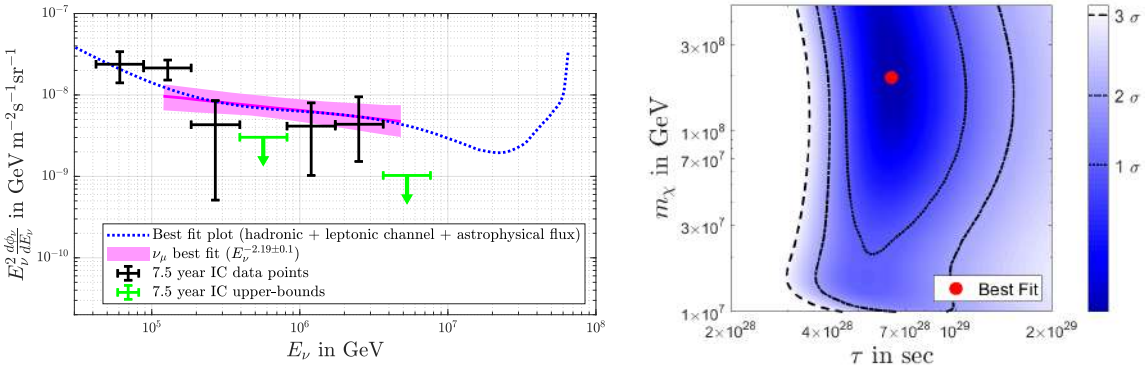

(a) (b)

Figure 11.5: (a) Flux, (b) contour by considering all points, all channels (The astrophysical flux is computed from Eq. 11.9). See text for details.

11.4 Summary

In this Chapter, we have explored the possibility that the UHE neutrino detected by IceCube in the PeV energy region could have originated from the decay of SHDM. Such SHDM could be created at the early Universe during spontaneous symmetry breaking at the GUT scale and they decay to leptons at the electroweak scale involving the processes of QCD cascade and electroweak cascade. The numerical evolutions of such processes are generally done by MC methods or by evolving the DGLAP equations treated numerically. In a recent work M. Kachelriess *et al.* [499]

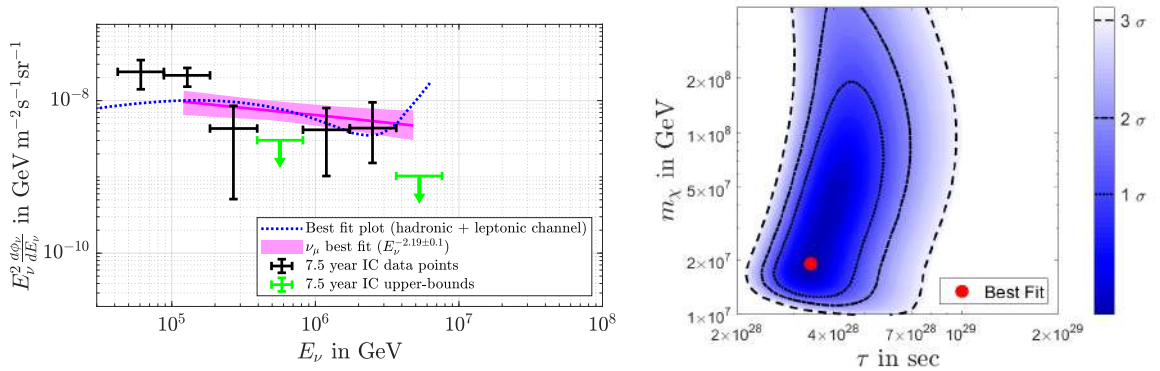

(a) (b)

Figure 11.6: (a) Flux, (b) contour by considering all points, leptonoic+hadronic channels. See text for details.

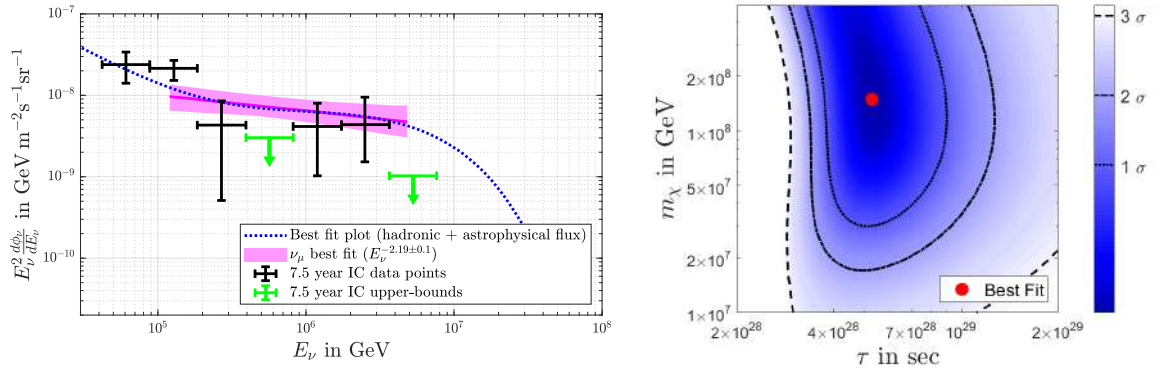

(a) (b)

Figure 11.7: (a) Flux, (b) contour by considering all points, hadronic+astro channels (the astrophysical flux is computed from Eq. 11.9). See text for details.

made a MC analysis for such heavy dark matter decay to leptons such as $\nu\bar{\nu}$ pair and e^+e^- pair as well as the photons where the recently updated limits of diffuse gamma ray flux has also been incorporated. In this Chapter, we compute the neutrino spectrum from the heavy dark matter decay as prescribed in reference and obtained the galactic and extragalactic neutrino fluxes from such decays. We then constrain the two unknown parameters namely the heavy dark matter mass (m_χ) and its decay lifetime (τ) by making a χ^2 fit of the calculated neutrino flux with those given from

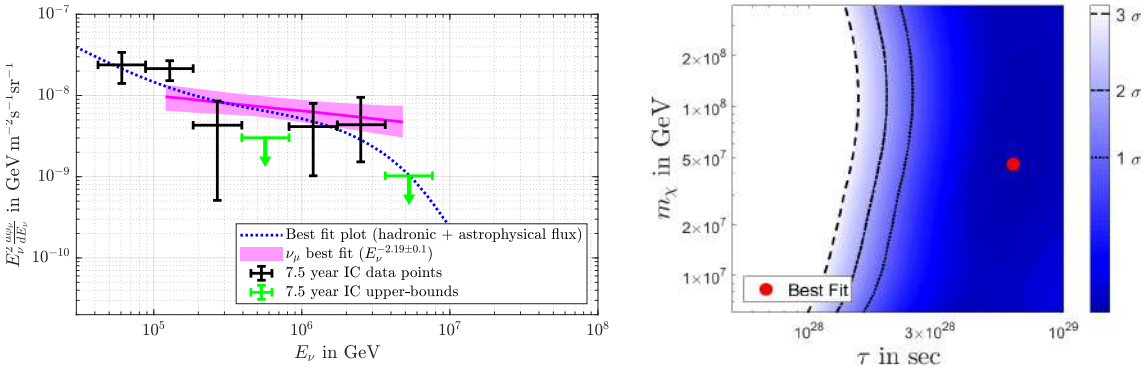

(a) (b)

Figure 11.8: (a) Flux, (b) contour by considering first 5 points with hadronic+astro channels (Eq. 11.9 is considered as the astrophysical flux). See text for details.

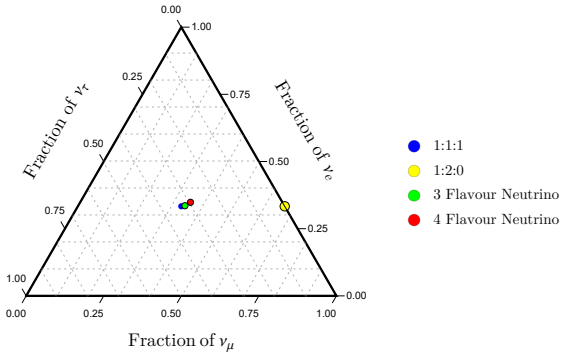

Figure 11.9: Ternary plot showing the neutrino flavour ratios on arriving the Earth from high energy sources.

the observed events at IceCube by the IceCube Collaboration. For this purpose, we have chosen the region given by the IceCube Collaboration corresponding to the upgoing muon neutrinos with two energies ranges - 10^5 GeV - 5×10^6 GeV (**Analysis A**) and 60 TeV - 5 PeV (**Analysis B**).

For **Analysis A**, we have considered 6 years of IceCube Collaboration data (Fig. 2 of [372]). The IceCube Collaboration analysis designated this region by a pink band of 1σ width in their published data and plots. We have made a χ^2 fit adopting a data set from this region that includes the observed points as well as other points chosen from within this pink band. For this analysis, we have considered the decay of SHDM only through the hadronic decay channel and no astrophysical

origin of neutrinos is taken into account. Our χ^2 fit yield the best fit value for the parameters m_χ, τ as $m_\chi = 5.2 \times 10^7$ GeV, $\tau = 7.05 \times 10^{28}$ sec. We also furnish $1\sigma, 2\sigma$ and 3σ C.L. contours in the parameter space $m_\chi - \tau$.

For **Analysis B**, we consider the UHE neutrino events reported by IceCube Collaboration in the energy range $\sim$ 60 TeV - $\sim$ 5 PeV with 7.5 years of data [494]. The lower energy range between $\sim$ 60 TeV to $\sim$ 120 TeV represented by two event data points (Fig. 11.4) appears to be consistent with the flux of astrophysical origin, while for the higher energy range between $\sim 1.2 \times 10^5$ GeV - $\sim 5 \times 10^6$ GeV, the neutrinos could have originated from the SHDM decay. In addition to the astrophysical origin, both the hadronic and leptonic decay channels are considered in this analysis. We have considered four different cases and made two parameter χ^2 fit for each of the four different cases, which are mentioned in Table 11.3. Both 3- and 4-flavour neutrino oscillations are also taken into account and there is no significant changes appear in the flavour ratio with those obtained for 3-flavour case (see Fig. 11.9). Thus from our analyses it appears that the UHE neutrino signals in the energy range $\sim 1.2 \times 10^5$ GeV - $\sim 5 \times 10^6$ GeV reported by IceCube could have originated from the decay of SHDM of mass $\sim 10^7 - 10^8$ GeV and decay lifetime $\sim 10^{28}$ sec.

CHAPTER 12

THE VIOLATION OF EQUIVALENCE PRINCIPLE AND FOUR NEUTRINO OSCILLATIONS FOR LONG BASELINE NEUTRINOS

A consequence of violation of equivalence principle (VEP) is that different types of neutrinos can couple to gravity with different strengths. In this scenario, if the gravity eigenstates are not the same as the avour eigenstates then it may lead to avour mixing and hence gravity induced neutrino oscillations. But there is no de nite evidence of VEP in nature. Even if the equivalence principle is indeed violated, their measure is expected to be extremely small. The possibility to probe such a small VEP is considered for the case of long baseline (LBL) neutrinos in a 4- avour neutrino framework (3 active + 1 sterile) where both mass and gravity induced oscillations are taken into account. For the muon neutrino ux from a neutrino factory or accelerator, the muon yields are computed and compared at a far end detector with and without VEP.

12.1 Introduction

The neutrinos undergo avour oscillations due to the phase difference that is acquired by a neutrino eigenstate during its propagation and this phase difference depends on the baseline length and the mass squared difference of two neutrino mass eigenstates for the case of mass- avour oscillation. In addition to the mass induced oscillations, VEP [515, 516] can also induce neutrino oscillations. If the equivalence principle is indeed violated in nature, different types of neutrinos couple differently with gravity which means that different neutrino avour eigenstates interact with the gravitational eld with different strengths. Thus in this situation the gravitational coupling (constant) G is different for different types of neutrinos. If the gravity eigenstates of neutrinos are not identical to those of their weak interaction eigenstates then a gravity- avour mixing may result similar to the mass- avour mixing. An important feature of Einstein's general theory of relativity is the equivalence principle which leads to the equivalence of the inertial mass and the gravitational mass. This is stated that an observer standing on the Earth experiences the gravitational force which is same as the pseudo force experienced by the same observer in accelerated reference frame. Therefore, if the equivalence principle is indeed violated, then the coupling strengths of neutrinos with the gravitational eld as well as the gravitational constant (G) are no more universal. While propagating through a gravitational eld, the energy E of a neutrino will be shifted by an amount $E' = \sqrt{g_{00}}E = E(1 - \frac{GM}{R}) = E(1 + \phi)$ [516, 517], where the gravitational potential (ϕ) is de ned as $\phi = \frac{GM}{R}$, M and R being the mass of the source and the distance over which the gravitational eld operates respectively [1]. This is known as the gravitational redshift. By virtue of the equivalence principle, energies of different types of neutrinos are shifted by an equal amount and

[1] In the presence of gravitational eld, the proper time in a curve manifold is $d\tau = \sqrt{g_{\mu\nu}dx^\mu dx^\nu}$ which can lead to the relation $E' = \sqrt{g_{00}}E$. The proper time ($d\tau$) relates to the coordinate time (dt) through $d\tau = \sqrt{g_{\mu\nu}dx^\mu dx^\nu}$ (when clock is at rest). If a distant star is emitting N number of waves having frequency $f_{\rm star}$ and proper time interval $\Delta\tau_{\rm star}$ respectively and if the Earth is detecting the same with frequency $f_{\rm Earth}$ and proper time interval $\Delta\tau_{\rm Earth}$, then $\frac{f_{\rm star}}{f_{\rm Earth}} = \frac{\Delta\tau_{\rm Earth}}{\Delta\tau_{\rm star}} = \frac{\sqrt{g_{00}(x_{\rm Earth})}}{\sqrt{g_{00}(x_{\rm star})}} = \sqrt{\left(\frac{1+2\phi_{\rm Earth}}{1+2\phi_{\rm star}}\right)} = 1 + |\Delta\phi|$.

the phase difference induced by gravity between two types of neutrinos may not be generated in this case. But if the equivalence principle is violated then for different types of neutrinos the energies would be shifted differently. The VEP will induce a phase $\sim \Delta EL$, $\Delta E = |E_i - E_j|$, E_i and E_j being the redshifted energies of the neutrino species i and j respectively (and are different since gravitational coupling G is different for different neutrinos) and L de nes the baseline length from the source to the detector, E_i, E_j are the energy eigenstates in gravity basis. Similar to the case for mass- avour oscillations, the acquired phase difference will generate a gravity induced oscillations between different avours of neutrinos. The quantity $\frac{L}{\lambda_{ij}}$ (λ_{ij} denoting the oscillation length) in the oscillatory part $\left[\sin^2\left(\frac{\pi L}{\lambda_{ij}}\right)\right]$ then takes a form $\sim |\Delta EL| = |\Delta f_{ij}|LE$, where $|\Delta f_{ij}| = |f_i - f_j|$, f_i is de ned as $f_i = \frac{G_i M}{R} = (\frac{GM}{R})\alpha_i = \phi\alpha_i$, G_i being the gravitational coupling of the neutrino having index i. The effects of VEP on neutrino oscillation are addressed here along with usual mass- avour oscillations with three active neutrinos and one sterile. Using the latest experimental limits on active-sterile neutrino mixing and mass squared difference Δm^2_{41} for normal hierarchy of neutrino mass eigenstates (and assumed normal hierarchy for neutrino gravity eigenstates) and best t values of active neutrino mixing parameters (mixing angles and mass squared differences), combined four avour gravity induced and mass induced neutrino oscillation probabilities are obtained including the matter effect induced by the matter through which the neutrinos travel. VEP will induce new set of parameters Δf_{ij} which change the neutrino oscillation probabilities signi cantly. This is demonstrated in this Chapter for a neutrino beam propagating through an assumed baseline of 7000 Kms inside Earth matter. Therefore, even if VEP is very small, it would signi cantly affect the number of muon yields (from ν_μ) at the far detector in a long baseline (LBL) neutrino experiment. In this Chapter, estimates are made for neutrino induced muon yields for these neutrino yields considering an LBL neutrino experiment with a baseline length of around 7359 Kms with the end detector to be an iron calorimeter (ICAL) of 50 kTon such as the one proposed for the India-based Neutrino Observatory or INO [181]. The neutrinos are originated from a neutrino factory or accelerator such as CERN. The number of right sign and wrong sign (explained later) muon yields at the

end detector are estimated for different values of Δf_{ij} (the VEP effect).

12.2 Neutrino Oscillations in Matter with VEP in 4-Flavour Scenario

In the case of massive neutrinos, the neutrino avour eigenstates $|\nu_\alpha\rangle$ produced in a charged current (CC) weak interactions can be expressed as the linear combination of the mass eigenstates $|\nu_i\rangle$ via a unitary mixing matrix U.

$$|\nu_\alpha\rangle \;=\; \sum_{i=1}^{n} U_{\alpha i}|\nu_i\rangle \;, \tag{12.1}$$

where the number of neutrino species is indicated by n. As mentioned, an extra sterile neutrino (ν_s) in addition to the three active neutrinos (ν_e, ν_μ, ν_τ) is considered here.

For the 4- avour scenario, the mixing matrix is given by (Chapter 8)

$$U_{(4\times4)} \;=\; \begin{pmatrix} c_{14}\tilde{U}_{e1} & c_{14}\tilde{U}_{e2} & c_{14}\tilde{U}_{e3} & s_{14} \\ -s_{14}s_{24}\tilde{U}_{e1} + c_{24}\tilde{U}_{\mu1} & -s_{14}s_{24}\tilde{U}_{e2} + c_{24}\tilde{U}_{\mu2} & -s_{14}s_{24}\tilde{U}_{e3} + c_{24}\tilde{U}_{\mu3} & c_{14}s_{24} \\ \begin{matrix}-c_{24}s_{14}s_{34}\tilde{U}_{e1}\\ -s24s34\tilde{U}_{\mu1}\\ +c_{34}\tilde{U}_{\tau1}\end{matrix} & \begin{matrix}-c_{24}s_{14}s_{34}\tilde{U}_{e2}\\ -s24s34\tilde{U}_{\mu2}\\ +c_{34}\tilde{U}_{\tau2}\end{matrix} & \begin{matrix}-c_{24}s_{14}s_{34}\tilde{U}_{e3}\\ -s24s34\tilde{U}_{\mu3}\\ +c_{34}\tilde{U}_{\tau3}\end{matrix} & c_{14}c_{24}s_{34} \\ \begin{matrix}-c_{24}c_{34}s_{14}\tilde{U}_{e1}\\ -s_{24}c_{34}\tilde{U}_{\mu1}\\ -s_{34}\tilde{U}_{\tau1}\end{matrix} & \begin{matrix}-c_{24}c_{34}s_{14}\tilde{U}_{e2}\\ -s_{24}c_{34}\tilde{U}_{\mu2}\\ -s_{34}\tilde{U}_{\tau2}\end{matrix} & \begin{matrix}-c_{24}c_{34}s_{14}\tilde{U}_{e3}\\ -s_{24}c_{34}\tilde{U}_{\mu3}\\ -s_{34}\tilde{U}_{\tau3}\end{matrix} & c_{14}c_{24}c_{34} \end{pmatrix} , \tag{12.2}$$

where $\tilde{U}_{\alpha i}$ etc. indicate the elements of the avour mixing matrix in 3- avour scenario, which is given in Eq. 8.15 (Chapter 8).

The time evolution equation in the case of four neutrino avours, $|\nu_e\rangle$, $|\nu_\mu\rangle$, $|\nu_\tau\rangle$ and $|\nu_s\rangle$ is given by

$$i\frac{d}{dt}\begin{pmatrix}\nu_e\\ \nu_\mu\\ \nu_\tau\\ \nu_s\end{pmatrix} = H\begin{pmatrix}\nu_e\\ \nu_\mu\\ \nu_\tau\\ \nu_s\end{pmatrix} , \tag{12.3}$$

where

$$H = U_{(4\times4)}H_d U^{\dagger}_{(4\times4)} . \tag{12.4}$$

In the above, the Hamiltonian in the mass basis is given by

$$H_d = \begin{pmatrix}E_1 & 0 & 0 & 0\\ 0 & E_2 & 0 & 0\\ 0 & 0 & E_3 & 0\\ 0 & 0 & 0 & E_4\end{pmatrix} , \tag{12.5}$$

where $E_i (i = 1-4)$ are the energy eigen values which can be expressed in terms of the momentum p and mass eigen values m_i, as

$$E_i = \sqrt{p_i^2 + m_i^2} \simeq p_i + \frac{m_i^2}{2p_i} \simeq p + \frac{m_i^2}{2E} , \tag{12.6}$$

with $i = 1, 2, 3, 4$ and $p_i \simeq p$. With this H_d can be rewritten as

$$H_d = \begin{pmatrix} p & 0 & 0 & 0 \\ 0 & p & 0 & 0 \\ 0 & 0 & p & 0 \\ 0 & 0 & 0 & p \end{pmatrix} + \frac{1}{2E} \begin{pmatrix} m_1^2 & 0 & 0 & 0 \\ 0 & m_2^2 & 0 & 0 \\ 0 & 0 & m_3^2 & 0 \\ 0 & 0 & 0 & m_4^2 \end{pmatrix} . \tag{12.7}$$

In Eq. 12.7, the matrix $\mathrm{diag}(p, p, p, p)$ does not contribute to the neutrino oscillations as it does not induce any phase differences between the neutrinos and hence we do not consider this term further in the calculation. Subtracting m_1^2 from all the diagonal elements of the matrix $\mathrm{diag}(m_1^2, m_2^2, m_3^2, m_4^2)$, we have

$$H_d = \frac{1}{2E}\mathrm{diag}(0, \Delta m_{21}^2, \Delta m_{31}^2, \Delta m_{41}^2) , \tag{12.8}$$

where $\Delta m_{21}^2 = m_2^2 - m_1^2, \Delta m_{31}^2 = m_3^2 - m_1^2, \Delta m_{41}^2 = m_4^2 - m_1^2$.

We explore the mass- avour oscillations in matter and gravity induced oscillations in a single framework by considering $|\nu_\alpha\rangle \neq |\nu_i\rangle \neq |\nu_{Gi}\rangle$. Here the gravity basis and mass basis are approximately identical and do not coincide with the avour basis. Therefore, as in the case for mass basis, in 4- avour framework, the gravity eigenstates $|\nu_{Gi}\rangle (i = 1, 2, 3, 4)$ are connected to the avour eigenstates $|\nu_\alpha\rangle (\alpha = e, \mu, \tau, s)$ through a mixing matrix $U'_{(4\times4)}$ with avour-gravity mixing angle $\theta'_{ij} (i \neq j), i, j = 1, 2, 3, 4$ in the presence of the gravitational eld. Thus

$$|\nu_\alpha\rangle = U'_{(4\times4)} |\nu_{G_i}\rangle , \tag{12.9}$$

where the avour-gravity mixing matrix ($U^{'}_{(4\times4)}$) can be represented as

$$U^{'}_{(4\times4)} = \begin{pmatrix} c'_{14}U'_{e1} & c'_{14}U'_{e2} & c'_{14}U'_{e3} & s'_{14} \\ -s'_{14}s_{24}U'_{e1} + c'_{24}U'_{\mu1} & -s'_{14}s_{24}U'_{e2} + c'_{24}U'_{\mu2} & -s'_{14}s_{24}U'_{e3} + c'_{24}U'_{\mu3} & c'_{14}s_{24} \\ \begin{matrix} -c'_{24}s_{14}s'_{34}U'_{e1} \\ -s'24s'34U'_{\mu1} \\ +c'_{34}U'_{\tau1} \end{matrix} & \begin{matrix} -c'_{24}s'_{14}s'_{34}U'_{e2} \\ -s'24s'34U'_{\mu2} \\ +c'_{34}U'_{\tau2} \end{matrix} & \begin{matrix} -c'_{24}s'_{14}s'_{34}U'_{e3} \\ -s'24s'34U'_{\mu3} \\ +c'_{34}U'_{\tau3} \end{matrix} & c'_{14}c'_{24}s'_{34} \\ \begin{matrix} -c'_{24}c'_{34}s'_{14}U'_{e1} \\ -s'_{24}c'_{34}U'_{\mu1} \\ -s'_{34}U'_{\tau1} \end{matrix} & \begin{matrix} -c'_{24}c'_{34}s'_{14}U'_{e2} \\ -s'_{24}c'_{34}U'_{\mu2} \\ -s'_{34}U'_{\tau2} \end{matrix} & \begin{matrix} -c'_{24}c'_{34}s'_{14}U'_{e3} \\ -s'_{24}c'_{34}U'_{\mu3} \\ -s'_{34}U'_{\tau3} \end{matrix} & c'_{14}c'_{24}c'_{34} \end{pmatrix} . \tag{12.10}$$

The evolution equation in avour basis due to the presence of the gravitational eld is therefore written as

$$i\frac{d}{dt}|\nu_\alpha\rangle = H'|\nu_\alpha\rangle \ , \tag{12.11}$$

where $H' = U'_{(4\times4)}H_G U'^{\dagger}_{(4\times4)}$ and for 4- avour scenario $H_G = \mathrm{diag}(E_{G1}, E_{G2}, E_{G3}, E_{G4})$. If the equivalence principle is indeed violated, all the gravitational energy eigenvalues will induce phase differences to neutrino eigenstates and therefore we have

$$H_G = \mathrm{diag}((1-\phi\alpha_1)E, (1-\phi\alpha_2)E, (1-\phi\alpha_3)E, (1-\phi\alpha_4)E))$$

with $\phi\alpha_i = \frac{G_i M}{R} = \frac{GM}{R}\alpha_i$. In this case, the phase differences can be expressed as

$$\Delta E_{ij,G} = \frac{GM}{R}\Delta\alpha_{ij}E = \frac{GM}{R}(\alpha_i - \alpha_j)E = \phi\Delta\alpha_{ij}E = \Delta f_{ij}E \ , \tag{12.12}$$

where $\Delta f_{ij} = \frac{GM}{R}\Delta\alpha_{ij} = \Delta\alpha_{ij}\phi; i, j = 1, 2, 3, 4$. After subtracting $(1-\phi\alpha_1)E$ term from all the diagonal elements of H_G, we have $H_G = \mathrm{diag}(0, \Delta f_{21}E, \Delta f_{31}E, \Delta f_{41}E)$. In the present neutrino oscillations formalism, we also include the matter (MSW) effect. The effective Hamiltonian of the system including both gravity effect and matter effect is given by

$$\begin{aligned} H'' &= H + H' + V \\ &= U_{(4\times4)}H_d U^{\dagger}_{(4\times4)} + U'_{(4\times4)}H_G U'^{\dagger}_{(4\times4)} + V \ . \end{aligned} \tag{12.13}$$

In the above, the matter potential (V) can be written as

$$V = \mathrm{diag}(V_{\mathrm{CC}}, 0, 0, -V_{\mathrm{NC}}) \ , \tag{12.14}$$

where V_{CC} is the CC potential that appears due to the interactions of neutrinos with the electrons of the medium, which are mediated by the $W^{\pm}$ exchange and V_{NC} denotes the NC potential responsible for the interactions mediated by Z^0 bosons. With $V_{\mathrm{CC}} = \sqrt{2}G_F N_e$ and $V_{\mathrm{NC}} = \frac{G_F N_n}{\sqrt{2}}$, the matter potential (V) can be expressed as

$$V = \mathrm{diag}(\sqrt{2}G_F N_e, 0, 0, G_F N_n/\sqrt{2}) \ , \tag{12.15}$$

where G_F is the Fermi constant, N_e and N_n are the number densities of electron and neutrons respectively inside the matter through which neutrinos propagate. In the present formalism, for the purpose of the calculation the mass mixing angles (θ_{ij}) and gravity mixing angles (θ'_{ij}) with the avour eigenstates are assumed same, and hence $U_{(4\times4)} = U'_{(4\times4)} = U$. The effective Hamiltonian

according to this assumption takes the form

$$\begin{aligned} H'' &= U(H_d + H_G)U^\dagger + V \\ &= U(\mathrm{diag}(0, \frac{\Delta m^2_{21}}{2E}, \frac{\Delta m^2_{31}}{2E}, \frac{\Delta m^2_{41}}{2E}) \\ &\quad +\mathrm{diag}(0, \Delta f_{21}E, \Delta f_{31}E, \Delta f_{41}E))U^\dagger + V \ . \end{aligned} \tag{12.16}$$

We neglect the terms Δm^2_{21} and Δf_{21} by assuming that both the neutrino mass eigenstates $|\nu_1\rangle$, $|\nu_2\rangle$ and gravity eigenstates $|\nu_{G1}\rangle, |\nu_{G2}\rangle$ are very close to each other. Thus the above equation can be written as

$$\begin{aligned} H'' &= U\,\mathrm{diag}(0, 0, \frac{\Delta m^2_{31}}{2E} + \Delta f_{31}E, \frac{\Delta m^2_{41}}{2E} + \Delta f_{41}E)U^\dagger + V \\ &= U\,\mathrm{diag}(0, 0, \frac{\Delta \mu^2_{31}}{2E}, \frac{\Delta \mu^2_{41}}{2E})U^\dagger + V \ . \end{aligned} \tag{12.17}$$

In the above,

$$\begin{aligned} \frac{\Delta \mu^2_{31}}{2E} &= \frac{\Delta m^2_{31}}{2E} + \Delta f_{31}E \ , \\ \frac{\Delta \mu^2_{41}}{2E} &= \frac{\Delta m^2_{41}}{2E} + \Delta f_{41}E \ . \end{aligned} \tag{12.18}$$

In Eq. 12.17, the unitary matrix U is the 4×4 matrix similar to that given in Eq. 12.2. The active neutrino mixing angles described in 3×3 PMNS matrix (Eq. 8.15, Chapter 8) are obtained from the latest bounds given by different neutrino experiments [417] and these are

$$\begin{aligned} \theta_{12} = 33.96^0, \quad \theta_{23} = 48.3^0, \quad \theta_{13} = 8.61^0 \\ \Delta m^2_{21} = 7.53 \times 10^{-5}\mathrm{eV}^{-2}, \quad \Delta m^2_{31} = 2.5 \times 10^{-3}\mathrm{eV}^{-2} \ . \end{aligned} \tag{12.19}$$

For simplicity, normal hierarchy for neutrino eigenstates has been considered and CP violating phase $\delta_{\mathrm{CP}} = 0$.

Apart from the active neutrino oscillation parameters mentioned in Eq. 12.19, there are three active-sterile neutrino mixing angles $\theta_{14},\ \theta_{24},\ \theta_{34}$. Several neutrino oscillation experiments such as MINOS [137–148], Daya Bay [127–133], Bugey [174], T2K [149], IceCube [371] etc. provide stringent limits on these mixing angles ($\theta_{i4},\ i = 1 - 3$) for different values of mass squared difference Δm^2_{41}. For the calculations in this Chapter, combined limit on mixing angle θ_{14} obtained from the analyses by Daya Bay, MINOS and Bugey-3 [148] has been used. Also considered is the constraints from cosmological data [Adams *et al.*] [518] along with the neutrino oscillation results from other experiments. In this reference, it is concluded that PLANCK data exclude the regions when $\Delta m^2_{41} \geq 5 \times 10^{-2}$ eV^2 and for $\Delta m^2_{41} \leq 5 \times 10^{-2}$ eV^2, limits from the combined analysis of Daya Bay, MINOS and Bugey-3 [148] become signi cant (see Fig. 2 and Fig. 4 of Ref. [518] for details). With these constraints, in this Chapter, $\theta_{14} = 3.6^0$ has been adopted and results are presented for two chosen values of Δm^2_{41} namely, $\Delta m^2_{41} = 1 \times 10^{-3}$ eV^2 and $\Delta m^2_{41} = 3 \times 10^{-3}$ eV^2, consistent with the latest experimental ndings. MINOS and MINOS+ [139, 519] also provide limits on the active-sterile mixing angle θ_{24}. From their analyses, it is found that for $\Delta m^2_{41} \geq 10^{-2}$ eV^2, MINOS+ provides strong upper bound on the mixing angle θ_{24}. However, it is observed that $\theta_{24} \leq 26.7^0$ when $\Delta m^2_{41} = 1 \times 10^{-3}$ eV^2 and $\theta_{24} \leq 50.7^0$ when $\Delta m^2_{41} = 3 \times 10^{-3}$ eV^2. Recent analysis for the search of sterile neutrinos performed by T2K far detector with 295 Kms baseline length [149] predicts $\theta_{24} \leq 22.7^0$ for $\Delta m^2_{41} = 1 \times 10^{-3}$ eV^2 and for $\Delta m^2_{41} = 3 \times 10^{-3}$ eV^2 the limit on mixing angle is $\theta_{24} \leq 15.3^0$. With the above limit on θ_{24} for $\Delta m^2_{41} = 3 \times 10^{-3}$ eV^2, the limit on θ_{34} is found to be $\theta_{34} \leq 53.1^0$ (see Fig. 4 of Ref. [149] for details). Therefore, it may be observed that for smaller values of $\Delta m^2_{41} \sim 10^{-3}$ eV^2, although the mixing angle θ_{14} is very much constrained, limits on other mixing angles namely $\theta_{24},\ \theta_{34}$ are not that stringent. In this Chapter, two different sets of active-sterile neutrino mixing angles are adopted and these are given in Table 12.1 which are in agreement with different neutrino oscillation experimental results for smaller values of $\Delta m^2_{41} \sim 10^{-3}$ eV^2.

It is to be noted that apart from the CP phase δ_{CP} appearing in the 3×3 PMNS matrix for

Table 12.1: Chosen 4- avour mixing angle parameter sets for the calculation of gravity induced 4- avour oscillations in matter.

Set	θ_{14}	θ_{24}	θ_{34}
1	3.6°	4.0°	18.48°
2	2.5°	10.0°	30.0°

3 active neutrino case, the 3+1 scenario involves two new CP phases δ_{14} and δ_{24}. However, as mentioned in [148], experiments like MINOS, Daya Bay and Bugey-3 are based on disappearance measurements which makes them insensitive to CP phases. Apart from that, IceCube [371] experiment also analyse data to t active-sterile mixing angle considering CP phases to be zero. In the present calculations also a CP conserving scenario is assumed and all CP phases are zero.

With the two sets of mixing angles tabulated in Table 12.1 and neutrino mass squared differences mentioned above, the four neutrino oscillation probabilities in matter is to be obtained including the effects of VEP principle with VEP parameters Δf_{31} and Δf_{41}. The Hamiltonian H'' is then diagonalised by a new 4×4 unitary matrix U^m whose elements are similar to that of the matrix U (as in Eq. 12.2) but with new modi ed mixing angles. Therefore, the oscillation probability for a neutrino $|\nu_\alpha\rangle$ having avour α oscillate to a neutrino $|\nu_\beta\rangle$ of avour β is given by the expression [464, 520]

$$P_{\nu_\alpha \to \nu_\beta} = \delta_{\alpha\beta} - 4 \sum_{j>i} U^m_{\alpha i} U^m_{\beta i} U^m_{\alpha j} U^m_{\beta j} \sin^2 \left(\frac{\pi L}{\lambda_{ij}} \right) , \tag{12.20}$$

where $U^m_{\alpha i}$ etc. are the matrix elements of the unitary matrix (U^m), which is computationally obtained by diagonalising the effective Hamiltonian H'' in Eq. 12.17 and L indicates the baseline length. The oscillation length (λ_{ij}) in the presence of both mass and gravity induced oscillations in matter can be expressed as

$$\lambda_{ij} = \frac{2\pi}{E'_j - E'_i} = \frac{2\pi}{\Delta E'_{ij}} , \tag{12.21}$$

where $E'_i, E'_j (i, j = 1, 2, 3, 4; i \neq j)$ are the eigenvalues of the effective Hamiltonian H'' (Eq. 12.17). Since the mass eigenstates $|\nu_1\rangle$ and $|\nu_2\rangle$ can be assumed to be almost degenerate ($\Delta m^2_{21} \sim 10^{-5}$ eV^2), we have $\Delta m^2_{31} \simeq \Delta m^2_{32}$, $\Delta m^2_{41} \simeq \Delta m^2_{42}$. We follow similar convention for neutrino gravity eigenstates, such that $|\nu_{G1}\rangle$ and $|\nu_{G2}\rangle$ are also almost degenerate ($\Delta f_{21} = 0$) and adopt $\Delta f_{31} \simeq \Delta f_{32}$ and $\Delta f_{41} \simeq \Delta f_{42}$. Therefore, in the 4- avour framework, the oscillation probability equations are given by

$$\begin{aligned} P^4_{ee} &= 1 - 4\Bigg[|U^m_{e1}|^2|U^m_{e2}|^2 \sin^2\left(\frac{\Delta E'_{12}L}{2}\right) + |U^m_{e1}|^2|U^m_{e3}|^2 \sin^2\left(\frac{\Delta E'_{13}L}{2}\right) + \\ &\quad |U^m_{e1}|^2|U^m_{e4}|^2 \sin^2\left(\frac{\Delta E'_{14}L}{2}\right) + |U^m_{e2}|^2|U^m_{e3}|^2 \sin^2\left(\frac{\Delta E'_{23}L}{2}\right) + \\ &\quad |U^m_{e2}|^2|U^m_{e4}|^2 \sin^2\left(\frac{\Delta E'_{24}L}{2}\right) + |U^m_{e3}|^2|U^m_{e4}|^2 \sin^2\left(\frac{\Delta E'_{34}L}{2}\right)\Bigg] \end{aligned} \tag{12.22}$$

$$\begin{aligned} P^4_{\mu\mu} &= 1 - 4\Bigg[|U^m_{\mu1}|^2|U^m_{\mu2}|^2 \sin^2\left(\frac{\Delta E'_{12}L}{2}\right) + |U^m_{\mu1}|^2|U^m_{\mu3}|^2 \sin^2\left(\frac{\Delta E'_{13}L}{2}\right) + \\ &\quad |U^m_{\mu1}|^2|U^m_{\mu4}|^2 \sin^2\left(\frac{\Delta E'_{14}L}{2}\right) + |U^m_{\mu2}|^2|U^m_{\mu3}|^2 \sin^2\left(\frac{\Delta E'_{23}L}{2}\right) + \\ &\quad |U^m_{\mu2}|^2|U^m_{\mu4}|^2 \sin^2\left(\frac{\Delta E'_{24}L}{2}\right) + |U^m_{\mu3}|^2|U^m_{\mu4}|^2 \sin^2\left(\frac{\Delta E'_{34}L}{2}\right)\Bigg] \end{aligned} \tag{12.23}$$

$$\begin{aligned} P^4_{\tau\tau} &= 1 - 4\Bigg[|U^m_{\tau1}|^2|U^m_{\tau2}|^2 \sin^2\left(\frac{\Delta E'_{12}L}{2}\right) + |U^m_{\tau1}|^2|U^m_{\tau3}|^2 \sin^2\left(\frac{\Delta E'_{13}L}{2}\right) + \\ &\quad |U^m_{\tau1}|^2|U^m_{\tau4}|^2 \sin^2\left(\frac{\Delta E'_{14}L}{2}\right) + |U^m_{\tau2}|^2|U^m_{\tau3}|^2 \sin^2\left(\frac{\Delta E'_{23}L}{2}\right) + \\ &\quad |U^m_{\tau2}|^2|U^m_{\tau4}|^2 \sin^2\left(\frac{\Delta E'_{24}L}{2}\right) + |U^m_{\tau3}|^2|U^m_{\tau4}|^2 \sin^2\left(\frac{\Delta E'_{34}L}{2}\right)\Bigg] \end{aligned} \tag{12.24}$$

$$
\begin{aligned}
P^4_{ss} &= 1 - 4\left[|U^m_{s1}|^2|U^m_{s2}|^2\sin^2\left(\frac{\Delta E'_{12}L}{2}\right) + |U^m_{s1}|^2|U^m_{s3}|^2\sin^2\left(\frac{\Delta E'_{13}L}{2}\right) + \right. \\
&\quad |U^m_{s1}|^2|U^m_{s4}|^2\sin^2\left(\frac{\Delta E'_{14}L}{2}\right) + |U^m_{s2}|^2|U^m_{s3}|^2\sin^2\left(\frac{\Delta E'_{23}L}{2}\right) + \\
&\quad \left. |U^m_{s2}|^2|U^m_{s4}|^2\sin^2\left(\frac{\Delta E'_{24}L}{2}\right) + |U^m_{s3}|^2|U^m_{s4}|^2\sin^2\left(\frac{\Delta E'_{34}L}{2}\right)\right]
\end{aligned}
\tag{12.25}
$$

$$
\begin{aligned}
P^4_{e\mu} &= 4\left[|U^m_{e1}||U^m_{\mu1}||U^m_{e2}||U^m_{\mu2}|\sin^2\left(\frac{\Delta E'_{12}L}{2}\right) + |U^m_{e1}||U^m_{\mu1}||U^m_{e3}||U^m_{\mu3}|\sin^2\left(\frac{\Delta E'_{13}L}{2}\right) + \right. \\
&\quad |U^m_{e1}||U^m_{\mu1}||U^m_{e4}||U^m_{\mu4}|)\sin^2\left(\frac{\Delta E'_{14}L}{2}\right) + |U^m_{e2}||U^m_{\mu2}||U^m_{e3}||U^m_{\mu3}|\sin^2\left(\frac{\Delta E'_{23}L}{2}\right) + \\
&\quad \left. |U^m_{e2}||U^m_{\mu2}||U^m_{e4}||U^m_{\mu4}|\sin^2\left(\frac{\Delta E'_{24}L}{2}\right) + |U^m_{e3}||U^m_{\mu3}||U^m_{e4}||U^m_{\mu4}|\sin^2\left(\frac{\Delta E'_{34}L}{2}\right)\right]
\end{aligned}
\tag{12.26}
$$

$$
\begin{aligned}
P^4_{e\tau} &= 4\left[|U^m_{e1}||U^m_{\tau1}||U^m_{e2}||U^m_{\tau2}|\sin^2\left(\frac{\Delta E'_{12}L}{2}\right) + |U^m_{e1}||U^m_{\tau1}||U^m_{e3}||U^m_{\tau3}|\sin^2\left(\frac{\Delta E'_{13}L}{2}\right) + \right. \\
&\quad |U^m_{e1}||U^m_{\tau1}||U^m_{e4}||U^m_{\tau4}|)\sin^2\left(\frac{\Delta E'_{14}L}{2}\right) + |U^m_{e2}||U^m_{\tau2}||U^m_{e3}||U^m_{\tau3}|\sin^2\left(\frac{\Delta E'_{23}L}{2}\right) + \\
&\quad \left. |U^m_{e2}||U^m_{\tau2}||U^m_{e4}||U^m_{\tau4}|\sin^2\left(\frac{\Delta E'_{24}L}{2}\right) + |U^m_{e3}||U^m_{\tau3}||U^m_{e4}||U^m_{\tau4}|\sin^2\left(\frac{\Delta E'_{34}L}{2}\right)\right]
\end{aligned}
\tag{12.27}
$$

$$
\begin{aligned}
P^4_{es} &= 4\left[|U^m_{e1}||U^m_{s1}||U^m_{e2}||U^m_{s2}|\sin^2\left(\frac{\Delta E'_{12}L}{2}\right) + |U^m_{e1}||U^m_{s1}||U^m_{e3}||U^m_{s3}|\sin^2\left(\frac{\Delta E'_{13}L}{2}\right) + \right. \\
&\quad |U^m_{e1}||U^m_{s1}||U^m_{e4}||U^m_{s4}|)\sin^2\left(\frac{\Delta E'_{14}L}{2}\right) + |U^m_{e2}||U^m_{s2}||U^m_{e3}||U^m_{s3}|\sin^2\left(\frac{\Delta E'_{23}L}{2}\right) + \\
&\quad \left. |U^m_{e2}||U^m_{s2}||U^m_{e4}||U^m_{s4}|\sin^2\left(\frac{\Delta E'_{24}L}{2}\right) + |U^m_{e3}||U^m_{s3}||U^m_{e4}||U^m_{s4}|\sin^2\left(\frac{\Delta E'_{34}L}{2}\right)\right]
\end{aligned}
\tag{12.28}
$$

$$P^4_{\mu\tau} = 4\Bigg[|U^m_{\mu1}||U^m_{\tau1}||U^m_{\mu2}||U^m_{\tau2}|\sin^2\left(\frac{\Delta E'_{12}L}{2}\right) + |U^m_{\mu1}||U^m_{\tau1}||U^m_{\mu3}||U^m_{\tau3}|\sin^2\left(\frac{\Delta E'_{13}L}{2}\right) + |U^m_{\mu1}||U^m_{\tau1}||U^m_{\mu4}||U^m_{\tau4}|)\sin^2\left(\frac{\Delta E'_{14}L}{2}\right) + |U^m_{\mu2}||U^m_{\tau2}||U^m_{\mu3}||U^m_{\tau3}|\sin^2\left(\frac{\Delta E'_{23}L}{2}\right) + |U^m_{\mu2}||U^m_{\tau2}||U^m_{\mu4}||U^m_{\tau4}|\sin^2\left(\frac{\Delta E'_{24}L}{2}\right) + |U^m_{\mu3}||U^m_{\tau3}||U^m_{\mu4}||U^m_{\tau4}|\sin^2\left(\frac{\Delta E'_{34}L}{2}\right)\Bigg] \tag{12.29}$$

$$P^4_{\mu s} = 4\Bigg[|U^m_{\mu1}||U^m_{s1}||U^m_{\mu2}||U^m_{s2}|\sin^2\left(\frac{\Delta E'_{12}L}{2}\right) + |U^m_{\mu1}||U^m_{s1}||U^m_{\mu3}||U^m_{s3}|\sin^2\left(\frac{\Delta E'_{13}L}{2}\right) + |U^m_{\mu1}||U^m_{s1}||U^m_{\mu4}||U^m_{s4}|)\sin^2\left(\frac{\Delta E'_{14}L}{2}\right) + |U^m_{\mu2}||U^m_{s2}||U^m_{\mu3}||U^m_{s3}|\sin^2\left(\frac{\Delta E'_{23}L}{2}\right) + |U^m_{\mu2}||U^m_{s2}||U^m_{\mu4}||U^m_{s4}|\sin^2\left(\frac{\Delta E'_{24}L}{2}\right) + |U^m_{\mu3}||U^m_{s3}||U^m_{\mu4}||U^m_{s4}|\sin^2\left(\frac{\Delta E'_{34}L}{2}\right)\Bigg] \tag{12.30}$$

$$P^4_{\tau s} = 4\Bigg[|U^m_{\tau1}||U^m_{s1}||U^m_{\tau2}||U^m_{s2}|\sin^2\left(\frac{\Delta E'_{12}L}{2}\right) + |U^m_{\tau1}||U^m_{s1}||U^m_{\tau3}||U^m_{s3}|\sin^2\left(\frac{\Delta E'_{13}L}{2}\right) + |U^m_{\tau1}||U^m_{s1}||U^m_{\tau4}||U^m_{s4}|)\sin^2\left(\frac{\Delta E'_{14}L}{2}\right) + |U^m_{\tau2}||U^m_{s2}||U^m_{\tau3}||U^m_{s3}|\sin^2\left(\frac{\Delta E'_{23}L}{2}\right) + |U^m_{\tau2}||U^m_{s2}||U^m_{\tau4}||U^m_{s4}|\sin^2\left(\frac{\Delta E'_{24}L}{2}\right) + |U^m_{\tau3}||U^m_{s3}||U^m_{\tau4}||U^m_{s4}|\sin^2\left(\frac{\Delta E'_{34}L}{2}\right)\Bigg] \tag{12.31}$$

It is to be noted that, earlier studies of VEP with IceCube neutrino data by Esmaili *et. al* set a stringent bound on $\Delta f_{31} \leq 7 \times 10^{-27}$ [521]. Therefore, in the calculations, $\Delta f_{31} = 5 \times 10^{-27}$ is adopted which is in agreement with previous analysis. However, since the value of Δf_{31} is negligibly small, no signi cant VEP effect due to Δf_{31} is expected. On the other hand, there exists no bound on the VEP associated with the sterile neutrino Δf_{41}. In the next Section, VEP induced four avour neutrino oscillations in matter are explored by actual computation of such probabilities.

12.3 Calculations and Results

12.3.1 Gravity Induced Neutrino Oscillations in Matter

In order to estimate the effect of the gravity induced oscillations in presence of matter for a 4 neutrino (3 active (ν_e, ν_μ, ν_τ) + 1 sterile (ν_s)) scenario in the context of long baseline neutrinos, a baseline length of 7000 Kms is chosen within the Earth. For the demonstrative purpose, a matter density is chosen to be 4.15 gm/cc. However, for the actual estimation of neutrino induced muon yields at a far detector where ν_μ and ν_τ are produced in a neutrino factory, actual densities of the layers of the Earth matter through which the neutrino would propagate from the source to the detector, has been incorporated for the computation of the probabilities. The probabilities are computed using the Eqs. 12.13 - 12.31. In this Section, mainly the nature of the probabilities and their variations (with neutrino energy) are demonstrated by the combined effect of the gravity induced factors as well as the mass- avour oscillations in matter. From Eqs. 12.20 - 12.31, it is clear that the oscillatory part of the probability equations are controlled by the phase factor $\Delta E'_{ij} L/2$, where $\Delta E'_{ij}$ are the difference of the eigen values E'_i and E'_j of the eigenstates designated by i and j respectively. The eigenvalues E'_i, E'_j etc. are computationally obtained by explicitly diagonalising the Hamiltonian H'' (Eq. 12.17) that includes both the mass induced effects, matter effects as also the gravity induced effects.

In Figs 12.1-12.4, the variations of 4 neutrino oscillation probabilities for different gravity induced effects (designated by Δf_{ij}) are shown when the mass squared differences Δm^2_{ij} are kept xed. Note that in all the gures $P^4_{\alpha\beta}$ signi es the oscillation probabilities $P_{\nu_\alpha \to \nu_\beta}$ $(\alpha, \beta \equiv e, \mu, \tau, s)$.

In Fig. 12.1 the variations of 4 neutrino probabilities as described earlier are shown in ve plots (a)-(e) for $P^4_{ee}, P^4_{e\mu}, P^4_{\mu\mu}, P^4_{es}$ and $P^4_{\mu s}$ respectively. In each of these plots the variations are shown for three different values of $\Delta f_{41} = 0, 10^{-24}, 10^{-23}$. The computations for all the plots are made

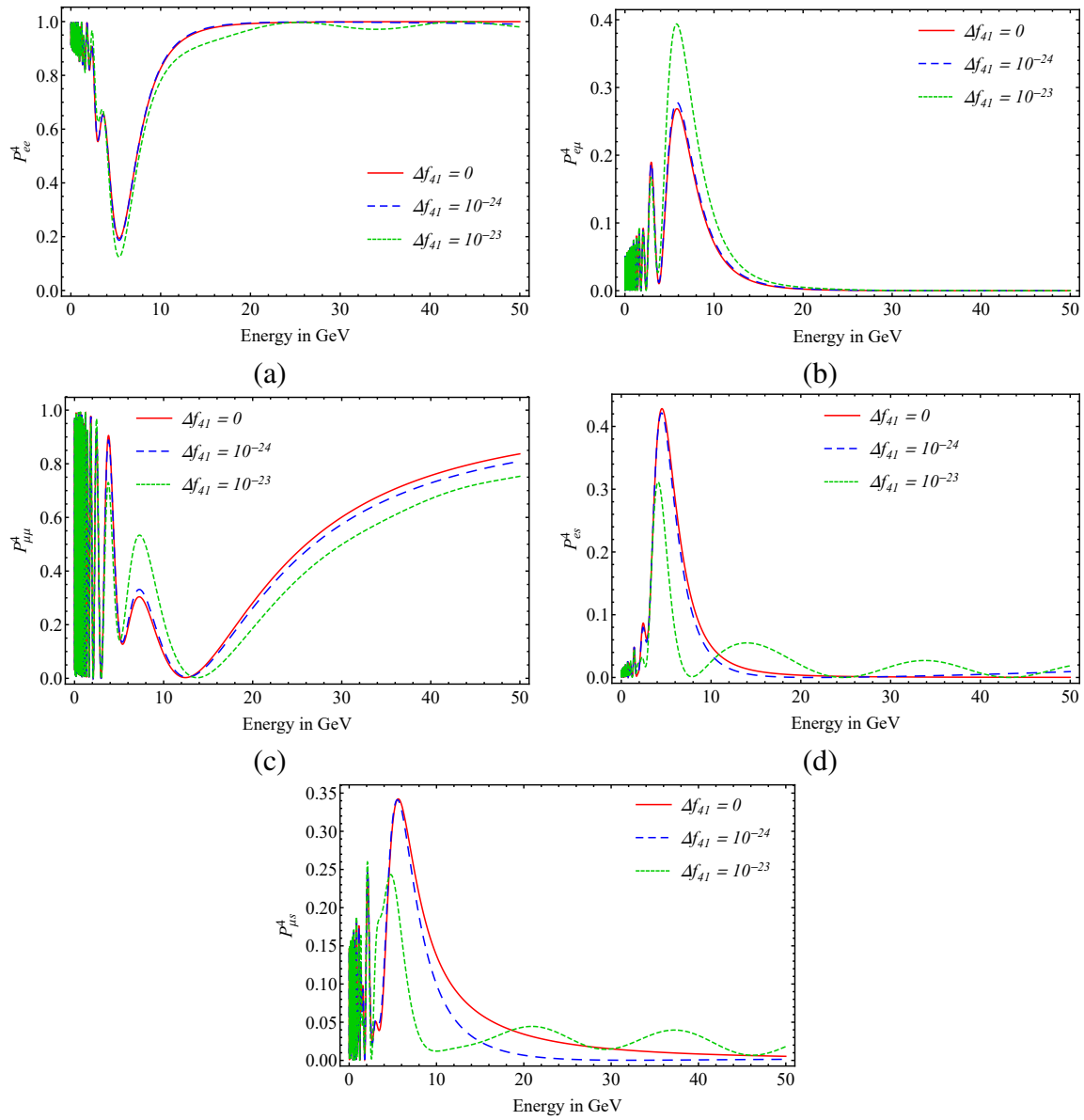

Figure 12.1: Neutrino oscillation probabilities in matter for a fixed value of $\Delta m^2_{41} = 1 \times 10^{-3}$ eV^2, $\Delta f_{31} = 5 \times 10^{-27}$ and for Set-1 with baseline length L = 7000 Kms.

with $\Delta m^2_{41} = 1 \times 10^{-3}$ eV^2 and $\Delta f_{31} = 5 \times 10^{-27}$ for a baseline length of 7000 Kms. For other four flavour mixing angles, Set 1 of Table 12.1 is adopted. The three values of flavour mixing angles and mass squared differences are given earlier in Section 12.2. From Fig. 12.1(a-e) it is

evident that the nature of variation of the probabilities changes when the value of Δf_{41} is changed. It is also observed from these gures that the changes in oscillation probabilities are more prominent when $\Delta f_{41} = 10^{-23}$ (in comparison to what is obtained when $\Delta f_{41} = 0$). For the cases P^4_{es} and $P^4_{\mu s}$, these variations are more distinctive and the oscillatory behaviours of these probabilities are observed beyond energy $\sim$ 10 GeV when $\Delta f_{41} = 10^{-23}$ and for $E_\nu \leq 10$ GeV, the probabilities suffer very rapid oscillations.

Similar computations of the probabilities are performed and the results are plotted in Fig. 12.2(a-e) using the same set of parameters (Set-1 of Table 12.1) but for a different chosen value of $\Delta m^2_{41} = 3 \times 10^{-3}$ eV^2. Although results similar to what is observed in Fig. 12.1 are obtained, the oscillation patterns for the case of $P^4_{\alpha s}$ ($\alpha = e, \mu$) show signi cant difference when compared with the same for Fig. 12.1. We observe that the probability P^4_{es} is reduced by one order for $\Delta m^2_{41} = 3 \times 10^{-3}$eV^2. Moreover, behaviours of both the probability plots $P^4_{\alpha s}$ ($\alpha = e, \mu$) change signi cantly with increasing values of Δf_{41} and becomes oscillatory in nature for $\Delta f_{41} = 10^{-23}$.

In Figs. 12.3-12.4 the ve probability plots are shown but with the Set-2 for active-sterile mixing angles as given in Table 12.1. For each of the probabilities, the variations are shown for same set of three Δf_{41} values while the value of Δf_{31} is kept xed at 5×10^{-27} as for Fig. 12.1. Shown in Fig. 12.3 (Fig. 12.4), the probability plots for $\Delta m^2_{41} = 1 \times 10^{-3}$ eV^2 ($\Delta m^2_{41} = 3 \times 10^{-3}$ eV^2) with baseline length of 7000 Kms as before. It can be easily noticed that the nature of the plots in Fig. 12.3 (Fig. 12.4) are similar to that of Fig. 12.1 (Fig. 12.2) the computations of which differ only in different sets of mixing angles that have been used. However comparing Fig. 12.1 with Fig. 12.3 reveals that the probability $P^4_{\mu\mu}$ also changes signi cantly with the variations of Δf_{41}. The probability plots for $P^4_{\mu\mu}$ in Fig. 12.2 and Fig. 12.4 exhibit similar nature when compared. These deviations can play signi cant role for the case of long baseline neutrino experiments which will be discussed later. Comparing Fig. 12.3 and Fig. 12.4 it is also observed that the probabilities P^4_{es} and $P^4_{\mu s}$ become oscillatory in nature for $E \geq 10$ GeV and P^4_{es} suffers a suppression of one order when $\Delta m^2_{41} = 3 \times 10^{-3}$ eV^2 is adopted. In addition it appears that the natures of the probabilities

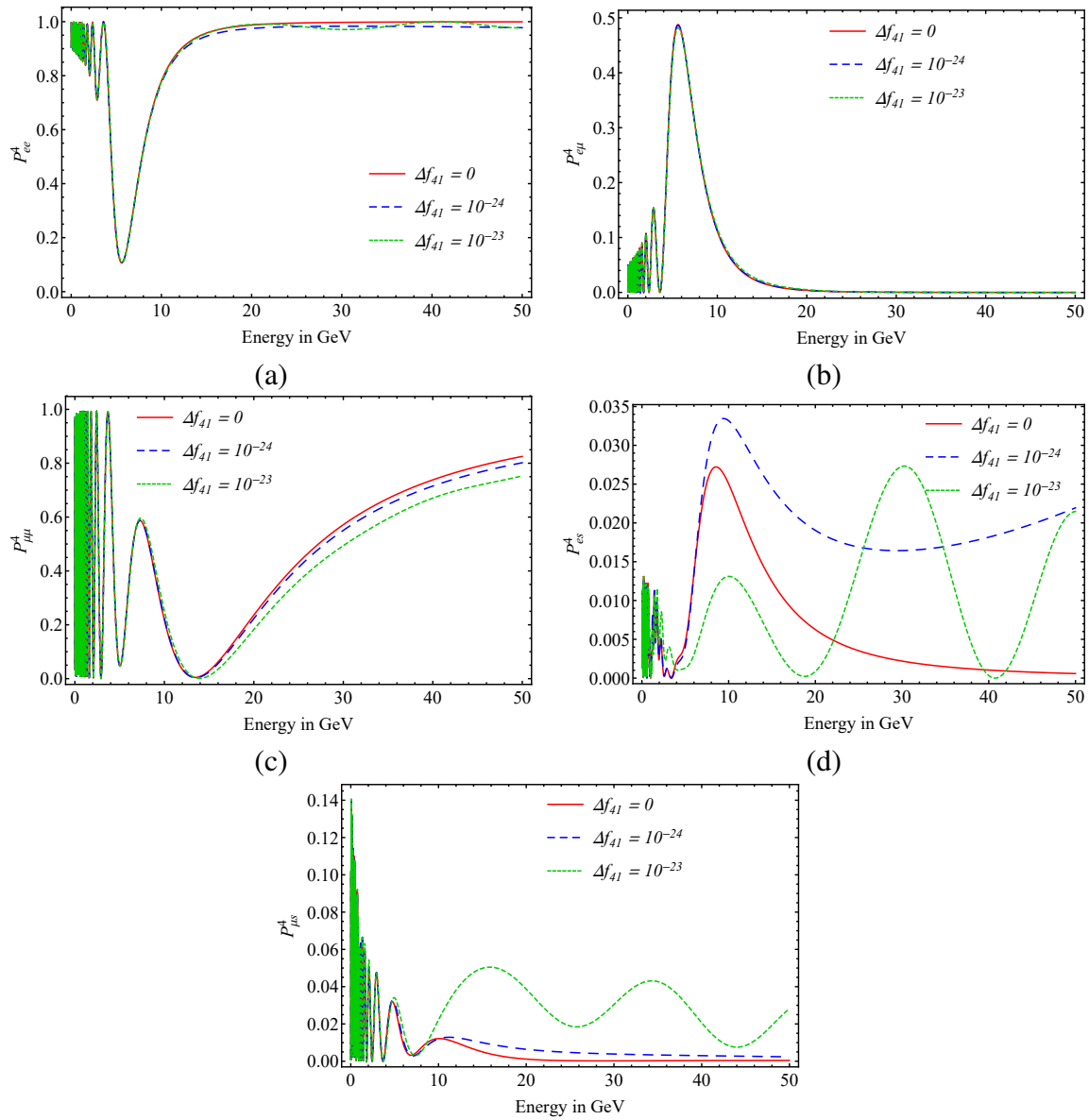

Figure 12.2: Neutrino oscillation probabilities in matter for a fixed value of $\Delta m^2_{41} = 3 \times 10^{-3}$ eV^2, $\Delta f_{31} = 5 \times 10^{-27}$ and for Set-1 with baseline length L = 7000 Kms.

are more affected when $\Delta f_{41} = 10^{-23}$ as compared to the case $\Delta f_{41} = 0$. This is also evident in case of Figs. 12.1-12.2. Thus it is demonstrated from Figs. 12.1-12.4 that for these calculations, the probabilities are most affected by the gravity induced effects when $\Delta f_{41} = 10^{-23}$.

12.3.2 Effect of Gravity Induced Oscillation on a LBL Neutrino Experiment

In this Section, we estimate the neutrino induced muon yields in a LBL experiment. In a LBL neutrino experiment neutrinos are usually produced in an accelerator based neutrino factory which then propagate to a distant detector where these are detected. In this set up, pions are initially produced in neutrino factories by directing a proton beam incident on a target. Pions decay into muons which suffer further decay in a muon storage ring producing neutrinos. Neutrinos are generated from 3-body decay of muons as

$$\mu^- \to e^- + \bar{\nu}_e + \nu_\mu \,, \qquad (12.32)$$
$$\mu^+ \to e^+ + \nu_e + \bar{\nu}_\mu \ .$$

Neutrinos produced in neutrino factory are then directed towards a neutrino detector far away from the source of the neutrinos and traverse through Earth matter to reach the detector. The muon neutrinos ($\nu_\mu,\ \bar{\nu}_\mu$) generated in neutrino factory will suffer oscillations due to its passage through the Earth matter along the baseline. The $\nu_\mu(\bar{\nu}_\mu)$ will produce μ^- (μ^+) at the detector by CC interaction with the detector material. If it is pure μ^- at the source then only ν_μ beam will propagate along the baseline and μ^- will be produced at the detector end which the detector would detect. Those muons are called right sign muons. Needless to mention that ν_μ ux at the source will suffer depletion due to the oscillation and same will happen to the expected muon yield. However if the detector detects a μ^+ instead, then it must be that $\bar{\nu}_\mu$ reaches the detector and $\bar{\nu}_\mu$ can only be created in the beam (produced by the decay of μ^-) through the oscillation $\bar{\nu}_e \to \bar{\nu}_\mu$ during the passage of $\bar{\nu}_e$ through the baseline. These events are termed as wrong sign muon events. The situation is just reversed if $\bar{\nu}_\mu$ beam is produced at the storage ring from the decay of μ^+. But the right sign and the wrong sign muon events can be distinguished by an iron calorimeter detector (such as

the one considered for the calculation of muon yields in this Chapter) when the ICAL detector is magnetized.

As mentioned above, we first consider the neutrino (antineutrino) flux in the neutrino factory which is expressed as [522, 523]

$$\frac{d^2\Phi_{\nu_\mu,\bar{\nu}_\mu}}{dydA} = \frac{4n_\mu}{\pi L^2 m_\mu^6}\, E_\mu^4 y^2 (1-\beta)\, \left[3m_\mu^2 - 4E_\mu^2 y (1-\beta)\right] \tag{12.33}$$

and similarly ν_e ($\bar{\nu}_e$) flux is given by

$$\frac{d^2\Phi_{\nu_e,\bar{\nu}_e}}{dydA} = \frac{24n_\mu}{\pi L^2 m_\mu^6}\, E_\mu^4 y^2 (1-\beta)\, \left[m_\mu^2 - 2E_\mu^2 y (1-\beta)\right] \ , \tag{12.34}$$

where different terms are given as follows

- E_μ : muon energy
- n_μ : number of injected muons
- L : distance between neutrino factory and the end detector (baseline length)
- $y = \frac{E_\nu}{E_\mu}$ where E_ν is energy of neutrino
- β is the boost factor

It is to be noted that the expressions for neutrino fluxes in Eqs. 12.33, 12.34 are derived under the following approximations; i) neutrinos are not polarised and ii) the angle between the direction of neutrino beam towards the detector and the beam axis is assumed to be zero. For the computations of neutrino flux using Eqs. 12.33,12.34, $\sim 10^{21}$ protons on target per year and muon injection energy of 50 GeV are considered. In Fig. 12.5 the calculated fluxes for ν_μ and $\bar{\nu_e}$ are shown.

As mentioned, a magnetized ICAL detector is considered. Such a detector of 50 kTon mass has been suggested for the proposed INO [181]. The proposed ICAL detector at INO [181] is basically a

stack of 151 iron plates of thickness 5.6 cm and the plates are separated by a gap of 4 cm containing a total of 50 kTon of detector iron. Here we consider a baseline length of 7359 Kms which is roughly the distance between CERN and proposed INO site. Beam of ν_μ ($\bar{\nu}_\mu$) from a neutrino factory after reaching such a magnetized ICAL detector will undergo CC interactions and produce μ^- (μ^+) which form muon tracks of different curvature due to magnetic eld while passing through different layers of the detector. Observing the direction and curvature of the muon tracks one can distinguish the right sign and wrong sign muons inside detector. As mentioned, the ux of neutrino (antineutrino) beam will undergo gravity induced and mass induced four avour oscillations in matter before reaching the detector. Thus the neutrino (antineutrino) ux at the detector is to be folded by corresponding probabilities. For a beam with ν_μ and $\bar{\nu}_e$ (produced from the decay of μ^- at the storage ring), if μ^+ is registered in ICAL then this is referred to as appearance channel since it originates due the oscillation $\bar{\nu}_e \to \bar{\nu}_\mu$ while for the same beam μ^- at the detector is considered as disappearance channel as ν_μ disappears via the oscillation $\nu_\mu \to \nu_x, x \neq \mu$. In this Section, we present the expected yield of right sign muons (μ^-) and wrong sign muons (μ^+) at ICAL detector in presence of gravity induced neutrino oscillations in four avour scenario.

Different neutrino oscillation probabilities are calculated and presented in previous Section assuming average Earth density $\rho = 4.15$ gm/cc. However for the present scenario, where the baseline length $\sim$ 7359 Kms, neutrinos travel through Earth crust and mantle. Width of Earth crust is very small $\sim$ 10-15 Kms compared to the long baseline oscillation length 7359 Kms. Therefore, oscillation effects due to crust can be ignored safely and we consider neutrino oscillations through upper and lower mantle only, as demonstrated in Fig. 12.6. Density of upper (lower) mantle of Earth is $\rho_{up} = 3.9$ gm/cc ($\rho_{low} = 4.5$ gm/cc) [524]. From Fig. 12.6, we observe that for the chosen LBL length, neutrinos traverse through upper mantle initially for rst 1603 Kms and then enters lower mantle where it travels a distance of 4153 Kms and nally enters again into the upper mantle through which they travel another 1603 Kms to reach the detector. We use the above two-layer formalism to calculate neutrino oscillation probabilities within Earth for the calculation of right sign and wrong

sign muon events at the detector. For this purpose, we need to evaluate new probability amplitudes for neutrino oscillation within two layers of mantle. For example, the probability amplitude for the channel $\nu_l \rightarrow \nu_{l'}$ with the two layers of mantle considered is expressed as

$$A_{ll'} = \sum_{k,k',k'',\alpha,\beta} A_{lk} A^{up}_{kk}(d) A_{k\alpha} A_{\alpha k'} A^{low}_{k'k'}(D) A_{k'\beta} A_{\beta k''} A^{up}_{k''k''}(d) A_{k''l'} \tag{12.35}$$

where $l, l', \alpha, \beta = e, \mu, \tau, s$; $k, k', k'' = 1, 2, 3, 4$ and superscripts up (low) correspond to upper and lower mantle with density ρ_{up} (ρ_{low}). Eq. 12.35 can be explained as follows. The matter effect on neutrinos as they pass through the matter is related to neutrino interaction with matter. The coherent neutrino weak interaction scattering with matter proceeds via weak interaction eigenstates or avour eigen states of neutrinos and depends on the particle density (and hence matter density) inside the medium through which the neutrino is propagating (as discussed earlier in Chapter 4). But it is the mass eigenstates of neutrino in matter (within that medium) which propagate through a distance in that medium. The neutrino in this case, is produced in a particular avour eigenstate in a source and enters the earth matter in the upper mantle with a certain density, through which it will rst propagate. The possible mass eigenstates (in matter of the upper mantle) in the initial avour eigenstate (due to neutrino mixing) is of relevance here. These mass eigenstates initially propagate a distance of $d = 1603$ Kms inside the upper mantle as $\exp(-iEd)$ (E represents the energy eigen value of the neutrino; the propagation Hamiltonian is diagonal in mass basis) till they reach the boundary of the upper and the lower mantle (Fig. 12.6). As the lower mantle has a different matter density, the neutrino needs to be converted from its mass eigenstate (in upper mantle matter) to possible avour eigenstates which then enter the lower mantle. But since neutrino will now propagate a distance of $D = 4153$ Kms inside the lower mantle with matter density different from that of the upper mantle, these are the mass eigenstates in lower mantle matter (and not the avour eigenstates) that are relevant since these mass eigenstates will now propagate as $\exp(-iED)$ till they reach the boundary of the lower mantle and the upper mantle (Fig. 12.6). As they propagate from lower mantle to upper mantle, another change of matter density will occur.

Table 12.2: The right sign μ yield and the wrong sign μ yield in the presence of gravity induced 4- avour oscillations in matter for Set-1 and for the xed values of $\Delta f_{31} = 5 \times 10^{-27}$. The muon injection energy is xed at 50 GeV. See text for details.

Δm^2_{41} in eV^2	Δf_{41}	Right sign μ	Wrong sign μ
1×10^{-3}	0	3115191.8	6031.1
	10^{-24}	2973398.1	5920.1
	10^{-23}	2662702.8	6332.4
3×10^{-3}	0	3006509.5	8349.9
	10^{-24}	2896293.3	8465.6
	10^{-23}	2654969.2	7687.9

Following the similar procedure, nally, the neutrino mass eigenstates in the upper mantle will reach the detector on earth after traversing a distance of $d = 1603$ Kms (see Fig. 12.6). But again, since the neutrinos will undergo weak interaction with detector material inside the detector (and a neutrino of a particular avour will be detected), the relevant avour eigen state is to be obtained from the mass eigenstates that reach the detector. In Eq. 12.35, $A_{lk} = \langle \nu_l | \nu_k \rangle = U_{lk}$ is the element of neutrino mixing matrix before oscillation within matter whereas $A_{k\alpha} \rightarrow U_{k\alpha}(\theta_{up})$, $A_{\alpha k'} \rightarrow U_{\alpha k'}(\theta_{low})$, $A_{k'\beta} \rightarrow U_{k'\beta}(\theta_{low})$, $A_{\beta k''} \rightarrow U_{\beta k''}(\theta_{up})$ (θ_{up} and θ_{low} denote the mixing angles in the matters of upper and lower mantle respectively) correspond to oscillation within matter and $A^{up}_{kk} = \langle \nu_k | \nu^{up}_k(d) \rangle = e^{-iEd}$ with E being a function of Δm^2_{ij}, $\Delta f_{ij}, V$. Finally the oscillation probability $P_{\nu_l \nu_{l'}}$ between two different neutrino avours l and l' can be calculated from the amplitude $P_{ll'} = |A_{ll'}|^2$. In Fig. 12.7 we show the oscillation probabilities for the case $\nu_e \rightarrow \nu_\mu$ and $\nu_\mu \rightarrow \nu_\mu$ which are computed using Eq. 12.19, Eq. 12.35 and new mixing angles mentioned in Set-1 of Table 12.1 for $\Delta m^2_{41} = 1 \times 10^{-3}$ eV^{-2} with different Δf_{41} values and xed $\Delta f_{31} = 5 \times 10^{-27}$.

In Table 12.2, we furnish the estimated right sign and wrong sign muon yields for ve year run of a magnetized ICAL detector with the benchmark set of active-sterile mixing angles given in Set-1 of Table 12.1. As mentioned, the energy of injected muon is taken to be 50 GeV at the muon storage ring assumed to be directed towards the ICAL detector. The estimated numbers are shown for two values of chosen $\Delta m^2_{41} = 1 \times 10^{-3}$ eV^2 and $\Delta m^2_{41} = 3 \times 10^{-3}$ eV^2. As we have discussed

Table 12.3: The right sign μ yield and the wrong sign μ yield in the presence of gravity induced 4- avour oscillations in matter for Set-2 and for the xed values of $\Delta f_{31} = 5 \times 10^{-27}$ with injected muon energy xed at 50 GeV. See text for details.

Δm^2_{41} in eV^2	Δf_{41}	Right sign μ	Wrong sign μ
1×10^{-3}	0	3386440.6	6052.6
	10^{-24}	2891732.9	5101.3
	10^{-23}	1832335.8	4037.9
3×10^{-3}	0	3006874.9	8692.3
	10^{-24}	2605873.5	8631.2
	10^{-23}	1805902.2	7634.0

before, keeping $\Delta f_{31} = 5 \times 10^{-27}$ xed, the right sign and wrong sign muon yields are estimated at the ICAL detector (considered here) for three different Δf_{41} values discussed in previous Section. From Table 12.2, we observe that for both the chosen xed values of $\Delta m^2_{41} = 1(3) \times 10^{-3}$ eV^2, increase in Δf_{41} results in depletion of the right sign muon yields while wrong sign muon yields do not suffer any signi cant change. The right and wrong sign muon yields are also computed for a set of different benchmark points for active-sterile mixing given in Set 2 of Table 12.1 keeping the other parameters same as those used in Table 12.2. These results are furnished in Table 12.3. Similar trend, as in Table 12.2, is also observed for the computed right and wrong sign muon yield values given in Table 12.3. From these calculations it appears that LBL neutrino experiment can be very effective and important not only to address, in addition to other neutrino physics issues, the four neutrino avour scenario but also to probe a possible tiny violation, if any, of equivalence principle.

In order to demonstrate, how both the right sign and wrong sign muon yields for 4- avour scenario differ from those when only three active avours are considered with and without VEP effects, comparison has been shown in Table 12.4 of the yields for the two cases by computing the right sign and wrong sign muon yields when three avour mixing parameters are same for both the scenarios. The other parameters of active-sterile mixing are adopted as given in Set 1 and Set 2 of Table 12.1 (and also shown in Table 12.4). The value of $\Delta f_{31} = 5 \times 10^{-27}$, as in Tables 12.2 and

Table 12.4: Comparison of the right sign and the wrong sign μ yields for the 4- avour case compared to the same for 3- avour case for two sets of active-sterile neutrino mixing angles and for two different values of Δm^2_{41}. We consider $\Delta f_{41} = 0$ for this comparison and muon injection energy is kept xed at 50 GeV. See text for details.

Δm^2_{41} in eV^2	θ_{14}	θ_{24}	θ_{34}	Right sign μ in 4- avour	Wrong sign μ in 4- avour	Right sign μ in 3- avour	Wrong sign μ in 3- avour
1×10^{-3}	3.6°	4.0°	18.48°	3115191.8	6031.1	2250267.65	463.18
	2.5°	10.0°	30.0°	3386440.6	6052.6	2250267.65	463.18
3×10^{-3}	3.6°	4.0°	18.48°	3006509.5	8349.9	2250267.65	463.18
	2.5°	10.0°	30.0°	3006874.9	8692.3	2250267.65	463.18

12.3 is xed from the bounds on Δf_{31} given in Ref. [521] and $\Delta f_{41} = 0$. All computations are for ve year run of the chosen 50 kTon ICAL detector, assumed to be placed at a distance of 7359 Kms from a neutrino factory with muon injection energy of 50 GeV.

From Table 12.4, it is clear that for both the cases (two adopted values of Δm^2_{41}), right sign and wrong sign muon yields are enhanced for 4- avour (3 active + 1 sterlile) scenario when compared with 3- avour oscillations. The difference is more striking for the case of wrong sign muon yields. For example, when $\Delta m^2_{41} = 3 \times 10^{-3}$ is chosen, the wrong sign muon yield for 4- avour case is 20 times larger in magnitude than the same for 3- avour case. If the active-sterile VEP oscillation is made non-zero ($\Delta f_{41} \neq 0$), the 4- avour results will be modi ed as seen from Tables 12.2 and 12.3 but the similar trend in difference of wrong sign muon yields are maintained. However, for increasing Δf_{41}, right sign muon yield reduces considerably and can become even smaller than the 3- avour case as observed in Table 12.3 for $\Delta f_{41} = 10^{-23}$. From the estimated results of muon yields obtained in Tables 12.2, 12.3 at the chosen ICAL detector, it is now evident that the presence of gravity induced four neutrino oscillations in matter will signi cantly affect the right sign and wrong sign muon yields for non zero Δf_{41}. Therefore, LBL neutrino experiment can be a viable probe to investigate the VEP appearing in four avour scenario.

In the 3-D plots in Fig. 12.8, simultaneous variations of each of the right sign and wrong sign

muon yields with θ_{24} (ranging from $0^0 \leq \theta_{24} \leq 10^0$) and θ_{34} (ranging from $0^0 \leq \theta_{34} \leq 30^0$) for xed values of $\theta_{14} = 2.5^0$ and $\Delta f_{31} = 5 \times 10^{-27}$ are shown. The chosen ranges of θ_{24} and θ_{34} are within the allowed regions given by 4- avour analyses of oscillation experiment data. We compute the muon yields with muon injection energy 50 GeV in proposed ICAL detector with baseline length 7359 Kms for ve year run and compare the muon yield values for $\Delta m^2_{41} = 10^{-3}$ eV^2, $\Delta f_{41} = 0$ with $\Delta f_{41} = 10^{-23}$. In the left panel of Fig. 12.8, it is to be noticed that for $\Delta f_{41} = 0$, right sign muon yields do not change signi cantly with the variations of θ_{24} and θ_{34}. However, with $\Delta f_{41} = 10^{-23}$, one observes considerable depletion in right sign muon yield as θ_{34} increases while the changes are negligible with the variations of θ_{24}. This result is also in agreement with the muon yield events reported earlier in Table 12.2-12.4, where a reduction has been observed in right sign muon yield for increase in Δf_{41}. A similar plot with the same set of parameters for wrong sign muon yield events at ICAL detector with 50 GeV muon injection energy (and ve year run) is shown in the right panel of Fig. 12.8. Comparing the values of wrong sign muon yields for $\Delta f_{41} = 0$ with $\Delta f_{41} = 10^{-23}$, we observe very mild variation in wrong sign muon yields as the values of θ_{24}, θ_{34} are changed. The nature of this 3-D plot is consistent with the results shown in Tables 12.2-12.4 for wrong sign muons. Thus, this may be concluded that in case of 4- avour oscillations the VEP, if exists in nature can in uence considerable effect on muon yields in a LBL neutrino experiment.

12.4 Summary

If the equivalence principle is indeed violated in nature, this will induce different gravitational couplings for different types of neutrinos. In this Chapter, a study has been made to estimate how such a probability affects the neutrino oscillations in matter and the possibility that even a very small VEP principle can be probed by a LBL neutrino experiment. To this end, a four neutrino (3+1) framework has been considered, where one extra sterile neutrino is assumed to exist in addition to

the three active neutrinos. In a possible scenario that the equivalence principle is violated in nature, the three active neutrinos as well as the sterile neutrino couple differently with gravity which result in a gravity induced oscillations of neutrinos in addition to mass avour oscillations. In addition, one must also take into account the matter effects if neutrinos propagate through medium. In this Chapter, the effective Hamiltonian for four neutrino oscillations is derived in presence of gravity induced effects along with usual mass- avour oscillations with matter effects. These formalisms are then used to study the effects of VEP in a LBL neutrino oscillation experiment, by estimating the detector yields at a far detector.

The new oscillation probabilities in this scenario are derived assuming the mixing angles between mass and avour eigenstates to be identical with those between gravity and avour eigenstates. The resulting new unknown parameters (under certain viable approximations) are Δf_{31}, Δf_{41} which are responsible for gravity induced neutrino oscillations and can be attributed to the signature and measure of VEP. However, IceCube data of atmospheric neutrino puts stringent constraint on Δf_{31}. Using the bounds on neutrino mixing angles from different experiments and Δf_{31}, the behaviour of four neutrino oscillation probabilities are studied. Two benchmark sets of active-sterile neutrino mixing angles $\theta_{14},\ \theta_{24},\ \theta_{34}$ are adopted and these choices are within experimental limits of possible sterile neutrino oscillations. Signi cant deviations in oscillation probabilities $P_{\nu_\alpha \to \nu_\beta}$ occur with the changes in Δf_{41} (for a chosen baseline length of $\sim$ 7000 Kms) indicating that even a very weak VEP will affect the oscillation probabilities over a chosen representative baseline of $\sim$ 7000 Kms.

Using this formalism and computational procedure, the possible signatures of VEP is estimated at the end detector of an assumed LBL neutrino experiment where the neutrinos are produced in a neutrino factory and are detected at a far detector of magnetized ICAL with a baseline length of around 7359 Kms. The magnetized ICAL detector can ef ciently measure the number of μ^- and μ^+ produced upon CC interaction of muon neutrinos and muon antineutrinos at the detector. Flux of muon neutrinos (ν_μ) will suffer gravity induced and mass induced oscillations in matter

while propagating to the far ICAL detector from a neutrino factory where neutrinos are produced and thus the neutrino ux will be depleted on reaching the detector. Hence this oscillation channel is referred to as disappearance channel. Similarly detection of μ^+ at magnetized ICAL indicates the appearance channel due to neutrino oscillation $\bar{\nu}_e \rightarrow \bar{\nu}_\mu$. It is demonstrated that for a baseline of $\sim$ 7000 Kms, effect of VEP becomes prominent with four avour oscillations for non zero values of Δf_{41}. This is further justi ed by the calculation of muon yields ($\mu^\mp$) in an assumed LBL neutrino experiment with baseline length 7359 Kms (which is approximately a baseline that one would obtain if the neutrino source is considered to be at CERN and the end detector is a ICAL detector at the proposed INO site). The results show signi cant changes in muon yields arising due to VEP parameter Δf_{41} responsible for gravity induced neutrino oscillations. Therefore, LBL neutrino experiment can be used to probe even a very small VEP principle, if exists in nature.

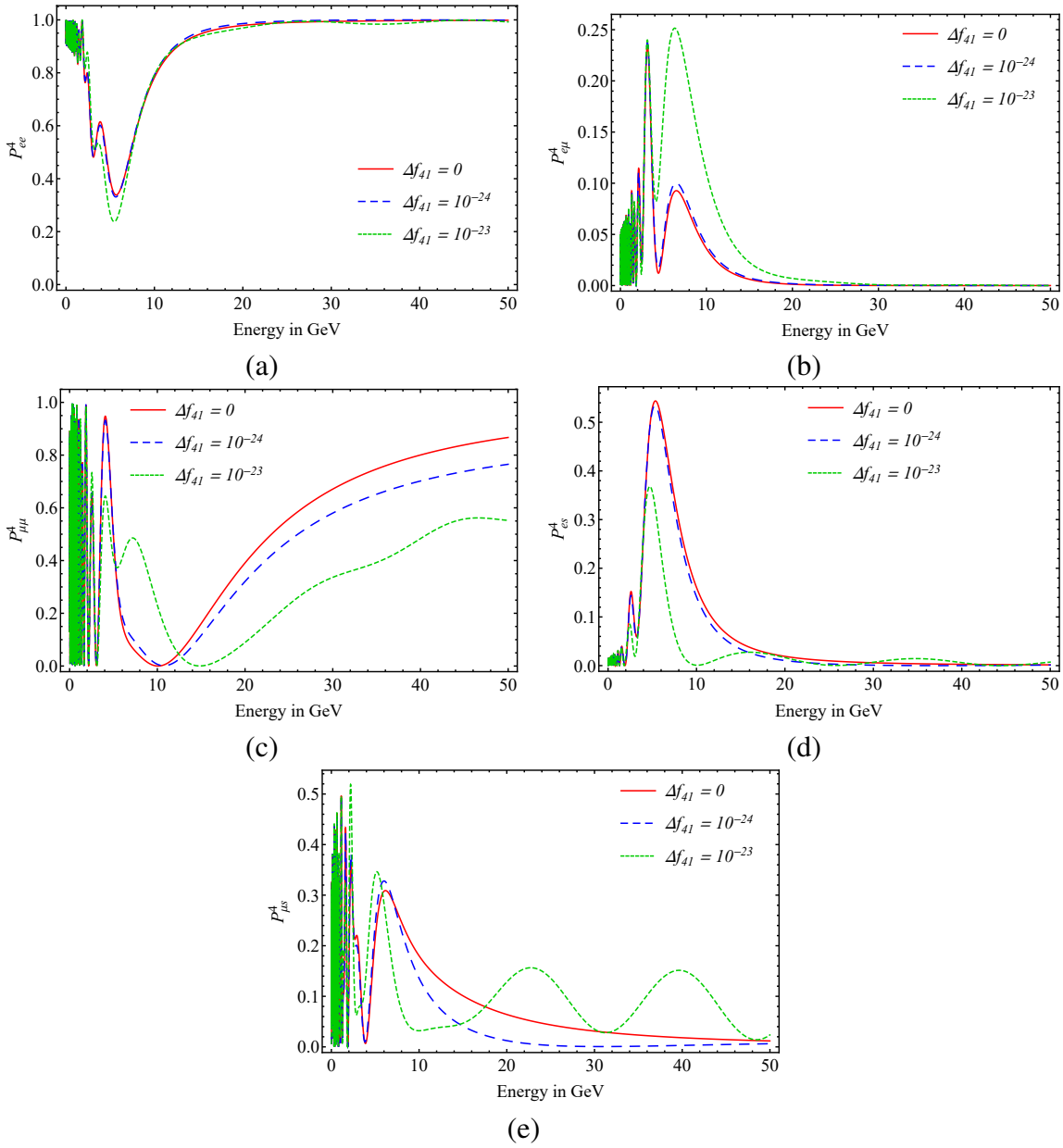

Figure 12.3: Neutrino oscillation probabilities in matter for a xed value of $\Delta m^2_{41} = 1 \times 10^{-3}$ eV^2, $\Delta f_{31} = 5 \times 10^{-27}$ and for Set-2 with baseline length L = 7000 Kms.

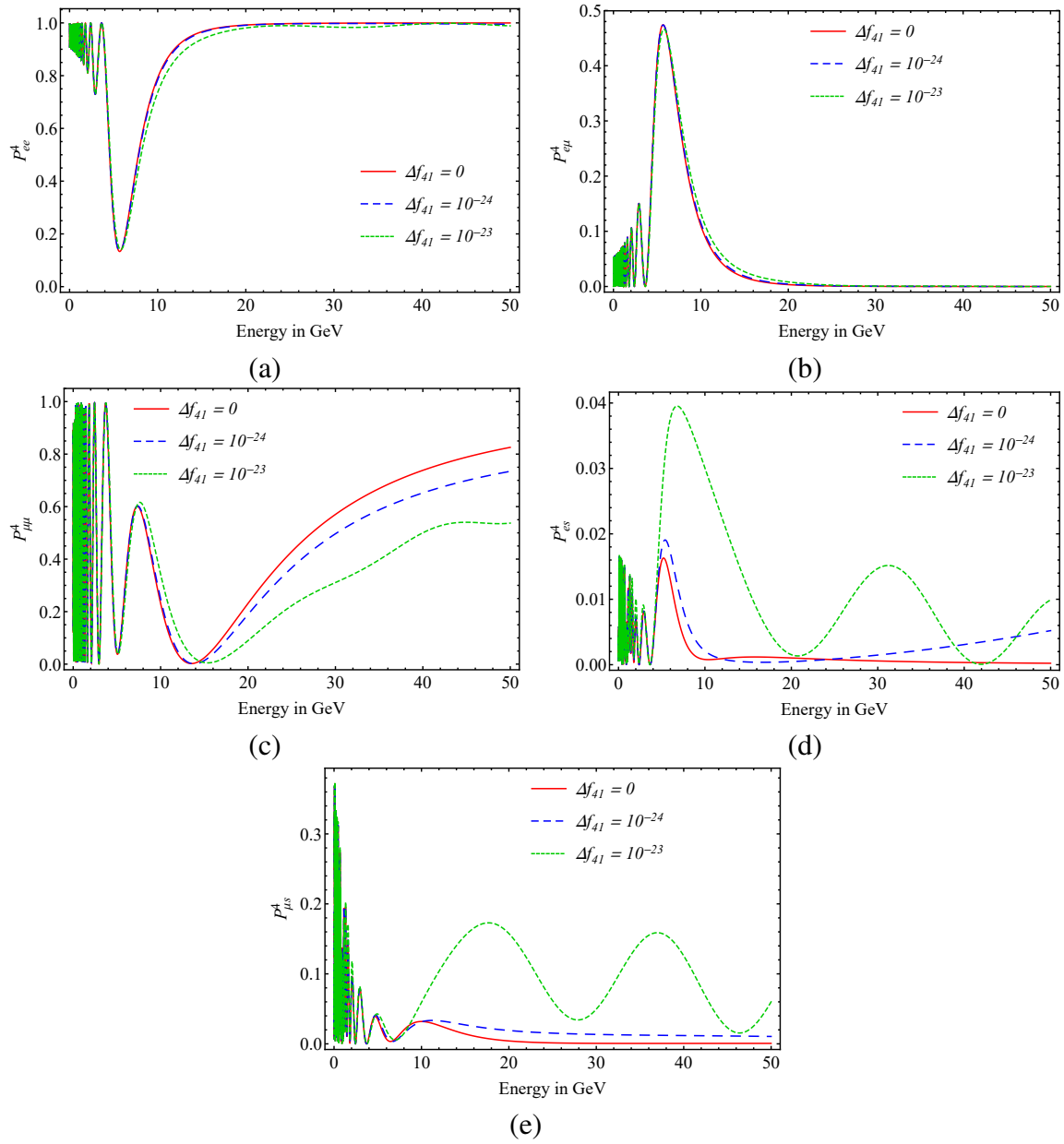

Figure 12.4: Neutrino oscillation probabilities in matter for a xed value of $\Delta m^2_{41} = 3 \times 10^{-3}$ eV^2, $\Delta f_{31} = 5 \times 10^{-27}$ and for Set-2 with baseline length L = 7000 Kms.

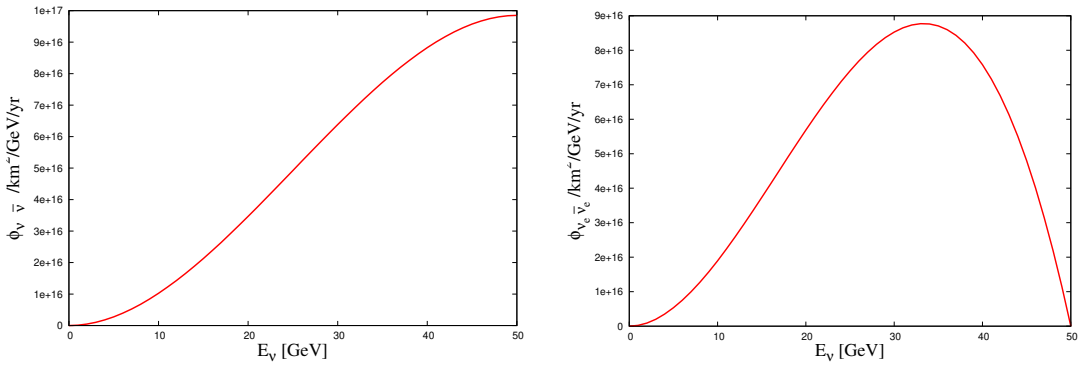

(a) (b)

Figure 12.5: Flux of a) ν_μ and b) $\bar{\nu_e}$ for muon decay at muon storage ring with muon injection energy of 50 GeV. See text for details.

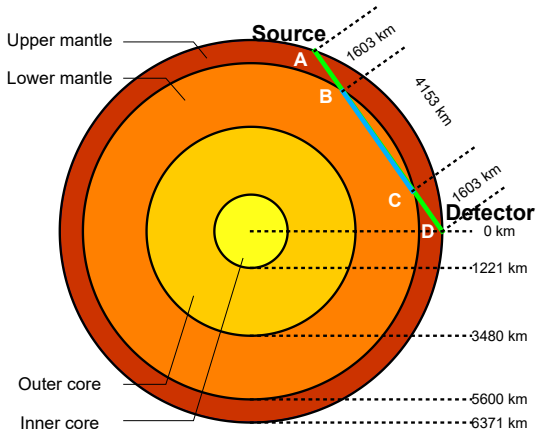

Figure 12.6: Different layers of earth and projected travel path of neutrinos for long basline neutrino detector placed at 7359 Kms from source.

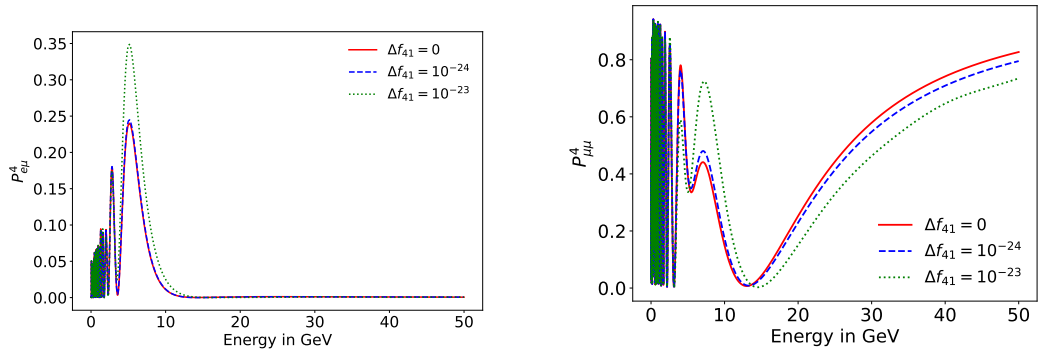

(a) (b)

Figure 12.7: Neutrino oscillation probabilities within matter for varying density with two layer approximation and baseline length $L = 7359$ Kms. See text for details.

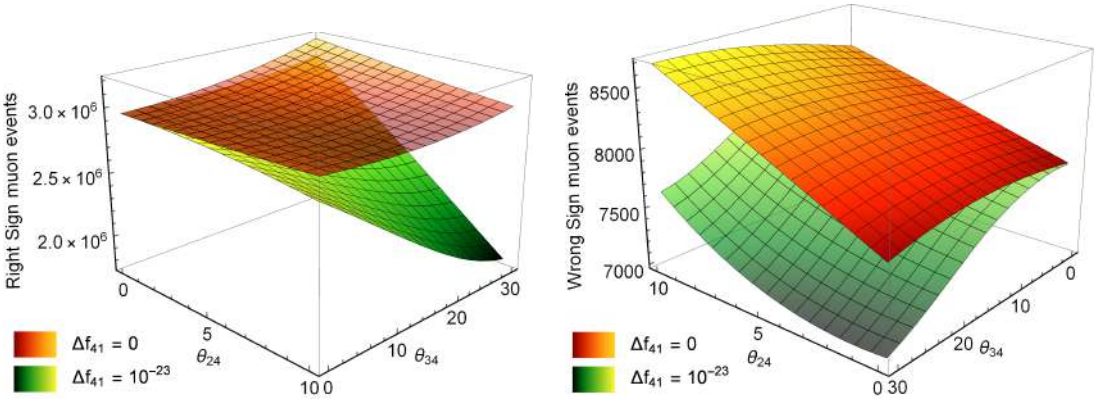

(a) (b)

Figure 12.8: Right sign and wrong sign muon yield variations with θ_{24} and θ_{34} for xed $\theta_{14} = 2.5^0$, $\Delta f_{31} = 5 \times 10^{-27}$ and two chosen values of $\Delta f_{41} = 0, 10^{-23}$. See text for details.

CHAPTER 13

GRAVITATIONAL WAVE EMISSIONS FROM FIRST ORDER PHASE TRANSITIONS WITH TWO COMPONENT FIMP DARK MATTER

In this Chapter, we explore the emissions of the Gravitational Waves (GWs) from a strong first order electroweak phase transition (SFOEWPT). To this end, a dark matter (DM) model has been investigated in Feebly Interacting Massive Particle (FIMP) scenario, where the DM particles are produced through "freeze-in" mechanism in the early Universe described briefly in Chapter 3 (Section 3.3). In this context, we extend scalar sector of Standard Model (SM) of particle physics by two additional scalar singlets whose stabilities are protected by an unbroken discrete $Z_2 \times Z_2'$ symmetry and they are assumed to develop no vacuum expectation values (VEVs) after spontaneous symmetry breaking (SSB). We have elaborately discussed this two component FIMP DM model in Chapter 6. We study the first order phase transition (FOPT) within the framework of this present model. Both ana-

lytical and numerical computations have been done to calculate the consequent production of GWs and then we investigate the detectabilities of such GWs at the future space-based detectors such as LISA, BBO, ALIA, DECIGO, aLIGO and aLIGO+, etc. We also find that the smaller Higgs portal couplings play a signifant role in the relic density calculations for the considered two component FIMP DM model whereas the DM self couplings have a considerable influence on GWs production in the present scenario.

13.1 Introduction

In 2015 the Laser Interferometer Gravitational Wave Observatory (LIGO) collaboration [525] had detected Gravitational Waves (GW150914) reaching the Earth from the distant violent astrophysical phenomenon involving inward spiralling and eventual merger of a pair of massive black holes and subsequent ringdown after the merger opens up new vistas to GW astronomy. This has been followed by the detections of a number of such other GWs and the study of these GWs help to explore high energy cosmic phenomena such as neutron stars, pulsars, black holes etc. Other than the likes detected by LIGO where the GWs are generally originated from the collision of black holes and/or neutron stars, primordial GWs can be produced via inflationary quantum fluctuations [526], topological defects of the domain walls and cosmic strings [527], FOPT in the early Universe [528, 529] etc. Study of these GWs could be very useful to understand the cosmic evolution and the processes in the early Universe. In this Chapter, we address the case where the GWs can be produced from FOEWPT mediated by a viable dark matter candidate. Similar issues have been addressed in the literatures [530–543] but here a two component DM model has been considered (discussed earlier in Chapter 6) instead of just a one component DM, where both the components are Feebly Interacting Massive Particles or FIMPs. The simple extension of SM of particle physics ($SU(2)_L \times U(1)_Y$ electroweak symmetry) with additional particles (to accommodate the two component particle DM candidate) may lead the elctroweak phase transition (EWPT) to be a FOPT instead of a just a smooth

crossover.

The EWPT followed by the SSB of electroweak symmetry ($SU(2)_L \times U(1)_Y$) as formulated in SM is a smooth transition rather than a first order one. In this Chapter, GWs from a FOEWPT is addressed in the framework of a proposed DM model. Though the SM of particle physics can describe the descriptions of several experimental observations, it may not be considered as a fundamental theory as it fails to describe DM phenomena and the baryon asymmetry of the Universe (BAU). In order to explain the latter a SFOEWPT is required which can provide a non-equilibrium environment if the electroweak baryogenesis mechanism [544–547] generates the BAU. There are many models and theories where the extension of the SM has been studied to address the EWPT and the DM phenomena simultaneously [530–543]. Different types of phase transitions (PT) namely one-step [62, 63, 548–550] and two-step (or more step) [535, 551–558] PT , may lead to a SFOEWPT. For one-step PT only initial and final phases exist whereas the temperature of the Universe drops down to the barrier between the electroweak symmetry and the broken phases appear from loop corrections of the potential. On the other hand, for two-step (or multi step) PT an intermediate metastable state arises between the initial and the final phases and the barrier between two minima appears at the tree level of the potential. As a result the transition may happen as a FOPT through a tunneling process and it may proceed through electroweak bubble nucleation [559, 560], which can expand, collide and coalesce and eventually the Universe turns into the electroweak broken phase. Initially all possible sizes of bubbles having different surface tension and pressure are taken into account. The bubble with the size which is large enough to avoid any kind of collapses are claimed as a critical bubble. The bubbles having size smaller than the critical one tend to collapse whereas the bubbles having size larger than the critical bubble tend to expand. Due to the pressure difference between the true and false vacua, nucleations of electroweak bubbles occur. These bubbles could not sustain their spherical symmetry which generates phase transitions and eventually these phase transitions may produce the GWs. The GW production mechanisms through the bubble nucleation and bubble collision have been addressed in literatures [561–566]. The three mechanisms based on

which the GW production arises mainly are bubble collisions and shock waves [561–566], sound waves [567–570] and magnetohydrodynamic turbulance in the plasma [571–577].

In this Chapter, we address the issues of SFOEWPT as well as the particle DM candidate by adopting a minimally extended SM where two real scalar singlets produced via freeze-in mechanism are added to the SM. We have already described this freeze-in mechanism in Chapter 3 (Section 3.3). The detail study of the two component FIMP DM model as well as the bounds and the constraints on the parameters of our proposed DM model from both theoretical and experimental aspects are elaborately dicussed in Chapter 6. The proposed model also satisfies the upper limit of the DM self interacting cross-sections obtained from the observations of 72 colliding galaxy clusters [217] and this is also discussed in Chapter 6. Though the relic density calculations of the proposed DM model can be done by considering the Higgs portal, however the couplings of the DM self interactions dominate over the Higgs portal couplings in the case of generating SFOEWPT as the Higgs portal couplings (couplings of DM with the SM particles) are very negligible ($\sim 10^{-9} - 10^{-11}$). Our purpose is to demonstrate the viability of the present extended SM to induce the SFOEWPT and at the same time yields a viable DM candidate. We have chosen three benchmark points (BPs) from the allowed parameter space for the analytical and numerical calculations of the GW production due to SFOEWPT in the present model. We have checked that the three chosen BPs can satisfy the criterion $\frac{v_c}{T_c} \gtrsim 1$ [578, 579], where v_c indicates the Higgs VEV at the critical temperaure T_c required to produce SFOEWPT and hence the GWs are generated. The detectabilities of such GWs by calculating the GW frequencies and intensities for the present formalism has also been addressed in this Chapter. We then compare them with the estimated sensitivity predictions of the future space borne detector such as Big Bang Observer (BBO) [580], Laser Interferometer Space Antenna (LISA) [581], Advanced Laser Interferometer Antenna (ALIA) [582], DECi-hertz Interferometer Gravitational Wave Observatory (DECIGO) [583] and ground-based detector such as advanced Laser Interferometer Gravitational Wave Observatory (aLIGO) [584].

13.2 Two Component FIMP DM Model

In this Chapter, a two component FIMP DM model is adopted, where the dark matter candidates are produced through freeze-in mechanism. The model is a renormalizable extension of the SM of particle physics with two singlet scalar fields S_2 and S_3 as discussed in Chapter 6. These two real scalars (S_2 and S_3) compose the dark sector in the present scenario. As already mentioned in Chapter 6, the scalars S_2 and S_3 are singlets under the SM gauge group $(\mathrm{SU}(2)_L \times \mathrm{U}(1)_Y)$ and a discrete $Z_2 \times Z_2'$ symmetry is imposed on the real scalar fields to ensure their stabilities. After SSB, these scalars do not generate any VEVs, which prevent mixing between the real scalars and the SM scalar. The DM candidates can interact only through the Higgs portal with the SM sector. The Lagrangian of the model is given as

$$\mathcal{L} = \mathcal{L}_{\rm SM} + \mathcal{L}_{\rm DM} + \mathcal{L}_{\rm int} \ , \tag{13.1}$$

where $\mathcal{L}_{\rm SM}$ represents the SM Lagrangian. $\mathcal{L}_{\rm DM}$ stands for the dark sector Lagrangian including two real singlet scalars. All these terms for this model is briefly elaborated in Chapter 6. The renormalizable potential term of the scalar sector of the two component DM model in FIMP scenario (V) as

$$\begin{aligned} V &= \mu_H^2\, H^\dagger H + \lambda_H\, (H^\dagger H)^2 + \frac{\mu_{S_2}^2}{2} S_2^2 + \frac{\lambda_{S_2}}{4} S_2^4 + \frac{\mu_{S_3}^2}{2} S_3^2 + \frac{\lambda_{S_3}}{4} S_3^4 \\ &\quad + \lambda_{HS_2} H^\dagger H\, S_2^2 + \lambda_{HS_3} H^\dagger H\, S_3^2 + \lambda_{S_2S_3} S_2^2\, S_3^2 \, . \end{aligned} \tag{13.2}$$

After SSB, only the Higgs acquires a VEV $\left[H = \begin{pmatrix} 0 \\ \frac{v+h}{\sqrt{2}} \end{pmatrix} \right]$ and the scalar fields S_2 and S_3 acquire no VEV. Therefore $S_2 = s_2 + 0$, $S_3 = s_3 + 0$. As a result, after SSB the scalar potential

(V) takes the form

$$\begin{aligned} V &= \frac{\mu_H^2}{2}(v+h)^2 + \frac{\lambda_H}{4}(v+h)^4 + \frac{\mu_{S_2}^2}{2}s_2^2 + \\ &\quad \frac{\lambda_{S_2}}{4}s_2^4 + \frac{\mu_{S_3}^2}{2}s_3^2 + \frac{\lambda_{S_3}}{4}s_3^4 + \\ &\quad \frac{\lambda_{HS_2}}{2}(v+h)^2 s_2^2 + \frac{\lambda_{HS_3}}{2}(v+h)^2 s_3^2 + \lambda_{S_2S_3}s_2^2 s_3^2 \ . \end{aligned} \tag{13.3}$$

From the minimisation condition

$$\left(\frac{\partial V}{\partial h}\right), \left(\frac{\partial V}{\partial s_2}\right), \left(\frac{\partial V}{\partial s_3}\right)\Bigg|_{h=0,\, s_2=0,\, s_3=0} = 0 \ , \tag{13.4}$$

one obtains

$$\mu_H^2 + \lambda_H v^2 = 0 \ . \tag{13.5}$$

The mass matrix is diagonal as there is no mixing between the scalars since S_3 and S_3 do not generate any VEVs. Therefore the diagonal mass matrix is written as

$$\mathcal{M}^2_{\text{scalar}} = \begin{pmatrix} 2\lambda_H v^2 & 0 & 0 \\ 0 & \mu_{S_2}^2 + \lambda_{HS_2}v^2 & 0 \\ 0 & 0 & \mu_{S_3}^2 + \lambda_{HS_3}v^2 \end{pmatrix} \ , \tag{13.6}$$

where

$$m_h^2 = \mu_h^2 + 3\lambda_h v^2 = 2\lambda_h v^2 \ , \tag{13.7}$$

$$m_{s_2}^2 = \mu_{S_2}^2 + \lambda_{HS_2}v^2 \ , \tag{13.8}$$

$$m_{s_3}^2 = \mu_{S_3}^2 + \lambda_{HS_3} v^2 \ , \tag{13.9}$$

$$m_{hs_2}^2 = m_{hs_3}^2 = m_{s_2 s_3}^2 \ . \tag{13.10}$$

13.3 Electroweak Phase Transition (EWPT)

In order to study the EWPT in the proposed two component FIMP DM model, the finite temperature correction is required to be considered with the tree level scalar potential. The effective potential at finite temperature T is given as [585]

$$V_{\text{eff}} = V_{\text{tree-level}}^{T=0} + V_{1-\text{loop}}^{T=0} + V_{1-\text{loop}}^{T\neq 0} \ , \tag{13.11}$$

where $V_{\text{tree-level}}^{T=0}$, $V_{1-\text{loop}}^{T=0}$ and $V_{1-\text{loop}}^{T\neq 0}$ are the tree level potential at $T = 0$, the Coleman - Weinberg one loop corrected potential at $T = 0$ and the same at finite temperaure ($T \neq 0$) respectively. By replacing s_2 and s_3 fields with their corresponding classical fields v_1 (VEV of S_2) and v_2 (VEV of S_3), we can express the tree level potential ($V_{\text{tree-level}}^{T=0}$) as

$$\begin{aligned} V_{\text{tree-level}}^{T=0} \quad = \quad & \frac{\mu_H^2}{2} v^2 + \frac{\lambda_H}{4} v^4 + \frac{\mu_{S_2}^2}{2} v_1^2 + \\ & \frac{\lambda_{S_2}}{4} v_1^4 + \frac{\mu_{S_3}^2}{2} v_2^2 + \frac{\lambda_{S_3}}{4} v_2^4 + \\ & \frac{\lambda_{HS_2}}{2} v^2 v_1^2 + \frac{\lambda_{HS_3}}{2} v^2 v_2^2 + \lambda_{S_2 S_3} v_1^2 v_2^2 \ . \end{aligned} \tag{13.12}$$

The Coleman - Weinberg one loop correction of the effective potential at zero temperature $V_{1-\text{loop}}^{T=0}$ is written as [432, 585]

$$V_{1-\text{loop}}^{T=0} = \pm \frac{1}{64\pi^2} \sum_i n_i m_i^4 \left[\log \frac{m_i^2}{Q^2} - C_i \right] \ , \tag{13.13}$$

where '+' and '−' indicate bosons and fermions respectively and the summation is taken over i particles ($i \equiv h, s_2, s_3, W^{\pm}, z, t$). In Eq. 13.13, n_i represents the number of degrees of freedom. The degrees of freedom for the gauge bosons ($W^{\pm}, Z$), fermions (t), Higgs bosons (h) and scalars (s_2, s_3) are $(n_{W^{\pm}})_L = 4$, $(n_{W^{\pm}})_T = 2$, $(n_Z)_L = 2$, $(n_Z)_T = 1$, n_t = 12, n_h = 1 and $n_{s_2,s_3} = 1$ respectively and the subscript 'L' and 'T' stand for the longitudinal and transverse components of the gauge bosons ($W^{\pm}, Z$). The field dependent square masses of the gauge bosons, fermions and scalars in terms of their corresponding classical fields v (VEV of H), v_1 (VEV of S_2) and v_2 (VEV of S_3) at zero temperature can be written as

$$m_t^2 = \frac{1}{2} y_t^2 v^2 \ , \tag{13.14}$$

$$m_W^2 = \frac{1}{4} g^2 v^2 \ , \tag{13.15}$$

$$m_Z^2 = \frac{1}{4} (g^2 + g'^2) v^2 \ , \tag{13.16}$$

$$m_h^2 = \mu_H^2 + 3\lambda_H v^2 + \lambda_{HS_2} v_1^2 + \lambda_{HS_3} v_2^2 \ , \tag{13.17}$$

$$m_{s_2}^2 = \mu_{S_2}^2 + \lambda_{HS_2} v^2 + 3\lambda_{S_2} v_1^2 + 2\lambda_{S_2S_3} v_2^2 \ , \tag{13.18}$$

$$m_{s_3}^2 = \mu_{S_3}^2 + \lambda_{HS_3} v^2 + 3\lambda_{S_3} v_2^2 + 2\lambda_{S_2S_3} v_1^2 \ , \tag{13.19}$$

$$m_{G^+}^2 = 2\mu_H^2 + 2\lambda_H v^2 + 2\lambda_{HS_2} v_1^2 + 2\lambda_{HS_3} v_2^2 \ , \tag{13.20}$$

$$m_{G_0}^2 = \mu_H^2 + \lambda_H v^2 + \lambda_{HS_2} v_1^2 + \lambda_{HS_3} v_2^2 \ , \tag{13.21}$$

where y_t, g and g' correspond to the top Yukawa coupling, SU(2)$_L$ and U(1)$_Y$ gauge SM couplings respectively. Note that for $v_1 = v_2 = 0$ the Eqs. 13.17 - 13.19 will be similar to the Eqs. 13.7 - 13.9 mentioned in Section 13.2. Here we impose Landau gauge ($\xi = 0$), where at $T \neq 0$ the Goldstone bosons acquire masses but for zero temperature they are massless and also the ghost contribution does not exist here [586]. For further calculations, we consider the values of the renormalizable scale, Q (mentioned in Eq. 13.13) as ~ 246.22 GeV. However, one can vary Q as the selection of Q is not unique. In Eq. 13.13 C_i indicates a numerical constant and it depends on the renormalization scheme. For the transverse component of gauge bosons ($W_T^{\pm}, Z_T$), $(C_{W,Z})_T = 1/2$ while for the longitudinal component of gauge bosons ($W_L^{\pm}, Z_L$), $(C_{W,Z})_L = 3/2$ and for the other particles considered in this model (h, s_2, s_3, t), $C_{h,s_2,s_3,t} = 3/2$. The one loop corrected effective potential at finite temperature takes the form

$$V_{1-\text{loop}}^{T\neq 0} = \frac{T^4}{2\pi^2} \sum_i n_i J_{\pm} \left[\frac{m_i^2}{T^2} \right] , \tag{13.22}$$

where the function $J_{\pm}$ is given as

$$J_{\pm} \left(\frac{m_i^2}{T^2} \right) = \pm \int_0^{\infty} dy \, y^2 \log \left(1 \mp e^{-\sqrt{y^2 + \frac{m_i^2}{T^2}}} \right) . \tag{13.23}$$

We add the temperature corrected terms to the boson masses by including the Daisy resummation procedure in $V_{1-\text{loop}}^{T\neq 0}$ [587]. Therefore, the temperature dependent masses can be expressed as $\mu_H^2(T) = \mu_H^2 + c_1 T^2$, $\mu_{S_2}^2(T) = \mu_{S_2}^2 + c_2 T^2$ and $\mu_{S_3}^2(T) = \mu_{S_3}^2 + c_3 T^2$, where

$$c_1 = \frac{6\lambda_H + 2\lambda_{HS_2}}{12} + \frac{3g^2 + g'^2}{16} + \frac{1}{6}\lambda_{HS_3} + \frac{y_t^2}{4} \ , \tag{13.24}$$

$$c_2 = \frac{1}{8}\lambda_{S_2} + \frac{1}{6}\lambda_{HS_2} + \frac{1}{6}\lambda_{S_2S_3} \ , \tag{13.25}$$

$$c_3 = \frac{1}{8}\lambda_{S_3} + \frac{1}{6}\lambda_{HS_3} + \frac{1}{6}\lambda_{S_2S_3} \ . \tag{13.26}$$

For the longitudinal components of gauge bosons ($W_L^{\pm}$, Z_L), the temperture corrected mass terms are given by [586]

$$m_W^2\left(T\right) = m_W^2 + 2g^2T^2 \ , \tag{13.27}$$

and

$$m_Z^2\left(T\right) = \frac{1}{2}m_Z^2 + \left(g^2 + g'^2\right)T^2 + \frac{1}{8}\sqrt{\left[\left(g^2 - g'^2\right)^2\left(64T^2 + 16T^2v^2\right) + \left(g^2 + g'^2\right)^2 v^4\right]} \ . \tag{13.28}$$

For our calculation the CosmoTransition package [585] has been used to compute the correction to the tree level potential at $T \neq 0$.

13.4 Gravitational Waves Production from FOEWPT

The onset of bubble nucleation when the system attains a vacuum state at a finite temperature is central to the occurence of FOEWPT. The temperature when the bubble nucleation sets in is generally known as the nucleation temperature. The bubble nucleation rate per unit volume at a particular temperature (T) can be written as [588]

$$\Gamma = \Gamma_0\left(T\right)e^{-S_3(T)/T} \ , \tag{13.29}$$

where $\Gamma_0\,(T) \propto T^4$. In the above, $S_3(T)$ signifies the Euclidean action of the critical bubble, which is given as

$$S_3 = 4\pi \int dr\, r^2 \left[\frac{1}{2}\left(\partial_r \vec{\phi}\right)^2 + V_{\text{eff}}\right], \tag{13.30}$$

where $\vec{\phi} = (h, s_2, s_3)$ and V_{eff} denotes the effective finite temperature potential (Eq. 13.11). The bubble nucleation occurs when the nucleation temperature (T_n) satisfies the condition $\frac{S_3(T_n)}{T_n} \simeq 140$. The three mechanisms via which the GWs are generated from FOEWPT are bubble collisions [561–566], sound waves [567–570] and turbulance effect in the plasma [571–577]. With the contributions of these three mechanisms, the total GW intensity ($\Omega_{\text{GW}}h^2$) as a function of frequency is given as [561–577]

$$\Omega_{\text{GW}}h^2 = \Omega_{\text{col}}h^2 + \Omega_{\text{SW}}h^2 + \Omega_{\text{turb}}h^2\ , \tag{13.31}$$

where $\Omega_{\text{col}}h^2$ denotes the contribution of the bubble collisions to the total GW intensity (for more detail derivations see Ref. [589, 590]), which can be expressed as

$$\Omega_{\text{col}}h^2 = 1.67\times 10^{-5}\left(\frac{\beta}{H}\right)^{-2}\frac{0.11 v_w^3}{0.42+v_w^2}\left(\frac{\kappa\alpha}{1+\alpha}\right)^2\left(\frac{g_*}{100}\right)^{-\frac{1}{3}}\frac{3.8\left(\frac{f}{f_{col}}\right)^{2.8}}{1+2.8\left(\frac{f}{f_{\text{col}}}\right)^{3.8}}\ , \tag{13.32}$$

with the parameter β

$$\beta = \left[HT\frac{d}{dT}\left(\frac{S_3}{T}\right)\right]\Bigg|_{T_n}. \tag{13.33}$$

In the above equation (Eq. 13.33), H is the Hubble parameter at T_n. The bubble wall velocity (v_w) is generally estimated as [565, 591]

$$v_w = \frac{1/\sqrt{3}+\sqrt{\alpha^2+2\alpha/3}}{1+\alpha}. \tag{13.34}$$

The choice of the bubble wall velocity varies from literature to literature [535, 592]. For simplicity in some literatures v_w is considered to be 1 [540, 541, 593]. In this Chapter, we use Eq. 13.34 for the calculation of the bubble wall velocity. In Eq. 13.32, κ denotes the fraction of laten heat deposited in a thin shell, which is given as

$$\kappa = 1 - \frac{\alpha_\infty}{\alpha}, \tag{13.35}$$

with [540, 581]

$$\alpha_\infty = \frac{30}{24\pi^2 g_*}\left(\frac{v_n}{T_n}\right)^2\left[6\left(\frac{m_W}{v}\right)^2 + 3\left(\frac{m_Z}{v}\right)^2 + 6\left(\frac{m_t}{v}\right)^2\right] , \tag{13.36}$$

where v_n indicates the VEV of Higgs at T_n. The masses of $W^\pm, Z$ and top quarks are represented as m_W, m_Z and m_t repectively in the above. The parameter α is defined as the ratio of the vacuum energy density ($\rho_{\rm vac}$) released by EWPT to the background energy density ($\rho^*_{\rm rad}$) at T_n.

$$\alpha = \left[\frac{\rho_{\rm vac}}{\rho^*_{\rm rad}}\right]\Bigg|_{T_n} , \tag{13.37}$$

where $\rho_{\rm vac}$ and $\rho^*_{\rm rad}$ are given as

$$\rho_{\rm vac} = \left[\left(V^{\rm high}_{\rm eff} - T\frac{dV^{\rm high}_{\rm eff}}{dT}\right) - \left(V^{\rm low}_{\rm eff} - T\frac{dV^{\rm low}_{\rm eff}}{dT}\right)\right] \tag{13.38}$$

and

$$\rho^*_{\rm rad} = \frac{g_*\pi^2 T_n^4}{30} . \tag{13.39}$$

It is to be mentioned that one may calculate $\rho_{\rm vac}$ by using the trace anomaly [570], where we need to include an additional factor $\frac{1}{4}$ with the term $T\frac{dV}{dT}$ (Eq. 13.38).

The peak frequency produced by the bubble collisions (the parameter $f_{\rm col}$ in Eq. 13.32) can be

expressed as

$$f_{\rm col} = 16.5 \times 10^{-6}\ {\rm Hz} \left(\frac{0.62}{v_w^2 - 0.1 v_w + 1.8}\right) \left(\frac{\beta}{H}\right) \left(\frac{T_n}{100\ {\rm GeV}}\right) \left(\frac{g_*}{100}\right)^{\frac{1}{6}}. \tag{13.40}$$

In Eq. 13.31, $\Omega_{\rm SW}h^2$ stands for the sound wave component of the GW intensity which takes the form

$$\Omega_{\rm SW}h^2 = 2.65 \times 10^{-6} \left(\frac{\beta}{H}\right)^{-1} v_w \left(\frac{\kappa_v \alpha}{1+\alpha}\right)^2 \left(\frac{g_*}{100}\right)^{-\frac{1}{3}} \left(\frac{f}{f_{\rm SW}}\right)^3 \left[\frac{7}{4 + 3\left(\frac{f}{f_{\rm SW}}\right)^2}\right]^{\frac{7}{2}}. \tag{13.41}$$

In Eq. 13.41, the fraction of latent heat transformed into the bulk motion of the fluid is defined as κ_v, which is given as

$$\kappa_v = \frac{\alpha_\infty}{\alpha} \left[\frac{\alpha_\infty}{0.73 + 0.083\sqrt{\alpha_\infty} + \alpha_\infty}\right]. \tag{13.42}$$

The peak frequency $f_{\rm SW}$ produced by the sound wave mechanisms (in Eq. 13.41) has the following form

$$f_{\rm SW} = 1.9 \times 10^{-5}\ {\rm Hz} \left(\frac{1}{v_w}\right) \left(\frac{\beta}{H}\right) \left(\frac{T_n}{100\ {\rm GeV}}\right) \left(\frac{g_*}{100}\right)^{\frac{1}{6}}. \tag{13.43}$$

In order to check whether the contribution of sound wave component to the total GW intensity is significant or not, it is useful to estimate a factor $\frac{HR_*}{\overline{U}_f}$, which is known as suppression factor, where $\overline{U}_f$ and R_* are the root mean square (RMS) fluid velocity and the mean bubble separation respectively [581, 594, 595]. For a given model if the suppression factor $\left(\frac{HR_*}{\overline{U}_f}\right)$ turns out to be < 1, then we need to include this factor to the sound wave component of the GW intensity as it is an overestimate to the GW signal. On the other hand, for $\frac{HR_*}{\overline{U}_f} > 1$ the sound wave survives more

than the Hubble time.

The third mechanism which takes part in the production of GWs is the turbulance component ($\Omega_{\text{turb}}h^2$) arising out of the turbulance in plasma

$$\Omega_{\text{turb}}h^2 = 3.35\times10^{-4}\left(\frac{\beta}{H}\right)^{-1} v_w \left(\frac{\epsilon\kappa_v\alpha}{1+\alpha}\right)^{\frac{3}{2}} \left(\frac{g_*}{100}\right)^{-\frac{1}{3}} \frac{\left(\frac{f}{f_{\text{turb}}}\right)^3 \left(1+\frac{f}{f_{\text{turb}}}\right)^{-\frac{11}{3}}}{\left(1+\frac{8\pi f}{h_*}\right)}, \quad (13.44)$$

where $\epsilon = 0.1$ and the peak frequency f_{turb} is

$$f_{\text{turb}} = 2.7\times10^{-5}\ \text{Hz}\left(\frac{1}{v_w}\right)\left(\frac{\beta}{H}\right)\left(\frac{T_n}{100\ \text{GeV}}\right)\left(\frac{g_*}{100}\right)^{\frac{1}{6}}. \quad (13.45)$$

In Eq. 13.44, the parameter h_* takes the form

$$h_* = 16.5\times10^{-6}\ \text{Hz}\left(\frac{T_n}{100\ \text{GeV}}\right)\left(\frac{g_*}{100}\right)^{\frac{1}{6}}. \quad (13.46)$$

The GW intensity can now be computed using Eqs. 13.31 - 13.46.

13.5 Calculations and Results

In this Section, we calculate the intensities of GW signals produced from the FOEWPT in a two component FIMP DM model discussed in detail in Chapter 6 and the calculated signals are compared with the sensitivity curves of such GWs at different proposed future detectors such as ALIA, BBO, DECIGO, aLIGO, aLIGO+ and LISA. In order to compute the GW intensities we choose three sets of BPs from the allowed model parameter space. These three BPs are chosen in such a way that they satisfy various bounds and constraints on the model parameters from both theoretical considerations (vacuum stability [227], perturbativity [11, 227, 277–280] etc.) and experimental observations, e.g. the PLANCK observational results for the DM relic density, the collider bounds

BP	m_h in GeV	m_{s_1} in GeV	m_{s_3} in GeV	λ_{HS_2}	λ_{HS_3}	λ_{S_2}	λ_{S_3}	$\lambda_{S_2S_3}$	$\Omega_{\rm DM}h^2$
1	125.5	10×10^{-6}	5×10^{-6}	2×10^{-9}	1×10^{-9}	0.089	0.59	1.59	0.1217
2	125.5	0.01	0.005	6.36×10^{-11}	2.67×10^{-11}	0.029	0.96	0.98	0.119
3	125.5	10×10^{-6}	5×10^{-6}	2×10^{-9}	1×10^{-9}	1.57	0.025	0.18	0.1217

Table 13.1: The chosen three benchmark points (BPs) are tabulated. We use the parameter values of these chosen BPs to calculate the GW intensities produced from a two component FIMP DM model. The relic density values corresponding to each of the BPs are also furnished in this table.

and the upper limit on the DM self interaction cross-section. All the necessary constraints mentioned above and the relic density calculations of the present model have been worked out in detail in Chapter 6. In Chapter 6, the authors have shown that the two real singlet scalars constitute a viable two component DM candidate. The considered BPs are tabulated in Table 13.1. In addition to the model parameters, we have also furnished the values of the DM relic densities corresponding to each of the three BPs in Table 13.1. A discussion is in order. From the observations of 72 colliding galaxy clusters by Harvey *et al.* Ref. [217], the upper limit on the DM self interaction cross-section is found to be $\sigma_{\rm DM}/m < 0.47$ cm^2/gm with 95% confidence limit (C.L.). The study of DM self interaction by Campbell *et al.* [219] claims that the DM produced by the freeze-in mechanism can explain the DM self interaction results $\sigma_{\rm DM}/m \sim 1.5$ cm^2/gm from Abell 3827 clusters performed by [218]. The choice of the self couplings in Table 13.1 of the two components s_2, s_3 of the FIMP DM are made as follows. In Chapter 6, the calculations are made for similar model (Fig. 6.12 of Chapter 6) by varying the self couplings from 0 to $\frac{2\pi}{3}$. In this Chapter we found that smaller choices of self couplings (although allowed) does not yield significant GW intensity. The values of self couplings in Table 13.1 are therefore chosen within the allowed limits so as to obtain strong first order phase transitions (SFOPTs) and the subsequent productions of GWs.

The thermal parameters which play a major role for GW emissions are the time-scale of the phase transition ($1/\beta$), the strength of the FOPT (α), the bubble wall velocity (v_w), the nucleation temperature (T_n) and VEV of Higgs (v_n) at T_n. To estimate the GW intensity, firstly we need to compute the above mentioned thermal parameters and for that we consider a finite temperature

BP	v_n in GeV	v_c in GeV	T_c in GeV	$\frac{v_c}{T_c}$	T_n in GeV	α	$\frac{\beta}{H}$	$\frac{HR_*}{\bar{U}_f}$
1	170.30	136.93	120.49	1.14	103.62	0.36	1455.44	0.78
2	173.59	130.42	122.74	1.06	99.06	0.42	1075.66	0.92
3	122.04	140.42	125.59	1.12	101.96	0.39	793.32	3.72

Table 13.2: The values of the thermal parameters used for computing the GW intensity for each of the corresponding chosen BPs. See text for details.

effective potential which is obtained by adding the thermal correction terms with the tree level potential (Eq. 13.12). The calculations related to the thermal parameters have been done using CosmoTransition package [585]. The calculated values of the phase transition parameters such as $v_n, v_c, T_c, v_c/T_c, T_n, \alpha, \beta/H$ are furnsihed in Table 13.2. All the chosen BPs satisfy the SFOPT condition $v_c/T_c > 1$ which is shown in Table 13.2. Here we note again that calculations made with choice of low values of DM self couplings ($\lesssim 10^{-2}$) do not yield results feasible for SFOEWPT and eventual productions of GWs. In the proposed model the Higgs portal couplings of the FIMP DM particles are small due to their freeze-in production mechanism. Though these feeble Higgs portal couplings take no part in the generation of GWs, but they play an important role in the DM relic density calculation. Therefore the GW production from the FOEWPT occurs purely in the dark sector through the self interaction in the FIMP DM particles (S_2 and S_3 in the proposed two component FIMP DM model). It is to be noted that the phase transition occurs in between the critical temerature and the temperature at the present epoch. Therefore, T_n is always smaller than T_c and this is true for all the considered BPs (Table 13.2). For all the calculations the renormalizable scale (Q) is kept fixed at 246.22 GeV. We use Eqs. 13.31-13.46 to compute the intensities of the GWs. As mentioned earlier, in order to estimate the contribution of the sound wave component to the total GW intensity, the suppression factor $\frac{HR_*}{\bar{U}_f}$ is computed (following Refs. [581, 594, 595]) and we obtain that $\frac{HR_*}{\bar{U}_f} < 1$ for BP1 and BP2 but in case of BP3 we found $\frac{HR_*}{\bar{U}_f} > 1$. The SFOEWPT properties for BP1 are shown in Fig. 13.1 (a and b). In Fig. 13.1(a) we have plotted the phase structure of the model as a function of the temperature for the chosen values of the benchmark

parameter values of BP1 are chosen. From the Fig. 13.1(a) it is observed that the SFOEWPT occurs at T_n = 103.62 GeV and at this temperature a potential separation between a high (indicated as blue line) and low (indicated as orange line) phase appears. We also study the phase transition properties of other two BP points (BP2, BP3) and we found that the nature of the plots are similar to what is shown in Fig. 13.1(a) (BP1). The parameter β (Eq. 13.33) can be estimated from the slope of the plot S_3/T vs T (Fig. 13.1(b)) around T_n. This is seen to satisfy the condition S_3/T_n = 140. For the demonstrating purpose we show the variation of the parameter S_3/T with the temperature T for BP1 in Fig. 13.1(b).

In Fig. 13.2 the calculated GW intensities for three BPs have been plotted as a function of frequency and we make a comparison with the estimated detectability [1] of such GWs at the future generation ground-based telescopes (aLIGO and aLIGO+) and space-based telescopes (ALIA, BBO, DECIGO and LISA). For BP1, BP2 and BP3 the GW intensities acquire peaks at the frequencies 6.29×10^{-3} Hz, 4.4×10^{-3} Hz and 3.40×10^{-3} Hz respectively. It is observed from Fig. 13.2 that the GW intensities for all the BPs (BP1 - BP3) fall within the sensitivity curves of ALIA, BBO and DECIGO. From Table 13.2 we obtain the lowest value of the parameter β for BP3 compared to the other two BPs (BP1, BP2) which reflects the fact that the GW intensity is higher for BP3 and it is also evident from Fig. 13.2. Therefore, it appears that the principal dependence of GW intensity is on the parameter β.

13.6 Summary

In this Chapter, we have considered the emission of GWs from FOEWPT involving a two component FIMP DM and the detectabilities of these GWs by some proposed space-based detectors in future. We consider a two component DM model where the scalar sector of SM is extended by introducing two real scalars and both the components of this two component DM model are pro-

[1] We consider the power-law-integrated sensitivity approach [539, 596]. For an alternate method see [597–599].

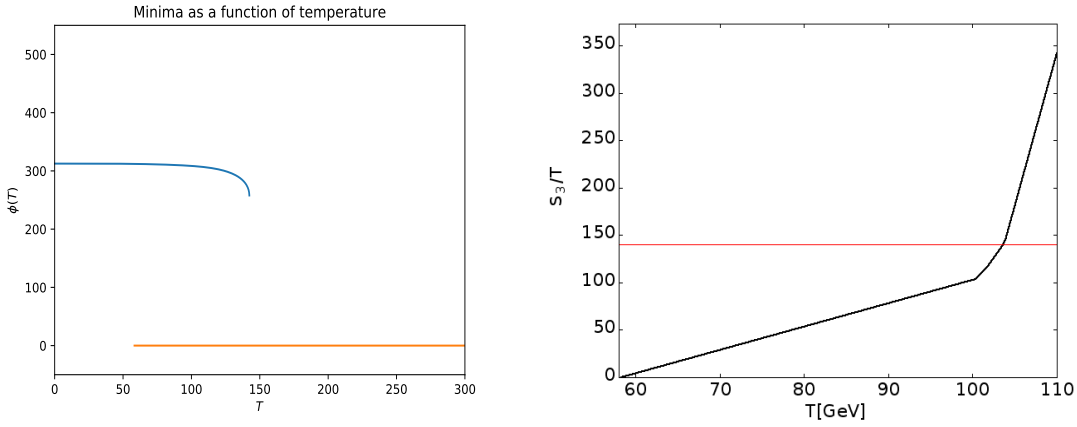

(a) (b)

Figure 13.1: Variations of the phase transition properties with temperature for BP1. In the left panel (a) we show the variations of the positions of minima of the field $\phi(T)$ with the temperature and it creates a potential separation at T_n = 103.62 GeV. The right panel (b) gives the variation of the parameter S_3/T with T and the red solid line indicates that nucleation occurs for the condition S_3/T =140. See text for details.

duced via “freeze-in" mechanism. The masses of these FIMP DM particles in the present scenario are within the range of few keV to few MeV. The extensive study of the DM phenomenology of the considered model as well as the theoretical and experimental constraints on the model parameters have been discussed in Chapter 6. We explore the possibility of FOEWPT with this model and subsequent productions of GWs. From the allowed parameter space we choose three BPs for both the analytical and numerical calculations of the GW intensity. Finite temperature corrections of the tree level potential have been introduced for the calculations of the GW signals. For the model chosen parameters we compute the intensities of GWs from the FOEWPT initiated by the present extended SM. We compare our results with the projected sensitivities of future space-based (ALIA, BBO, DECIGO amd LISA) as well as ground-based (aLIGO and aLIGO+) GW detectors that would detect such primordial GWs. From our calculations it is observed that the peak values of such GWs lie within the detectable range of the future detectors such as ALIA, BBO and DECIGO. We also find that in the present DM model though the DM phenomenology (e.g. relic density calculations)

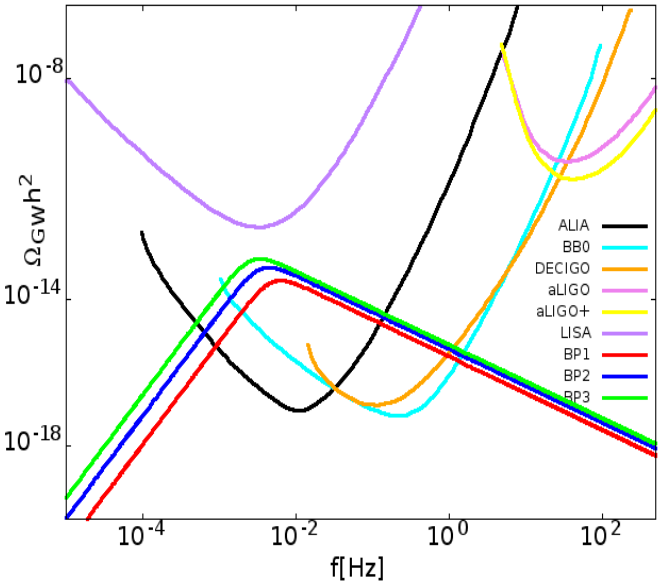

Figure 13.2: The variations of the GW intensities with frequency for each of the three BPs and their comparisons with the sensitivity curves of the detectors namely aLIGO, aLIGO+, ALIA, BBO, DECIGO and LISA. See text for details.

can be addressed by considering very small Higgs portal couplings in FIMP mechanism, but the production of the GW signals is mostly governed by the couplings of the DM self interactions. Therefore, our considered two component FIMP DM model can be a viable candidate for particle DM as well as it can also explain the production of GWs from FOEWPT.

CHAPTER 14

CONCLUSIONS AND FUTURE OUTLOOK

In the thesis, three important aspects of Astroparticle Physics have been addressed, namely, particle dark matter (DM) phenomenology, neutrino oscillation and primordial Gravitational Waves (GWs) from first order electroweak phase transition.

The known luminous object in the Universe accounts for only about 4.9 $\%$ of the total mass-energy budget of the Universe. The analysis of satellite borne PLANCK experiment on the anisotropy of Cosmic Microwave Background Raditaion or CMBR suggests that the Universe ovewhelmingly contains unknown DM and dark energy. The former one is an unseen unknown matter, whose only definite evidence so far is due to their gravitational effects, makes up for around 26.8 $\%$ of the Universe's contents. The rest around 68.3 $\%$ is yet another unknown energy known as dark energy thought to invoke a negative pressure opposite to gravity and cause the recent accelerated expansion of the Universe. Although Standard Model (SM) of particle physics very satisfactorily explains the known fundamental particles in nature with which the luminous matter of the Universe is made up of, it cannot explain the particle nature of DM. SM cannot also explain the neutrino mass and hence mass induced oscillation. Theories are proposed in the thesis for particle DM by simple extension of SM, by a scalar, a pseudo scalar or a fermion or combinations of all. It is then shown in the

thesis that such models can well explain some of the possible indirect DM signatures from different astrophysical bodies such as Galactic Centre (GC), dwarf galaxies etc.

A two component DM model is proposed in the thesis where the SM is extended by a scalar, a fermion and a pseudo scalar. The scalar and the fermion constitute each of the components of this two component DM while the fermion component is of Weakly Interacting Massive Particle or WIMP in nature, the other scalar component is the Feebly Interacting Massive Particle or FIMP. The stability of the fermionic component is assured by imposing a global $\mathrm{U}(1)_{\mathrm{DM}}$ symmetry on this fermion such that this Dirac fermion is a singlet under SM gauge group and it has a global $\mathrm{U}(1)_{\mathrm{DM}}$ charge. On the other hand, a Z_2 symmetry is imposed on the scalar component to ensure its stability. It is shown in the thesis that, while the annihilation end product of the fermionic component can explain the observed gamma-ray (γ-ray) excess from GC in the 1-3 GeV energy range, the other scalar component accounts for the emission of 3.55 keV X-ray lines reported to have observed from Persues and Andromeda galaxies. The FIMP component is also found to be useful in explaining the self interaction of DM. The experimental bound for the cross-section of this self interaction is $\sigma_{\mathrm{DM}}/m < 0.47\,\mathrm{cm}^2/\mathrm{gm}$ [217].

A two component DM model where both the components are scalars and FIMPs are also proposed and explored in the thesis in order to explain the DM self interaction.

Dwarf satellite galaxies of Milky Way can be rich in DM. The Fermi-LAT satellite borne experiment provided upper bounds of the γ-ray flux observed from dwarf satellite galaxies. Proposing that the γ-rays from the dwarf galaxies are produced by the annihilations of DM present in the dwarf galaxies, γ-rays from 45 dwarf galaxies are analysed in the thesis with two different particle DM models. One is the WIMP-FImP model proposed in the thesis by simple extension of SM while the other is Kaluza-Klein or KK DM in theories of extra dimension - a beyond SM theory. These two DM candidates are also explored to explain the extragalactic γ-ray flux observed by Fermi-LAT. It is seen that the γ-rays from annihilation of KK DM when added to other possible background sources for γ-rays such as BL LAC objects, Gamma Ray Bursts (GRBs) etc. very well satisfy the

Fermi-LAT data for extragalactic γ-rays.

It is also explored in the thesis, whether the decay of primordial superheavy dark matter (SHDM) may produce the ultrahigh energy (UHE) neutrinos as a secondary product. Southpole based IceCube observatory reported UHE neutrinos in the energy range $\sim$ 120 TeV to $\sim$ 50 PeV from their 6 year data analysis known as HESE (High Energy Starting Event) data. From a through χ^2 analysis of HESE energy region of IceCube ($\sim 10^5$ GeV - $\sim 5 \times 10^6$ GeV), in the thesis a prediction is made for the mass and lifetime of a primordial SHDM that can explain the HESE results of UHE neutrino. It is found that the decay of a primordial SHDM mass $\sim 10^8$ GeV with a lifetime $\sim 10^{28}$ sec, can explain the HESE results of UHE neutrinos. The SHDM undergoes cascading decay and such decay process can proceed through two decay channels namely hadronic and leptonic. While the former study was only assuming the hadronic decay cascade, the scope of the analysis has latter been broadened by including the leptonic channel as well. In addition, the energy range of the analysis has been extended further in the lower energy regime to include the two IceCube data of astrophysical origin. A combined analysis is then performed in the thesis including the astrophysical flux and the hadronic and leptonic decay channels of the SHDM of the 7.5 year IceCube HESE data and the two astrophysical neutrino data. From this analysis, again the SHDM mass and decay lifetime are obtained.

The possible existence of a sterile fourth neutrino in addition to the usual 3 active neutrino flavours is a long standing issue. Although it is not conclusively confirmed but several terrestrial neutrino detectors analyse their experimental data for neutrino ocillations assuming 4 neutrino (3 active + 1 sterile) oscillations and determined bounds on various 4 neutrino oscillation parameters. In the thesis, this issue of sterile neutrino has been explored. Considering the UHE neutrinos from distant GRB sources, the possible detection yields of the observed UHE signal at a km^2 detector such as IceCube have been computed in the thesis for both 3-flavour and 4-flavour scenarios. For this case, a detailed formalism for 4-flavour mixing matrix and 4-flavour neutrino oscillations have been worked out in the thesis. It is to be noted that due to astronomical distances between the Earth

and the UHE neutrino sources, the oscillatory part of a neutrino oscillation probability equation is averaged to $\frac{1}{2}$ and a neutrino flavour would suffer flavour suppression instead of flavour oscillation while traversing such astronomical baselines. To this end, a ratio of muon yields to shower yields at the detector induced by such UHE neutrinos is defined for the purpose. It is seen that this ratio grossly differs for the two cases of 3-flavour and 4-flavour oscillation formalisms. Thus, this ratio for UHE neutrino events in a km^2 detector could be a viable probe for the existence of sterile neutrinos.

On September 22, 2017 the IceCube collaboration detected a cosmic neutrino event IceCube-170922A of energy $\sim$ 290 TeV from the direction of the Blazar TXS 0506+056. The Fermi-LAT collaboration also reported a state of enhanced γ-ray emission of the same Blazar around that time. This revealations of multimessenger astronomy suggest a common high energy cosmic source of neutrinos and γ-rays. In addition 13 neutrino events IceCube-141209A are also observed by IceCube during 2014-2015 from the direction of the Blazars PKS 0502+049/TXS 0506+056 and GB6 J1040+0617. All of them were found to be in the state of enhanced γ-ray emission during these detections suggesting blazars to be a source of cosmic rays and their acceleration in blazar jets. The UHE γ-rays and neutrinos can be produced either by the interaction of cosmic rays accelerated by blazar jets with the surrounding photons or electromagnetic radiations ($p\gamma$ interaction) or by the interaction of blazar-accelerated cosmic rays with ambient matter (pure hadronic (pp) interactions). In the thesis, a proton blazar model for the blazars has been explored to show that it not only can explain consistently the spectral behaviour of the high energy bump of electromagnetic spectral energy distribution (SED) but also the observed neutrinos from the three blazars mentioned above. This model is more realistic than cloud-in-jet model.

The Standard Model (SM) of particle physics does not have scale invariance since most of the SM particles are massive and scale invariance is manifestly broken by the masses of SM particles. But the scale invariance may be restored at a much higher scale. But it had been observed by Georgi that if an unseen scale invariant sector exists at low energy and interacts very weakly with

SM particles then this non trivial scale invariant sector is characterised by “Unparticles". In this theoretical set up, scale invariance sector sets in at an energy scale $\Lambda_{\mathcal{U}}$ and the renormalizable couplings of the fields of the scale invariant sector induce dimensional transmutation at $\Lambda_{\mathcal{U}}$ and the particles are described by massless unparticles. Below $\Lambda_{\mathcal{U}}$ the scale invariant fields match onto unparticle operators. The scale dimension $d_{\mathcal{U}}$ of unparticles is a non-integral number. The unparticle physics may lead to very unexpected phenomenologies. In the thesis, the consequences of neutrino decay to unparticles has been explored in a 4 neutrino framework with UHE neutrinos from distant GRB by explicitly writing the analytical expressions for the neutrino flux undergoing such unparticle decay and then computing their possible signatures at a km^2 detector. The effect of unparticle coupling strength and the scaling dimension $d_{\mathcal{U}}$ on the detector yield are also addressed.

A consequence of the principle of equivalence is that all the three types of neutrinos couple with same strength G with gravity. Although the equivalence principle is not reported to be violated in nature but even a very weak violation of equivalence principle or VEP would result in different coupling strengths with which different types of neutrinos interact with gravity. This in turn would induce a phase difference between two types of neutrinos in a coherent neutrino beam while traversing a distance in a gravitation field. In the event therefore, if the neutrinos in gravitational basis are not identical to that in gravity basis, this results in flavour-gravity mixing of neutrinos in addition to the mass-flavour mixing and would lead to gravity induced oscillations along with the usual mass-flavour oscillations. In the thesis, a possibility is explored to probe a very tiny violation of equivalence principle in case of a long baseline (LBL) neutrino experiment by considering a 4 neutrino framework. Since for an LBL neutrino experiment, the accelerator neutrinos (in a neutrino factory) would travel through different layers of Earth matter before reaching a distant detector, in the thesis, a rigorous analytical expressions for neutrino oscillation probabilities in matter are derived where matter induced mass-flavour oscillations along with gravity induced oscillations are considered in the same framework for 4-flavour neutrino scenario. This is accomplished in the thesis by explicitly diagonalising the relevant 4×4 matrices and elaborate computation of the same

as the neutrinos propagate through different density layers within the Earth matter to reach the far detector. Finally in the thesis, wrong sign (in appearence channel, where a ν_e oscillates to ν_μ) and right sign (in disappearence channel, where the ν_μ flux is suppressed due to oscillation of ν_μ) muon yields are computed at the far detector assumed to be at a baseline length of $\sim$ 7000 km from the neutrino source. The detector is taken to be a 50 kTon iron calorimeter (ICAL) with magnetic field applied across it so that the neutrino induced μ^+ and μ^- could be identified at the detector (and hence the incident neutrino or an antineutrino could be differentiated). From this study, two important observations have been made in the thesis. One is that the VEP effect on neutrino oscillations is very prominent if violation is as small as $\sim 10^{-23}$ in comparison to no VEP case for both the 3-flavour and 4-flavour scenarios. The other is that the computed wrong sign muon yields for the 3-flavour case are found to be remarkably suppressed than the same when computed for the 4-flavour scenario for both VEP and no VEP considerations. These studies indicate that the LBL neutrinos could not only offer viable mechanisms to probe very small VEP, if exists, but is suitable as well to investigate the possible existence of sterile neutrinos.

The emissions of the Gravitational Waves (GWs) from a strong first-order electroweak phase transition have been explored in the thesis. To this end, a dark matter model has been investigated in Feebly Interacting Massive Particle (FIMP) scenario, where the dark matter particles are produced through "freeze-in" mechanism in the early Universe. The first-order phase transition has been studied within the framework of this present model. Both analytical and numerical computations have been done to calculate the consequent production of GWs and then the detectabilities of such GWs have been investigated at the future space-based detectors such as LISA, BBO, ALIA, DECIGO, aLIGO and aLIGO+, etc. It is also observed that the smaller Higgs portal couplings plays a signifant role in the relic density calculations for the considered two component FIMP dark matter model whereas the dark matter self-couplings has a considerable influence on GW production in the present scenario.

Future Outlook

The topics of Astroparticle Physics that has been addressed in the thesis have very wide scope for future expansion and studies. In the following, some of the future research topics are mentioned.

- An interesting FIMP scenario is the Clockwork FIMP scenario involving a number of Beyond Standard Model Fields and their interactions through which FIMPs are produced. In one such approach discussed in A. Goudelis *et al.*, [600], the scalar FIMP DM has been considered to have originated from the consideration of the spontaneous breakdown of a global symmetry $\Pi_{i=0}^{N} \otimes \mathrm{U}(1)_{\mathrm{i}}$ at scales f_is (for each $\mathrm{U}(1)_{\mathrm{i}}$) where $f = f_i$ is assumed to be leading to the gereration of $N+1$ massless Goldstone bosons and this $\mathrm{U}(1)^{N+1}$ is further softly broken giving rise to mass parameters. The resulting mass matrix, on diagonalisation produces a tower of discrete levels of masses much like the Kaluza-Klein tower in extra-dimensional theories, the lowest one of which is attributed to a FIMP candidate. The self interaction of such a Clockwork FIMP candidate will also be addressed where in addition to $2 \to 2$ processes, $4 \to 2$ and $3 \to 2$ processes can also be investigated.

- It is also interesting to investigate the possibility of one of the three right handed (RH) neutrinos (singlets) introduced in see-saw mechanism to be a DM candidate. This RH neutrino is almost decoupled from the Yukawa interaction term of the Lagrangian and is produced by the freeze-in mechanism assisted by a thermalized scalar singlet having odd Z_2 parity. The Yukawa couplings of other two heavy neutrinos which are related to the light neutrino masses and mixing also play a crucial role in the DM production. A successful hierarchical leptogenesis will also be addressed while the Yukawa couplings are expressed in terms of the low energy parameters via Casas-Ibarra parametrization.

- Primordial Black Holes (PBH) are believed to be formed during the radiation dominated era due to the collapse of the overdensity region characterized by the size of the region which should be greater than the Jeans length. The PBHs may account for DM or it may evaporate DM along with other SM particles. The evaporation of Primordial Black Holes can inject

more energy to the system. This may affect the 21 cm signal of hydrogen from the dark ages of the Universe as well as the 21 cm signal from the epoch of reionisation (EoR). It will be an important topic for further investigation.

- Fuzzy dark matter or FDM is considered to be composed of scalar particles with mass as low as 10^{-22} eV. Therefore the de Broglie wavelength is of the order of astrophysical scales ($\sim$ kpc) and is hypothesised to address the cusp-core problem of DM density profile. The FDM is well motivated by the ubiquitous presence of ultra-light scalars (such as axion like particles) in beyond Standard Model theories. The implications of FDM as against the ususal cold dark matter (CDM) can be investigated via the fluctuations in 21 cm signal of hydrogen during the EoR along with the Lyman-α background as also from the dark ages. The future data from upcoming radio telescope, the square kilometer array or SKA would help obtain tighter bounds on FDM. These also is a topic for future exploration.

- The long baseline (LBL) accelerator neutrinos will be probed mainly with respect to DUNE, NOνA and other LBL neutrino experiments and the questions such as CP violations in neutrino sector, the possibility of a fourth sterile neutrino, neutrino mixing angle and neutrino mass hierarchy will be a study worth pursued in future. The origin of neutrino mass and its possible DM origin is also be probed.

- When a discrete symmetry is spontaneously broken it leads to the formation of domain walls. These are in fact topological defects. In general, the average number of domain walls per Hubble horizon remains constant, which may lead to overclosure of the Universe due to the slower decrease of their energy densities with respect to radiation or matter. Thus the domain wall has to be unstable and should eventually break down. The domain wall could be unstable if the discrete symmetry is approximate. The domain walls are annihilated when the pressure on the walls induced by the energy bias between the true and false vacua superceeds the tensions of the domain walls. The process of annihilations of such domain walls triggers

Gravitational Wave emissions and these GWs retain in them the information of the physics following which these were created. Thus, study of such domain wall induced relic GWs may enable us to probe events in the early Universe and the ultraviolet physics as well. The study of such GWs for several possible discrete symmetries in the early Universe era is worth pursuing. Possible generations of baryon asymmetry from domain wall annihilations may also be looked into.

APPENDIX A

ANNIHILATION CROSS-SECTION AND DECAY TERMS OF WIMP-FIMP DARK MATTER CANDIDATES

The fermion dark matter χ (in Chapter 5) can annihilate in several channels namely the fermions ($f\bar{f}$), the gauge bosons ($W^{\pm}, Z$) or Higgs boson (h). The annihilation cross-sections of such channels are furnished below

$$\sigma v_{\chi\chi\to f\bar{f}} = N_c \frac{g^2}{32\pi} s \frac{m_f^2}{v_1^2} \left(1 - \frac{4m_f^2}{s}\right)^{3/2} F(s, m_1, m_2) \ ,$$

$$\sigma v_{\chi\chi\to W^+W^-} = \frac{g^2}{64\pi} \left(1 - \frac{4m_W^2}{s}\right)^{1/2} \left(\frac{m_W^2}{v_1}\right)^2 \left(2 + \frac{(s-2m_W^2)^2}{4m_W^4}\right) F(s, m_1, m_2) \ ,$$

$$\sigma v_{\chi\chi\to ZZ} = \frac{g^2}{128\pi}\left(1-\frac{4m_Z^2}{s}\right)^{1/2}\left(\frac{m_Z^2}{v_1}\right)^2\left(2+\frac{(s-2m_Z^2)^2}{4m_Z^4}\right)F(s,m_1,m_2)\ ,$$

$$\begin{aligned} F(s,m_1,m_2) &= \left[\frac{a_{12}^2a_{11}^2}{(s-m_1^2)^2+m_1^2\Gamma_1^2}+\frac{a_{21}^2a_{22}^2}{(s-m_2^2)^2+m_2^2\Gamma_2^2}\right. \\ &\left. +a_{12}a_{11}a_{22}a_{21}\frac{2(s-m_1^2)(s-m_2^2)+2m_1m_2\Gamma_1\Gamma_2}{[(s-m_1^2)^2+m_1^2\Gamma_1^2][(s-m_2^2)^2+m_2^2\Gamma_2^2]}\right]\ , \end{aligned}$$

$$\begin{aligned} \sigma v_{\chi\chi\to h_1h_1} &= \frac{g^2}{32\pi}\left(1-\frac{4m_1^2}{s}\right)^{1/2}\left[\frac{a_{12}^2\lambda_{111}^2}{(s-m_1^2)^2+m_1^2\Gamma_1^2}\right. \\ &\left. +\frac{a_{22}^2\lambda_{211}^2}{(s-m_2^2)^2+m_2^2\Gamma_2^2}+\frac{2a_{12}a_{22}\lambda_{111}\lambda_{211}((s-m_1^2)(s-m_2^2)+m_1m_2\Gamma_1\Gamma_2)}{[(s-m_1^2)^2+m_1^2\Gamma_1^2][(s-m_2^2)^2+m_2^2\Gamma_2^2]}\right]\ , \end{aligned}$$

$$\begin{aligned} \sigma v_{\chi\chi\to h_2h_2} &= \frac{g^2}{32\pi}\left(1-\frac{4m_2^2}{s}\right)^{1/2}\left[\frac{a_{12}^2\lambda_{122}^2}{(s-m_1^2)^2+m_1^2\Gamma_1^2}\right. \\ &\left. +\frac{a_{22}^2\lambda_{222}^2}{(s-m_2^2)^2+m_2^2\Gamma_2^2}+\frac{2a_{12}a_{22}\lambda_{122}\lambda_{222}((s-m_1^2)(s-m_2^2)+m_1m_2\Gamma_1\Gamma_2)}{[(s-m_1^2)^2+m_1^2\Gamma_1^2][(s-m_2^2)^2+m_2^2\Gamma_2^2]}\right]\ , \end{aligned}$$

$$\begin{aligned} \sigma v_{\chi\chi\to h_3h_3} &= \frac{g^2}{32\pi}\left(1-\frac{4m_3^2}{s}\right)^{1/2}\left[\frac{a_{12}^2\lambda_{133}^2}{(s-m_1^2)^2+m_1^2\Gamma_1^2}\right. \\ &\left. +\frac{a_{22}^2\lambda_{233}^2}{(s-m_2^2)^2+m_2^2\Gamma_2^2}+\frac{2a_{12}a_{22}\lambda_{133}\lambda_{233}((s-m_1^2)(s-m_2^2)+m_1m_2\Gamma_1\Gamma_2)}{[(s-m_1^2)^2+m_1^2\Gamma_1^2][(s-m_2^2)^2+m_2^2\Gamma_2^2]}\right]\ . \end{aligned}$$

Decay and annihilation terms for scalar DM candidate h_3 in Chapter 5 can be written as

$$\Gamma_{h_j \to h_3 h_3} = \frac{\lambda_{j33}^2}{8\pi m_j}\sqrt{1-\frac{4m_3^2}{m_j^2}}\ , j=1,2\ ,$$

$$\sigma_{f\bar{f}\to h_3 h_3} = N_c \frac{1}{16\pi s}\sqrt{(s-4m_3^2)(s-4m_f^2)}\left(\frac{m_f}{v_1}\right)^2 F'(s,m_1,m_2)\ ,$$

$$\sigma_{W^+W^-\to h_3 h_3} = \frac{1}{18\pi s}\sqrt{\frac{s-4m_3^2}{s-4m_W^2}}\left(\frac{m_W^2}{v_1}\right)^2\left(2+\frac{(s-2m_W^2)^2}{4m_W^4}\right)F'(s,m_1,m_2)\ ,$$

$$\sigma_{ZZ\to h_3 h_3} = \frac{1}{18\pi s}\sqrt{\frac{s-4m_3^2}{s-4m_Z^2}}\left(\frac{m_Z^2}{v_1}\right)^2\left(2+\frac{(s-2m_Z^2)^2}{4m_Z^4}\right)F'(s,m_1,m_2)\ ,$$

$$\begin{aligned} F'(s,m_1,m_2) &= \left[\frac{a_{11}^2\lambda_{133}^2}{(s-m_1^2)^2+m_1^2\Gamma_1^2}+\frac{a_{21}^2\lambda_{233}^2}{(s-m_2^2)^2+m_2^2\Gamma_2^2}\right. \\ &\left. +a_{11}\lambda_{133}a_{21}\lambda_{233}\frac{2(s-m_1^2)(s-m_2^2)+2m_1m_2\Gamma_1\Gamma_2}{[(s-m_1^2)^2+m_1^2\Gamma_1^2][(s-m_2^2)^2+m_2^2\Gamma_2^2]}\right]\ , \end{aligned}$$

$$\sigma_{h_1 h_1\to h_3 h_3} = \frac{1}{2\pi s}\sqrt{\frac{s-4m_3^2}{s-4m_1^2}}\left(\lambda_{1133}+3\frac{\lambda_{111}\lambda_{133}}{(s-m_1^2)}+\frac{\lambda_{211}\lambda_{233}}{(s-m_2^2)}\right)^2\ ,$$

$$\sigma_{h_2 h_2\to h_3 h_3} = \frac{1}{2\pi s}\sqrt{\frac{s-4m_3^2}{s-4m_2^2}}\left(\lambda_{2233}+3\frac{\lambda_{222}\lambda_{233}}{(s-m_2^2)}+\frac{\lambda_{122}\lambda_{133}}{(s-m_1^2)}\right)^2\ .$$

PMNS matrix with $\delta = 0$ is given as

$$U = \begin{pmatrix} c_{13}c_{12} & s_{12}c_{13} & s_{13} \\ -s_{12}c_{23} - s_{23}s_{13}c_{12} & c_{23}c_{12} - s_{23}s_{13}s_{12} & s_{23}c_{13} \\ s_{23}s_{12} - s_{13}c_{23}c_{12} & -s_{23}c_{12} - s_{13}s_{12}c_{23} & c_{23}c_{13} \end{pmatrix} .$$

Couplings between different physical scalars obtained from the expression of potential

$$\begin{aligned}
-\lambda_{111} &= \lambda_H v_1 a_{11}^3 + \lambda_\Phi v_2 a_{12}^3 + \lambda_{H\Phi}(v_2 a_{11}^2 a_{12} + v_1 a_{11} a_{12}^2) + \lambda_{HS} v_1 a_{11} a_{13}^2 + 2\lambda_{\Phi S} v_2 a_{12} a_{13}^2 , \\
-\lambda_{222} &= \lambda_H v_1 a_{21}^3 + \lambda_\Phi v_2 a_{22}^3 + \lambda_{H\Phi}(v_2 a_{21}^2 a_{22} + v_1 a_{21} a_{22}^2) + \lambda_{HS} v_1 a_{21} a_{23}^2 + 2\lambda_{\Phi S} v_2 a_{22} a_{23}^2 , \\
-\lambda_{122} &= 3\lambda_H v_1 a_{11} a_{21}^2 + 3\lambda_\Phi v_2 a_{12} a_{22}^2 + \lambda_{H\Phi}(v_2(a_{21}^2 a_{12} + 2a_{11} a_{21} a_{22}) + v_1(a_{11} a_{22}^2 + 2a_{21} a_{12} a_{22}) \\
&\quad + \lambda_{HS} v_1(a_{11} a_{23}^2 + 2a_{21} a_{13} a_{23}) + 2\lambda_{\Phi S} v_2(a_{12} a_{23}^2 + 2a_{22} a_{13} a_{23}) , \\
-\lambda_{211} &= 3\lambda_H v_1 a_{11}^2 a_{21} + 3\lambda_\Phi v_2 a_{12}^2 a_{22} + \lambda_{H\Phi}(v_2(a_{11}^2 a_{22} + 2a_{11} a_{21} a_{12}) + v_1(a_{21} a_{12}^2 + 2a_{11} a_{12} a_{22}) \\
&\quad + \lambda_{HS} v_1(a_{21} a_{13}^2 + 2a_{11} a_{13} a_{23}) + 2\lambda_{\Phi S} v_2(a_{22} a_{31}^2 + 2a_{12} a_{13} a_{23}) , \\
-\lambda_{133} &= 3\lambda_H v_1 a_{11} a_{31}^2 + 3\lambda_\Phi v_2 a_{12} a_{32}^2 + \lambda_{H\Phi}(v_2(a_{31}^2 a_{12} + 2a_{11} a_{31} a_{32}) + v_1(a_{11} a_{32}^2 + 2a_{31} a_{12} a_{32}) \\
&\quad + \lambda_{HS} v_1(a_{11} a_{33}^2 + 2a_{31} a_{13} a_{33}) + 2\lambda_{\Phi S} v_2(a_{12} a_{33}^2 + 2a_{32} a_{13} a_{33}) , \\
-\lambda_{233} &= 3\lambda_H v_1 a_{21} a_{31}^2 + 3\lambda_\Phi v_2 a_{22} a_{32}^2 + \lambda_{H\Phi}(v_2(a_{31}^2 a_{22} + 2a_{21} a_{31} a_{32}) + v_1(a_{21} a_{32}^2 + 2a_{31} a_{22} a_{32}) \\
&\quad + \lambda_{HS} v_1(a_{21} a_{33}^2 + 2a_{31} a_{23} a_{33}) + 2\lambda_{\Phi S} v_2(a_{22} a_{33}^2 + 2a_{32} a_{23} a_{33}) , \\
-\lambda_{1133} &= \frac{3}{2}(\lambda_H a_{11}^2 a_{31}^2) + \frac{3}{2}(\lambda_\Phi a_{12}^2 a_{32}^2) + \frac{3}{2}(\lambda_S a_{13}^2 a_{33}^2) + \frac{\lambda_{H\Phi}}{2}(a_{12}^2 a_{31}^2 + a_{11}^2 a_{32}^2 + 4a_{11} a_{12} a_{31} a_{32}) \\
&\quad + \frac{\lambda_{HS}}{2}(a_{11}^2 a_{33}^2 + a_{13}^2 a_{31}^2 + 4a_{11} a_{13} a_{31} a_{33}) + \lambda_{\Phi S}(a_{12}^2 a_{33}^2 + a_{13}^2 a_{32}^2 + 4a_{12} a_{13} a_{32} a_{33}) , \\
-\lambda_{2233} &= \frac{3}{2}(\lambda_H a_{21}^2 a_{31}^2) + \frac{3}{2}(\lambda_\Phi a_{22}^2 a_{32}^2) + \frac{3}{2}(\lambda_S a_{23}^2 a_{33}^2) + \frac{\lambda_{H\Phi}}{2}(a_{22}^2 a_{31}^2 + a_{21}^2 a_{32}^2 + 4a_{21} a_{22} a_{31} a_{32}) \\
&\quad + \frac{\lambda_{HS}}{2}(a_{21}^2 a_{33}^2 + a_{23}^2 a_{31}^2 + 4a_{21} a_{23} a_{31} a_{33}) + \lambda_{\Phi S}(a_{22}^2 a_{33}^2 + a_{23}^2 a_{32}^2 + 4a_{22} a_{23} a_{32} a_{33}) , \\
-\lambda_{3333} &= \frac{1}{4}(\lambda_H a_{31}^4 + \lambda_\Phi a_{32}^4 + \lambda_S a_{33}^4) + \frac{\lambda_{H\Phi}}{2} a_{31}^2 a_{32}^2 + \frac{\lambda_{HS}}{2} a_{31}^2 a_{33}^2 + \lambda_{\Phi S} a_{32}^2 a_{33}^2 \sim \lambda_S/4 .
\end{aligned}$$

APPENDIX B

EXPRESSIONS FOR COUPLINGS

The expressions for the couplings in between the scalars (h, s_2, s_3) as well as the couplings of Higgs with the gauge bosons and fermions used in Chapter 6 are listed below

$$
\begin{aligned}
g_{hhh} &= -\lambda_H v \ , \\
g_{hs_2s_2} &= -\lambda_{HS_2} v \ , \\
g_{hs_3s_3} &= -\lambda_{HS_3} v \ , \\
g_{hhs_2s_2} &= -\frac{\lambda_{HS_2}}{2} \ , \\
g_{hhs_3s_3} &= -\frac{\lambda_{HS_3}}{2} \ , \\
g_{s_2s_2s_3s_3} &= -\lambda_{S_2S_3} \ , \\
g_{s_2s_2s_2s_2} &= -\frac{\lambda_{S_2}}{4} \ , \\
g_{s_3s_3s_3s_3} &= -\frac{\lambda_{S_3}}{4} \ , \\
g_{WWh} &= \frac{2m_W^2}{v} \ , \\
g_{ZZh} &= \frac{m_Z^2}{v} \ , \\
g_{ffh} &= \frac{m_f}{v} \ .
\end{aligned}
$$

BIBLIOGRAPHY

[1] S. L. Glashow, *The renormalizability of vector meson interactions*, *Nucl. Phys.* **10** (1959) 107–117.

[2] A. Salam and J. C. Ward, *Weak and electromagnetic interactions*, *Il Nuovo Cimento* **11** (Feb., 1959) 568–577.

[3] S. Weinberg, *A Model of Leptons*, Phys. Rev. Lett. **19** (Nov., 1967) 1264–1266.

[4] P. W. Higgs, *Broken Symmetries and the Masses of Gauge Bosons*, *Phys. Rev. Lett.* **13** (1964) 508–509.

[5] P. Pal, *An Introductory Course of Particle Physics*. CRC Press, 2014.

[6] N. Cabibbo, *Unitary Symmetry and Leptonic Decays*, *Phys. Rev. Lett.* **10** (1963) 531–533.

[7] M. Kobayashi and T. Maskawa, *CP-Violation in the Renormalizable Theory of Weak Interaction*, *Progress of Theoretical Physics* **49** (Feb., 1973) 652–657.

[8] J. Beringer, J. F. Arguin, R. M. Barnett, K. Copic, O. Dahl, D. E. Groom et al., *Review of Particle Physics*, Phys. Rev. D **86** (July, 2012) 010001.

[9] M. Luscher and P. Weisz, *Is There a Strong Interaction Sector in the Standard Lattice Higgs Model?*, *Phys. Lett. B* **212** (1988) 472–478.

[10] N. Cabibbo, L. Maiani, G. Parisi and R. Petronzio, *Bounds on the Fermions and Higgs Boson Masses in Grand Unified Theories*, *Nucl. Phys. B* **158** (1979) 295–305.

[11] WMAP collaboration, G. Hinshaw et al., *Nine-Year Wilkinson Microwave Anisotropy Probe (WMAP) Observations: Cosmological Parameter Results*, *Astrophys. J. Suppl.* **208** (2013) 19, [1212.5226].

[12] PLANCK collaboration, P. A. R. Ade et al., *Planck 2013 results. XVI. Cosmological parameters*, *Astron. Astrophys.* **571** (2014) A16, [1303.5076].

[13] M. Bartelmann and P. Schneider, *Weak gravitational lensing*, *Phys. Rept.* **340** (2001) 291–472, [astro-ph/9912508].

[14] Y. Sofue and V. Rubin, *Rotation curves of spiral galaxies*, *Ann. Rev. Astron. Astrophys.* **39** (2001) 137–174, [astro-ph/0010594].

[15] D. Clowe, A. Gonzalez and M. Markevitch, *Weak lensing mass reconstruction of the interacting cluster 1E0657-558: Direct evidence for the existence of dark matter*, *Astrophys. J.* **604** (2004) 596–603, [astro-ph/0312273].

[16] F. Dyson, A. Eddington and C. Davidson, *A Determination of the Deflection of Light by the Sun's Gravitational Field, from Observations Made at the Total Eclipse of May 29, 1919*, *Phil. Trans. Roy. Soc. Lond. A* **220** (1920) 291–333.

[17] D. Walsh, R. Carswell and R. Weymann, *0957 + 561 A, B - Twin quasistellar objects or gravitational lens*, *Nature* **279** (1979) 381–384.

[18] R. A. Cabanac, D. Valls-Gabaud, A. O. Jaunsen, C. Lidman and H. Jerjen, *Discovery of a high-redshift Einstein ring*, *Astron. Astrophys.* **436** (2005) L21–L25, [astro-ph/0504585].

[19] M. J. Jee et al., *Discovery of a Ringlike Dark Matter Structure in the Core of the Galaxy Cluster Cl 0024+17*, *Astrophys. J.* **661** (2007) 728–749, [0705.2171].

[20] J.-P. Kneib, Y. Mellier, B. Fort and G. Mathez, *The distribution of dark matter in distant cluster lenses - modelling a:370*, A&A **273** (06, 1993) 367.

[21] Y. Mellier, *Probing the universe with weak lensing*, *Ann. Rev. Astron. Astrophys.* **37** (1999) 127–189, [astro-ph/9812172].

[22] N. Kaiser and G. Squires, *Mapping the Dark Matter with Weak Gravitational Lensing*, ApJ **404** (Feb., 1993) 441.

[23] B. Paczynski, *Gravitational Microlensing by the Galactic Halo*, ApJ **304** (May, 1986) 1.

[24] R. Massey, T. Kitching and J. Richard, *The dark matter of gravitational lensing*, *Rept. Prog. Phys.* **73** (2010) 086901, [1001.1739].

[25] H. C. van de Hulst, E. Raimond and H. van Woerden, *Rotation and density distribution of the Andromeda nebula derived from observations of the 21-cm line*, Bull. Astron. Inst. Netherlands **14** (Nov., 1957) 1.

[26] M. Schmidt, *The distribution of mass in M 31*, Bull. Astron. Inst. Netherlands **14** (Nov., 1957) 17.

[27] L. M. J. S. Volders, *Neutral hydrogen in M 33 and M 101*, Bull. Astron. Inst. Netherlands **14** (Sept., 1959) 323.

[28] V. C. Rubin and J. Ford, W. Kent, *Rotation of the Andromeda Nebula from a Spectroscopic Survey of Emission Regions*, ApJ **159** (Feb., 1970) 379.

[29] K. G. Begeman, A. H. Broeils and R. H. Sanders, *Extended rotation curves of spiral galaxies: Dark haloes and modified dynamics*, *Mon. Not. Roy. Astron. Soc.* **249** (1991) 523.

[30] M. Kamionkowski, *Possible relics from new physics in the early universe: Inflation, the cosmic microwave background, and particle dark matter*, in *Workshop on The Early and Future Universe*, 6, 1998. astro-ph/9809214.

[31] L. Bergström, *Nonbaryonic dark matter: Observational evidence and detection methods*, *Rept. Prog. Phys.* **63** (2000) 793, [hep-ph/0002126].

[32] D. Clowe, M. Bradac, A. H. Gonzalez, M. Markevitch, S. W. Randall, C. Jones et al., *A direct empirical proof of the existence of dark matter*, *Astrophys. J. Lett.* **648** (2006) L109–L113, [astro-ph/0608407].

[33] G. Bertone, D. Hooper and J. Silk, *Particle dark matter: evidence, candidates and constraints*, Phys. Rep. **405** (Jan., 2005) 279–390, [hep-ph/0404175].

[34] D. Fabricant, M. Lecar and P. Gorenstein, *X-ray measurements of the mass of M 87.*, ApJ **241** (Oct., 1980) 552–560.

[35] D. Fabricant and P. Gorenstein, *Further evidence for M87's massive, dark halo.*, ApJ **267** (Apr., 1983) 535–546.

[36] J. P. Hughes, *The Mass of the Coma Cluster: Combined X-Ray and Optical Results*, ApJ **337** (Feb., 1989) 21.

[37] E. Bulbul, M. Markevitch, A. Foster, R. K. Smith, M. Loewenstein and S. W. Randall, *Detection of An Unidentified Emission Line in the Stacked X-ray spectrum of Galaxy Clusters*, *Astrophys. J.* **789** (2014) 13, [1402.2301].

[38] D. J. Fixsen, *The Temperature of the Cosmic Microwave Background*, ApJ **707** (Dec., 2009) 916–920, [0911.1955].

[39] SDSS collaboration, P. McDonald et al., *The Lyman-alpha forest power spectrum from the Sloan Digital Sky Survey*, *Astrophys. J. Suppl.* **163** (2006) 80–109, [astro-ph/0405013].

[40] A. Blaauw and M. Schmidt, *Jan Hendrik Oort (1900-1992)*, PASP **105** (July, 1993) 681.

[41] R. Clausius, *On a Mechanical Theorem Applicable to Heat*, *The Kinetic Theory Of Gases. Series: History of Modern Physical Sciences* **1** (July, 2003) 172–178.

[42] F. Zwicky, *Die Rotverschiebung von extragalaktischen Nebeln*, *Helv. Phys. Acta* **6** (1933) 110–127.

[43] F. Zwicky, *On the Masses of Nebulae and of Clusters of Nebulae*, *Astrophys. J.* **86** (1937) 217–246.

[44] S. D. M. White, J. F. Navarro, A. E. Evrard and C. S. Frenk, *The baryon content of galaxy clusters: a challenge to cosmological orthodoxy*, Nature **366** (Dec., 1993) 429–433.

[45] S. Smith, *The Mass of the Virgo Cluster*, *Astrophys. J.* **83** (1936) 23–30.

[46] P. Gondolo and G. Gelmini, *Cosmic abundances of stable particles: Improved analysis*, *Nucl. Phys. B* **360** (1991) 145–179.

[47] E. W. Kolb and M. S. Turner, *The Early Universe*, vol. 69. 1990.

[48] M. Taoso, G. Bertone and A. Masiero, *Dark Matter Candidates: A Ten-Point Test*, *JCAP* **03** (2008) 022, [0711.4996].

[49] G. Jungman, M. Kamionkowski and K. Griest, *Supersymmetric dark matter*, *Phys. Rept.* **267** (1996) 195–373, [hep-ph/9506380].

[50] V. Silveira and A. Zee, *SCALAR PHANTOMS*, *Phys. Lett. B* **161** (1985) 136–140.

[51] J. McDonald, *Gauge singlet scalars as cold dark matter*, *Phys. Rev. D* **50** (1994) 3637–3649, [hep-ph/0702143].

[52] C. P. Burgess, M. Pospelov and T. ter Veldhuis, *The Minimal model of nonbaryonic dark matter: A Singlet scalar*, *Nucl. Phys. B* **619** (2001) 709–728, [hep-ph/0011335].

[53] V. Barger, P. Langacker, M. McCaskey, M. J. Ramsey-Musolf and G. Shaughnessy, *LHC Phenomenology of an Extended Standard Model with a Real Scalar Singlet*, *Phys. Rev. D* **77** (2008) 035005, [0706.4311].

[54] E. Ma, *Verifiable radiative seesaw mechanism of neutrino mass and dark matter*, *Phys. Rev. D* **73** (2006) 077301, [hep-ph/0601225].

[55] L. Lopez Honorez, E. Nezri, J. F. Oliver and M. H. G. Tytgat, *The Inert Doublet Model: An Archetype for Dark Matter*, *JCAP* **02** (2007) 028, [hep-ph/0612275].

[56] D. Majumdar and A. Ghosal, *Dark Matter candidate in a Heavy Higgs Model - Direct Detection Rates*, *Mod. Phys. Lett. A* **23** (2008) 2011–2022, [hep-ph/0607067].

[57] M. Gustafsson, E. Lundstrom, L. Bergstrom and J. Edsjo, *Significant Gamma Lines from Inert Higgs Dark Matter*, *Phys. Rev. Lett.* **99** (2007) 041301, [astro-ph/0703512].

[58] E. Lundstrom, M. Gustafsson and J. Edsjo, *The Inert Doublet Model and LEP II Limits*, *Phys. Rev. D* **79** (2009) 035013, [0810.3924].

[59] S. Andreas, M. H. G. Tytgat and Q. Swillens, *Neutrinos from Inert Doublet Dark Matter*, *JCAP* **04** (2009) 004, [0901.1750].

[60] L. Lopez Honorez and C. E. Yaguna, *The inert doublet model of dark matter revisited*, *JHEP* **09** (2010) 046, [1003.3125].

[61] L. Lopez Honorez and C. E. Yaguna, *A new viable region of the inert doublet model*, *JCAP* **01** (2011) 002, [1011.1411].

[62] T. A. Chowdhury, M. Nemevsek, G. Senjanovic and Y. Zhang, *Dark Matter as the Trigger of Strong Electroweak Phase Transition*, *JCAP* **02** (2012) 029, [1110.5334].

[63] D. Borah and J. M. Cline, *Inert Doublet Dark Matter with Strong Electroweak Phase Transition*, *Phys. Rev. D* **86** (2012) 055001, [1204.4722].

[64] A. Arhrib, R. Benbrik and N. Gaur, $H \to \gamma\gamma$ *in Inert Higgs Doublet Model*, *Phys. Rev. D* **85** (2012) 095021, [1201.2644].

[65] A. Goudelis, B. Herrmann and O. Stål, *Dark matter in the Inert Doublet Model after the discovery of a Higgs-like boson at the LHC*, *JHEP* **09** (2013) 106, [1303.3010].

[66] A. Dutta Banik and D. Majumdar, *Inert doublet dark matter with an additional scalar singlet and 125 GeV Higgs boson*, *Eur. Phys. J. C* **74** (2014) 3142, [1404.5840].

[67] Y. G. Kim, K. Y. Lee and S. Shin, *Singlet fermionic dark matter*, *JHEP* **05** (2008) 100, [0803.2932].

[68] M. M. Ettefaghi and R. Moazzemi, *Annihilation of singlet fermionic dark matter into two photons*, *JCAP* **02** (2013) 048, [1301.4892].

[69] M. Fairbairn and R. Hogan, *Singlet Fermionic Dark Matter and the Electroweak Phase Transition*, *JHEP* **09** (2013) 022, [1305.3452].

[70] T. Hambye, *Hidden vector dark matter*, *JHEP* **01** (2009) 028, [0811.0172].

[71] C.-H. Chen and T. Nomura, $SU(2)_X$ *vector DM and Galactic Center gamma-ray excess*, *Phys. Lett. B* **746** (2015) 351–358, [1501.07413].

[72] S. Di Chiara and K. Tuominen, *A minimal model for SU(N) vector dark matter*, *JHEP* **11** (2015) 188, [1506.03285].

[73] G. Gentile, P. Salucci, U. Klein, D. Vergani and P. Kalberla, *The Cored distribution of dark matter in spiral galaxies*, *Mon. Not. Roy. Astron. Soc.* **351** (2004) 903, [astro-ph/0403154].

[74] A. A. Klypin, A. V. Kravtsov, O. Valenzuela and F. Prada, *Where are the missing Galactic satellites?*, *Astrophys. J.* **522** (1999) 82–92, [astro-ph/9901240].

[75] M. Boylan-Kolchin, J. S. Bullock and M. Kaplinghat, *Too big to fail? The puzzling darkness of massive Milky Way subhaloes*, MNRAS **415** (July, 2011) L40–L44, [1103.0007].

[76] M. S. Turner, *Cosmological parameters*, in *COSMO-98* (D. O. Caldwell, ed.), vol. 478 of *American Institute of Physics Conference Series*, pp. 113–128, July, 1999. astro-ph/9904051. DOI.

[77] D. Hooper and S. Profumo, *Dark Matter and Collider Phenomenology of Universal Extra Dimensions*, *Phys. Rept.* **453** (2007) 29–115, [hep-ph/0701197].

[78] D. J. H. Chung, P. Crotty, E. W. Kolb and A. Riotto, *On the Gravitational Production of Superheavy Dark Matter*, *Phys. Rev. D* **64** (2001) 043503, [hep-ph/0104100].

[79] M. Y. Khlopov, *Primordial black holes*, *Research in Astronomy and Astrophysics* **10** (may, 2010) 495–528.

[80] R. D. Peccei and H. R. Quinn, *CP Conservation in the Presence of Instantons*, *Phys. Rev. Lett.* **38** (1977) 1440–1443.

[81] I. G. Irastorza and J. Redondo, *New experimental approaches in the search for axion-like particles*, *Prog. Part. Nucl. Phys.* **102** (2018) 89–159, [1801.08127].

[82] J. F. Navarro, C. S. Frenk and S. D. M. White, *The Structure of cold dark matter halos*, *Astrophys. J.* **462** (1996) 563–575, [astro-ph/9508025].

[83] J. F. Navarro, C. S. Frenk and S. D. M. White, *A Universal density profile from hierarchical clustering*, *Astrophys. J.* **490** (1997) 493–508, [astro-ph/9611107].

[84] F. Prada, A. Klypin, J. Flix, M. Martínez and E. Simonneau, *Dark matter annihilation in the milky way galaxy: Effects of baryonic compression*, *Phys. Rev. Lett.* **93** (Dec, 2004) 241301.

[85] B. Moore, F. Governato, T. Quinn, J. Stadel and G. Lake, *Resolving the structure of cold dark matter halos*, *The Astrophysical Journal* **499** (may, 1998) L5–L8.

[86] J. Diemand, B. Moore and J. Stadel, *Convergence and scatter of cluster density profiles*, *Mon. Not. Roy. Astron. Soc.* **353** (2004) 624, [astro-ph/0402267].

[87] J. N. Bahcall and R. M. Soneira, *The universe at faint magnitudes. I. Models for the Galaxy and the predicted star counts.*, ApJS **44** (Sept., 1980) 73–110.

[88] A. Burkert, *The structure of dark matter halos in dwarf galaxies*, *The Astrophysical Journal* **447** (jul, 1995) .

[89] A. V. Kravtsov, A. A. Klypin, J. S. Bullock and J. R. Primack, *The Cores of dark matter dominated galaxies: Theory versus observations*, *Astrophys. J.* **502** (1998) 48, [astro-ph/9708176].

[90] A. W. Graham, D. Merritt, B. Moore, J. Diemand and B. Terzic, *Empirical models for Dark Matter Halos. I. Nonparametric Construction of Density Profiles and Comparison with Parametric Models*, *Astron. J.* **132** (2006) 2685–2700, [astro-ph/0509417].

[91] J. F. Navarro, A. Ludlow, V. Springel, J. Wang, M. Vogelsberger, S. D. M. White et al., *The Diversity and Similarity of Cold Dark Matter Halos*, *Mon. Not. Roy. Astron. Soc.* **402** (2010) 21, [0810.1522].

[92] DAMA collaboration, R. Bernabei et al., *First results from DAMA/LIBRA and the combined results with DAMA/NaI*, *Eur. Phys. J. C* **56** (2008) 333–355, [0804.2741].

[93] UK DARK MATTER collaboration, G. J. Alner et al., *First limits on nuclear recoil events from the ZEPLIN I galactic dark matter detector*, *Astropart. Phys.* **23** (2005) 444–462.

[94] COGENT collaboration, C. E. Aalseth et al., *Results from a Search for Light-Mass Dark Matter with a P-type Point Contact Germanium Detector*, *Phys. Rev. Lett.* **106** (2011) 131301, [1002.4703].

[95] D. Muna, *The drift-ii directional dark matter detector*, *Nuclear Physics B - Proceedings Supplements* **173** (2007) 172–175.

[96] M. F. Altmann et al., *Results and plans of the CRESST dark matter search*, in *20th International Symposium on Lepton and Photon Interactions at High Energies (LP 01)*, 6, 2001. astro-ph/0106314.

[97] CDMS-II collaboration, Z. Ahmed et al., *Dark Matter Search Results from the CDMS II Experiment*, *Science* **327** (2010) 1619–1621, [0912.3592].

[98] SUPERCDMS collaboration, R. Agnese et al., *Search for Low-Mass Weakly Interacting Massive Particles with SuperCDMS*, *Phys. Rev. Lett.* **112** (2014) 241302, [1402.7137].

[99] EDELWEISS collaboration, E. Armengaud et al., *Final results of the EDELWEISS-II WIMP search using a 4-kg array of cryogenic germanium detectors with interleaved electrodes*, *Phys. Lett. B* **702** (2011) 329–335, [1103.4070].

[100] XENON100 collaboration, E. Aprile et al., *Dark Matter Results from 225 Live Days of XENON100 Data*, *Phys. Rev. Lett.* **109** (2012) 181301, [1207.5988].

[101] LUX collaboration, D. S. Akerib et al., *First results from the LUX dark matter experiment at the Sanford Underground Research Facility*, *Phys. Rev. Lett.* **112** (2014) 091303, [1310.8214].

[102] V. N. Lebedenko et al., *Result from the First Science Run of the ZEPLIN-III Dark Matter Search Experiment*, *Phys. Rev. D* **80** (2009) 052010, [0812.1150].

[103] G. Angloher, M. Bauer, I. Bavykina, A. Bento, C. Bucci, C. Ciemniak et al., *Results from 730 kg days of the CRESST-II Dark Matter search*, *European Physical Journal C* **72** (Apr., 2012) 1971, [1109.0702].

[104] H. Kraus et al., *EURECA: The European future of dark matter searches with cryogenic detectors*, *Nucl. Phys. B Proc. Suppl.* **173** (2007) 168–171.

[105] J. R. Ellis, A. Ferstl and K. A. Olive, *Reevaluation of the elastic scattering of supersymmetric dark matter*, *Phys. Lett. B* **481** (2000) 304–314, [hep-ph/0001005].

[106] S. Archambault et al., *Searching for Dark Matter with PICASSO*, *Phys. Procedia* **61** (2015) 107–111.

[107] PICO collaboration, C. Amole et al., *Dark Matter Search Results from the PICO-2L C_3F_8 Bubble Chamber*, *Phys. Rev. Lett.* **114** (2015) 231302, [1503.00008].

[108] LUX collaboration, D. S. Akerib et al., *Results from a search for dark matter in the complete LUX exposure*, *Phys. Rev. Lett.* **118** (2017) 021303, [1608.07648].

[109] PICO collaboration, C. Amole et al., *Dark matter search results from the PICO-60 CF_3I bubble chamber*, *Phys. Rev. D* **93** (2016) 052014, [1510.07754].

[110] PICO collaboration, C. Amole et al., *Improved dark matter search results from PICO-2L Run 2*, *Phys. Rev. D* **93** (2016) 061101, [1601.03729].

[111] P. L. Nolan, A. A. Abdo, M. Ackermann, M. Ajello, A. Allafort, E. Antolini et al., *Fermi Large Area Telescope Second Source Catalog*, ApJS **199** (Apr., 2012) 31, [1108.1435].

[112] H.E.S.S. collaboration, F. Aharonian et al., *The h.e.s.s. survey of the inner galaxy in very high-energy gamma-rays*, *Astrophys. J.* **636** (2006) 777–797, [astro-ph/0510397].

[113] T. C. Weekes et al., *VERITAS: The Very energetic radiation imaging telescope array system*, *Astropart. Phys.* **17** (2002) 221–243, [astro-ph/0108478].

[114] R. Abbasi, Y. Abdou, M. Ackermann, J. Adams, M. Ahlers, K. Andeen et al., *Limits on a Muon Flux from Neutralino Annihilations in the Sun with the IceCube 22-String Detector*, Phys. Rev. Lett. **102** (May, 2009) 201302, [0902.2460].

[115] M. Ageron, J. A. Aguilar, I. Al Samarai, A. Albert, F. Ameli, M. André et al., *ANTARES: The first undersea neutrino telescope*, *Nuclear Instruments and Methods in Physics Research A* **656** (Nov., 2011) 11–38, [1104.1607].

[116] O. Adriani, G. C. Barbarino, G. A. Bazilevskaya, R. Bellotti, M. Boezio, E. A. Bogomolov et al., *An anomalous positron abundance in cosmic rays with energies 1.5-100GeV*, Nature **458** (Apr., 2009) 607–609, [0810.4995].

[117] AMS collaboration, M. Aguilar et al., *First Result from the Alpha Magnetic Spectrometer on the International Space Station: Precision Measurement of the Positron Fraction in Primary Cosmic Rays of 0.5–350 GeV*, *Phys. Rev. Lett.* **110** (2013) 141102.

[118] A. Askew, S. Chauhan, B. Penning, W. Shepherd and M. Tripathi, *Searching for Dark Matter at Hadron Colliders*, *Int. J. Mod. Phys. A* **29** (2014) 1430041, [1406.5662].

[119] L. Carpenter, A. DiFranzo, M. Mulhearn, C. Shimmin, S. Tulin and D. Whiteson, *Mono-Higgs-boson: A new collider probe of dark matter*, *Phys. Rev. D* **89** (2014) 075017, [1312.2592].

[120] A. A. Petrov and W. Shepherd, *Searching for dark matter at LHC with Mono-Higgs production*, *Phys. Lett. B* **730** (2014) 178–183, [1311.1511].

[121] Z. Maki, M. Nakagawa and S. Sakata, *Remarks on the unified model of elementary particles*, *Prog. Theor. Phys.* **28** (1962) 870–880.

[122] B. T. Cleveland, T. Daily, J. Davis, Raymond, J. R. Distel, K. Lande, C. K. Lee et al., *Measurement of the Solar Electron Neutrino Flux with the Homestake Chlorine Detector*, ApJ **496** (Mar., 1998) 505–526.

[123] A. Bellerive, J. Klein, A. McDonald, A. Noble and A. Poon, *The sudbury neutrino observatory*, *Nuclear Physics B* **908** (2016) 30–51.

[124] S. Fukuda, Y. Fukuda, T. Hayakawa, E. Ichihara, M. Ishitsuka, Y. Itow et al., *The Super-Kamiokande detector*, *Nuclear Instruments and Methods in Physics Research A* **501** (Apr., 2003) 418–462.

[125] KamLAND-Zen collaboration, A. Gando et al., *Limit on Neutrinoless $\beta\beta$ Decay of ^{136}Xe from the First Phase of KamLAND-Zen and Comparison with the Positive Claim in ^{76}Ge*, *Phys. Rev. Lett.* **110** (2013) 062502, [1211.3863].

[126] KamLAND-Zen collaboration, A. Gando et al., *Search for Majorana Neutrinos near the Inverted Mass Hierarchy Region with KamLAND-Zen*, *Phys. Rev. Lett.* **117** (2016) 082503, [1605.02889].

[127] Daya Bay collaboration, F. P. An et al., *Observation of electron-antineutrino disappearance at Daya Bay*, *Phys. Rev. Lett.* **108** (2012) 171803, [1203.1669].

[128] Daya Bay collaboration, F. P. An et al., *Improved Search for a Light Sterile Neutrino with the Full Configuration of the Daya Bay Experiment*, *Phys. Rev. Lett.* **117** (2016) 151802, [1607.01174].

[129] Daya Bay collaboration, F. P. An et al., *The Detector System of The Daya Bay Reactor Neutrino Experiment*, *Nucl. Instrum. Meth. A* **811** (2016) 133–161, [1508.03943].

[130] Daya Bay collaboration, F. P. An et al., *Spectral measurement of electron antineutrino oscillation amplitude and frequency at Daya Bay*, *Phys. Rev. Lett.* **112** (2014) 061801, [1310.6732].

[131] DAYA BAY collaboration, F. P. An et al., *Measurement of the Reactor Antineutrino Flux and Spectrum at Daya Bay*, *Phys. Rev. Lett.* **116** (2016) 061801, [1508.04233].

[132] DAYA BAY collaboration, F. P. An et al., *New Measurement of Antineutrino Oscillation with the Full Detector Configuration at Daya Bay*, *Phys. Rev. Lett.* **115** (2015) 111802, [1505.03456].

[133] DAYA BAY collaboration, F. P. An et al., *Search for a Light Sterile Neutrino at Daya Bay*, *Phys. Rev. Lett.* **113** (2014) 141802, [1407.7259].

[134] J. K. Ahn, S. Chebotaryov, J. H. Choi, S. Choi, W. Choi, Y. Choi et al., *Observation of Reactor Electron Antineutrinos Disappearance in the RENO Experiment*, Phys. Rev. Lett. **108** (May, 2012) 191802, [1204.0626].

[135] M. Apollonio, A. Baldini, C. Bemporad, E. Caffau, F. Cei, Y. Déclais et al., *Search for neutrino oscillations on a long base-line at the CHOOZ nuclear power station*, *European Physical Journal C* **27** (Apr., 2003) 331–374, [hep-ex/0301017].

[136] M. H. Ahn, E. Aliu, S. Andringa, S. Aoki, Y. Aoyama, J. Argyriades et al., *Measurement of neutrino oscillation by the K2K experiment*, Phys. Rev. D **74** (Oct., 2006) 072003, [hep-ex/0606032].

[137] P. Adamson et al., *The NuMI Neutrino Beam*, *Nucl. Instrum. Meth. A* **806** (2016) 279–306, [1507.06690].

[138] MINOS collaboration, P. Adamson et al., *Search for Sterile Neutrinos Mixing with Muon Neutrinos in MINOS*, *Phys. Rev. Lett.* **117** (2016) 151803, [1607.01176].

[139] MINOS+ collaboration, P. Adamson et al., *Search for sterile neutrinos in MINOS and MINOS+ using a two-detector fit*, *Phys. Rev. Lett.* **122** (2019) 091803, [1710.06488].

[140] MINOS collaboration, P. Adamson et al., *Electron neutrino and antineutrino appearance in the full MINOS data sample*, *Phys. Rev. Lett.* **110** (2013) 171801, [1301.4581].

[141] MINOS collaboration, P. Adamson et al., *Active to sterile neutrino mixing limits from neutral-current interactions in MINOS*, *Phys. Rev. Lett.* **107** (2011) 011802, [1104.3922].

[142] MINOS collaboration, D. G. Michael et al., *Observation of muon neutrino disappearance with the MINOS detectors and the NuMI neutrino beam*, *Phys. Rev. Lett.* **97** (2006) 191801, [hep-ex/0607088].

[143] MINOS collaboration, P. Adamson et al., *Search for active neutrino disappearance using neutral-current interactions in the MINOS long-baseline experiment*, *Phys. Rev. Lett.* **101** (2008) 221804, [0807.2424].

[144] MINOS collaboration, P. Adamson et al., *Combined analysis of ν_μ disappearance and $\nu_\mu \to \nu_e$ appearance in MINOS using accelerator and atmospheric neutrinos*, *Phys. Rev. Lett.* **112** (2014) 191801, [1403.0867].

[145] MINOS collaboration, P. Adamson et al., *Search for sterile neutrino mixing in the MINOS long baseline experiment*, *Phys. Rev. D* **81** (2010) 052004, [1001.0336].

[146] MINOS collaboration, D. G. Michael et al., *The Magnetized steel and scintillator calorimeters of the MINOS experiment*, *Nucl. Instrum. Meth. A* **596** (2008) 190–228, [0805.3170].

[147] MINOS collaboration, P. Adamson et al., *A Study of Muon Neutrino Disappearance Using the Fermilab Main Injector Neutrino Beam*, *Phys. Rev. D* **77** (2008) 072002, [0711.0769].

[148] DAYA BAY, MINOS collaboration, P. Adamson et al., *Limits on Active to Sterile Neutrino Oscillations from Disappearance Searches in the MINOS, Daya Bay, and Bugey-3 Experiments*, *Phys. Rev. Lett.* **117** (2016) 151801, [1607.01177].

[149] T2K collaboration, K. Abe et al., *Search for light sterile neutrinos with the T2K far detector Super-Kamiokande at a baseline of 295 km*, *Phys. Rev. D* **99** (2019) 071103, [1902.06529].

[150] DUNE collaboration, R. Acciarri et al., *Long-Baseline Neutrino Facility (LBNF) and Deep Underground Neutrino Experiment (DUNE): Conceptual Design Report, Volume 2: The Physics Program for DUNE at LBNF*, 1512.06148.

[151] DUNE collaboration, R. Acciarri et al., *Long-Baseline Neutrino Facility (LBNF) and Deep Underground Neutrino Experiment (DUNE): Conceptual Design Report, Volume 4 The DUNE Detectors at LBNF*, 1601.02984.

[152] DUNE collaboration, R. Acciarri et al., *Long-Baseline Neutrino Facility (LBNF) and Deep Underground Neutrino Experiment (DUNE): Conceptual Design Report, Volume 1: The LBNF and DUNE Projects*, 1601.05471.

[153] DUNE collaboration, J. Strait et al., *Long-Baseline Neutrino Facility (LBNF) and Deep Underground Neutrino Experiment (DUNE): Conceptual Design Report, Volume 3: Long-Baseline Neutrino Facility for DUNE June 24, 2015*, 1601.05823.

[154] NOvA collaboration, P. Adamson et al., *Search for active-sterile neutrino mixing using neutral-current interactions in NOvA*, *Phys. Rev. D* **96** (2017) 072006, [1706.04592].

[155] NOvA collaboration, D. S. Ayres et al., *NOvA: Proposal to Build a 30 Kiloton Off-Axis Detector to Study $\nu_\mu \to \nu_e$ Oscillations in the NuMI Beamline*, hep-ex/0503053.

[156] NOvA collaboration, P. Adamson et al., *First measurement of electron neutrino appearance in NOvA*, *Phys. Rev. Lett.* **116** (2016) 151806, [1601.05022].

[157] NOvA collaboration, P. Adamson et al., *Constraints on Oscillation Parameters from ν_e Appearance and ν_μ Disappearance in NOvA*, *Phys. Rev. Lett.* **118** (2017) 231801, [1703.03328].

[158] NOvA collaboration, P. Adamson et al., *First measurement of muon-neutrino disappearance in NOvA*, *Phys. Rev. D* **93** (2016) 051104, [1601.05037].

[159] NOvA collaboration, P. Adamson et al., *Measurement of the neutrino mixing angle θ_{23} in NOvA*, *Phys. Rev. Lett.* **118** (2017) 151802, [1701.05891].

[160] R. Abbasi, M. Ackermann, J. Adams, M. Ahlers, J. Ahrens, K. Andeen et al., *The IceCube data acquisition system: Signal capture, digitization, and timestamping*, *Nuclear Instruments and Methods in Physics Research A* **601** (Apr., 2009) 294–316, [0810.4930].

[161] M. G. Aartsen, K. Abraham, M. Ackermann, J. Adams, J. A. Aguilar, M. Ahlers et al., *PINGU: a vision for neutrino and particle physics at the south pole*, *Journal of Physics G: Nuclear and Particle Physics* **44** (apr, 2017) 054006.

[162] R. Abbasi, Y. Abdou, T. Abu-Zayyad, M. Ackermann, J. Adams, J. Aguilar et al., *The design and performance of icecube deepcore*, *Astroparticle Physics* **35** (2012) 615–624.

[163] ANTARES collaboration, A. Albert et al., *The search for high-energy neutrinos coincident with fast radio bursts with the ANTARES neutrino telescope*, *Mon. Not. Roy. Astron. Soc.* **482** (2019) 184–193, [1807.04045].

[164] BOREXINO collaboration, G. Alimonti et al., *Science and technology of BOREXINO: A Real time detector for low-energy solar neutrinos*, *Astropart. Phys.* **16** (2002) 205–234, [hep-ex/0012030].

[165] G. Prior, *The SNO+ experiment physics goals and background mitigation*, in *Prospects in Neutrino Physics*, 4, 2017. 1704.06647.

[166] C. Guo, *Status of the Jiangmen Underground Neutrino Observatory*, *arXiv e-prints* (Oct., 2019) arXiv:1910.10343, [1910.10343].

[167] HiRes collaboration, D. J. Bird et al., *Evidence for correlated changes in the spectrum and composition of cosmic rays at extremely high-energies*, *Phys. Rev. Lett.* **71** (1993) 3401–3404.

[168] S. Chakraborty and I. Izaguirre, *Diffuse neutrinos from extragalactic supernova remnants: Dominating the 100 TeV IceCube flux*, *Phys. Lett. B* **745** (2015) 35–39, [1501.02615].

[169] F. W. Stecker, C. Done, M. H. Salamon and P. Sommers, *High-energy neutrinos from active galactic nuclei*, *Phys. Rev. Lett.* **66** (1991) 2697–2700.

[170] E. Waxman and J. N. Bahcall, *High-energy neutrinos from cosmological gamma-ray burst fireballs*, *Phys. Rev. Lett.* **78** (1997) 2292–2295, [astro-ph/9701231].

[171] KM3NeT collaboration, A. Margiotta, *The KM3NeT deep-sea neutrino telescope*, *Nucl. Instrum. Meth. A* **766** (2014) 83–87, [1408.1392].

[172] L. Wolfenstein, *Neutrino Oscillations in Matter*, *Phys. Rev. D* **17** (1978) 2369–2374.

[173] S. P. Mikheyev and A. Y. Smirnov, *Resonance Amplification of Oscillations in Matter and Spectroscopy of Solar Neutrinos*, *Sov. J. Nucl. Phys.* **42** (1985) 913–917.

[174] Y. Declais et al., *Search for neutrino oscillations at 15-meters, 40-meters, and 95-meters from a nuclear power reactor at Bugey*, *Nucl. Phys. B* **434** (1995) 503–534.

[175] LSND collaboration, C. Athanassopoulos et al., *Evidence for anti-muon-neutrino —> anti-electron-neutrino oscillations from the LSND experiment at LAMPF*, *Phys. Rev. Lett.* **77** (1996) 3082–3085, [nucl-ex/9605003].

[176] LSND collaboration, A. Aguilar-Arevalo et al., *Evidence for neutrino oscillations from the observation of $\bar{\nu}_e$ appearance in a $\bar{\nu}_\mu$ beam*, *Phys. Rev. D* **64** (2001) 112007, [hep-ex/0104049].

[177] J. M. Conrad, W. C. Louis and M. H. Shaevitz, *The LSND and MiniBooNE Oscillation Searches at High Δm^2*, *Ann. Rev. Nucl. Part. Sci.* **63** (2013) 45–67, [1306.6494].

[178] MiniBooNE collaboration, A. A. Aguilar-Arevalo et al., *Significant Excess of ElectronLike Events in the MiniBooNE Short-Baseline Neutrino Experiment*, *Phys. Rev. Lett.* **121** (2018) 221801, [1805.12028].

[179] OPERA collaboration, N. Agafonova et al., *Observation of a first ν_τ candidate in the OPERA experiment in the CNGS beam*, *Phys. Lett. B* **691** (2010) 138–145, [1006.1623].

[180] MINERvA collaboration, D. Coplowe et al., *Probing nuclear effects with neutrino-induced charged-current neutral pion production*, *Phys. Rev. D* **102** (2020) 072007, [2002.05812].

[181] ICAL collaboration, S. Ahmed et al., *Physics Potential of the ICAL detector at the India-based Neutrino Observatory (INO)*, *Pramana* **88** (2017) 79, [1505.07380].

[182] ANITA collaboration, S. Wissel, C. Burch, W. Carvalho, J. Crowley, J. Alvarez-Muniz, A. Cummings et al., *Comprehensive estimate of the sensitivity of ANITA to tau neutrinos*, *PoS* **ICRC2019** (2021) 1034.

[183] XENON collaboration, E. Aprile et al., *Physics reach of the XENON1T dark matter experiment*, *JCAP* **04** (2016) 027, [1512.07501].

[184] PandaX-II collaboration, A. Tan et al., *Dark Matter Results from First 98.7 Days of Data from the PandaX-II Experiment*, *Phys. Rev. Lett.* **117** (2016) 121303, [1607.07400].

[185] F. Calore, I. Cholis, C. McCabe and C. Weniger, *A Tale of Tails: Dark Matter Interpretations of the Fermi GeV Excess in Light of Background Model Systematics*, *Phys. Rev. D* **91** (2015) 063003, [1411.4647].

[186] A. Boyarsky, O. Ruchayskiy, D. Iakubovskyi and J. Franse, *Unidentified Line in X-Ray Spectra of the Andromeda Galaxy and Perseus Galaxy Cluster*, *Phys. Rev. Lett.* **113** (2014) 251301, [1402.4119].

[187] R. Krall, M. Reece and T. Roxlo, *Effective field theory and keV lines from dark matter*, *JCAP* **09** (2014) 007, [1403.1240].

[188] J.-C. Park, S. C. Park and K. Kong, *X-ray line signal from 7 keV axino dark matter decay*, *Phys. Lett. B* **733** (2014) 217–220, [1403.1536].

[189] M. T. Frandsen, F. Sannino, I. M. Shoemaker and O. Svendsen, *X-ray Lines from Dark Matter: The Good, The Bad, and The Unlikely*, *JCAP* **05** (2014) 033, [1403.1570].

[190] S. Baek and H. Okada, *7 keV Dark Matter as X-ray Line Signal in Radiative Neutrino Model*, 1403.1710.

[191] K. Nakayama, F. Takahashi and T. T. Yanagida, *The 3.5 keV X-ray line signal from decaying moduli with low cutoff scale*, *Phys. Lett. B* **735** (2014) 338–339, [1403.1733].

[192] K.-Y. Choi and O. Seto, *X-ray line signal from decaying axino warm dark matter*, *Phys. Lett. B* **735** (2014) 92–94, [1403.1782].

[193] M. Cicoli, J. P. Conlon, M. C. D. Marsh and M. Rummel, *3.55 keV photon line and its morphology from a 3.55 keV axionlike particle line*, *Phys. Rev. D* **90** (2014) 023540, [1403.2370].

[194] C. Kolda and J. Unwin, *X-ray lines from R-parity violating decays of keV sparticles*, *Phys. Rev. D* **90** (2014) 023535, [1403.5580].

[195] R. Allahverdi, B. Dutta and Y. Gao, *keV Photon Emission from Light Nonthermal Dark Matter*, *Phys. Rev. D* **89** (2014) 127305, [1403.5717].

[196] S. P. Liew, *Axino dark matter in light of an anomalous X-ray line*, *JCAP* **05** (2014) 044, [1403.6621].

[197] K. Nakayama, F. Takahashi and T. T. Yanagida, *Anomaly-free flavor models for Nambu–Goldstone bosons and the 3.5keV X-ray line signal*, *Phys. Lett. B* **734** (2014) 178–182, [1403.7390].

[198] E. Dudas, L. Heurtier and Y. Mambrini, *Generating X-ray lines from annihilating dark matter*, *Phys. Rev. D* **90** (2014) 035002, [1404.1927].

[199] K. S. Babu and R. N. Mohapatra, *7 keV Scalar Dark Matter and the Anomalous Galactic X-ray Spectrum*, *Phys. Rev. D* **89** (2014) 115011, [1404.2220].

[200] K. P. Modak, *3.5 keV X-ray Line Signal from Decay of Right-Handed Neutrino due to Transition Magnetic Moment*, *JHEP* **03** (2015) 064, [1404.3676].

[201] S. Baek, P. Ko and W.-I. Park, *The 3.5 keV X-ray line signature from annihilating and decaying dark matter in Weinberg model*, 1405.3730.

[202] S. Chakraborty, D. K. Ghosh and S. Roy, *7 keV Sterile neutrino dark matter in $U(1)_R-$ lepton number model*, *JHEP* **10** (2014) 146, [1405.6967].

[203] C.-W. Chiang and T. Yamada, *3.5-keV X-ray line from nearly-degenerate WIMP dark matter decays*, *JHEP* **09** (2014) 006, [1407.0460].

[204] B. Dutta, I. Gogoladze, R. Khalid and Q. Shafi, *3.5 keV X-ray line and R-Parity Conserving Supersymmetry*, *JHEP* **11** (2014) 018, [1407.0863].

[205] N. Haba, H. Ishida and R. Takahashi, *ν_R dark matter-philic Higgs for 3.5 keV X-ray signal*, *Phys. Lett. B* **743** (2015) 35–38, [1407.6827].

[206] J. M. Cline and A. R. Frey, *Nonabelian dark matter models for 3.5 keV X-rays*, *JCAP* **10** (2014) 013, [1408.0233].

[207] Y. Farzan and A. R. Akbarieh, *Decaying Vector Dark Matter as an Explanation for the 3.5 keV Line from Galaxy Clusters*, *JCAP* **11** (2014) 015, [1408.2950].

[208] T. Higaki, N. Kitajima and F. Takahashi, *Hidden axion dark matter decaying through mixing with QCD axion and the 3.5 keV X-ray line*, *JCAP* **12** (2014) 004, [1408.3936].

[209] S. Patra, N. Sahoo and N. Sahu, *Dipolar dark matter in light of the 3.5 keV x-ray line, neutrino mass, and LUX data*, *Phys. Rev. D* **91** (2015) 115013, [1412.4253].

[210] K. S. Babu, S. Chakdar and R. N. Mohapatra, *Warm Dark Matter in Two Higgs Doublet Models*, *Phys. Rev. D* **91** (2015) 075020, [1412.7745].

[211] Y. Mambrini and T. Toma, *X-ray lines and self-interacting dark matter*, *Eur. Phys. J. C* **75** (2015) 570, [1506.02032].

[212] K. Cheung, W.-C. Huang and Y.-L. S. Tsai, *Non-abelian Dark Matter Solutions for Galactic Gamma-ray Excess and Perseus 3.5 keV X-ray Line*, *JCAP* **05** (2015) 053, [1411.2619].

[213] T. E. Jeltema and S. Profumo, *Discovery of a 3.5 keV line in the Galactic Centre and a critical look at the origin of the line across astronomical targets*, *Mon. Not. Roy. Astron. Soc.* **450** (2015) 2143–2152, [1408.1699].

[214] E. Carlson, T. Jeltema and S. Profumo, *Where do the 3.5 keV photons come from? A morphological study of the Galactic Center and of Perseus*, *JCAP* **02** (2015) 009, [1411.1758].

[215] HITOMI collaboration, F. A. Aharonian et al., *Hitomi constraints on the 3.5 keV line in the Perseus galaxy cluster*, *Astrophys. J. Lett.* **837** (2017) L15, [1607.07420].

[216] D. Harvey, E. Tittley, R. Massey, T. D. Kitching, A. Taylor, S. R. Pike et al., *On the cross-section of Dark Matter using substructure infall into galaxy clusters*, *Mon. Not. Roy. Astron. Soc.* **441** (2014) 404–416, [1310.1731].

[217] D. Harvey, R. Massey, T. Kitching, A. Taylor and E. Tittley, *The non-gravitational interactions of dark matter in colliding galaxy clusters*, *Science* **347** (2015) 1462–1465, [1503.07675].

[218] F. Kahlhoefer, K. Schmidt-Hoberg, J. Kummer and S. Sarkar, *On the interpretation of dark matter self-interactions in Abell 3827*, *Mon. Not. Roy. Astron. Soc.* **452** (2015) L54–L58, [1504.06576].

[219] R. Campbell, S. Godfrey, H. E. Logan, A. D. Peterson and A. Poulin, *Implications of the observation of dark matter self-interactions for singlet scalar dark matter*, *Phys. Rev. D* **92** (2015) 055031, [1505.01793].

[220] A. Biswas, D. Majumdar and P. Roy, *Nonthermal two component dark matter model for Fermi-LAT γ-ray excess and 3.55 keV X-ray line*, *JHEP* **04** (2015) 065, [1501.02666].

[221] A. Biswas, D. Majumdar and P. Roy, *Dwarf galaxy γ-excess and 3.55 keV X-ray line in a nonthermal Dark Matter model*, *EPL* **113** (2016) 29001, [1507.04543].

[222] V. Barger, P. Langacker, M. McCaskey, M. Ramsey-Musolf and G. Shaughnessy, *Complex Singlet Extension of the Standard Model*, *Phys. Rev. D* **79** (2009) 015018, [0811.0393].

[223] A. Friedland, H. Murayama and M. Perelstein, *Domain walls as dark energy*, *Phys. Rev. D* **67** (2003) 043519, [astro-ph/0205520].

[224] Y. Mambrini, S. Profumo and F. S. Queiroz, *Dark Matter and Global Symmetries*, *Phys. Lett. B* **760** (2016) 807–815, [1508.06635].

[225] ATLAS collaboration, G. Aad et al., *Observation of a new particle in the search for the Standard Model Higgs boson with the ATLAS detector at the LHC*, *Phys. Lett.* **B716** (2012) 1–29, [1207.7214].

[226] CMS collaboration, S. Chatrchyan et al., *Observation of a New Boson at a Mass of 125 GeV with the CMS Experiment at the LHC*, *Phys. Lett. B* **716** (2012) 30–61, [1207.7235].

[227] K. Kannike, *Vacuum Stability Conditions From Copositivity Criteria*, *Eur. Phys. J. C* **72** (2012) 2093, [1205.3781].

[228] M. S. Turner and F. Wilczek, *MIGHT OUR VACUUM BE METASTABLE?*, *Nature* **298** (1982) 633–634.

[229] J. McDonald, *Thermally generated gauge singlet scalars as selfinteracting dark matter*, *Phys. Rev. Lett.* **88** (2002) 091304, [hep-ph/0106249].

[230] L. J. Hall, K. Jedamzik, J. March-Russell and S. M. West, *Freeze-In Production of FIMP Dark Matter*, *JHEP* **03** (2010) 080, [0911.1120].

[231] ATLAS collaboration, *Updated ATLAS results on the signal strength of the Higgs-like boson for decays into WW and heavy fermion final states*, .

[232] G. Belanger, B. Dumont, U. Ellwanger, J. F. Gunion and S. Kraml, *Status of invisible Higgs decays*, *Phys. Lett. B* **723** (2013) 340–347, [1302.5694].

[233] L. Lopez-Honorez, T. Schwetz and J. Zupan, *Higgs portal, fermionic dark matter, and a Standard Model like Higgs at 125 GeV*, *Phys. Lett. B* **716** (2012) 179–185, [1203.2064].

[234] K. Ghorbani, *Fermionic dark matter with pseudo-scalar Yukawa interaction*, *JCAP* **01** (2015) 015, [1408.4929].

[235] A. Biswas, *Explaining Low Energy γ-ray Excess from the Galactic Centre using a Two Component Dark Matter Model*, *J. Phys. G* **43** (2016) 055201, [1412.1663].

[236] R. Barbieri, L. J. Hall and V. S. Rychkov, *Improved naturalness with a heavy Higgs: An Alternative road to LHC physics*, *Phys. Rev. D* **74** (2006) 015007, [hep-ph/0603188].

[237] FERMI-LAT collaboration, W. B. Atwood et al., *The Large Area Telescope on the Fermi Gamma-ray Space Telescope Mission*, *Astrophys. J.* **697** (2009) 1071–1102, [0902.1089].

[238] FERMI-LAT collaboration, M. Ackermann et al., *Searching for Dark Matter Annihilation from Milky Way Dwarf Spheroidal Galaxies with Six Years of Fermi Large Area Telescope Data*, *Phys. Rev. Lett.* **115** (2015) 231301, [1503.02641].

[239] FERMI-LAT, DES collaboration, A. Drlica-Wagner et al., *Search for Gamma-Ray Emission from DES Dwarf Spheroidal Galaxy Candidates with Fermi-LAT Data*, *Astrophys. J. Lett.* **809** (2015) L4, [1503.02632].

[240] S. K. Lee, M. Lisanti, B. R. Safdi, T. R. Slatyer and W. Xue, *Evidence for Unresolved γ-Ray Point Sources in the Inner Galaxy*, *Phys. Rev. Lett.* **116** (2016) 051103, [1506.05124].

[241] R. Bartels, S. Krishnamurthy and C. Weniger, *Strong support for the millisecond pulsar origin of the Galactic center GeV excess*, *Phys. Rev. Lett.* **116** (2016) 051102, [1506.05104].

[242] H. A. Clark, P. Scott, R. Trotta and G. F. Lewis, *Dark matter substructure cannot explain properties of the Fermi Galactic Centre excess*, *JCAP* **07** (2018) 060, [1612.01539].

[243] FERMI-LAT, DES collaboration, A. Albert et al., *Searching for Dark Matter Annihilation in Recently Discovered Milky Way Satellites with Fermi-LAT*, *Astrophys. J.* **834** (2017) 110, [1611.03184].

[244] M. Cirelli, G. Corcella, A. Hektor, G. Hutsi, M. Kadastik, P. Panci et al., *PPPC 4 DM ID: A Poor Particle Physicist Cookbook for Dark Matter Indirect Detection*, *JCAP* **03** (2011) 051, [1012.4515].

[245] S. Nurmi, T. Tenkanen and K. Tuominen, *Inflationary Imprints on Dark Matter*, *JCAP* **11** (2015) 001, [1506.04048].

[246] P. S. B. Dev, A. Mazumdar and S. Qutub, *Constraining non-thermal and thermal properties of dark matter*, *Frontiers in Physics* **2** (2014) 26.

[247] K. Kainulainen, S. Nurmi, T. Tenkanen, K. Tuominen and V. Vaskonen, *Isocurvature Constraints on Portal Couplings*, *JCAP* **06** (2016) 022, [1601.07733].

[248] S. Bhattacharya, A. Drozd, B. Grzadkowski and J. Wudka, *Two-Component Dark Matter*, *JHEP* **10** (2013) 158, [1309.2986].

[249] S. Profumo, K. Sigurdson and L. Ubaldi, *Can we discover multi-component WIMP dark matter?*, *JCAP* **12** (2009) 016, [0907.4374].

[250] G. B. Gelmini, *Dark matter searches: Looking for the cake or its frosting? Detectability of a subdominant component of the CDM*, *Nucl. Phys. B Proc. Suppl.* **138** (2005) 32–34, [hep-ph/0310022].

[251] G. Duda, G. Gelmini, P. Gondolo, J. Edsjo and J. Silk, *Indirect detection of a subdominant density component of cold dark matter*, *Phys. Rev. D* **67** (2003) 023505, [hep-ph/0209266].

[252] G. Duda, G. Gelmini and P. Gondolo, *Detection of a subdominant density component of cold dark matter*, *Phys. Lett. B* **529** (2002) 187–192, [hep-ph/0102200].

[253] A. Drozd, B. Grzadkowski and J. Wudka, *Multi-Scalar-Singlet Extension of the Standard Model - the Case for Dark Matter and an Invisible Higgs Boson*, *JHEP* **04** (2012) 006, [1112.2582].

[254] Q.-H. Cao, E. Ma, J. Wudka and C. P. Yuan, *Multipartite dark matter*, 0711.3881.

[255] D. Feldman, Z. Liu, P. Nath and G. Peim, *Multicomponent Dark Matter in Supersymmetric Hidden Sector Extensions*, *Phys. Rev. D* **81** (2010) 095017, [1004.0649].

[256] M. Aoki, M. Duerr, J. Kubo and H. Takano, *Multi-Component Dark Matter Systems and Their Observation Prospects*, *Phys. Rev. D* **86** (2012) 076015, [1207.3318].

[257] J. Heeck and H. Zhang, *Exotic Charges, Multicomponent Dark Matter and Light Sterile Neutrinos*, *JHEP* **05** (2013) 164, [1211.0538].

[258] K. M. Zurek, *Multi-Component Dark Matter*, *Phys. Rev. D* **79** (2009) 115002, [0811.4429].

[259] Y. Tomozawa, *Two components of dark matter in the DAMA data*, *Int. J. Mod. Phys. A* **23** (2008) 4811–4816, [0806.1501].

[260] J.-H. Huh, J. E. Kim and B. Kyae, *Two dark matter components in dark matter extension of the minimal supersymmetric standard model and the high energy positron spectrum in PAMELA/HEAT data*, *Phys. Rev. D* **79** (2009) 063529, [0809.2601].

[261] Y. Daikoku, H. Okada and T. Toma, *Two Component Dark Matters in $S_4 \times Z_2$ Flavor Symmetric Extra U(1) Model*, *Prog. Theor. Phys.* **126** (2011) 855–883, [1106.4717].

[262] M. Aoki, J. Kubo and H. Takano, *Two-loop radiative seesaw mechanism with multicomponent dark matter explaining the possible γ excess in the Higgs boson decay and at the Fermi LAT*, *Phys. Rev. D* **87** (2013) 116001, [1302.3936].

[263] A. Biswas, D. Majumdar, A. Sil and P. Bhattacharjee, *Two Component Dark Matter : A Possible Explanation of 130 GeV $\gamma-$ Ray Line from the Galactic Centre*, *JCAP* **12** (2013) 049, [1301.3668].

[264] P.-H. Gu, *Multi-component dark matter with magnetic moments for Fermi-LAT gamma-ray line*, *Phys. Dark Univ.* **2** (2013) 35–40, [1301.4368].

[265] M. Cirelli and J. M. Cline, *Can multistate dark matter annihilation explain the high-energy cosmic ray lepton anomalies?*, *Phys. Rev. D* **82** (2010) 023503, [1005.1779].

[266] L. Bian, R. Ding and B. Zhu, *Two Component Higgs-Portal Dark Matter*, *Phys. Lett. B* **728** (2014) 105–113, [1308.3851].

[267] M. Heikinheimo, A. Racioppi, M. Raidal, C. Spethmann and K. Tuominen, *Dark Supersymmetry*, *Nucl. Phys. B* **876** (2013) 201–214, [1305.4182].

[268] Z. G. Berezhiani and M. Y. Khlopov, *Physics of cosmological dark matter in the theory of broken family symmetry. (In Russian)*, *Sov. J. Nucl. Phys.* **52** (1990) 60–64.

[269] Y. Kajiyama, H. Okada and T. Toma, *Multicomponent dark matter particles in a two-loop neutrino model*, *Phys. Rev. D* **88** (2013) 015029, [1303.7356].

[270] P. T. Winslow, K. Sigurdson and J. N. Ng, *Multi-State Dark Matter from Spherical Extra Dimensions*, *Phys. Rev. D* **82** (2010) 023512, [1005.3013].

[271] K. R. Dienes and B. Thomas, *Dynamical Dark Matter: I. Theoretical Overview*, *Phys. Rev. D* **85** (2012) 083523, [1106.4546].

[272] K. R. Dienes and B. Thomas, *Dynamical Dark Matter: II. An Explicit Model*, *Phys. Rev. D* **85** (2012) 083524, [1107.0721].

[273] M. V. Medvedev, *Cosmological Simulations of Multicomponent Cold Dark Matter*, *Phys. Rev. Lett.* **113** (2014) 071303, [1305.1307].

[274] V. Semenov, S. Pilipenko, A. Doroshkevich, V. Lukash and E. Mikheeva, *Dark matter halo formation in the multicomponent dark matter models*, 1306.3210.

[275] A. Merle and A. Schneider, *Production of Sterile Neutrino Dark Matter and the 3.5 keV line*, *Phys. Lett. B* **749** (2015) 283–288, [1409.6311].

[276] A. Merle and M. Totzauer, *keV Sterile Neutrino Dark Matter from Singlet Scalar Decays: Basic Concepts and Subtle Features*, *JCAP* **06** (2015) 011, [1502.01011].

[277] K. P. Modak, D. Majumdar and S. Rakshit, *A Possible Explanation of Low Energy γ-ray Excess from Galactic Centre and Fermi Bubble by a Dark Matter Model with Two Real Scalars*, *JCAP* **03** (2015) 011, [1312.7488].

[278] S. Bhattacharya, P. Poulose and P. Ghosh, *Multipartite Interacting Scalar Dark Matter in the light of updated LUX data*, *JCAP* **04** (2017) 043, [1607.08461].

[279] S. Bhattacharya, P. Ghosh, T. N. Maity and T. S. Ray, *Mitigating Direct Detection Bounds in Non-minimal Higgs Portal Scalar Dark Matter Models*, *JHEP* **10** (2017) 088, [1706.04699].

[280] B. W. Lee, C. Quigg and H. B. Thacker, *Weak Interactions at Very High-Energies: The Role of the Higgs Boson Mass*, *Phys. Rev. D* **16** (1977) 1519.

[281] M. Heikinheimo, T. Tenkanen, K. Tuominen and V. Vaskonen, *Observational Constraints on Decoupled Hidden Sectors*, *Phys. Rev. D* **94** (2016) 063506, [1604.02401].

[282] A. Dutta Banik, M. Pandey, D. Majumdar and A. Biswas, *Two component WIMP–FImP dark matter model with singlet fermion, scalar and pseudo scalar*, *Eur. Phys. J. C* **77** (2017) 657, [1612.08621].

[283] N. Bernal and X. Chu, $\mathbb{Z}_2$ *SIMP Dark Matter*, *JCAP* **01** (2016) 006, [1510.08527].

[284] J. Edsjo and P. Gondolo, *Neutralino relic density including coannihilations*, *Phys. Rev. D* **56** (1997) 1879–1894, [hep-ph/9704361].

[285] A. Biswas and D. Majumdar, *The Real Gauge Singlet Scalar Extension of Standard Model: A Possible Candidate of Cold Dark Matter*, *Pramana* **80** (2013) 539–557, [1102.3024].

[286] M. Kaplinghat, T. Linden and H.-B. Yu, *Galactic Center Excess in γ Rays from Annihilation of Self-Interacting Dark Matter*, *Phys. Rev. Lett.* **114** (2015) 211303, [1501.03507].

[287] M. Markevitch, A. H. Gonzalez, D. Clowe, A. Vikhlinin, L. David, W. Forman et al., *Direct constraints on the dark matter self-interaction cross-section from the merging galaxy cluster 1E0657-56*, *Astrophys. J.* **606** (2004) 819–824, [astro-ph/0309303].

[288] J. R. Espinosa, G. F. Giudice and A. Riotto, *Cosmological implications of the Higgs mass measurement*, *JCAP* **05** (2008) 002, [0710.2484].

[289] J. Elias-Miro, J. R. Espinosa, G. F. Giudice, G. Isidori, A. Riotto and A. Strumia, *Higgs mass implications on the stability of the electroweak vacuum*, *Phys. Lett. B* **709** (2012) 222–228, [1112.3022].

[290] K. Enqvist, T. Meriniemi and S. Nurmi, *Generation of the Higgs Condensate and Its Decay after Inflation*, *JCAP* **10** (2013) 057, [1306.4511].

[291] M. Ackermann et al., *Searching for Dark Matter Annihilation from Milky Way Dwarf Spheroidal Galaxies with Six Years of Fermi Large Area Telescope Data*, *Physical Review Letters* **115** (Dec., 2015) 231301, [1503.02641].

[292] A. A. Abdo, M. Ackermann, M. Ajello, W. B. Atwood, L. Baldini, J. Ballet et al., *Spectrum of the Isotropic Diffuse Gamma-Ray Emission Derived from First-Year Fermi Large Area Telescope Data*, Phys. Rev. Lett. **104** (Mar., 2010) 101101, [1002.3603].

[293] FERMI-LAT collaboration, M. Ackermann et al., *The spectrum of isotropic diffuse gamma-ray emission between 100 MeV and 820 GeV*, *Astrophys. J.* **799** (2015) 86, [1410.3696].

[294] H.-C. Cheng, J. L. Feng and K. T. Matchev, *Kaluza-Klein dark matter*, *Phys. Rev. Lett.* **89** (2002) 211301, [hep-ph/0207125].

[295] G. Servant and T. M. P. Tait, *Is the lightest Kaluza-Klein particle a viable dark matter candidate?*, *Nucl. Phys.* **B650** (2003) 391–419, [hep-ph/0206071].

[296] D. Majumdar, *Relic densities for Kaluz-Klein dark matter*, *Mod. Phys. Lett.* **A18** (2003) 1705–1710.

[297] D. Hooper, G. Zaharijas, D. P. Finkbeiner and G. Dobler, *Prospects For Detecting Dark Matter With GLAST In Light Of The WMAP Haze*, *Phys. Rev.* **D77** (2008) 043511, [0709.3114].

[298] T. Appelquist, H.-C. Cheng and B. A. Dobrescu, *Bounds on universal extra dimensions*, *Phys. Rev.* **D64** (2001) 035002, [hep-ph/0012100].

[299] K. Kong and K. T. Matchev, *Phenomenology of universal extra dimensions*, *AIP Conf. Proc.* **903** (2007) 451–454, [hep-ph/0610057].

[300] P. Ullio, L. Bergstrom, J. Edsjo and C. G. Lacey, *Cosmological dark matter annihilations into gamma-rays - a closer look*, *Phys. Rev.* **D66** (2002) 123502, [astro-ph/0207125].

[301] L. Bergström, J. Edsjö and P. Ullio, *Spectral gamma-ray signatures of cosmological dark matter annihilations*, *Physical Review Letters* **87** (2001) 251301.

[302] Y.-T. Gao, F. W. Stecker and D. B. Cline, *The lightest supersymmetric particle and the extragalactic gamma-ray background*, *Astronomy and Astrophysics* **249** (Sept., 1991) 1–4.

[303] F. W. Stecker, *The cosmic gamma-ray background from the annihilation of primordial stable neutral heavy leptons*, *The Astrophysical Journal* **223** (Aug., 1978) 1032–1036.

[304] J. E. Taylor and J. Silk, *The clumpiness of cold dark matter: implications for the annihilation signal*, MNRAS **339** (02, 2003) 505–514.

[305] K. C. Y. Ng, R. Laha, S. Campbell, S. Horiuchi, B. Dasgupta, K. Murase et al., *Resolving small-scale dark matter structures using multisource indirect detection*, *Phys. Rev. D* **89** (Apr, 2014) 083001.

[306] T. Bringmann, F. Calore, M. Di Mauro and F. Donato, *Constraining dark matter annihilation with the isotropic γ-ray background: Updated limits and future potential*, *Phys. Rev. D* **89** (Jan, 2014) 023012.

[307] I. Cholis, D. Hooper and S. D. McDermott, *Dissecting the gamma-ray background in search of dark matter*, *Journal of Cosmology and Astroparticle Physics* .

[308] M. Tavakoli, I. Cholis, C. Evoli and P. Ullio, *Constraints on Dark Matter Annihilations from Diffuse Gamma-Ray Emission in the Galaxy*, *JCAP* **1401** (2014) 017, [1308.4135].

[309] E. Sefusatti, G. Zaharijas, P. D. Serpico, D. Theurel and M. Gustafsson, *Extragalactic gamma-ray signal from dark matter annihilation: an appraisal*, MNRAS **441** (05, 2014) 1861–1878.

[310] M. Ajello, D. Gasparrini, M. Sánchez-Conde, G. Zaharijas, M. Gustafsson, J. Cohen-Tanugi et al., *The Origin of the Extragalactic Gamma-Ray Background and Implications for Dark Matter Annihilation*, *The Astrophysical Journal Letters* **800** (Feb., 2015) L27, [1501.05301].

[311] M. Di Mauro and F. Donato, *Composition of the Fermi-LAT isotropic gamma-ray background intensity: Emission from extragalactic point sources and dark matter annihilations*, *Phys. Rev.* **D91** (2015) 123001, [1501.05316].

[312] M. Di Mauro, *Isotropic diffuse gamma-ray background: unveiling Dark Matter components beyond the contribution of astrophysical sources*, in *5th International Fermi Symposium Nagoya, Japan, October 20-24, 2014*, 2015. 1502.02566.

[313] FERMI-LAT collaboration, M. Ackermann et al., *Limits on Dark Matter Annihilation Signals from the Fermi LAT 4-year Measurement of the Isotropic Gamma-Ray Background*, *JCAP* **1509** (2015) 008, [1501.05464].

[314] A. Dutta Banik, M. Pandey, D. Majumdar and A. Biswas, *Two component wimp–fimp dark matter model with singlet fermion, scalar and pseudo scalar*, *The European Physical Journal C* **77** (Oct, 2017) 657.

[315] Planck Collaboration, N. Aghanim, Y. Akrami, M. Ashdown, J. Aumont, C. Baccigalupi et al., *Planck 2018 results. VI. Cosmological parameters*, *arXiv e-prints* (July, 2018) arXiv:1807.06209, [1807.06209].

[316] K. Boddy, J. Kumar, D. Marfatia and P. Sandick, *Model-independent constraints on dark matter annihilation in dwarf spheroidal galaxies*, *Phys. Rev. D* **97** (2018) 095031, [1802.03826].

[317] A. B. Pace and L. E. Strigari, *Scaling Relations for Dark Matter Annihilation and Decay Profiles in Dwarf Spheroidal Galaxies*, *Mon. Not. Roy. Astron. Soc.* **482** (2019) 3480–3496, [1802.06811].

[318] W. B. Atwood et al., *The Large Area Telescope on the Fermi Gamma-Ray Space Telescope Mission*, *The Astrophysical Journal* **697** (June, 2009) 1071–1102, [0902.1089].

[319] H.-N. Lin and X. Li, *The dark matter profiles in the Milky Way*, MNRAS **487** (06, 2019) 5679–5684, [https://academic.oup.com/mnras/article-pdf/487/4/5679/28897927/stz1698.pdf]

[320] S. Ando, *Can dark matter annihilation dominate the extragalactic gamma-ray background?*, *Phys. Rev. Lett.* **94** (May, 2005) 171303.

[321] T. Oda, T. Totani and M. Nagashima, *Gamma-ray background from neutralino annihilation in the first cosmological objects*, *The Astrophysical Journal* **633** (oct, 2005) L65–L68.

[322] L. Pieri, G. Bertone and E. Branchini, *Dark matter annihilation in substructures revised*, MNRAS **384** (02, 2008) 1627–1637, [https://academic.oup.com/mnras/article-pdf/384/4/1627/2838096/mnras0384-162

[323] M. Cirelli et al., *PPPC 4 DM ID: a poor particle physicist cookbook for dark matter indirect detection*, *Journal of Cosmology and Astroparticle Physics* **2011** (mar, 2011) 051–051.

[324] A. Franceschini, G. Rodighiero and M. Vaccari, *Extragalactic optical-infrared background radiation, its time evolution and the cosmic photon-photon opacity*, *Astronomy and Astrophysics* **487** (Sept., 2008) 837–852, [0805.1841].

[325] A. Domínguez et al., *Extragalactic background light inferred from AEGIS galaxy-SED-type fractions*, MNRAS **410** (Feb., 2011) 2556–2578, [1007.1459].

[326] W. H. Press and P. Schechter, *Formation of Galaxies and Clusters of Galaxies by Self-Similar Gravitational Condensation*, *The Astrophysical Journal* **187** (Feb., 1974) 425–438.

[327] A. Jenkins, C. S. Frenk, S. D. M. White, J. M. Colberg, S. Cole, A. E. Evrard et al., *The mass function of dark matter haloes*, MNRAS **321** (Feb., 2001) 372–384, [astro-ph/0005260].

[328] R. K. Sheth, H. J. Mo and G. Tormen, *Ellipsoidal collapse and an improved model for the number and spatial distribution of dark matter haloes*, MNRAS **323** (May, 2001) 1–12, [astro-ph/9907024].

[329] W. J. Percival, *The build-up of haloes within Press-Schechter theory*, MNRAS **327** (Nov., 2001) 1313–1322, [astro-ph/0107437].

[330] R. K. Sheth and G. Tormen, *Large-scale bias and the peak background split*, MNRAS **308** (Sept., 1999) 119–126, [astro-ph/9901122].

[331] A. Jenkins, C. S. Frenk, F. R. Pearce, P. A. Thomas, J. M. Colberg, S. D. M. White et al., *Evolution of structure in cold dark matter universes*, *The Astrophysical Journal* **499** (may, 1998) 20–40.

[332] S. Murray, C. Power and A. Robotham, *HMFcalc: An Online Tool for Calculating Dark Matter Halo Mass Functions*, 1306.6721.

[333] R. H. Wechsler, J. S. Bullock, J. R. Primack, A. V. Kravtsov and A. Dekel, *Concentrations of dark halos from their assembly histories*, *The Astrophysical Journal* **568** (Mar, 2002) 52–70.

[334] G. L. Bryan and M. L. Norman, *Statistical properties of x-ray clusters: Analytic and numerical comparisons*, *The Astrophysical Journal* **495** (mar, 1998) 80–99.

[335] A. Klypin, G. Yepes, S. Gottlöber, F. Prada and S. Heß, *MultiDark simulations: the story of dark matter halo concentrations and density profiles*, MNRAS **457** (02, 2016) 4340–4359, [https://academic.oup.com/mnras/article-pdf/457/4/4340/18515365/stw248.pdf].

[336] A. V. Macciò, A. A. Dutton and F. C. van den Bosch, *Concentration, spin and shape of dark matter haloes as a function of the cosmological model: WMAP1, WMAP3 and WMAP5 results*, MNRAS **391** (Dec., 2008) 1940–1954, [0805.1926].

[337] A. F. Neto et al., *The statistics of ΛCDM halo concentrations*, MNRAS **381** (10, 2007) 1450–1462.

[338] G. D. Martinez, J. S. Bullock, M. Kaplinghat, L. E. Strigari and R. Trotta, *Indirect Dark Matter Detection from Dwarf Satellites: Joint Expectations from Astrophysics and Supersymmetry*, *JCAP* **0906** (2009) 014, [0902.4715].

[339] T. Bringmann, *Particle models and the small-scale structure of dark matter*, *New Journal of Physics* **11** (oct, 2009) 105027.

[340] A. V. Maccio', A. A. Dutton and F. C. v. d. Bosch, *Concentration, Spin and Shape of Dark Matter Haloes as a Function of the Cosmological Model: WMAP1, WMAP3 and WMAP5 results*, *Mon. Not. Roy. Astron. Soc.* **391** (2008) 1940–1954, [0805.1926].

[341] MINIBOONE collaboration, A. A. Aguilar-Arevalo et al., *A Search for Electron Neutrino Appearance at the $\Delta m^2 \sim 1eV^2$ Scale*, *Phys. Rev. Lett.* **98** (2007) 231801, [0704.1500].

[342] MINIBOONE collaboration, A. A. Aguilar-Arevalo et al., *Event Excess in the MiniBooNE Search for $\bar{\nu}_\mu \to \bar{\nu}_e$ Oscillations*, *Phys. Rev. Lett.* **105** (2010) 181801, [1007.1150].

[343] T. A. Mueller et al., *Improved Predictions of Reactor Antineutrino Spectra*, *Phys. Rev. C* **83** (2011) 054615, [1101.2663].

[344] P. Huber, *On the determination of anti-neutrino spectra from nuclear reactors*, *Phys. Rev. C* **84** (2011) 024617, [1106.0687].

[345] G. Mention, M. Fechner, T. Lasserre, T. A. Mueller, D. Lhuillier, M. Cribier et al., *The Reactor Antineutrino Anomaly*, *Phys. Rev. D* **83** (2011) 073006, [1101.2755].

[346] GALLEX collaboration, P. Anselmann et al., *First results from the Cr-51 neutrino source experiment with the GALLEX detector*, *Phys. Lett. B* **342** (1995) 440–450.

[347] GALLEX collaboration, W. Hampel et al., *Final results of the Cr-51 neutrino source experiments in GALLEX*, *Phys. Lett. B* **420** (1998) 114–126.

[348] D. N. Abdurashitov et al., *The Russian-American gallium experiment (SAGE) Cr neutrino source measurement*, *Phys. Rev. Lett.* **77** (1996) 4708–4711.

[349] SAGE collaboration, J. N. Abdurashitov et al., *Measurement of the response of the Russian-American gallium experiment to neutrinos from a Cr-51 source*, *Phys. Rev. C* **59** (1999) 2246–2263, [hep-ph/9803418].

[350] J. N. Abdurashitov et al., *Measurement of the response of a Ga solar neutrino experiment to neutrinos from an Ar-37 source*, *Phys. Rev. C* **73** (2006) 045805, [nucl-ex/0512041].

[351] HYPER-KAMIOKANDE WORKING GROUP collaboration, T. Ishida, *T2HK: J-PARC upgrade plan for future and beyond T2K*, in *15th International Workshop on Neutrino Factories, Super Beams and Beta Beams*, 11, 2013. 1311.5287.

[352] Y. Abe, Y. Asano, N. Haba and T. Yamada, *Heavy neutrino mixing in the T2HK, the T2HKK and an extension of the T2HK with a detector at Oki Islands*, *Eur. Phys. J. C* **77** (2017) 851, [1705.03818].

[353] S. Choubey, D. Dutta and D. Pramanik, *Imprints of a light Sterile Neutrino at DUNE, T2HK and T2HKK*, *Phys. Rev. D* **96** (2017) 056026, [1704.07269].

[354] P. Coloma, D. V. Forero and S. J. Parke, *DUNE Sensitivities to the Mixing between Sterile and Tau Neutrinos*, *JHEP* **07** (2018) 079, [1707.05348].

[355] S. Dado, A. Dar and A. D. Rujula, *On the optical and X-ray afterglows of gamma-ray bursts*, *Astron. Astrophys.* **388** (2002) 1079, [astro-ph/0107367].

[356] A. Dar and A. De Rujula, *Towards a complete theory of gamma-ray bursts*, *Phys. Rept.* **405** (2004) 203–278, [astro-ph/0308248].

[357] A. Dar, *Fireball and cannonball models of gamma-ray bursts confront observations*, *Chin. J. Astron. Astrophys.* **6** (2006) 301, [astro-ph/0511622].

[358] S. Dado and A. Dar, *The cannonball model of long GRBs - overview*, *AIP Conf. Proc.* **1111** (2009) 333–343, [0901.4260].

[359] S. K. Kang, Y.-D. Kim, Y.-J. Ko and K. Siyeon, *Four-Neutrino Analysis of 1.5 km Baseline Reactor Antineutrino Oscillations*, *Adv. High Energy Phys.* **2013** (2013) 138109, [1408.3211].

[360] H. Athar, M. Jezabek and O. Yasuda, *Effects of neutrino mixing on high-energy cosmic neutrino flux*, *Phys. Rev. D* **62** (2000) 103007, [hep-ph/0005104].

[361] E. Waxman and J. N. Bahcall, *High-energy neutrinos from astrophysical sources: An Upper bound*, *Phys. Rev. D* **59** (1999) 023002, [hep-ph/9807282].

[362] R. Gandhi, C. Quigg, M. H. Reno and I. Sarcevic, *Neutrino interactions at ultrahigh-energies*, *Phys. Rev. D* **58** (1998) 093009, [hep-ph/9807264].

[363] R. Gandhi, C. Quigg, M. H. Reno and I. Sarcevic, *Ultrahigh-energy neutrino interactions*, *Astropart. Phys.* **5** (1996) 81–110, [hep-ph/9512364].

[364] T. K. Gaisser, F. Halzen and T. Stanev, *Particle astrophysics with high-energy neutrinos*, *Phys. Rept.* **258** (1995) 173–236, [hep-ph/9410384].

[365] N. Gupta, *Neutrino induced upward going muons from a gamma-ray burst in a neutrino telescope of Km**2 area*, *Phys. Rev. D* **65** (2002) 113005, [astro-ph/0201509].

[366] A. M. Dziewonski and D. L. Anderson, *Preliminary reference earth model*, *Physics of the Earth and Planetary Interiors* **25** (1981) 297–356.

[367] A. Dar, J. J. Lord and R. J. Wilkes, *On the Nature of the High-energy Particles From Cygnus X-3*, *Phys. Rev. D* **33** (1986) 303.

[368] D. Guetta, D. Hooper, J. Alvarez-Muniz, F. Halzen and E. Reuveni, *Neutrinos from individual gamma-ray bursts in the BATSE catalog*, *Astropart. Phys.* **20** (2004) 429–455, [astro-ph/0302524].

[369] S. I. Dutta, M. H. Reno and I. Sarcevic, *Tau neutrinos underground: Signals of muon-neutrino —> tau neutrino oscillations with extragalactic neutrinos*, *Phys. Rev. D* **62** (2000) 123001, [hep-ph/0005310].

[370] N. Gupta, *The appearance of tau neutrinos from a gamma-ray burst*, *Phys. Lett. B* **541** (2002) 16–21, [astro-ph/0205451].

[371] ICECUBE collaboration, M. G. Aartsen et al., *Search for sterile neutrino mixing using three years of IceCube DeepCore data*, *Phys. Rev. D* **95** (2017) 112002, [1702.05160].

[372] ICECUBE collaboration, C. Kopper, *Observation of Astrophysical Neutrinos in Six Years of IceCube Data*, *PoS* **ICRC2017** (2018) 981.

[373] EXO-200 collaboration, J. B. Albert et al., *Search for Majorana neutrinos with the first two years of EXO-200 data*, *Nature* **510** (2014) 229–234, [1402.6956].

[374] J.-H. Liu and S. Zhou, *Another look at the impact of an eV-mass sterile neutrino on the effective neutrino mass of neutrinoless double-beta decays*, *Int. J. Mod. Phys. A* **33** (2018) 1850014, [1710.10359].

[375] ICECUBE collaboration, M. G. Aartsen et al., *Searches for Sterile Neutrinos with the IceCube Detector*, *Phys. Rev. Lett.* **117** (2016) 071801, [1605.01990].

[376] P. L. Biermann and P. A. Strittmatter, *Synchrotron emission from shock waves in active galactic nuclei*, *Astrophys. J.* **322** (1987) 643–649.

[377] C. M. Urry and P. Padovani, *Unified schemes for radio-loud active galactic nuclei*, *Publ. Astron. Soc. Pac.* **107** (1995) 803, [astro-ph/9506063].

[378] G. Ghisellini, L. Maraschi and A. Treves, *Inhomogeneous synchrotron-self-compton models and the problem of relativistic beaming of BL Lac objects.*, A&A **146** (May, 1985) 204–212.

[379] G. Ghisellini and F. Tavecchio, *Canonical high power blazars*, *Mon. Not. Roy. Astron. Soc.* **397** (2009) 985–1002, [0902.0793].

[380] M. Sikora, M. C. Begelman and M. J. Rees, *Comptonization of diffuse ambient radiation by a relativistic jet: The source of gamma rays from blazars?*, *Astrophys. J.* **421** (1994) 153.

[381] J. Albert et al., *Variable VHE gamma-ray emission from Markarian 501*, *Astrophys. J.* **669** (2007) 862–883, [astro-ph/0702008].

[382] F. Aharonian et al., *An Exceptional Very High Energy Gamma-Ray Flare of PKS 2155-304*, *Astrophys. J. Lett.* **664** (2007) L71–L78, [0706.0797].

[383] ICECUBE, FERMI-LAT, MAGIC, AGILE, ASAS-SN, HAWC, H.E.S.S., INTEGRAL, KANATA, KISO, KAPTEYN, LIVERPOOL TELESCOPE, SUBARU, SWIFT NUSTAR, VERITAS, VLA/17B-403 collaboration, M. G. Aartsen et al., *Multimessenger observations of a flaring blazar coincident with high-energy neutrino IceCube-170922A*, *Science* **361** (2018) eaat1378, [1807.08816].

[384] ICECUBE collaboration, M. G. Aartsen et al., *Neutrino emission from the direction of the blazar TXS 0506+056 prior to the IceCube-170922A alert*, *Science* **361** (2018) 147–151, [1807.08794].

[385] MAGIC collaboration, S. Ansoldi et al., *The blazar TXS 0506+056 associated with a high-energy neutrino: insights into extragalactic jets and cosmic ray acceleration*, *Astrophys. J. Lett.* **863** (2018) L10, [1807.04300].

[386] Y. T. Tanaka, S. Buson and D. Kocevski, *Fermi-LAT detection of increased gamma-ray activity of TXS 0506+056, located inside the IceCube-170922A error region.*, *The Astronomer's Telegram* **10791** (Sept., 2017) 1.

[387] A. Keivani et al., *A Multimessenger Picture of the Flaring Blazar TXS 0506+056: implications for High-Energy Neutrino Emission and Cosmic Ray Acceleration*, *Astrophys. J.* **864** (2018) 84, [1807.04537].

[388] R. Mirzoyan, *First-time detection of VHE gamma rays by MAGIC from a direction consistent with the recent EHE neutrino event IceCube-170922A*, *The Astronomer's Telegram* **10817** (Oct., 2017) 1.

[389] P. Padovani, P. Giommi, E. Resconi, T. Glauch, B. Arsioli, N. Sahakyan et al., *Dissecting the region around IceCube-170922A: the blazar TXS 0506+056 as the first cosmic neutrino source*, *Mon. Not. Roy. Astron. Soc.* **480** (2018) 192–203, [1807.04461].

[390] H.-N. He, Y. Inoue, S. Inoue and Y.-F. Liang, *High-energy neutrino flare from cloud-jet interaction in the blazar PKS 0502+049*, 1808.04330.

[391] FERMI-LAT, ASAS-SN, ICECUBE collaboration, S. Garrappa et al., *Investigation of two Fermi-LAT gamma-ray blazars coincident with high-energy neutrinos detected by IceCube*, *Astrophys. J.* **880** (2019) 880:103, [1901.10806].

[392] P. Banik and A. Bhadra, *Describing correlated observations of neutrinos and gamma-ray flares from the blazar TXS 0506+056 with a proton blazar model*, *Phys. Rev. D* **99** (2019) 103006, [1908.11849].

[393] S. Gao, A. Fedynitch, W. Winter and M. Pohl, *Modelling the coincident observation of a high-energy neutrino and a bright blazar flare*, *Nature Astron.* **3** (2019) 88–92, [1807.04275].

[394] M. Cerruti, A. Zech, C. Boisson, G. Emery, S. Inoue and J. P. Lenain, *Leptohadronic single-zone models for the electromagnetic and neutrino emission of TXS 0506+056*, *Mon. Not. Roy. Astron. Soc.* **483** (2019) L12–L16, [1807.04335].

[395] R.-Y. Liu, K. Wang, R. Xue, A. M. Taylor, X.-Y. Wang, Z. Li et al., *Hadronuclear interpretation of a high-energy neutrino event coincident with a blazar flare*, *Phys. Rev. D* **99** (2019) 063008, [1807.05113].

[396] N. Sahakyan, *Lepto-hadronic γ-ray and neutrino emission from the jet of TXS 0506+056*, *Astrophys. J.* **866** (2018) 109, [1808.05651].

[397] K. Murase, F. Oikonomou and M. Petropoulou, *Blazar Flares as an Origin of High-Energy Cosmic Neutrinos?*, *Astrophys. J.* **865** (2018) 124, [1807.04748].

[398] A. Celotti and A. C. Fabian, *The Kinetic Power and Luminosity of Parsecscale Radio Jets - an Argument for Heavy Jets*, *Mon. Not. Roy. Astron. Soc.* **264** (1993) 228.

[399] G. Ghisellini, F. Tavecchio, L. Foschini, G. Ghirlanda, L. Maraschi and A. Celotti, *General physical properties of bright Fermi blazars*, *Mon. Not. Roy. Astron. Soc.* **402** (2010) 497, [0909.0932].

[400] K. Katarzyński, H. Sol and A. Kus, *The multifrequency emission of Mrk 501. From radio to TeV gamma-rays*, A&A **367** (Mar., 2001) 809–825.

[401] M. Boettcher, A. Reimer, K. Sweeney and A. Prakash, *Leptonic and Hadronic Modeling of Fermi-Detected Blazars*, *Astrophys. J.* **768** (2013) 54, [1304.0605].

[402] D. Eichler and E. Waxman, *The Efficiency of electron acceleration in collisionless shocks and GRB energetics*, *Astrophys. J.* **627** (2005) 861–867, [astro-ph/0502070].

[403] D. Caprioli, A.-R. Pop and A. Spitkovsky, *SIMULATIONS AND THEORY OF ION INJECTION AT NON-RELATIVISTIC COLLISIONLESS SHOCKS*, *The Astrophysical Journal* **798** (dec, 2014) L28.

[404] J. Giacalone, D. Burgess, S. J. Schwartz and D. C. Ellison, *Hybrid simulations of protons strongly accelerated by a parallel collisionless shock*, Geophys. Res. Lett. **19** (Mar., 1992) 433–436.

[405] A. M. Bykov and P. Meszaros, *Electron acceleration and efficiency in nonthermal gamma-ray sources*, *Astrophys. J. Lett.* **461** (1996) L37–L40, [astro-ph/9602016].

[406] F. Vazza, D. Eckert, M. Brüggen and B. Huber, *Electron and proton acceleration efficiency by merger shocks in galaxy clusters*, *Mon. Not. Roy. Astron. Soc.* **451** (2015) 2198–2211, [1505.02782].

[407] G. R. Blumenthal and R. J. Gould, *Bremsstrahlung, synchrotron radiation, and compton scattering of high-energy electrons traversing dilute gases*, *Rev. Mod. Phys.* **42** (1970) 237–270.

[408] S. Inoue and F. Takahara, *Electron acceleration and gamma-ray emission from blazars*, *Astrophys. J.* **463** (1996) 555–564.

[409] C. D. Dermer and R. Schlickeiser, *Transformation properties of external radiation fields, energy-loss rates and scattered spectra, and a model for blazar variability*, *Astrophys. J.* **575** (2002) 667–686, [astro-ph/0202280].

[410] M. Malkov and L. O. Drury, *Nonlinear theory of diffusive acceleration of particles by shock waves*, *Rept. Prog. Phys.* **64** (2001) 429–481.

[411] M. Cerruti, A. Zech, C. Boisson and S. Inoue, *A hadronic origin for ultra-high-frequency-peaked BL Lac objects*, *Mon. Not. Roy. Astron. Soc.* **448** (2015) 910–927, [1411.5968].

[412] L. A. Anchordoqui, J. F. Beacom, H. Goldberg, S. Palomares-Ruiz and T. J. Weiler, *TeV γ^- rays and neutrinos from photo-disintegration of nuclei in Cygnus OB2*, *Phys. Rev. D* **75** (2007) 063001, [astro-ph/0611581].

[413] P. Banik, B. Bijay, S. K. Sarkar and A. Bhadra, *Probing the cosmic ray mass composition in the knee region through TeV secondary particle fluxes from solar surroundings*, *Phys. Rev. D* **95** (2017) 063014, [1703.05083].

[414] S. R. Kelner, F. A. Aharonian and V. V. Bugayov, *Energy spectra of gamma-rays, electrons and neutrinos produced at proton-proton interactions in the very high energy regime*, *Phys. Rev. D* **74** (2006) 034018, [astro-ph/0606058].

[415] F. Aharonian, D. Khangulyan and L. Costamante, *Formation of hard VHE gamma-ray spectra of blazars due to internal photon-photon absorption*, *Mon. Not. Roy. Astron. Soc.* **387** (2008) 1206–1214, [0801.3198].

[416] A. M. Atoyan and C. D. Dermer, *Neutral beams from blazar jets*, *Astrophys. J.* **586** (2003) 79–96, [astro-ph/0209231].

[417] PARTICLE DATA GROUP collaboration, M. Tanabashi et al., *Review of Particle Physics*, *Phys. Rev. D* **98** (2018) 030001.

[418] F. Halzen, *High-energy neutrino astrophysics*, *Nature Phys.* **13** (2016) 232–238.

[419] ICECUBE collaboration, M. G. Aartsen et al., *Observation and Characterization of a Cosmic Muon Neutrino Flux from the Northern Hemisphere using six years of IceCube data*, *Astrophys. J.* **833** (2016) 3, [1607.08006].

[420] A. Maselli, F. Massaro, R. D'Abrusco, G. Cusumano, V. La Parola, A. Segreto et al., *New blazars from the cross-match of recent multi-frequency catalogs*, *Astrophys. Space Sci.* **357** (2015) 141, [1504.07236].

[421] SDSS collaboration, C. P. Ahn et al., *The Ninth Data Release of the Sloan Digital Sky Survey: First Spectroscopic Data from the SDSS-III Baryon Oscillation Spectroscopic Survey*, *Astrophys. J. Suppl.* **203** (2012) 21, [1207.7137].

[422] S. Paiano, R. Falomo, A. Treves and R. Scarpa, *The redshift of the BL Lac object TXS 0506+056*, *Astrophys. J. Lett.* **854** (2018) L32, [1802.01939].

[423] N. Sahakyan, *Origin of the multiwavelength emission of PKS 0502+049*, *Astron. Astrophys.* **622** (2019) A144, [1812.06338].

[424] M. J. Drinkwater, R. L. Webster, P. J. Francis, J. J. Condon, S. L. Ellison, D. L. Jauncey et al., *The parkes half-jansky flat-spectrum sample*, *Mon. Not. Roy. Astron. Soc.* **284** (1997) 85, [astro-ph/9609019].

[425] X. Rodrigues, S. Gao, A. Fedynitch, A. Palladino and W. Winter, *Leptohadronic Blazar Models Applied to the 2014–2015 Flare of TXS 0506+056*, *Astrophys. J. Lett.* **874** (2019) L29, [1812.05939].

[426] CTA collaboration, R. A. Ong, *Cherenkov Telescope Array: The Next Generation Gamma-ray Observatory*, *PoS* **ICRC2017** (2018) 1071, [1709.05434].

[427] LHAASO collaboration, C. Liu et al., *The dynamic range extension system for the LHAASO-WCDA experiment*, *PoS* **ICRC2017** (2018) 424.

[428] H. Georgi, *Unparticle physics*, *Phys. Rev. Lett.* **98** (2007) 221601, [hep-ph/0703260].

[429] H. Georgi, *Another odd thing about unparticle physics*, *Phys. Lett. B* **650** (2007) 275–278, [0704.2457].

[430] K. Cheung, W.-Y. Keung and T.-C. Yuan, *Collider signals of unparticle physics*, *Phys. Rev. Lett.* **99** (2007) 051803, [0704.2588].

[431] T. Banks and A. Zaks, *On the Phase Structure of Vector-Like Gauge Theories with Massless Fermions*, *Nucl. Phys. B* **196** (1982) 189–204.

[432] S. R. Coleman and E. J. Weinberg, *Radiative Corrections as the Origin of Spontaneous Symmetry Breaking*, *Phys. Rev. D* **7** (1973) 1888–1910.

[433] T. Kikuchi and N. Okada, *Unparticle physics and Higgs phenomenology*, *Phys. Lett. B* **661** (2008) 360–364, [0707.0893].

[434] C.-H. Chen and C.-Q. Geng, *Unparticle physics on direct CP violation*, *Phys. Rev. D* **76** (2007) 115003, [0705.0689].

[435] T. M. Aliev, A. S. Cornell and N. Gaur, *Lepton flavour violation in unparticle physics*, *Phys. Lett. B* **657** (2007) 77–80, [0705.1326].

[436] T. M. Aliev, A. S. Cornell and N. Gaur, *B —> K(K*) missing energy in Unparticle physics*, *JHEP* **07** (2007) 072, [0705.4542].

[437] X.-Q. Li and Z.-T. Wei, *Unparticle Physics Effects on D0 - anti-D0 Mixing*, *Phys. Lett. B* **651** (2007) 380–383, [0705.1821].

[438] M. Duraisamy, *Unparticle physics in e+ e- —> P P annihilation*, 0705.2622.

[439] D. Choudhury, D. K. Ghosh and Mamta, *Unparticles and Muon Decay*, *Phys. Lett. B* **658** (2008) 148–154, [0705.3637].

[440] C.-D. Lu, W. Wang and Y.-M. Wang, *Lepton flavor violating processes in unparticle physics*, *Phys. Rev. D* **76** (2007) 077701, [0705.2909].

[441] N. Greiner, *Constraints on unparticle physics in electroweak gauge boson scattering*, *Phys. Lett. B* **653** (2007) 75–80, [0705.3518].

[442] H. Davoudiasl, *Constraining Unparticle Physics with Cosmology and Astrophysics*, *Phys. Rev. Lett.* **99** (2007) 141301, [0705.3636].

[443] P. Mathews and V. Ravindran, *Unparticle physics at hadron collider via dilepton production*, *Phys. Lett. B* **657** (2007) 198–206, [0705.4599].

[444] D. Majumdar, *Unparticle decay of neutrinos and it's effect on ultra high energy neutrinos*, 0708.3485.

[445] G.-J. Ding and M.-L. Yan, *Signals of unparticles in low energy parity violation and the NuTeV experiment*, *Phys. Rev. D* **78** (2008) 075015, [0706.0325].

[446] A. Lenz, *Unparticle physics effects in $B_s - \bar{B}_s$ mixing*, *Phys. Rev. D* **76** (2007) 065006, [0707.1535].

[447] D. Choudhury and D. K. Ghosh, *Top off the unparticle*, *Int. J. Mod. Phys. A* **23** (2008) 2579–2590, [0707.2074].

[448] M. Luo and G. Zhu, *Some phenomenologies of unparticle physics*, *Phys. Lett. B* **659** (2008) 341–344, [0704.3532].

[449] N. G. Deshpande, X.-G. He and J. Jiang, *Supersymmetric Unparticle Effects on Higgs Boson Mass and Dark Matter*, *Phys. Lett. B* **656** (2007) 91–95, [0707.2959].

[450] M. Neubert, *Unparticle Physics with Jets*, *Phys. Lett. B* **660** (2008) 592–596, [0708.0036].

[451] G. Bhattacharyya, D. Choudhury and D. K. Ghosh, *Unraveling unparticles through violation of atomic parity and rare beauty*, *Phys. Lett. B* **655** (2007) 261–268, [0708.2835].

[452] Z.-H. Li, Y. Li and H.-X. Xu, *Unparticle-Induced Lepton Flavor Violating Decays tau- —> l-(V0, P0)*, *Phys. Lett. B* **677** (2009) 150–156, [0901.3266].

[453] A. Delgado, J. R. Espinosa, J. M. No and M. Quiros, *A Note on Unparticle Decays*, *Phys. Rev. D* **79** (2009) 055011, [0812.1170].

[454] E. O. Iltan, *Lepton flavor violating Higgs decays induced by massive unparticle*, *Acta Phys. Polon. B* **41** (2010) 2423, [1006.2095].

[455] G. A. Kozlov and I. N. Gorbunov, *On decays of Z' into unparticle stuff*, *Adv. High Energy Phys.* **2011** (2011) 975237, [1009.0103].

[456] K.-S. Sun, T.-F. Feng, L.-N. Kou, F. Sun, T.-J. Gao and H.-B. Zhang, *Lepton flavor violation decays of vector mesons in unparticle physics*, *Mod. Phys. Lett. A* **27** (2012) 1250172, [1312.2072].

[457] M. Ettefaghi, R. Moazzemi and M. Rousta, *Constraining unparticle physics from CP violation in Cabibbo-favored decays of D mesons*, *Phys. Rev. D* **95** (2017) 095027, [1705.06330].

[458] M. M. Ettefaghi and M. Dehghani, *The Decay of singlet scalar dark matter to unparticle and photon*, 0805.0682.

[459] M. Jamil, D. Momeni and M. A. Rashid, *Notes on dark energy interacting with dark matter and unparticle in loop quantum cosmology*, *Eur. Phys. J. C* **71** (2011) 1711, [1107.1558].

[460] D. Guetta, M. Spada and E. Waxman, *On the neutrino flux from gamma-ray bursts*, *Astrophys. J.* **559** (2001) 101, [astro-ph/0102487].

[461] N. Gupta and P. Bhattacharjee, *Detecting TeV gamma-rays from gamma-ray bursts by ground based muon detectors*, astro-ph/0108311.

[462] P. Baerwald, M. Bustamante and W. Winter, *Neutrino Decays over Cosmological Distances and the Implications for Neutrino Telescopes*, *JCAP* **10** (2012) 020, [1208.4600].

[463] S. Zhou, *Neutrino Decays and Neutrino Electron Elastic Scattering in Unparticle Physics*, *Phys. Lett. B* **659** (2008) 336–340, [0706.0302].

[464] M. Pandey, D. Majumdar and A. Dutta Banik, *Probing a four flavor vis-a-vis three flavor neutrino mixing for ultrahigh energy neutrino signals at a 1* Km^2 *detector*, *Phys. Rev. D* **97** (2018) 103015, [1711.05018].

[465] J. F. Beacom, N. F. Bell, D. Hooper, S. Pakvasa and T. J. Weiler, *Decay of High-Energy Astrophysical Neutrinos*, *Phys. Rev. Lett.* **90** (2003) 181301, [hep-ph/0211305].

[466] S. Pakvasa, *CHARGED LEPTON OSCILLATIONS*, *Lett. Nuovo Cim.* **31** (1981) 497.

[467] Y. Farzan and A. Y. Smirnov, *Leptonic unitarity triangle and CP violation*, *Phys. Rev. D* **65** (2002) 113001, [hep-ph/0201105].

[468] PLANCK collaboration, P. A. R. Ade et al., *Planck 2015 results. XIII. Cosmological parameters*, *Astron. Astrophys.* **594** (2016) A13, [1502.01589].

[469] A. Loeb and E. Waxman, *The Cumulative background of high energy neutrinos from starburst galaxies*, *JCAP* **05** (2006) 003, [astro-ph/0601695].

[470] K. Murase, M. Ahlers and B. C. Lacki, *Testing the Hadronuclear Origin of PeV Neutrinos Observed with IceCube*, *Phys. Rev. D* **88** (2013) 121301, [1306.3417].

[471] O. Kalashev, D. Semikoz and I. Tkachev, *Neutrinos in IceCube from active galactic nuclei*, *J. Exp. Theor. Phys.* **120** (2015) 541–548, [1410.8124].

[472] A. Anisimov and P. Di Bari, *Cold Dark Matter from heavy Right-Handed neutrino mixing*, *Phys. Rev. D* **80** (2009) 073017, [0812.5085].

[473] J. Zavala, *Galactic PeV neutrinos from dark matter annihilation*, *Phys. Rev. D* **89** (2014) 123516, [1404.2932].

[474] A. Bhattacharya, R. Gandhi and A. Gupta, *The Direct Detection of Boosted Dark Matter at High Energies and PeV events at IceCube*, *JCAP* **03** (2015) 027, [1407.3280].

[475] E. Dudas, Y. Mambrini and K. A. Olive, *Monochromatic neutrinos generated by dark matter and the seesaw mechanism*, *Phys. Rev. D* **91** (2015) 075001, [1412.3459].

[476] C. El Aisati, C. Garcia-Cely, T. Hambye and L. Vanderheyden, *Prospects for discovering a neutrino line induced by dark matter annihilation*, *JCAP* **10** (2017) 021, [1706.06600].

[477] L. Covi, M. Grefe, A. Ibarra and D. Tran, *Neutrino Signals from Dark Matter Decay*, *JCAP* **04** (2010) 017, [0912.3521].

[478] A. Esmaili, S. K. Kang and P. D. Serpico, *IceCube events and decaying dark matter: hints and constraints*, *JCAP* **12** (2014) 054, [1410.5979].

[479] C. Rott, K. Kohri and S. C. Park, *Superheavy dark matter and IceCube neutrino signals: Bounds on decaying dark matter*, *Phys. Rev. D* **92** (2015) 023529, [1408.4575].

[480] A. Esmaili and P. D. Serpico, *Are IceCube neutrinos unveiling PeV-scale decaying dark matter?*, *JCAP* **11** (2013) 054, [1308.1105].

[481] A. Esmaili, A. Ibarra and O. L. G. Peres, *Probing the stability of superheavy dark matter particles with high-energy neutrinos*, *JCAP* **11** (2012) 034, [1205.5281].

[482] C. S. Fong, H. Minakata, B. Panes and R. Zukanovich Funchal, *Possible Interpretations of IceCube High-Energy Neutrino Events*, *JHEP* **02** (2015) 189, [1411.5318].

[483] C. El Aisati, M. Gustafsson and T. Hambye, *New Search for Monochromatic Neutrinos from Dark Matter Decay*, *Phys. Rev. D* **92** (2015) 123515, [1506.02657].

[484] S. M. Boucenna, M. Chianese, G. Mangano, G. Miele, S. Morisi, O. Pisanti et al., *Decaying Leptophilic Dark Matter at IceCube*, *JCAP* **12** (2015) 055, [1507.01000].

[485] S. Troitsky, *Search for Galactic disk and halo components in the arrival directions of high-energy astrophysical neutrinos*, *JETP Lett.* **102** (2015) 785–788, [1511.01708].

[486] M. Chianese, G. Miele, S. Morisi and E. Vitagliano, *Low energy IceCube data and a possible Dark Matter related excess*, *Phys. Lett. B* **757** (2016) 251–256, [1601.02934].

[487] M. Chianese, G. Miele and S. Morisi, *Dark Matter interpretation of low energy IceCube MESE excess*, *JCAP* **01** (2017) 007, [1610.04612].

[488] A. Bhattacharya, A. Esmaili, S. Palomares-Ruiz and I. Sarcevic, *Probing decaying heavy dark matter with the 4-year IceCube HESE data*, *JCAP* **07** (2017) 027, [1706.05746].

[489] M. Chianese, G. Miele and S. Morisi, *Interpreting IceCube 6-year HESE data as an evidence for hundred TeV decaying Dark Matter*, *Phys. Lett. B* **773** (2017) 591–595, [1707.05241].

[490] ICECUBE collaboration, M. G. Aartsen et al., *Search for neutrinos from decaying dark matter with IceCube*, *Eur. Phys. J. C* **78** (2018) 831, [1804.03848].

[491] P. S. B. Dev, D. Kazanas, R. N. Mohapatra, V. L. Teplitz and Y. Zhang, *Heavy right-handed neutrino dark matter and PeV neutrinos at IceCube*, *JCAP* **08** (2016) 034, [1606.04517].

[492] Y. Sui and P. B. Dev, *A combined astrophysical and dark matter interpretation of the IceCube HESE and throughgoing muon events*, *Journal of Cosmology and Astroparticle Physics* **2018** (jul, 2018) 020–020.

[493] N. Hiroshima, R. Kitano, K. Kohri and K. Murase, *High-energy neutrinos from multibody decaying dark matter*, *Phys. Rev. D* **97** (2018) 023006, [1705.04419].

[494] C. Wiebusch, *Review on high energy neutrino measurements*, in *Contributed Talk at SSP - Aachen, 2018*, 2018.

[495] V. A. Kuzmin and I. I. Tkachev, *Ultrahigh-energy cosmic rays and inflation relics*, *Phys. Rept.* **320** (1999) 199–221, [hep-ph/9903542].

[496] R. Aloisio, V. Berezinsky and M. Kachelriess, *Fragmentation functions in SUSY QCD and UHECR spectra produced in top - down models*, *Phys. Rev. D* **69** (2004) 094023, [hep-ph/0307279].

[497] G. Bertone, *Particle Dark Matter : Observations, Models and Searches*. 2010.

[498] M. Kachelriess, O. E. Kalashev and M. Y. Kuznetsov, *Heavy decaying dark matter and IceCube high energy neutrinos*, *Phys. Rev. D* **98** (2018) 083016, [1805.04500].

[499] V. Berezinsky, M. Kachelriess and S. Ostapchenko, *Electroweak jet cascading in the decay of superheavy particles*, *Phys. Rev. Lett.* **89** (2002) 171802, [hep-ph/0205218].

[500] C. T. Hill, *Monopolonium*, *Nucl. Phys. B* **224** (1983) 469–490.

[501] P. Bhattacharjee and G. Sigl, *Monopole annihilation and highest energy cosmic rays*, *Phys. Rev. D* **51** (1995) 4079–4091, [astro-ph/9412053].

[502] V. Berezinsky and A. Vilenkin, *Cosmic necklaces and ultrahigh-energy cosmic rays*, *Phys. Rev. Lett.* **79** (1997) 5202–5205, [astro-ph/9704257].

[503] V. Berezinsky and M. Kachelriess, *Monte Carlo simulation for jet fragmentation in SUSY QCD*, *Phys. Rev. D* **63** (2001) 034007, [hep-ph/0009053].

[504] V. N. Gribov and L. N. Lipatov, *Deep inelastic e p scattering in perturbation theory*, *Sov. J. Nucl. Phys.* **15** (1972) 438–450.

[505] G. Altarelli and G. Parisi, *Asymptotic Freedom in Parton Language*, *Nucl. Phys. B* **126** (1977) 298–318.

[506] M. Ciafaloni, P. Ciafaloni and D. Comelli, *Towards collinear evolution equations in electroweak theory*, *Phys. Rev. Lett.* **88** (2002) 102001, [hep-ph/0111109].

[507] P. Ciafaloni and D. Comelli, *Sudakov enhancement of electroweak corrections*, *Phys. Lett. B* **446** (1999) 278–284, [hep-ph/9809321].

[508] M. Beccaria, P. Ciafaloni, D. Comelli, F. Renard and C. Verzegnassi, *Logarithmic expansion of electroweak corrections to four-fermion processes in the tev region*, *Phys. Rev. D* **61** (Mar, 2000) 073005.

[509] V. S. Fadin, L. N. Lipatov, A. D. Martin and M. Melles, *Resummation of double logarithms in electroweak high energy processes*, *Phys. Rev. D* **61** (Mar, 2000) 094002.

[510] W. Beenakker and A. Werthenbach, *New insights into the perturbative structure of electroweak Sudakov logarithms*, *Phys. Lett. B* **489** (2000) 148–156, [hep-ph/0005316].

[511] M. Hori, H. Kawamura and J. Kodaira, *Electroweak Sudakov at two loop level*, *Phys. Lett. B* **491** (2000) 275–279, [hep-ph/0007329].

[512] A. Denner and S. Pozzorini, *One loop leading logarithms in electroweak radiative corrections. 1. Results*, *Eur. Phys. J. C* **18** (2001) 461–480, [hep-ph/0010201].

[513] V. Berezinsky and M. Kachelriess, *Monte carlo simulation for jet fragmentation in susy qcd*, *Phys. Rev. D* **63** (Jan, 2001) 034007.

[514] M. Chianese, *IceCube PeV Neutrinos and Leptophilic Dark Matter*, *J. Phys. Conf. Ser.* **718** (2016) 042014, [1605.05749].

[515] M. Gasperini, *Testing the Principle of Equivalence with Neutrino Oscillations*, *Phys. Rev. D* **38** (1988) 2635–2637.

[516] M. Gasperini, *Experimental constraints on a minimal and nonminimal violation of the equivalence principle in the oscillations of massive neutrinos*, *Phys. Rev. D* **39** (Jun, 1989) 3606–3611.

[517] M. Gasperini, *Testing the principle of equivalence with neutrino oscillations*, *Phys. Rev. D* **38** (Oct, 1988) 2635–2637.

[518] M. Adams, F. Bezrukov, J. Elvin-Poole, J. J. Evans, P. Guzowski, B. O. Fearraigh et al., *Direct comparison of sterile neutrino constraints from cosmological data, ν_e disappearance data and $\nu_\mu \to \nu_e$ appearance data in a $3+1$ model*, *Eur. Phys. J. C* **80** (2020) 758, [2002.07762].

[519] MINOS, MINOS+ collaboration, S. De Rijck, *Latest Results from MINOS and MINOS+*, *J. Phys. Conf. Ser.* **873** (2017) 012032.

[520] D. Majumdar and A. Ghosal, *Probing deviations from tri-bimaximal mixing through ultra high energy neutrino signals*, *Phys. Rev. D* **75** (2007) 113004, [hep-ph/0608334].

[521] A. Esmaili, D. R. Gratieri, M. M. Guzzo, P. C. de Holanda, O. L. G. Peres and G. A. Valdiviesso, *Constraining the violation of the equivalence principle with IceCube atmospheric neutrino data*, *Phys. Rev. D* **89** (2014) 113003, [1404.3608].

[522] S. Geer, *Neutrino beams from muon storage rings: Characteristics and physics potential*, *Phys. Rev. D* **57** (1998) 6989–6997, [hep-ph/9712290].

[523] A. Donini, D. Meloni and P. Migliozzi, *The Silver channel at the neutrino factory*, *Nucl. Phys. B* **646** (2002) 321–349, [hep-ph/0206034].

[524] A. M. Dziewonski and D. L. Anderson, *Preliminary reference earth model*, *Phys. Earth Planet. Interiors* **25** (1981) 297–356.

[525] LIGO SCIENTIFIC, VIRGO collaboration, B. P. Abbott et al., *Observation of Gravitational Waves from a Binary Black Hole Merger*, *Phys. Rev. Lett.* **116** (2016) 061102, [1602.03837].

[526] A. A. Starobinsky, *Spectrum of relict gravitational radiation and the early state of the universe*, *JETP Lett.* **30** (1979) 682–685.

[527] A. Vilenkin and E. P. S. Shellard, *Cosmic Strings and Other Topological Defects*. Cambridge University Press, 7, 2000.

[528] E. Witten, *Cosmic Separation of Phases*, *Phys. Rev. D* **30** (1984) 272–285.

[529] C. J. Hogan, *Gravitational radiation from cosmological phase transitions*, *Mon. Not. Roy. Astron. Soc.* **218** (1986) 629–636.

[530] J. Kozaczuk, S. Profumo, L. S. Haskins and C. L. Wainwright, *Cosmological Phase Transitions and their Properties in the NMSSM*, *JHEP* **01** (2015) 144, [1407.4134].

[531] S. Profumo, M. J. Ramsey-Musolf, C. L. Wainwright and P. Winslow, *Singlet-catalyzed electroweak phase transitions and precision Higgs boson studies*, *Phys. Rev. D* **91** (2015) 035018, [1407.5342].

[532] I. Baldes and C. Garcia-Cely, *Strong gravitational radiation from a simple dark matter model*, *JHEP* **05** (2019) 190, [1809.01198].

[533] D. Croon, V. Sanz and G. White, *Model Discrimination in Gravitational Wave spectra from Dark Phase Transitions*, *JHEP* **08** (2018) 203, [1806.02332].

[534] P. Schwaller, *Gravitational Waves from a Dark Phase Transition*, *Phys. Rev. Lett.* **115** (2015) 181101, [1504.07263].

[535] V. Vaskonen, *Electroweak baryogenesis and gravitational waves from a real scalar singlet*, *Phys. Rev. D* **95** (2017) 123515, [1611.02073].

[536] W. Chao, H.-K. Guo and J. Shu, *Gravitational Wave Signals of Electroweak Phase Transition Triggered by Dark Matter*, *JCAP* **09** (2017) 009, [1702.02698].

[537] T. Hasegawa, N. Okada and O. Seto, *Gravitational waves from the minimal gauged $U(1)_{B-L}$ model*, *Phys. Rev. D* **99** (2019) 095039, [1904.03020].

[538] M. Artymowski, M. Lewicki and J. D. Wells, *Gravitational wave and collider implications of electroweak baryogenesis aided by non-standard cosmology*, *JHEP* **03** (2017) 066, [1609.07143].

[539] P. S. B. Dev, F. Ferrer, Y. Zhang and Y. Zhang, *Gravitational Waves from First-Order Phase Transition in a Simple Axion-Like Particle Model*, *JCAP* **11** (2019) 006, [1905.00891].

[540] V. R. Shajiee and A. Tofighi, *Electroweak Phase Transition, Gravitational Waves and Dark Matter in Two Scalar Singlet Extension of The Standard Model*, *Eur. Phys. J. C* **79** (2019) 360, [1811.09807].

[541] A. Mohamadnejad, *Gravitational waves from scale-invariant vector dark matter model: Probing below the neutrino-floor*, *Eur. Phys. J. C* **80** (2020) 197, [1907.08899].

[542] A. Mazumdar and G. White, *Review of cosmic phase transitions: their significance and experimental signatures*, *Rept. Prog. Phys.* **82** (2019) 076901, [1811.01948].

[543] F. P. Huang and J.-H. Yu, *Exploring inert dark matter blind spots with gravitational wave signatures*, *Phys. Rev. D* **98** (2018) 095022, [1704.04201].

[544] V. A. Kuzmin, V. A. Rubakov and M. E. Shaposhnikov, *On the Anomalous Electroweak Baryon Number Nonconservation in the Early Universe*, *Phys. Lett. B* **155** (1985) 36.

[545] A. G. Cohen, D. B. Kaplan and A. E. Nelson, *Progress in electroweak baryogenesis*, *Ann. Rev. Nucl. Part. Sci.* **43** (1993) 27–70, [hep-ph/9302210].

[546] A. Riotto and M. Trodden, *Recent progress in baryogenesis*, *Ann. Rev. Nucl. Part. Sci.* **49** (1999) 35–75, [hep-ph/9901362].

[547] D. E. Morrissey and M. J. Ramsey-Musolf, *Electroweak baryogenesis*, *New J. Phys.* **14** (2012) 125003, [1206.2942].

[548] G. Gil, P. Chankowski and M. Krawczyk, *Inert Dark Matter and Strong Electroweak Phase Transition*, *Phys. Lett. B* **717** (2012) 396–402, [1207.0084].

[549] J. M. Cline and K. Kainulainen, *Improved Electroweak Phase Transition with Subdominant Inert Doublet Dark Matter*, *Phys. Rev. D* **87** (2013) 071701, [1302.2614].

[550] S. S. AbdusSalam and T. A. Chowdhury, *Scalar Representations in the Light of Electroweak Phase Transition and Cold Dark Matter Phenomenology*, *JCAP* **05** (2014) 026, [1310.8152].

[551] C. Cheung and Y. Zhang, *Electroweak Cogenesis*, *JHEP* **09** (2013) 002, [1306.4321].

[552] S. Inoue, G. Ovanesyan and M. J. Ramsey-Musolf, *Two-Step Electroweak Baryogenesis*, *Phys. Rev. D* **93** (2016) 015013, [1508.05404].

[553] H. H. Patel, M. J. Ramsey-Musolf and M. B. Wise, *Color Breaking in the Early Universe*, *Phys. Rev. D* **88** (2013) 015003, [1303.1140].

[554] M. Chala, G. Nardini and I. Sobolev, *Unified explanation for dark matter and electroweak baryogenesis with direct detection and gravitational wave signatures*, *Phys. Rev. D* **94** (2016) 055006, [1605.08663].

[555] S. J. Huber, T. Konstandin, G. Nardini and I. Rues, *Detectable Gravitational Waves from Very Strong Phase Transitions in the General NMSSM*, *JCAP* **03** (2016) 036, [1512.06357].

[556] D. Land and E. D. Carlson, *Two stage phase transition in two Higgs models*, *Phys. Lett. B* **292** (1992) 107–112, [hep-ph/9208227].

[557] W. Huang, Z. Kang, J. Shu, P. Wu and J. M. Yang, *New insights in the electroweak phase transition in the NMSSM*, *Phys. Rev. D* **91** (2015) 025006, [1405.1152].

[558] N. Blinov, J. Kozaczuk, D. E. Morrissey and C. Tamarit, *Electroweak Baryogenesis from Exotic Electroweak Symmetry Breaking*, *Phys. Rev. D* **92** (2015) 035012, [1504.05195].

[559] S. R. Coleman, *The Fate of the False Vacuum. 1. Semiclassical Theory*, *Phys. Rev. D* **15** (1977) 2929–2936.

[560] A. D. Linde, *Fate of the False Vacuum at Finite Temperature: Theory and Applications*, *Phys. Lett. B* **100** (1981) 37–40.

[561] A. Kosowsky, M. S. Turner and R. Watkins, *Gravitational radiation from colliding vacuum bubbles*, *Phys. Rev. D* **45** (1992) 4514–4535.

[562] A. Kosowsky and M. S. Turner, *Gravitational radiation from colliding vacuum bubbles: envelope approximation to many bubble collisions*, *Phys. Rev. D* **47** (1993) 4372–4391, [astro-ph/9211004].

[563] S. J. Huber and T. Konstandin, *Gravitational Wave Production by Collisions: More Bubbles*, *JCAP* **09** (2008) 022, [0806.1828].

[564] A. Kosowsky, M. S. Turner and R. Watkins, *Gravitational waves from first order cosmological phase transitions*, *Phys. Rev. Lett.* **69** (1992) 2026–2029.

[565] M. Kamionkowski, A. Kosowsky and M. S. Turner, *Gravitational radiation from first order phase transitions*, *Phys. Rev. D* **49** (1994) 2837–2851, [astro-ph/9310044].

[566] C. Caprini, R. Durrer and G. Servant, *Gravitational wave generation from bubble collisions in first-order phase transitions: An analytic approach*, *Phys. Rev. D* **77** (2008) 124015, [0711.2593].

[567] M. Hindmarsh, S. J. Huber, K. Rummukainen and D. J. Weir, *Gravitational waves from the sound of a first order phase transition*, *Phys. Rev. Lett.* **112** (2014) 041301, [1304.2433].

[568] J. T. Giblin, Jr. and J. B. Mertens, *Vacuum Bubbles in the Presence of a Relativistic Fluid*, *JHEP* **12** (2013) 042, [1310.2948].

[569] J. T. Giblin and J. B. Mertens, *Gravitional radiation from first-order phase transitions in the presence of a fluid*, *Phys. Rev. D* **90** (2014) 023532, [1405.4005].

[570] M. Hindmarsh, S. J. Huber, K. Rummukainen and D. J. Weir, *Numerical simulations of acoustically generated gravitational waves at a first order phase transition*, *Phys. Rev. D* **92** (2015) 123009, [1504.03291].

[571] C. Caprini and R. Durrer, *Gravitational waves from stochastic relativistic sources: Primordial turbulence and magnetic fields*, *Phys. Rev. D* **74** (2006) 063521, [astro-ph/0603476].

[572] T. Kahniashvili, A. Kosowsky, G. Gogoberidze and Y. Maravin, *Detectability of Gravitational Waves from Phase Transitions*, *Phys. Rev. D* **78** (2008) 043003, [0806.0293].

[573] T. Kahniashvili, L. Campanelli, G. Gogoberidze, Y. Maravin and B. Ratra, *Gravitational Radiation from Primordial Helical Inverse Cascade MHD Turbulence*, *Phys. Rev. D* **78** (2008) 123006, [0809.1899].

[574] T. Kahniashvili, L. Kisslinger and T. Stevens, *Gravitational Radiation Generated by Magnetic Fields in Cosmological Phase Transitions*, *Phys. Rev. D* **81** (2010) 023004, [0905.0643].

[575] A. Paul, B. Banerjee and D. Majumdar, *Gravitational wave signatures from an extended inert doublet dark matter model*, *JCAP* **10** (2019) 062, [1908.00829].

[576] B. Barman, A. Dutta Banik and A. Paul, *Singlet-doublet fermionic dark matter and gravitational waves in a two-Higgs-doublet extension of the Standard Model*, *Phys. Rev. D* **101** (2020) 055028, [1912.12899].

[577] C. Caprini, R. Durrer and G. Servant, *The stochastic gravitational wave background from turbulence and magnetic fields generated by a first-order phase transition*, *JCAP* **12** (2009) 024, [0909.0622].

[578] M. E. Shaposhnikov, *Possible Appearance of the Baryon Asymmetry of the Universe in an Electroweak Theory*, *JETP Lett.* **44** (1986) 465–468.

[579] M. E. Shaposhnikov, *Baryon Asymmetry of the Universe in Standard Electroweak Theory*, *Nucl. Phys. B* **287** (1987) 757–775.

[580] G. M. Harry, P. Fritschel, D. A. Shaddock, W. Folkner and E. S. Phinney, *Laser interferometry for the big bang observer*, *Class. Quant. Grav.* **23** (2006) 4887–4894.

[581] C. Caprini et al., *Science with the space-based interferometer eLISA. II: Gravitational waves from cosmological phase transitions*, *JCAP* **04** (2016) 001, [1512.06239].

[582] X. Gong et al., *Descope of the ALIA mission*, *J. Phys. Conf. Ser.* **610** (2015) 012011, [1410.7296].

[583] N. Seto, S. Kawamura and T. Nakamura, *Possibility of direct measurement of the acceleration of the universe using 0.1-Hz band laser interferometer gravitational wave antenna in space*, *Phys. Rev. Lett.* **87** (2001) 221103, [astro-ph/0108011].

[584] LIGO Scientific collaboration, G. M. Harry, *Advanced LIGO: The next generation of gravitational wave detectors*, *Class. Quant. Grav.* **27** (2010) 084006.

[585] C. L. Wainwright, *CosmoTransitions: Computing Cosmological Phase Transition Temperatures and Bubble Profiles with Multiple Fields*, *Comput. Phys. Commun.* **183** (2012) 2006–2013, [1109.4189].

[586] P. Basler, M. Krause, M. Muhlleitner, J. Wittbrodt and A. Wlotzka, *Strong First Order Electroweak Phase Transition in the CP-Conserving 2HDM Revisited*, *JHEP* **02** (2017) 121, [1612.04086].

[587] P. B. Arnold and O. Espinosa, *The Effective potential and first order phase transitions: Beyond leading-order*, *Phys. Rev. D* **47** (1993) 3546, [hep-ph/9212235].

[588] A. D. Linde, *Decay of the False Vacuum at Finite Temperature*, *Nucl. Phys. B* **216** (1983) 421.

[589] R. Jinno and M. Takimoto, *Gravitational waves from bubble collisions: An analytic derivation*, *Phys. Rev. D* **95** (2017) 024009, [1605.01403].

[590] R. Jinno and M. Takimoto, *Gravitational waves from bubble dynamics: Beyond the Envelope*, *JCAP* **01** (2019) 060, [1707.03111].

[591] P. J. Steinhardt, *Relativistic Detonation Waves and Bubble Growth in False Vacuum Decay*, *Phys. Rev. D* **25** (1982) 2074.

[592] E. Madge and P. Schwaller, *Leptophilic dark matter from gauged lepton number: Phenomenology and gravitational wave signatures*, *JHEP* **02** (2019) 048, [1809.09110].

[593] M. Chala, V. V. Khoze, M. Spannowsky and P. Waite, *Mapping the shape of the scalar potential with gravitational waves*, *Int. J. Mod. Phys. A* **34** (2019) 1950223, [1905.00911].

[594] J. Ellis, M. Lewicki and J. M. No, *On the Maximal Strength of a First-Order Electroweak Phase Transition and its Gravitational Wave Signal*, *JCAP* **04** (2019) 003, [1809.08242].

[595] J. Ellis, M. Lewicki, J. M. No and V. Vaskonen, *Gravitational wave energy budget in strongly supercooled phase transitions*, *JCAP* **06** (2019) 024, [1903.09642].

[596] E. Thrane and J. D. Romano, *Sensitivity curves for searches for gravitational-wave backgrounds*, *Phys. Rev. D* **88** (2013) 124032, [1310.5300].

[597] C. J. Moore, R. H. Cole and C. P. L. Berry, *Gravitational-wave sensitivity curves*, *Class. Quant. Grav.* **32** (2015) 015014, [1408.0740].

[598] T. Alanne, T. Hugle, M. Platscher and K. Schmitz, *A fresh look at the gravitational-wave signal from cosmological phase transitions*, *JHEP* **03** (2020) 004, [1909.11356].

[599] K. Schmitz, *New Sensitivity Curves for Gravitational-Wave Signals from Cosmological Phase Transitions*, *JHEP* **01** (2021) 097, [2002.04615].

[600] A. Goudelis, K. A. Mohan and D. Sengupta, *Clockworking FIMPs*, *JHEP* **10** (2018) 014, [1807.06642].

Thesis Highlight

Name of the Student: Madhurima Pandey

Name of the CI/OCC: Saha Institute of Nuclear Physics, Kolkata

Enrolment No.: PHYS05201504019

Thesis Title: ASTROPARTICLE PHYSICS WITH PARTICLE DARK MATTER MODELS, NEUTRINOS AND GRAVITATIONAL WAVES FROM FIRST ORDER ELECTROWEAK PHASE TRANSITION

Discipline: Physical Sciences

Sub-Area of Discipline: Astroparticle Physics and Cosmology

Date of viva voce: 26th June, 2021

The thesis pursues three major topics of astroparticle physics namely particle dark matter (DM) phenomenology, neutrino oscillations and primordial Gravitational Waves (GWs) in the early Universe. Although the properties of the fundamental building blocks of the elementary particles as well as their fundamental interactions (not including gravity) can be immensely described by the Standard Model (SM) of particle physics but it fails to address sine phenomena like explaining the neutrino mass, the particle nature of DM and other issues such as triviality, naturalness problem etc. It is unknown to us whether the DM is constituted by single particle component or multi type of particles. In addition, the sources of the ultrahigh energy (UHE) neutrinos observed by Km^2 IceCube detector still remains a mystery. Apart from these above mentioned phenomena, it is believed that even though the electroweak phase transition is a smooth crossover within the SM framework, but it can be of first order phase transition if simple extensions of SM is considered by adding some scalars which could be well a candidate of DM. The highlights of thesis dealing with these issues are following. The thesis explores two component Weakly Interacting Massive Particle (WIMP) – Feebly Interacting Massive Particle (FIMP) DM model by extending the SM with a fermion and a scalar. Th observed gamma-ray (γ-ray) excess from the Galactic Centre (GC), DM self interaction from 72 colliding galaxy clusters as well as the 3.55 keV X-ray line etc. can be simultaneously explained in the present model. Also in order to explain DM self interaction a two component FIMP (both are scalars) DM model is proposed in the thesis. A detailed analysis of the γ-ray fluxes from 45 dwarf galaxies produced from possible DM annihilation have been done in the thesis with two different particle DM models, one is WIMP-FimP model and the other one is Kaluza-Klein (KK) DM in theories of extra dimensions. The possible cascading decay of superheavy dark matter (SHDM) into UHE neutrinos (PeV energy range) in the context of UHE neutrino spectrum at IceCube is also addressed in the thesis, where some constraints on SHDM mass and its decay lifetime have been given. The possible existence of the sterile neutrino as well as the effect of the neutrinos decaying unparticles on the detection yield at IceCube in 4-flavour (3 active + 1 sterile) neutrino framework are also investigated in the thesis. In addition a proton blazar model is proposed in the thesis which can consistently explain the observed electromagnetic spectrum in combination with the neutrino events observed by the IceCube detector from the three blazars namely TXS 0506+056, PKS 0502+049 and GB6 J1040+0617. The thesis also probes the effects of violation of equivalence principle (VEP), if it has existence in nature, for the case of long baseline (LBL) neutrinos in 4-flavour scenario. Lastly the thesis deals with the GW emissions from a strong fist order electroweak phase transition by simple extensions of SM with scalars, which are produced via freeze-in mechanism. This transition may happen from a metastable minimum to the true minimum through electroweak bubble nucleation. The detectabilities of such GWs at the future space based detectors have also been investigated in the thesis.